

PROCEEDINGS

The First International Conference on DAMAGE MECHANICS ICDM 1

Editors

Chi L. Chow
J. Woody Ju
Dragoslav M. Šumarac

BELGRADE
JUNE 25-27, 2012.

The First International Conference on Damage Mechanics, ICDM 1, Belgrade, June 25-27, 2012

Editors

Chi L. Chow
J. Woody Ju
Dragoslav M. Šumarac

Computer editing

Miša Angeleski
Nenad Pantić

Press

“BeoTeleProm”, Belgrade

Circulation

150 copies

Published by

Serbian Chamber of Engineers, Belgrade

Faculty of Civil Engineering, Belgrade

Belgrade 25 - 27 June 2012

Preface

The First International Conference on Damage Mechanics (ICDM 1, 2012), Belgrade June 25-27th is the first in a new conference series whose main objective is to bring together leading educators, researchers and practitioners discussing and exchanging ideas on recent advances in damage and fracture mechanics. Since 1958, following the pioneering work of L. M. Kachanov, the theory of damage mechanics has in particular made significant progress and established itself capable of solving a wide range of engineering problems. This inaugural conference will provide a forum for scientists and practicing engineers alike to present the latest findings in their research endeavor and at the same time to explore future research directions in the fields of damage and fracture mechanics. The inauguration of the ICDM 1, 2012 is also considered timely as it coincides with the 20th anniversary of the founding of the *International Journal of Damage Mechanics*.

The ICDM 1, 2012 covers theoretical and experimental investigations from specific topics: Multiscale damage and fracture characterizations, Nano-micro damage mechanics and fracture in composites and bio-materials, Continuum damage mechanics, Computational damage mechanics and fracture, Experimental characterization and validation of damage and failure mechanisms, Diagnosis or quantification of material damage and failure, Dynamic damage, fracture and failure, Applications to metal forming and in-service structural integrity, Applications to concrete, cementations composites, and geomaterials, Applications to nano-materials and bio-materials, Applications to aging infrastructures and structures.

Many individuals have been involved in the production of these Proceedings, which started in the middle of 2010 launching of a Call for Papers. First Abstract was received by October 1st 2011 and reviewed by an external referee process over the next few months. Those selected by the International Scientific Committee were invited for Full paper (four pages) submission. The committee is gratifying to note that the papers received cover a variety of different topics and come from all around the world, including both developed and developing countries.

This Proceedings is organized such that Plenary lectures of Professors Chi L. Chow, George Z. Voyiadjis, J. Woody Ju and Khemais Saanouni are at the beginning, followed by the papers of Minisymposium: Damage Mechanics in Metal forming: Theory, Numerics and Application, organized by Professor Khemais Saanouni. Finally all papers are included in alphabetical order according to first authors' name.

We have enjoyed working with our friends in the International Scientific committee, to whom we are most grateful to their dedication, expertise, and professionalism and with the authors of the papers themselves. This Proceedings represents 30 countries from all parts of the world and from diversified academic backgrounds and interests who have worked together because of a shared interest in damage mechanics research and education.

It was our privilege but a challenging task, editing the Proceedings of the ICDM 1, 2012.

Conference Chairmen

Chi L. Chow - University of Michigan, Dearborn, USA

J. Woody Ju - University of California at Los Angeles, USA

Dragoslav M. Šumarac – Faculty of Civil Engineering, University of Belgrade, SERBIA

International Scientific Committee

J. L. Chaboche (France)

Olivier Allix (France)

Elias C. Aifantis (Greece)

Yilong Bai (China)

Michal Basista (Poland)

Zdenek P. Bazant (USA)

Josef Betten (Germany)

Wolfgang Brocks (Germany)

Michael Brunig (Germany)

Diego Celentano (Chile)

E. P. Chen (USA)

L. R. Dharani (USA)

Andre Dragon (France)

Emmanuel E. Gdoutos (Greece)

Jovo Jaric (Serbia)

Iwona Jasiuk (USA)

Kikuo Kishimoto (Japan)

Djimedo Kondo (France)

Shiro Kubo (Japan)

Pierre Ladeveze (France)

Jean Lemaitre (France)

Xikui Li (China)

Jianguo Lin (UK)

Y. W. Mai (Australia)

D. L. McDowell (USA)

Sinisa Mesarovic (USA)

Milan Mićunović (Serbia)

Martin Ostoja-Starzewski(USA)

Jwo Pan (USA)

Ekkehard Ramm (Germany)

Khemais Saanouni (France)

Bernhard Schrefler (Italy)

Raju Sethuraman (India)

Lizhi Sun (USA)

R. Talreja (USA)

T. E. Tay (Singapore)

Yutaka Toi (Japan)

Viggo Tvergaard (Denmark)

George Z. Voyiadjis, (USA)

Shou Wen Yu (China)

Soo Woo Nam (Korea)

Peter Wriggers (Germany)

Local Organizing Committee

Dragoslav Šumarac (Chair)

Dragoslav Kuzmanović

Nataša Trišović

Maja Todorović

Sreten Mastilović

Conference Secretariat

Miša Angeleski

Branko Marković

Lela Todorović-Padežanin

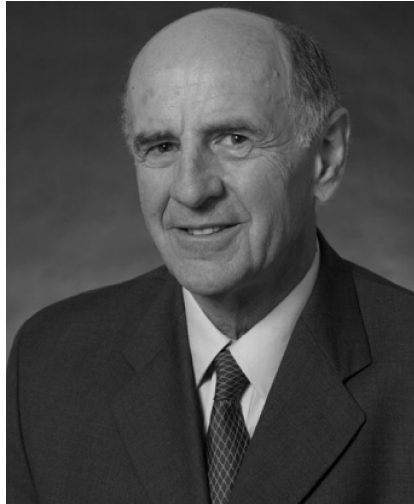
Olga Damnjanović

Tribute to

Dusan Krajcinovic

Professor dr Dusan Krajcinovic was born on March 28, 1935 in Zagreb, Kingdom of Yugoslavia; he passed away on August 10, 2007 in Madison, Wisconsin, USA.

Dusan Krajcinovic enrolled at Faculty of Civil Engineering, University of Belgrade in 1953, and received his Bachelor degree in 1958. He entered a Master degree program in Structural Mechanics in 1964 and completed it in 1966 with the averaged grade of 9.9 out of 10, as the first student in a highly competitive class. Afterwards, he moved with his family to USA following an invitation of Professor George Herrmann; entered Northwestern University, Evanston, Illinois; and earned his PhD in 1968.



Professor Krajcinovic started his career of a professional civil engineer in 1959 as a member of technical staff in Energoprojekt, Belgrade, Yugoslavia. He contributed to some major civil engineering projects such as Bajina Basta Dam (a 92-m high segmented hollow concrete dam); Otovica Dam (a 30-m high concrete arch dam); Glazanj Dam (a 90-m high concrete arch dam); two railroad bridges in Ljubljana; Orasje Bridge (an 800-m long continuous road bridge); Hotel-Apartment Tower in Belgrade. After earning his PhD in USA, he continued his career in Ingersoll Rand Research Inc., Princeton, New Jersey. From 1969 to 1973 he was at Argonne National Laboratory, Illinois in the Theoretical and Applied Mechanics Group.

Dusan Krajcinovic's academic development started 1961-66 at his alma mater, the Faculty of Civil Engineering, University of Belgrade. As an accomplished professional engineer and researcher he re-entered academia in 1973, when he became a faculty member at Department of Civil Engineering, University of Illinois, Chicago. From 1989 until retirement he was a Professor in Department of Mechanical and Aerospace Engineering, Arizona State University, Tempe, Arizona, where he was elected a Professor Emeritus in 2004.

Professor Krajcinovic's research had a profound impact on the development of damage and fracture mechanics, micromechanics, and physics of disordered materials. He had been an influential contributor and respected authority in the research community for over three decades. Professor Krajcinovic authored and co-authored over 250 publications, including refereed journals, proceedings, monograph chapters, books. The landmark of his scientific merit, "Damage Mechanics" (North-Holland, 1996), stands among mechanics of materials classics.

During his brilliant career his consulting services were solicited by prestigious names such as Argonne National Laboratory; US Department of Interior; US Department of Energy; Procedyne Corporation; Electric Power Research Institute; Conselho de Gestao, Gabinete da Area de Sines, Lisbon, Portugal; Power Project Ltd; Sargent and Lundy Engineers; The World Bank; Lufthansa; Enrico Fermi National Accelerator Laboratory; University of Michigan, Ann

Arbor; Wiss, Janney, Elstner Associates; Allied Signal; Sandia National Laboratories; Arizona Power Service.

Professor Krajcinovic was continuously involved with professional societies such as ASME (fellow and President of AMD Executive Committee 1996-2001, Chair 2001-2002); American Academy of Mechanics (fellow and President 1999-2001); US National Committee of Theoretical and Applied Mechanics (2002-2005). At various times he also participated in activities of Stability Research Council, International Association for Structural Engineering in Reactor Technology, ASCE (non-member advisor of the Committee for Inelastic Behavior of Materials), and Engineering Academy of Yugoslavia. He was an organizer of and a principal lecturer at courses at CISM – International Centre for Mechanical Sciences in Udine in 1985 and 1999; and Visiting Professor at Universite de Paris VI, University of Belgrade, Politecnico di Milano, Institute for Theoretical Physics, and University of California, Santa Barbara. He was a member of editorial boards of highly regarded scientific journals such as International Journal of Damage Mechanics (one of four founding editors with C.L.Chow, J.L. Chaboche and S. Murakami in 1992), Applied Mechanics Reviews (Associate Editor, 1988-1994), Mechanics of Materials (Regional Editor, since 2000), and International Journal of Non-Linear Mechanics (Advisory Editor, 2000-2006). Professor Krajcinovic was an invited and a main contributor to numerous workshops, scientific meetings, symposia, and conferences. His contributions to the education of almost two generations of professional engineers and researchers cannot be overemphasized. He mentored a dozen PhD dissertations that span a period of almost 30 years. Professor Krajcinovic was a very demanding mentor but also an inspiring and respected one.

Professor Krajcinovic's outstanding achievements gain admiration of his peers and resulted in a number of awards and distinctions including October Prize for Mathematical, Physical, and Engineering Sciences (with D. Sumarac; Belgrade, Yugoslavia, 1990); Gold Medal in Science and Technology (Technical University of Crete, Greece, 2001); Laurea Honoris Causa (Politecnico di Milano, Italy, 2001). His impressive record of academic achievements was honored by his colleagues in a specially dedicated volume of International Journal of Plasticity (Volume 23, Issues 10-11, 2007), a memorial issue of International Journal of Damage Mechanics (Volume 18, Issue 2, 2009), and a memorial issue of Theoretical and Applied Mechanics (Serbian; Volume 35, Issues 1-3, 2008).

This biographical sketch unavoidably resembles many others written in memory of Professor Krajcinovic. Admittedly, it falls very short in illuminating his unique personality and versatility. Many of us who were privileged to work with him would remember him in much more profound way. We may cherish a memory of not only a self-made man of fruitful life and exceptional accomplishments but also a lifelong athlete, avid reader, opera fan, witty conversationalist; an open-minded man of the Renaissance curiosity. He had an urge and gift for camaraderie. He was a riveting storyteller and his memories, which swept amazingly over wide range of temporal and social strata, provided a remarkable building material. His home was a memorable meeting place of colleagues, friends, and generations of students, who will remember his trademark smiles, hearty laughs, and passionate arguments as well as a genuine hospitality.

He was a loving and tender husband to Tanya and father to Ivana and Maya.

D. Šumarac

M. Basista

S. Mastilović

20th ANNIVERSARY OF THE INTERNATIONAL JOURNAL OF DAMAGE
MECHANICS – PAGE 1

20th ANNIVERSARY OF THE INTERNATIONAL JOURNAL OF DAMAGE
MECHANICS – PAGE 2

Contents

Preface	iii
Bridging Damage Mechanics and Digital Sensing Technique <i>C. L. Chow and J. Shen</i>	1
Coupled Viscoplastic Damage Model and Simulation for Metals and Composites <i>G. Z. Voyiadjis and D. Faghihi</i>	7
Size-Dependent Probabilistic Damage Micromechanics and Toughening Behavior of Particle/Fiber Reinforced Composites <i>J. W. Ju and K. Yanase</i>	13
Damage Mechanics in Metal Forming: Advanced Modeling, Numerics and Application <i>K. Saanouni</i>	19
Modelling and Numerical Simulation of Thick Sheets Slitting Using Continuum Damage Mechanics <i>Y. Ghozzi, C. Labergere and K. Saanouni</i>	25
Micromorphic Approach for Nonlocal Fully Coupled Elastoplastic-Damage Constitutive Equations <i>M. Hamed and K. Saanouni</i>	29
Micromechanical Modeling of a Duplex Stainless Steel – Comparison with Mesoscopic Measurement by Neutron Diffraction Leading to an Observation of Damage <i>L. Le Joncour, B. Panicaud, A. Baczmanski and M. François</i>	33
On Anisotropic Damage Coupled with Elastoplasticity at Finite Strain <i>T. D. Nguyen, H. Badreddine and K. Saanouni</i>	37
Anisotropic Ductile Damage Fully Coupled with Anisotropic Large Strain Plasticity for Metal Forming <i>W. Rajhi, K. Saanouni and H. Sidhom</i>	41
Failure Prediction and Validation of a Steel Automotive Safety Part <i>M. Achouri, G. Germain, P. Dal Santo and D. Saidane</i>	45
Modeling Creep Damage of an Aluminium-Silicon Eutectic Alloy <i>H. Altenbach, S. Kozhar, K. Naumenko, M. V. Cid Alfaro and C. H. L.j. ten Horn</i>	49
Assessment and Comparison of Non-Local Models for Ductile Damage <i>F. X. C. Andrade, J. M. A. Cesar de Sa and F. M. Andrade Pires</i>	53
Influence of Plasticity Reduction on Strength and Fracture of Turbine Runner Cover in Hydro Power Plant Đerdap 1 <i>M. Arsić, S. Bošnjak, Z. Odanović, V. Grabulov and B. Vistić</i>	57

Energy Release Rates at Interfacial Cracks in Residually Stressed Aluminum Based Fibre Metal Laminate (Glare): A Numerical Assessment <i>S. Bhat and R. Patibandla</i>	61
Damage and Rupture of Structural Materials under Complex Low Cycle Loading <i>M. Bobyr, O. Khalimon and V. Koval</i>	65
Creep Damage Processes in Cyclically Loaded Structural Members <i>D. Breslavsky and O. Morachkovsky</i>	69
Numerical Modeling of Localized Failure by Means of Strong Discontinuities at Finite Strain <i>O. T. Bruhns, R. Radulovic and J. Mosler</i>	73
Studies on the Effect of the Stress Triaxiality and the Lode Parameter on Ductile Damage Conditions <i>M. Brünig, S. Gerke and V. Hagenbrock</i>	77
Buckling of Imperfect CDM Structural Systems <i>N. Challamel and J. Helleland</i>	81
Study of the Blast-Resistant Response of a Reinforced Polymer Composite-Glass Laminate <i>Z. Chen, L. Shen, S. K. Khanna and H. Zhu</i>	85
Structural Health Monitoring with Advanced Nondestructive Methods Based on Wavelet Analysis <i>R. Cvelbar, M. Suban, B. Bundara, M. P. Lazarević and V. Vasić</i>	89
Microstructural Effects on the Mechanical Properties and Tribological Damage of Ti-6Al-4V Alloy <i>I. Cvijović-Alagić, M. Rakin, Z. Cvijović, N. Gubeljak and K. Gerić</i>	93
Transition From a Gradient Damage Model to a Cohesive Zone Model within the Framework of Quasi-Brittle Failure <i>S. Cuvilliez, F. Feyel, E. Lorentz and S. Michel-Ponnelle</i>	97
Modeling Progressive Damage in Electronic Systems <i>A. Dasgupta</i>	101
Behavior of an Interfacial Crack Between the Two Layers in the Stationary Temperature Field Conditions <i>J. M. Djoković and R. R. Nikolić</i>	105
Numerical Simulation of Damage in the Thin Plates <i>C. Dolicanin, K. Maksimovic, V. Nikolic-Stanojevic and M. Maksimovic</i>	109
A Multiscale Approach for Modelling Non-Linear Behaviour and Damage of Highly-Filled Particulate Composites <i>A. Dragon, C. Nadot-Martin, D. Halm, S. Dartois and M. Trombini</i>	113
Crack Initiation and Propagation in Nonlocal Ductile Media <i>S. Feld-Payet, J. Besson, F. Feyel and V. Chiaruttini</i>	117

Modeling of Corrosion Distribution for Self-Healing Nanomaterials <i>N. Filipovic, A. Jovanovic, D. Petrovic, M. Obradovic, M. Radovic, S. Jovanovic, D. Balos and M. Kojic</i>	121
Image-Based MPM Simulation of the Human Hip Structural Failure under Impact <i>Y. Gan, Z. Chen, Y. Shen, A. Horner, Y. Duan, C. Ward and J. Parker</i>	125
Material Damage Studied by the Strain Energy Density Theory <i>E. E. Gdoutos</i>	129
Evaluation of Cumulative Damage of RC Structures under Multiple Earthquakes <i>G. Hatzigeorgiou and A. Liolios</i>	133
Fe-Analysis of Damage in Steel Structures under Dynamic Loading <i>S. Heinrich, U. Kowalsky, J. Meyer and D. Dinkler</i>	137
Models of Dynamical Dislocation in Continuum <i>K. R. Hedrih Stevanović</i>	141
Avalanches in the Fracture Process Zone <i>P. C. Houlis and A. V. Dyskin</i>	145
Emi Shielding Simulation of CNT-Epoxy Film Coated Mortar Panels <i>Y. Y. Hwang, B. J. Yang and H. K. Lee</i>	149
On Anisotropic Elasticity Damage Mechanics <i>J. Jarić, D. Kuzmanović and D. Šumarac</i>	153
Predicting the Lifetime of Filled Elastomers under Inhomogeneous Loading Conditions <i>D. Juhre and T. Alshuth</i>	157
A Finite Element Calculation of Stress Intensity Factors in Structures with Multi- Site Damage (MSD) <i>G. Kastratović, A. Grbović and N. Vidanović</i>	161
Debonding in Beam-Reinforced Plates <i>J. T. Katsikadelis and N. G. Babouskos</i>	165
Application of Conservation Laws to Defect and Damage Mechanics <i>R. Kienzler</i>	169
High-Temperature Material Characteristics Analysis of Offshore Structural Steels Considering Damage Mechanics <i>S. J. Kim, Y. H. Choi, M. H. Kim and J. M. Lee</i>	173
Simulation of Anisotropic Damage in Quasifragile Materials Using the Truss-Like 3D Discrete Element Method <i>L. Kostaski, I. Iturrioz and J. D. Riera</i>	177

Analysis of Crack Displacements on Residential Structure Induced by Blasting and Earthquake Vibrations and Daily Changes of Temperature and Relative Humidity <i>L. Kričak, M. Negovanović, I. Janković, D. Zeković and S. Mitrović</i>	181
On the Creep-Fatigue Lifetime of Turbine Housings Affected by Application-Specific Load Conditions <i>F. Laengler, T. Mao and A. Scholz</i>	185
Effect of Anisotropic Characteristics on Failure of Reinforced Polyurethane Foam <i>C. S. Lee, C. H. Lee and J. M. Lee</i>	189
Stochastic Damage Mechanics of Concrete: A Review of Recent Progresses <i>J. Li and X. D. Ren</i>	193
Micromechanically Informed Macro-Damage Characterization of Granular Materials <i>X. Li and Y. Du</i>	197
Fiber Beam-Column Element for the Seismic Damage Analysis of RC Frames <i>Z. Li and G. Hatzigeorgiou</i>	201
Dynamic Soil - Pipeline Interaction under Environmental Damage Effects: A Linear Complementarity Numerical Approach <i>A. Liolios, G. Hatzigeorgiou and K. Liolios</i>	205
Numerical and Experimental Modelling Cortical Bone Tissue Deformation Processes <i>M. Lovrenić-Jugović, Z. Tonković, A. Bakić and D. Pustačić</i>	209
Computation Methods and Software in Fatigue Life Estimations of Structural Components under General Load Spectrum <i>S. Maksimović, I. Vasovic, M. Maksimovic and M. Djuric</i>	213
Damage and Recovery of ARS 1400 Conveyer's Lower Construction Support in a Surface Mine <i>T. Maneski, N. Trišović and D. Ignjatović</i>	217
Damage Phenomenology in Dynamically Loaded Brittle Lattices <i>S. Mastilovic</i>	221
Plasticity of Crystals and Interfaces: From Dislocation Mechanics to Size-Dependent Continuum <i>S. Dj. Mesarovic and R. Baskaran</i>	225
Thermal Ratchetting: Tensor Representation vs Classical Approach <i>M. Mićunović, L. Kudrjavceva and A. Sedmak</i>	229
Dynamic Failure of Inelastic Rods <i>D. D. Milašinović</i>	233
Microstructural Effects on Fatigue Crack Behavior of a Pressure Vessel Welded Joint Made of HSLA Steel <i>Lj. Milović, M. Manjgo, I. Blačić, T. Vuherer, K. Maksimović and M. Burzić</i>	237

Application of the Theory of Critical Distances on Failure Analysis - A Case Study <i>D. Momčilović, R. Mitrović and I. Atanasovska</i>	241
Experimental Assessment of Damage Mechanisms in Both One-Piece and Welded Aluminum Foam Sandwich Beams <i>M. Moncada, F. Cognini, U. De Angelis, D. Ferrara, G. De Santis, L. Pilloni, G. Barbieri and A. Rinaldi</i>	245
Effect of Micro-Alloying on Microstructure and Cyclic Mechanical Durability Response of Sn1.0Ag0.5Cu Joint-scale Solder Specimens <i>S. Mukherjee and A. Dasgupta</i>	249
Development of Hybrid Layered Structures Consisting of Silicone and Metal and Their Static Tensile Behavior <i>N. Nestic, R. Uhlig, U. Risto and L. Zentner</i>	253
Fracture Phenomena – Combined DM & FM Approach – A Tribute to Professors J. Janson and J. Hult <i>M. Pavisic</i>	257
Experimental Analysis of Low Cycle Fatigue of DC 90 Dampers <i>Z. Petrašković and D. Šumarac</i>	261
A Two-Dimensional Shell Element for Coupled Visco-Hyperelastic and Damage Behavior of Polymeric Fabrics <i>G. P. Potirniche, D. Stillman and T. L. Lin</i>	265
Models & Robust Algorithms in Crash Simulations <i>R. Prohl, A. Grillo and G. Wittum</i>	269
Modelling of Overall Material Properties and Crack Reinforcement by Bridging Fibres in Metalc ceramic Composites with Interpenetrating Phase Microstructure <i>Z. Ponižnik and M. Basista</i>	273
Multiscale Modeling of Collective Behavior of Carbon Nanotubes <i>H. Radhakrishnan, S. Dj. Mesarovic, A. Qiu and D. F. Bahr</i>	277
Damage and Failure Assessment of Pipes with Local Thin Areas <i>M. Rakin, B. Medjo, M. Arsić, Ž. Šarkočević, V. Grabulov and A. Sedmak</i>	281
Use of Global Minimum Optimization in Identifying Damage Micromechanical Model Parameters with a Damage Deactivation Phenomenon <i>D. Razafindramary and A. Abdul-Latif</i>	285
Anisotropic Plastic Deformation and Damage in Commercial Al 2198 T8 Sheet Metal <i>D. Steglich, H. Wafai and J. Besson</i>	289
Damage Prediction of a Graded Porous Biocomposite Implant Using the Finite Element Method <i>C. P. Tsui, C. Y. Tang, H. Y. Wang and L. C. Chan</i>	293
Modelling Damage and Failure in High Velocity Impact on CFRP <i>R. Vignjevic, N. Djordjevic and J. Campbell</i>	297

Stability of Quasi-Static Fractal Cracks at Meso and Nano Scale Levels <i>M. P. Wnuk</i>	301
Modelling of Compressive Failure in Z-Pinned Composite Laminates <i>S. Xie and J. Zhang</i>	305
Quasi-Static Test Till Failure of the Connection of Reinforced Pan Slab with Floor Support Joists <i>S. Zdravković, T. Igić, D. Zlatkov and D. Turnić</i>	309
Index of Contributors	11

PLENARY LECTURE

**BRIDGING DAMAGE MECHANICS AND DIGITAL SENSING
TECHNIQUE****Chi L. Chow, Jie Shen**

¹Department of Mechanical Engineering
The University of Michigan, Dearborn, Michigan, U.S.A.
e-mail: clchow@umich.edu

²Department of Computer and Information Science,
The University of Michigan, Dearborn, Michigan, U.S.A.
e-mail: shen@umich.edu

Abstract. This paper presents a method of bridging damage mechanics and digital sensing technique to investigate the damage mechanism of engineering materials. Nondestructive X-ray computed tomography is our focus on the digital sensing.

1. Introduction

Damage mechanics provides a mechanics-based analysis to characterize the material damage via a set of state variables. The change in these state variables based on the irreversible thermodynamics reflects the material degradation via its constitutive modeling. An evolution equation is developed and used to describe a complete process from damage initiation to material failure. Continuum damage mechanics [1-4] presents an effective way to characterize an average measure of material damage. Micromechanical damage mechanics emphasizes the relation between the macroscopic state of material damage and the irreversible change of microstructures [5-15]. How to represent a huge number of arbitrarily-shaped three-dimensional material defects is, however, still not well solved. Recently, some researchers have revived interests in discrete lattice models for linking the simulation results at molecular scale with macroscopic material damage directly [16-18]. Although scaling relations are valid for both hardening and softening phases, an open issue is how all the micro/macro-scale material defects could be incorporated into such a framework.

Dynamic spatial distribution and evolution of voids/cracks in engineering materials are crucial information for both engineers and scientists to understand damage¹ and failure² mechanisms under varying loading conditions. Unfortunately, there are very few published experimental data with respect to the spatial distribution and evolution of multiple three-

¹ Damage is defined as physical deterioration in mechanical properties of engineering materials due to micro/mesoscale crack initiation and evolution to the formation of macrocrack.

² Failure refers to a critical state in which engineering material specimens completely lose their mechanical functionality in brittle fracture or reach their maximum mechanical resistance capacity in ductile fracture.

dimensional (3D) voids/cracks throughout a complete loading process from damage initiation to final rupture. Although *electron microscopy* has been used to achieve a nanometer level resolution, only surface microstructures can be observed unless tedious and destructive dissection of samples is involved. The dissection is not only prohibitively labor-intensive and costly, but also destructive to some micro/mesoscale 3D voids/cracks. *Optical microscope* shares the same drawbacks as above with relatively lower resolutions and restricted depths of field. Computer tomography on the basis of *microfocus X-ray microscope*, has been recently extended from medical field to material research [19], providing an affordable opportunity to nondestructively investigate the dynamic propagation of 3D voids/cracks in complete loading processes.

Rapid advance in digital sensing field provides us with a new way to evaluate material damage, and an emerging opportunity to bridge damage mechanics and digital sensing technique. Figure 1 demonstrates a distribution of material defects in an aluminum alloy. A multiresolution processing of this defect distribution will provide us with a rich set of information about material damage and degradation process. In the following three sections, we will summarize recent advances at the University of Michigan in an effort of applying the digital sensing technology in the study of material damage.

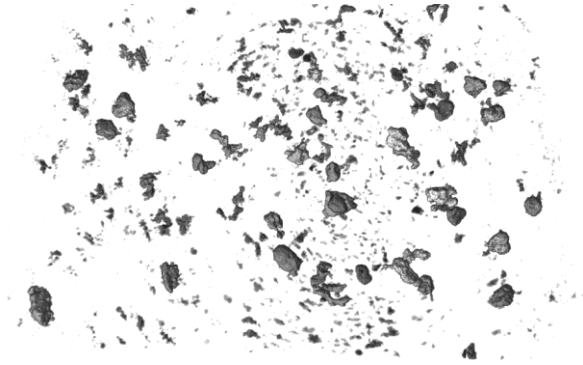


Figure 1: Three-dimensional distribution of material defects in a light-weight aluminum alloy (Grey color represents defects and white color refers to material.)

2. Multiresolution Transformation Rule of Material Damage

As illustrated in Figure 1, a large countless quantity of defects with different sizes and shapes are observed in a material domain. This poses a serious challenge to the finite element simulation of material degradation even if high-performance computing is utilized. To circumvent this problem, we have developed a multiresolution transformation rule to characterize the material damage. Its basic premise is that we first categorize all the material defects into n levels ($n \geq 1$) on the basis of their characteristic sizes. For instance, Level 1 refers to a group of all the smallest defects less than a certain characteristic size. Level 2 contains a group of defects larger than that of level 1 but less than a specified characteristic size. This multiresolution analysis continues progressively up to m -level of the entire population of material defects. The proposed multiresolution transformation is carried out from level 1 sequentially up to level m such that the impact of all defects in a

material element is reflected via a set of the material damage variables in the constitutive model.

For the sake of illustration, a simplified example shown in Figure 2(A) is conducted for the damage transformation of material defects consisting of only two levels of fine and coarse defects [20]. Based on the sequentially transformation analysis, we initially calculate the effects of all the fine defects of material damage on the original Young's modulus, E_0 . The resulting effective modulus known as E_1 reflects only the first level of the fine defects. The influence of all the coarse defects is then determined on the degraded material with a modified effective modulus, E_1 . The effect of coarse defects leads to a new secant modulus, E_2 , as a final material degradation consisting of those two levels of defects. Alternatively, both levels of defects could be considered simultaneously, leading to another effective modulus, E_3 , which is degraded from E_0 . The closeness between E_2 and E_3 in Figure 2(B) demonstrates feasibility of analyzing material degradation based on the proposed multiresolution algorithm. For better accuracy, the same transformation analysis can be readily extended to several levels of defects described in the previous section.

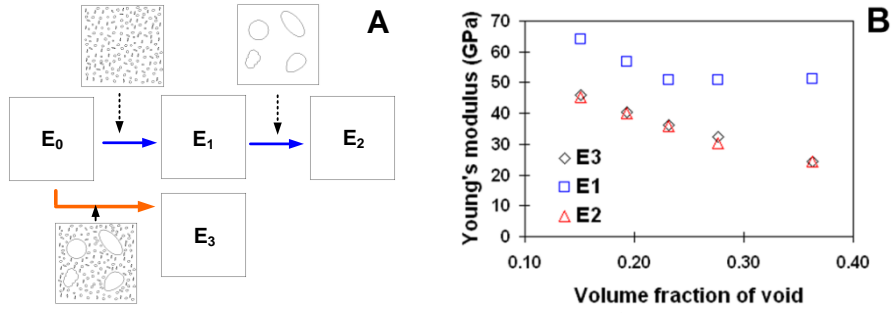


Figure 2: Transformation of Material Defects. (A) A simple case with two levels of defects. (blue and orange colors represent two different routes in the transformation of material defects.) (B) Numerical equivalence of E_2 and E_3 in finite element analysis [20].

In our previous study [20], a theoretical derivation was conducted to establish a transformation rule of material damage contributed by defects at $i+1$ and $i+2$ levels. For instance, a two-level damage transformation is formulated as:

$$\mathbf{C}_{i+2}^{-1} = \mathbf{M}(d\mathbf{D}_{i+2})^T : \mathbf{M}(d\mathbf{D}_{i+1})^T : \mathbf{C}_i^{-1} : \mathbf{M}(d\mathbf{D}_{i+1}) : \mathbf{M}(d\mathbf{D}_{i+2}) + \hat{\mathbf{C}}_{i+2}^{cor}, \quad (1)$$

where \mathbf{D} and \mathbf{M} are a damage tensor and a damage effect tensor ($\tilde{\sigma}_{\mathbf{D}} = \mathbf{M}(d\mathbf{D}) : \sigma_{\mathbf{D}+d\mathbf{D}}$), respectively. The $:$ operator denotes a tensor product contracted over two indices. σ and $\tilde{\sigma}$ are Cauchy stress and effective stress tensors due to damage, respectively. \mathbf{C}_i^{-1} refers to the inverse of a stiffness tensor at level i . $\hat{\mathbf{C}}_{i+2}^{cor}$ is a correction term, which should be used

when the damage increment in $d\mathbf{D}_1$ or $d\mathbf{D}_2$ is sufficiently large (greater than 0.15 in one dimension).

3. Multiresolution Analysis of Material Damage

Our recent results indicate that many existing models in micromechanics [21-25] and damage mechanics [3] do not provide an accurate estimation of material degradation due to voids and cracks of arbitrary degree and size [26]. Traditional homogenization method, which relies upon a statistical mean to link microscale to macroscale, does not give a consistent answer. The statistical treatment is suitable only to a uniformly randomized distribution of material defects. This hypothesis becomes invalid whenever asymmetric voids/cracks occur during a loading process, after a manufacturing procedure, or in a given service period. Although asymptotic homogenization [27] normally works well on cellular structures, it is not suited for handling arbitrary cell structures with asymmetric defects.

A mechanics-based two-scale or multiscale bridging strategy known as Super Representative Volume (SRV) method is proposed [26] and considered to be an accurate method for linking microscale mechanical properties to macroscopic behavior. In SRV, the mechanical property at microscale is estimated by:

$$\begin{aligned} C_{ijpm}^{micro} &= C_{ijpm}^{RVE_k} = \frac{1}{|V_{micro}|} \int_{V_{micro}} C_{ijkl} L_{klpm}^{micro} dV_{micro} = \frac{1}{|V_{RVE_k}|} \int_{V_{RVE_k}} C_{ijkl} L_{klpm}^{RVE_k} dV_{RVE_k}, \quad (k=1, n), \\ \int_{V_{micro}} C_{ijpm} \varepsilon_{ij}(v^{micro}) \varepsilon_{pm}^{qs}(u^{micro}) dV_{micro} &= \int_{V_{RVE_k}} C_{ijpm} \varepsilon_{ij}(v^{RVE_k}) \varepsilon_{pm}^{qs}(u^{RVE_k}) dV_{RVE_k} \\ &= \int_{\partial V_{micro}} \lambda v_i^{micro} ((u_i^{micro})^{qs} - (d_i^{micro})^{qs}) d\partial V_{micro} = \int_{\partial V_{RVE_k}} \lambda v_i^{RVE_k} ((u_i^{RVE_k})^{qs} - (d_i^{RVE_k})^{qs}) d\partial V_{RVE_k}, \quad (k=1, n), \end{aligned} \quad (2a,b)$$

where superscript/subscript ‘‘micro’’ and ‘‘RVE’’ mean quantities at the microscale and within a representative volume element, respectively. V_{RVE} refers to the domain of RVE.

RVE_k represents the k -th RVE within the material test specimen or a structural domain. n is the number of sampling RVEs in the domain of a specimen or structure. u and v are the displacement and virtual displacement, respectively. d is a specified displacement. C_{ijkl} is a stiffness tensor, and L_{klpm} can be computed by a weak form of the RVE equilibrium equations:

$$\int_{V_{RVE_k}} C_{ijpm} \varepsilon_{ij}(v) \varepsilon_{pm}^{qs}(u) dV_{RVE_k} = \int_{\partial V_{RVE_k}} \lambda v_i (u_i^{qs} - d_i^{qs}) d\partial V_{RVE_k} \quad (k=1, n), \quad (2c)$$

in which λ is a penalty parameter. d refers to the specified displacement. ∂V means the boundary surface of V . $\varepsilon_{kl} = L_{klpm} \bar{\varepsilon}_{pm}$, where ε_{kl} and $\bar{\varepsilon}_{pm}$ are strain and average strain tensors within V_{RVE_k} , and these two strains are determined by solving Equation (2c). At the macroscale, the mechanical property is computed by:

$$\begin{aligned}
C_{ijpm}^{macro} &= C_{ijpm}^{\Omega} = \frac{1}{|V_{macro}|} \int_{V_{macro}} C_{ijkl}^{micro} L_{klpm}^{macro} dV_{macro} = \frac{1}{|\Omega|} \int_{\Omega} C_{ijkl}^{RVE} L_{klpm}^{\Omega} d\Omega, \\
\int_{V_{macro}} C_{ijpm}^{micro} \varepsilon_{ij}(v^{macro}) \varepsilon_{pm}^{qs}(u^{macro}) dV_{macro} &= \int_{\Omega} C_{ijpm}^{RVE} \varepsilon_{ij}(v^{\Omega}) \varepsilon_{pm}^{qs}(u^{\Omega}) d\Omega \\
= \int_{\partial V_{macro}} \hat{\lambda}_i^{macro} ((u_i^{macro})^{qs} - (d_i^{macro})^{qs}) d\partial V_{macro} &= \int_{\partial \Omega} \hat{\lambda}_i^{\Omega} ((u_i^{\Omega})^{qs} - (d_i^{\Omega})^{qs}) d\partial \Omega,
\end{aligned} \tag{3a,b}$$

in which $\varepsilon_{kl}^{macro} = L_{klpm}^{macro} \bar{\varepsilon}_{pm}^{macro}$. Superscript and subscript ‘‘macro’’ refers to quantities at the macroscale. Ω represents the domain of material specimens or volumes of interest at the macroscopic scale. The remaining variables are similar to those in Equation (2).

Figure 3 shows the predicted effective modulus based on the proposed method of Super RVE, compared with that of several conventional approaches based on the measured moduli of AL 2024 reported in [26]. This figure indicates that the proposed method yields a more accurate prediction than that of several conventional formulae in micromechanics including the Eshelby’s method, the Self-consistent method, the Voigt and Reuss approximations [25, 28]. Among those formulae, Voigt and Reuss approximations defines upper and lower bounds, respectively. The prediction of Voigt approximation is very close to that of Gibson model in this figure. The predicted SuperRVE results also yield more accurate overall predictions than that of the tradition RVE based on the statistical mean (i.e., averaging operation).

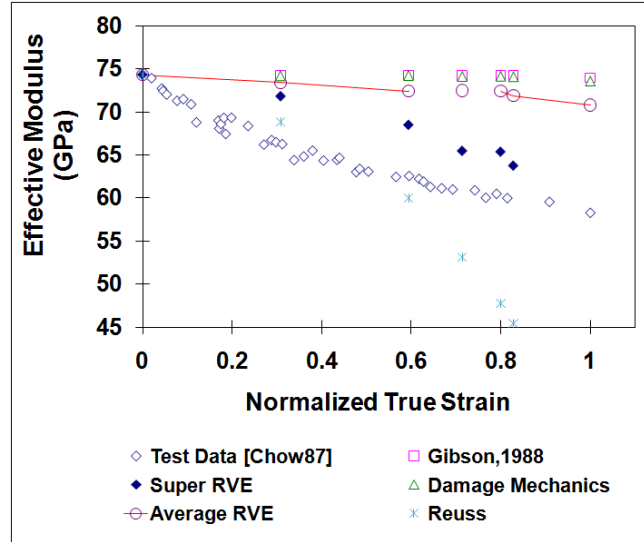


Figure 3: Experimental and numerical results of an aluminum alloy specimen.

Acknowledgement. This work was in part supported by U.S. National Science Foundation CMMI-0721625 and ECCS-1039563.

References

- [1] D. Krajcinovic, *Damage mechanics: accomplishments, trends and needs*. International Journal of Solids and Structures 37, 267-277 (2000).

- [2] J. Lemaitre, A Course on Damage Mechanics, Springer, 1996.
- [3] J. Lemaitre and R. Desmorat, Engineering Damage Mechanics, Springer, 2005.
- [4] L. M. Kachanov, Introduction to continuum damage mechanics, Martinus Nijhoff Publishers, the Netherlands 1986.
- [5] M. Kachanov, I. Tsukrov and B. Shafiro, *Effective moduli of solids with cavities of various shapes*. In *Micromechanics of Random Media, ASME book AMR 139*. (Ed. M. Ostoja-Starzewski and I. Jasiuk) p. S151-S174, 1994.
- [6] I. Jasiuk, J. Chen and M. F. Thorpe. Elastic moduli of two-dimensional materials with polygonal and elliptical holes. *Applied Mechanics Reviews* 47[1], S18-S28. 1994.
- [7] Q. S. Zheng and I. F. Collins. The relationship between damage variables and the evolution laws and microstructure and physical properties. *Proceedings of the Royal Society of London. Series A* 454[1973], 1469-1498. 1997.
- [8] J. W. Ju and K. H. Tseng. An improved two-dimensional micromechanical theory for brittle solids with randomly located interacting microcracks. *International Journal of Damage Mechanics* 4[1], 23-57. 1995.
- [9] D. Krajcinovic. Effective material properties in the limit of large defect concentration. *Engineering Fracture Mechanics* 57[2/3], 227-240. 1997.
- [10] Y. Fu, K. J. Klimkowski, G. J. Rodin, E. Berger, J. C. Browne, J. K. Singer, R. A. van de Geijn and K. S. Vemaganti. A fast solution method for three-dimensional many-particle problems of linear elasticity. *International Journal for Numerical Methods in Engineering* 42[7], 1215-1229. 1998.
- [11] J. Fish, Q. Yu and K. Shek. Computational damage mechanics for composite materials based on mathematical homogenization. *International Journal for Numerical Methods in Engineering* 45[11], 1657-1679. 1999.
- [12] J. L. Chaboche, S. Kruch, J. F. Maire and T. Pottier. Towards a micromechanic based inelastic and damage modeling of composites. *International Journal of Plasticity* 17[4], 411-439. 2001.
- [13] J. W. Ju and H. K. Lee. A micromechanical damage model for effective elastoplastic behavior of partially debonded ductile matrix composites. *International Journal of Solids and Structures* 38[36-37], 6307-6332. 2001.
- [14] S. Ghosh, K. Lee and P. Raghavan. A multi-level computational model for multi-scale damage analysis in composite and porous materials. *International Journal of Solids and Structures* 38[14], 2335-2385. 2001.
- [15] S. Ghosh, D. M. Valiveti, S. J. Harris and J. Boileau. A domain partitioning based pre-processor for multi-scale modeling of cast aluminium alloys. *Modeling and Simulation in Materials Science and Engineering* 14[8], 1363-1396. 2006.
- [16] D. Krajcinovic and A. Rinaldi, *Thermodynamics and statistical physics of damage process in quasi-ductile solids*. *Mechanics of Materials* 37, 299-315 (2005).
- [17] D. Krajcinovic and A. Rinaldi. Statistical damage mechanics - I : Theory. *Journal of Applied Mechanics* 72[1], 76-85. 2005.
- [18] A. Rinaldi, D. Krajcinovic, P. Peralta and Y. C. Lai. Lattice models of polycrystalline microstructures: A quantitative approach. *Mechanics of Materials* 40[1-2], 17-36. 2008.
- [19] L. Salvo, P. Cloetens, E. Maire, S. Zabler, J. J. Blandin, J. Y. Buffiere, W. Ludwig, E. Boller, D. Bellet and C. Josserond, *X-ray micro-tomography an attractive characterisation technique in materials science*. *Nuclear Instruments and Methods in Physics Research B* 200, 273-286 (2003).
- [20] J. Shen, Y. Mao, G. Reyes, C. L. Chow, J. Boileau, J. Su and J. M. Wells. A multiresolution transformation rule of material defects. *International Journal of Damage Mechanics* 18[8], 739-758. 2009.
- [21] B. Budiansky and T. T. Wu. Theoretical prediction of plastic strains of polycrystals. 1175-1185. 1962. *Proceedings of the 4th US National Congress on Applied Mechanics*.
- [22] J. D. Eshelby. The determination of the elastic field of an ellipsoidal inclusion, and related problems. *Proceedings of the Royal Society of London. Series A* 241[1226], 376-396. 1957.
- [23] J. D. Eshelby, *Elastic inclusions and inhomogeneities*. In. (Ed. I. N. Sneddon and R. Hill) pp. 89-104, 1961.
- [24] B. Budiansky. On the elastic moduli of some heterogeneous materials. *Journal of the Mechanics and Physics of Solids* 13[4], 223-227. 1965.
- [25] T. Mura, *Micromechanics of defects in solids*, Martinus Nijhoff, New York 1987.
- [26] J. Shen, D. Yoon, S. Wei, J. Boileau, J. Mao, W. Shi, J. M. Wells, G. Reyes and C. L. Chow. Material Damage Estimated via Linking Micro/Macroscale Defects to Macroscopic Mechanical Properties. *International Journal of Damage Mechanics* (to be submitted). 2012.
- [27] S. J. Hollister and N. Kikuchi. A comparison of homogenization and standard mechanics analyses for periodic porous composites. *Computational Mechanics* 10[2], 73-95. 1992.
- [28] S. Nemat-Nasser and M. Hori, *Micromechanics: overall properties of heterogeneous materials*, North-Holland, 1999.

PLENARY LECTURE

COUPLED VISCOPLASTIC DAMAGE MODEL AND SIMULATION FOR METALS AND COMPOSITES**George Z. Voyiadjis¹, D. Faghihi²**

¹Faculty of Civil and Environmental Engineering,
Louisiana State University, Baton Rouge, LA 70803
e-mail: voyiadjis@eng.lsu.edu

²PhD Candidate of Civil and Environmental Engineering,
Louisiana State University, Baton Rouge, LA 70803
e-mail: dfaghi1@tigers.lsu.edu

Abstract. In this work a nonlocal viscoplastic-viscodamage model is presented using a consistent mathematical and mechanical framework that allows for total coupling of geometrical and material nonlinearities. Computational aspects and implementing the presented model in the commercial finite element code ABAQUS as a user defined subroutine (VUMAT) are also discussed. Numerical integration algorithms, verification and validation process of the theory is discussed. The finite element simulations are also performed using this model for various localization phenomena. The available experimental data are also compared to the numerical simulation results in order to verify the model.

1. Introduction

Metals and composites are among those materials that are often used in various parts of the structural components of the engineering structure in aerospace, automobile and defense industries. The need for a micro-mechanical damage model that accounts for the nonlocal microscopic interactions between material points (i.e. to take into account the influence of an internal state variable at a point on its neighborhood) in the simulation of metal impact problems has been recognized recently [1-3]. This nonlocal microdamage model is formulated based on the enhanced gradient-dependent theory which is successful in explaining the size effects encountered at the micron scale and in preserving the well-posed nature of the initial boundary value problem that governs the solution of material instability triggering strain localization. Moreover, the viscoplasticity theory (rate-dependency) allows the spatial difference operator in the governing equations to retain its ellipticity and consequently the initial boundary value problem is hence well-posed [4-11]. However, the gradient dependent theories enhance a stronger regularization of the localization problem than the rate-dependent theory. Moreover, the rate-dependent theory cannot explain the size effect of the microdamage zone (i.e. the void/crack size and spacing) on the material failure while the gradient theory can address that. Therefore, the objective of this work is to present a novel microdamage constitutive model that possesses several material length scales. This model can be used to produce physically meaningful and numerically converging results within strain localization computations.

2. A coupled rate-dependent (viscoplasticity) continuum damage:

Materials with microstructure are nonlocal in behavior due to the interplay of characteristic lengths including sizes or spacing of defect clusters (e.g. micro-cracks, micro-voids, dislocations). As traditional continuum mechanics does not contain characteristic lengths, the use of the nonlocal concept is required in order to incorporate a microstructural length scale that introduces long-range microstructural interactions where the stress response at a material point is assumed to depend on the state of its neighborhood in addition to the state of the material point itself. Moreover, this length scale preserves the well-posed nature of the initial boundary value problem governing the solution of material instability triggering strain localization. In the following, the nonlocality is incorporated through the use of the gradient-dependent theory such that if $\boldsymbol{\phi}$ is some 'local' field (second order tensor) in a domain V , the corresponding nonlocal field, $\widehat{\boldsymbol{\phi}}$, is defined as follows:

$$\widehat{\boldsymbol{\phi}} = \boldsymbol{\phi} + \frac{1}{2} \ell^2 \nabla^2 \boldsymbol{\phi} \quad (1)$$

where ℓ is the internal material length scale, which weights each component of the gradient term identically, and ∇^2 is the Laplacian operator. The length scale ℓ should be obtained from gradient-dominant experiments such as indentation tests, bending tests, or torsion tests [2]. The role of the material length scale in solving the impact damage problem and in preserving the objectivity of the continuum modeling and numerical simulation of the localization problem is the main concern of this paper. The first-order gradients are disregarded since the isotropic nonlocal influence is assumed. The viscoplastic rate of deformation, \mathbf{d}^{vp} , the viscodamage rate of deformation, \mathbf{d}^{vd} , the rate of the second-order damage tensor $\boldsymbol{\phi}$, and viscoplastic rate of deformation in the undamaged configuration, $\bar{\mathbf{d}}^{vp}$, are given as follows:

$$\mathbf{d}^{vp} = \lambda^{vp} \frac{\partial f}{\partial \boldsymbol{\tau}}, \quad \mathbf{d}^{vd} = \lambda^{vd} \frac{\partial g}{\partial \boldsymbol{\tau}}, \quad \dot{\boldsymbol{\phi}} = \lambda^{vp} \frac{\partial f}{\partial \mathbf{V}} + \lambda^{vd} \frac{\partial g}{\partial \mathbf{V}}, \quad \bar{\mathbf{d}}^{vp} = \lambda^{vp} \frac{\partial f}{\partial \bar{\boldsymbol{\tau}}}, \quad (2)$$

where the potentials f and g are the nonlocal viscoplastic and viscodamage conditions given in the undamaged (effective) configuration, respectively, by

$$f = \sqrt{(\bar{\boldsymbol{\tau}}' - \bar{\boldsymbol{\chi}}):(\bar{\boldsymbol{\tau}}' - \bar{\boldsymbol{\chi}})} - [\bar{Y}_{yp} + \bar{R}(\bar{\boldsymbol{p}})] \left[1 + (\eta^v \dot{\bar{\boldsymbol{p}}})^{1/m} \right] [1 - (T/T_m)^n] \leq 0 \quad (3)$$

and

$$g = \sqrt{(\bar{\mathbf{Y}} - \bar{\mathbf{H}}):(\bar{\mathbf{Y}} - \bar{\mathbf{H}})} - [r_0 + \bar{K}(\hat{r})] \left[1 + (\eta^v \dot{\hat{r}})^{1/m} \right] [1 - (T/T_m)^n] \leq 0 \quad (4)$$

where $\bar{\boldsymbol{\tau}}'$ is the effective deviatoric stress tensor; \bar{Y}_{yp} is the initial yield strength (at zero absolute temperature, zero plastic strain, and static strain rate); $\bar{R}(\bar{\boldsymbol{p}})$ is the nonlocal isotropic hardening function; $\bar{\boldsymbol{\chi}}$ is the nonlocal anisotropic (kinematic) hardening stress; $\bar{p} = \int_0^t \sqrt{\frac{2}{3} \bar{\mathbf{d}}_{ij}^{vp} \bar{\mathbf{d}}_{ij}^{vp}} dt$ is the effective accumulative viscoplastic strain; m and n are material constants; η^v is the relaxation time; the nonlocal damage forces $\bar{\mathbf{Y}}$ and $\bar{K}(\hat{r})$ are, respectively, characterizing the energy release rate and the damage isotropic hardening function; r_0 is the initial damage threshold; $\hat{r} = \sqrt{\widehat{\boldsymbol{\phi}}:\widehat{\boldsymbol{\phi}}}$ is the nonlocal damage accumulation; and T_m is the melting temperature.

If $f \leq 0$ and $g \leq 0$, the process is clearly undamaged elastic and the trial stress is in fact the final state. On the other hand, if $f > 0$ and $g > 0$, the Kuhn-Tucker loading/unloading

conditions, are violated by the trial stress which now lies outside f and g (see Figure 1). Consistency is restored by a generalization of the classical return mapping algorithm to rate-dependent problems [12]. Since the objective rates reduce to a simple time derivative due to the fact that the global configuration is held fixed, the coupled viscoplastic-viscodamage corrector problem may then be rephrased

Another complication is the higher-order boundary conditions that are necessary from the mathematical point of view and have to be prescribed on the moving elasto-inelastic boundary (Figure 1). These internal boundaries are not always easy to interpret physically. In the following, the robust numerical technique that have been developed in [13, 14] is used to calculate the Laplacian terms $\nabla^2 \dot{\lambda}^{vp}$ and $\nabla^2 \dot{\lambda}^{vd}$.

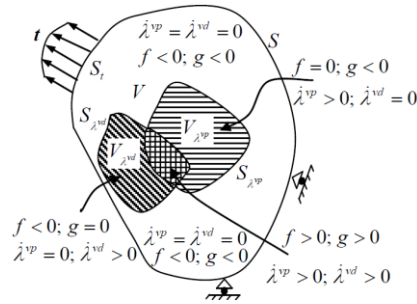


Figure 1. Schematic Representation of Elastic, Viscoplastic, and Viscodamage Boundaries [15].

The aforementioned constitutive relations implemented into finite element code, ABAQUS [16] as the user material subroutine. In the context of the finite element method, the discrete problem can be obtained via a spatial displacement-based projection of the semidiscrete (i.e. discrete in space and continuous in time) problem into a finite dimensional subspace of admissible continuous shape functions. In order to integrate the set of constitutive equations, a return mapping algorithm is also developed.

3. Application of the theory in studying high velocity contact problems

3.1. A blunt projectile impacting a target

The proposed constitutive equations are used here to describe the structural response to projectile impact damage when different failure modes are expected to occur. This is done by conducting numerical simulations of the experimental tests presented by Borvik et al. [17] for a blunt projectile made of hardened Arne tool steel impacting a circular plate made of Weldox 460 E steel. In these simulations a 4-node 2D axisymmetric element with one integration point and a stiffness based on hourglass control is used. The contact between the projectile and the target was modeled using an automatic 2D single surface penalty formulation available in ABAQUS [16] (for more details regarding the experiments and numerical simulations please refer to [18]).

Numerical plots showing perforation of the target plate by a blunt projectile at impact velocity close to the ballistic limit of 210m/s is shown in Figure 2(a). The contours of accumulated viscoelastic strain are plotted on the deformed mesh. It can be seen that limited inelastic deformation occurs outside the localized shear zone.

A direct comparison between the numerical and experimental residual velocity curves for blunt projectiles is shown in Figure 2(b). As seen, there is a good agreement with the experimental results.

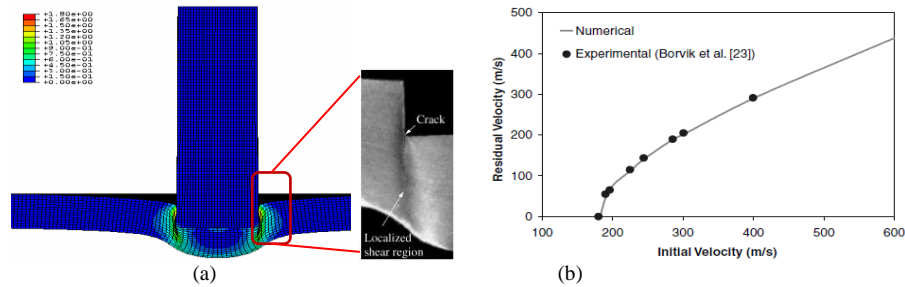


Figure 2. Penetration of the target plate by a blunt projectile. (a) macrograph of sectioned and etched target plate close to perforation [17] and simulation plotted as contours of accumulated inelastic strain [18]; (b) The initial impact velocity versus residual projectile velocity.

3.2. Shear localizations in cylindrical hat-shaped samples

The hat-shaped sample geometry is commonly used to study shear localization growth. Numerical simulations of the dynamic deformation response of tantalum hat-shaped specimens are performed in this study under prescribed conditions. Comparisons of these results to experiments conducted by three different authors [19-21] are also made. The finite element mesh, simulation results, and comparison with the corresponding experimental data for tantalum are given in Figure 3. This figure shows that the shear localization corresponding to pure tantalum deformed at the above mentioned loading condition compares well with the optical micrographs taken at the forced localized shear region. In addition to the good comparisons between the results from simulations and experiments, the width of the shear region increases with increasing shear strain within a given specimen.

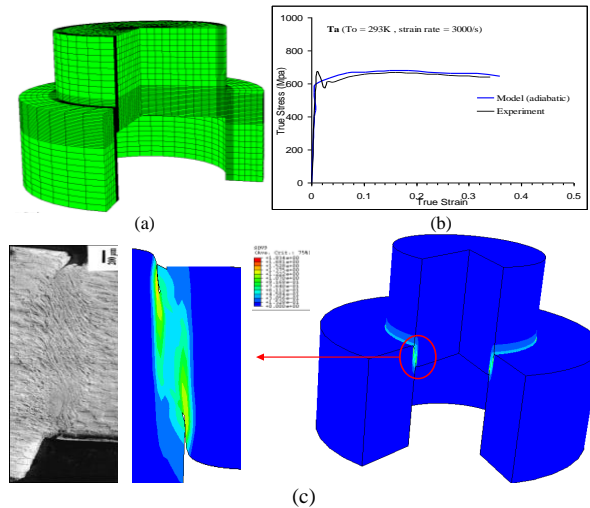


Figure 3. Cylindrical Hat-shaped specimen for tantalum under adiabatic condition: (a) A three-dimensional shape corresponding to 3/4 of the sample [12]; (b) comparison between experiment and simulation results in shear stress versus displacement; (c) shear localization results from experimental observations [21] and contour plots of model simulation [12].

3.3. A projectile impacting a composite plate

The proposed model is used to simulate a hemi-spherically tipped cylindrical steel projectile, 5.5mm long and 7.5mm diameter, impacting and penetrating into a 50x50x5mm

laminated metal matrix composite plate subjected to an initial velocity of 1000m/s (for more details regarding the geometry and material parameters please see [22]). Figure 4 shows the sequence of stages of impact. Global bending and dishing is observed in the third stage. Numerical plots of the perforation of the target plate by the projectile shows the limited inelastic deformation that occurs outside of the localized shear zone. These plots clearly indicate that the numerical model qualitatively captures the overall physical behavior of the target during penetration and perforation. In the third and fourth stages of deformation of the plate it can be seen that the elements in the impacted area are significantly distorted. However, stable results are nevertheless obtained. This distortion caused delay in the damage evolution process and, consequently the erosion of the failed elements. This simulation also indicates that the initiation and propagation of the microdefects depend on both the amplitude and distribution of the inelastic strain/stress in the vicinity around the microdefects. This implies that the evolution of the material inelasticity is practically a nonlocal process. Hence, such nonlocality in the material response requires such a micromechanical approach that incorporates material length scale parameter into the classical constitutive relations.

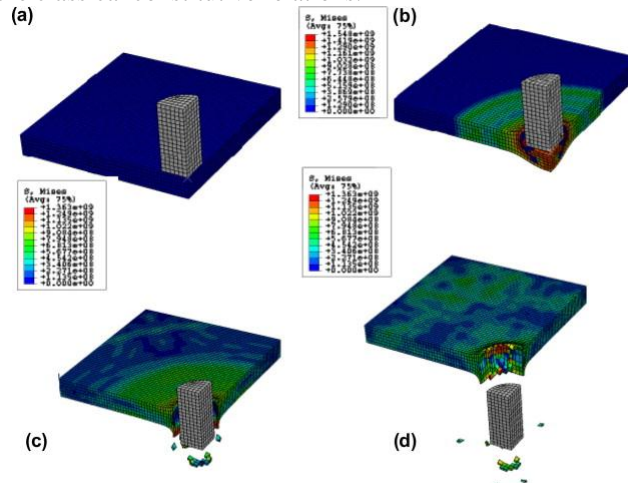


Figure 4. Deformation Stages of the Plate during the Impact Process [22].

4. Conclusions

The authors presented the micro-mechanical damage model that accounts for the nonlocal microscopic interactions between material points in the simulation of metal/composite localization, impact and severe contact stress problems. The presented nonlocal microdamage model is based on the enhanced gradient-dependent theory which is successful in explaining the size effects encountered at the micron scale and in preserving the well-posed nature of the initial boundary value problem that governs the solution of material instability triggering strain localization. This is modeled through coupling continuum damage with strain gradient plasticity.

The finite element simulations are performed by implementing the presented model in the commercial finite element code ABAQUS [16] as a user defined subroutine (VUMAT) in order to perform the simulations.

This model provides a potential feature for enabling one to relate the non-local continuum plasticity and damage of the bulk material to friction and wear at the contact interfaces. The

findings of this research effort is invaluable in providing a material model and numerical procedure that will be used within a hydrocode to better facilitate the design components of severe contact stress applications.

References

- [1] Voyiadjis, G.Z., Abu Al-Rub, R.K., and Palazotto, A.N. (2003). Non-local coupling of viscoplasticity and anisotropic viscodamage for impact problems using the gradient theory, *Arch Mech*, **55**(1): pp. 39-89.
- [2] Voyiadjis, G.Z., Abu Al-Rub, R.K., and Palazotto, A.N. (2004). Thermodynamic framework for coupling of non-local viscoplasticity and non-local anisotropic viscodamage for dynamic localization problems using gradient theory, *Int J Plasticity*, **20**(6): pp. 981-1038.
- [3] Abu Al-Rub, R.K. and Voyiadjis, G.Z. (2006). A finite strain plastic-damage model for high velocity impact using combined viscosity and gradient localization limiters: Part I - Theoretical formulation, *Int J Damage Mech*, **15**(4): pp. 293-334.
- [4] Needleman, A. (1988). Material Rate Dependent and Mesh Sensitivity in Localization Problems, *Computer Methods in Applied Mechanics and Engineering*, **67**(1): pp. 69-85.
- [5] Loret, B. and Prevost, H. (1990). Dynamics Strain Localization in Elasto-(Visco-)Plastic Solids, Part 1: General Formulation and One-Dimensional Examples, *Computer Methods in Applied Mechanics and Engineering*, **83**(3): pp. 247-273.
- [6] Molinari, A. (1997). Collective Behavior and Spacing of Adiabatic Shear Bands, *Journal of the Mechanics and Physics of Solids*, **45**: pp. 1551-1575.
- [7] Sluys, L.J., *Wave Propagation, Localization and Dispersion in Softening Solids* (1992), The Delft Univ. of Technology: Delft, Netherlands.
- [8] Batra, R.C., and Wei, Z. G., (2006). Shear Bands Due to Heat Flux Prescribed at Boundaries, *International Journal of Plasticity*, **22**: pp. 1-15.
- [9] Batra, R.C. and Chen, L. (1999). Shear Band Spacing in Gradient-Dependent Thermoviscoplastic Materials, *Computational Mechanics*, **23**: pp. 8-19.
- [10] Batra, R.C. and Kim, C.H. (1988). Effect of material characteristic length on the initiation, growth and band width of adiabatic shear bands in dipolar materials, *Journal De Physique* pp. 41-46.
- [11] Batra, R.C. and Kim, C.H. (1990). The interaction among adiabatic shear bands in simple and dipolar materials *International Journal of Engineering Science*, **28**: pp. 927-942.
- [12] Voyiadjis, G.Z. and Abed, F.H. (2006). Implicit algorithm for finite deformation hypoelastic-viscoplasticity in fcc metals, *Int J Numer Meth Eng*, **67**(7): pp. 933-959.
- [13] Abu Al-Rub, R.K. and Voyiadjis, G.Z. (2005). A direct finite element implementation of the gradient-dependent theory, *Int J Numer Meth Eng*, **63**(4): pp. 603-629.
- [14] Voyiadjis, G.Z. and Abu Al-Rub, R.K. (2006). A Finite Strain Plastic-Damage Model for High Velocity Impacts Using Combined Viscosity and Gradient Localization Limiters, Part II: Numerical Aspects and Simulations *International Journal of Damage Mechanics*, **15**(14): pp. 335-373.
- [15] Deliktas, B., Voyiadjis, G.Z., and Palazotto, A.N. (2009). Simulation of perforation and penetration in metal matrix composite materials using coupled viscoplastic damage model, *Compos Part B-Eng*, **40**(6): pp. 434-442.
- [16] ABAQUS, *Use Manual* (2008), Habbt, Karlsson and sorenson, Inc: Providence, RI.
- [17] Borvik, T., Clausen, A.H., Eriksson, M., Berstad, T., Hopperstad, O.S., and Langseth, M. (2005). Experimental and numerical study on the perforation of AA6005-T6 panels, *International Journal of Impact Engineering*, **32**(1-4): pp. 35-64.
- [18] Voyiadjis, G.Z., Al-Rub, R.K.A., and Palazotto, A.N. (2008). Constitutive modeling and simulation of perforation of targets by projectiles, *Aiaa J*, **46**(2): pp. 304-316.
- [19] Nemat-Nasser, S., Isaacs, J.B., and Liu, M. (1998). Microstructure of high-strain, high-strain-rate deformed tantalum, *Acta Metallurgica*, **46**: pp. 1307-1325.
- [20] Bronkhorst, C.A., Cerreta, E.K., Xue, Q., Maudlin, P.J., Mason, T.A., and Gray, G.T. (2006). An experimental and numerical study of the localization behavior of tantalum and stainless steel, *International Journal of Plasticity*, **22**: pp. 1304-1335.
- [21] Perez-Prado, M.T., Hines, J.A., and Vecchio, K.S. (2001). [Microstructural evolution in adiabatic shear bands in Ta and Ta-W alloys, *Acta Materialia*, **49**: 2905-2917., **49**: pp. 2905-2917.
- [22] Deliktas, B., Voyiadjis, G.Z., and Palazotto, A.N. (2009). Simulation of perforation and penetration in metal matrix composite materials using coupled viscoplastic damage model, *Composites Part B: Engineering*, **40**(6): pp. 434-442.

PLENARY LECTURE

**SIZE-DEPENDENT PROBABILISTIC DAMAGE
MICROMECHANICS AND TOUGHENING BEHAVIOR OF
PARTICLE/FIBER REINFORCED COMPOSITES****J.W. Ju¹, K. Yanase²**

¹Department of Civil and Environmental Engineering,
University of California, Los Angeles, CA 90095, USA
e-mail: juj@ucla.edu

²Department of Mechanical Engineering,
Fukuoka University, Fukuoka City, Fukuoka 814-0180, Japan
e-mail: kyanase@fukuoka-u.ac.jp

Abstract. A size-dependent micromechanical framework is rendered to predict the deformation responses of particle-reinforced metal matrix composites by incorporating essential features of the dislocation plasticity. Within the framework of probabilistic micromechanical formulation, the damage caused by the manufacturing process and by the external mechanical loading in the presence of thermal residual stresses is considered. The density of dislocations due to the thermal contraction misfit and the plastic deformation misfit are taken into consideration within the micromechanical methodology to account for the dislocation strengthening. To predict the overall elastoplastic damage behavior of composites, a size-dependent hybrid effective yield function is presented based on the ensemble-volume averaging and modified matrix yield strength.

1. Introduction

Composite materials have been widely studied and employed in diverse fields of science and engineering disciplines due to their superior structural performance, versatile capabilities, and customizable design potentials. In comparison with many conventional materials, fiber-reinforced or particle-reinforced composites offer salient features such as low density, high strength-to-weight ratio, high stiffness, high toughness, improved creep resistance, enhanced wear resistance, superior environmental durability, custom microstructure-morphology, and preferred directionality, etc. The matrix material may consist of metal, ceramic, or polymer. The inclusions (particles or fibers) can be unidirectionally aligned, bi-directional, or randomly dispersed in a matrix material.

2. Effective elastic moduli of multi-phase composites*2.1. Manufacturing process induced damage*

The particle fracture caused by manufacturing processes is a common phenomenon, and has a dominant effect upon the performance of MMCp [1]. Since the cracked particles may not carry any load effectively, they can be treated as voids. However, cracked particles can still contribute to the composite stiffness. Moreover, the amount of particle fracture is

dependent on the particle size; therefore the deformation behavior of MMCp is particle-size dependent [2]. The stiffness of a cracked particle $\mathbf{C}^{(2)}$ can be represented as:

$$\mathbf{C}^{(2)} = (1-D) \cdot \mathbf{C}^{(1)}, \quad \text{where } D = 1 \quad (1)$$

Here, $\mathbf{C}^{(1)}$ represent the elastic stiffness of an intact particle and can be expressed as:

$$C_{ijkl}^{(1)} = \lambda^{(1)} \delta_{ij} \delta_{kl} + \mu^{(1)} (\delta_{ik} \delta_{jl} + \delta_{il} \delta_{jk}), \quad i, j, k, l = 1, 2, 3 \quad (2)$$

where $\lambda^{(1)}$ and $\mu^{(1)}$ denote the isotropic Lamé constants of intact particles. The manufacturing process often induces anisotropic damage, hence the fourth-order tensor is suitable to characterize the damage in Eq. (1), if the detailed microstructural information is available. In addition, an exponential cumulative density function (CDF) is adopted to account for the probable size-dependent particle fracture as follows:

$$\phi^{(2)} = P_m \cdot \phi, \quad \text{where } P_m = 1 - \exp(-R_{mf} \cdot a) \quad (3)$$

Here, the coefficient R_{mf} and the particle radius a control the amount of damage or fracture probability of particles as shown in **Figure 1**. Further, ϕ and $\phi^{(2)}$ denote the volume fraction of the original (intact) particles and the damaged particles caused by the manufacturing process, respectively.

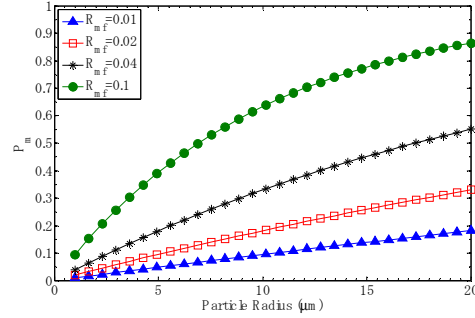


Figure 1. The probability function P_m with various particle radii.

2.2. Thermal residual stress and relaxation

Eigenstrain is introduced in micromechanics to represent inelastic strains such as the thermal strain, phase transformation strain, plastic strain, and misfit strain. The *thermal contraction misfit* can be simulated by the thermal eigenstrain as follows:

$$\varepsilon_{ij}^* = \alpha^* \delta_{ij}, \quad \text{where } \alpha^* = (\alpha_1 - \alpha_0) \Delta T \quad (4)$$

Here, α_0 and α_1 signify the coefficients of thermal expansion (CTE) of the matrix and inclusion, respectively, and δ_{ij} is the Kronecker delta. Since the thermal eigenstrain is the stress-free strain within the inclusion, Eshelby's equivalence principle can be expressed

with the total or fictitious eigenstrain ε^{**} as

$$\mathbf{C}^{(r)} : (\varepsilon^0 + \varepsilon' - \varepsilon^*) = \mathbf{C}_0 : (\varepsilon^0 + \varepsilon' - \varepsilon^{**}) \quad (5)$$

During the manufacturing process, the internal stress caused by *thermal expansion mismatch* can be quickly relaxed by the dislocation punching. For example, the internal stress relaxation leads to a decreased amount of residual compressive cramping force around inclusions. On the other hand, in terms of yielding, such relaxation is particularly favored for fiber-reinforced composites because the residual deviatoric stress in a matrix can also be reduced. We simulate the domain of punched-out dislocations by an additional prolate spheroid as rendered in **Figure 2**. By taking advantage of the respective dislocation loop configuration as displayed, the following thermal eigenstrain decomposition is considered for the *relaxed state* (cf. **Figure 2(b)**):

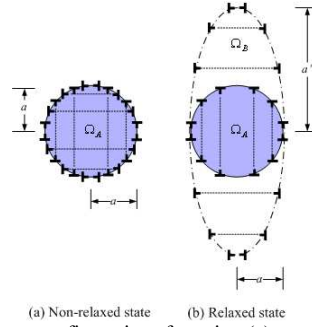


Figure 2. The dislocation loops configurations featuring (a) non-relaxed state; (b) relaxed state.

$$\boldsymbol{\varepsilon}_{ij}^{A*} = \begin{bmatrix} 0 & 0 & 0 \\ 0 & \alpha^* & 0 \\ 0 & 0 & \alpha^* \end{bmatrix} \quad \text{in } \Omega_A \quad (6)$$

$$\boldsymbol{\varepsilon}_{ij}^{B*} = \begin{bmatrix} \alpha^* \cdot (a/a') & 0 & 0 \\ 0 & 0 & 0 \\ 0 & 0 & 0 \end{bmatrix} \quad \text{in } \Omega_B \quad (7)$$

Here, a represents the particle radius. We define the punching distance a' directly with the mean center-to-center distance of particles λ_p as follows:

$$a' = \lambda_p / 2, \quad \text{where } \lambda_p = 2 \left[\left(\frac{\pi}{6\phi} \right)^{1/2} - \frac{2}{\pi} + 1 \right] a \quad (8)$$

The relaxed internal stress state can be emulated by the following equivalence equation:

$$\mathbf{C}^{(1)} \bullet (\mathbf{S}^{(B)} : \boldsymbol{\varepsilon}^{B*} - \boldsymbol{\varepsilon}^{B*} + \mathbf{S}^{(A)} : \boldsymbol{\varepsilon}^{**} - \boldsymbol{\varepsilon}^{A*}) = \mathbf{C}_0 \bullet (\mathbf{S}^{(B)} : \boldsymbol{\varepsilon}^{B*} - \boldsymbol{\varepsilon}^{B*} + \mathbf{S}^{(A)} : \boldsymbol{\varepsilon}^{**} - \boldsymbol{\varepsilon}^{**}) \quad (9)$$

Therefore, the total eigenstrain for a *relaxed state* can be expressed as

$$\boldsymbol{\varepsilon}_R^{**} = [\mathbf{C}_0 + \Delta\mathbf{C}^{(1)} \bullet \mathbf{S}^{(A)}]^{-1} \bullet [-\Delta\mathbf{C}^{(1)} \bullet (\mathbf{S}^{(B)} - \mathbf{I}) : \boldsymbol{\varepsilon}^{B*} + \mathbf{C}^{(1)} : \boldsymbol{\varepsilon}^{A*}] \quad (10)$$

By contrast, based on Eqs. (4) and (5), the equivalence equation for a non-relaxed state is given as

$$\mathbf{C}^{(1)} \bullet (\mathbf{S}^{(A)} : \boldsymbol{\varepsilon}^{**} - \boldsymbol{\varepsilon}^*) = \mathbf{C}_0 \bullet (\mathbf{S}^{(A)} : \boldsymbol{\varepsilon}^{**} - \boldsymbol{\varepsilon}^{**}) \quad (11)$$

Accordingly, in contrast to Eq. (10), we obtain the total eigenstrain for a *non-relaxed state*:

$$\boldsymbol{\varepsilon}_{NR}^{**} = \left(\mathbf{C}_0 + \Delta \mathbf{C}^{(1)} \bullet \mathbf{S}^{(A)} \right)^{-1} \bullet \mathbf{C}^{(1)} : \boldsymbol{\varepsilon}^* \quad (12)$$

Finally, by assuming that the dislocation punching occurs in every possible direction, the amount of stress relaxation is estimated by the following equation:

$$\Delta T_{ref} = \eta \cdot \Delta T, \quad \text{where } \eta = \langle \boldsymbol{\varepsilon}_R^{**} \rangle_{ij}^{Angle} / \boldsymbol{\varepsilon}_{NR-ij}^{**} \quad (13)$$

The angle-ensemble averaging can be performed by the following equation:

$$\langle \boldsymbol{\varepsilon}_R^{**} \rangle^{Angle} = \frac{1}{4\pi} \int_0^{2\pi} \left(\int_{-\pi/2}^{\pi/2} \mathbf{Q} : \boldsymbol{\varepsilon}_R^{**} : \mathbf{Q}^T \cos \phi \, d\phi \right) d\theta \quad (14)$$

2.3. Concept of equivalent inclusion method

While the tensile radial stress reaches a critical interfacial debonding stress σ_{cri} , the local debonding criterion can be characterized as [3]:

$$\begin{aligned} \sigma^{Interface} &\geq \sigma_{cri} = 0, & \text{then the interface is partially debonded} \\ \sigma^{Interface} &< \sigma_{cri} = 0, & \text{then the interface is perfectly bonded} \end{aligned} \quad (15)$$

Since thermal residual stresses are induced before the mechanical loading due to the manufacturing process, the presence of residual stress plays an important role for the interfacial damage evolution. To estimate the extent of damage, we make use of the approximate interface stress of intact particle based on the micromechanical equations [3]:

$$\boldsymbol{\sigma}^{Interface} = \boldsymbol{\beta} \cdot \mathbf{F} : \bar{\boldsymbol{\sigma}} + \mathbf{G} : \boldsymbol{\varepsilon}^* \quad (16)$$

In order to emulate the reduction in load-transfer capability of particles, the following equivalent orthotropic stiffness is defined for the partially debonded particles:

$$\mathbf{C}_{ijkl}^{(3)} = \lambda_{ik}^{(3)} \delta_{ij} \delta_{kl} + \mu_{il}^{(3)} (\delta_{ik} \delta_{jl} + \delta_{il} \delta_{jk}), \quad i, j, k, l = 1, 2, 3 \text{ and } I, J, K = 1, 2, 3 \quad (17)$$

where

$$\lambda_{ik}^{(3)} = \lambda^{(1)} (1 - D_i) \cdot (1 - D_k); \quad \mu_{il}^{(3)} = \mu^{(1)} (1 - D_i) \cdot (1 - D_l) \quad (18)$$

3. Effective elastoplastic-damage behavior

3.1. Effective elastic-damage moduli of 4-phase composites

Since the self-equilibrium residual stresses do not influence the elastic properties of composites, the effective stiffness tensor of four-phase composites can be expressed as

$$\bar{\boldsymbol{\sigma}} = \mathbf{C}^* : \bar{\boldsymbol{\varepsilon}}^e \quad (19)$$

3.2. Effective yield function for elastoplastic composites with damage and residual stress

The effective yield function for a composite is defined by the following equation:

$$\bar{F} = \sqrt{\langle H(\mathbf{x}) \rangle} - K (\bar{e}^p)^p \leq 0 \quad (20)$$

The ensemble-volume-averaged stress norm $\langle H(\mathbf{x}) \rangle_m$ for the matrix material with three distinct phases of particles is approximated as

$$\langle H(\mathbf{x}) \rangle_m \equiv H^0 + \sum_{r=1}^3 \left[\int_{|\mathbf{x}-\mathbf{x}_r| \neq \Omega_r} \{H(\mathbf{x}|\mathbf{x}_r) - H^0\} \cdot P(\mathbf{x}_r) \right] \quad (21)$$

The far-field stress $\boldsymbol{\sigma}^0$ is expressed in terms of macroscopic stress and thermal eigenstrain:

$$\boldsymbol{\sigma}^0 = \mathbf{P} : \bar{\boldsymbol{\sigma}} + \mathbf{Q} : \boldsymbol{\varepsilon}^* \quad (22)$$

By making use of Eq. (22), we obtain

$$\langle H(\mathbf{x}) \rangle_m = \bar{\boldsymbol{\sigma}} : \bar{\mathbf{T}}^A : \bar{\boldsymbol{\sigma}} + 2 \cdot \bar{\boldsymbol{\sigma}} : \bar{\mathbf{T}}^B : \boldsymbol{\varepsilon}^* + \boldsymbol{\varepsilon}^* : \bar{\mathbf{T}}^C : \boldsymbol{\varepsilon}^* \quad (23)$$

As only the intact particles can *effectively constrain* the deformation of surrounding matrix material, the ensemble-volume-averaged current stress norm for a composite is:

$$\sqrt{\langle H(\mathbf{x}) \rangle} = (1 - \phi^{(1)}) \sqrt{\bar{\boldsymbol{\sigma}} : \bar{\mathbf{T}}^A : \bar{\boldsymbol{\sigma}} + 2 \cdot \bar{\boldsymbol{\sigma}} : \bar{\mathbf{T}}^B : \boldsymbol{\varepsilon}^* + \boldsymbol{\varepsilon}^* : \bar{\mathbf{T}}^C : \boldsymbol{\varepsilon}^*} \quad (24)$$

3.3. Dislocation strengthening

To account for the dislocation strengthening, we consider the thermal contraction misfit and plastic deformation misfit between the matrix and particles. The dislocation density generated by the thermal contraction misfit is estimated as:

$$\rho^T = \frac{6\phi\alpha^*}{ab} \quad (25)$$

where b is the Burgers vector of the matrix material. Since only intact particles can *effectively constrain* the deformation of surrounding matrix, only the plastic deformation mismatch between the matrix and intact particles is considered. Accordingly, by invoking the volume fraction of intact particles, the following incremental form is considered:

$$\dot{\rho}^p = \frac{3\phi^{(1)}}{a \cdot b} \dot{e}_m^p, \quad \text{where } \dot{e}_m^p = \frac{\dot{e}^p}{1 - \phi^{(1)}} \quad (26)$$

Since the increased dislocation density in composites leads to the higher yield strength of matrix material, the yield strength of the matrix in composite is expressed as:

$$\sigma_y = \sigma_y^m + \Delta\sigma_y \quad (27)$$

Here, σ_y^m represents the yield strength of the unreinforced matrix, and $\Delta\sigma_y$ signifies the amount of dislocation strengthening. The mechanisms of similar strengthening are most suitably combined with the square root sum; thus the net strengthening is expressed as

$$\Delta\sigma_y = \sqrt{(\Delta\sigma_y^T)^2 + (\Delta\sigma_y^p)^2} \quad (28)$$

4. Numerical simulations

In the experiment, the uniaxial tensile behaviors were observed for T6-A356/SiC and T4-A356/SiC composites, respectively. As exhibited by **Figures 3, 4** and **5**, the interfacial debonding cannot be observed instantly after the mechanical loading is applied.

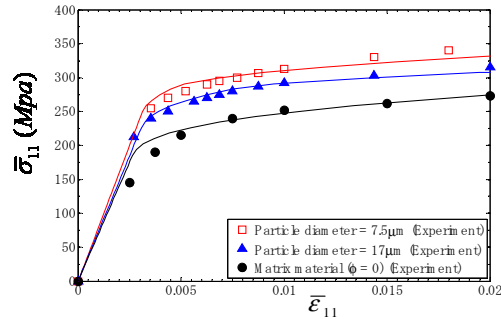


Figure 3. The comparisons between the theoretical predictions and experimental data (T6-A356/SiC 15% composite by [4]).

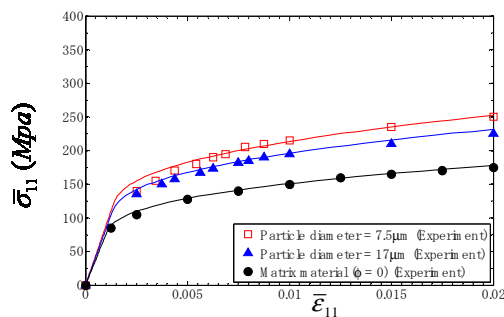


Figure 4. The comparisons between the theoretical predictions and experimental data (T4-A356/SiC 15% composite by [4]).

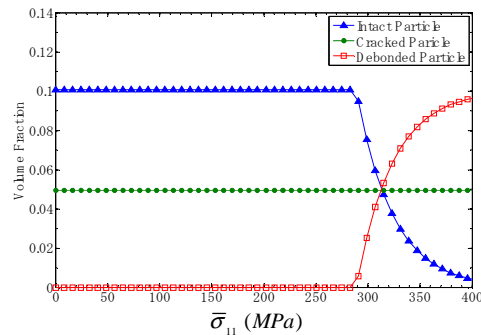


Figure 5. The theoretical predictions on the particle volume fraction evolutions for T6-A356/SiC 15% composite (the volume fraction = 0.15, the particle diameter = 7.5 μm).

References

- [1] Sun, L.Z., Liu, H.T., and Ju, J.W. (2003), Effect of particle cracking on elastoplastic behavior of metal matrix composites, *Int. J. for Numer. Meth. in Eng.*, **56**, pp. 2183-2198.
- [2] Chawla, N., and Shen, Y.L. (2001), Mechanical behavior of particle reinforced metal matrix composites, *Advanced Engineering Materials*, **3**, pp. 357-370.
- [3] Ju, J.W. and Chen, T.M. (1994a), Micromechanics and effective moduli of elastic composites containing randomly dispersed ellipsoidal inhomogeneities, *Acta Mech.*, **103**, pp. 103-121.
- [4] Lloyd, D.J., (1994), Particle reinforced aluminum and magnesium matrix composites, *Int. Mater. Rev.*, **39**, pp. 1-23.

PLENARY LECTURE

DAMAGE MECHANICS IN METAL FORMING: ADVANCED MODELING, NUMERICS AND APPLICATION

K. Saanouni

Professor, ICD/LASMIS, STMR UMR-CNRS 6279, University of Technology of Troyes
12, Rue Marie Curie – BP2060- 10000 Troyes cedex France
khemais.saanouni@utt.fr

Abstract. This paper describes the needs required in modern virtual metal forming including both sheet and bulk metal forming of mechanical components. These concern the advanced modeling of thermomechanical behavior including the multiphysical phenomena and their interaction or strong coupling, as well as the associated numerical aspects using fully adaptive simulation strategies. First a survey of advanced constitutive equations accounting for the main thermomechanical phenomena as the thermo-elasto-plastic finite strains with isotropic and kinematic hardenings fully coupled with ductile damage will be presented. Only the macroscopic phenomenological approach with state variables (mono-scale approach) will be discussed in the general framework of the rational thermodynamics for generalized micromorphic continua. The micro-macro (multi-scales approach) in the framework of polycrystalline inelasticity is not presented here for the sake of shortness but will be presented during the oral presentation. The main numerical aspects related to the resolution of the associated initial and boundary value problem will be outlined. A fully adaptive numerical methodology will be briefly described and some numerical examples will be given in order to show the high predictive capabilities of this adaptive methodology for virtual metal forming simulations.

1. Introduction

To increase their highly competitive market share, manufacturers have to constantly innovate to design new high added value products. These new products should be produced under low cost and severe environmental constraints to reduce significantly the carbon emission in conformity with the European code REACH. In this context, there is no longer place for the classical and very expensive trial and error approaches which have characterized manufacturing industry for long years. In recent decades, these costly methods have gradually replaced by concurrent engineering methods which break with sequential methods by placing the product in the form of a digital mockup put in the middle of all the actors of a given project team.

In this framework of concurrent engineering using an appropriate digital mockup, each part from any mechanical system should be designed and its manufacturing process optimized numerically before its physical realization. This defines what we call virtual metal forming. As with other scientific fields where numerical simulation is essential, predictive capabilities of virtual metal forming methods require: (i) advanced thermomechanical constitutive equations representing the mechanisms of the main thermomechanical phenomena involved and their various strong couplings; (ii) high-performing numerical methods adapted to the problem's various nonlinearities; (iii) adaptive and user friendly

geometric tools for the spatial representation and adaptive spatial discretization of 3D geometrically complex solids undergoing large inelastic strains.

These aspects have been extensively developed during the last decades in order to provide engineers by helpful numerical tools in order to design and optimize the best forming process. These numerical methodologies are mainly based on the widely used finite element method (FEM) as in ([1], [2], [3]) or even on more recent numerical methods as Meshfree or Meshless methods [4]. In the most of these works, constitutive equations describing the thermomechanical behavior of the metallic materials are very simplified neglecting many important phenomena and their mutual interactions (coupling) as the kinematic hardening, the ductile damage, the microstructural nature of metals etc.

More recent works have focused on the use of advanced constitutive equations which try to take into account the main phenomena without neglecting their strong coupling and full interactions. The works developed by our team (UTT/LASMIS) since twenty years can be accounted among these recent works dedicated to the virtual metal forming using advanced fully coupled constitutive equations ([5] to [11]). A comprehensive summary and recent state of the art of these works can be found in the recent books by Saanouni ([10], [11]).

In this invited paper, a very short summary of the main aspects of virtual metal forming using advanced multiphysical constitutive equations will be discussed and one illustrative example will be given.

2. About the advanced thermomechanical constitutive equations

As discussed in the introduction above, constitutive equations with high predictive capabilities are required for virtual metal forming where highly nonlinear phenomena are exhibited as large inelastic strains, nonlinear isotropic and kinematic hardening, ductile damage initiation and growth, initial and induced anisotropies due to the inelastic flow or to the ductile damage, strong thermal exchanges with highly localized thermal zones, ductile fracture initiation and growth inside intensive (adiabatic) shear bands, microstructure evolution under severe mechanical and thermal loading conditions, ... To model these phenomena and their mutual interactions or strong coupling, two approaches can be used: the macroscopic or mono-scale approach and the micro-macro or multi-scale approach. In both approaches, the ductile damage effects lead to induced softening which modifies completely the nature of the initial and boundary value problems and induces a high sensitivity to the time and space discretization. This requires the use of the mechanics of the generalized continua called the nonlocal mechanics based either on higher grade continua or higher order continua ([10] to [14]).

2.1. Micromorphic nonlocal fully coupled constitutive equations

A complete set of fully coupled constitutive equations can be developed in the framework of the rational thermodynamics of irreversible processes with couples of state variables representing the required thermomechanical phenomena. The detailed derivation of these constitutive equations can be found in our publications given in references list and mainly in the two recent books ([10], [11]). Here, for the sake of shortness, we limit ourselves to giving the final equations of the fully coupled nonlocal constitutive equations for isotropic metallic material developed in the framework of micromorphic continua under isothermal condition for the sake of simplicity. This consists in introducing additional micromorphic

(isotropic) state variables corresponding to the micromorphic damage $((\bar{d}, \bar{Y}))$ and $(\bar{\nabla}\bar{d}, \bar{Y})$, micromorphic isotropic hardening $((\bar{r}, \bar{R}), (\bar{\nabla}\bar{r}, \bar{R}))$ and micromorphic kinematic hardening $((\bar{\alpha}, \bar{X}), (\bar{\nabla}\bar{\alpha}, \bar{X}))$. This defines a first gradient micromorphic theory as can be found in [10, 11] and leads to the enrichment of the state relations and the evolution equations by nonlocal terms which are simply added to the classical local contributions. Also the application of the principle of virtual power when the corresponding micromorphic degrees of freedom \bar{d} , \bar{r} and $\bar{\alpha}$ are introduced, leads to additional micromorphic balance equations (see later in §3).

Accordingly, if we limit ourselves to the fully isotropic and isothermal case for the sake of shortness, the micromorphic constitutive equations write as following:

Micromorphic state variables: defined in the rotated configuration by :

$$\text{- Cauchy stress tensor } \bar{\sigma} = \bar{\sigma}_{loc} = (1-d) \left[2\mu_e \bar{\varepsilon}^e + \lambda_e \text{tr}(\bar{\varepsilon}^e) \mathbf{1} \right] \quad (1)$$

$$\text{- Kinematic hardening stress tensor: } \bar{X} = \bar{X}_{loc} + \bar{X}_{nloc} \text{ and } \bar{X}_{loc} = (2/3)(1-d)C\bar{\alpha}, \\ \bar{X}_{nloc} = -\sqrt{(1-d)}\bar{X}. \quad (2)$$

$$\text{- Isotropic hardening stress: } \bar{R} = \bar{R}_{loc} + \bar{R}_{nloc} \text{ and } \bar{R}_{loc} = (1-d)Qr, \bar{R}_{nloc} = -\sqrt{(1-d)}\bar{R} \quad (3)$$

$$\text{- Damage force } Y = Y_{loc} + Y_{nloc} : \begin{cases} Y_{loc} = (1/2)\bar{\varepsilon}^e : \underline{A} : \bar{\varepsilon}^e + (1/2)Qr^2 + (1/3)C\bar{\alpha} : \bar{\alpha} \\ Y_{nloc} = \bar{Y} - [\bar{R}r + \bar{X} : \bar{\alpha}] / (2\sqrt{1-d}) \end{cases} \quad (4)$$

$$\text{- Micromorphic back stress tensors: } \bar{X} = -\frac{1}{3}\bar{C} \left(\sqrt{(1-d)}\bar{\alpha} - \bar{\alpha} \right) \text{ and } \bar{X} = \bar{C}_g (\bar{\nabla}\bar{\alpha}) \quad (5)$$

$$\text{- Micromorphic isotropic stresses: } \bar{R} = -\bar{Q} \left(\sqrt{(1-d)}r - \bar{r} \right) \text{ and } \bar{R} = \bar{Q}_g (\bar{\nabla}\bar{r}). \quad (6)$$

$$\text{- Micromorphic damage forces: } \bar{Y} = -\bar{H}(d - \bar{d}) \text{ and } \bar{Y} = \bar{H}_g (\bar{\nabla}\bar{d}). \quad (7)$$

In addition to the classical elasticity (μ_e, λ_e) and hardening (C, Q) modules, new micromorphic modules $(\bar{C}, \bar{C}_g, \bar{Q}, \bar{Q}_g, \bar{H}$ and $\bar{H}_g)$ are added to characterize the three micromorphic phenomena under concern.

Micromorphic evolution equations: defined in the rotated single surface fully non-associative theory assuming the small elastic strain (i.e. $\bar{D} = \bar{\varepsilon}^e + 2(\bar{\varepsilon}^e \cdot \bar{Q})^{sym} + \bar{D}^p$) by:

$$\text{- Plastic strain rate: } \bar{D}^p = \bar{D}_{loc}^p = \lambda \bar{n} / \sqrt{1-d} \text{ where } \bar{n} = 3(\bar{\sigma}^{dev} - \bar{X}) / (2\|\bar{\sigma} - \bar{X}\|) \quad (8)$$

- Kinematic strain rate:

$$\dot{\bar{\alpha}} = \dot{\bar{\alpha}}_{loc} + \dot{\bar{\alpha}}_{nloc} \text{ where } \begin{cases} \dot{\bar{\alpha}}_{loc} = \bar{D}_{loc}^p - a\lambda\bar{\alpha} \\ \dot{\bar{\alpha}}_{nloc} = -\lambda a(\bar{C}/C) \left(\sqrt{(1-d)}\bar{\alpha} - \bar{\alpha} \right) / \sqrt{(1-d)} \end{cases} \quad (9)$$

- Isotropic strain rate: $\dot{r} = \dot{r}_{loc} + \dot{r}_{nloc}$ where
$$\begin{cases} \dot{r}_{loc} = \dot{\lambda}(1-br\sqrt{1-d})/\sqrt{1-d} \\ \dot{r}_{nloc} = -\dot{\lambda}b(\bar{Q}_r/Q)(\sqrt{(1-d)r-\bar{r}})/\sqrt{(1-d)} \end{cases} \quad (10)$$

- Damage rate: $\dot{d} = \dot{\lambda}[\langle Y - Y_y \rangle / S]^s / (1-d)^\beta$. (11)

- Total rotation rate tensor: $\underline{\dot{Q}}\underline{Q}^T = \underline{\dot{Q}} - \bar{\underline{Q}}$ with $\underline{Q}(t=0) = \underline{1}$. (12)

where $\dot{\lambda}$ is the single plastic multiplier $\dot{\lambda}$ can be deduced from the consistency condition applied to the yield criterion $f(\bar{\underline{\sigma}}, \bar{\underline{X}}, \bar{R}) = \|\bar{\underline{\sigma}} - \bar{\underline{X}}\| - \bar{R} - \sigma_y$, σ_y being the limit yield stress and Y_y is the threshold for the damage force invariant below which the damage rate is zero and β_d , S_d and s_d are material parameters characterizing the ductile damage growth. The norms defined in the stress space : $\|\bar{\underline{\sigma}} - \bar{\underline{X}}\| = \sqrt{3(\bar{\underline{\sigma}}^{dev} - \bar{\underline{X}}) : (\bar{\underline{\sigma}}^{dev} - \bar{\underline{X}}) / 2}$ for this isotropic plastic flow. Finally, $\underline{\dot{Q}} - \bar{\underline{Q}}$ is the relative total rotation rate (spin) depending on the choice of the rotating frame (Green-Naghdi, Zaremba-Jaumann, ...).

2.2. About the identification methodology

As can be clearly noticed from the constitutive equations presented above, numerous material parameters should be determined for each material before using these constitutive equations in virtual metal forming. This can be done using an appropriate methodology combining the well known inverse approach together with appropriate experimental results obtained on a wide range of loading conditions (loading paths, velocity, temperature, etc). This kind of identification methodology can be found in Chapter 4 of [10] or [11] which allows the determination of the overall material parameters for each material used.

3. About numerical aspects

As mentioned above the initial and boundary value problem (IBVP) defining the virtual metal forming problems, is defined by various strong forms which are, in this micromorphic formulation, for a solid \wp_t of boundary Γ_t and at each time t ([10], [11]):

- the equilibrium equations:

$$\begin{cases} \overline{\text{div}}(\underline{\sigma}) + \bar{f} = \rho_t \bar{\gamma} & \text{in } \wp_t \\ \underline{\sigma} \cdot \bar{n} = \bar{F} & \text{on } \Gamma_t \end{cases} \quad (13)$$

- the micromorphic damage balance equations:

$$\begin{cases} \ell_{\bar{d}}^2 \overline{\text{Lap}}(\bar{d}) + (d - \bar{d}) = \rho \frac{\zeta_{\bar{d}}}{\bar{H}} \ddot{\bar{d}} & \text{in } \wp_t \\ (\bar{H}_g(\bar{\nabla} \bar{d})) \cdot \bar{n} = 0 & \text{on } \Gamma_t \end{cases} \quad \text{where } \ell_{\bar{d}} = \sqrt{\frac{\bar{H}_g}{\bar{H}}} \quad (14)$$

- the micromorphic isotropic hardening balance equations:

$$\begin{cases} \ell_{\bar{r}}^2 \text{Lap}(\bar{r}) + (\sqrt{(1-d)r - \bar{r}}) = \frac{\rho \zeta_{\bar{r}}}{Q} \ddot{\bar{r}} & \text{in } \mathcal{P}_t \\ (\bar{Q}_g(\bar{\nabla}\bar{r})) \cdot \bar{n} = 0 & \text{on } \Gamma_t \end{cases} \quad \text{where } \ell_{\bar{r}} = \sqrt{\frac{\bar{Q}_g}{Q}}. \quad (15)$$

- the micromorphic kinematic hardening balance equations:

$$\begin{cases} \ell_{\bar{\alpha}}^2 \text{Lap}(\bar{\alpha}) + (\sqrt{(1-D)\underline{\alpha} - \bar{\alpha}}) = \rho \frac{\zeta_{\bar{\alpha}}}{C} \ddot{\bar{\alpha}} & \text{in } \mathcal{P}_t \\ (\bar{C}_g(\bar{\nabla}\bar{\alpha})) \cdot \bar{n} = \underline{0} & \text{on } \Gamma_t \end{cases} \quad \text{where } \ell_{\bar{\alpha}} = \sqrt{\frac{\bar{C}_g}{C}}. \quad (16)$$

where the overall micromorphic body forces and contact forces have been neglected for the sake of simplicity, and $\zeta_{\bar{d}}$, $\zeta_{\bar{r}}$ and $\zeta_{\bar{\alpha}}$ are parameters which map the classical local density to the micromorphic densities; $\ddot{\bar{d}}$, $\ddot{\bar{r}}$ and $\ddot{\bar{\alpha}}$ are the micromorphic accelerations related to the micromorphic damage, isotropic hardening and kinematic hardening; Θ_{in}^v is the classical local intrinsic dissipation. Finally, $\ell_{\bar{d}}$, $\ell_{\bar{r}}$ and $\ell_{\bar{\alpha}}$ are nothing but the internal lengths related to the three micromorphic phenomena under concern.

These four strong forms lead to four associated weak forms at the basis of the finite element formulation giving five fully coupled algebraic systems to be solved using either a dynamic iterative implicit (Newton-Raphson) or dynamic explicit resolution scheme. Note that for virtual metal forming, the dynamic explicit resolution scheme is preferred due to the difficulties to obtain consistent tangent matrix and to the contact with friction as well the damage induced softening.

The global resolution scheme requires the local numerical integration, at each integration point of each finite element, of the fully coupled constitutive equations (Eq. (1) to (12)). This can be performed thanks to a fully implicit iterative integration scheme based on the elastic prediction and plastic correction algorithm combined with an asymptotic scheme applied to the hardening constitutive equations.

A fully adaptive numerical methodology can be constructed in order to solve the IBVP over each time increment using a fully adaptive remeshing procedure. This latter uses various error indicators based on the local curvature of the contact surfaces as well as the plastic and damage dissipation. A 2D or 3D mesh generator is used to generate the new mesh after the fully damaged elements deletion, and appropriate operators are used to transfer the thermomechanical fields from the old to the new mesh after each loading sequence ([9], [10], [11]).

4. One illustrative example

The numerical methodology outlined above has been extensively used in ([5] to [11]) in order to perform various sheet and bulk metal forming processes. Without going more in detail, one illustrative example is given in Fig.1 concerning the simulation of the expansion test performed in order to measure the ductile fracture of thick sheets made in high strength steel. The results compare the numerically simulated process where clearly four main cracks are predicted at the end in accordance with the experimental result shown in Fig. 1d.

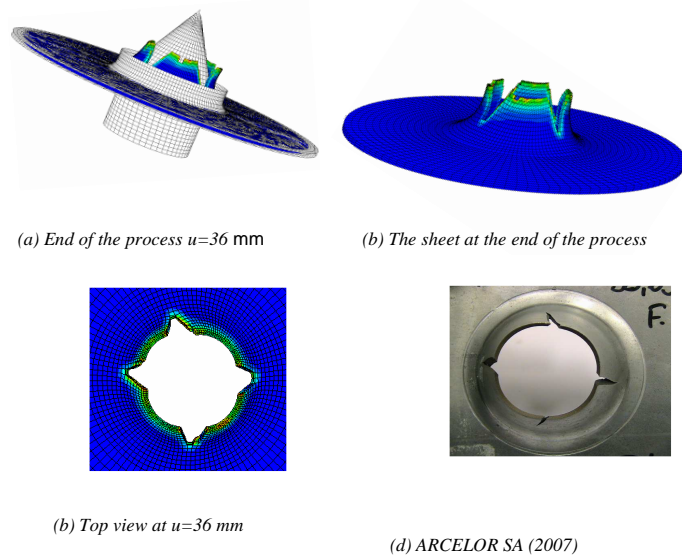


Figure 1. Final results of the expansion process of a thick sheet (from [10], [11])

Acknowledgement. This paper summarizes the results obtained by our research team (ICD/LASMIS) during more than 10 years. Many thanks are due to all my PhD students as well as to my colleagues C. Labergère and H. Badreddine.

References

- [1] Kobayashi S., Oh S.I., Altan T., Metal Forming and the Finite Element Method, Oxford University Press, Oxford, 1989)
- [2] Wagoner R.H., Chenot J.L., Metal Forming Analysis, Cambridge University Press, Cambridge, 2001.
- [3] Dixit P.M., Dixit U.S., Modeling of Metal Forming and Machining Processes by Finite Element and Soft Computing Methods, Springer Verlag, London, 2008
- [4] Chinesta F., Cescotto S., Cueto E., Lorong P., La méthode des éléments naturels en calcul des structures et simulation des procédés, Hermès, Paris, 2009
- [5] Saanouni K., On the numerical prediction of the ductile fracture in metal forming, Engineering Fracture Mechanics, Volume 75, 2008, pp: 3545-3559
- [6] Badreddine H., Saanouni K., Dogui A., On non associative anisotropic finite plasticity fully coupled with isotropic ductile damage for metal forming, International Journal of Plasticity, 26, 2010, 1541-1575
- [7] Saanouni K., Belamri N., Autesserre P., Finite element simulation of 3D sheet metal guillotining using advanced fully coupled elasto-plastic damage constitutive equations, Journal of Finite Elements in Analysis & Design, 46 (2010) 535-550
- [8] Saanouni K., Lestriez P., Labergère C., 2D adaptive simulations in finite thermo-elasto-viscoplasticity with ductile damage : Application to orthogonal metal cutting by chip formation and breaking, Int. J. of Damage Mechanics, Vol: 20, N°:1, January 2011, pp. 23-61
- [9] Labergère C., Rassineux A., Saanouni K., 2D adaptive mesh methodology for the simulation of metal forming processes with damage, Int. J. Mater. Forming, 4, 2011, pp:317-328
- [10] Saanouni K., 'Modélisation et simulation numériques en formage Virtuel', Hermes, Paris 2012, ISBN: 978-2746232259.
- [11] Saanouni K., 'Damage Mechanics in metal forming. Advanced modeling and numerical simulation', John Wiley, London 2012, ISBN: 978-1848213487
- [12] Eringen A.C., Microcontinuum Field Theories. I: Foundation and Solids, Springer Verlag, New York, 1999
- [13] Eringen A.C., Nonlocal Continuum Field Theories, Springer Verlag, New York, 2002
- [14] Forest S., Milieux continus généralisés et milieux hétérogènes, Presses de l'école des Mines, Paris, 2006

MODELLING AND NUMERICAL SIMULATION OF THICK SHEETS SLITTING USING CONTINUUM DAMAGE MECHANICS

Y.GHOZZI, C. LABERGERE, K. SAANOUNI

ICD/LASMIS, STMR UMR-CNRS 6279, University of Technology of Troyes
12, Rue Marie Curie – BP2060- 10000 Troyes cedex France
E-mail : yosr.ghozzi@utt.fr, carl.labergere@utt.fr, khemais.saanouni@utt.fr

Abstract. The continuum damage mechanics (CDM) has now reached a high level of maturity and is currently used to solve various engineering problems involving the development of various kinds of fracture [1], [2], [9], [11], [13], [14]. This work consists in the modelling and numerical simulation of specific cutting processes of more or less thick sheets using CDM. First, a thermodynamically-consistent constitutive equations strongly coupled with ductile damage is presented [10], [11], [12]. Attention is paid to the strong coupling between all the mechanical fields accounted for and the ductile damage. The associated numerical aspects dealing with either the local integration scheme as well as the global resolution scheme using the standard FEM are then briefly presented. Application is made to the modelling and numerical simulation of some sheet slitting processes. The obtained numerical results show the ability of the proposed CDM-based methodology to reproduce accurately the slitting process. A parametric study aiming to examine the sensitivity of the process parameters such as the sheet thickness, step of blade advance and clearance cutting is presented.

1. Introduction

Sixty years ago, industrialists optimize cutting processes to choose the required technological parameters based on the trial-error expensive approach. Indeed, studies concentrate on decreasing the cutting effort and energy by studying closely tool penetration till fracture. Some research works took lead with regard to the simulation of cutting processes of thin sheets. Two approaches are often used to model the material behavior including the ductile fracture effects. The first is introduced by Gurson ([3]) and the second one is based on CDM approach as developed in Lemaitre [7]. Nowadays, numerical simulation of thick sheet metal cutting processes gives a very useful optimization tool for engineering industries. In the present work, we are interested in cutting processes by shearing of thick sheet metal using a thermodynamically-consistent constitutive equations strongly coupled with isotropic damage. In fact, the local CDM approach is now currently used to introduce the ductile damage effect [7], [12] in order to predict metal cutting processes [10], [11], [12]. Thus, we propose a double slitting modeling process, more particularly for the tools motion and the choice of boundary conditions. A numerical analysis of fracture topographies and cutting force for different configurations (thickness, clearance...) are studied.

2. Coupled constitutive equations

The coupling between the ductile damage and the elastoplastic constitutive equations is formulated in the framework of the thermodynamics of irreversible processes together with the Continuum Damage Mechanics (CDM) approach [10], [11], [12]. Here, we are interested in the strongly coupled isothermal elastoplasticity and ductile isotropic damage. Thus, the following state variables are used: $(\underline{\epsilon}^e, \underline{\sigma})$ for small elastic strain tensor and the Cauchy stress tensor, $(\underline{\alpha}, \underline{X})$ for the back-strain and back-stress deviator tensors describing the kinematic hardening, (r, R) equivalent plastic driving strain and stress representing the isotropic hardening and (D, Y) for isotropic ductile damage and its conjugate force, which is also known as a damage strain energy release rate. The coupled constitutive equations formulated in the rotated configuration according to the objectivity requirement using the below defined state variables [4], [12]:

$$\text{Cauchy stress tensor: } \underline{\sigma} = (1-D)[\lambda^e \text{tr} \underline{\epsilon}^e \mathbf{1} + 2\mu^e \underline{\epsilon}^e] \quad (1)$$

$$\text{Kinematic hardening stress tensor: } \underline{X} = \frac{2}{3}(1-D)C\underline{\alpha} \quad (2)$$

$$\text{Isotropic hardening stress: } R = Q(1-D^\omega)r \quad (3)$$

$$\text{Isotropic damage: } Y = Y_e + Y_{ine} = \left[\frac{1}{2} \lambda (\text{tr} \underline{\epsilon}^e)^2 + \mu \text{tr} (\underline{\epsilon}^e)^2 \right] + \left[\frac{2}{3} C \underline{\alpha} : \underline{\alpha} + \frac{1}{2} \omega D^{\omega-1} Q r^2 \right] \quad (4)$$

To accounts for the effect of dissymmetry in the damage evolution and effects under tension and compression due to the microcracks closure [7], the Cauchy stress tensor is decomposed according to:

$$\tilde{\underline{\sigma}} = \frac{\underline{\sigma}^+}{\sqrt{1-D}} + \frac{\underline{\sigma}^-}{\sqrt{1-hD}} \quad (5)$$

Thus, a new form of the elastic contribution of the damage driving force is obtained in the stress principal frame:

$$Y_e = \frac{1}{2E(1-D)} \left[\begin{array}{l} (1+\nu) [\langle \sigma_I \rangle^2 + \langle \sigma_{II} \rangle^2 + \langle \sigma_{III} \rangle^2] - 9\nu \langle \sigma_H \rangle^2 \text{Tension} \\ + h(1+\nu) [\langle -\sigma_I \rangle^2 + \langle -\sigma_{II} \rangle^2 + \langle -\sigma_{III} \rangle^2] - 9\nu \langle -\sigma_H \rangle^2 \text{Compression} \end{array} \right] \quad (6)$$

where $\sigma_H = 1/3 \text{tr}(\underline{\sigma})$ and $\sigma_I, \sigma_{II}, \sigma_{III}$ are the principal stresses. Some materials exhibit some microstructural instabilities at the beginning of the plastic flow due to the nucleation of the so-called Piobert-Lüders bands. To accounts for this phenomenon, the plasticity is chosen as rigid plastic during the first percentages of the plastic strain. Therefore, an additional parameter noted “ p^* ” which serves as a threshold in terms of accumulated plastic strain:

$$\underline{D}_p = \delta \underline{n}, \text{ where } \underline{n} = \tilde{n} / \sqrt{1-D} \quad (7)$$

$$\text{if } (p > p^*) \dot{\underline{\alpha}} = \delta (\underline{n} - a\underline{\alpha}) \text{ else } \dot{\underline{\alpha}} = \underline{0} \quad (8)$$

$$\text{if } (p > p^*) \dot{r} = \delta \left(\frac{1}{\sqrt{1-D^\omega}} - br \right) \text{ else } \dot{r} = 0 \quad (9)$$

$$\dot{D} = \left(\frac{\langle Y - Y_0 \rangle}{S} \right)^s \frac{\delta}{(1-D)^\beta} \quad (10)$$

with δ is the plastic multiplier, a and b are the nonlinearity parameters for kinematic and isotropic hardening, respectively and \underline{n} is the outward normal to the isotropic von Mises yield function. These constitutive equations have been discretized using a fully implicit time discretization scheme together with the elastic predictor and plastic corrector method. This algorithm has been implemented in ABAQUS/EXPLICIT FE package using the user's subroutine VUMAT (see references [11], [12] for more detail). The initial and boundary value problem is solved thanks to the dynamic explicit resolution scheme available in ABAQUS/EXPLICIT [6].

3. Double slitting process modeling

The double slitting process is schematized in Figure 1. By a combination of connecting rods, the cutting press requires an oscillatory motion of the longitudinal blade (Fig.1). From a kinematic diagram, we have developed the motion equation of the transversal and longitudinal blade which is introduced in Abaqus using a specific VUAMP subroutine. In the modeling the tools are taken as rigid bodies. The Coulomb model is used to define the friction between the upper blade and the sheet metal with the friction coefficient $\eta=0.3$. The sheet is discretized using 3D hexahedral elements (C3D8R) with a mesh size progressively

evolving from the smallest size of (1x1x4) in the shearing area to the maximum size of 2.5x6.0x12.0 away from the shearing zone. An inverse identification procedure gives the following material parameters for specific steel: $E=220$ GPa, $\nu=0.29$, $\sigma_y=738$ MPa, $Q=1680$ MPa, $b=8$, $C=6800$ MPa, $a=120$, $S=2.5$ MPa, $s=1.2$, $\beta=0.5$, $Y_0=0.7$, $\omega=4$.

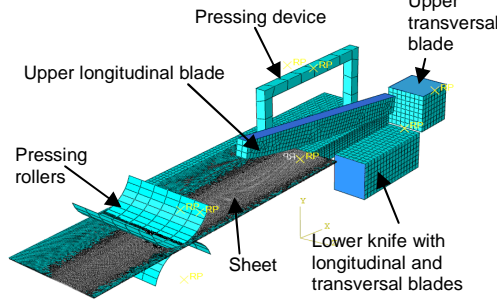


Fig.1: Schematic representation of the double slitting

4. Process parameter influence

Fig.2 shows different steps along cutting cycles. One cycle is divided on four stages. Stage 1: the sheet is clamped to the lower blade by a pressing device. Stage 2: oscillatory motion of the upper blade leading to the sheet cutting operation. Stage 3: back pressing device. Stage 4: rotation of pressing roller which results from longitudinal (x axis) displacement of the sheet at a distance "p". The time of one cycle process is 0.1s.

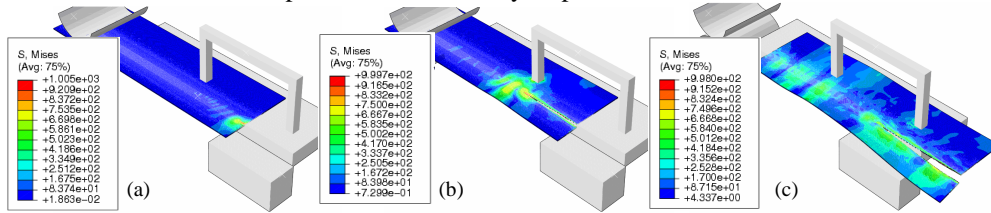


Fig.2: von Mises iso-values: (a) time=3.66e-2s, (b) time=5.46e-2s, (c) time=7.4e-2s

Figure 3 shows the evolution of the cutting force for various thicknesses. The cutting force is quite proportional to the thickness of sheet. For large thick sheet, the cutting force can be divided to four stages. Stage I represents a fast increase in the cutting force until its maximum because the upper blade comes in contact with sheet metal that hardens; Stage II corresponds to the progressive failure of the sheet; stage III corresponds to a constant force which corresponds to the bottom dead center of the blade and stage IV corresponds to the release of the blade. After cutting, the sheet metal moves with a step displacement p. For the first cycle, p represents the initial longitudinal position of the sheet to the lower blade.

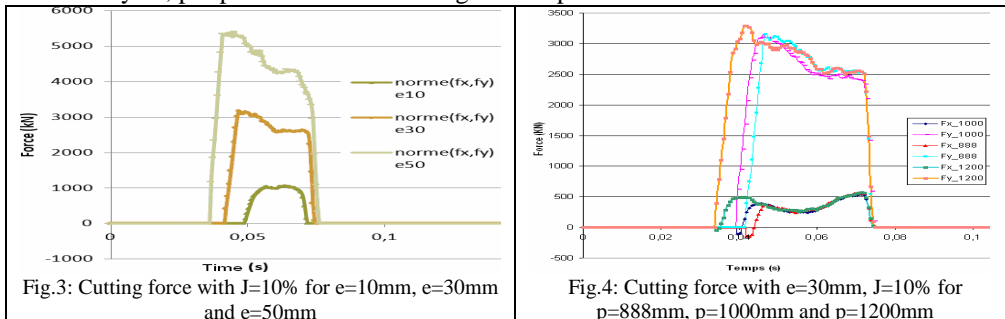
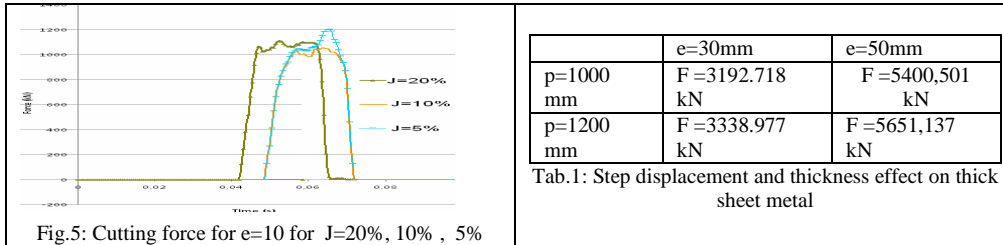


Fig.3: Cutting force with $J=10\%$ for $e=10$ mm, $e=30$ mm and $e=50$ mm

Fig.4: Cutting force with $e=30$ mm, $J=10\%$ for $p=888$ mm, $p=1000$ mm and $p=1200$ mm



The evolution of the cutting force is also proportional to “p” (Fig.4) simply because the quantity of sheet shearing zone increase when p increase. According to the data in table 1, for e=30mm, the cutting force increases with 4.38% from p=1000mm to 1200mm, and with about 4.43% for e=50mm. Figure 5 shows that the clearance has very little influence on the cutting force, but often helps to improve the fracture topography (this aspect is quite presented in [5]). Nonetheless, these results are extremely dependent on the element size in the cutting zone and a sensitivity analysis of the mesh size would be necessary to fully achieve the studies of the numerical simulation of the double slitting process.

5. Conclusion

We proposed in this paper a complete numerical simulation of the double slitting process with particular emphasis on the behavioral model and modeling of the ductile damage effect. A sensitivity study of some of process parameters (thickness, displacement “p” and clearance), cutting force was proposed and analyzed. Application to the 3D double slitting of thick sheet validates the proposed numerical approach with the adapted process parameters. In fact, the obtained results are encouraging and the methodology is then useful to optimize the specific shearing process. Further, an adaptive meshing procedure is required to improve the modelling procedure.

References

- [1] Brokken D., Brekelmans W.A.M., Baaijens F.P.T., (2000), Discrete ductile fracture modelling for the metal blanking process, *Comp. Mech.*, **26**, pp. 104-114
- [2] Ghosh S., Li M., Khadke A., (2005), 3D modeling of shear-slitting process for aluminum alloys. *Journal of materials processing technology*, Volume 167, Issue 1, Pages 91-102
- [3] Gurson A.L., (1977), Continuum theory of ductile rupture by void nucleation and growth: Part I-Yield criteria and flow rules for porous ductile media, *J. Eng. Mat. Tech.*, vol. 99.
- [4] Issa M., Saanouni K., Labergere C., Rassineux A., (2011), Prediction of serrated chip formation in orthogonal metal cutting by advanced adaptive 2D numerical methodology, *International Journal of Machining and Machinability*, vol 9, 295-315
- [5] Komori K., (2001), Simulation of shearing by node separation method, *Comput. Struct.*, **79** , pp. 197–207
- [6] Labergere C., Rassineux A., Saanouni K., (2010), 2D adaptive mesh methodology for the simulation of metal forming processes with damage, *International Journal of Material Forming*, pp 1-12
- [7] Lemaitre J., (1992), *A Course of Damage Mechanics*, Springer-Verlag, Heidelberg
- [8] Lemiale V., (2004), Contribution à la modélisation et à la simulation numérique et à la simulation numérique du découpage des métaux, Thèse de doctorat, Université de Franche-Comté, Besançon
- [9] Pyttel T., John R., Hoogen M., (2000), A finite element based model for the description of aluminum sheet blanking, *Int. J. Machine Tools Manuf.*, **40** , pp. 1993–2002
- [10] Saanouni K., (2008) On the numerical prediction of the ductile fracture in metal forming, *Engineering Fracture Mechanics*, Volume 75, , pages 3545-3559
- [11] Saanouni K., Belamri N., Autesserre P., (2010), Finite element simulation of 3D sheet metal guillotining using advanced fully coupled elasto-plastic damage constitutive equations, *Journal of Finite Elements in Analysis & Design*, **46** , 535-550
- [12] Saanouni K., Chaboche J.L., (2003), Computational damage mechanics. Application to metal forming, *Numerical and Computational methods*. chap. 3, p. 321-376.
- [13] Taupin E., Breiting J., Wu T.W., Atlan T., (1996), Materials fracture and burr formation in blanking results of FEM simulations and comparison with experiments, *J. Mater. Proc. Tech.*, **59**, pp. 68–78
- [14] Wisselink H. H., Huélink J., (2004) 3D FEM simulation of stationary metal forming processes with applications to slitting and rolling. *Journal of materials process. Tech.*, Vol.148, Issue 3, , pp. 328-341

MICROMORPHIC APPROACH FOR NONLOCAL FULLY COUPLED ELASTOPLASTIC-DAMAGE CONSTITUTIVE EQUATIONS

M. Hamed, K. Saanouni

ICD/LASMIS, STMR UMR-CNRS 6279, University of Technology of Troyes
12, Rue Marie Curie – BP2060- 10000 Troyes cedex France
khemais.saanouni@utt.fr , Mohamed.hamed@utt.fr

Abstract. The present paper is devoted to solving the pathological mesh dependency of FEM numerical results of Initial and boundary value problems (IBVP) exhibiting damage-induced softening. A thermodynamically-consistent formulation incorporating micromorphic damage gradient in the framework of micromorphic continuum is proposed. In this formulation the damage field is strongly coupled with a mixed isotropic and kinematic nonlinear hardening together with micromorphic damage variables. The micromorphic damage variable is introduced as a Degree of Freedom (DoF) in the principle of virtual power and its first gradient as a state variable in the state potential. By using the principle of virtual power in the framework of the micromorphic continuum, an additional Partial Differential Equations (PDE) together with appropriate boundary conditions are obtained. A new finite element using one additional DoF for the micromorphic damage field is developed, and implemented into ABAQUS/EXPLICIT using the user's subroutine VUEL. While the micromorphic model is implemented using the VUMAT subroutine. For the validation purpose, the 2D strain plane uniaxial compression of metallic cylinder is performed using fully coupled elastoplastic constitutive equations with mixed hardening fully coupled with the ductile isotropic damage. For a given choice of the model parameters, the proposed micromorphic methodology is shown to be efficient in avoiding the pathological mesh dependency.

1. Introduction

It is well established, nowadays, that the initial and boundary value problems (IBVPs) exhibiting some induced softening due to damage phenomena, lead to solutions highly sensitive to the space and time discretization. Many works were developed to avoid this problem with several methods. One can find two types of methods: the approximate nonlocal methods and the straightforward nonlocal methods. The approximate methods consist in introducing some "localization limiters" in the classical local constitutive equations under concern, using either higher order of strain-gradients, damage-gradients or equivalently some averaging using specific integral equations ([1], [2], [3], [4] among many others). The straightforward theories are based on the framework of generalized continua that makes it possible the natural introduction of the characteristic lengths into the constitutive equations of materials with microstructure ([5], [6], [7] among others). The present work uses the generalized micromorphic theory in order to formulate additional micromorphic balance equation governing the micromorphic damage as well as damage-

gradient micromorphic constitutive equations deduced from the thermodynamics of irreversible processes with additional micromorphic state variables. The IBVP resulting from this formulation is formulated and numerically discretized using specific finite element with the micromorphic damage as an additional DoF. Applications to some typical examples show the efficiency of the proposed micromorphic formulation in ensuring a mesh independent solution [8].

2. Formulation of the micromorphic evolution problem

Damage, which is the main cause of the mesh dependency to the solution of IBVP, is selected as the sole target micromorphic phenomenon represented by the micromorphic scalar variable \tilde{D} . Following, the micromorphic theory [5], \tilde{D} is taken as the additional DoF in the principle of virtual power. On the other hand, two new pairs of micromorphic state variables namely (\tilde{D}, \tilde{Y}) and $(\tilde{\nabla}\tilde{D}, \tilde{\tilde{Y}})$ are added to the state variables space.

2.1. The additional micromorphic balance equation

By writing the generalized principle of the virtual power while taking the displacement vector \tilde{u} and the micromorphic damage \tilde{D} as degrees of freedom, one easily obtain the following balance equations [7, 8]:

$$\left\{ \begin{array}{l} \text{div}(\underline{\sigma}) + \rho \tilde{f}^u = \rho \ddot{\tilde{u}} \\ \underline{\sigma} \cdot \tilde{n} = \tilde{F}^u \end{array} \right. \quad \text{in } \Omega \quad \text{on } \Gamma_u \quad \text{(a)} \quad \left\{ \begin{array}{l} \text{div}(\tilde{Y} - \tilde{f}^{s\tilde{D}}) - (\tilde{Y} - f^{\tilde{D}}) = \rho \zeta_d \ddot{\tilde{d}} \\ (\tilde{Y} - \tilde{f}^{s\tilde{D}}) \cdot \tilde{n} = F^{\tilde{D}} \end{array} \right. \quad \text{in } \Omega \quad \text{on } \Gamma_{F^{\tilde{D}}} \quad \text{(b)} \quad (1)$$

The first one is nothing but the classical equilibrium equations while the second one is a new balance equation related to the micromorphic damage.

2.2. Micromorphic constitutive equations

The standard space of local state variables is enriched by the new pairs of micromorphic state variables (\tilde{D}, \tilde{Y}) and $(\tilde{\nabla}\tilde{D}, \tilde{\tilde{Y}})$. By using the well known framework of the thermodynamics of irreversible processes with state variables the state relation as well the evolution equations of all the dissipative phenomena can be deduced from both the state and dissipation potentials. Adopting the non associative theory and assuming the isothermal and fully isotropic conditions, one can find [8]:

$$\underline{\sigma} = (1 - D) \left[\lambda_e \text{tr}(\underline{\varepsilon}^e) \underline{1} + 2\mu_e \underline{\varepsilon}^e \right] \quad \text{(a)} \quad \underline{\chi} = \frac{2}{3} (1 - D) C \underline{\alpha} \quad \text{(b)} \quad (2)$$

$$R = (1 - D) Q r \quad \text{(a)} \quad Y = \frac{1}{2} \underline{\varepsilon}^e : \underline{A} : \underline{\varepsilon}^e + \frac{1}{2} Q r^2 + \frac{1}{3} C \underline{\alpha} : \underline{\alpha} - \tilde{H} (D - \tilde{D}) \quad \text{(b)} \quad (3)$$

$$\tilde{Y} = -\tilde{H} (D - \tilde{D}) \quad \text{(a)} \quad \tilde{\tilde{Y}} = \tilde{H}^s (\tilde{\nabla}\tilde{D}) \quad \text{(b)} \quad (4)$$

where $\underline{\underline{A}} = \lambda_e \underline{\underline{1}} \otimes \underline{\underline{1}} + 2\mu_e \underline{\underline{1}}$ is the elastic properties tensor, Q and C are the isotropic and kinematic hardening moduli and \tilde{H} and \tilde{H}^s are the micromorphic damage moduli. On the other hand, by neglecting the micromorphic dissipation and using the non associative plasticity theory in fully isothermal and isotropic case, it comes [8]:

$$\dot{\underline{\underline{\epsilon}}}^p = \dot{\lambda}^p \underline{\underline{n}} = \dot{\lambda}^p \frac{\tilde{\underline{\underline{n}}}}{\sqrt{(1-D)}} \quad (\text{a}) \quad \tilde{\underline{\underline{n}}} = \frac{3(\underline{\underline{\sigma}}^{dev} - \underline{\underline{X}})}{2\|\underline{\underline{\sigma}} - \underline{\underline{X}}\|} \quad (\text{b}) \quad (5)$$

$$\dot{\underline{\underline{\alpha}}} = \frac{\dot{\lambda}^p}{\sqrt{(1-D)}} \left(\tilde{\underline{\underline{n}}} - a\sqrt{(1-D)}\underline{\underline{\alpha}} \right) \quad (\text{a}) \quad \dot{r} = \frac{\dot{\lambda}^p}{\sqrt{(1-D)}} \left(1 - b\sqrt{(1-D)}r \right) \quad (\text{b}) \quad (6)$$

$$\dot{D} = \frac{\dot{\lambda}^p}{(1-D)^\beta} \left(\frac{\langle Y - Y_0 \rangle}{S} \right)^s = \dot{\lambda}^p Y_D^* \quad (\text{a}) \quad f = \frac{\|\underline{\underline{\sigma}} - \underline{\underline{X}}\| - R}{\sqrt{(1-D)}} - \sigma_y \leq 0 \quad (\text{b}) \quad (7)$$

where $\dot{\lambda}^p$ is the classical plastic multiplier fulfilling the well known kahn-Tucker conditions.

3. Associated numerical aspects

The constitutive equations developed above have been implemented into ABAQUS/Explicit using the VUMAT user's developed subroutine. Also a new finite element with additional DoF (\bar{D}) has been implemented thanks to the user's subroutine VUEL. The IBVP has two fully coupled weak forms derived from eq. (1a and 1b). Their resolution was performed using a dynamic explicit sequential resolution scheme. The local integration scheme, used to compute the stress and state variables at each Gauss point and at each time step, is of iterative Newton-type based on the classical elastic-prediction and plastic correction procedure. All these numerical aspects can be found in [8].

4. Some applications

To illustrate the efficiency of the proposed micromorphic modelling and the associated numerical approach, some results are presented. The principal aim is to illustrate the ability of the proposed micromorphic model to give a numerical solution independent from the mesh discretization at convergence. The material parameters are defined by $E = 210 \text{ GPa}$, $\nu = 0.29$, $\sigma_y = 400 \text{ MPa}$, $Q = 1000 \text{ MPa}$, $b = 50$, $C = 10000 \text{ MPa}$, $a = 100$, $\beta = 1$, $S = 0.8$, $s = 1$, $Y_0 = 0$ and $\tilde{H}_d = 200 \text{ MPa}$ and $\tilde{H}_{gd} = 200 \text{ MPa.mm}^2$ leading to $\ell_{\bar{d}} = 1 \text{ mm}$. Due to the plane strain assumption only one section of the cylinder is considered and meshed using the micromorphic element (linear T3) of size $h_{\min} = 0.5 \text{ mm}$ as shown in Fig. 1a. The distribution of the damage inside the cyclinder is independent from the mesh size (fig. 1b). Further results and other examples available in [8] will be shown during the oral presentation.

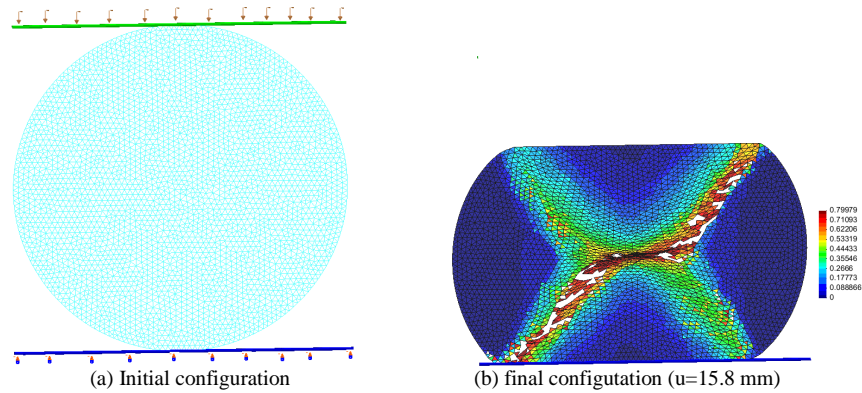


Figure 1. Side pressing of an infinite cylinder.

5. Conclusion

The micromorphic formulation of the initial and boundary value problem exhibiting some damage induced softening is shortly presented. The numerical results show the effective ability of the proposed micromorphic formulation to ensure a solution independent from the mesh size.

Acknowledgement. The financial support of the French ministry of high education is acknowledged.

References

- [1] Saanouni K, Chaboche J.L., Lesne P. M. (1989), On the creep crack-growth prediction by a nonlocal damage formulation, *European Journal of Mechanics, A/Solids*, 8, No:6, p.437-459
- [2] Jirasek M. (1996), Nonlocal Models for damage and fracture : comparison of approaches, *Int. J. Solids structures* Vol 35, Nos 31. 32, pp 4133-4145 elsevier
- [3] Peerlings R.H.J., Geers M.G.D, de Borst R., Brekelmans W.A.M. (2001), A critical comparison of nonlocal and gradient-enhanced softening continua, *Int. J. Solids and Structures*, 38, p. 7723-7746
- [4] Polizzotto (2003), Unified thermodynamic framework for non local/gradient continuum theories, *European Journal of Mechanics A/Solids* 22 2003 651-668, Elsevier
- [5] Eringen A. C. (1999), *Microcontinuum field theories: Foundation and solids*. Springer Verlag, New York
- [6] Eringen A. C. (2002), *Nonlocal continuum field theories*. Springer Verlag, New York, 2002.
- [7] Forest S. (2009), Micromorphic approach for gradient elasticity, viscoplasticity and damage, *ASCE Journal of Engineering Mechanics*, 135, 3, p.117-131.
- [8] Hamed M. (2012), *Formulations micromorphiques en élastoplasticité non locale avec endommagement en transformations finies.*, PhD thesis, UTT.

MICROMECHANICAL MODELING OF A DUPLEX STAINLESS STEEL – COMPARISON WITH MESOSCOPIC MEASUREMENT BY NEUTRON DIFFRACTION LEADING TO AN OBSERVATION OF DAMAGE

L. Le Joncour¹, B. Panicaud¹, A. Baczmanski², M. François¹.

¹ ICD-LASMIS, Université de Technologie de Troyes (UTT), UMR CNRS 6279, 12 rue Marie Curie, 10010 Troyes, France.

e-mail : benoit.panicaud@utt.fr, lea.le_joncour@utt.fr, manuel.francois@utt.fr.

² Faculty of Physics and Applied Computer Science, AGH- University of Science and Technology, Al Mickiewicza 30, 30-059 Krakow, Poland

e-mail: baczman@newton.ftj.agh.edu.

Abstract. In the present study, a two-phase polycrystalline plasticity model in the framework of scale transition methods is investigated. This model is an elastoplastic self-consistent model developed by Lipinski and Berveiller. Because of the microstructural complexity of the material under concern, some particular developments of the micromechanical approaches are considered. The modeling is justified from previous experimental results obtained especially by neutrons diffraction on a duplex stainless steel. These measurements, compared with numerical simulations, allow observing elasticity behavior, plasticity hardening of the duplex steel and a softening attributed to damage in the ferritic phase. Experimental damage values can eventually be extracted from a particular methodology at mesoscopic scale.

1. Introduction

Ductile damage is a consequence of large strains more or less localized inside intensive shear bands. Taking into account damage in constitutive behavior of metallic materials is necessary to model various engineering problems involved in sheet or bulk forming processes (deep drawing, hydroforming, forging, punching, shearing...). Damage can be described at macroscopic scale with continuum damage mechanics theories [1-2]. Moreover, introducing microstructural features can lead to more accurate predictions by accounting for the main physical phenomena. However, damage at mesoscopic scale is difficult to observe [3].

2. Experimental part

2.1. Material, sample and applied loading path

The studied material is an austeno-ferritic stainless steel, containing approximately 50% (vol.) austenite and 50% ferrite. It was obtained by continuous casting, and then hot rolled down to 15 mm sheet thickness. Its chemical composition is given in [4]. The characteristic microstructure of this steel consists of austenitic islands elongated along the rolling direction and embedded in a ferritic matrix. EBSD method showed that all crystallites of the ferritic phase have almost the same orientation, while austenitic islands are divided into smaller grains with different orientations of the lattice [5]. The sample (designated as UR45N) was annealed during 1000 hours at a

temperature of 400 °C and next cooled in ambient air. Tensile tests have been performed on cylindrical samples of 8 mm diameter along rolling direction RD.

2.2. Neutron diffraction

The ENGIN-X diffractometer [6] was used to measure interplanar spacings $\langle d \rangle_{\{hkl\}}$ applying time-of-flight (TOF) neutron diffraction method at the ISIS spallation neutron source. The experimental setup is detailed in [5]. The gauge volume size is 8 x 4 x 4 mm³. The elastic lattice strains $\langle \varepsilon_{RD} \rangle_{\{hkl\}}$ with respect to the initial interplanar spacings were calculated for different {hkl} reflections of the scattering vector, using a least square fitting procedure based on theoretical pseudo-Voigt function [7-8]:

$$\langle \varepsilon_{RD}^{elastic} \rangle_{\{hkl\}} = \ln \left(\frac{\langle d_{RD}^{\Sigma} \rangle_{\{hkl\}}}{\langle d_{RD}^0 \rangle_{\{hkl\}}} \right) \quad (1)$$

where $\langle d_{RD}^{\Sigma} \rangle_{\{hkl\}}$ and $\langle d_{RD}^0 \rangle_{\{hkl\}}$ are the interplanar spacings measured for a sample with and without external load; while the $\langle \rangle_{\{hkl\}}$ brackets denote the average over the volume of diffracting grains for which the scattering vector is perpendicular to the {hkl} planes. Integral width of the peaks have also been calculated and normalized in order to be compared with yield stress.

2. Modelling

The interpretation of neutron diffraction results is based on an elastoplastic self-consistent model without damage developed by Lipinski and Berveiller [9]. It was applied for neutron measurements on duplex steels by Baczmanski et al. [10]. This model have been presently modified to take into account non-linearity of hardening thanks to Voce equation, sometimes applied in self-consistent model for comparison with diffraction measurements:

$$f_{Voce}^g = \tilde{\tau}^s - \left(\tau_{C0}^g + (\tau_1^g + \theta_1^g \tilde{\vartheta}^g) \left[1 - \exp \left(- \frac{\theta_0^g}{\tau_1^g} \tilde{\vartheta}^g \right) \right] \right) \leq 0 \quad (2)$$

where $\tau_{C0}^g, \tau_1^g, \theta_1^g, \theta_0^g$ are material parameters and $\tilde{\vartheta}^g$ the accumulated slip inside a single grain.

The model as presented here is not able to represent damage. Simulations will be compared to the measured elastic lattice strain and normalized integral peak width with the theoretical values.

3. Results

3.1. Hardening

Comparison between ISIS measurements and self-consistent elastoplastic modelling is thus used to extract precisely plasticity thresholds and other plastic parameters from an optimization method directly at mesoscopic scale. Corresponding elasticity limits and hardening moduli by phases and obtained with an inverse method are summarized in Table 1.

Phase	Elasticity limit (MPa)	Hardening modulus (MPa)
Ferrite	350	130
Austenite	140	270

Table 1. Parameters of plastic deformation determined in tensile tests.

The yield stress τ_c is supposed to be directly linked with dislocation density [11], with b the burger vector norm, μ the shear modulus, α a material parameter and τ_c^0 the initial yield stress :

$$\tau_c = \tau_c^0 + \alpha\mu b\sqrt{\rho} \quad (3)$$

If dislocation density can be considered as homogenous, integral peak width from neutron diffraction is expected to be proportional to the yield stress variation (more precisely to the average of the Critical Resolved Shear Stress averaged on the diffracting grains). Before being compared with the yield stress, it has to be normalized using the following relation [12]:

$$\langle \Delta a_{RD} \rangle_{\{hkl\}} = \langle \Delta d_{RD} \rangle_{\{hkl\}} \sqrt{h^2 + k^2 + l^2} \quad (4)$$

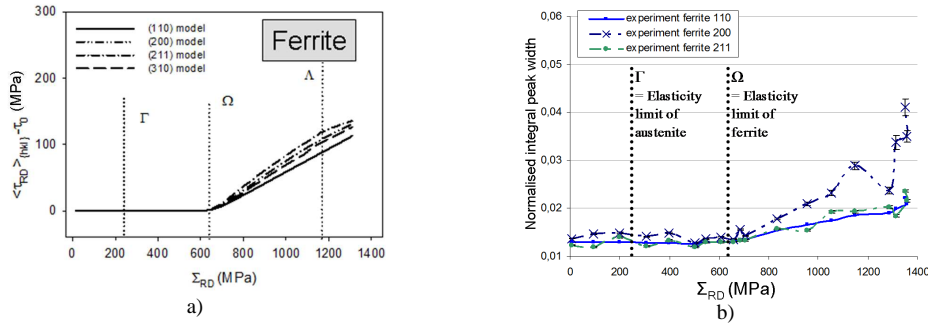


Fig 1. Yield stress evolution given by the model (a) compared with normalised integral peak width evolution (b) in $\{hkl\}$ lattice plans of ferrite, during tensile test.

In Fig. 1, the evolutions of normalized integral peak width and resolved shear stress in ferrite are shown. These results present a good correlation between model and experiments.

The limit Γ corresponding to the beginning of plasticity in austenite (observed at a macrostress around 250 MPa) has little impact on curves of integral width in Fig. 1 b), due to the elasticity of the ferritic phase that balances the load. It corresponds to the prediction of the model.

However, the plasticity of ferrite corresponding to the Ω limit can easily be observed in Fig. 1, when curves slopes are increasing at a macrostress of 600 MPa.

After this threshold, hardening is different in each family $\{hkl\}$ of grains. Experimental curves go up sharply at the end of the test just before failure. The slope of every integral width seems to increase, but the influence of damage on these curves cannot easily be established.

3.2. Damage

Elastic strains per $\{hkl\}$ lattice plans can also be observed. By making the average per phases, we can obtain distribution of elastic strains into ferrite and austenite that are proportional to stress into each phase. As said before, plastification of each phase can easily be seen on these curves.

As mentioned in section 2, damage process is not taken into account in the self-consistent calculations. Consequently, at the end of the loading, the discrepancy observed between experiment and modeling, seems to be due to damage effect. Moreover, this is well known that aging treatment causes transformation into ferritic phases that increases its hardness and can cause a higher fragility [12]. This damage in ferrite seems to cause relaxation of stresses into the ferritic phase due to the appearance of micro-cracks or cavities before the global failure of the sample, as depicted in Fig. 2. Damage per families $\{hkl\}$ of grain can be extracted using formula (5) established in [4]:

$$\delta_{\{hkl\}meso} = 1 - \left(\frac{\langle \varepsilon_{RD}^{elastic} \rangle_{\{hkl\}exp}}{\langle \varepsilon_{RD}^{elastic} \rangle_{\{hkl\}mod}} \right)^2 \quad (5)$$

Decrease of elastic strain before fracture can be observed in every families of diffracting grains in ferrite. Fig 3 shows the damage extracted for grains having {211} lattice plan in diffraction position. This family is the first in which the discrepancy with modeling can be observed. Furthermore, this family is also the one with the higher hardening in ferritic phase (Fig 1 a).

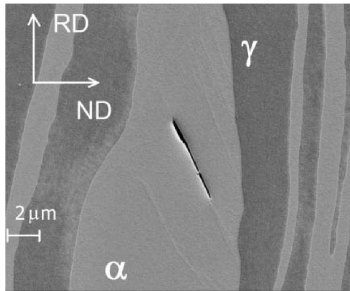


Fig 2. Micrography of UR45N showing a micro-crack into ferritic phase [5]

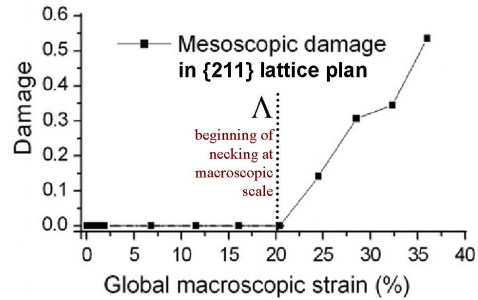


Fig 3 . Mesoscopic damage versus total macroscopic strain in a family of grains which {211} lattice plan is in diffraction position, during the tensile test

The beginning of damage for {211} grains family corresponds, at macroscopic scale, approximately at the beginning of necking. For other families, damage appears at the very end just before fracture of the sample. A limit corresponding to the beginning of damage is thus proposed at around 1150 MPa.

4. Conclusion

In the present work, diffraction method, compared to a micromechanical modelling, enables to investigate UR45N behavior until fracture. Damage and resolved shear stress evolution have been qualitatively measured and plasticity thresholds have been extracted at mesoscopic scale. Moreover the presented curves have shown a very good correlation between simulations and measurements that indicated a link between relaxation of stresses in {211} family of grains and necking, a damage limit was consequently introduced.

References

- [1] Saanouni K., Nesnas K. and Hammi Y. (July 2000), Damage modelling in metal forming processes. *International Journal of Damage Mechanics*, Vol. 9, pp 196-240.
- [2] Chaboche J.-L., Boudifa M., Saanouni K., (2006), A CDM approach of ductile damage with plastic compressibility, *International Journal of Fracture*, 137, pp 51-75.
- [3] Montheillet, F., and Moussy, F., (1986). *Physique et mécanique de l'endommagement*. Les éditions de la physique.
- [4] Le Joncour, L., Panicaud, B., Baczmanski, A., François, M., Braham, C., Paradowska, A.M., Wronski, S., Chiron, R. (2010), Damage in duplex steel studied at mesoscopic and macroscopic scales, *Mechanics of Materials*, 42-12, pp 1048-1063.
- [5] Baczmanski, A., Le Joncour, L., Panicaud, B., Francois, M., Braham, C., Paradowska, A. M., Wronski, S., Amara, S. and Chiron R., (2011), Neutron time-of-flight diffraction used to study aged duplex stainless at small and large deformation until sample fracture, *J. Appl. Cryst.* 44, pp 966-982.
- [6] Santisteban, J., James, J., Daymond, M., Edwards, L., (2006). *Journal of Applied Crystallography*. 39, pp 812-825.
- [7] François, M., Bourmiquel, B., Not, C., Guillén, R., Duval, C., (2000), *Zeitschrift für metallkunde*. 91/5, pp 414-420.
- [8] Courant, B., Bourmiquel, B., François, M., Bessière, M., (2000), *Materials Science Forum*. 347/3, pp161-165.
- [9] Lipinski, P., M. Berveiller, M., (1989) *Int. J. Plastic.* 5, pp 149-172.
- [10] Baczmański, A., C. Braham, C., (2004) *Acta Mater.* 52, pp 1133-1142.
- [11] Dakhlaoui, R., (2006), Analyse du comportement mécanique des constituants d'un alliage polycristallin multiphasé par diffraction des rayons X et neutronique, Phd manuscript, ENSAM
- [12] Le Joncour, L., (2011), *Analyses expérimentales et modélisations multi-échelles de l'endommagement d'un acier UR45N laminé vieilli*, Université de Technologie de Troyes.

ON ANISOTROPIC DAMAGE COUPLED WITH ELASTO-PLASTICITY AT FINITE STRAIN

T.Dung NGUYEN, H. BADREDDINE, K. SAANOUNI

ICD-LASMIS, Université de Technologie de Troyes (UTT), UMR CNRS 6279, 12 rue Marie Curie, 10010 Troyes, France
e-mail: trong_dung.nguyen@utt.fr, houssem.badreddine@utt.fr, khemais.saanouni@utt.fr

Abstract. This paper discusses an anisotropic damage constitutive model which is developed within the framework of thermodynamics and continuum damage mechanics. The anisotropic damage is taken into account by using a second-rank tensor while the effect of damage on the mechanical fields (stress, hardening, plastic deformation, etc...) is described by a fourth-rank damage effect operator that is defined in the context of the total energy equivalence hypothesis. This model is developed with the finite strain assumption based on multiplicative decomposition of the total transformation gradient and using the rotating frame formulation concept. A fully non associative plasticity theory is considered, while the coupling with the anisotropic ductile damage is based on a separate yield surface and plastic potential. The implementation of this model into ABAQUS finite element code is shortly presented and application to the bulge test forming process is discussed and compared to the isotropic damage case.

1. Introduction

In this work we propose a formulation of anisotropic plastic model coupled with anisotropic ductile damage in the thermodynamically-consistent framework. In this model the anisotropy of damage is described by a symmetric second-rank tensor [2, 3, 5, 6, 7, 10]. The effect of damage on the other mechanical fields is defined through the effective variables based on the assumption of the total energy equivalence. A fourth-rank damage effect tensor originally proposed in [3] and redefined in [2] and [5] is used while the coupling with the stress and elastic strain tensors is carried out separately on the hydrostatic and deviatoric parts. The plastic anisotropy is described by a non-associative plasticity theory to define separately the yield criterion and plastic potential [1]. The generalization to finite strains is provided by using the rotating frame formulation with the multiplicative decomposition of the total transformation into elastic and plastic parts [1, 9]. A mixed nonlinear hardening (kinematic and isotropic) strongly coupled with ductile anisotropic damage is taken into account. Some results of the bulge test are shown to highlight the effect of the damage anisotropy compared to the isotropic case.

2. Theoretical formulation

The finite strains are accounted for through the concept of intermediate configuration with an elastoplastic kinematics assuming multiplicative decomposition of the total transformation into elastic and plastic parts [1, 9]. The rotating frame formulation (RFF) is

used to ensure the objectivity of the constitutive equations by defining a rotation tensor \underline{Q} allowing a rotational transport of the overall tensorial variables defined on the current configuration to rotated local configuration having the same orientation as the initial undeformed configuration. Using the framework of the well-known thermodynamics of irreversible processes and neglecting the thermal effect (isothermal case), the pairs of state variables under concern are: $(\underline{\sigma}, \underline{\varepsilon}^e)$ for the elasticity, $(\underline{\alpha}, \underline{X})$ for kinematic hardening, (r, R) for isotropic hardening and $(\underline{d}, \underline{Y})$ for anisotropic hardening. In order to define the effect of damage on the others variables, we use the concept of effective state variables based on the total energy equivalence assumption [8], which leads to the following definitions of the effective state variables:

$$\underline{\tilde{\sigma}} = \underline{\overline{M}}^{-1} : \underline{\sigma}, \quad \underline{\tilde{\varepsilon}}^e = \underline{\overline{M}} : \underline{\varepsilon}^e, \quad \underline{\tilde{X}} = \underline{\overline{M}}^{-1} : \underline{X}, \quad \underline{\tilde{\alpha}} = \underline{\overline{M}} : \underline{\alpha}, \quad \tilde{R} = \frac{R}{\sqrt{1 - \|\underline{d}\|^\gamma}}, \quad \tilde{r} = \sqrt{1 - \|\underline{d}\|^\gamma} \cdot r \quad (1)$$

where $\underline{\overline{M}}$ is a fourth-rank tensor representing damage effect operator [2, 3, 6, 7, 10] which is here decomposed as in [5] into two parts $\underline{\overline{M}} = \underline{\overline{M}}^D + \underline{\overline{M}}^S$ in which $\underline{M}_{ijkl}^S = \frac{1}{3} \sqrt{1 - \|\underline{d}\|^\gamma} \delta_{ij} \delta_{kl}$ is the hydrostatic part while $\underline{M}_{ijkl}^D = \frac{1}{2} (\overline{h}_{ik} \overline{h}_{jl} + \overline{h}_{il} \overline{h}_{jk}) - \frac{1}{3} (\overline{h}_{ij}^2 \delta_{kl} + \overline{h}_{kl}^2 \delta_{ij}) + \frac{1}{9} \text{tr}(\overline{h}_{rs}^2) \delta_{ij} \delta_{kl}$ is the deviatoric part. The notation $\|\underline{d}\|$ define the first damage tensor invariant by $\|\underline{d}\| = \frac{1}{3} \text{tr}(\underline{d})$ and $\underline{\overline{h}}$ is a second-rank tensor that is defined by $\underline{\overline{h}} = (1 - \underline{d})^{1/k}$. The state relations are obtained by replacing the expressions of the effective variables in the classical state potential given in to have:

$$\underline{\tilde{\sigma}} = \underline{\tilde{\Lambda}} : \underline{\tilde{\varepsilon}}^e = \underline{\overline{M}} : \underline{\underline{\Lambda}} : \underline{\overline{M}} : \underline{\varepsilon}^e, \quad \underline{\tilde{X}} = \underline{\tilde{C}} : \underline{\tilde{\alpha}} = \frac{2}{3} C [\underline{\overline{M}} : \underline{\overline{M}}] : \underline{\alpha}, \quad R = \tilde{Q} r = Q (1 - \|\underline{d}\|^\gamma) r \quad (2)$$

$$\underline{\underline{Y}} = \underline{\underline{Y}}^e + \underline{\underline{Y}}^\alpha + \underline{\underline{Y}}^r = -\underline{\underline{\varepsilon}}^e : \frac{\partial \underline{\overline{M}}}{\partial \underline{d}} : \underline{\tilde{\sigma}} - \underline{\underline{\alpha}} : \frac{\partial \underline{\overline{M}}}{\partial \underline{d}} : \underline{\tilde{X}} + \frac{\gamma}{6} \|\underline{d}\|^{\gamma-1} Q r^2 \cdot 1 \quad (3)$$

where $\underline{\tilde{\Lambda}}$ and $\underline{\tilde{C}}$ are the symmetric fourth-rank tensors defining the elastic and the kinematic hardening moduli for the damaged material .

In this work we adopt the same expressions of the plastic potential and yield criterion as in [1, 8]. They are characterized by the equivalent stress σ_c (criterion) and σ_p (potential) that are anisotropic and quadratic of Hill type:

$$\sigma_i(\underline{\tilde{\sigma}}^D - \underline{\tilde{X}}) = \sqrt{(\underline{\tilde{\sigma}}^D - \underline{\tilde{X}}) : \underline{\underline{H}}^i : (\underline{\tilde{\sigma}}^D - \underline{\tilde{X}})} = \sqrt{(\underline{\sigma}^D - \underline{X}) : \underline{\underline{H}}^i : (\underline{\sigma}^D - \underline{X})} \quad i = c, p \quad (4)$$

with $\underline{\tilde{\sigma}}^D = \underline{\overline{M}}^{-1} : \underline{\sigma}^D$ and $\underline{\underline{H}}^i (i = c, p)$ are the initial anisotropic operators of the undamaged material, each of them is characterized by six constants F^i, G^i, H^i, L^i, M^i and N^i . $\underline{\underline{H}}^i (i = c, p)$ are the anisotropic operators of the damaged material. The evolution equations

governing the overall dissipative phenomena are obtained by the normality rule applied to the plastic potential:

$$\dot{\bar{D}}^p = \dot{\lambda} \bar{n}^p, \quad \dot{\bar{\alpha}} = \dot{\bar{D}}^p - a \dot{\lambda} \bar{\alpha}, \quad \dot{r} = \frac{\dot{\lambda}}{\sqrt{1 - \|\bar{d}\|^{\gamma}}} (1 - b \bar{r}), \quad \dot{\bar{d}} = \dot{\lambda} \frac{1}{(1 - \|\bar{d}\|^{\beta})^s} \left\langle \frac{\|\bar{Y}\| - Y_0}{S} \right\rangle^s \frac{3\bar{Y}}{\|\bar{Y}\|} \quad (5)$$

$$\text{with } \bar{n}^p = \frac{\bar{M}^{-1} : \bar{H}^p : (\bar{\sigma}^D - \bar{X})}{\sigma^p (\bar{\sigma}^D - \bar{X})} = \frac{\bar{H}^p : (\bar{\sigma}^D - \bar{X})}{\sigma^p (\bar{\sigma}^D - \bar{X})}$$
 is the outward normal to the plastic potential,

$\dot{\lambda}$ is the plastic multiplier deduced from the classical consistency condition applied to the yield function $\dot{f} = 0$ and $\|\bar{Y}\| = \sqrt{3\bar{Y} : \bar{Y}}$.

This model has been implemented into ABAQUS/EXPLICIT® using the VUMAT user's subroutine in which an implicit local integration scheme is used to compute the stress and the state variables at each integration point. The global equilibrium problem is then solved using an explicit dynamic resolution scheme available in ABAQUS/EXPLICIT®.

3. Application to Bulge test in 3D

In this section, we illustrate a comparison study between isotropic and anisotropic damage models through 3D bulge test of an AISI 304 thin sheet. The material parameters of the two models are: $E = 190$ GPa, $\nu = 0,3$, $\sigma_y = 300$ MPa, $C = 7000$ MPa, $a = 170$, $Q = 2600$ MPa, $b = 1,5$, $F_c = 0,863$, $G_c = 0,8$, $H_c = 0,2$, $N_c = 1,452$, $M_c = 1,5$, $L_c = 1,5$, $F_p = 0,461$, $G_p = 0,447$, $H_p = 0,553$, $N_p = 1,4$, $M_p = 1,5$, $L_p = 1,5$, and those related to anisotropic damage model are: $S = 18$, $s = 1$, $\beta = 2$, $Y_0 = 0$, $\chi = 1$, $\gamma = 6$, $k = 4$. The same damage parameters are used for the isotropic case except: $S = 12$ and $\beta = 1$.

The matrix has cylindrical shape with an external diameter $D_0 = 133$ mm, an internal diameter $d = 90$ mm and an edge radius $R = 6$ mm and the sheet specimen have an initial thickness $t_0 = 1$ mm and it is clamped on the matrix along his boundaries. During the test, an increasing internal pressure is applied on the down face of the sheet and the displacement of the dome pole is measured continuously. The numerical simulations of this process are made with Abaqus/Explicit® finite element code. The sheet is meshed with 156328 3D elements C3D8R with uniform size $\Delta x = 0,5$ mm and the matrix is meshed with 5000 rigid element R3D4.

The numerically predicted results show a quite difference in the damage distributions between the isotropic model (Fig.1 (a)) and the anisotropic model (Fig.1 (b)). However, the starting points of the macroscopic cracks predicted with the two models are the same and are located on the pole of the dome. Also, the applied pressure level just before the rupture is the same (about $P = 243$ MPa) for the two models. On the other hand we have observed that the two models give the same global results which are in agreement with the experimental results not shown here for the sake of shortness. This good agreement is essentially due to the non-associative anisotropic plasticity coupled with damage as shows in [1].

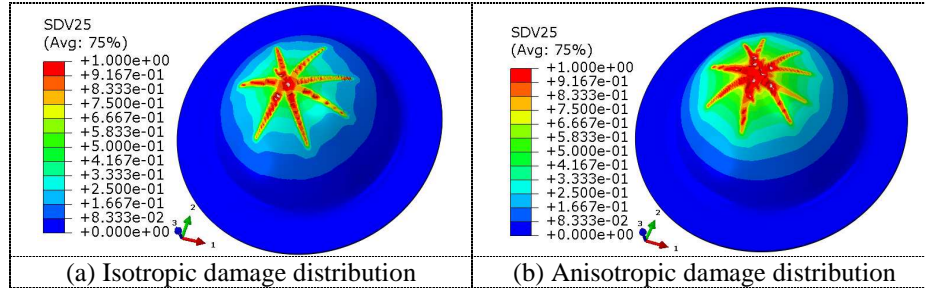


Figure 1. Fracture modes predicted by isotropic and anisotropic damage models at internal pressure $P=243$ MPa.

4. Conclusions

In this work, we have briefly presented a theoretical formulation of an anisotropic elastoplastic model coupled with anisotropic damage in finite strains. This model takes account also an initial plastic anisotropy with non-associative plasticity theory with a mixed nonlinear hardening. Some local and global numerical results of the bulge test simulations are presented and compared to the experimental results. In this study the attention is directed to the comparison between the isotropic and the anisotropic damage cases. The results obtained show a non-important effect of the anisotropic damage on the global pressure versus the dome pole displacement for this case. However, the local plastic strain and thickness distributions are quite different for the two models.

Acknowledgement. Thanks are due to Region Champagne – Ardenne (France) for the financial support.

References

- [1] Badreddine H., Saanouni K. and Dogui A. (2010), On non associative anisotropic finite plasticity fully coupled with isotropic ductile damage for metal forming, *International Journal of Plasticity*, **26**, pp 1541–1575.
- [2] Chow C.L., (1987) An anisotropic Theory of Continuum Damage Mechanics for Ductile Fracture, *Engng.Frac.Meche*, **27**, pp 547-558.
- [3] Cordebois J.L and Sidoroff F., (1982) Endommagement anisotrope en élasticité et plasticité, *Journal de Mécanique Théorique Appliqué*, pp 45-60.
- [4] Lemaitre J. and Chaboche. J-L., (1985) *Mécanique des milieux solides*, Dunod, Paris.
- [5] Lemaitre, J. and Desmorat, R., (2005) *Engineering Damage Mechanics: Ductile, Creep, Fatigue and Brittle Failures*, Springer.
- [6] Murakami S., (1988) Mechanical modeling of material damage. *J. Appl. Mech.*, **55**, 280–286.
- [7] Murakami.S and Ohno N., (1981) A continuum theory of creep and creep damage. *Creep of Structure IUTAM symp.*, A.R.S.Ponter, ed.,Springer-Verlag, Berlin, Federal Republic of Germany, pp 422-444.
- [8] Saanouni.K, Forster Ch., and Ben Hatira F., (1994) On the anelastic Flow with Damage, *J. Damage Mechanics*, **3**, pp 140-169.
- [9] Sidoroff F. and Dogui A., (2001) Some issues about anisotropic elastic-plastic models at finite strain, *Int. J. Sol. Str.*, **38**, pp 9569-9578.
- [10] Voyiadjis, G.Z., Kattan, P.L., (1999) *Advances in Damage Mechanics: Metals and Metal Matrix Composites*. Elsevier, Amsterdam, 1999.

ANISOTROPIC DUCTILE DAMAGE FULLY COUPLED WITH ANISOTROPIC LARGE STRAIN PLASTICITY FOR METAL FORMING

W. Rajhi^{1,2}, K. Saanouni¹, H. Sidhom²

¹ ICD/LASMIS, STMR UMR-CNRS 6279, University of Technology of Troyes 12, Rue Marie Curie – BP2060- 10000 Troyes cedex, France

e-mail: wajdirajhi@gmail.com, khemais.saanouni@utt.fr

² LMMP LAB-STI03, High School of Science and Technology of Tunisia, 5 street Taha Hussein, 1008 Tunis, Tunisia

e-mail: Habib.Sidhom@esstt.rnu.tn

Abstract. In this work, a second rank tensor is introduced to model the anisotropic effect of ductile damage in metal forming processes. Following the concept of effective stress together with the total energy equivalence assumption, the « Murakami » fourth order damage effect tensor is chosen to describe the anisotropic damage effect on the elastic-plastic behavior. The « Lemaitre » anisotropic damage evolution relation, where the principal directions of damage rate tensor are governed by those of the plastic strain rate tensor, is used in the thermodynamically-consistent framework. A nonlinear mixed hardening, isotropic and kinematic, is taken into account considering the full and strong damage effect. A non-associative plasticity assumption is considered, and the « Hill 1948 » quadratic equivalent stress norm is used to describe large plastic anisotropic flow. The obtained model was implemented into ABAQUS/Explicit® FE software thanks to the user's subroutine VUMAT for the validation purpose.

1. Introduction

The theory of CDM has been widely used to predict isotropic damage initiation and propagation in metal forming [1], [2]. However, for high performance engineering materials such as HLE steels and aluminum alloys, heterogeneous and strongly anisotropic materials such as composite and concrete which exhibit privileged directions of damage, it is less and less practical to preserve the hypothesis of the isotropy of damage. Different tensorial damage variables were used in the literature [3], [4], [5] especially in the framework of thermodynamics of irreversible processes with state variables in order to characterize different kinds of damage. In this work, the damage variable is introduced through a symmetric second order tensor in order to describe the ductile anisotropic damage effect on the elastic-plastic behavior [6], [7].

2. Constitutive equations with anisotropic damage

This section deals with the presentation of the elastic-plastic constitutive equations fully coupled to the anisotropic damage. Four pairs of internal state variables formally noted (a_i, A_i) are taken into account. Small elastic strain tensor associated with the Cauchy stress tensor $(\underline{\varepsilon}^e, \underline{\sigma})$. Kinematic hardening variables $(\underline{\alpha}, \underline{X})$ representing the displacement of the

center of the yield surface. Isotropic hardening variables (r, R) representing the size of the yield surface. The pair of second rank tensors ($\underline{\Omega}, \underline{Y}$) where $\underline{\Omega}$ is the damage tensor and \underline{Y} is the associated force representing the total damage energy release rate. Following the concept of effective stress ([8], [9]) together with the hypothesis of total energy equivalence ([9], [11]), the effective variables can be written as:

$$\underline{\tilde{\sigma}} = \underline{\underline{M}}^{-1} : \underline{\sigma} . \quad \underline{\tilde{X}} = \underline{\underline{M}}^{-1} : \underline{X} . \quad \tilde{R} = \frac{R}{\sqrt{1 - \|\underline{\Omega}\|}} . \quad (1)$$

$$\underline{\tilde{\varepsilon}}^e = \underline{\underline{M}} : \underline{\varepsilon}^e . \quad \underline{\tilde{\alpha}} = \underline{\underline{M}} : \underline{\alpha} . \quad \tilde{r} = r \sqrt{1 - \|\underline{\Omega}\|} . \quad (2)$$

where ($\underline{\underline{M}}$) is the Murakami and Ohno fourth rank damage-effect tensor defined from the eigenvalues ($\Omega_i, i \in \{1, 2, 3\}$) of the damage tensor $\underline{\Omega}$ [10]. The symmetric and positive definite fourth rank tensors $\underline{\underline{A}}$ and $\underline{\underline{C}}$ represent the elasticity and the kinematic hardening moduli respectively, and Q is the scalar isotropic hardening modulus.

If the Helmholtz free energy Ψ , defined in the effective strain-like variables space, is taken as a state potential, then the state relations are given by (see [9], [11]):

$$\underline{\sigma} = \rho \frac{\partial \Psi}{\partial \underline{\varepsilon}^e} = \underline{\underline{\tilde{A}}} : \underline{\varepsilon}^e . \quad \underline{X} = \rho \frac{\partial \Psi}{\partial \underline{\alpha}} = \underline{\underline{\tilde{C}}} : \underline{\alpha} . \quad R = \rho \frac{\partial \Psi}{\partial r} = \tilde{Q} r . \quad (3)$$

$$\underline{Y} = -\rho \frac{\partial \Psi}{\partial \underline{\Omega}} = -\frac{1}{2} \underline{\varepsilon}^e : \frac{\partial \underline{\underline{\tilde{A}}}}{\partial \underline{\Omega}} : \underline{\varepsilon}^e - \frac{1}{2} \underline{\alpha} : \frac{\partial \underline{\underline{\tilde{C}}}}{\partial \underline{\Omega}} : \underline{\alpha} - \frac{1}{2} \frac{\partial \tilde{Q}}{\partial \underline{\Omega}} r^2 . \quad (4)$$

The material properties affected by the damage have the following form:

$$\underline{\underline{\tilde{A}}} = \underline{\underline{M}} : \underline{\underline{A}} : \underline{\underline{M}} . \quad \underline{\underline{\tilde{C}}} = \underline{\underline{M}} : \underline{\underline{C}} : \underline{\underline{M}} . \quad \tilde{Q} = Q (1 - \|\underline{\Omega}\|) . \quad (5)$$

The anisotropic plastic flow is modeled using the classical yield function (f^p):

$$f^p(\underline{\sigma}, \underline{X}, R, \underline{\Omega}) = \|\underline{\tilde{\sigma}} - \underline{\tilde{X}}\|_H - \tilde{R} - \sigma_y . \quad (6)$$

where σ_y is the initial size of the plastic yield surface. The notation $\|\underline{\tilde{\sigma}} - \underline{\tilde{X}}\|_H$ defines the Hill 1948 quadratic norm of the effective equivalent stress given by $\|\underline{\tilde{\sigma}} - \underline{\tilde{X}}\|_H = \sqrt{(\underline{\tilde{\sigma}} - \underline{\tilde{X}}) : \underline{\underline{H}} : (\underline{\tilde{\sigma}} - \underline{\tilde{X}})}$ where the fourth order symmetric and positive definite operator ($\underline{\underline{H}}$) defines the anisotropy of plastic flow.

By choosing an appropriate form for the plastic potential (F^p) ([9], [11]), the constitutive equations are deduced from the normality rule by:

$$\underline{\dot{\varepsilon}}^p = \dot{\lambda} \frac{\partial F^p}{\partial \underline{\sigma}} = \dot{\lambda} \underline{n} . \quad \dot{r} = -\dot{\lambda} \frac{\partial F^p}{\partial R} = \frac{\dot{\lambda}}{\sqrt{1 - \|\underline{\Omega}\|}} (1 - b\tilde{r}) . \quad \underline{\dot{\alpha}} = -\dot{\lambda} \frac{\partial F^p}{\partial \underline{X}} = \underline{\dot{\varepsilon}}^p - a \dot{\lambda} \underline{\alpha} . \quad (7)$$

$$\underline{n} = \frac{\partial f^p}{\partial \underline{\sigma}} = \underline{M}^{-1} : \tilde{n} . \quad \tilde{n} = \frac{\underline{H} : (\underline{\sigma} - \underline{X})}{\|\underline{\sigma} - \underline{X}\|_H} . \quad (8)$$

Where the material constants a and b are the nonlinearity parameters for kinematic and isotropic hardening respectively. $(\dot{\lambda})$ is the plastic Lagrange multiplier that verifies the plastic loading/unloading condition. The deviatoric second rank tensors \underline{n} and \tilde{n} represent the outward unit normal to the plastic yield surface in the stress and effective stress spaces respectively.

In this work, the principal components of the damage rate tensor are considered to be proportional to the absolute value of the principal components of the plastic strain rate [6]. Thus, a direct generalization to the anisotropic case of the Lemaitre isotropic damage law [6] is proposed without defining specific damage potential:

$$\dot{\underline{\Omega}} = \left(\frac{\langle Y - Y_0 \rangle}{S} \right)^s \left| \dot{\underline{\epsilon}} \right| . \quad (9)$$

where the scalar Y is nothing but the total energy release rate according to the isotropic damage case. The parameters (S, s, Y_0) represent the material constants governing the nonlinear evolution of the ductile damage.

3. Elastic plastic model with anisotropic damage effect validation and numerical simulation results:

The fully coupled constitutive equations presented above have been implemented into ABAQUS/EXPLICIT® F.E software using the user's subroutine VUMAT (ABAQUS® Theory Manuel). The dynamic explicit DE resolution procedure has been used in order to solve the global mechanical equilibrium problem. This requires the numerical integration of the fully coupled constitutive equations in order to compute the stress tensor and the associated state variables at each integration point of each element. The plastic and damage evolution relationships are numerically integrated by using implicit incremental integration scheme. The asymptotic integration method is applied to both kinematic and isotropic hardening evolution relations. The incremental elastic predictor-plastic corrector algorithm is used for the local integration of the model [11].

Application is made to tensile test of flat specimen by using the following material constants: $E=195.000 \text{ MPa}$, $\nu=0.3$, $\sigma_y=320 \text{ MPa}$, $Q=5500 \text{ MPa}$, $b=10$, $C=38000 \text{ MPa}$, $a=290$, $F=0.5$, $G=0.5$, $H=0.5$, $L=1.5$, $M=1.5$, $N=1.5$, $S=20$, $s=1$ and $Y_0=0 \text{ MPa}$, where F , G , H , L , M and N are Hill48's anisotropic parameters.

The curves of the evolution of the von Mises equivalent stress and the anisotropic damage tensor components Ω_{ij} versus the accumulated plastic strain during tensile test loading are given by fig. 1. The damage components Ω_{11} , Ω_{22} and Ω_{33} evolve almost the same way during the early stage of tensile loading. Then, the damage component Ω_{11} increases significantly compared to Ω_{22} and Ω_{33} damage components and exceeds 70% at the end of the applied load. The damage components Ω_{22} and Ω_{33} evolve in the same way until 20% of the accumulated plastic strain, level from which the Ω_{33} component increases and bifurcates from Ω_{22} component. The evolution of damage 'shear' components Ω_{23} and

Ω_{23} remains very low during the tensile loading compared to Ω_{12} damage component which increases without exceeding 5% at the end of the loading.

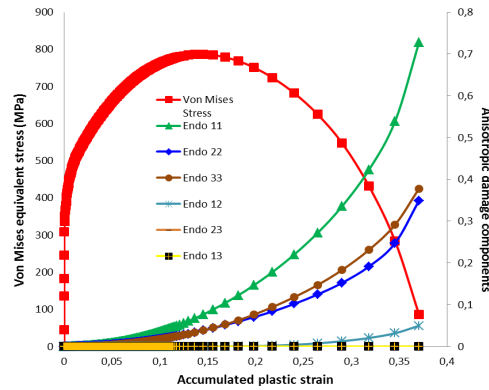


Figure 1. Evolution of the von Mises equivalent stress and the anisotropic damage tensor components versus the accumulated plastic strain during tensile test.

4. Conclusion:

In this work, a second order damage tensor is introduced in order to describe the anisotropic damage effect on the elastic-plastic behavior. The implementation of the proposed model into ABAQUS/Explicit® FE software allows to predict the anisotropic damage in loaded structures. Validation of this model using appropriate experimental results from highly anisotropic metallic material is still to perform.

References

- [1] Zhu, Y. Y. and Cescotto, S. (1995), A Fully Coupled Elasto-Visco-Plastic Damage Theory for Anisotropic Materials, *Int.J.Molids and Structures*, **32**, pp. 1607-1641.
- [2] Saanouni, K. (2008), On the Numerical Prediction of the Ductile Fracture in Metal Forming, *Engineering Fracture Mechanics*, **75**, pp. 3545-3559.
- [3] Dragon, A. and Mroz, Z. (1979), A Continuum Model for Plastic Brittle Behavior of Rock and Concrete, *International Journal of Engineering Science*, **17**, pp. 121-137.
- [4] Chaboche, J.L. (1984), Anisotropic Creep Damage in the Framework of Continuum Damage Mechanics, *Nuclear Engineering and Design*, **79**, pp. 309-319.
- [5] Onat, E. T. and Leckie, F. A. (1988), Representation of Mechanical Behaviour in the Presence of Changing Internal Structure, *Journal of Applied Mechanics*, **55**, pp. 1-10.
- [6] Lemaitre, J., Desmorat, R. and Sauzaya, M. (2000), Anisotropic damage law of evolution, *European Journal of Mechanics*, **19**, pp. 187-208.
- [7] Hammi Y., Horstemeyer M.F. (2007), A Physically Motivated Anisotropic Tensorial Representation of Damage with Separate Functions for Void Nucleation, Growth, and Coalescence, *International Journal of Plasticity*, **23**, pp. 1641-1678.
- [8] Chaboche, J.L. (1988), Continuum Damage Mechanics, Parts I and II, *Journal of Applied Mechanics*, **55**, pp. 59-72.
- [9] Saanouni, K., Forster, C. and Hatira, F.B. (1994), On the Anelastic Flow with Damage, *Journal of Damage Mechanics*, **3**, pp.140-169.
- [10] Murakami, S. and Ohno, N. (1981), Continuum Theory of Creep and Creep Damage, Creep in Structures, A. R. S. Ponter, Ed., Third IUTAM Symposium, Springer- Verlag, New York pp. 422-453.
- [11] Saanouni, K. and Chaboche, J.L. (2003), 3.06 - Computational Damage Mechanics: Application to Metal Forming Simulation, *Comprehensive Structural Integrity*, **3**, pp. 321-376.

FAILURE PREDICTION AND VALIDATION OF A STEEL AUTOMOTIVE SAFETY PART

M. Achouri¹, G. Germain¹, P. Dal Santo¹, D. Saidane², M. V. Cid Alfaro³, C.H.L.J. ten Horn³

¹LAMPA(EA1427), 2 Boulevard du Ronceray BP 93525, 49035 Angers-France

e-mails: Mohamed.Achouri@ensam.eu, Guenael.Germain@ensam.eu, Philippe.DalSanto@ensam.eu,

²DEVILLE ASC, ZI de Beauregard 49150 Baugé-France, delphine.saidane@devillesa.fr

³Tata Steel Research, Development & Technology, PO BOX 10000 1970 CA IJmuiden-The Netherlands, e-mail: Carel.ten-Horn@tatasteel.com

Abstract. The objective of this work was to investigate the failure behaviour of a HSLA steel component subjected to a bending-unbending operation. This study was conducted through a combined experimental and numerical approach to better understand the limitations of current models and generate more suitable data that can be used to further optimise the manufacturing process. The numerical approach was carried out using two finite element codes (ABAQUS and PAM-STAMP) and two fracture models (Gurson and CrachFEM). Bending and unbending tests were performed with the purpose of validating the models and study the operating performance of this material when subjected to these kinds of loading. The final purpose of this work is to present a numerical approach that can accurately predict the mechanical and failure behaviour of a real automotive safety component.

1. Introduction

Material damage, created during forming, is critical to the component specification to avoid the risk of fracture in service. Therefore, the damage prediction is a key point in the optimization of these processes. The automobile manufacturers are increasingly relying on numerical simulation software in order to predict strain localization or tool wear. Concerning these aspects, the results obtained by simulation are usually fairly reliable. The objective of this work is to present a study of damage problems that can occur in forming processes, such as bending which is one of the processes frequently applied during manufacturing of these kinds of components that are obtained after blanking [1]. Bending and unbending tests were performed with the purpose to validate our models and study the operating performance of this material applied to these kinds of loading. Two finite element codes will also be used to determine the limits of each law and each calculation code.

2. Experimental study

The material tested in this study is the S500MC HSLA steel. This material is commonly used in manufacture of automotive safety parts such as the buckle belt safety. The bending operation has been done by a device mounted on a press with force and displacement sensors. The bending device is shown in Fig. 1. The specimen is bent at the oblong hole to study its bending behaviour after the blanking operation. After the specimen has been bent, it is clamped in a tensile test machine and pulled until fracture occurs (Fig. 2). This test determines the strength of part after bending and represents loading that the part might see during crash.

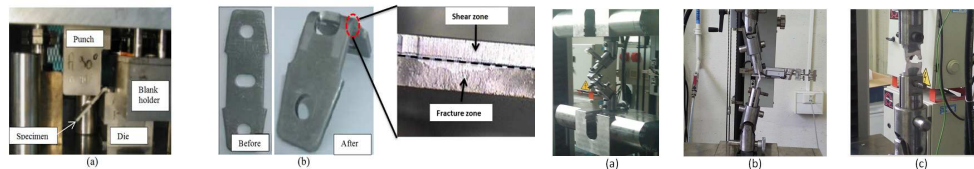


Figure 1: (a) bending device, (b) shape of the specimen

Figure 2: (a) before, (b) during, (c) after unbending

3. Numerical modelling

The bending and unbending operations of the experiments were simulated using two finite element codes: ABAQUS / Standard and PAM-STAMP. The results of these simulations were compared with the experiments in order to compare behaviour and damage models and their ability to predict

the stress distribution and location of damage on the specimen. Fig. 3 shows the tools used in the simulation by the two codes and different steps of simulation. The tools in ABAQUS / Standard are modelled by analytical rigid body. Quadratic elements were used in the middle of the part. Particular attention has been devoted to areas adjacent to the oblong hole, because at this zone it will be bent and therefore the strain and stress levels will be important. In the explicit FE code PAM-STAMP, the Hill'48 yield locus, the Bergström-van Liempt hardening law [5] and the CrachFEM fracture model [6] were used. The model was built using 2D shell elements, these elements are not ideal for bending thick material however, in PAM-STAMP CrachFEM is currently only available for shell elements.

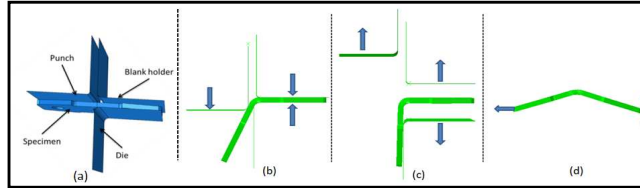


Figure 3. Tools and steps of simulation: (a) tools used in simulation, (b) bending phase, (c) end of bending and decline of tools, (d) unbending phase

3.1. Models used by ABAQUS Software

The behaviour law is the elastic-plastic law of Ludwick written as: $\sigma_e = \sigma_{e0} + K(\bar{\epsilon}^p)^n$ (1)

With σ_{e0} is the initial yield strength, K is the hardening modulus, n is the hardening exponent and $\bar{\epsilon}^p$ is the plastic equivalent strain.

The GTN damage model was implemented in ABAQUS [2]. The yield potential is described as follows [3]:

$$\Phi(\sigma_{eq}, \sigma_H) = \left(\frac{\sigma_{eq}}{\sigma_e}\right)^2 + 2q_1 f^* \cosh\left(\frac{3q_2 \sigma_H}{2\sigma_e}\right) - (1 + q_3 f^*) = 0 \quad (2)$$

q_1 , q_2 and q_3 are the constitutive parameters of the model, σ_{eq} is the von Mises equivalent stress, σ_H the hydrostatic stress and σ_e is the yield stress of matrix material.

The total variation of void volume fraction is: $\dot{f} = A\dot{\epsilon}^p + (1 - f)\dot{\epsilon}_{kk}^p$ (3)

$\dot{\epsilon}_{kk}^p$ is the plastic strain rate due to hydrostatic stress and $\dot{\epsilon}^p$ is the equivalent plastic strain rate. A and f^* the form of a Gaussian probability are given in [4].

3.2. Models used by PAM-STAMP Software

The damage model used in PAM-STAMP in this study is the commercially available CrachFEM model [6]. This model is a local fracture model that predicts three failure risks: instability risk, ductile normal fracture risk and ductile shear fracture risk. For each of the failure mechanisms, CrachFEM has a separate failure curve. The risk of fracture is evaluated by looking at the distance between the current strain state and the failure curve. As the instability curve is calculated based on the deformation history, it may shift depending on the type of loading. For example, in bending, instability is suppressed and ductile normal and shear fracture become dominant. For a constant strain path, the failure risk is determined by the distance to the failure curve. At a failure risk of 1, fracture is predicted. In order to take some strain path dependency into account, the failure risk is integrated over the strain history.

4. Results – Discussion

We can decompose the experimental curves in Fig. 5-a in three mean zones. AB zone that corresponds to the elastic zone of material. The BC zone shows the plastic behaviour of bending zone, the maximum value of bending load is equal to 6640N. The end zone CD shows the decrease of bending load, in this zone the contact surface between punch and specimen increase. We can observe a large difference between the experimental curves and ABAQUS prediction, due to the insufficient of models used by ABAQUS. However, the prediction by PAM-STAMP on the AB and BC zones are acceptable. The oscillations observed are due to the problems of inertia. The

zone CD is not predicted well by PAM-STAMP as shell elements are not able to account for stresses normal to the sheet plane that occur in this phase of bending. Fig. 5-b shows the evolution of unbending load versus displacement of the cross-head. We can decompose the curves on two zones: AB zone that corresponds an unbending phase, this operation requires a displacement of about 70mm with a relatively small effort to achieve an almost straight specimen. The second zone BC represents the tension phase where the load increases rapidly till a maximum value of 32 kN which corresponds to fracture of the specimens. The numerical models used by ABAQUS gives an evolution of load almost close to the real case, except for the fracture point due to the absence of parameters responsible to fracture in GTN damage model implemented in ABAQUS\Standard. For PAM-STAMP, there are initially some inertia effects but the force needed for unbending is predicted quite well. PAM-STAMP predicts fracture to occur at a force of 34 kN; which is close to the experiments.

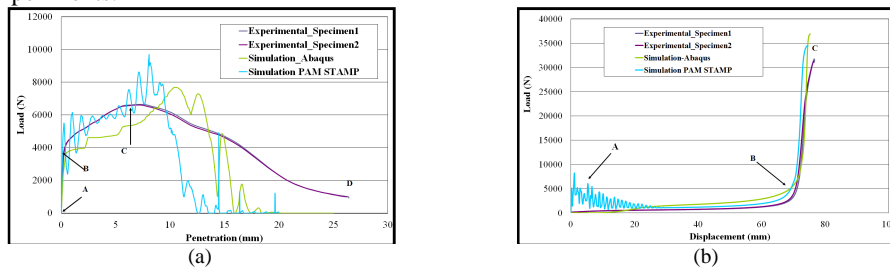


Figure 5: Comparison of curves: (a) bending test, (b) unbending test

Fig. 6-a shows a micrographic observation of the bent zone of two specimens, changing the face of the specimen to study the effect of the blanking zones (Fig. 1-b) on the damage to the part. The specimen 1 shows an appearance of microcracks on the top of the bent zone in the level of fracture zone. The specimen 2 was bent in the opposite direction (shear zone) which indicates the absence of microcracks. This observation allows us to highlight the interaction of the bending process with blanking process. The maximum equivalent stress obtained by ABAQUS (744MPa) appears inside the crease on the side of compressed fibres and on the edge of the hole. There is a stress concentration at the bended area (Fig. 7-b) where equivalent plastic strains are very important because they can reach 48%. For the PAM-STAMP simulation, the equivalent plastic strain at the bending area reached values up to 47% however, the fracture risks remain small and no fracture is predicted. The contour plot of the equivalent stress at the end of the bending operation is depicted in Fig. 6-c where maximum values reached 789 MPa; this is slightly higher than the results of ABAQUS. Overall, the results of ABAQUS and PAM-STAMP are quite close.

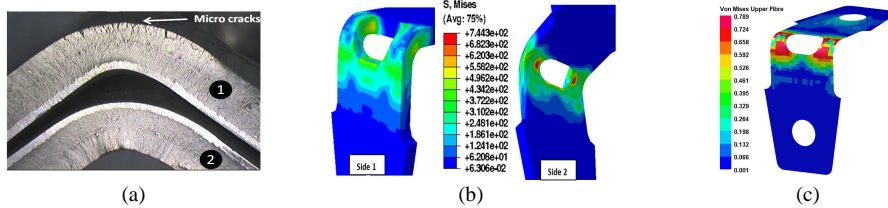


Figure 6: Profile of specimen after bending and spring-back phenomena: (a) experimental observation, (b) stress distribution obtained by ABAQUS in two sides and (c) Stress distribution obtained by PAM STAMP

Fig. 7 shows the profile of the specimen during unbending. The stress prediction by simulation (Figs. 7-b-c) shows the concentration of stress with a maximum value equal to 1168 MPa. The damage is localised at the level of hole in the below side, this conclusion is validated by micrographic observation (Fig. 7-a). For the PAM STAMP simulation, the maximum equivalent stress before fracture was 942 MPa and the location of fracture is predicted correctly. Damage parameter and failure risk after bending and at the moment of fracture during unbending are shown in Fig. 8.

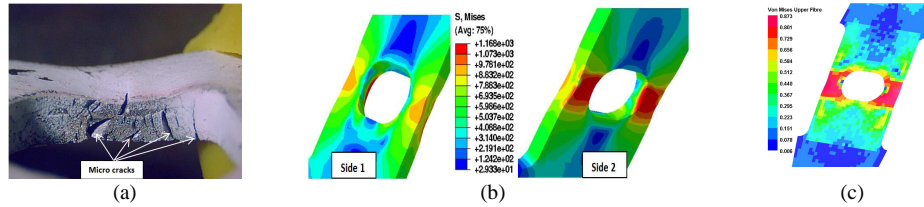


Figure 7: Unbending results: (a) experimental, (b) stress by ABAQUS and (c) stress obtained by PAM STAMP

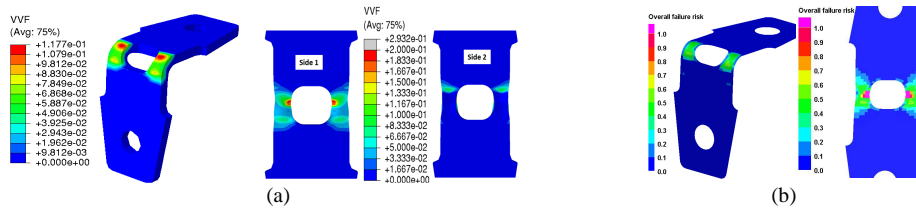


Figure 8: (a) Damage parameter (G), (b) Overall failure risk (CrachFEM)

Conclusion

From comparison of the simulations using ABAQUS and PAM-STAMP with the experiments, the following conclusions can be drawn:

- Force displacement curve for bending and unbending obtained from PAM STAMP simulations are close to experiments. The end of the bending operation is not well predicted as the shell elements cannot handle stresses in the normal direction that are present in the experiment.
- The overall evolution of force-displacement curves obtained from ABAQUS is close to experimental curve. However, should be tested other models to consider similar phenomena to those kinds of processes and to get a more accuracy. The prediction of stress and damage fields in the bending zone is acceptable compared to experimental observations. The use of 3D elements in ABAQUS compared to shell elements is allows us to analyze the part on both sides.
- The microcracks that occur at the edge of the specimen are influenced by the quality of the cut edge. This has not been accounted for in the simulations.
- The study will continue to develop more relevant models and to study the influence of process parameters, also to analyze the residual stresses in the bending zone.

References

- [1] Bahloul, R., Mkaddem, A., Dal Santo, Ph., Potiron, A. (2006), Sheet metal bending optimisation using response surface method, numerical simulation and design of experiments, *International Journal of Mechanical Sciences*, **48**, pp. 991 – 1003.
- [2] Abaqus, 2010. Reference Manuals, v 6.10. Abaqus Inc.
- [3] Tvergaard, V., *International Journal of Fracture* 18 (1982) 237–252.
- [4] Needleman, A. and V. Tvergaard (1987), An analysis of ductile rupture modes at a crack tip, *Journal Of The Mechanics And Physics Of Solids*, **35**, pp.151-183
- [5] Vegter, H., ten Horn, C.H.L.J., An, Y., H. Atzema, E., H. Pijlman, H., van den Boogaard, T. H., Huétink, H. (2003) ,Characterisation And Modelling Of The Plastic Material Behaviour And Its Application In Sheet Metal Forming Simulation, *Proceedings of the Seventh International conference on Computational Plasticity*, Barcelona (Spain).
- [6] ten Horn, C.H.L.J., Lambriks, M.P.J. and Unruh , K. (2009), Testing Methods for Fracture Modelling: The Need for Harmonisation, *Conference proceedings of Werkstoffprüfung*.

MODELING CREEP DAMAGE OF AN ALUMINIUM-SILICON EUTECTIC ALLOY

H. Altenbach¹, S. Kozhar², and K. Naumenko¹

Abstract. Aluminum-silicon casting alloys are widely used in the automotive industry. The creep and creep damage of the eutectic AlSi12CuNiMg cast piston alloy will be analyzed and a constitutive model with inner variables that reflect basic features of deformation, ageing and damage behavior is presented. Creep and force-controlled low cycle fatigue tests are carried out at several levels of temperature. The creep curves exhibit classical three stages. The tertiary creep stage is controlled by damage processes, mainly due to failure of the brittle inclusions and ageing processes of the aluminum matrix. Ruptured specimens are analyzed with the help of optical and scanning electron microscopy to establish the fracture mode. A constitutive model is developed to describe the high temperature creep and ratcheting behavior. The proposed model involves three inner variables including a back stress, an ageing parameter and a damage variable. The model is calibrated against the creep and tensile curves and verified by numerical simulations of cyclic creep tests.

¹ Institute of Mechanics, Otto-von-Guericke-Universität Magdeburg, Universitätsplatz 2, D-39106 Magdeburg, Germany

e-mail: holm.altenbach@ovgu.de, konstantin.naumenko@ovgu.de

² Institute of Solids Process Engineering and Particle Technology, Hamburg University of Technology, D-21073 Hamburg, Germany

e-mail: sergii.kozhar@tu-harburg.de

1. Introduction

Cast Al-Si base alloys belong to the most important aluminium alloys attributed to their low density, high specific strength, excellent castability, good mechanical properties and wear resistance. These alloys are applied in automotive, aerospace and other branches of industry. The considered here eutectic aluminium alloy AlSi12CuNiMg is widely used for load-bearing structural components, for example pistons for combustion engines, gears or pump parts. These components may be subjected to complex thermo-mechanical loading paths. Therefore it is important to analyze the considered alloy under applied cyclic loading conditions at high temperature.

Numerous studies of Al-Si alloys show that the static strength and fatigue behavior strongly depend on casting defects and microstructural characteristics. The presence of casting porosity and oxide films decreases the fatigue life [1, 2]. On the other hand, in the absence of casting imperfections, the fatigue fracture of cast Al-Si alloys is mainly characterized by cracking and debonding of silicon and intermetallic particles and nucleation of voids in the aluminium matrix. Dendrite arm spacing, grain size, shape and distribution of silicon particles and intermetallic compounds can also significantly influence the behavior of cast aluminium-silicon alloys [3].

Table 1. Chemical composition of the studied alloy (wt.%)

Si	Cu	Ni	Mg	Mn	Fe	Ti	P	Sr	Al
12.72	1.07	0.95	1.12	0.16	0.41	0.05	0.005	< 0.0005	Balance

In this study, the alloy behavior with respect to tensile strength, creep as well as isothermal mechanical fatigue at different temperatures is examined. To describe the results of conducted tests, a constitutive model is developed. The model is calibrated against the creep and tensile curves and verified by numerical simulations of cyclic creep tests .

2. Experimental Procedure

The material used in this study is cast aluminium alloy EN AC-48000. The chemical composition of the alloy is given in Table 1.

The base alloy was supplied in the form of ingots which were cut and melted in a preheated silicon carbide crucible of 3 kg-capacity, using an electrical resistance furnace and keeping the melting temperature at 740°C. Phosphorous was added with the help of the AlCu19P1,4 master alloy. Subsequently, the melts were degassed with the tablet degassing method. The melt was then poured into a permanent steel mould and preheated to 250°C. Samples were heat-treated under T6 conditions, i.e. solution treated at 510°C for 6 h in an air circulate furnace, water quenched, naturally aged at room temperature for 24 h, and then artificially aged at 165°C for 8 h. Microstructural changes were examined using optical and scanning electron microscopy. Specimens for creep testing with a diameter of 5 mm, length of 120 mm and gauge length of 50 mm were machined from the ingots. The surfaces of the specimens were polished to avoid crack initiation from the surface due to machining imperfections. Tests were performed on a servohydraulic testing machine MTS-810 with maximum load of 250 kN. Creep tests were carried out at temperatures of 250°C and 300°C. Some of the broken specimens were analyzed with the help of light microscopy and scanning electron microscopy to determine the damage mechanisms.

Figure 1 shows the creep strain vs. time curves. Owing to the scatter of test results, creep curves are averaged. Figure 2(a) shows the creep strength (stress vs. time to rupture) curves for the temperature levels of 250°C and 300°C. The experimental data at 350°C published in [4] is added to the plot. In the double logarithmic scale the data can be fitted by straight lines. The slopes of the lines depend on temperature levels. This indicates that different fracture mechanism may operate depending on stress and temperature values. The rupture strain vs. stress plot is presented in Figure 2(b). We observe that values of rupture strain tend to decrease with an increase in the stress.

3. Constitutive Model

As experimental data show, at high temperatures the tensile behavior is strain rate dependent. A unified theory of viscoplasticity has been developed to describe inelastic responses of engineering materials under different loading conditions, e.g. [5]. The constitutive equations characterize basic features of inelastic material behavior such as uni- and multi-axial ratcheting, creep, thermo-mechanical fatigue, etc. Any viscoplastic constitutive equation

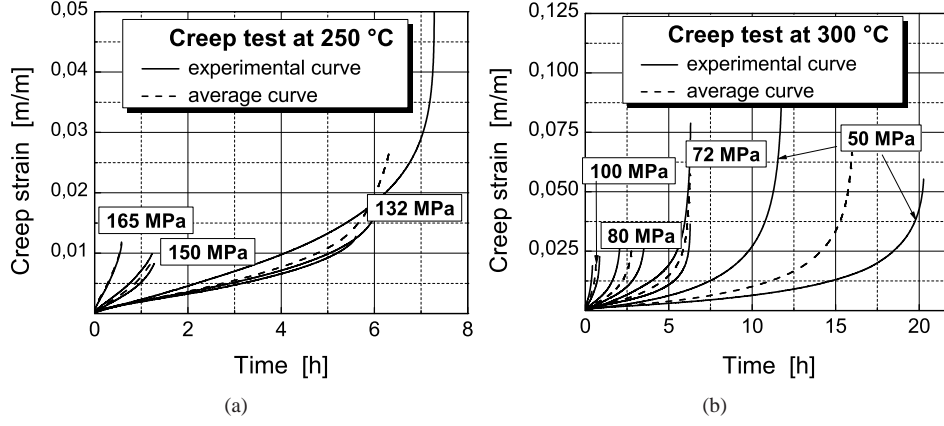


Figure 1. Experimental and averaged creep curves at (a) 250°C and (b) 300°C.

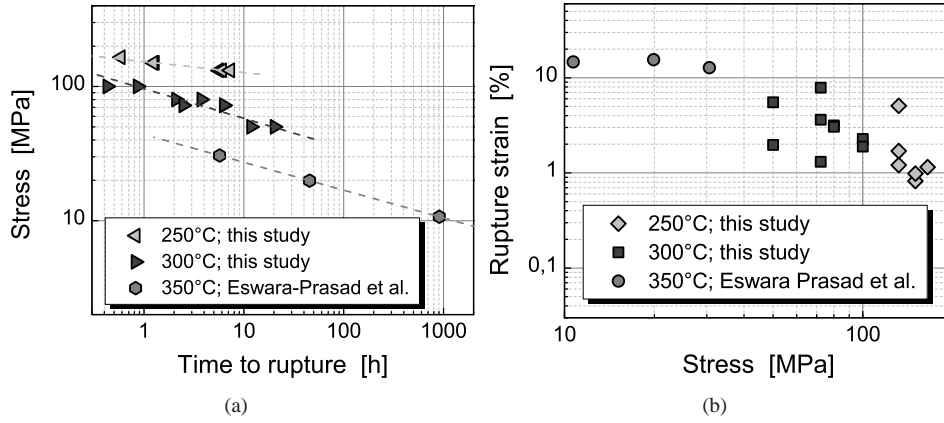


Figure 2. Variation of rupture time with stress (a) and the rupture strain vs. stress (b).

must include the viscosity function and the internal state variables together with appropriate evolution equations [5].

The constitutive equation for inelastic strain rate tensor can be formulated as follows

$$\dot{\boldsymbol{\epsilon}}^{\text{in}} = \frac{3}{2} A \sinh \left\{ \frac{\sigma_{\text{eq}}}{\sigma_0 (1 - \omega) (1 - \phi)} \right\} \frac{\boldsymbol{s} - \boldsymbol{\beta}}{\sigma_{\text{eq}}}, \quad (1)$$

$$\boldsymbol{s} = \boldsymbol{\sigma} - \frac{1}{3} \text{tr} \boldsymbol{\sigma} \boldsymbol{I}, \quad \boldsymbol{\beta} = \boldsymbol{\alpha} - \frac{1}{3} \text{tr} \boldsymbol{\alpha} \boldsymbol{I}, \quad (2)$$

$$\dot{\boldsymbol{\beta}} = A_h \left(\frac{2}{3} \dot{\boldsymbol{\epsilon}}^{\text{in}} - \dot{\epsilon}_{\text{eq}} \frac{\boldsymbol{\beta}}{\beta_*} \right), \quad \dot{\epsilon}_{\text{eq}} = \sqrt{\frac{2}{3} \text{tr} (\dot{\boldsymbol{\epsilon}}^{\text{in}})^2}, \quad \sigma_{\text{eq}} = \sqrt{\frac{3}{2} \text{tr} (\boldsymbol{s} - \boldsymbol{\beta})^2}. \quad (3)$$

In Eqs. (1)-(3) $\boldsymbol{\beta}$ is the deviatoric part of the back stress tensor $\boldsymbol{\alpha}$, \boldsymbol{s} is the deviatoric part of the stress tensor $\boldsymbol{\sigma}$, $\dot{\boldsymbol{\epsilon}}^{\text{in}}$ is the inelastic strain rate tensor, A , A_h , β_* and σ_0 are parameters, $\dot{\epsilon}_{\text{eq}}$ and σ_{eq} are the equivalent strain rate and the equivalent stress, respectively. To take into

account over-ageing processes such as coarsening of the strengthening phases Mg_2Si , for instance, the state variable ϕ is introduced in Eq. (4). The corresponding evolution equation is postulated here as follows

$$\dot{\phi} = K_c (C_{\text{sat}} - \phi), \quad (4)$$

where K_c and C_{sat} are material parameters. The choice of evolution law for ϕ is based on the experimental relationships between the time and the basic mechanical properties of the alloy exposed at different temperatures.

To consider damage processes including particles cracking and nucleation of voids and dimples in the matrix around the brittle particles, a scalar damage variable ω in the sense of continuum damage mechanics [6] is introduced. The evolution equation for damage is assumed as follows

$$\dot{\omega} = g(\omega)h(\boldsymbol{\sigma})\frac{\dot{\epsilon}_{\text{eq}}}{\epsilon_*(\boldsymbol{\sigma})}, \quad (5)$$

where $g(\omega)$, $h(\boldsymbol{\sigma})$ and $\epsilon_*(\boldsymbol{\sigma})$ are response functions. Examples for the response functions $g(\omega)$ are given in [6, 7] A frequently used response function $h(\boldsymbol{\sigma})$ can be written as follows [7]

$$h(\boldsymbol{\sigma}) = \frac{\sigma_1 + |\sigma_1|}{2\sigma_{\text{vM}}}, \quad \sigma_{\text{vM}} = \sqrt{\frac{3}{2}\text{tr}(\mathbf{s})^2}. \quad (6)$$

where σ_1 is the first principal stress and σ_{vM} is the von Mises equivalent stress. The response function $\epsilon_*(\boldsymbol{\sigma})$ describes the dependence of the creep rupture strain on stress. The response functions in constitutive and evolution equations as well as the values of material constants are identified in [8]. Furthermore, the model is validated in [8] for inelastic behavior under various loading paths.

References

- [1] M.J. Couper, A.E. Neeson, and J.R. Griffiths. Casting Defects and the Fatigue Life of an Aluminum Casting Alloy. *Fatigue & Fracture of Engineering Materials & Structures*, 13:213–227, 1990.
- [2] H. Stroppe. Einfluß der Porosität auf die mechanische Eigenschaften von Gußlegierungen. *Giessereiforschung*, 252:58–60, 2000.
- [3] H. Ye. An overview of the development of Al-Si-alloy based material for engine applications. *Journal of Materials Engineering and Performance*, 12:288–297, 2002.
- [4] N. Eswara-Prasad, D. Vogt, T. Bildingmaier, A. Wanner, and E. Arzt. Effect of prior fatigue exposure on the creep behaviour of an aluminium alloy (Al-12Si-CuMgNi). *Zeitschrift Fur Metallkunde*, 91:190–195, 2000.
- [5] J.L. Chaboche. A review of some plasticity and viscoplasticity constitutive theories. *International Journal of Plasticity*, 24:1642–1693, 2008.
- [6] J. Lemaitre and R. Desmorat. *Engineering Damage Mechanics*. Springer-Verlag Berlin Heidelberg, 2005.
- [7] K. Naumenko, H. Altenbach, and A. Kutschke. A combined model for hardening, softening, and damage processes in advanced heat resistance steels at elevated temperature. *International Journal of Damage Mechanics*, 20:578–597, 2011.
- [8] S. Kozhar. *Festigkeitsverhalten der Al-Si-Gusslegierung AlSi12CuNiMg bei erhöhten Temperaturen*. PhD thesis, Otto-von-Guericke University, Magdeburg, 2011.

ASSESSMENT AND COMPARISON OF NON-LOCAL MODELS FOR DUCTILE DAMAGE

F.X.C. Andrade¹, J.M.A. Cesar de Sa^{2,*}, F.M. Andrade Pires²

¹ DYNAmore GmbH
Industriestr. 2, 70565 Stuttgart, Germany

² Faculty of Engineering, University of Porto
Rua Dr. Roberto Frias s/n, 4200-465 Porto, Portugal
*e-mail: cesarsa@fe.up.pt

Abstract. Aiming to answer the question of which non-local formulations effectively lead to mesh-insensitive results, we select in this contribution several constitutive variables to be non-local quantities by taking both Lemaitre and GTN models as the base for the non-local enhancement. The resulting non-local constitutive models are employed in the numerical simulation of various specimens which are subjected to different values of stress triaxiality and Lode angle at the fracture zone. The goal is to find which models present the best performance in the task of providing mesh-insensitive solutions. The results show that strain-softening mesh dependency is much stronger in plane strain and pure shear stress states than in the axisymmetric case. It is also found that the variables that regularise the solution in the axisymmetric case do not necessarily eliminate mesh sensitivity in the other cases.

1. Introduction

Non-local models have been successfully used in the last two decades in the task of circumventing the pathological mesh dependency. Such issue is inherently present in local strain-softening media which is the case of many commonly employed constitutive models. Mesh sensitivity takes place when the partial differential equilibrium equations lose ellipticity (or hyperbolicity, in the transient case) due to the negative material modulus in the softening regime. Since the pioneering work of Pijaudier-Cabot and Bazant [1], who applied the non-local formulation of Edelen and co-workers [2-3] in the context of an elastic-damage model, many advances have been accomplished by many authors, who developed reliable and efficient algorithms for the implementation of the non-local theory, both in its integral and differential counter-parts [4-9]. It is worth mentioning that both formulations of non-locality are, in general, equivalent and render a similar behaviour if employed under the same circumstances.

Despite the many advances in this topic, many questions still remain unanswered. For instance, up to this date, there is no exact guideline for how should non-locality be introduced in most existing local models. In general, authors have usually chosen a promising candidate variable to be a non-local quantity and have then developed and assessed their models based on this candidate. In view of that, the objective of the present work is to enhance with non-locality the classical models of Lemaitre [10] and GTN [11],

which are very often adopted to simulate ductile materials. We select different variables to be taken as non-local and assess the established non-local models through numerical simulation under different stress states. The main goal is to identify which options lead to a completely mesh insensitive material description when subjected to different loading conditions.

2. Non-local models

In the present assessment, the constitutive frameworks proposed by Lemaitre [10] and Tvergaard and Needleman [11], often called GTN-Model, have been enhanced with non-locality by regularising different constitutive variables. In the case of the GTN-Model, an additional damaging mechanism, based on the work of Nahshon and Hutchinson [12], has been added into the underlying constitutive model in order to trigger damage under shear-dominated stress states. The aforementioned shear mechanism reads:

$$\dot{f}^{shear} = kf\dot{\epsilon}_{eqv}^p (1 - \xi^2) \quad (1)$$

where ξ is the normalised third invariant of the deviatoric stress tensor. The several non-local models are schematically summarised in Tables 1 and 2.

Table 1 – Lemaitre-based non-local models.

Variable	Symbol	Evolution Equation	REF.
Damage	D	$\dot{D}(\mathbf{x}) = \int_V \beta(\mathbf{x}, \xi) \dot{D}(\xi) dV(\xi)$	L-D
Isotropic Hardening	R	$\dot{R}(\mathbf{x}) = \int_V \beta(\mathbf{x}, \xi) \dot{R}(\xi) dV(\xi)$	L-R
Energy Release Rate	$-Y$	$-\dot{\bar{Y}}(\mathbf{x}) = \int_V \beta(\mathbf{x}, \xi) (-\dot{Y}(\xi)) dV(\xi)$	L-Y

Table 2 – GTN-based non-local models.

Variable	Symbol	Evolution Equation	REF.
Damage	f	$\dot{f}(\mathbf{x}) = \int_V \beta(\mathbf{x}, \xi) \dot{f}(\xi) dV(\xi)$	G-F
Isotropic Hardening	R	$\dot{R}(\mathbf{x}) = \int_V \beta(\mathbf{x}, \xi) \dot{R}(\xi) dV(\xi)$	G-R
Equivalent Plastic Strain	ϵ_{eqv}^p	$\dot{\epsilon}_{eqv}^p = \int_V \beta(\mathbf{x}, \xi) \dot{\epsilon}_{eqv}^p(\xi) dV(\xi)$	G-EP

3. Assessment under different stress states

It has been widely recognised that ductile materials behave quite differently under different stress states; therefore, this statement highly suggests that the issues of pathological mesh dependency may also behave quite differently under different loading conditions. Thus, aiming to unfold the question of which variable should be regularised in a given ductile damage model, a comprehensive comparison of different non-local formulations, when applied in the simulation of different stress states, will be carried out in this contribution. Figure 1 shows four different specimens that have been selected for the present assessment. It is worth noting that each specimen provides a different stress state when subjected to external loading.

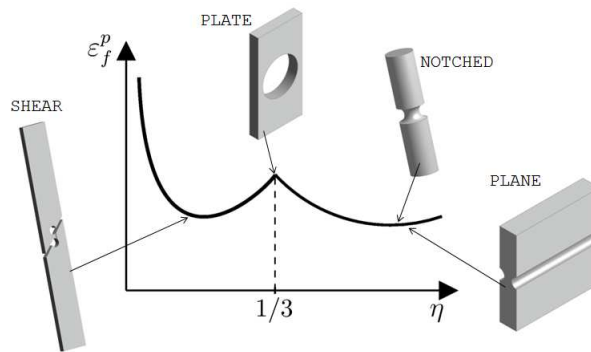


Figure 1. Specimens subjected to different stress states.

4. Results

The large number of analysis that the present assessment has required makes the scrutiny of the results difficult if one aims to have a general overview. Thus, in order to facilitate comprehension, we have schematically summarised all the results obtained in Table 3. A more detailed account can be found in [13]. Reference values for the initial triaxiality and the average normalised third invariant have been given for convenience.

Table 3 – Summary of results.

Analysis	η_0	ξ_{avg}	L-D	L-R	L-Y	G-F	G-R	G-EP
NOTCHED	0.8	1.0	++	--	++	++	++	++
PLANE	0.7	0.0	++	--	--	++	--	+
PLATE	1/3		++	--	--	++	++	++
SHEAR	0.0	0.0	++	--	+	++	--	+

Close observation of Table 3 shows that the solutions in which damage has been regularised have been effective in all cases. We remark that the conclusion that damage is the preferred variable to be regularised in the case of Lemaitre- and Gurson-based models is significantly important. It seems that this is an inherent characteristic of implicit damage models. In the case of explicit damage models, often used to model quasi-brittle materials, the conclusion is completely different. As reported by Jirásek and Rolshoven [14], the damage variable is a bad candidate for non-local variable for such explicit damage models and should be avoided. This utterly implies that one has to be very careful when choosing

the non-local variable for a given constitutive model; in particular, it should be analysed if the damage formulation of such material model is done in an implicit or explicit fashion.

5. Conclusions

The main goal of this contribution was to unfold the question of which variable should be regularised in order to obtain mesh-insensitive results under strain-softening regimes. Therefore, several non-local models based on the constitutive theories of Lemaitre and Gurson have been established. Scrutiny of the results have revealed that in both cases (Lemaitre- and Gurson-based models) the damage variable seems to be the optimal candidate for non-local variable.

Acknowledgements. F.X.C. Andrade was supported by the Programme Alþan, the European Union Programme of High Level Scholarships for Latin America, scholarship no. E07D401751BR. J.M.A. Cesar de Sa and F.M. Andrade Pires gratefully acknowledge the financial support provided by Ministério da Ciência e Tecnologia e do Ensino Superior – Fundação para a Ciência e Tecnologia (Portugal), under the projects PTDC/EME-TME/74589/2006 and PTDC/EME-TME/71325/2006.

References

- [1] G. Pijaudier-Cabot and Z.P. Bazant (1987), Nonlocal damage theory, *Journal of Engineering Mechanics*, **113**(10), pp.1512–1533.
- [2] D.G.B. Edelen and N. Laws (1971), On the thermodynamics of systems with nonlocality, *Archive for Rational Mechanics and Analysis*, **43**, pp. 24–35.
- [3] D.G.B. Edelen, A.E. Green, and N. Laws (1971), Nonlocal continuum mechanics, *Archive for Rational Mechanics and Analysis*, **43**, pp. 36–44.
- [4] L. Stromberg and M. Ristinmaa (1996), FE-formulation of a nonlocal plasticity theory, *Computer Methods in Applied Mechanics and Engineering*, **136**, pp. 127– 144.
- [5] R.H.J. Peerlings, R. De Borst, W.A.M. Brekelmans, and J.H.P. De Vree (1996), Gradient-enhanced damage for quasi-brittle materials, *International Journal for Numerical Methods in Engineering*, **39**, pp. 1512–1533.
- [6] G. Borino, B. Failla, and C. Polizzotto (2003), A symmetric nonlocal damage theory, *International Journal of Solids and Structures*, **40**, pp. 3621–3645.
- [7] M.G.D. Geers, R.L.J.M. Ubachs, and R.A.B. Engelen (2003), Strongly non-local gradient-enhanced finite strain elastoplasticity, *International Journal for Numerical Methods in Engineering*, **56**, pp. 2039–2068.
- [8] J.M.A. Cesar de Sa, F.M. Andrade Pires, and F.X.C. Andrade (2010), Local and nonlocal modeling of ductile damage, In M. Vaz Jr., E.A. De Souza Neto, and P.A. Muñoz-Rojas, editors, *Advanced Computational Materials Modelling: From Classical to Multi-Scale Techniques*, Chapter 2, pp. 23–72. Wiley-VCH, Weinheim.
- [9] F.X.C. Andrade, J.M.A. Cesar de Sa, and F.M. Andrade Pires (2011), A ductile damage nonlocal model of integral-type at finite strains: formulation and numerical issues, *International Journal of Damage Mechanics*, **20**, pp. 515–557.
- [10] J. Lemaitre (1985), A continuous damage mechanics model for ductile fracture, *Journal of Engineering Materials and Technology*, **107**, pp. 83–89.
- [11] V. Tvergaard and A. Needleman (1984), Analysis of cup-cone fracture in a round tensile bar, *Acta Metallurgica*, **32**, pp. 157–169.
- [12] K. Nahshon and J.W. Hutchinson (2008), Modification of the Gurson model for shear failure, *European Journal of Mechanics A/Solids*, **27**, pp. 1–17.
- [13] F.X.C. Andrade (2012), *Non-local modelling of ductile damage: formulation and numerical issues*, PhD Thesis, University of Porto, Portugal.
- [14] M. Jirásek and S. Rolshoven (2003), Comparison of integral-type nonlocal plasticity models for strain-softening materials, *International Journal of Engineering Science*, **41**, pp. 1553–1602.

INFLUENCE OF PLASTICITY REDUCTION ON STRENGTH AND FRACTURE OF TURBINE RUNNER COVER IN HYDRO POWER PLANT ĐERDAP 1

Miodrag Arsić¹, Srđan Bošnjak², Zoran Odanović¹,
Vencislav Grabulov¹, Brane Vistić¹

¹Institute for Materials Testing,
Bulevar vojvode Mišića 43, 11000 Belgrade
e-mail: miodrag.arsic@institutims.rs

²Faculty of Mechanical Engineering,
The University of Belgrade, Kraljice Marije 16, 11120 Belgrade
e-mail: sbosnjak@mas.bg.ac.rs

Abstract. Vertical Kaplan turbines, with 200 MW of nominal output power, manufactured in Russia, are built into six hydro-electric generating units of hydro power plant „Đerdap 1”. In this paper results of experimental examinations of four specimens taken from the runner cover which is made of cast steel 20GSL are presented. These results indicated that values of yield strength, tensile strength and impact energy for all specimens met the demands of the standard, while two specimens had significantly lower values of elongation ($A_5 = 8\%$ and 9%). Taking into account that values A_5 i Z are not universal and the fact that it is impossible to estimate whether fracture mechanism will be implemented in material the runner cover was made of, analytical and numerical calculations of stress state and experimental examinations of fracture mechanics parameters have been carried out. Obtained results of fatigue crack growth rate da/dN indicated that internal deformations of circular or elliptical shape (flaws detected by ultrasonic testing), of initial size up to 6 mm, enable 29 year long reliable operation of the runner cover.

Keywords: hydro turbine, runner cover, plasticity, life

1. Introduction

Designing, construction and putting into operation of a hydro power plant comprises complex tasks. Due to limited possibilities of periodic inspections and state analyses, hydro turbines and their components are being designed in order to endure 40 years of operation. Therefore, extensive researches and testing of hydro power plant equipment have been carried out all over the world for a long time. Turbine and hydromechanical equipment testing has been introduced recently at a modest level when serbian hydro power plants are concerned.

2. Experimental Tests

Turbine runner cover at the hydro power plant "Djerdap 1" is presented in fig. 1. Along with experimental tests carried out on the cover, tests were performed in order to

determine mechanical properties and fracture mechanics parameters. Test results for four specimens taken from the cover, made of cast steel 20GSL, showed that yield strength (R_{02}), tensile strength (R_m) and impact energy (KCU) values for all specimens meet the demands of the GOST 108.11.158-86 standard, as well as that values which define the plasticity of the base material, elongation (A_5) and contraction (Z) have a large dispersion. Two specimens met the demands of the standard ($A_5 = 23\%$ and 27%), while two had significantly lower values of elongation ($A_5 = 8\%$ and 9%). Obtained values of fracture mechanics parameters (critical stress intensity factor - K_{Ic} , critical fatigue crack length - a_c , fatigue threshold - ΔK_{th} , constant in Paris equation - C , exponent in Paris equation - m_p , fatigue crack growth rate - da/dN) are presented in table 1.

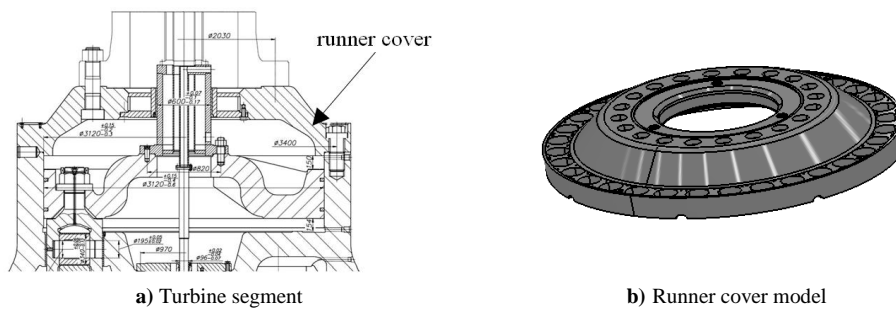


Figure 1. Vertical Kaplan turbine, with nominal output power of 200 MW

Table 1. Fracture mechanics parameters at 23°C, for the stress intensity factor range $\Delta K = 10$ [MPa·m^{1/2}]

Specimen	K_{Ic} [MPa·m ^{1/2}]	a_c [mm]	ΔK_{th} [MPa·m ^{1/2}]	C [(m/cycle)/ (MPa·m ^{1/2}) ^{m_p}]	m_p	da/dN [m/cycle]
With reduced plasticity	46,3	9,3	7,4	$5,7 \cdot 10^{-11}$	3,15	$6,36 \cdot 10^{-08}$
With adequate plasticity	50,4	10,2	8,7	$3,0 \cdot 10^{-11}$	3,02	$5,11 \cdot 10^{-08}$
Minimum allowed value of K_{Ic} for 20GSL at temperatures below 0° C is $K_{Ic} = 41 - 44$ [MPa·m ^{1/2}]						

2. Influence of Plasticity Reduction During Runner Cover Casting on Fatigue Strength

Influence of plasticity reduction and internal defects on fatigue of cast steel 20GSL is important concerning the establishment of technical conditions for casting, norms for allowable defects and quality inspection. For that purpose and with participation of representatives of LMZ factory and Mechanical Engineering Institute from Saint Petersburg, the mechanisms of microcrack initiation and conditions of propagation of microcracks to macrocracks have been established. Tests have been carried out on large specimens of dimensions from 100 to 300 mm. Analysis of test results helped the establishment of the empirical dependency which enabled the evaluation of resistance to fatigue of cast steel with internal defects, or in other words with reduced plasticity:

$$\sigma_{-1}^* = \frac{\sigma_{-1}}{(1 + \beta \cdot d_{max})^{1/2}} \quad (1)$$

where: σ_{-1} - lower limit of fatigue strength dispersion;
 β - coefficient which depends on properties of the metal;

d_{\max} - maximum size of the defect in cast material.

As a result of testing of cast steels with reduced plasticity, the following dependency between stress amplitude σ_{-1} and maximum number of loading cycles N has been obtained:

$$\lg(\sigma_{-1}) = 2,69 - 0,155 \times \lg(N) \quad (2)$$

It was determined that defect sizes from 0,2 to 0,5 mm in 20GSL do not influence fatigue strength, as well as that maximum allowable defect size of $d = 1.5$ mm causes the reduction of fatigue strength from $\sigma_{-1} = 118,5$ MPa to $\sigma_{-1} = 91,15$ MPa, in which case the corrosion-fatigue strength reserve (safety factor) is still satisfactory, $S_{\sigma} = 1,63$.

3. Estimation of Service Life of the Runner Cover through the Use of Fracture Mechanics

Estimation of runner cover service life through the use of fracture mechanics has been carried out according to methodology presented in paper [3]. In the area of stable crack growth, Paris' equation describes the behaviour of the material with sufficient accuracy:

$$\frac{da}{dN} = C \cdot (\Delta K)^{m_p} \quad (3)$$

where: ΔK - stress intensity factor range, which is being calculated by the following equation:

$$\Delta K = \Delta\sigma \sqrt{\frac{1,21\pi a}{Q}} \quad (4)$$

For the internal defect measuring 6 mm in diameter in the steel cast 20GSL, detected by ultrasonic inspection, characteristic value is circle radius or half-length of the short axis of the ellipse, which value a_0 is being calculated by the following equation:

$$a_0 = \frac{\sqrt{3}}{2} d = \frac{\sqrt{3}}{2} 6 = 5,2\text{mm} \quad (5)$$

Stress intensity factor K_I is being calculated by the following equation, in case of existence of an internal defect:

$$K_I = \sigma_{\max} \sqrt{Ma_0} = 98,5 \sqrt{2,38 \times 0,0052} = 11 \text{ MPa} \sqrt{\text{m}} \quad (6)$$

where: σ_{\max} - maximum operational stress ;

M - coefficient which depends on shape and dimensions of defects and structure,
 $M = 1,25 \pi / Q$;

a_0 - characteristic size of the defect;

Q - defect shape parameter;

$\Delta\sigma$ - stress range, which is being calculated by the following equation:

$$\Delta\sigma = \frac{\sigma_{\max} - \sigma_{\min}}{2} = \frac{98,5 - 93,6}{2} = 2,45\text{mm} \quad (7)$$

For the ratio of half-lengths of the short and long axis of the defect ellipse $a/2c = 0,3$, as well as for the ratio of the maximum projected stress on the turbine cover and yield

strength for the specimen with the lowest plasticity $\sigma_{\max} / R_{02} = 98,5 / 309 = 0,32$, value of the defect shape parameter is $Q = 1.65$ [3].

Critical length of the internal crack in cast steel in which deformation weakening occurs, which can cause the fracture in the structure, can be calculated by equation (6):

$$a_{cr} = \frac{1}{M} \left(\frac{K_{Ic}}{\sigma_{\max}} \right)^2 = \frac{1}{2,38} \left(\frac{46,3}{98,5} \right)^2 = 92,8 \text{ mm} \quad (8)$$

Number of cycles until reaching the critical size of the internal defect within the turbine runner cover, made of cast steel 20GSL with reduced plasticity, gets calculated through the integration of Paris' equation, as well as values from table 1 and other calculated values:

$$N = \frac{2}{C_p \cdot M^{\frac{m_p}{2}} \cdot \Delta \sigma^{m_p}} \left(\frac{1}{a_0^{\frac{m_p-2}{2}}} - \frac{1}{a_{cr}^{\frac{m_p-2}{2}}} \right) = 2,61 \cdot 10^{10} \quad (9)$$

Number of load cycles for a one year period is:

$$N_u = n_h \cdot 60 \cdot 7000 \cdot 30 = 71,43 \cdot 60 \cdot 7000 \cdot 30 = 9 \cdot 10^8 \text{ cycles} \quad (10)$$

where: n_h – number of revolutions of the hydroelectric generating set, $n_h = 71.43$ o/min;

60 – number of minutes per hour;

7000 – overall number of hours of operation of the hydroelectric generating set during a one year period;

30 – number of years of operation of the hydroelectric generating set.

Estimated service life of the turbine runner cover with reduced plasticity is:

$$n = \frac{N}{N_u} = \frac{2,61 \cdot 10^{10}}{9 \cdot 10^8} = 29 \text{ years} \quad (11)$$

6. Conclusion

Results of fatigue strength tests carried out on large specimens, as well as obtained values of fracture mechanics parameters, enabled the estimation of service life of turbine runner cover with reduced plasticity.

Acknowledgement. The authors acknowledge the support from the Serbian Ministry of Education and Science for projects TR 35002 and TR 35006.

References

- [1] Arsić M. and Vistić B. (2005), Analysis of operational capability and a possibility of operational safety of the turbine cover in a life cycle at least 30 years long, Institute for Materials Testing, Belgrade.
- [2] Tests carried out by LMZ factory and Institute for Mechanical Engineering AN, (2005), Saint Petersburg.
- [3] Bošnjak S., Arsić M., Zrnić N., Rakin M., Pantelic M. (2011), Bucket wheel excavator: Integrity assessment of the bucket wheel boom tie – rod welded joint, *Engineering Failure Analysis*, Vol.18, pp. 212 – 222.
- [4] Hertzberg R. (1995), *Deformation and fracture mechanics of engineering materials*, New York, John Wiley & Sons, Inc.

ENERGY RELEASE RATES AT INTERFACIAL CRACKS IN RESIDUALLY STRESSED ALUMINUM BASED FIBRE METAL LAMINATE (GLARE): A NUMERICAL ASSESSMENT

Sunil Bhat¹, Rajasekhar Patibandla²

¹School of Mechanical and Building Sciences
Vellore Institute of Technology, Vellore-632014, Tamil Nadu, India, e-mail: sbhat_789@rediffmail.com

²School of Mechanical and Building Sciences
Vellore Institute of Technology, Vellore-632014, Tamil Nadu, India
e-mail: rajasekhar1408@gmail.com

Abstract. Mode I fatigue cracks in Glare (Aluminum based fibre metal laminate) nucleate and propagate in soft aluminum layers whereas strong fibre layers don't fracture and remain intact. This results in the development of interfacial cracks and delaminations between aluminum and fibre layers. The interfacial cracks subsequently grow as Mode II cracks under cyclic load. Different residual stresses in material layers also influence the cracks. The paper presents finite element analysis of, a residually stressed, cracked and delaminated Glare to determine energy release rates at the tips of interfacial cracks for checking their growth stability. Multiple cracks in various orientations viz. normal to and across the property mismatched interfaces, leading to several delaminations, are examined. The delaminations are modeled by cohesive elements. Various sizes of interfacial cracks are considered. The model is successfully validated over a cracked and delaminated CentrAL, the laminate with similar ingredients as that of Glare but with different dimensions, the results of which are reported elsewhere.

1. Introduction

Fibre metal laminate (FML) is a hybrid composite that consists of layers of thin metallic sheets bonded and cured by heat and pressure with prepregs., each prepreg. built up of resin impregnated fibre cloth layers laid in similar or different orientations. Glare is one such aluminum and glass fibre based FML. Several property mismatched interfaces exist in Glare because the materials on either side of each interface in it have un-identical elasticity and plasticity properties. Also variable residual stresses develop in material layers during curing of the laminate due to their different stiffness and coefficients of thermal expansion. Consequently, material property mismatch and residual stresses influence fracture characteristics of Glare.

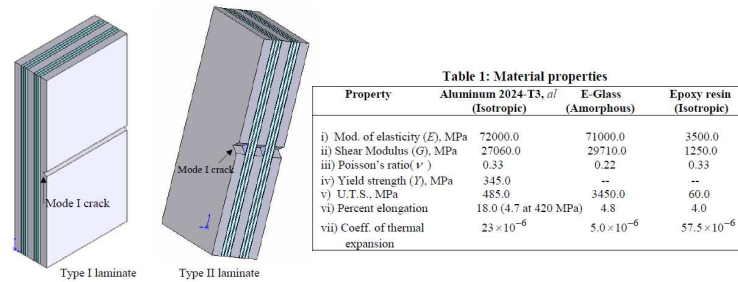


Fig. 1 Cracked Glare laminates

Refer Fig. 1. A cracked and delaminated Glare in the present work is classified into two types depending upon the orientation of cracks in it viz. Type I and Type II. In Type I laminate, the parent Mode I cracks in aluminum layers grow normally towards the composite prepregs. before deflecting into the interfaces of fibres in prepregs. since cracks can't penetrate the fibres. This results in development of interfacial cracks and delaminations between aluminum and fibre layers. On the other hand, in Type II laminates, the normal parent Mode I cracks in aluminum layers are oriented across the interfaces and their advancement simultaneously leads to the generation of interfacial cracks and delaminations governed by debonding curve between aluminum and fibre layers, the parent and interfacial crack growths forming a balanced and coupled process. The interfacial cracks in both the types of laminates propagate as Mode II cracks under cyclic loads.

The paper aims at numerical analysis of, a residually stressed, cracked and delaminated Glare for obtaining energy release rate, G , at the tips of interfacial cracks to check their stability by the criterion, $G < G_c$, where the critical value, G_c , represents the inter-laminar fracture toughness of the laminate. Multiple interfacial cracks of various sizes are examined in both the types of laminates. The approach is successfully validated over a different type of laminate, CentrAL, results of which are reported elsewhere.

2. Characterization of Glare

Refer Fig. 2. Glare is assumed to comprise three layers of 0.4 mm thick 2024-T3 aluminum sheets bonded alternatively with two prepreg. layers., each prepreg. layer built up of three composite layers in the sequence, c0-c90-c0. A composite layer consists of 0.0165 mm (app.) thick epoxy resin on either side of a 4 mil or 0.1mm thick unidirectional E-glass fibre. Composite c0 has fibres laid in y direction i.e. along the direction of the load whereas composite c90 has fibres laid in x direction i.e. perpendicular to the direction of the load. Material properties are displayed in Table 1. The longitudinal (y dir.) and transverse (x dir.) coefficients of thermal expansion of the laminate are found as $18.62 \times 10^{-6} \text{ C}^{-1}$ and $17.25 \times 10^{-6} \text{ C}^{-1}$ respectively.

The laminate is 200 mm long, 50 mm wide and 2 mm thick. It is subjected to far field monotonic tensile stress of 150 MPa in y direction. Since the layers are un-identical, classical theory of laminates is employed to obtain stress distribution in them. Curing temperature of the laminate is assumed as 120 deg.. Effect of curing is incorporated by superimposing residual curing strain with the applied strain. Difference in stress values obtained with and without the effect of curing provides the magnitude of residual stresses. As expected, their value in y direction in plane strain condition used for Type I laminate are close to those in plane stress condition used for Type II laminate. Difference between the values in x direction is inconsequential as these values don't influence the computations carried out in y - z plane.

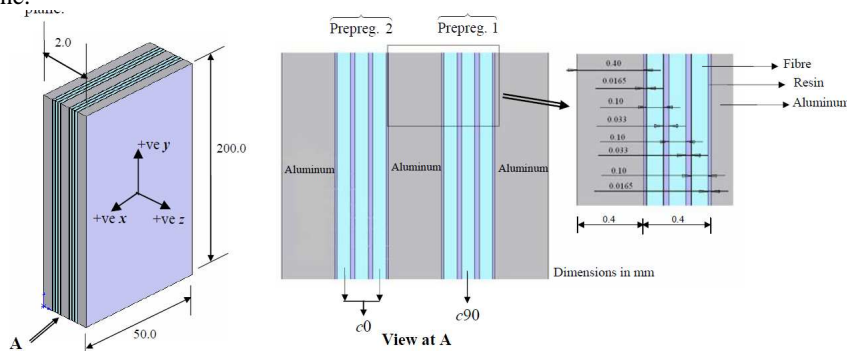


Fig. 2 Constitution of Glare

3. Finite element analysis of damaged Glare

Refer Fig. 3. Four cases of Type I laminate *viz.* a) one crack with one delamination b) two cracks with two delaminations c) two cracks with three delaminations and d) three cracks with four delaminations and two cases of Type II laminate *viz.* a) two cracks with two delaminations and b) three cracks with four delaminations are modeled. Two interfacial crack lengths, d , of 2 mm and 30 mm are investigated in Type I laminate whereas the fixed value of d with parent crack depth is chosen as 9.4 mm and 25 mm respectively in Type II laminate.

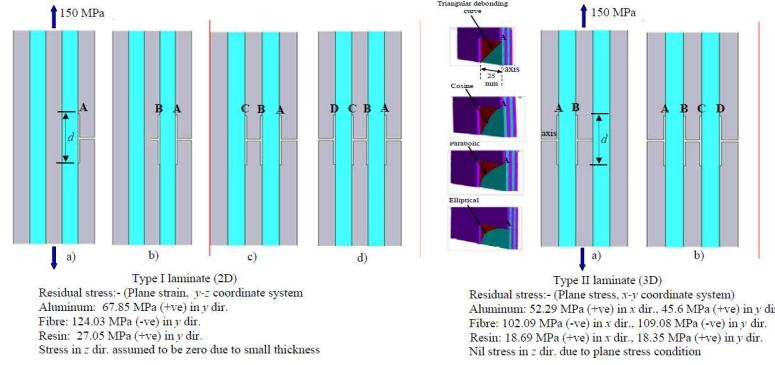


Fig. 3 Orientation of cracks and delaminations in damaged Glare

Half of the laminates are only modeled due to the conditions of symmetry. Each material layer is considered separately. 2D mesh model of Type I laminate is created with solid 183 elements in aluminum layers and shell 281 elements in resin and fibre layers under plane strain condition. Number of elements and nodes generated are equal to 40912 and 123727 respectively. 3D mesh model of Type II laminate is created with 8 noded, solid 185 elements in aluminum and 8 noded, layered solid shell 190 elements in fibre and resin layers. Number of nodes and elements generated are equal to 55827 and 53066 respectively. Delaminations are modeled by cohesive elements in the form of 2D, 6 noded, inter cohesive element 203 in Type I and 3D, 8 noded, inter cohesive element 205 in Type II laminate. Values of maximum normal traction (σ_z), width and maximum equivalent shear traction of τ_{zy} and τ_{zx} in the delamination zone are input as C1, C2 and C3 respectively in the cohesive element code. In Type II laminate, triangular, cosine, parabolic and elliptical debonding curves are assumed because they can be defined mathematically. Since the type of de-bonding curve influences C1, C2 and C3 values, albeit marginally, the cohesive element data are found for each of them by modeling cracked laminates without delaminations but with the use of a chosen debonding curve to note the maximum values developing near the curve. Sample values of C1, C2 and C3 in case a) of Type I laminate are of the order of 39.24 MPa, 0.001 mm and 34.32 MPa and in case a) of Type II laminate with triangular debonding are of the order of 19.5 MPa, 0.001 mm and 15.03 MPa respectively. Artificial damping coefficient of 1×10^{-5} s is used wherever necessary to achieve numerical convergence.

Ramberg-Osgood formulation, Eq. (1), is employed to obtain non-linear stress-strain values beyond yield point in aluminum

$$\varepsilon = \frac{\sigma}{E_{al}} + \frac{Y_{al} m'}{E_{al}} \left(\frac{\sigma}{Y_{al}} \right)^{m''} \quad (1)$$

The material constants, using stress-strain values at the break and at an intermediate point provided in Table 1, are obtained as $m' = 1.2$ and $m'' = 10$. The nodes representing cracks at the bottom surface in aluminum and resin layers of the model are unconstrained while all the nodes of fibre layers are constrained in y direction ($y = 0$). Load is applied as monotonic stress at the top edge of each laminate whereas the residual stresses are introduced over respective material nodes in x and y directions. All the interface layers are glued and the common nodes are merged. The nodes are thoroughly checked for connectivity before executing the models for solution.

As yielding levels are of small scale, G is considered equal to the value of J integral. J integral over a cyclic path, P , around interfacial crack tip [1] is defined in y-z plane by Eq. (2) as

$$J = \int_P \left(W_e(-dz) - T_y \frac{\partial v_n}{\partial y} ds - T_z \frac{\partial w_n}{\partial y} ds \right) \quad (2)$$

where W_e is the strain energy density, v_n and w_n are the nodal displacements in y and z directions, traction terms $T_y = \sigma_y n_y + \tau_{zy} n_z$, $T_z = \sigma_z n_z + \tau_{zy} n_y$ with n_y and n_z being unit normal vectors. Numerical values of J are obtained over three paths, denoted by 1, 2 and 3, near interfacial crack tips.

3.1 Results

Sample deformations with case a) of both the types of laminates are provided at Fig. 4. G values are displayed at Table 2. The value of G_c of the laminate is experimentally obtained as 0.85 N/mm. Since $G < G_c$ in all the cases of Type I laminate, the interfacial crack growth is concluded to be stable. In Type II laminate also, the values are safe except in interfacial cracks at one extreme end of case b) for all the types of debonding curves indicating crack instability.

3.2. Validation

The present model is applied over a different laminate referred to as CentrAL [2]. CentrAL has ingredients similar to that of Glare but with different dimensions. Its constitution and properties are presented in Fig. 5. All three aluminum layers in it are assumed to be cracked with delaminations existing between aluminum and prepreg. layers resembling case d) of Type I laminate. Interfacial cracks of 0.032 in. size are considered. Half of the laminate is again modeled under far field load line displacement of 0.0015 in. Prepregs. are considered as single units with given properties. Cohesive element data, C1, C2 and C3 used are of the order of 500000 msi, 0.0001in. and 920000 msi respectively. The results obtained are compared with the reported results in Table 3. They are in good agreement that validates the model.

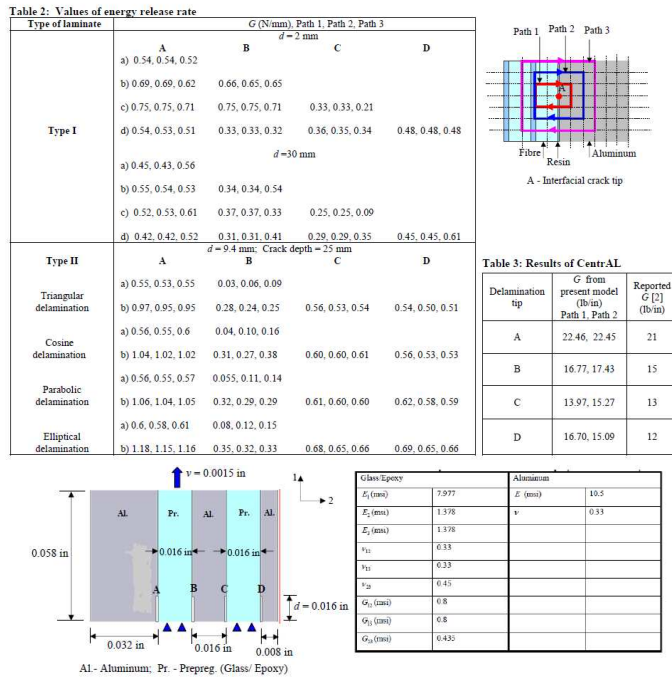


Fig. 5 Constitution of Centr-AL

4. Conclusion

A numerical approach to obtain energy release rate at interfacial crack tips in a, residually stressed, cracked and delaminated Glare is presented. Validity of the finite element model is well substantiated.

Acknowledgment. The work is funded by the Science and Engineering Research Council (SERC), Department of Science and Technology (DST), India.

References

[1] Rice, J.R. (1968), A path independent integral and approximate analysis of strain concentration by notches and cracks, *Journal of Applied Mechanics*, **35**, pp. 379-386.
 [2] Wang J. T. (2009), Calculation of stress intensity factors for interfacial cracks in fiber metal laminates, *Proceedings of 50th AIAA/ASME/ASCE/AHS/ASC Structures, Structural Dynamics, and Materials Conference*, Palm Springs, California, pp. 1-21.

DAMAGE AND RUPTURE OF STRUCTURAL MATERIALS UNDER COMPLEX LOW CYCLE LOADING

M. Bobyr, O. Khalimon, V. Koval

Institute of Mechanical Engineering
National Technical University of Ukraine "Kyiv Polytechnic Institute", Prospekt Peremohy,
37, 03056 Kyiv, Ukraine
e-mail: khalimon@gmail.com

Abstract. In this work application of phenomenological damage accumulation model for a case of the complex stress-strain mode is presented. Results of numerical calculation in ANSYS for a constructive element in the form of a plate with a hole (damage distribution for different diameters) are shown. On the basis of experiments the effective stress-strain curve for aluminum alloy is built and parameters of damage model are defined. For damage estimation at tension method on specific electrical resistance change has been used. The modified Neuber-Makhutov definition approach of stress and strain concentration factors with the damage account is discussed. Dependences of the given factors on the reduced stress and hardening rate of aluminum alloy from number of cycles are shown. Engineering and effective curves of a Morrow's diagram received as a result of strain controlled tests.

1. Introduction

The majority of responsible elements of designs contain stress concentrators (holes, fillet, neck and other). As any concentrator is the probable initiation center of a construction fracture, and the stress concentration is one of major factors which influence its strength and lifetime, so research of the stress-strain mode in the area of the concentrator and its improvement by means of existing approaches modification is an actual problem [1, 2, 3]. The majority of constructions analyses are carried out with use of the engineering stress-strain diagram of a material (engineering stress) that does not consider true stress in the specimen, and processes of growth and accumulation of microdefects in a plastic zone.

2. Damage Model

In the field of the concentrator there is a local zone of a plastic deformation in which intensively take place processes of damage accumulation, authors offered at an estimation of the stress-strain mode near the concentrator, for its improvement, to take into consideration damage scalar parameter, estimation of which is based on the power approach that is in more details presented in publication [3].

Dependence of damage parameter from plastic strain level, taking into account factor of Pisarenko-Lebedev is defined as follows [4]

$$D = \left(\frac{A^2}{2EB} \left(\frac{2}{3} (1 + \mu) \left[\chi + (1 - \chi) \frac{\sigma_1}{\sigma_i} \right]^2 + 3(1 - 2\mu) \left(\frac{\sigma_0}{\sigma_i} \right)^2 \right) \right)^c \frac{1}{2n+1} (\varepsilon_i^{(p)})^{2n+1}, \quad (1)$$

A , B , c and $n = mc$ material parameters, E – Young modulus of elasticity; $\varepsilon_i^{(p)}$ – plastic strain rate. μ – Poisson ratio, χ – factor of Pisarenko-Lebedev, which allows to consider different properties of a material at tension and compression, σ_0 – mean stress,

σ_1 – maximum stress, σ_i – stress ratio. Parameters A and m were defined from approximation of the experimental true stress-strain curve with power law $\sigma_i = A(\varepsilon_i^{(p)})^m$.

3. Material and main experimental feature

For definition of model parameters at experimental equipment which allows to record continuously damage of material at straining [5], experiments on specimens of aluminum alloy D16T (4.1% Cu, 1.6% Mg, 0.64% Mn, 0.47% Fe, 0.33% Si, 0.03% Ti, 0.02% Cr, 0.18% Zn) have been made. The damage parameter is identified as relative change of specific electric resistance of the specimen [4]. For damage parameter calculation values of material parameters (Table 1) gained from experiments were used.

Table 1

Material	Material parameter						
	E , MPa	χ	b	A	l	B	μ
Aluminum Alloy	69608	0.7	1,17	748	0,1091	1,7	0.3

4. Numerical implementation

For the further researches the plate of thickness 3 mm with the central aperture which diameter varied from 1 to 15 mm has been chosen.

Using geometrical and force symmetry, at numerical modeling the quarter of the specimen with corresponding boundary conditions (Fig. 2) was considered. For modeling of a finite-element grid were elements PLANE 82 used. For solution were used the true stress-strain diagram of a material (the diagram considering necking of the specimen).

Criterion of grid selection was value of a calculation results difference obtained on two different grids at equal loading conditions. If the difference on two grids under equal conditions differed less than on 1% further "subdivision" of a grid was not made also result was considered as the reliable. As a result of the numerical calculation for aluminum alloy damage distribution which are presented on Fig. 3 have been obtained.

For an estimation of concentration at elastic-plastic straining, stress (K_σ) and strain (K_ε) concentration factors are used. The general approach to definition of these factors does not consider damage [1, 2], in zone of concentrator. The damage parameter account gives the chance to specify factors (K_σ) and (K_ε) thus more reliable estimate the stress-strain mode of the given constructive element.

In a general relation connecting concentration factors taking into account Makhutov approach and damage parameter, it is possible to write down a relationship [1, 6]:

$$\frac{K_\sigma K_\varepsilon}{\alpha_\sigma^2} = F[\alpha_\sigma, \bar{\sigma}_n, m, n]. \quad (2)$$

Using the data of numerical calculations and experimental data, built curves of change of stress intensity concentration factors with damage account (effective) and without taking damage into account (engineering) (see Fig. 4).

Fig. 4 shows that the damage account at factor K_σ calculation increases its value, at the same time, for factor K_ε we have an opposite situation: the damage account reduces its value.

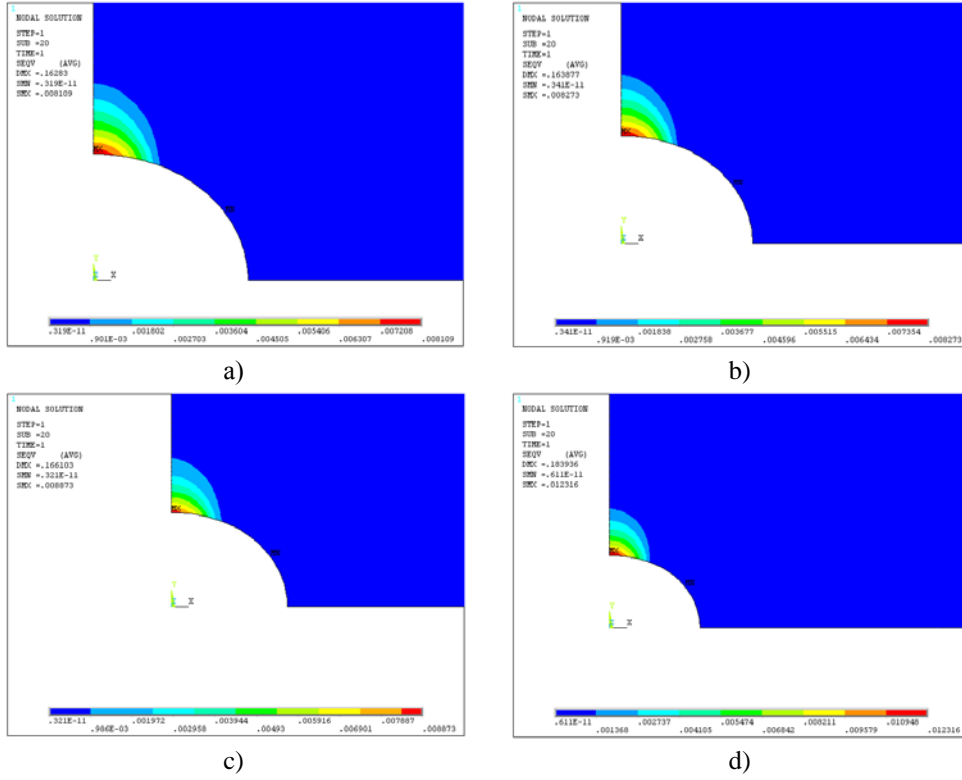


Figure 3. Damage distribution for an aluminum alloy, $\sigma = 280 \text{ MPa}$
 a – hole $\varnothing 1\text{mm}$, b – hole $\varnothing 3\text{mm}$, c – hole $\varnothing 5\text{mm}$, d – hole $\varnothing 10\text{mm}$

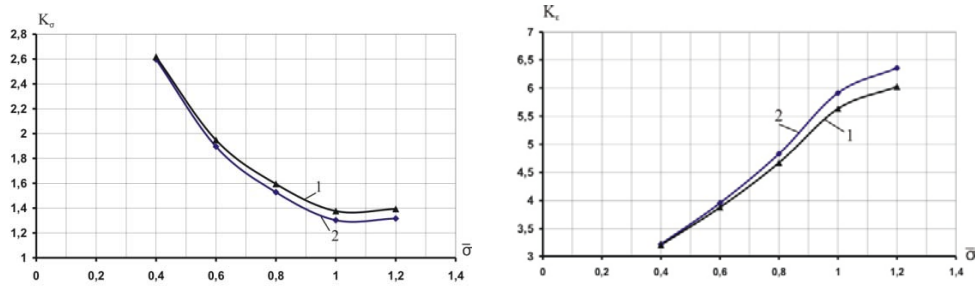


Figure 4. Stress K_σ and strain K_ϵ concentration factors vs. reduced stress $\bar{\sigma}$,
 $\alpha_\sigma = 3,0$ (1 – effective, 2 – engineering)

Dependence of hardening rate from number of load half-cycles can be presented [1, 6]:

$$M(k) = \frac{\lg \bar{\epsilon}_{\max}^{(0)M}}{\lg \left[\bar{\epsilon}_{\max}^{(0)M} + \frac{R}{2} (\bar{\epsilon}_{\max}^{(0)M} - 1) G(k) \right]} \quad (3)$$

Effect of damage on value of hardening rate is shown on Fig. 5.

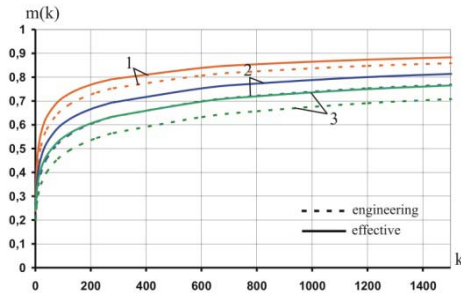


Figure 5. Hardening rate vs. number of load half-cycles (1- $\bar{\epsilon} = 1,1$; 2- $\bar{\epsilon} = 5,0$; 3- $\bar{\epsilon} = 10,0$)

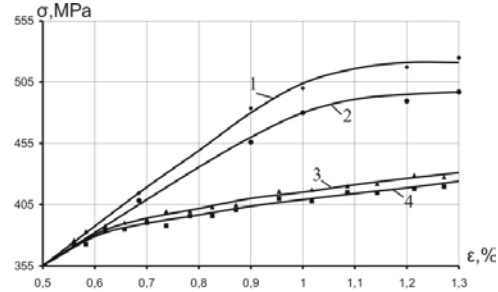


Figure 6. Static load curves (3 - effective, 4 - engineering) and the Morrow's diagram (1 - effective, 2 - engineering) for aluminum alloy

From Fig. 5 influence of damage on hardening rate grows with increase in value of the reduced strain $\bar{\epsilon}$, and also grows calculation error using engineering stress-strain diagram parameters. For calculation of stress and strain concentration factors taking damage into account it is necessary to use the parameters obtained from the effective stress-strain diagram [6] which allows to improve concentration factors.

For an evaluation of damage effect on stress-strain mode under low-cycle fatigue have been made strain control tests. As a result of experiments have been obtained the Morrow's diagram with account and without taking into account damage for a load cycle $N = 0.5N_R$, where N_R - number of cycles to rupture. Comparison of the Morrow's diagram and static load curves is resulted on Fig. 6. It is clear from Fig.6, that damage have essential influence on definition of the maximum stress in stabilized cycle of a loading.

Thus, calculations of the stress-strain mode of constructive elements with stress concentrators and the estimation of a stress and strain concentration by Neuber-Makhotov approach with use of engineering stress add error, by ignoring damage which occurs at plastic deformation. Use of an introduced calculation method, gives the opportunity to decrease error by introduction scalar isotropic damage parameter in consideration.

References

- [1] Махутов Н.А. Деформационные критерии разрушения и расчет элементов конструкций на прочность. – М.: Машиностроение, 1981. – 272 с.
- [2] Нейбер Г. Концентрация напряжений. – М.-Л.: ОГИЗ Государственное издательство технико-теоретической литературы, 1947. – 204 с.
- [3] Lemaitre J., Desmorat R. Engineering Damage Mechanics. Ductile, Creep, Fatigue and Brittle Failures. – Springer-Verlag Berlin Heidelberg, 2005. – 372 p.
- [4] Bobyr N., Grabovskii A., Khalimon A., Timoshenko A., Maslo A. Kinetics of scattered fracture in structural metals under elastoplastic deformation. Strength of Materials, Vol. 39, No. 3, 2007, pp.237-245.
- [5] О.В. Тимошенко, В.В. Коваль, Р.В. Кравчук Вплив виду напруженого стану на критичне значення пошкоджуваності для конструкційних матеріалів при пружно-пластичному деформуванні.- Київ: «Вісник НТУУ «КПІ». Машинобудування», № 63, 2011 р., стор. 103-107
- [6] M. Bobyr, O. Khalimon, V. Koval, Damage and failure of the structural components at low cycle loading, 03056 Six International Conference on low cycle loading LCF 6. – Berlin, Germany, 2008, pp. 499-50.

CREEP DAMAGE PROCESSES IN CYCLICALLY LOADED STRUCTURAL MEMBERS

D. Breslavsky¹, O. Morachkovsky²

¹Department of Control Systems and Processes
National Technical University 'Kharkiv Polytechnic Institute'
21 Frunze str. 61002, Kharkiv, Ukraine
e-mail: brdm@kpi.kharkov.ua

²Department of Theoretical Mechanics,
National Technical University 'Kharkiv Polytechnic Institute'
21 Frunze str. 61002, Kharkiv, Ukraine
e-mail: morachko@kpi.kharkov.ua

Abstract. The paper contains the description of the cyclic creep damage law that allows to estimate the long-term strength of metallic materials in wide range of frequencies of loading and heating. Asymptotic methods and procedures of averaging in a period were used for deriving the damage laws.

1. Introduction

Traditionally the deformation of structural members is studied separately for static and varying loading, especially in the cases of the loading frequencies which take place in the processes of forced oscillations and exceed 1-3Hz. However, for high-temperature creep processes, which flow in different engines, power turbine etc, such separation is impossible due to non-linear character of the phenomena. The important contribution of the dynamic stresses, which occur following to fast load or temperature varying, can essentially change the rate of creep strain and damage accumulation as well as the place of macro crack initiation. From the other hand, the real loading presents the combination of the cycles with large (hours or days, caused by loading, operating and unloading, heating and cooling (etc) and small (fractions of a second, caused by forced oscillations) periods.

The aim of a paper is introducing the unified approach to the description of different creep damage phenomena, which occur due to joint action of static and varying loading. The case of initially elastic stress-strain state, which has to be realized in different industrial applications, where creep strain growth and damage accumulation are started from the stress level which is less then yield limit, is considered.

2. Cyclic creep damage averaged laws

Let us regard the mostly common case. The long-term strength of the structure is determined by the action of the temperature $\bar{T}(t)$ and stress fields $\bar{\sigma}(t)$. It is well known, that mechanical behaviour of structural element subjected by cyclic loading, is significantly

depends upon its frequency. The cyclic creep-damage processes in a solid which are originated by the action of temperature fields, can be divided by the action of low or high cycle loading or heating.

In the case of high cycle loading, when the frequencies of oscillations correspond to the phenomenon of forced vibrations, the processes of 'dynamic creep' [1] as well as the creep-high cycle fatigue interaction can occurred [2]. These processes are divided by the value of so-called critical stress cycle asymmetry coefficient $A_{cr} = \sigma^a / \sigma$ where σ^a and σ are amplitude and mean stress correspondingly. The big values of A_{cr} , which are arisen when the significant values of varying stresses are acted, characterize the high cycle high temperature fatigue damage accumulation which is coupled with creep one. The low values of A_{cr} caused to substantial acceleration of pure creep damage accumulation. This process was called the 'dynamic creep' and the damage occurs here by creep mechanism [1].

Otherwise, the loading of structures at elevated temperatures very often corresponds to low-cycle with the frequency is less than 1Hz. The values of period can be hours or days, for example in power turbines, where one cycle contains the time from starting to transition into the operating mode, some peak loading and finishing.

In real working conditions the low and high cycle creep processes are coupled. The main idea of the presented theory is subsequent studying of both processes. The approach of asymptotic methods [3] will be used. Due to the real situation in a structure, where the forced oscillations occur on the background of processes, caused by static or quasi-static loading, firstly let us regard the low cycle creep damage accumulation processes. The growth of creep strain c and scalar damage parameter ω can occur here due to the varying of loading as well as due to the varying of temperature.

Let us use the the Rabotnov-Kachanov kinetic law with scalar damage parameter ω

$$\dot{\omega} = D \frac{(\sigma)^r}{(1-\omega)^l} \quad (1)$$

The process of low-cycle loading will be described by the period T_σ and stress $\bar{\sigma} = \sigma + \sigma^l$, where σ and σ^l are its constant and varying parts:

$$\bar{\sigma} = \sigma + \sigma^l = \sigma \left(1 + \sum_{k=1}^{\infty} M_k \sin \left(\frac{2\pi k}{T_\sigma} t + \beta_k \right) \right) \quad (2)$$

Let us expand the damage parameter into asymptotic series on the small parameter μ [3] and limit by two terms of series:

$$\omega \cong \omega^0(t) + \mu \omega^l(\xi), \quad \dot{\omega} \cong \dot{\omega}^0(t) + \frac{1}{\mu} \frac{\partial \omega^l}{\partial \xi} \quad (3)$$

where $\omega^0(t)$, $\omega^l(\xi)$ are the functions which depends upon low t and fast time ξ , ($0 \leq \xi \leq 1$) [4]. After the substitution of the Eq.(3) into Eq.(1) and further averaging the damage law on the time interval ($0 \leq \xi \leq 1$):

$$\langle \omega^0(\xi) \rangle = \int_0^1 \omega^0(t) d\xi \cong \omega^0(t), \quad \langle \omega^l(\xi) \rangle = \int_0^1 \omega^l(\xi) d\xi \cong 0, \quad (4)$$

we obtain [4]:

$$\dot{\omega} = D g_r(M_k) \frac{(\sigma)^r}{(1-\omega)^l} \quad \omega(0) = \omega_0, \quad \omega(t^*) = \omega^*, \quad (5)$$

$$g_r(M_k) = \int_0^l \left(1 + \sum_{k=1}^{\infty} M_k \sin(2\pi k \xi) \right)^r d\xi, \quad M_k = \sigma^{ak} / \sigma.$$

If we consider more general low cycle process when not only stress but the temperature T varies through a cycle

$$\bar{T} = T + T^l = T \left(1 + \sum_{i=1}^{\infty} M_i^T \sin\left(\frac{2\pi i}{T} t + \beta_i^T\right) \right) \quad M_i^T = T_i^a / T, \quad (6)$$

the creep-damage law can be written in the following form:

$$\dot{\omega} = D \frac{\sigma^r}{(1-\omega)^l} \exp\left(-\frac{\bar{Q}}{T}\right) = D(T) \frac{\sigma^r}{(1-\omega)^l} \quad (7)$$

Now we can use the similar suggestions and reasoning, regarding the averaged damage parameter law Eq. (5) as an initial one. Finally we have

$$\dot{\omega} = g_r(M_k) g_r^{\omega}(T) \frac{\sigma^r}{(1-\omega)^l}, \quad \omega(0) = \omega_0, \quad \omega(t^*) = \omega^*. \quad (8)$$

where

$$g_r^{\omega}(T) = d \int_0^l \exp\left(\frac{-\bar{Q}}{T} \left(1 + \sum_{i=1}^{\infty} M_i^T \sin(2\pi i \xi) \right)^{-1}\right) d\xi.$$

Now let us consider the case of mono-harmonic loading with sine law, when frequencies of forced oscillations are more than 1 Hz. If the stress cycle asymmetry coefficient $A > A_{cr}$, the essential fatigue damage appears. We'll use the Yokobori suppose [2] that in this case the total damage increment contains from creep and high-temperature high cycle fatigue parts

$$d\omega = d\omega_c + d\omega_f = F_c(\sigma, \sigma^a, \bar{T}, \omega) dt + F_f(\sigma, \sigma^a, \bar{T}, \omega) dt \quad (9)$$

The creep damage law (1) and auto-model fatigue damage law

$$d\omega_f = \frac{F'(\sigma^a + b\sigma)^p}{(1-\omega_f)^q} dN = \frac{F(\sigma^a + b\sigma)^p}{(1-\omega_f)^q} dt, \quad N = \frac{t}{T_f} \quad (10)$$

can be used. In the case of $A < A_{cr}$ the influence of fatigue damage is marginal, but damage acceleration happens due to 'dynamic creep' mechanism [1, 5]. If we regard the slow varying of the loading with big period by law like Eq. (2), we have to slightly change the law Eq.(5) in order to account the multiplying on the coefficient A:

$$\dot{\omega} = D g_r(I + K_r) \frac{(\sigma)^r}{(1-\omega)^l} \quad K_r = \int_0^l (1 + A_r \sin(2\pi \xi))^r d\xi - 1, \quad A = \frac{\sigma^a}{\sigma} \quad (11)$$

$$g_r = \int_0^l \left(1 + \sum_{k=1}^{\infty} M_k \sin(2\pi k \xi) \right)^r d\xi \quad A_r = \frac{A}{g_r^{1/r}}$$

Here K_r is dynamic creep influence function had been obtained by asymptotic expansion and averaging procedure in [6]. Now we have to construct the universal damage law, which reflects above mentioned physical laws. Let us use the influence functions, which reflect the acceleration or retardation of appropriate damage processes. These functions have to operate with stress asymmetry coefficient A_{cr} and can be selected in the following form [5]:

$$\beta_f(A) = 1 - \exp\left(\pi \frac{A^2}{A_{kp}^2}\right); \quad \nu_f(A) = \exp\left(\pi \frac{A^2}{A_{kp}^2}\right); \quad (12)$$

Finally the damage law takes the following form:

$$\dot{\omega} = g_r g_f \alpha_f(A) D \frac{\sigma^r}{(1-\omega)^l} + \beta_f(A) F \frac{(\sigma^a + b\sigma)^p}{(1-\omega)^q} \quad (13)$$

$$\omega(0) = \omega_0, \quad \omega(t_*) = \omega_*, \quad \alpha_f(A) = 1 + K_r(A) \nu_f(A)$$

Constructed general damage law Eq.(13) have to be generalized for the case of complex stress state. Here the three invariants criterion for creep long term strength description as well as Sines criterion [7] for fatigue were used [4, 5].

3 Conclusions

The paper contains the creep damage law, which had been formulated for the wide range of cyclic loading and heating frequencies. By use of the same asymptotic procedures the flow rule for cyclic creep with different frequencies of loading and heating were obtained and averaged creep-damage law was added to the general system of equation of motion of the creeping solid [4-6].

References

- [1] Rabotnov, Yu.N (1969), *Creep Problems in Structural Members*, North Holland, Amsterdam.
- [2] Yokobori, T. (1978), *Scientific Foundations of Strength and Rupture of Materials*, Naukova dumka, Kiev (Translated into Russian).
- [3] Moiseev, N.N. (1969), *Asymptotic methods of nonlinear mechanics*, Nauka, Moscow (In Russian).
- [4] Breslavs'kyi, D.V., Korytko, Yu.M., Morachkovskiy, O.K. (2011), Cyclic Thermal Creep Model for the Bodies of Revolution, *Strength of Materials*, Vol. 43, 2, pp. 134-143.
- [5] Breslavsky, D.V., Morachkovsky O.K. (2004). High Cycle Creep-Fatigue Processes in Solids, Proceedings of the International Conference "Nonlinear dynamics", Sept. 14-16 2004, Kharkov, Ukraine, pp. 44-47.
- [6] Breslavsky, D. (1998), Simulation of Creep and Damage Effects in Structural Members under Fast Cyclic Load, *ZAMM*, 78 (S1), pp. S301-S302.
- [7] Lemaitre, J. and Chaboche, J.-L. (1990), *Mechanics of Solid Materials*, Cambridge University Press, Cambridge.

NUMERICAL MODELING OF LOCALIZED FAILURE BY MEANS OF STRONG DISCONTINUITIES AT FINITE STRAIN

O.T. Bruhns¹, R. Radulovic² and J. Mosler³

Abstract. An efficient numerical framework suitable for three-dimensional analyses of brittle material failure is presented. The proposed model is based on an (embedded) Strong Discontinuity Approach (SDA). Hence, the deformation mapping is elementwise additively decomposed into a conforming, continuous part and an enhanced part associated with the kinematics induced by material failure. To overcome locking effects and to provide a continuous crack path approximation, the approach is extended and combined with advantages known from classical interface elements. More precisely, several discontinuities each of them being parallel to a facet of the respective finite element are considered. By doing so, crack path continuity is automatically fulfilled and no tracking algorithm is necessary. However, though this idea is similar to that of interface elements, the novel SDA is strictly local and thus, it does not require any modification of the global data structure, e.g., no duplication of nodes. An additional positive feature of the advocated finite element formulation is that it leads to a symmetric tangent matrix. It is shown that several simultaneously active discontinuities in each finite element are required to capture highly localized material failure.

¹ Institute of Mechanics, Ruhr-Universität Bochum, D-44780 Bochum, Germany
e-mail: otto.bruhns@rub.de

² now at: Siemens AG, Energy Sector, Fossil Power Generation Division, D-45478
Mülheim/Ruhr, Germany

³ Institute of Mechanics, TU Dortmund, Leonhard-Euler-Str. 5, D-44227 Dortmund,
Germany
e-mail: joern.mosler@udo.edu

1. Kinematics of strong discontinuities

A domain $\Omega \in R^3$ is assumed to be separated into two parts Ω^+ and Ω^- by means of a localization surface $\partial_s \Omega$, which, depending on the context, can represent a crack surface or a shear band. Hence, the displacement field \mathbf{u} can be discontinuous at $\partial_s \Omega$. Following [1], \mathbf{u} is assumed to be of the type

$$\mathbf{u} = \bar{\mathbf{u}} + \llbracket \mathbf{u} \rrbracket (H_s - \varphi), \quad (1)$$

where $\bar{\mathbf{u}}$ is the standard continuous displacement field and $\llbracket \mathbf{u} \rrbracket$ denotes a displacement jump. In Eq. (1), H_s is the Heaviside function with respect to the discontinuity and φ is a smooth ramp function necessary for describing the Dirichlet boundary conditions in terms of the standard displacement field $\bar{\mathbf{u}}$. By applying the generalized derivative to Eq. (1), together with the approximation $\nabla \llbracket \mathbf{u} \rrbracket = \mathbf{0}$, the deformation gradient reads

$$\mathbf{F} = \mathbf{1} + \nabla \bar{\mathbf{u}} - \llbracket \mathbf{u} \rrbracket \otimes \nabla \varphi + \llbracket \mathbf{u} \rrbracket \otimes \mathbf{N} \delta_s \quad \text{with} \quad \nabla \bar{\mathbf{u}} = \frac{\partial \bar{\mathbf{u}}}{\partial \mathbf{X}}. \quad (2)$$

Here, δ_s represents the Dirac-delta distribution associated with the localization surface and \mathbf{N} is the normal vector of $\partial_s \Omega$. Analogously, in case of intersecting strong discontinuities, i.e. more than one displacement jump per element, the displacement field and the associated deformation gradient are computed as

$$\mathbf{u} = \bar{\mathbf{u}} + \sum_{i=1}^n [[\mathbf{u}]]^{(i)} (H_s^{(i)} - \varphi^{(i)}) \quad (i = \dots n) \quad (3)$$

and

$$\mathbf{F} = \mathbf{1} + \nabla \bar{\mathbf{u}} - \sum_{i=1}^n [[\mathbf{u}]]^{(i)} \otimes \nabla \varphi^{(i)} + \sum_{i=1}^n [[\mathbf{u}]]^{(i)} \otimes \mathbf{N}^{(i)} \delta_s^{(i)}. \quad (4)$$

2. Material models

Since the deformation gradient is regularly distributed in Ω^\pm , standard stress-strain based continuum models can be applied. For the sake of simplicity, the bulk material is assumed to be purely elastic (neo-Hookean material with λ and μ the Lamé constants), while inelastic deformations localized at $\partial_s \Omega$ are governed by a damage-like cohesive potential of the type

$$\Psi_s = \frac{1}{2} (1 - d) [[\mathbf{u}]] \cdot \mathbf{C}_s \cdot [[\mathbf{u}]] \quad (5)$$

with

$$d = 1 - \exp\left(-\frac{f_0}{\mathcal{G}_f} \kappa\right) \quad \text{and} \quad \mathbf{C}_s = \frac{f_0}{\kappa} \mathbf{I} \quad (6)$$

where f_0 denotes the uniaxial tensile strength, \mathcal{G}_f is the fracture energy and κ represents an internal variable (maximum value of the displacement jump during the complete loading path). With Eq. (5), the stress vector acting at the discontinuity can be computed as

$$\mathbf{T}_s = \frac{\partial \Psi_s}{\partial [[\mathbf{u}]]} = (1 - d) f_0 \frac{[[\mathbf{u}]]}{\kappa}. \quad (7)$$

It is coupled to the stresses in Ω^\pm by the condition of traction continuity. An advantage of the above models is that only four parameters (λ , μ , f_0 and \mathcal{G}_f) are required to describe material behavior.

3. Finite element implementation

According to [1], one possible implementation of the SDA is based on the EAS concept. Though this approach is not new for a single discontinuity, it represents the background for the novel intersecting SDA as discussed in this paper. The numerical implementation of elements with strong discontinuities is based on the weak forms

$$\int_{\Omega} \mathbf{P}(\bar{\mathbf{u}}, [[\mathbf{u}]]) : \nabla \bar{\eta} \, dV - \int_{\Omega} \rho_0 \mathbf{B} \cdot \bar{\eta} \, dV - \int_{\Gamma_P} \mathbf{T}^* \cdot \bar{\eta} \, dA = 0 \quad (8)$$

$$\frac{1}{V} \int_{\Omega} \mathbf{P} \cdot \mathbf{N} \, dV = \frac{1}{A} \int_{\partial \Omega} \mathbf{T}_s \, dA \quad (9)$$

where \mathbf{P} is the Piola stress, $\bar{\eta}$ is a continuous test function, \mathbf{B} denotes body forces, \mathbf{T}^* are prescribed tractions on the Neumann boundary, V and A are the volume of the finite element

and the surface area of the discontinuity, respectively. Eq. (8) is the standard principle of virtual works and Eq. (9) represents the weak form of traction continuity, cf. [2].

One of the critical open issues concerning the implementation of elements with strong discontinuities is the prediction of crack path propagation. It is known, that a straightforward implementation of strong discontinuities can lead to locking effects. To overcome such problems different strategies like tracking algorithms have been developed. The aim of the present contribution is to show that simple local strategies without enforcing crack path continuity can lead to computationally efficient and robust numerical implementations. In what follows, two different methods will be explained.

3.1. Rotating SDA

After embedding a discontinuity in a finite element, a certain change in principle stress directions may occur. Consequently, keeping the normal vector \mathbf{N} fixed during subsequent loading does not necessarily provide the proper kinematics. As a consequence, after proper crack initiation, the crack normal \mathbf{N} is wrongly predicted in the elements ahead the crack tip. This can result in a dispersion of the macro-crack over neighboring elements. Therefore it is reasonable to allow the discontinuity to rotate. Thus, \mathbf{N} depending on the maximum principal stress direction is recomputed in each loading step. In this way, the aforementioned locking effects can be strongly reduced.

3.2. Intersecting SDA

In the context of the SDA, the numerical implementation of intersecting localization surfaces was introduced in [3]. The main idea of such approach is to enrich the space of admissible crack paths by introducing more than one discontinuity per elements, i.e. to model micro-defects in elements separately. Some of these micro-defects will significantly contribute to a macro-crack, while some of them will close under increasing loading. According to the standard SDA, the orientation of discontinuities is assumed to be invariant, i.e. $\dot{\mathbf{N}} = \mathbf{0}$.

The extension of the single crack concept to the intersecting SDA is relatively straightforward. Clearly, the implementation of intersecting discontinuities is computationally more expensive. Analogously to the standard SDA (one crack per element), the tangent stiffness matrix remains non-symmetric. Only if the discontinuities are parallel to the edges or the facets of the considered element, a symmetric tangent is obtained. Consequently, this case is similar to that characterizing classical interface formulations where the interface elements are inserted into the existing finite element formulation. Thus, discontinuities are a priori parallel to the facets of the underlying bulk elements. Further elaborating this similarity, the discontinuities of the proposed SDA are assumed to have the same topology. Besides this analogy, the SDA shows still several advantages compared to the nowadays classical interface approaches. For instance, the mesh topology has not to be modified (e.g. duplicating nodes). Evidently, the more discontinuities are considered, the softer and the more realistic is the predicted mechanical response. However, an increasing number of discontinuities increases the numerical effort as well. Therefore, the crucial question arises how many discontinuities in each element are needed to describe material failure and softening in a realistic manner. To answer this question, the discontinuities are successively introduced and the results are compared to each other.

4. Numerical Examples

The performance of the proposed methods is demonstrated by means of two fully three-dimensional numerical examples: a clamped L-shaped frame subject to off-center tension and asymmetric bending of a notched beam. Both examples are discussed in [6].

Example 1: L-shaped frame: The geometry, material parameters and loading conditions are in line with [4], where a concrete L-shaped frame has been experimentally investigated. A mesh containing 33202 tetrahedral elements is used. In case of intersecting SDA, only failure modes aligned with the element facets are taken into account. It has been observed in numerical experiments that three displacements jumps in each element are sufficient to describe the material response in a realistic manner. If only one or two jumps are accounted for, the softening effects are underestimated.

Example 2: Bending of a notched beam: The present example is taken from [5], where the authors documented a number of mixed mode failure experiments on notched beams. The geometry and the boundary conditions are shown in Fig. 1. Four different finite element discretizations are considered. Two of them are uniformly distributed, the remaining two are refined in the region where the crack path is expected to propagate, while they are relatively coarse in the remaining part of the specimen. For all triangulations a curved crack propagates from the notch toward the upper surface of the beam, building approximately an angle of 30° with respect to the vertical direction.

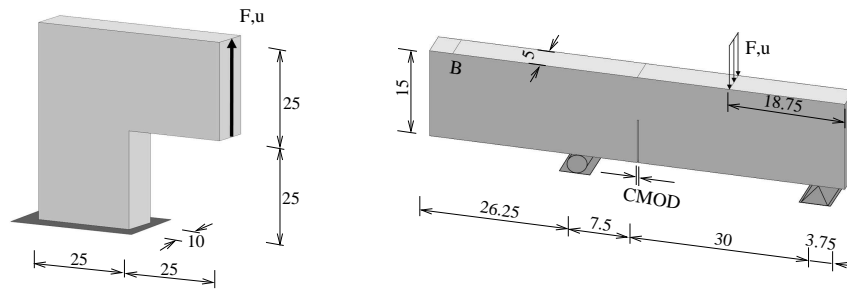


Figure 1. Numerical analysis of a L-shaped frame (left) and asymmetric bending of a notched beam (right): dimensions [cm] and loading of structures

References

- [1] Simo J C Oliver J and Armero F (1993) An analysis of strong discontinuities induced by strain-softening in rate-independent inelastic models, *Computational Mechanics*, **12**, pp. 277-296.
- [2] Mosler J (2004) On the Modeling of Highly Localized Deformations Induced by Material Failure: The Strong Discontinuity Approach, *Archives of Computational Methods in Engineering*, **11**, pp. 389-446.
- [3] Mosler J (2005) On advanced solution strategies to overcome locking effects in strong discontinuity approaches, *International Journal for Numerical Methods in Engineering* **63**, pp. 1313-1341.
- [4] Winkler B Hofstetter G and Lehar H (2004) Application of a constitutive model for concrete to the analysis of a precast segmental tunnel lining, *International Journal for Numerical and Analytical Methods in Geomechanics*, **28**, pp. 797-819.
- [5] Gálvez J Elices M Guinea G and Planas J (1998) Mixed mode fracture of concrete under proportional and nonproportional loading, *International Journal of Fracture*, **94**, pp. 267-284.
- [6] Radulovic R Bruhns O T and Mosler J (2011) Effective 3D failure simulations by combining the advantages of embedded Strong Discontinuity Approaches and classical interface elements, *Engineering Fracture Mechanics*, **78**, pp. 2470-2485.

STUDIES ON THE EFFECT OF THE STRESS TRIAXIALITY AND THE LODE PARAMETER ON DUCTILE DAMAGE CONDITIONS

Michael Brüning, Steffen Gerke, Vanessa Hagenbrock

Institut für Mechanik und Statik
Universität der Bundeswehr München, Werner-Heisenberg-Weg 39, D-85577 Neubiberg,
Germany
e-mail: michael.brueinig@unibw.de

Abstract. The paper deals with the effect of stress state on the damage behavior of aluminum alloys. The continuum damage model has been generalized to take into account stress-state-dependence of the damage criterion with different branches corresponding to various damage mechanisms depending on the stress triaxiality and the Lode parameter. Basic material parameters are identified using experiments with differently notched tension and shear specimens. To be able to get more insight in the complex damage and failure behavior additional series of micro-mechanical numerical analyses of void containing unit cells have been performed. These calculations cover a wide range of stress triaxialities and Lode parameters in the tension, shear and compression domains. The numerical results are used to show general trends, to develop equations for the damage criterion, and to identify parameters of the continuum model.

1. Introduction

Accurate and realistic modeling of inelastic behavior of ductile metals is evident in structural mechanics and corresponding numerical analyses. Thus, continuum models have been proposed to describe elastic-plastic behavior as well as material softening during the damage and failure processes under general loading conditions. Motivated by experimental observations or numerical analyses on the micro-scale, various phenomenological damage models have been developed. They are based on internal scalar or tensorial damage variables whose increase is governed by evolution laws.

Besides the stress intensity, the stress triaxiality and the Lode parameter are the most important factors controlling initiation and evolution of ductile damage. These dependencies can be studied by performing experiments and corresponding numerical simulations of a series of tests with carefully designed and differently loaded specimens experiencing a wide range of stress states [1-8]. In addition, to be able to detect features on the scale of the micro-defects, micro-mechanical numerical models are used solving boundary-value problems of representative volume elements with micro-structural details to predict the constitutive response at the macroscopic level. Thus, three-dimensional finite element calculations of microscopic cell models have been performed [9-13] to get more insight in the damage and failure mechanisms of ductile solids and to understand the stress-

state-dependent behavior of void growth and ductile damage mechanisms. The numerical results show that the void growth, the macroscopic deformation behavior of the unit cells and the critical failure strain remarkably depend on the value of the stress triaxiality. In addition, the rate of void expansion in different directions for constant stress triaxialities are sensitive to the Lode parameter.

Most published papers deal with void growth and coalescence only in regions with high hydrostatic stress. Thus, their results are only valid for moderate or high stress triaxialities where the effect of the Lode parameter on failure behavior has been shown to be marginal [5]. Therefore, further numerical calculations have to be performed to get detailed information on damage and failure mechanisms in ductile solids for a wide range of stress triaxialities and Lode parameters even in the shear and compression ranges. In this context, the present paper discusses results of numerical unit-cell simulations on the micro-scale covering a wide range of three-dimensional stress states. They are used to develop and to verify stress-state-dependent damage criteria taking into account different branches corresponding to various damage modes.

2. Continuum model

A continuum model is used to predict the irreversible material behavior taking into account information of the microscopic mechanisms of individual micro-defects and their interaction. Brünig [6] proposed a phenomenological framework to describe the inelastic deformations of ductile materials including anisotropic damage by micro-defects. This approach takes into account different damage mechanisms (Fig. 1): micro-shear-cracks for negative stress triaxialities, void growth for large positive stress triaxialities and mixed behavior for lower positive stress triaxialities. In the hydrostatic pressure regime a cut-off value of stress triaxiality [14] is taken into account below which damage does not occur. This stress-triaxiality-dependent concept will be generalized to be able to take also into account the effect of the Lode parameter on damage behavior.

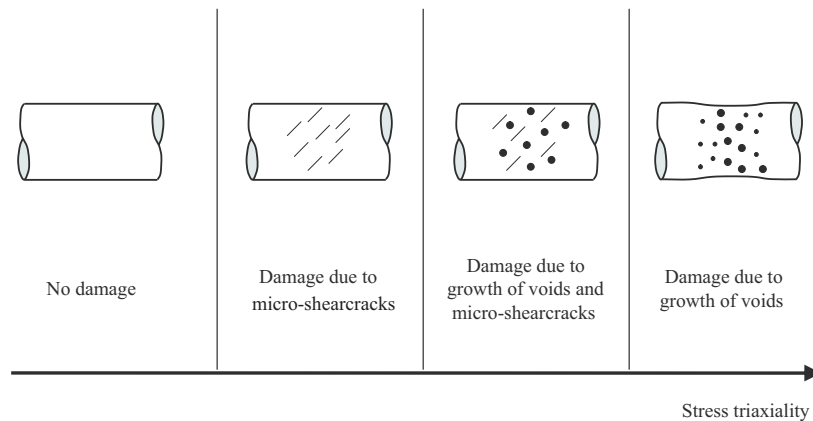


Figure 1. Damage mechanisms

Thus, the onset of damage is assumed to be governed by the damage criterion

$$f^{\text{da}} = \alpha I_1 + \beta \sqrt{J_2} - \sigma = 0 \quad (1)$$

where I_1 and J_2 denote the first and second deviatoric stress invariants, σ is the damage threshold and α and β represent the damage mode parameters taking into account the different branches depending on the stress triaxiality

$$\eta = \sigma_m / \sigma_{\text{eq}} = I_1 / (3\sqrt{3}J_2) \quad (2)$$

defined as the ratio of the mean stress σ_m and the von Mises equivalent stress σ_{eq} as well as on the Lode parameter

$$\omega = \frac{2\tilde{T}_2 - \tilde{T}_1 - \tilde{T}_3}{\tilde{T}_1 - \tilde{T}_3} \quad \text{with} \quad \tilde{T}_1 \geq \tilde{T}_2 \geq \tilde{T}_3 \quad (3)$$

expressed in terms of the principal stress components \tilde{T}_1 , \tilde{T}_2 and \tilde{T}_3 .

3. Experimental and numerical results

Tension and shear tests with smooth and pre-notched specimens as well as corresponding numerical simulations on the macro-scale have been performed to be able to identify material parameters appearing in the constitutive equations [15-17]. Based on these results it was possible to propose stress-triaxiality-dependent functions and a first estimate of Lode parameter dependence for the damage mode parameter. However, due to lack of reliable information on the effect of the Lode parameter on the damage criterion by experiments additional numerical simulations on the micro-scale are carried out to study in detail the dissipative and deteriorating mechanisms on the microscopic level. The behavior of unit cells with symmetry boundary conditions simulating periodic distributions of micro-defects is studied for a wide range of Lode parameters $\omega = -1, 0, \text{ and } 1$ as well as of the stress triaxiality coefficients $\eta = -1, -2/3, -1/3, 0, 1/3, 2/3, \text{ and } 1$. Based on the numerical results it was possible to compute different points shown in Fig. 2.

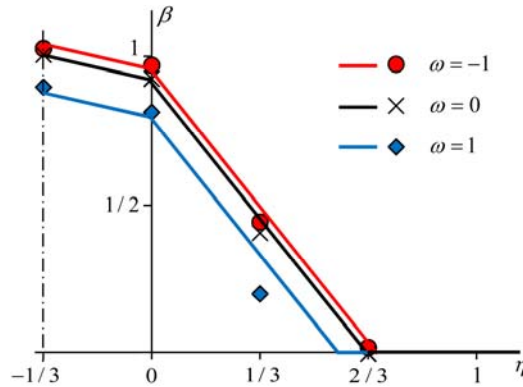


Figure 2. Damage mode parameter vs. stress triaxiality

For different Lode parameters ω and stress triaxiality coefficients η the damage mode parameters obtained from the micro-mechanical numerical analyses are used to propose the non-negative function

$$\beta(\eta, \omega) = \beta_0(\eta, \omega = 0) + \beta_\omega \geq 0 \quad (4)$$

and to identify the associated material parameters

$$\beta_0 = \begin{cases} -0.45\eta + 0.85 & \text{for } -1/3 \leq \eta \leq 0 \\ -1.28\eta + 0.85 & \text{for } \eta > 0 \end{cases} \quad (5)$$

and

$$\beta_\omega = \begin{cases} -0.021\omega & \text{for } \omega \leq 0 \\ -0.17\omega & \text{for } \omega > 0 \end{cases} \quad (6)$$

by curve fitting, see Fig. 2.

Acknowledgement. Financial support from the Deutsche Forschungsgemeinschaft (German Research Foundation, BR1793/12-1) is gratefully acknowledged.

References

- [1] Borvik, T., Hopperstad, O.S., Berstad, T. (2003). On the influence of stress triaxiality and strain rate on the behavior of a structural steel. Part II. Numerical study, *Eur. J. Mech. A/Solids* **22**, 15-32
- [2] Bao, Y., Wierzbicki, T. (2004). On fracture locus in the equivalent strain and stress triaxiality space, *Int. J. Mech. Sci.* **46**, 81-98
- [3] Bonora, N., Gentile, D., Pirondi, A., Newaz, G. (2005). Ductile damage evolution under triaxial state of stress: theory and experiment, *Int. J. Plast.* **21**, 981-1007
- [4] Oh, C.K., Kim, Y.J., Park, J.M., Baek, J.H., Kim, W.S. (2007). Development of stress-modified fracture strain for ductile failure of API X65 steel. *Int. J. Fract.* **143**, 119-133.
- [5] Bai, Y., Wierzbicki, T. (2008). A new model of metal plasticity and fracture with pressure and Lode dependence, *Int. J. Plast.* **24**, 1071-1096
- [6] Brünig, M. (2003). An anisotropic ductile damage model based on irreversible thermodynamics, *Int. J. Plast.* **19**, 1679-1713.
- [7] Brünig, M., Albrecht, D., Gerke, S. (2011). Numerical analyses of stress-triaxiality-dependent inelastic deformation behaviour of aluminium alloys. *Int. J. Damage Mech.* **20**, 299-317.
- [8] Gao, X., Zhang, T., Hayden, M., Roe, C. (2009). Effects of the stress state on plasticity and ductile failure of an aluminum 5083 alloy. *Int. J. Plasticity* **25**, 2366-2382.
- [9] Kuna, M., Sun, D.Z. (1996). Three-dimensional cell model analyses of void growth in ductile metals. *Int. J. Fract.* **81**, 235-258.
- [10] Zhang, K.S., Bai, J.B., Francois, D. (2001). Numerical analysis of the influence of the Lode parameter on void growth. *Int. J. Solids Struct.* **38**, 5847-5856.
- [11] Kim, J., Gao, X., Srivatsan, T.S. (2003). Modeling of crack growth in ductile solids: a three-dimensional analysis. *Int. J. Solids Struct.* **40**, 7357-7374.
- [12] Gao, X., Wang, T., Kim, J. (2005). On ductile fracture initiation toughness: Effects of void volume fraction, void shape and void distribution. *Int. J. Solids Struct.* **42**, 5097-5117.
- [13] Gao, X., Zhang, G., Roe, C. (2010). A study on the effect of the stress state on ductile fracture. *Int. J. Damage Mech.* **19**, 75-94
- [14] Bao, Y., Wierzbicki, T. (2005). On the cut-off value of negative triaxiality for fracture, *Eng. Frac. Mech.* **72**, 1049-1069
- [15] Brünig, M., Chyra, O., Albrecht, D., Driemeier, L., Alves, M. (2008). A ductile damage criterion at various stress triaxialities, *Int. J. Plast.* **24**, 1731-1755
- [16] Driemeier, L., Brünig, M., Micheli, G., Alves, M. (2010). Experiments on stress-triaxiality dependence of material behavior of aluminum alloys. *Mech. Mater.* **42**, 207-217.
- [17] Brünig, M., Albrecht, D., Gerke, S. (2011). Modeling of ductile damage and fracture behavior based on different micro-mechanisms, *Int. J. Damage Mech.* **20**, 558-577.

BUCKLING OF IMPERFECT CDM STRUCTURAL SYSTEMS

N. Challamel¹ and J. Helleland²

¹ Université Européenne de Bretagne, University of South Brittany UBS, LIMATB, Centre de Recherche, Rue de Saint Maudé, BP92116, 56321 Lorient cedex – France, email : noel.challamel@univ-ubs.fr; on sabbatical leave, Mechanics Division, Department of Mathematics, University of Oslo, P.O. Box 1053, Blindern, NO-0316 Oslo - Norway

² Mechanics Division, Department of Mathematics, University of Oslo, P.O. Box 1053, Blindern, NO-0316 Oslo – Norway, email: jostein.helleland@math.uio.no

Abstract. This paper is devoted to the buckling phenomenon of columns composed of a quasi-brittle material such as concrete. The constitutive law at the material or the structural scale is based on continuum damage mechanics arguments (CDM theory). We investigate, using a simple one-dimensional softening model based on continuum damage mechanics, how the buckling of reasonable slender reinforced concrete columns is associated with a limit load which decreases with the imperfection considered. The one-dimensional continuum problem is then analytically and numerically solved for an axially loaded cantilever column with some additional geometrical imperfection. The need of including some non-local properties is discussed for the post-buckling analysis. Though simplified, this column model will still give some qualitatively useful results for reinforced concrete columns.

1. Introduction

It is accepted that slender reinforced concrete columns must be designed taking into account the second order effects produced by the axial loads on the deformed member. The main international rules including for instance the European code for reinforced concrete design, Eurocode 2 (EC2), are based on this concept for the design of reinforced concrete columns. Slenderness limits that indicate when such effects can be neglected, have been investigated [e.g., 1, 2] and included in most reinforced concrete codes. Various empirical or theoretical based methods have been published in the past, that all introduced some necessary realistic imperfections through additional geometrical eccentricities [3, 4]. It means, from a theoretical stability point of view, that these nonlinear structural systems typically belong to the field of imperfection sensitive systems. There have been numerous papers and textbooks devoted to the study of elastic or inelastic buckling of columns (see for instance [4, 5]). But the link between imperfection sensitivity and the buckling phenomenon of reinforced concrete columns was not clearly highlighted in the authors' point of view, at least not from simple physically based model analysis. In this paper, we will demonstrate with some simple softening, one-dimensional models based on continuum damage mechanics (CDM), that the buckling of reinforced concrete columns is associated with a limit load, which decreases with the imperfection considered. The problem handled in this study is not so different from the elastica problem of a softening column, as already investigated numerically by Brojan et al [6] (see also references quoted in [6]). Global unstable softening post-buckling paths can be noticed for these nonlinear elastic problems, which in turn lead to the specific imperfection sensitivity phenomenon.

2. Buckling and post-buckling equations

A continuous softening CDM column of length L is studied. It has a bending-curvature constitutive law expressed by Eq. (1)

$$M = EI\kappa(1 - D) \quad \text{with } \kappa = \theta' \quad (1)$$

where M is the bending moment, κ is the curvature, θ is the rotation of the cross section, and D is the cross sectional damage variable. We first investigate the local problem associated with the loading function f expressed with local variables as

$$f(\kappa, D) = \frac{|\kappa|}{\kappa_Y} - 2D \quad \text{for } D \leq D_Y = \frac{1}{2} \quad (2)$$

where κ_Y is a material parameter associated with the maximum moment capacity of the cross section, and D_Y is the damage value at this section capacity. A similar model, at the beam scale like here, has been studied in [7] for time-dependent stability of beams (see also [8, 9] at the material scale, or [10], for the applications of similar models). The irreversible damage constitutive law, including the loading-unloading conditions, can be written as

$$\dot{D} \geq 0, \quad f(\kappa, D) \leq 0, \quad \dot{D} f(\kappa, D) = 0 \quad (3)$$

By applying the principle of virtual work for the so-called geometrically exact configuration, and assuming the softening column to be inextensible, we get

$$\int_0^L [EI(1 - D)\theta'\delta\theta' - P \sin \theta \delta\theta] ds - Pe_0 \cos \theta(L) \delta\theta(L) = 0 \quad (4)$$

where e_0 (considered as an imperfection) is the eccentricity of the applied axial load P at the end of the column. Integration by part of this equation gives the differential equation

$$[EI(1 - D)\theta'] + P \sin \theta = 0 \quad (5)$$

and the following natural and essential boundary conditions:

$$[EI(1 - D)\theta'\delta\theta]_0^L - Pe_0 \cos \theta(L) \delta\theta(L) = 0 \quad (6)$$

The dimensionless parameters below is introduced for convenience in the following:

$$p = \frac{PL^2}{EI}, \quad s^* = \frac{s}{L}, \quad \kappa_Y^* = \kappa_Y L \quad \text{and} \quad e_0^* = \frac{e_0}{L} \quad (7)$$

3. Numerical analysis

The computation of the non-linear boundary value problem is based on a finite difference code that implements the three-stage Lobatto IIIa formula. Results are presented in Fig. 1,

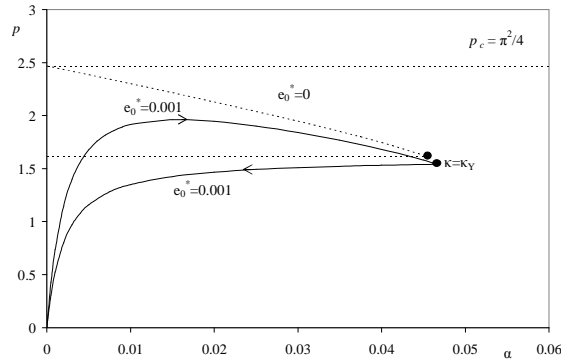


Figure 1. Unloading behavior of the local softening column after the critical point $\kappa^* = \kappa_Y^* = 0.1$; Wood's paradox found in the post-buckling range

where α is the rotation at the end of the column. For the local damage law considered in Eq. (2), there is a phenomenon known as Wood's paradox (elastic unloading). The softening zone along the column can be shown to necessarily vanish, which in turn leads to the zero dissipation phenomenon [11, 12, 13]. Due to this, the curvature of no column section will be located on the softening branch of the moment-curvature relationship. Thus, after the material instability point, $\kappa = \kappa_Y$, is reached at the maximum moment section, elastic unloading behaviour will result along all of the column. Fig. 1 shows the hysteresis loop linked to the loading-unloading phases. Wood's paradox is now solved with a nonlocal CDM model for this post-buckling and post-failure problem, as indicated in Fig. 2.

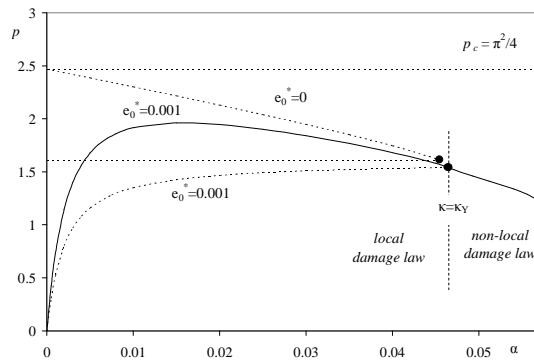


Figure 2. Propagation of the damage propagation in the nonlocal softening column after the critical point $\kappa^* = \kappa_Y^*$; $\kappa_Y^* = 0.1$; $e_0^* = 0.001$; $l_c^* = 0.1$

The nonlocal damage loading function was chosen in a strain-driven format (see also [14]):

$$f(\kappa, D) = \frac{|\bar{\kappa}|}{\kappa_Y} - 2D \quad \text{for} \quad D \geq D_Y = \frac{1}{2} \quad \text{with} \quad \bar{\kappa} - l_c^2 \bar{\kappa}'' = \kappa \quad (8)$$

l_c is an added internal length, specific to the nonlocal damage model; ($l_c^* = l_c/L$); and $\bar{\kappa}$ is the nonlocal curvature variable, defined from Eringen's differential equation [e.g., 15].

4. Conclusions

Including some nonlocality may cover the propagation phenomenon of localization in a post-buckling and post-failure structural problem. Some complementary stability studies could be envisaged in the future, especially regarding multiple bifurcated solutions [16].

Acknowledgement. The research leading to these results has received funding from the European Community's Seventh Framework Programme (FP7/2007-2013) under grant agreement n° PIEF-GA-2010-271610 STABELAS.

References

- [1] Robinson, J., Fouré, F. and Bourghli, M. (1975), Le flambement des poteaux en béton armé chargés avec des excentricités différentes à leurs extrémités, *Annales de l'ITBTP*, **333**, pp. 46-74(in French).
- [2] Mari, A.R. and Helleland, J. (2005), Lower slenderness limits for rectangular reinforced concrete columns, *J. Struct. Eng.*, **131**, 1, pp. 85-95.
- [3] Helleland, J. (2005), Nonslender column limits for braced and unbraced reinforced concrete members, *ACI Struct. J.*, **102**, 1, pp. 12-21.
- [4] Bažant, Z.P. and Cedolin, L. (2003), *Stability of structures – Elastic, Inelastic, Fracture, and Damage Theories*, Dover Publications, Inc., New-York, 2003.
- [5] Krauberger, N., Bratina, S., Saje, M., Schnabl, S. and Planinc, I. (2011), Inelastic buckling load of a locally weakened reinforced concrete column, *Engineering Structures*, **34**, pp. 278–288.
- [6] Brojan, M., Pukšić, A. and Kosel, F. (2007), Buckling and post-buckling of a nonlinearly elastic column, *ZAMM*, **87**, 7, pp. 518-527.
- [7] Challamel, N., Lanos, C. and Casandjian, C. (2007), Creep failure of a simply-supported beam through a uniaxial Continuum Damage Mechanics model, *Acta Mechanica*, 192, **1-4**, pp. 213-234.
- [8] Challamel, N., Lanos, C. and Casandjian, C. (2005), Creep damage modelling for quasi-brittle materials, *Eur. J. Mech. A/Solids*, **24**, pp. 593-613.
- [9] Cimetiere, A., Halm, D. and Molines, E. (2007), A damage model for concrete beam in compression, *Mech. Res. Comm.*, **34**, pp. 91-96.
- [10] Challamel, N. and Helleland, J. (2011), Simplified buckling analysis of imperfection sensitive reinforced concrete columns, Proceedings of the 24th Nordic Seminar on Computational Mechanics, November 3-4 2011, Aalto University, Helsinki, Finland.
- [11] Challamel, N., Lanos C. and Casandjian, C. (2009), Some closed-form solutions to simple beam problems using non-local (gradient) damage theory, *Int. J. Damage Mech.*, **18**, 6, pp. 569-598.
- [12] Challamel, N., Lanos C. and Casandjian, C. (2010), On the propagation of localization in the plasticity collapse of hardening-softening beams, *Int. J. Eng. Sc.*, **48**, 5, pp. 487-506.
- [13] Challamel, N. (2010), A variationally-based nonlocal damage model to predict diffuse microcracking evolution, *Int. J. Mech. Sc.*, **52**, pp. 1783-1800.
- [14] Pijaudier-Cabot, G. and Bažant, Z.P., (1987), Nonlocal damage theory, *J. Eng. Mech.*, **113**, pp. 1512-1533.
- [15] Peerlings, R.H.J., de Borst, R., Brekelmans, W.A.M. and de Vree, J.H.P. (1996), Gradient-enhanced damage for quasi-brittle materials, *Int. J. Num. Meth. Engng.*, **39**, pp. 3391-3403.
- [16] Pham, K., Marigo, J.J. and Maurini, C. (2011), The issues of the uniqueness and the stability of the homogeneous response in uniaxial tests with gradient damage models, *J. Mech. Phys. Solids*, **59**, 6, 1163-90.

Study of the Blast-Resistant Response of a Reinforced Polymer Composite-Glass Laminate

Zhen Chen^{1*}, Luming Shen², Sanjeev K. Khanna³ and Hua Zhu³

¹Department of Civil & Environmental Engineering, University of Missouri, Columbia, MO 65211, USA

*Department of Engineering Mechanics, Dalian University of Technology, Dalian 116024, P. R. China

E-mail: chenzh@missouri.edu

²School of Civil Engineering, University of Sydney, NSW 2006, Australia

E-mail: luming.shen@sydney.edu.au

³Department of Mechanical and Aerospace Engineering, University of Missouri, Columbia, MO 65211, USA

E-mail: khannas@missouri.edu

Abstract. A transparent fiber-reinforced polymer composite is being developed as the interlayer in a composite-glass laminate system to provide the cost-effective protection against blast loading. To evaluate and improve the system performance for the blast resistance, model-based simulation is being conducted to investigate the effects of key material and loading parameters on the wave patterns in the composite-glass laminate structure, and to estimate its failure response to different explosive environments based on available experimental data. To predict and simulate the rate-dependent transition from microcracking to macrocracking, discontinuous bifurcation analysis has been performed to formulate a decohesion model for the composite interlayer, and the material model with its solver has been implemented into the coupled computational fluid dynamics and solid dynamics code with the Material Point Method. The preliminary results and the comparison with the available experimental data are presented to illustrate the proposed procedure.

1. Introduction

Critical civil infrastructures such as airports or defense establishments and transport vehicles are vulnerable to manually delivered small explosive devices. Such structures are increasingly using composite materials, which include laminated composites also. An integrated analytical, experimental and computational effort is being made to develop a transparent glass fiber reinforced plastic composite laminated with glass sheets to fabricate a blast-resistant structural composite system for protection against manually transportable explosives. The use of transparent composite interlayer is helpful in visualizing the failure patterns in real time and in post-mortem. The new layered panel consists of heat-strengthened glass plies laminated with a novel damage-resistant and transparent composite as the interlayer. The candidate transparent composite interlayer consists of glass fiber reinforcement in an engineered polymer matrix. The interlayer is laminated with the glass sheets using an adhesive.

Traditionally blast-resistant glazing designs have been commonly based on laminated glass [1]. As can be seen from the open literature, however, there is no information available on the blast-resistant response of a reinforced composite-glass layered system. Especially,

there is a lack of understanding about the effect of mechanical impedances in different layers on the formation and evolution of failure in the system, although the impedance effect must be considered when designing composite structures that have to withstand blast loads [2]. To establish a quantitative design tool for evaluating the effects of system parameters on the blast resistance, therefore, model-based simulation is performed here to investigate the effects of key material and loading parameters on the wave patterns in the composite laminate system, and to estimate its failure response to different explosive environments based on available experimental data.

To perform coupled computational fluid dynamics (CFD) and computational solid dynamics (CSD) simulation of the responses involving multi-material phases in a single computational domain, a robust spatial discretization procedure is a necessity. The Material Point Method (MPM) [3 and 4; among others], which is an extension to solid dynamics problems from a hydrodynamics code, is used in this investigation. The motivation for developing the MPM was to simulate the problems such as impact/contact, penetration and perforation with history-dependent internal state variables. The essential idea is to take advantage of both the Eulerian and Lagrangian methods while avoiding the shortcomings of each. Hence, different material phases can be discretized in space with the MPM to simulate the failure evolution in the composite-glass laminate subject to blast loading.

2. Effects of Key Parameters

Due to the duration of the blast loads, the formation and evolution of failure across different layers in a composite structure depend on both wave and bending effects. Shock-induced microcracking results in macrocracking and final collapse of the structure under subsequent dynamic pressure (bending effects). The mechanical impedance plays an important role in inducing tensile failure of the interfacial bonding at a given interface under a compressive load of short duration. Since the impedance ratio could be adjusted via the amount of glass fibers reinforcement and since the wave patterns could also be controlled with the change in layer thickness for a given duration of impulse, the effects of selected parameters on the elastic wave patterns are investigated in a uniaxial strain configuration subject to incident impulses of triangular shape with a given peak and different durations. Based on the relation among the incident, reflected and transmitted stress waves in the composite glass consisting of 5 layers (glass, adhesive, composite interlayer, adhesive and glass), the major findings from the parametric study are summarized as follows:

1. The effect of representative thickness of the first adhesive layer on the maximum stress (compressive or tensile) in the rear glass layer (not facing blast wave) is small, and a similar effect could be observed for the second adhesive layer.
2. The effect of representative thickness of the composite interlayer on the maximum stress in the rear glass layer is larger than that of the adhesive layer, with an optimized value depending on the geometry and wave impedance.
3. The effect of incident impulse duration on the maximum stress in the rear glass layer changes with the duration. With the increase of duration, the wave effect decreases while the bending mode becomes dominant.
4. The increase of Young's modulus in the composite interlayer results in an increase in the maximum stress of the rear glass layer, but this effect diminishes with the further increase of Young's modulus. The effect of Young's modulus in either or both adhesive layers is similar to that in the composite interlayer.

3. Evaluation of the failure response

Much work has been done by the research community to understand and model the rate-dependent behaviors of individual candidate material components used in the composite-glass laminate [5-8, among others]. However, only quasi-static and low velocity impact experimental data are available for characterizing the constitutive responses of the material components being used in fabricating the transparent composite-glass laminate system [9-11]. Especially, there is a lack of understanding on the formation and evolution of debonding and cracking across different material layers. Hence, an attempt is made here to qualitatively model and evaluate the failure response of the laminate to different explosive environments based on available experimental data.

The essential feature of a complete failure evolution process is characterized by the transition between discontinuities of different degrees, which is governed by the jump forms of conservation laws [12]. Based on the discontinuous bifurcation analysis, it is known that the transition from continuous to discontinuous failure modes is identified by the onset of localization. There are certain kinds of applicability and limitation for different modeling approaches, depending on the scale of the problem and the degrees of discontinuity considered [13]. To better evaluate the blast resistance of various potential composite-glass laminates, a continuous modeling approach is integrated here with a discontinuous one via the discontinuous bifurcation analysis. As a result, the essential feature of the failure evolution could be effectively simulated while the governing equations remain well-posed. Based on the previous research [14-18], a combined rate-dependent tensile damage and decohesion model is used to describe glass fragmentation under explosion, while a coupled von Mises plasticity and decohesion model is applied to the simulation of the blast response of the composite interlayer and adhesion layer, respectively. Discontinuous bifurcation analysis is performed to identify the initiation and orientation of discontinuous failure.

Based on the parametric study, the normal stresses in the direction perpendicular to the blast wave direction dominate the evolution of failure in the glass layers due to the bending effect. For the purpose of simplicity, hence, a plane strain problem is considered here to demonstrate the proposed model-based simulation procedure. A slice of the composite-glass laminate with the total thickness of 10 mm and height of 431.8 mm is discretized via the MPM with the top and bottom sides being fixed. The thickness of the two glass layers and the composite interlayer is 3.2 mm, respectively, while the thickness of the two adhesion layers is 0.2 mm each. The blast wave is assumed to be applied uniformly on the left side glass layer, with the origin of the x-y coordinates being located at the lower-left corner of the panel section. The MPM discretization consists of square cells with each side being 0.2 mm long. Initially, one material point per cell is used to discretize each material layer so that there is one material point along the thickness direction of each adhesion layer. With the evolution of localization and decohesion, the number of material points per cell would change but the cell size remains fixed. An explicit time integrator is adopted for the MPM code. A series of simulations corresponding to the field experiments for different amounts of TNT at different standoff distances have been performed to calibrate the model-based simulation procedure. It appears from the comparison between experimental data and numerical results that the proposed procedure could qualitatively evaluate the evolution of damage in the composite-glass laminate. Governing equations, solution procedure and simulation results will be presented in the conference.

4. Concluding remarks

A parametric study has been performed to understand the effects of key model and loading parameters on the composite structural response to blast loading. Based on the parametric study and available experimental data, model-based simulations have been conducted to estimate the failure response to different explosive environments, in combination with field experiments. It appears from the preliminary investigation that the proposed model-based simulation procedure could qualitatively describe the experimental observation, and be used to better design the composite system.

Acknowledgement This research project was supported by the US Department of Homeland Security. The assistance of Dr. Jason Baird in the Rock Mechanics and Explosives Research Center at the Missouri University of Science and Technology, Rolla, Missouri, USA, in performing the explosive tests is greatly appreciated. Luming Shen also wishes to thank the support from the Australian Research Council under grant no. DP0772478.

References

1. Norville H.S., Conrath E.J. (2006) Blast-resistant glazing design. *Journal Architectural Engineering* **12**, 129-136.
2. Achenbach J.D., Hemann J.H., Ziegler F. (1968) Tensile failure of interface bonds in a composite body subjected to compressive loads. *AIAA Journal* **6**, 2040-2043.
3. Sulsky D., Chen Z., Schreyer H.L. (1994) A particle method for history-dependent materials. *Computer Methods in Applied Mechanics and Engineering* **118**, 179-196.
4. Sulsky D., Zhou S.J., Schreyer H.L. (1995) Application of a particle-in-cell method to solid mechanics. *Computer Physics Communications* **87**, 236-252.
5. Gilat A., Goldberg R.K., Roberts G.D. (2002) Experimental study of strain-rate-dependent behavior of carbon/epoxy composite. *Composites Science and Technology* **62**, 1469-1476.
6. Tsai J., Sun C.T. (2002) Constitutive model for high strain rate response of polymeric composites. *Composites Science and Technology* **62**, 1289-1297.
7. Song B., Chen W., Weerasooriya T. (2003) Quasi-static and dynamic compressive behaviors of an S-2 glass/SC15 composite. *Journal of Composite Materials* **37**, 1723-1743.
8. Vural M., Ravichandran G. (2004) Transverse failure in thick S2-glass/epoxy fiber-reinforced composites. *Journal of Composite Materials* **38**, 609-623.
9. Kalluri R.S. (2007) *Failure of Transparent Polymer Composite Laminated Glass Panels under Impact Loading*. M.S. Thesis, University of Missouri.
10. Ellingsen, M.D. (2009) *Static Interfacial Fracture in Orthotropic-Orthotropic Composite Bimaterials Using Photoelasticity*. Ph.D. dissertation, University of Missouri.
11. Khanna S.K., Ellingsen M.D., Winter R.M. (2004) Investigation of fracture in transparent glass fiber reinforced polymer composites using photoelasticity. *ASME Journal of Engineering Materials and Technology* **126**, 1-7.
12. Chen Z. (1996) Continuous and discontinuous failure modes. *Journal of Engineering Mechanics* **122**, 80-82.
13. Bazant Z.P., Chen E.P. (1997) Scaling of structural failure. *Applied Mechanics Reviews* **50**, 593-627.
14. Chen Z, Schreyer H.L. (1995) *Formulation and computational aspects of plasticity and damage models with application to quasi-brittle materials*. SAND95-0329, Sandia National Laboratories, Albuquerque, NM.
15. Chen Z., Deng M., Chen E.P. (2001) Rate-dependent transition from tensile damage to discrete fracture in dynamic brittle failure. *Theoretical and Applied Fracture Mechanics* **35**, 229-235.
16. Shen L., Liu Y., Chen, Z. (2001) Bifurcation analysis of steel and concrete with rate-dependent properties - Part Two: Bifurcation analyses and demonstrations. *Advances in Structural Engineering* **4**, 225-232.
17. Chen Z., Shen L., Mai Y.W., Shen, Y.G. (2005) A bifurcation-based decohesion model for simulating the transition from localization to decohesion with the MPM. *Zeitschrift für Angewandte Mathematik und Physik (ZAMP)* **56**, 908-930.
18. Hu W., Chen Z. (2006) Model-based simulation of the synergistic effects of blast and fragmentation on a concrete wall using the MPM. *International Journal of Impact Engineering* **32**, 2066-2096.

STRUCTURAL HEALTH MONITORING WITH ADVANCED NONDESTRUCTIVE METHODS BASED ON WAVELET ANALYSIS

Cvelbar, R.¹, Suban M.¹, Bundara B.¹, Lazarević, M.P.², Vasić, V.²

¹ Institute for metal construction, Mencingerjeva 8, SI-1000 Ljubljana
e-mail: robert.cvelbar@imk.si

² Faculty of Mechanical Engineering,
The University of Belgrade, Kraljice Marije 16, 11120 Belgrade 35
e-mail: mlazarevic@mas.bg.ac.rs

Abstract. Steel structures, especially if they are exposed to the demanding loading or environmental conditions, need to be monitored concerning the actual in-service properties. For reliable monitoring it is important to know the initial properties in order to diagnose possible degradation with time. The target result of the presented research is to develop and apply the procedure for the degradation identification. The obtained results would serve as input for the model analysis that enables estimation of the structure condition and to support decision on the maintenance activities.

In the experimental part of the presented research the model of the steel bridge was made to analyze the anomalous structural behavior and to optimize the selection of the appropriate monitoring methods. Various static and dynamic loads have been utilized on the model, with intentionally inserted steel structure failures (e.g. cracked bar, loosened screw joint). The structural responses are very well suited for the wavelet transforms and related wavelet analysis. This paper presents the procedure to correlate results of the wavelet analysis with the inflicted failures within the structure.

1. Introduction

Reliable and safe behavior of the structures is desire of the end user. Material ageing, environmental affects, damages, etc, are affecting the durability, reliability and safety of structures. Structural integrity monitoring (SIM) is a necessity to know and foresee the condition of the structure [1]. The system degradation affects the time-frequency characteristics of the system's response. [2].

It would be useful to determine the possible location of the structural damage with the method which evaluates structure in general and if possible with the excitation which is already present at the object under observation, i.e. truck moving over the bridge, wind acting on the tower or building, [2].

Analysis of the response could be presented in the time and/or frequency domain. Analysis in the frequency domain has some shortcuts since the time of certain event occurrence is not known. To overcome this deficiency the wavelet transform can be used in order to

provide information in the time and frequency domain. To analyze the suitability of the classical FFT approach and of the wavelet analysis to characterize dynamical behavior of the structure with some induced damages in the elements, we performed analysis on the model of the steel space truss bridge. Firstly the responses were calculated and then compared to the experimental values.

2. Numerical analysis of the problem

We were applying the analysis on the real 3D bridge model, which is presented on Fig. 1 [4]. Structure is space truss, assembled by two longitudinal truss frames of the 3600 mm in length, divided on 8 sectors of the 450 mm in length. Height of the frames is 440 mm, and width is 360 mm. Upper compression loaded and lower tensile loaded elements are made of cold formed elements HOP U30/30/2 mm, verticals are made of HOP U 30/20/2 mm, and diagonals are assembled from two HOP U15/30/2 mm and from two HOP L20/20/2 mm (Figs. 2 and 3). Upper compression loaded elements are connected by the HOP U 50/25/3 mm and centrally connection is made of round bars ϕ 6 mm. Lower tensile loaded elements are in the location of the supports connected with the HOP U 30/20/2 mm. For the numerical modeling the quality of the material S235 with the modulus of elasticity $E = 210$ GPa was used.

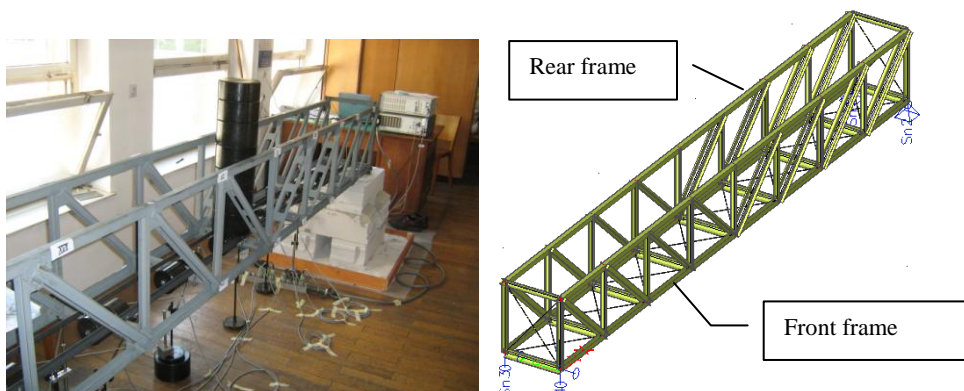


Figure 1: a) Laboratory bridge model

b) 3D FE bridge model.

In the model the rigid connection are assumed since the joints are made with the rigid bolted connections. In the model the sliding moment free supports were used.

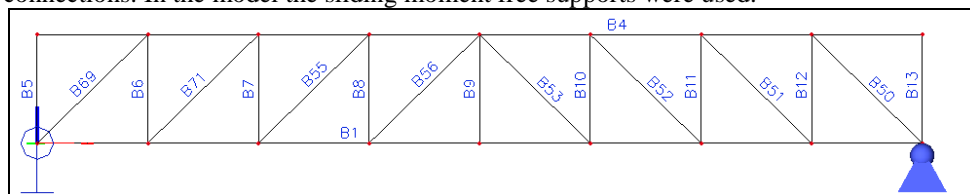


Figure 2: Elements of the front frame.

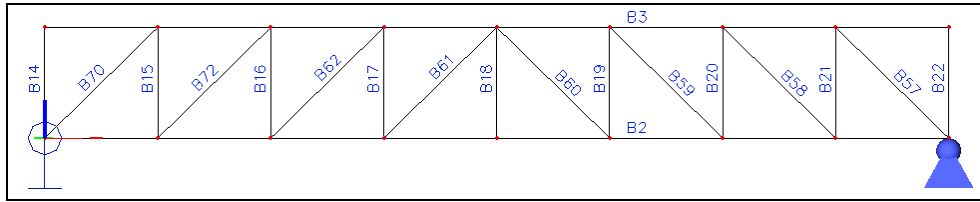


Figure 3: Elements of the rear frame.

Dynamic analysis, i.e. eigenfrequencies and modes of vibrations were calculated for the loading case presented on Fig.1 (57N on all joints at the bottom of the front and rear frame).

The analysis of the dynamic behavior of a structure was performed for cases where some of the diagonal elements in the structure were eliminated. Since diagonals are assembled of two L elements one was removed, i.e. rigidity of the diagonal was reduced to one half. Location of removed elements and calculated first natural frequencies for individual cases are presented in table 1.

Table 1: 1st natural frequencies for different “damage” cases

Case	Removed element	1 st eigenfrequency [Hz]
0	none	43,27
I	B69	43,01
II	B69 + B70	42,74
III	B71	43,12
IV	B71 + B72	42,96
V	B71 + B72 + B69	42,71
VI	B69 + B70 + B71 + B72	42,45
XIV	B69+B70+B50+B57+B71+B72+B51+B58	41,71

Even in the case when more than half diagonals have reduced stiffness to one half, the frequency is not changed significantly. From this numerical analysis we can conclude that conclusions on the possible structural damage based on the measurements of the global structure first natural frequency could be misleading. Even if the change of the cycle time would be determined, it would not be necessary the consequence of the rigidity change but could be caused by the temperature change.

3. Experimental analysis

On the model of the bridge measurements were performed for the case 0 (no-loose) and I (loose) from the table 1. Accelerometer was positioned on the middle of the bridge in vertical direction. The sampling rate was 5 kHz and loading was induced with the sudden release of the 100N from the middle of the bridge model. Response is for both cases presented on Fig. 4. The 1st natural frequencies determined by the FFT are 41,7 and 41,2 Hz for the case 0 and I respectively.

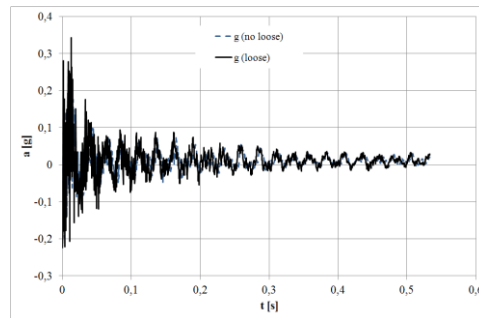


Figure 4: Measured response of the bridge model.

Since the conclusion based on the time domain and FFT analysis is the same as conclusion based on numerical analysis we performed the wavelet analysis. We applied Daubechies 3 kernels [4] and significant differences can be observed on the wavelet coefficient as presented for the third level coefficients on Fig. 5.

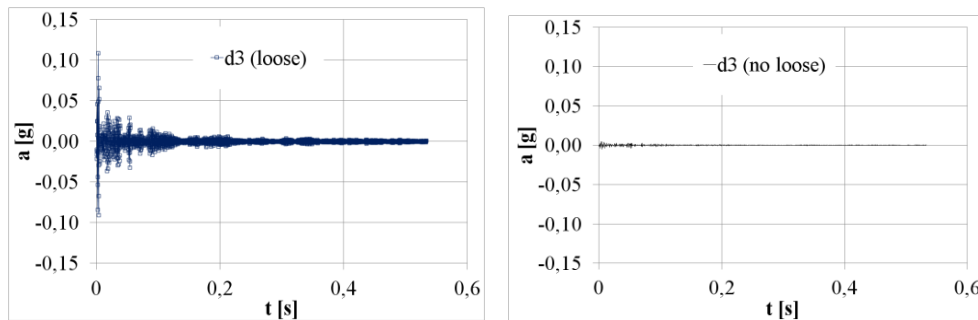


Figure 5: Wavelet coefficient on third level.

5. Conclusion

On the space truss bridge model comparison of the un-damaged and damaged bridge response to the sudden load was performed. With the analysis in the time domain and with the FFT we can conclude that conclusions on the possible structural damage based on the measurements of the global structure first natural frequency could be misleading. Wavelet analysis enables to distinguish the differences in the responses.

Acknowledgement. This work is supported by EUREKA program- E!4930 AWAST and partially supported by the Ministry of Education and Science of Serbia as R.P.-No. 35006.

6. References

- [1] W. Rücker, F. Hille, R. Rohrmann (2006), *Guideline for the Assessment of Existing Structure*, SAMCO Final Report 2006, F08a Guideline for the Assessment of Existing Structures, pp. 48.
- [2] Biswajit Basu (2005), *Identification of stiffness degradation in structures using wavelet analysis*, Construction and Building Materials 19, pp. 713–721.
- [3] A.V. Ovanesova, L.E. Suarez (2004), *Applications of wavelet transforms to damage detection in frame structures*, Engineering Structures 26, p.p. 39–49
- [4] Tomaž Rojc, Zdenko Savšek, (1994), *Report on the dynamical analysis on the bridge model (in Slovenian)*, IMK pp. 48.
- [5] R. Cvelbar, D. Močnik, A discrete wavelet transform , IMK, pp. 8.

MICROSTRUCTURAL EFFECTS ON THE MECHANICAL PROPERTIES AND TRIBOLOGICAL DAMAGE OF Ti-6Al-4V ALLOY

I. Cvijović-Alagić¹, M. Rakin², Z. Cvijović³, N. Gubelj⁴, K. Gerić⁵

¹Institute of Nuclear Sciences „Vinča“,
University of Belgrade, Mike Petrovića Alasa 12-14, 11001 Belgrade, Serbia
e-mail: ivanac@vinca.rs

²Faculty of Technology and Metallurgy,
University of Belgrade, Karnegijeva 4, 11120 Belgrade, Serbia
e-mail: marko@tmf.bg.ac.rs

³Faculty of Technology and Metallurgy,
University of Belgrade, Karnegijeva 4, 11120 Belgrade, Serbia
e-mail: zocvij@tmf.bg.ac.rs

⁴Faculty of Mechanical Engineering,
University of Maribor, Smetanova 17, 2000 Maribor, Slovenia
e-mail: nenad.gubelj@uni-mb.si

⁵Faculty of Technical Sciences,
University of Novi Sad, Trg Dositeja Obradovića 6, 21000 Novi Sad, Serbia
e-mail: gerick@uns.ac.rs

Abstract. The tensile properties and reciprocating sliding wear behavior in a Ringer's solution of Ti-6Al-4V alloy with fully lamellar, equiaxed and martensitic microstructures were examined with particular emphasis on identifying the damage mechanisms during frictional sliding. It was found that martensitic microstructure has a lowest elastic modulus, although its yield and ultimate tensile strength are similar to that of the equiaxed microstructure, exhibiting the highest values of all tensile properties. However, surface damage extent attributed to the predominant wear mechanism is strongly dependent on the microstructural features. The adhesive wear contributing to severe delamination is dominant in the lamellar microstructure with lowest tensile strength, while the martensitic microstructure is especially susceptible to oxidative wear and produces considerable amount of hard oxide debris that can score the surface. The extent of the surface damage is smallest for equiaxed microstructure in which the wear mechanism is mainly abrasive. This indicates that the martensitic microstructure attains a best combination of mechanical properties, while the equiaxed microstructure has superior frictional performance under investigated conditions.

1. Introduction

The Ti-6Al-4V alloy is presently most often used for biomedical applications because of its well balanced mechanical properties, corrosion resistance and biocompatibility [1,2]. However, relatively high elastic modulus, high friction coefficient and low wear resistance of this $\alpha+\beta$ titanium alloy might cause further bone degradation and orthopedic implant

failure due to the surface damage resulting in premature nucleation and subsequent propagation of fatigue cracks [2]. Therefore, it is important to reduce elastic modulus and improve tribological properties of this implant material.

The alloy properties, including mechanical and wear properties, can be controlled by alloy microstructure. The microstructure of titanium alloys is sensitive on both thermomechanical processing and heat treatment, so it is possible to obtain a suitable microstructure for optimal mechanical and tribological performance. In this study, the various microstructures developed under different heat treatments of the Ti-6Al-4V alloy were correlated with its tensile properties and reciprocating sliding wear behavior in simulated physiological solution. The friction coefficients were estimated for different applied load/sliding speed combinations and worn surfaces were observed to identify the damage mechanisms.

2. Material and experimental procedure

The Ti-6Al-4V ELI (Extra Low Interstitial) alloy bars (diameter of 38 mm) supplied by Krupp VDM GmbH, Germany, were used as the initial material. Three different microstructures were obtained by holding at 1000 °C (above the β transus) and 750 °C (below the β transus) for 1h under the protective argon atmosphere, followed by water quenching (WQ) and/or furnace cooling (FC). Tensile tests were performed in an INSTRON 1255 servo-hydraulic MTS (Micro Tensile Specimen) machine in order to determine elastic modulus, E , yield strength (0.2 % proof stress), $\sigma_{0.2}$, ultimate tensile strength, σ_{UTS} , and elongation to fracture, A , at room temperature. The tribological behavior was evaluated under linear-reciprocating sliding conditions using a ball-on-flat type CSM Nanotribometer in Ringer's solution at room temperature. The tests were done against 1.5 mm diameter alumina ball at different normal loads (100, 500 and 1000 mN) and sliding speeds (4 and 12 mm/s). All tests were conducted using a 0.5 mm stroke length for $\cdot 10^4$ cycles. After the tests, the worn surfaces were characterized using a scanning electron microscope (SEM).

3. Results and discussion

The heat treatment conditions and resulting microstructural morphology along with tensile properties are given in Table 1. It can be seen that the microstructure and mechanical properties of Ti-6Al-4V ELI alloy vary considerably with solution treatment (ST) temperature and cooling rate.

Table 1. Heat treatment conditions for studied alloy along with its microstructure and tensile properties.

Heat treatment	Microstructure	E (GPa)	$\sigma_{0.2}$ (MPa)	σ_{UTS} (MPa)	A (%)
1000 °C/1h + WQ	Martensitic	120.2	1002	1101	3.1
1000 °C/1h + FC	Fully lamellar	124.8	737	773	5.4
750 °C/1h + FC	Equiaxed	136.0	1063	1119	15.1

When the alloy is subjected to water cooling from β phase field, the microstructure consists of almost complete acicular α' martensite identified in previous study [3]. In the FC

condition, alloy exhibits a two-phase ($\alpha+\beta$) microstructure. The slow furnace cooling from β phase field leads to a fully lamellar microstructure comprising colonies of alternating laths of α and β phase. After furnace cooling from ($\alpha+\beta$) phase field, microstructure consists of the equiaxed primary α phase and intergranular β phase.

Among the three microstructures, the equiaxed microstructure has the highest values of all tensile properties. Compared to it, the martensitic microstructure shows similar yield and ultimate tensile strength. However, its elastic modulus and elongation values are much lower than those of the equiaxed microstructure. Moreover, the martensitic microstructure has the smallest modulus of elasticity and elongation among all three investigated microstructures. Its elastic modulus is comparable with that of the fully lamellar microstructure, having the lowest values of the yield and ultimate tensile strength with moderate elongation. Although the E value of martensitic microstructure is much higher than that of human bones (≈ 30 GPa), it is about 5 GPa and 16 GPa lower than those of lamellar and equiaxed microstructure, respectively, demonstrating that the Ti-6Al-4V ELI alloy rapidly cooled from β phase field has better biocompatibility.

On the other hand, the equiaxed microstructure exhibits the best frictional behavior. Although the coefficient of friction (COF) for all microstructural morphologies decreases with applied load increase or sliding speed decrease, the Ti-6Al-4V ELI alloy furnace cooled from ($\alpha+\beta$) phase field shows the lowest COF values (0.10-0.57) irrespective of load and speed. The lamellar microstructure provides comparable COF values (0.12-0.71), whereas the COF of martensitic microstructure varies from 0.13 to 1.79. The highest values (0.42-1.79) correspond to the lowest load (100 mN). At higher sliding speed, the difference in COF is much higher. The COF of equiaxed and lamellar microstructures is very close to 0.60, while of martensitic microstructure increases to 1.79. At 500 mN, the COF values for both sliding speeds are significantly lower (0.12-0.27) and remain more or less the same (0.10-0.19) as load further increases. This behavior strongly implies that wear mechanisms for the investigated microstructures are different.

The morphology of worn surfaces is shown in Fig. 1. The wear of the martensitic microstructure is controlled by an oxidative mechanism. Its worn surface is characterized by the presence of cracking and plastically deformed grooves with considerable amount of hard oxide debris trapped within and around the contact region (Figs. 1a and d). With the increase in either load or speed, the intensity of the oxidative wear decreases. The wear mechanism is essentially abrasion, but the extent of plastic deformation is much smaller. Intense delamination in some regions suggests that adhesive wear also contributes to the total wear. The wear of lamellar microstructure occurs predominantly by adhesion (Fig. 1b). Severe delamination can be easily detected on the worn surfaces. The wear tracks are rough with large grooves where material has been removed and some patches of transfer layer. At the lower load and speed, the presence of oxide debris is not observed. As the load or speed is increased, the occurrence of delamination is more prominent (Fig. 1e). The worn surface reveals the cracks in craters and fine debris accumulated at the edges of the wear track. The major damage mechanism in case of the equiaxed microstructure is abrasion. The wear track is surrounded by an accumulation of oxide debris scoring the surface (Fig. 1c), but the severity of the abrasion is much lesser as compared to the martensitic microstructure. As the load and speed are increased, the contribution of delamination increases while the amount of debris tends to be reduced (Fig. 1f).

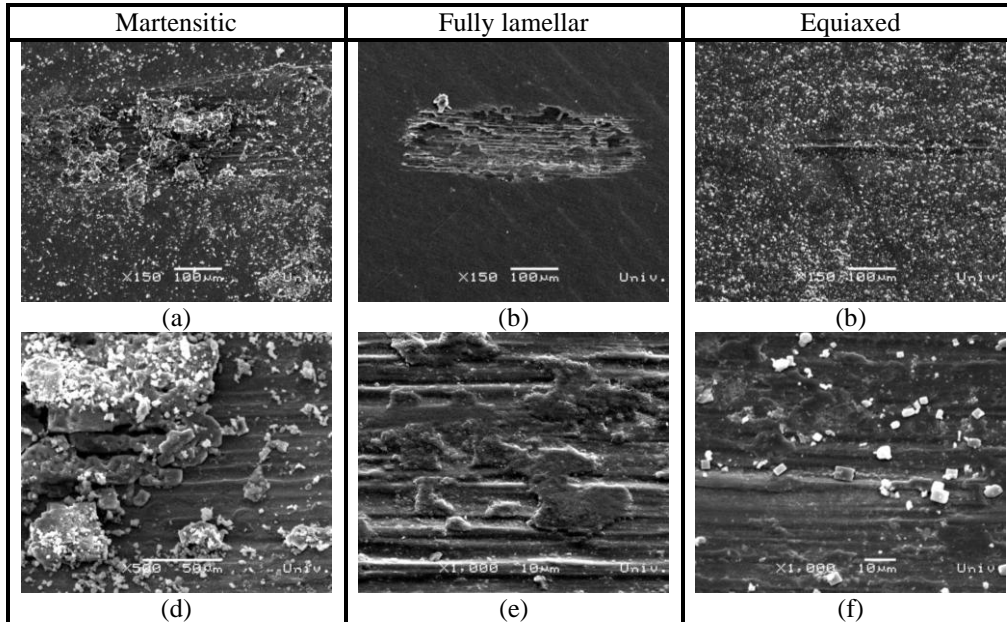


Figure 1. SEM micrographs of Ti-6Al-4V ELI worn surfaces tested at 100 mN and 4 mm/s (a-d) or 12 mm/s (e, f).

4. Conclusions

The mechanical properties, tribological behavior in Ringer's solution and resulting damage extent of Ti-6Al-4V ELI alloy are strongly dependent on the microstructural morphology. The fully martensitic microstructure possesses the best tensile strength/elastic modulus combination and biocompatibility among the investigated microstructures. However, the equiaxed and fully lamellar microstructures show the better frictional properties and smaller surface damage extent, particularly at low applied load and sliding speed. Under the present experimental conditions, the best frictional performance is obtained for the equiaxed microstructure. The observed behavior can be explained by different damage mechanisms.

Acknowledgement. This work was financially supported by the Ministry of Education and Science of the Republic of Serbia through the Project No. 174004.

References

- [1] Geetha, M., Singh, A.K., Asokamani, P. and Gogia, A.K. (2009), Ti based biomaterials, the ultimate choice for orthopaedic implants - A review, *Progress in Materials Science*, **54**, pp. 397-425.
- [2] Long, M. and Rack, H.J. (1998), Titanium alloys in total joint replacement - a materials science perspective, *Biomaterials*, **19**, pp. 1621-1639.
- [3] Cvijović-Alagić, I., Cvijović, Z., Mitrović, S., Panić, V. and Rakin, M. (2011), Wear and corrosion behaviour of Ti-13Nb-13Zr and Ti-6Al-4V alloys in simulated physiological solution, *Corrosion Science*, **53**, pp. 796-808.

TRANSITION FROM A GRADIENT DAMAGE MODEL TO A COHESIVE ZONE MODEL WITHIN THE FRAMEWORK OF QUASI-BRITTLE FAILURE

S. Cuvilliez¹, F. Feyel², E. Lorentz¹, S. Michel-Ponnelle¹

¹LaMSID – UMR EDF/CNRS/CEA 2832,
EDF R&D, 1 avenue du Général de Gaulle, 92141 Clamart Cedex, France
e-mail: sam.cuvilliez@edf.fr

²ONERA, BP72 – 29 avenue de la Division Leclerc, 92322 Châtillon Cedex, France

Abstract. The present work aims at studying the transition from a non local damage model to a cohesive zone model. An analytical one-dimensional study is first carried out (on a bar submitted to tensile loading) in order to identify a set of cohesive laws that enable to switch from a localized solution obtained with the continuous gradient damage model to cohesive crack opening. These interface laws are constructed so that energetic equivalence between both model remains ensured whatever the damage level reached when switching. The strategy is then extended to the bi-dimensional (and tri-dimensional) case of rectilinear (and plane) crack propagation under mode I loading conditions, in a finite element framework.

1. Introduction

Continuum damage mechanics (CDM) [3] is now a common computational framework used by engineers to describe fracture of quasi-brittle materials, especially in structural analysis for civil engineering, with materials such as concrete. Strain-softening damage constitutive laws are known to lead to pathological mesh sensitivity that can be overcome by means of regularization techniques such as non local formulations. In the present work we focus on a gradient damage model [5] (in which the gradient of damage is considered as an additional state variable). Finite element (FE) analysis performed with such non local damage models provide satisfactory results, but can still be improved in several ways, in particular at the late stage of damage growth when material separation is supposed to occur. The aim of this work is then to develop a strategy that enables to switch before complete damage from a continuous to a discrete failure model, by combining a gradient damage model and a cohesive zone model [1] (CZM) in the same FE framework.

2. Gradient damage model

The gradient damage model proposed in [5] is here briefly recalled. The material state is defined by the strain tensor $\boldsymbol{\varepsilon}$ and a scalar damage variable d , and the stress – strain relation is brittle elastic, where the damage progressively weakens the initial stiffness:

$$\boldsymbol{\sigma} = A(d)\mathbf{E} : \boldsymbol{\varepsilon} . \quad (1)$$

The stress is denoted $\boldsymbol{\sigma}$, \mathbf{E} is Hooke's tensor, and $0 \leq A(d) \leq 1$ is the stiffness function. In particular, $d = 0$ corresponds to the sound material and $d = 1$ corresponds to the ultimate damage state: $A(0) = 1$, $A(1) = 0$. The damage driving force derives from the elastic energy which reads:

$$Y = -\frac{1}{2} A'(d) \boldsymbol{\varepsilon} : \mathbf{E} : \boldsymbol{\varepsilon}. \quad (2)$$

In order to control the localisation of strain and damage, the damage Laplacian $\nabla^2 d$ is introduced into the yield function f :

$$f(Y, \nabla^2 d) = Y + c \nabla^2 d - k. \quad (3)$$

where $k > 0$ is a yield threshold, and $c > 0$ a parameter which governs the intensity of the non local term. The Kuhn – Tucker consistency condition takes its usual form:

$$f \leq 0; \quad \dot{d} \geq 0; \quad \dot{d} f = 0. \quad (4)$$

3. One-dimensional analytical study

In this section we consider a brittle one-dimensional bar of length $2L$, submitted to a tensile displacement at its both extremities $x = \pm L$, and we focus on the inhomogeneous symmetrical solution where damage localizes at the centre of the bar (see Fig. 1).

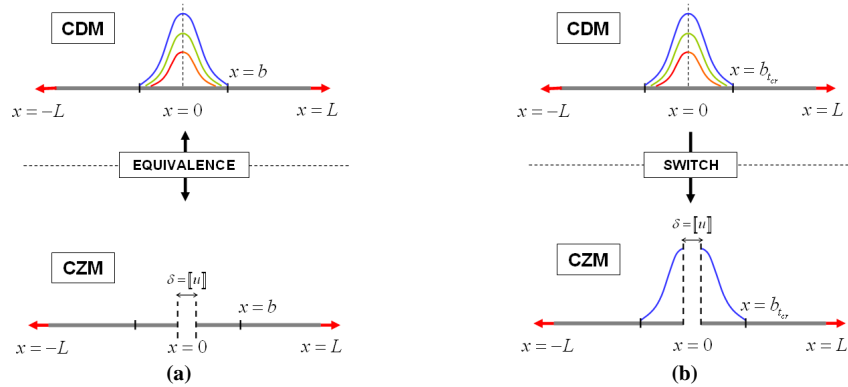


Figure 1. (a) equivalence between non local CDM and CZM, (b) .switching from CDM to CZM

A closed-form solution proposed in [4] is available for the gradient damage model when the width of the localization band $2b$ (see Fig. 1 again) is an increasing function of the load parameter. This condition is satisfied with the following expression of stiffness function:

$$A(d) = \left(\frac{1-d}{1+\gamma d} \right)^2; \quad \gamma \geq 2.8. \quad (5)$$

3.1. Identification of an equivalent cohesive law

Starting from this closed-form solution, we first want to identify an equivalent cohesive law in the sense that it provides the same stress – displacement global response as the one obtained by means of the gradient damage model. In that case (see Fig. 1a), we consider the same bar with a linear elastic material behavior, and a potential displacement discontinuity (punctual cohesive interface) located on its center (corresponding to the center of the localization band of the damageable bar). Let us call U^{CDM} and U^{CZM} the prescribed displacements at the abscissa $x=L$ respectively for the non local and the cohesive approaches:

$$U^{CDM} = \frac{\sigma}{E} \int_0^L \frac{dx}{A(d(x))}; \quad U^{CZM} - \frac{\delta^{EQU}}{2} = \frac{\sigma}{E} L \quad (6)$$

where δ^{EQU} denotes the displacement jump at $x=0$. The load level is then parameterised by the homogeneous stress σ , which decreases from its elastic yield value σ_y to 0. By enforcing the equality between U^{CDM} and U^{CZM} at each σ , one can extract the expression of the displacement jump $\delta^{EQU}(\sigma)$ of the equivalent cohesive law:

$$\forall \sigma, \quad U^{CDM} = U^{CZM} \Rightarrow \delta^{EQU}(\sigma) = \frac{2\sigma}{E} \left(\int_0^b \frac{dx}{A(d(x))} - b \right) \quad (7)$$

with b the half width of the localization band.

3.2. Switching from damage growth to cohesive crack opening

From now on we only consider the damageable bar, where material degradation is described through the gradient damage model until the top damage value at the center of the localization band reaches an arbitrary critical value denoted d_{cr} . (corresponding to the instant t_{cr}). At this stage, we switch from a continuous to a discontinuous failure representation by inserting a cohesive interface at the center of the localization band. When the cohesive interface is activated, the bar becomes elastic while maintaining the inhomogeneous stiffness distribution related to the “critical” damage field $d_{t_{cr}}(x)$.

In order to preserve the energetic equivalence with the stand-alone gradient damage model, the same strategy than in Eq. (7) is applied. The notation U_t^{CDM} is preserved to denote the prescribed displacement for the non local approach at time t , while U_t^{SWI} designates the prescribed displacement at time $t > t_{cr}$ once the transition has been triggered (where exponent “SWI” refers to “switch”). These two quantities read:

$$\forall t, \quad U_t^{CDM} = \frac{\sigma_t}{E} \int_0^L \frac{dx}{A(d_t(x))} \quad (8)$$

$$\forall t > t_{cr}, \quad U_t^{SWI} - \frac{\delta_t^{SWI}}{2} = \frac{\sigma_t}{E} \int_0^L \frac{dx}{A(d_{t_{cr}}(x))} \quad (9)$$

After some calculation, the expression of the “switch” displacement jump reads:

$$\forall t > t_{cr}, \delta^{SWI}(\sigma_t) = \delta^{EQU}(\sigma_t) - \frac{2\sigma_t}{E} \left(\int_0^{b_{cr}} \frac{dx}{A(d_{t_{cr}}(x))} - b_{t_{cr}} \right) \quad (10)$$

with $b_{t_{cr}}$ the half width of the localization band when switching. Eq. (10) indicates that the equivalent cohesive law $\delta^{EQU}(\sigma)$ is a master curve from which one can compute any cohesive law $\delta^{SWI}(\sigma)$ allowing to switch from CDM to CZM at an arbitrary critical damage value $d_{cr} = d_{t_{cr}}(0)$. Moreover, the corrective term in Eq. (10) is a linear function of the stress.

4. Extension to 2D/3D crack propagation in a FE framework

Under restrictive hypothesis such as straight (or plane) crack propagation under mode I loading conditions, the preliminary one-dimensional results related to the tensile bar can be extended as in [2] to a bi-dimensional (or tri-dimensional) FE context. This extension has been implemented in the case of postulated crack paths, allowing thus to take into account the cohesive interface into the discretisation (at the center of the expected localization band) prior to the FE computation. At the beginning of the computation, the interface is maintained in perfect adherence, and cohesive elements are gradually activated at the end of each converged time step as damage reaches a critical value at the center of the localization band. The mode I decohesion law of each activated cohesive integration point is then calculated according to Eq. (10). FE computations have been conducted with *Code_Aster* [6], an open source FE software.

References

- [1] G.I. Barenblatt (1962). The mathematical theory of equilibrium cracks in brittle fracture. *Advances in Applied Mechanics* 7, 55-129.
- [2] C. Comi, S. Mariani, U. Perego (2007). An extended FE strategy for transition from continuum damage to mode I cohesive crack propagation. *International Journal for Numerical and Analytical Methods in Geomechanics* 31 (2), 213-238.
- [3] J. Lemaitre, J.L. Chaboche (1985). *Mécanique des matériaux solide*. Dunod.
- [4] E. Lorentz, S. Cuvilliez, K. Kazymyrenko (2011). Convergence of a gradient damage model toward a cohesive zone model. *Comptes Rendus Mécanique* 339 (1), 20-26.
- [5] E. Lorentz, V. Godard (2011). Gradient damage models: Toward full-scale computations. *Computer Methods in Applied Mechanics and Engineering* 200 (21-22), 1927-1944.
- [6] *Code_Aster*, FE software distributed by EDF, open-source and freely available on www.code-aster.org

Modeling Progressive Damage in Electronic Systems

Abhijit Dasgupta¹

¹Center for Advanced Life Cycle Engineering (CALCE),
Faculty of Mechanical Engineering Department
University of Maryland, College Park, MD 20742, USA
e-mail: dasgupta@umd.edu

Abstract. This paper addresses progressive fatigue damage accumulation in copper metallizations and solder interconnects in electronic systems due to thermal and mechanical cyclic loading. A simple nonlinear continuum damage mechanics approach is presented, to capture the finite time for damage growth and propagation before final failure. The method uses either energy-based or strain based damage metrics to model incremental damage growth, and can be easily implemented within the context of conventional finite element analyses. Two examples are presented. The first example consists of fatigue failures in copper traces of leadless quad flatpack (QFN) components due to mechanical cycling of circuit card assemblies. The mechanical cycling can be due to quasi-static flexure or due to vibration or repeated shock/drop. The failure site is usually in the copper traces, at the outer edge of solder interconnects. The second example consists of fatigue failures in solder joints of chip-scale ball grid array (BGA) components due to cyclic thermomechanical stresses caused by temperature cycling.

1. Introduction

This paper addresses cyclic fatigue failures in electronic systems due to quasi-static mechanical or temperature cycling. The time required for progressive fatigue damage accumulation is important because of the opportunity it provides for early warning prognostics before catastrophic failure. Hence it is important to have design tools that can use simple methods to estimate the damage propagation period. This paper reports the use of simple incremental continuum methods to model nonlinear fatigue damage propagation.

2. Approach

Consistent with classical continuum damage mechanics concepts, an isotropic scalar state function $D(\mathbf{x})$ is used to represent the state of accumulated damage at location \mathbf{x} . The cyclic evolution dD/dN , is a function of the loading history at location \mathbf{x} . The loading history is quantified in terms of either the cyclic range of von Mises' strain $\Delta\epsilon(\mathbf{x})$ or stress $\Delta\sigma(\mathbf{x})$ or the density of cyclic inelastic work dissipation $\Delta W(\mathbf{x})$. The first example below uses $\Delta\epsilon(\mathbf{x})$ while the second example uses $\Delta W(\mathbf{x})$. The cumulative damage is then determined by integrating dD/dN over the cyclic loading history at the failure site.

Cyclic fatigue in ductile materials causes localization of distributed damage at regions of local stress concentration, and redistributes the stress distributions because of local softening and consequent loss of load-carrying capability. In this paper we use finite element analysis (FEA) to determine the history of the local stress and strain distributions for estimating the monotonic damage evolution. In the finite element context, this is captured through an incremental nonlinear analysis scheme where the material properties of each element are updated as a function of the cumulative damage value in the element. The

algorithm is applied in a piece-wise linear manner, to reduce the computational burden. Each element ‘fails’ when stiffness $\rightarrow 0$, as $D \rightarrow 1$. As critical elements ‘die’, ultimately the structure becomes mechanically unstable, leading to final failure.

3. Results:

We present 2 examples of this incremental damage propagation approach below, to address cyclic fatigue failures in electronic products. The first example addresses copper trace fatigue failures on printed wiring boards (PWBs) that are subjected to mechanical cycling. The second example deals with temperature cycling failure in the solder interconnect of surface mount area-array electronic assemblies. The fatigue process is dominated by cyclic plastic deformations in the first example and by cyclic creep deformations in the second.

3.1. Example 1: PWB Copper Trace Fatigue under Quasi-static Cycling

Figure 1 shows a PWB with 12 surface mount components, subjected to 3-point, cyclic, zero-to-max bending. The components and the PWB are daisy-chained so the electrical continuity can be monitored in real time during the cyclic testing. The copper pads containing the solder pads of this component experience large local stress concentrations. Fatigue cracks initiate and propagate to final failure in the copper trace, at the edge of the solder pad. Failure is defined by loss of electrical continuity. Data is collected from different cyclic amplitudes and described by Weibull distributions.

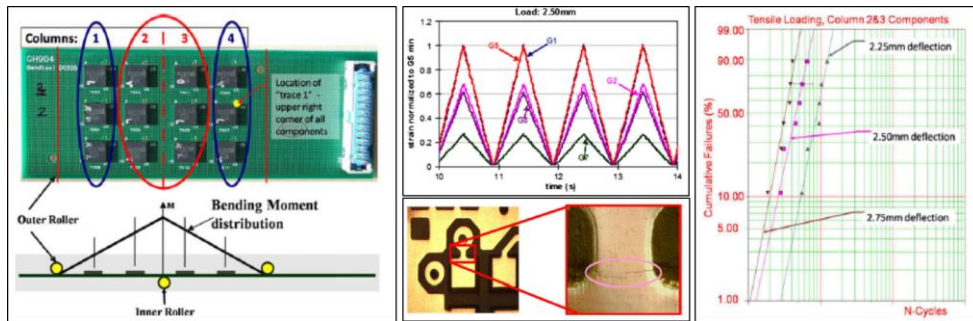


Figure 1: 3-Point cyclic bend tests for copper trace fatigue failures

In view of the symmetries of the setup, only one periodic strip of the PWB is modeled with FEA, as shown in Figure 2. In view of the geometric complexity, a multi-scale (global-local) modeling strategy is used to extract the strain and stress histories at the failure site shown in Figure 1 (in the copper stress at the edge of the solder joint).

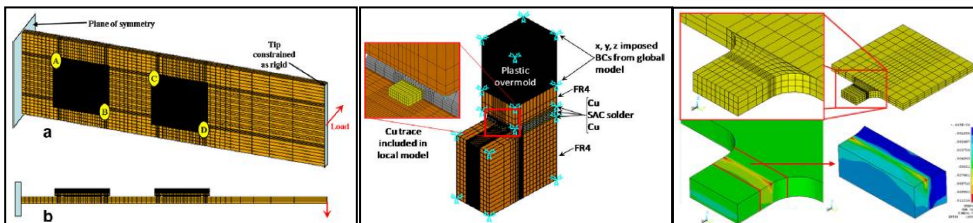


Figure 2: Multi-scale finite element model of test setup and local stress state at the failure site in the copper trace

To estimate the resulting dD/dN , we modify the generalized Coffin-Manson [1] damage model here. This model expresses dD/dN in terms of the cyclic range of the von Mises' strain ($\Delta\varepsilon$) when the loading is completely reversed. When there are non-zero means stresses, the cyclic mean of the hydrostatic stress is also included in the damage model, as shown below in Equation (1). There are 7 model constants (material properties) in this model. Details can be found in Ref [2].

$$\frac{\Delta\varepsilon}{2} = \frac{\sigma_f'}{E} \left[1 - A_i \cdot \tanh\left(\frac{m_i \cdot \sigma_m}{\sigma_f'}\right) \right] (2N_f)^b + \varepsilon_f' (2N_f)^c \quad (1)$$

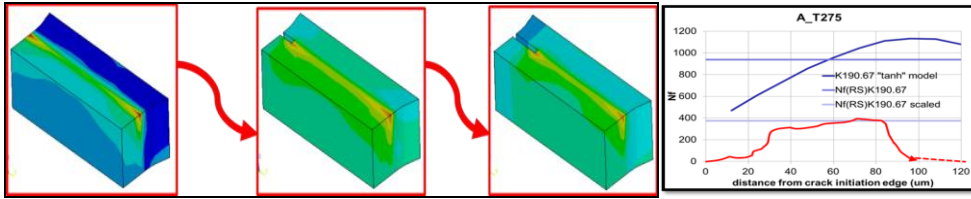


Figure 3. Damage zone propagating through cross section of the copper trace.

The damage propagation curve, using this incremental scheme is shown in Figure 3. The damage zone stably grows through about 5/6 of the cross-section, as characterized by the rising slope. At this point the remaining cross-section becomes unstable resulting in catastrophic failure. This gives us an expression for final failure in terms of the model constants in Eqn (1). By equating this expression to final measured failure for a series of fatigue tests, we are able to extract the best-fit model constants. The resulting fatigue S-N curves and the fit quality are shown in Figure 4.

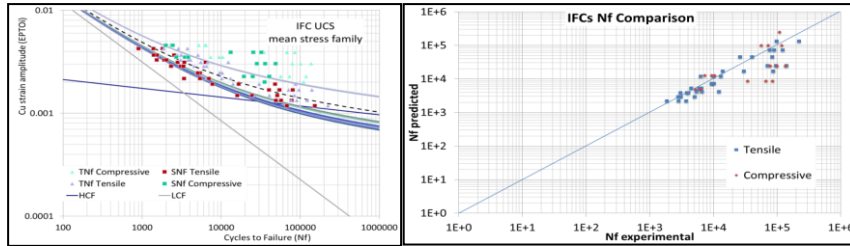


Figure 4. Extracted fatigue curves for copper and quality of model fit to test data

3.2 Example 2: Solder joint fatigue in BGA assemblies under temperature cycling:

In this example, we consider the thermal cycling durability of ball grid array (BGA) assemblies with 256 I/O solder joints each. Since solder is a viscoplastic material, we model it with a partitioned constitutive model so that the total von Mises' strain is a sum of the elastic, plastic and creep contributions. As shown in Eqn (2), the plastic deformations are modeled with a Ramberg-Osgood Power-law and the creep deformations are modeled with the Garofalo secondary creep model. Model constants may be found in ref [4].

$$\sigma = C_p \varepsilon_p^{n_p} \quad \frac{d\varepsilon_{sc}}{dt} = A(\sinh(\alpha\sigma))^{n_c} \exp\left(-\frac{Q}{RT}\right) \quad (2)$$

The temperature cycles generate cyclic stress strain histories within each solder joint because of the thermal expansion mismatches between the component and the PWB. The damage evolution model in this example partitions the cyclic work density into its plastic

and creep contributions, as shown in Eqn (3) [3]. The energy densities are obtained from FEA or similar analysis. Here the cyclic energy densities are: U_e for elastic, W_p for plastic and W_c for creep deformations. The model constants are material properties [4].

$$1/N_f = 1/N_{fe} + 1/N_{fp} + 1/N_{fc} = \left(\frac{U_{e0}}{U_e}\right)^{1/b} + \left(\frac{W_{p0}}{W_p}\right)^{1/c} + \left(\frac{W_{c0}}{W_c}\right)^{1/d} \quad (3)$$

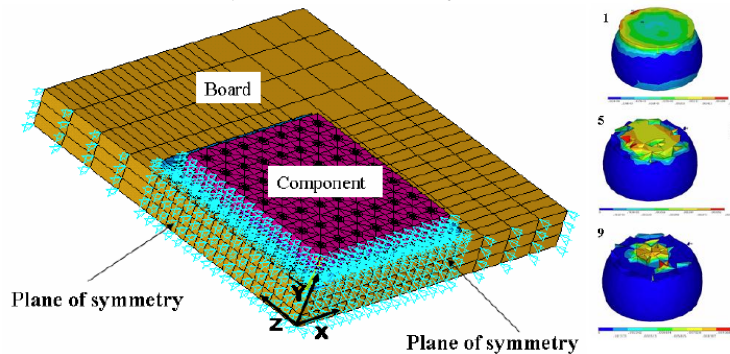


Figure 5. Quarter-symmetry FEA model of BGA256, and progressive damage evolution in critical solder joint, under temperature cycling

The quarter-symmetry FEA model for the BGA is shown in Figure 5. The work densities are monitored at the critical region of the critical joint (at outer corner of die footprint), and used to estimate the damage accumulation rate dD/dN per thermal cycle. The successive damage propagation analysis then follows an incremental scheme, similar to that described above in Example 1. Figure 5 also shows the results of this successive damage propagation analysis and shows three snapshots during the evolution of the fatigue damage zone (fatigue “crack”) through the top region of the critical solder ball from the beginning until final failure of the joint. Details of this study can be found in the literature [4]

4. Summary and Conclusions

This study has presented two examples of the use of progressive damage modeling concepts for computational estimates of cyclic fatigue damage in electronic assemblies. The method uses simple concept in continuum damage mechanics and is implemented in a computational framework since it involves incremental nonlinear analysis of complex geometries in our examples. The results are most useful since they allow us to separately model the initiation phase and propagation of cyclic fatigue damage in complex structures. This type of propagation early analysis can also provide valuable clues regarding the best windows for detecting early-warning signatures of impending failure, for prognostic and health management purposes.

Acknowledgement. The material in this paper comes from the Ph.D. dissertation research of Drs. Leila Ladani and Daniel Farley. Support for this research was provided by the sponsors of the CALCE consortium at the University of Maryland.

References

- [1] Dowling, N., “Mechanical Behavior of Materials,” 3rd Edition; Prentice Hall, 2007.
- [2] Farley, D., Dissertation, Mechanical Engineering Department, College Park, MD 20742, 2010.
- [3] Dasgupta, A., Oyan, C., Barker, D., and Pecht, M., “Solder Creep Fatigue Analysis by An Energy Partitioning Approach,” ASME Transactions, Journal of Electronic Packaging, Vol. 114, No.2, pp. 152-160, 1992.
- [4] Ladani, L. and Dasgupta, A., “Damage Initiation and Propagation in Voided Joints,” ASME Journal of Electronic Packaging, Vol 130, Issue 1, Paper Number 011008, March 2008.

BEHAVIOR OF AN INTERFACIAL CRACK BETWEEN THE TWO LAYERS IN THE STATIONARY TEMPERATURE FIELD CONDITIONS

J.M. Djoković¹, R.R. Nikolić^{2,3}

¹ Technical Faculty of Bor,
University of Belgrade, Vojske Jugoslavije 12, 19210 Bor, Serbia,
E-mail: jelenarapp@gmail.com

² Faculty of Engineering,
University of Kragujevac, Sestre Janjić 6, 34000 Kragujevac, Serbia

³ Faculty of Civil Engineering,
University of Žilina, Univerzitna 1, 01026 Žilina, Slovakia
E-mail: ruzicarnikolic@yahoo.com

Abstract. Thin films, coatings and multi-layered samples, which are made of different materials, are used for various purposes, like for thermo insulating coatings that are applied in thermal power plants turbines. The brittle coatings that operate in conditions of the elevated temperatures and high heat exchange are prone to delamination. In layers made of different materials, due to the environmental temperature change, appear thermal stresses as a consequence of a difference in their thermal expansion coefficients.

In this paper are considered driving forces that are causing the interfacial fracture in the two-layered bimaterial sample, when the external surfaces temperatures are different. Analysis in this paper is limited to consideration that the two-layered bimaterial sample is exposed to the stationary temperature field. In this case, the interfacial fracture driving force is the energy release rate G . The variation of energy release rate with temperature load is determined and it is noticed that it has a tendency to increase with increase of the temperature difference. This relation can be used for predicting the maximal temperature difference which the two-layered sample can withstand without delamination.

1. Introduction

In layers made of different materials, during the environmental temperature change, appear thermal stresses, which are the result of difference in the thermal expansion coefficients [1-3]. Those stresses are causing the appearance of an interfacial crack. When such a crack is formed, the energy release rate, which is the driving force for the crack propagation, depends on intensities of stresses in both layers. If one assumes that the layers were made of the elastic isotropic materials, the stresses would depend on the elastic and thermal characteristics of the layers' materials, as well as on the temperature variations, [4]. The driving force of the interfacial fracture, in this case, is the energy release rate G .

2. Problem formulation

Let $2a$ be the length of a crack under plane strain conditions, which is located at a distance H_1 from the upper surface and at a distance H_2 from the bottom surface of infinitely large two-layer plate of thickness $H=H_1+H_2$, as shown in Figure 1.

The upper surface of the sample is exposed to a uniform temperature T_1 and the lower surface to temperature T_2 . This means that the crack is opened. T_A and T_B are the temperatures at the upper and lower surface of crack. The two-layer sample has homogeneous characteristics and it is orthotropic with respect to the (x, y, z) axes.

The idea of this analysis is to determine the boundaries for which the crack is long enough that the temperature and stress distribution ahead of the crack tip depend only on z . By

determining this dependence, one can calculate the energy release rate and stress intensity factor by application of the linear elastic fracture mechanics concept to interfacial fracture.

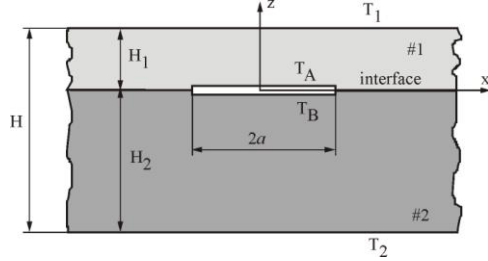


Figure 1. The two-layer sample with a crack under thermal loading.

In areas of the two-layer sample far ahead of the crack tip, the temperature distribution within each layer is linear in z . The temperature jump across the crack is given by:

$$T_A - T_B = \frac{T_1 - T_2}{1 + B_i}, \quad (1)$$

where: $B_i = Hh_c / k_z$, h_c is the conductivity across the interface and k_z is thermal conductivity of the body in the z direction. The dimensionless Biot number, B_i , controls the heat flow through crack surface. When $B_i = 0$, the crack is perfectly insulated so that $T_A = T_1$ and $T_B = T_2$. When B_i tends to infinity, the crack does not interrupt the heat flow.

Based on [5], the energy release rate for the problem shown in Figure 1 can be written as:

$$G = \frac{\eta(1 + \eta^3)}{2(1 + B_i)^2(1 + \eta)^5} \bar{E}H[\bar{\alpha}(T_1 - T_2)]^2, \quad (2)$$

where $\eta = H_1 / H_2$, $\bar{E} = (E_y - \nu_{xy}^2 E_x) / E_x E_y$ and $\bar{\alpha} = \alpha_x + \nu_{xy} \alpha_y$. The mode mixity, that measures the relative size of the Mode II with respect to Mode I, is:

$$\psi = \arctg \frac{K_{II}}{K_I} = \arctg \left[\frac{4\sqrt{\lambda} \frac{2(1 + \eta^3)\sqrt{V} \sin \omega + \eta^2(1 + \eta)\sqrt{U} \cos(\omega + \gamma)}{2(1 + \eta^3)\sqrt{V} \cos \omega - \eta^2(1 + \eta)\sqrt{U} \sin(\omega + \gamma)}}{1} \right], \quad (3)$$

where: $F = \frac{\sqrt{\lambda}}{4\sqrt{2(1 + \rho)}} \frac{\sqrt{\eta}(1 + \eta^3)}{(1 + B_i)\sqrt{(1 + \eta)^9}}$, $\lambda = \frac{E_z}{E_x}$, $\rho = \frac{1}{G_{xz}\sqrt{\lambda}} - \nu_{xz}$, $\omega \cong 52.1 - 3\eta$ [°],

$V = \frac{1}{12(1 + \Sigma\eta^3)}$, $U = \frac{1}{1 + \Sigma(4\eta + 6\eta^2 + 3\eta^3)}$ and $\gamma = \arcsin(6\Sigma\eta^2(1 + \eta)\sqrt{UV})$.

In order to eliminate the Biot's number, as an unknown from equation (2) the relationship is used between the energy release rate, G , and the size of the crack opening, δ . If the sample is isotropic i.e. $\lambda = \rho = 1$, eliminating B_i in (2) results in relation between the energy release rate, G and the temperature loading, $(T_1 - T_2)$, as:

$$\left(\frac{k_g H^4 \sqrt{\lambda^3}}{4k_z n \cos \psi} \sqrt{\frac{\pi \bar{E}}{Ga}} \right)^2 G = \frac{\eta(1 + \eta^3)}{2(1 + \eta)^5} \bar{E}H \bar{\alpha}(T_1 - T_2)^2. \quad (4)$$

where k_g is the conductivity of the gas.

3. Results and discussion

The energy release rate curves as functions of the crack distance from the upper sample surface, based on equation (2), for different values of B_i are shown in Figure 2. Diagrams were obtained with the help of the programming package *Mathematica*[®], and for the case of an isotropic sample. Figure 3 shows results for the mode mixity that does not depend on the Biot's number, for $T_1 > T_2$.

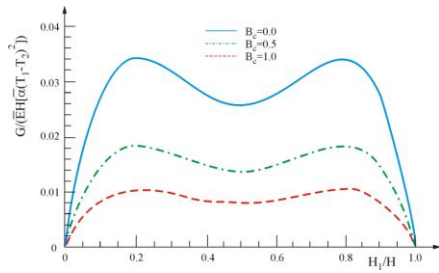


Figure 2. Dependence of the energy release rate on the crack distance from the upper sample surface for different values of B_i .

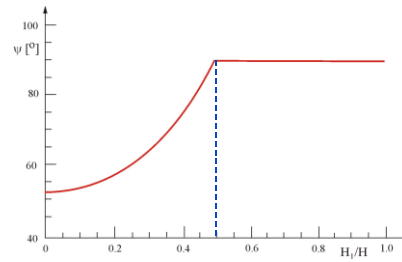


Figure 3. Dependence of the mode mixity on the crack distance from the upper sample surface

As shown in Figure 3, the crack tip is opened with a positive stress intensity factor for Mode I, as long as the crack is above or in the middle of the sample. Crack tip is closed in terms of pure Mode II, when the crack is below the mid-thickness of the sample, i.e. when $H_1/H > 0.5$.

Figure 2 shows that the highest value of the energy release rate is for a crack located at approximately one fifth of the sample thickness, i.e. for $H_1/H = 0.211$, what means that it is the most likely that at this distance lies the crack, which causes the sample delamination.

Figure 4 shows the dependence of the energy release rate, G , on the temperature loading $T_1 - T_2$ for $H_1/H = 0.211$, and different values of B_i .

As shown in Figure 4, an important role in heat flow through the crack plays the Biot's number, B_i . At temperatures below 1500K, the dominant mechanism of heat transfer through the crack is due to gaseous transport. Approximate formula for B_i , when the size of the crack opening δ , is larger than $0.1\mu\text{m}$, is $B_i = k_z H / k_g \delta$, where k_g is the gas conductivity. From Figure 4, follows that for large values of the Biot's number, the energy release rate G has a relatively lower value, which means that the crack opening is small. On the other hand, when B_i is small, the energy release rate will be large, as well as the crack opening, i.e. crack is completely and totally isolated, and as such is suitable for delamination of the sample if the temperature gradient is sufficiently large.

The relationship between the energy release rate and the temperature loading is shown in Figure 5, for three different values of k_g for an isotropic sample. The crack length $2a$ is equal to the thickness of the sample H . A surprising feature of these curves is that when once the threshold of $(T_1 - T_2)$ is reached, the energy release rate below it becomes zero, while for a very small increase in $(T_1 - T_2)$, the energy release rate becomes large very quickly.

In Figure 5 is shown that with increasing temperature on the crack the threshold of the temperature difference also increases, while k_g increases with temperature. If the threshold exceeds the temperature difference, to which the sample is exposed, delamination of the sample should not be expected. Heat flow through the crack can be significant and the

assumption of a perfectly isolated crack would be wrong. Another loading, causing a significant crack opening, would further reduce the heat transfer through the crack.

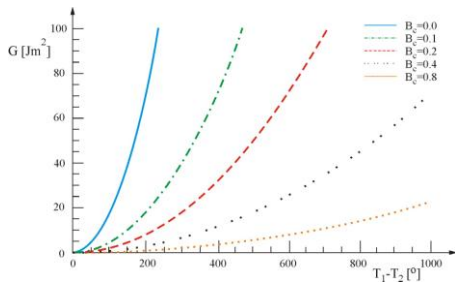


Figure 4. Dependence of the energy release rate on the temperature loading for different values of B_i .

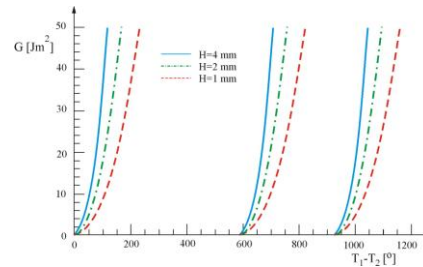


Figure 5. Dependence of the energy release rate on the temperature loading for different values of the sample thickness.

4. Conclusion

In this paper is presented the theoretical basis for determining the driving forces of interface fracture in a two-layer bimaterial specimen under conditions when the temperatures of the outer surface layers are different. The analysis in this paper is limited to the fact that the two-layer bimaterial sample is exposed to a stationary temperature field. The driving force of the interfacial fracture, in this case, is the energy release rate G . It is determined as a function of the temperature loading. It was noticed that the energy release rate tends to increase with increasing temperature difference. This relation can be used to predict the maximum temperature differences the two-layer sample can sustain without delamination. For future analysis remains the case when the two-layer bimaterial sample is subjected to unsteady temperature field.

Acknowledgement. This research was partially supported by the Ministry of Education and Science of Republic of Serbia through Grants ON174001 "Dynamics of hybrid systems with complex structures. Mechanics of materials", ON174004 "Micromechanics criteria of damage and fracture" and TR 32036 "Development of software for solving the coupled multi-physical problems".

5. References

- [1] Evans, A. G. and Hutchinson, J. W. (2007), The mechanics of coating delamination in thermal gradients, *Surface and Coatings Technology*, **201**, 18, pp. 179-184.
- [2] Hutchinson, J. W. and Evans, A. G. (2002), On the delamination of thermal barrier coatings in thermal gradients, *Surface and Coatings Technology*, **149**, 2-3, pp. 7905-7916.
- [3] Xue, Z., Evans, A. G., Hutchinson, J.W. (2009), Delamination Susceptibility of coatings under high thermal flux, *Journal of Applied Mechanics*, **76**, 4, pp. 1-7.
- [4] Djokovic, J. M., Nikolic, R. R., Tadic, S. S. (2010), Influence of temperature on behavior of the interfacial crack between the two layers, *Thermal Science*, **14**, pp. S259-S268.
- [5] Hutchinson, J. W. and Suo Z., (1992) Mixed mode cracking in layered materials, *Advances in Applied Mechanics*, **29**, pp. 63-191.

NUMERICAL SIMULATION OF DAMAGE IN THE THIN PLATES

C. Dolicanin¹, K. Maksimovic², V. Nikolic-Stanojevic³, M. Maksimovic⁴

^{1,3} State University of Novi Pazar

Vuka Karadžića bb, Novi Pazar

e-mail: rektorat@np.ac.rs, e-mail: veranikolic1@gmail.com

²Republic Serbia, City Administration of City of Belgrade,

Secretariat for Utilities and Housing Services Water Management,

Kraljice Marije 1, Belgrade, Serbia, e-mail: k.maksimovic@open.telekom.rs

⁴Water Supplies, Belgrade, Serbia

ABSTRACT: The rapid development of computer technology, which marked the last two decades has brought about real solutions to problems are increasingly demanding in terms of numerical simulations. With proper application of numerical methods is possible to reduce the cost and time required to develop new or to monitor the integrity of existing products in the real exploitation conditions. The basic dependences between the geometric and physical variables in the theory of thin plates, consists mainly in setting up links between the state of stress and strain and external load, which is described by differential equations, ordinary or partial. In the case of complex and large construction systems exposed to arbitrary loads, including complex boundary conditions, solving differential equations by analytic methods is very difficult or impossible. Then the solution requires using numerical methods, most often, using finite element method (FEM). This paper considers the finite element modelling to evaluate fracture behaviour of cracked thin-walled structural components. To determine stress intensity factors (SIF's) of cracked thin-walled stiffened panels singular finite elements are used. The effects of the stiffeners on SIF's is considered.

1. Introduction

Structural components that form part of a structure are, in most cases, of complex geometric shapes. Examinations have shown that, in places where cross section decreases, the stress increase. This phenomenon is called the stress concentration. The presence of cracks in a material generally reduces the static strength of the material because the stress and strain are highly magnified at the crack tip [2]. Parameters deduced from linear fracture mechanics (LEFM) can be used to determine the stress and strain magnification at the crack tip. These parameters, the stress intensity factor (SIF), incorporate applied stress levels, geometry and crack size in a systematic manner and may be evaluated from the elastic stress analysis of cracked structures [3-6, 8].

A new concept, called the damage tolerance approach, based on the principles of fracture mechanics, is to assume the initial damages in the critical zones of the elements, which can lead to structural failure during the planned life. In this paper special attention is paid to analysis of real structural elements with damages in form of initial cracks. For that purpose cracked stiffened panel, represent aircraft wing structure, is considered using singular finite elements.

2. Determination of Stress Intensity Factors Using Finite Elements

In this paper for the modelling the continuum in plane condition of stress and strain, where plates belong too, are used special singular 2D finite elements. Special singular 2D finite elements are provided in the top of the crack, singular strain. We get extremely accurate results with relatively coarse finite element mesh around the tip of cracks.

In order to represent point singularities, the quadrilateral must be degenerated into a triangle. This is done by coalescing grids 1,4 and 8 as can be done for standard 8-node isoparametric elements and is schematically in Fig. 2.1. Barsoum, [2] also showed that a triangular quarter-point element, which is shown in Fig. 2.1, exhibits the $r^{-1/2}$ singularity both on the boundary of the element and the interior. In this work the 6-node, quarter-point triangular element, which degenerated from 8-node quadrilateral element, is used around crack tip.

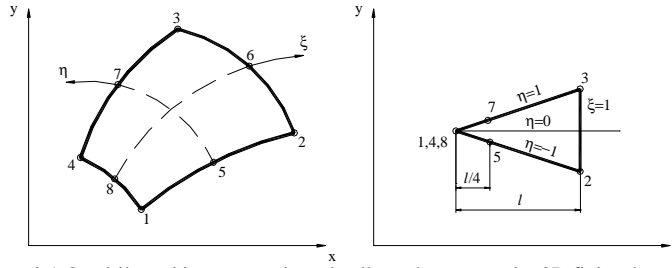


Figure 2.1 Quadrilateral isoparametric and collapsed quarter point 2D finite element

The finite element, which approximates the displacement field, must have nodes lying in the xy plane with displacements having components in the direction of x and y axis. Interpolation of geometry can be written in the following form, [1,2].

$$x = \sum_{i=1}^8 h_i(\xi, \eta) \cdot x_i; \quad y = \sum_{i=1}^8 h_i(\xi, \eta) \cdot y_i; \quad \text{or} \quad x_i = \sum_{k=1}^N h_k X_i^k \quad (2.1)$$

where h_i is interpolation matrix or shape function and x_i and y_i are coordinates, respectively, at the point i in the element. Thus, the displacement field of points can be defined by a vector field, [1], in the following way:

$$u = \sum_{i=1}^8 h_i(\xi, \eta) \cdot u_i; \quad v = \sum_{i=1}^8 h_i(\xi, \eta) \cdot v_i \quad \text{or} \quad u_i = \sum_{k=1}^N h_k U_i^k \quad (2.2)$$

Once a finite element solution has been obtained, the values of the stress intensity factor (SIF) can be extracted from it. Three approaches to the calculation of SIF can be used: the direct method, the indirect method and J-integral method. In this study the indirect method has been selected. In this method the values of stress intensity factors are calculated using the nodal displacements in the element around crack tip. The displacements can be expressed in terms of the nodal displacements A, B and C, Fig. 2.2.

$$\begin{aligned} u(r) &= u_A + (-3 \cdot u_A + 4 \cdot u_B - u_C) \cdot \sqrt{\frac{r}{l}} + (2 \cdot u_A - 4 \cdot u_B + 2 \cdot u_C) \cdot \frac{r}{l} \\ v(r) &= v_A + (-3 \cdot v_A + 4 \cdot v_B - v_C) \cdot \sqrt{\frac{r}{l}} + (2 \cdot v_A - 4 \cdot v_B + 2 \cdot v_C) \cdot \frac{r}{l} \end{aligned} \quad (2.3)$$

When r becomes small, the stress intensity factors can be obtained by comparing the \sqrt{r} in corresponding equations. Based on the results of displacements obtained using the FEM, one can determine the stress intensity factors

$$K_I = \frac{2 \cdot \sqrt{2} \cdot \pi \cdot G \cdot (4 \cdot v_B - v_C - 3 \cdot v_A)}{(k+1) \cdot \sqrt{l}}; \quad K_{II} = \frac{2 \cdot \sqrt{2} \cdot \pi \cdot G \cdot (4 \cdot u_B - u_C - 3 \cdot u_A)}{(k+1) \cdot \sqrt{l}} \quad (2.4)$$

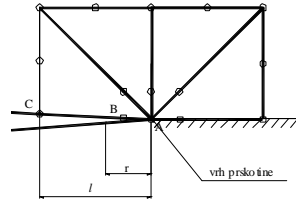
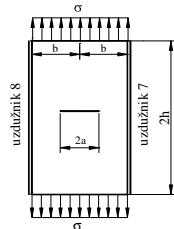


Figure 2.2. Element nodes along crack surface

The authors have performed a number of testing the accuracy of this singular finite element analysis and with other available solutions. Obtained a remarkable accuracy of the finite element and with a relatively coarse finite element mesh in the zone of damage.

3. Numerical results

To illustrate computation procedure for determination the parameters of fracture mechanics, based on FEM, here is considered cracked stiffened panel subject to tensile load, Fig. 3.1. This panel is representative of aircraft wing tip structures. Here is considered simplified cracked wing skin panel between two stringers. The effects of these stringers on SIF's are considered using singular finite elements.



2h = 345 mm
 2b = 155.7 mm
 t = 0.6 mm
 2a = 6.35 mm
 $\sigma = 700.35 \text{ daN/cm}^2$

Fig. 3.1 A Cracked stiffened panel

Graphical illustrations of stress distributions of un-stiffened and stiffened panels using singular finite elements are given in Fig. 3.2. As stiffener in this analysis are used two L-type profile as shown in Figure 3.1. The analysis carried out using a special 6-node singular finite elements, as described in paragraph 2 of this paper.

In Table 3.1 are given comparisons presented finite element and analytical results of SIF's for the stiffened panel of wing skin, defined in Figure 3.1.

Table 3.1: Comparisons finite element and analytic SIF results for cracked panel

$j = 1.5$	$2b$ [mm]	a_0 [mm]	K_I^{ANAL} [N / mm ^{3/2}]	K_I^{FEM} [N / mm ^{3/2}]	Panel of wing skin
$\sigma = 71.7$ N / mm ²	155.7	3.175	229.9 110.5	206.2 113.6	Panel without stringers Panel with stringers

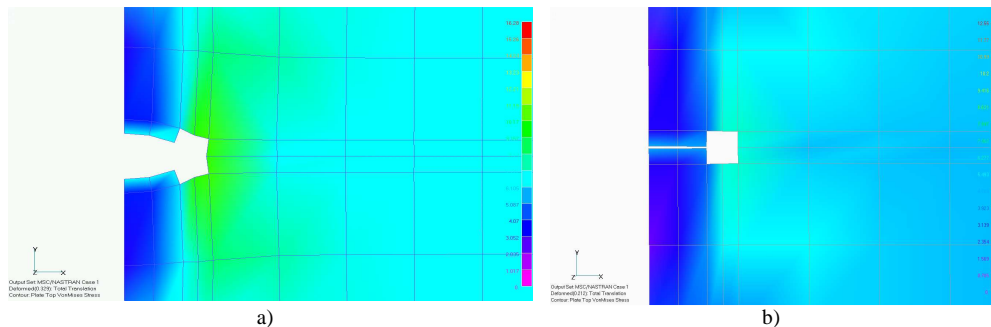


Fig. 3.2 Von Mises stresses distributions around the crack of un-stiffened panel (a) and stiffened panel (b)

The effects of the stiffeners on the stress intensity factors is evident, Table 3.1. Good agreement between finite element with analytic solutions is obtained.

4 Conclusion

This paper presents the finite element formulation to evaluate fracture behavior of cracked thin-walled structural components. Singular finite elements are used for modeling of cracked thin-walled structures. Here is shown that the finite elements can solve very complex thin-walled problems in fracture mechanics. Good agreement between present computation SIF's using singular finite elements and analytic solution is obtained. Based on the obtained data for singular displacement at the crack tip, the stress intensity factor with sufficient accuracy can be determined.

Acknowledgement: Parts of this research were supported by the Ministry of Sciences, Technologies and Development of Republic Serbia through Mathematical Institute SANU Belgrade, State University of Novi Pazar and Mathematical institute Belgrade: Grants No. ON174001 The dynamics of hybrid systems of complex structures. Mechanics of Materials and and TR 35011.

References

1. Zienkiewicz, O.C and Taylor, R.L, Finite Element Method, Butterworth Heinemann, Oxford, 2000.
2. Barsoum, R.S., On the use of isoparametric finite elements in linear fracture mechanics, Int. J. Numerical Methods in Engineering, vol. 10, 1976, p. 25-37
3. C.B. Dolicanin, V.B.Nikolic, D.C.Dolicanin, Application of finite Difference Method to Study of the Phenomenon in the Theory of thin plates, Scientific Publications of the State University of Novi Pazar, Series A, Applied Mathematics, Informatics and Mechanics, No 1, Volume 2, 2010.
4. Maksimović, K., Nikolić, V., Maksimović, S., Efficient computation method in fatigue life estimation of damaged structural components, Facta Universitatis, Series Mechanics, Automatic Control and Robotics, Vol. 4, No 16, 2004, pp 101-114
5. Maksimović, K., Nikolić, V., Maksimović, S., Modeling of the surface cracks and fatigue life estimation, ECF 16 2006, Minisymposium integrity of dynamical systems, p. 113...116, Alexandroupolis, JULY 3..7, 2006.
6. Maksimovic S., Posavljak S., Maksimovic K., Nikolic-Stanojevic V. and Djurkovic V., Total Fatigue Life Estimation of Notched Structural Components Using Low-Cycle Fatigue Properties, J. Strain (2011), **47** (suppl.2), pp 341-349.
7. Nikolic, V., Dolicanin C., Radojkovic, M. (2011), Application of Finite Element Method of thin steel Plate with holes, *Technical Gazette (Tehnički vjesnik 18)*, Vol. 18, No 1(2011), pp. 57-62.
8. Stamenkovic D., Maksimovic S., Maksimovic K., Nikolic-Stanojevic V., Maksimovic S., Stupar S, Vasovic I., Fatigue Life Estimation of Notched Structural Components, *Strojniški vestnik - Journal of Mechanical Engineering* 56(2010)12, 846-852, UDC 629.7:620.178.3, <http://www.sv-jme.eu/current-volume/sv-jme-56-12-2010/>

A MULTISCALE APPROACH FOR MODELLING NON-LINEAR BEHAVIOUR AND DAMAGE OF HIGHLY-FILLED PARTICULATE COMPOSITES

A. Dragon¹, C. Nadot-Martin¹, D. Halm¹, S. Dartois², M. Trombini¹

¹ Institut Pprime CNRS-ENSMA-Université de Poitiers, Département Physique et Mécanique des Matériaux

ENSMA, BP40109, F86961 Futuroscope Chasseneuil Cedex, France

e-mails : andre.dragon@ensma.fr, carole.nadot@ensma.fr, damien.halm@ensma.fr, marion.trombini@ensma.fr

² Institut Jean Le Rond d'Alembert

Université Pierre et Marie Curie, 4 place Jussieu, F75252 Paris, France

e-mail : sophie.dartois@upmc.fr

Abstract. This contribution outlines a non-classical scale transition framework, called “Morphological Approach” (MA), specially designed for modelling non-linear behaviour of highly-filled particulate composites as e.g. propellant-like materials. The advances concerning finite strain behaviour of the sound material and the most recent developments incorporating progressive microstructural damage by interface debonding are emphasized. Some numerical examples are set out. Damage phenomena are being managed through a discret numerical solving procedure for the global and local levels. The corresponding procedure accounts for the sequence of damage events, i.e. for discrete damage evolution relative to nucleation/closure/reopening... of interfacial defects depending on a loading path and on local morphology. The homogenized response is discussed with special attention paid on the evolution of damage-induced anisotropy and unilateral effects involved.

1. Introduction

The multi-scale “Morphological Approach” (MA) under consideration is a non-classical scale transition methodology specially designed for modelling non-linear behaviour of highly-filled particulate composites. These materials, including propellant-like and other energetic composites present a complex behaviour coupling strong non-linearities as finite strain viscoelasticity and interface debonding. The multiscale modelling challenges in this context concern the high volume fraction of charges (particles) and their complex interactions conveyed through the scanty matrix phase ($\approx 30\%$ of total volume). These interactions generate strong field heterogeneity in the matrix (usually softer than the grains) that influences strongly interfacial debonding events. Even for the sound material, the local field fluctuations impress much upon the global non-linear response. The inability of classical mean field approaches to capture complex interaction effects before and during deterioration process in energetic materials is confirmed by several authors (see e.g. [1]). The internal viscoelastic interactions mentioned above – delayed in time, expanding in space – lead to the remarkable global consequence named the “long range memory effect”, described first by Suquet [2]. A number of micromechanical studies dealing with viscoelastic and/or elastic-viscoplastic heterogeneous materials were deficient in this regard, carrying concentration equations expressing merely elastic intergranular

interactions. This deficiency was first recognized at the beginning of the nineties [3] but even recent contributions regarding solid propellant materials find it difficult to respect long memory effects while acknowledging their importance [4]. The MA approach, developed throughout the past decade, is an alternative to the Eshelby inclusion-based micromechanics methods for the energetic composites. Its purpose is to provide reliable thermomechanical data required by reactive models. The work presented here focuses on the modelling of damage consisting, under quasi-static loadings, in grain/matrix debonding (dewetting). The specificity of the approach lies notably in an explicit upstream geometrical schematization of the real microstructure. Furthermore, a coupling between this geometrical/morphological insight and a local kinematics is postulated. These ingredients are largely connected with the work by Christoffersen [5] for sound, elastic, “bonded granulates”. The label MA concerns the further non-linear developments, including damage, made by some of the present authors [6-9]. In the following, some selected aspects of the MA modelling are considered:

(i) Section 2 recalls briefly the theoretical background, detailed in [6,9], concerning direct geometrical and kinematical schematization of the microstructure for the sound and damaged material and outlines basic steps of the localization-homogenization problem. The complementary analysis relevant to damage by interfacial debonding is outlined. The evolution of damage configuration on the local level and its connection to global damage parameters is sketched. This brief synthesis concerns the simplified context of isotropic, linear, elastic constituents and linearized deformation framework. The long memory effect in the context of viscoelastic interactions between a matrix and charge particles was studied within the MA framework in [6].

(ii) In Section 3, some results of numerical simulations for a specific global loading path regarding an aggregate volume containing 400 grains and involving defect nucleation and closure events on interfaces are shown and shortly commented. A discrete numerical solving procedure works on the global and local levels. The procedure accounts for the sequence of events, i.e. for discrete damage evolution due to nucleation, possible closure/reopening, etc. of defects, as depending on the loading path and on local morphology. The homogenized response is shown, with special attention paid on the global stiffness recovery (unilateral effect connected to damage deactivation). The capability of the MA to give access to the position and morphology of defects is commented (it is illustrated and discussed in oral presentation).

2. Microstructure schematization and local problem: sound vs. damaged material.

The initial random microstructure of a particulate composite is represented by an aggregate of polyhedral grains interconnected by thin matrix layers. For each layer α , a set of morphological parameters is identified: thickness, projected area, vector linking centroids of the polyhedra separated by a layer, unit normal vector to the interface grain/layer α . The direct and explicit character of the schematization at stake is to be stressed as it differentiates the MA from the Eshelby-based self-consistent-like estimates. Within the schematized “representative volume”, kinematical assumptions are made regarding the local displacement pattern. Here, for simplicity, they are summarized within the linearized deformation (small strain) context. While the grain centroids are displaced so as to conform to global displacement gradient, the grains are supposed homogeneously deformed and the corresponding displacement gradient assumed identical for all grains. Each interconnecting layer is subjected to its proper homogeneous deformation, some local disturbances near

grain edges are being neglected. A specific consistency relationship governs interactions within the so defined aggregate according to Christoffersen [5], see also [6]. The interfacial defects and relative displacement jumps have been incorporated by Nadot et al. [6] in a compatible way with the kinematical framework above. It is shown that the displacement discontinuity vectors across debonded interfaces are necessarily affine functions of the spatial coordinates. On a given facet of a grain there is either decohesion everywhere or no decohesion. Moreover, there is a simultaneous double decohesion on both parallel interfaces of adjacent grains. A particular supplementary displacement gradient-like term represents the specific contribution of two interfacial defects located at the interfaces of the debonded layer α considered. The compatibility between local motion defined above and the global motion, described by a given displacement gradient including now the contribution of defects, is ensured through a generalized consistency relationship to be satisfied by morphological parameters, see [6]. For a given number of open and/or closed defects, a specific form of the generalized Hill lemma – including the discontinuities – is obtained. Employing the local constitutive laws for the grains and the matrix and using possibly some simplifying hypotheses, e.g. infinite friction coefficient presumed tentatively on closed defect lips, the solving procedure for the local incremental problem is set off. A complementary stage, depending on the local behaviour of constituents, is required to identify some of the damage-induced local quantities. Thanks to its explicit schematization of the real microstructure, notably of the grain/matrix interfaces, in addition to the accessibility to an estimate of local fields, the MA allows damage evolution at the local scale (that of the constituents) to be treated. This direct, discrete modelling is put forward considering the sequence of discrete interfacial local damage events. Two criteria are formulated, see [9]. The first one concerns the nucleation of defects while the second one is a closure criterion, thus allowing describing the evolution of damage configuration, i.e. the respective proportion of open and closed defects for a given total number of defects.

3. Numerical illustration: tension / compression – like loading path

The composite studied is constituted of 400 polyhedral grains embedded in a matrix occupying 25 per cent of the total volume. The composite is subjected first to tension and then to compression. Fig. 1 presents the evolution of the homogenized stress Σ_{II} with macroscopic axial strain E_{II} . The progressive nucleation of defects with normal very close to I takes place between markers (2) and (4). The response becomes non linear with progressive softening. The stage between (4) and (5) corresponds to the unloading. The slope of the homogenized axial response is different from that of the loading confirming the degradation of the axial modulus. At point (5), all the defects close simultaneously leading to the instantaneous recovery of axial stiffness. This result illustrates the ability of the MA to deal with unilateral effects. Between (5) and (6), the homogenized response to the compressive loading is linear with a slope equal to the initial one. When pursuing the compression (6–7), defects normal to the transverse directions are progressively nucleated.

4. Concluding remarks

A scale transition method devoted to highly-filled particulate composites has been presented. It is particularly suitable for high grain concentration and allows an estimate of local fields to be made in addition to that of the homogenized response. In particular, the

estimated strain field in the matrix is not only influenced by global, but also, by local morphology and interfacial defects. Such heterogeneity in the matrix, governed by local morphology, is taken into account in the homogenized behaviour estimate. This feature is not captured by more classical homogenization techniques. The numerical simulation of a specific loading path (tension-compression) illustrates the non-linear response, followed by a softening phase, as well as the defect activation / deactivation phenomenon.

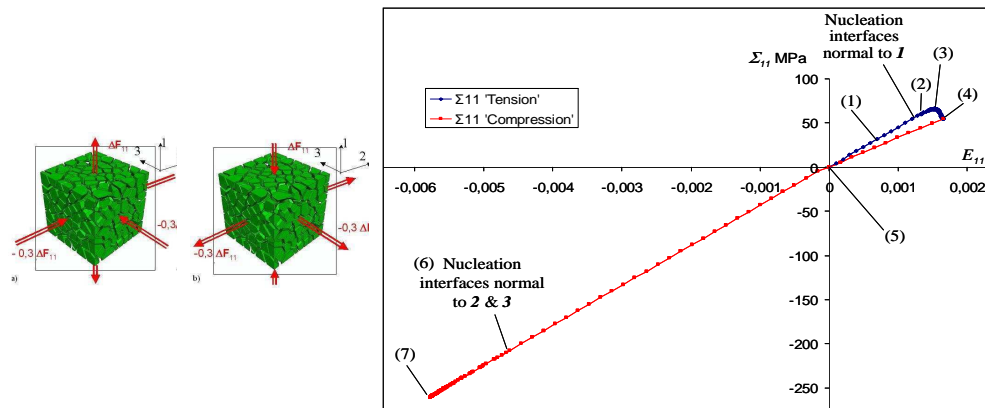


Figure 1. Loading path and homogenized Σ_{11} versus E_{11} for simulated “tension” - “compression”.

Acknowledgement. The Authors express their gratitude to the Commissariat à l'énergie atomique (CEA / Gramat), and in particular to Alain Fanget, for its support.

References

- [1] Inglis, H.M., Geubelle, P.H., Matous, K., Tan, H. and Huang, Y. (2007), Cohesive modelling of dewetting in particulate composites : Micromechanics vs. Multiscale Finite Element Analysis, *Mech. of Materials*, **39**, pp. 580-595.
- [2] Suquet, P. (1987), *Homogenization techniques for composite media*, Sanchez-Palencia, E., Zaoui, A. (Eds.), Springer-Verlag, Berlin, pp. 193-278
- [3] Zaoui, A. and Raphanel, J.L. (1993), Large plastic deformation, fundamentals and application to metal forming, *Proceedings of Mecamat '91 Conference*, Teodosiu, C., Raphanel, J.L., and Sidoroff, F. (Eds.), Rotterdam, Balkema edition, pp. 185-192.
- [4] Xu, F., Aravas N. and Sofronis, P. (2008), Constitutive modelling of solid propellant materials with evolving microstructural damage, *J. Mech. and Phys. of Solids*, **56**, pp. 2050-2073.
- [5] Christoffersen, J. (1983), Bonded granulates, *J. Mech. Phys. Solids*, **31**, pp. 55-83.
- [6] Nadot-Martin, C., Trumel, H. and Dragon, A. (2003), Morphology-based homogenization for viscoelastic particulate composites – Part I : viscoelasticity sole, *Eur. J. Mech. A Solids*, **22**, n°1(1), pp. 89-106.
- [7] Nadot, C., Dragon, A., Trumel, H. and Fanget, A. (2006), Damage modelling framework for viscoelastic particulate composites via a scale transition approach, *J. Theor. and Appl. Mech.*, **44**, pp. 553-583.
- [8] Dartois, S., Halm, D., Nadot, C., Dragon, A. and Fanget, A. (2007), Introduction of damage evolution in a scale transition approach for highly-filled particulate composites, *Eng. Frac. Mech.*, **75**, pp. 3428-3445.
- [9] Dartois, S., Nadot-Martin, C., Halm, D. and Dragon, A. (2009), Discrete damage modelling of highly-filled composites via a direct multiscale “morphological approach”, *J. of Multiscale Modelling*, **1**, pp. 347-368.

CRACK INITIATION AND PROPAGATION IN NONLOCAL DUCTILE MEDIA

S. Feld-Payet¹, J. Besson², F. Feyel¹, V. Chiaruttini¹

¹ ONERA - The French Aerospace Lab,
F-92322 Châtillon, France

e-mail: [\[sylvia.feld-payet, frederic.feyel, vincent.chiaruttini\]@onera.fr](mailto:[sylvia.feld-payet, frederic.feyel, vincent.chiaruttini]@onera.fr)

² Centre des Matériaux, Mines Paris, Paristech, CNRS UMR 7633
PB 87, F-91003, Evry Cedex, France

e-mail: jacques.besson@ensmp.fr

Abstract. A new strategy using remeshing techniques is proposed to model crack initiation and propagation for ductile media. The crack path is represented by an auxiliary mesh with a straight front which is completely independent of the volumetric mesh. The discontinuity is oriented depending on the continuous damage distribution by means of the sign of the projected gradient of the smoothed damage field. A mesh intersection algorithm is then used to insert the crack surface in the volumetric mesh and computation is resumed after the transfer of the fields from the old mesh to the new mesh. A numerical application is presented on a double notched specimen.

1. Introduction

The failure process of metals can be divided into two main phases. The first stage involves the nucleation and growth of voids in localized areas. For this stage, a continuous model is usually used to describe the failure of the underlying microstructure in an average sense by means of a damage variable. This continuous description is acceptable up to the onset of fracture. At this point, voids coalesce to form macroscopic cracks, and a continuous model cannot properly describe the kinematics associated to a crack opening. A discontinuous description has to be introduced to model crack propagation. In the last decades, several attempts have been made to propose a unified framework for the realistic description of the ductile failure process with a continuous-discontinuous approach.

In this paper, a novel methodology is presented which allows to model ductile damage evolution followed by crack initiation and propagation. After a brief description of the tools used to properly described damage evolution up to the onset of fracture in Section 2, a new strategy using remeshing techniques is proposed for crack initiation and propagation in Section 3.

2. Simulation up to the onset of fracture

First, damage evolution is properly described with a continuous model up to the onset of fracture. However, solving finite element problems involving elasto-plasticity coupled with damage softening faces two major difficulties: mesh dependence and volumetric locking.

The four-field mixed formulation proposed in [1] is used in order to solve simultaneously both problems within the small strain framework (with a quadratic interpolation for the displacements and a linear interpolation for the pressure, the volume change and the nonlocal variable).

Then, accuracy is improved and computational costs are minimized thanks to a mesh adaptivity procedure based on an error indicator using a recovery technique [2], described in [3]. The strategy combines a direct transfer of the smoothed fields at the old Gauss points to the new ones with a viscous model, so that computation can continue on the adapted mesh after reducing the time step.

This strategy has been applied in [3] on a double notched specimen proposed in [4] with an elasto-visco-plastic behavior featuring damage based on the constitutive behavior proposed in [5]. In two dimensions, the specimen is remeshed twice, for relatively small values of damage (see Fig.1).

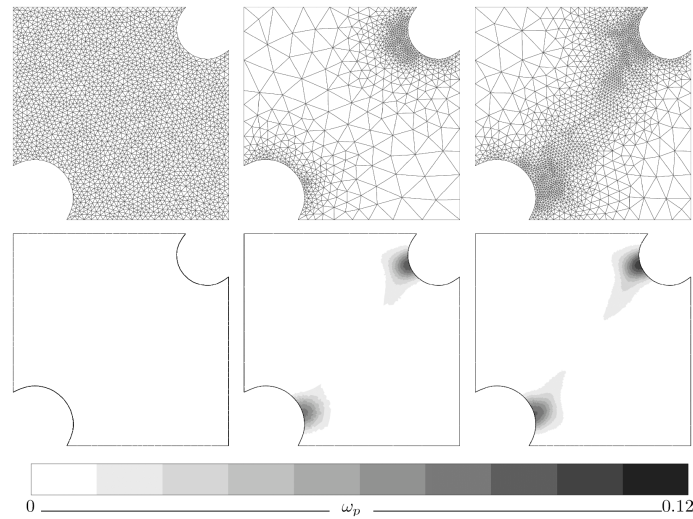


Figure 1. The different adapted meshes (top) and the corresponding damage patterns (bottom) - computation on 2D double notched specimen described in [2].

3. Crack insertion and propagation approach

A new strategy using remeshing techniques is proposed for crack initiation and propagation. The crack path is represented by an auxiliary mesh.

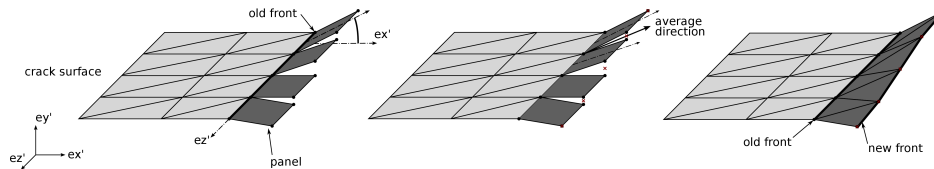


Figure 2. Left: a panel is associated to each segment of the old front; center: an average direction is computed for each node of the front; right: auxiliary mesh updated.

This auxiliary mesh is always built increment by increment based on a previously determined front, called the *old front*. The first step consists in dividing the old front into segments and to associate to each segment a rectangular panel. All the panels have the same prescribed length, which corresponds to the maximal increment length allowed by the user. At this point, an orientation criterion is used to select the rotation angle of each panel so as to place them in the maximum damage direction ahead of the old crack front (Fig. 2, left). A privileged tool to find the maximum of a continuous function being the study of its gradient, a new orientation criterion based on the change of sign of the scalar product of the damage gradient field and the orthoradial vector is proposed (Fig. 3).

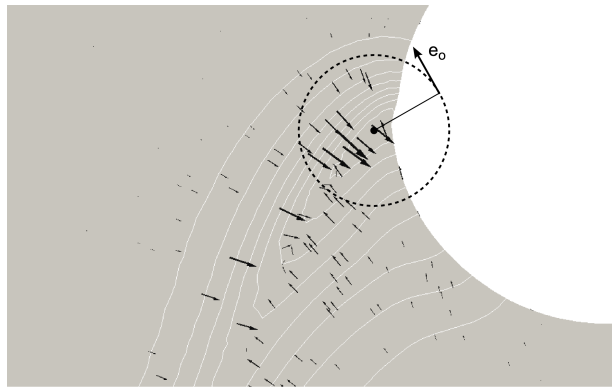


Figure 3. Representation of some damage gradient vectors and of the orthoradial vector.

Once the orientation of each panel has been set, the positions of the nodes on the *new front* are determined by averaging the rotation angles of the adjacent panels sharing the corresponding node on the old front (Fig. 2, center). The length of the crack increment being prescribed, the new front is thus completely defined.

A triangular surfacic mesh is then used to build the new crack increment between the old front and the new front. A mesh intersection algorithm [6] is used to obtain a new cracked mesh.

The question of energy conservation before and after the crack increment insertion is a difficult matter. In order to prevent a too important energy difference, the crack increments are inserted only when the corresponding area is almost completely damaged and has lost almost all its carrying capacity.

After inserting this crack in the volumetric mesh, the same strategy will be used to build the next crack increment from the new front, which then becomes an old front (Fig. 2, right).

The same orientation criterion can be used to determine the initial crack front too.

The crack initiation and propagation strategy is evaluated on a 3D double notched specimen, with the same behavior as Section 2. After being adapted to represent plane crack surfaces only, the proposed strategy allows to insert two cracks and simulate their propagation, as illustrated in Fig. 4. The resulting crack surfaces are consistent with damage (which is here proportional to the effective plastic strain) distribution. However, these results are only preliminary and future work should focus on providing more robustness to the methodology in 3D.

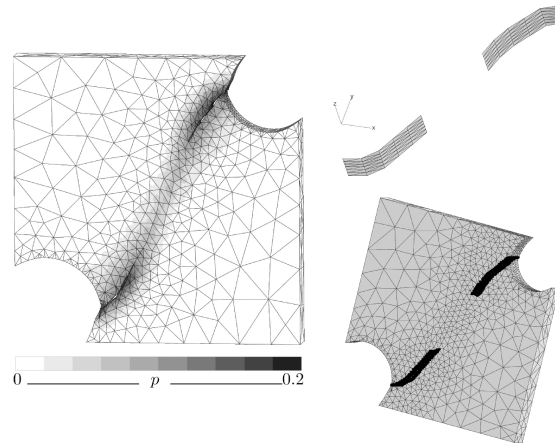


Figure 4. Left: effective plastic strain distribution before the last remeshing with a magnification factor of 2 ; top right corner: auxiliary mesh representing the final crack surface: right bottom corner: final mesh before divergence.

4. Conclusion

This paper has introduced a new crack insertion and propagation strategy using h-adaptive remeshing. The proposed strategy allowed to obtain very encouraging results in the case of a plane crack surface.

Future work will focus on the illustration of the strategy for more complex three-dimensional cases. Besides, ductile failure with intense localization often comes with large strains, so it would also be interesting to adapt this methodology to the large strains setting.

Acknowledgement. The authors gratefully acknowledge the always helpful suggestions contributed by H. Javani, R. Peerlings and M. Geers from the University of Technology of Eindhoven on many occasions.

References

- [1] Feld-Payet, S., Besson, J. and Feyel, F. (2011), Finite element analysis of damage in ductile structures using a nonlocal model combined with a three-field formulation, *International Journal of Damage Mechanics*, **20**, pp 655-680.
- [2] Boroomand, B. and Zienkiewicz, O.C. (1999), Recovery procedures in error estimation and adaptivity. Part II: Adaptivity in nonlinear problems of elasto-plasticity behaviour, *Comput. Methods Appl. Mech. Engrg.*, **176**, pp 127-146.
- [3] Feld-Payet, S., Besson, J. and Feyel, F., An h-adaptive remeshing strategy based on error estimation for elasto-plastic problems involving nonlocal damage, *Comput. Methods Appl. Mech. Engrg.* (submitted)
- [4] Mediavilla, J. (2005), Continuous and discontinuous modelling of ductile fracture, PhD thesis, Technische Universiteit Eindhoven.
- [5] Engelen, R.A.B., Geers, M.G.D., and Baaijens F.P.T., (2003), Nonlocal implicit gradient-enhanced elasto-elasticity for the modelling of softening behaviour, *International Journal of Plasticity*, **19**, pp 403-433.
- [6] Chiaruttini, V., Feyel, F. and Chaboche, J.L. (2010), A robust meshing algorithm for complex 3D crack growth simulation, *Proc. of IV European Conference on Computational Mechanics*, Paris, France.

MODELING OF CORROSION DISTRIBUTION FOR SELF-HEALING NANOMATERIALS

N. Filipovic¹, A. Jovanovic², D. Petrovic³, M. Obradovic¹, M. Radovic³, S. Jovanovic², D. Balos², M. Kojic^{3,4}

¹Faculty of Engineering,
University of Kragujevac, Sestre Janjica 6, 34000 Kragujevac, Serbia
e-mail: fica@kg.ac.rs

²Steinbeis Risk Technologies GmbH, Germany
e-mail: jovanovic@risk-technologies.com

³Research and Development Center for Bioengineering,
BioIRC, Kragujevac, Prvoslava Stojanovica 6, 34000 Kragujevac, Serbia
e-mail: racanac@kg.ac.rs

⁴Methodist Hospital Research Institute, Houston, USA
e-mail: mkojic@hsph.harvard.edu

Abstract. The “self-healing” is relative new term in material science which means self-recovery of the initial properties of the material after destructive actions of external environment. That is an urgent demand for industrial applications which initiates development of an active healing mechanism for the polymer coatings and adhesives. The continuum modeling uses Finite Element Method (FEM) with different diffusivity and fluxes. Randomizely distributions of nanocontainers with different percentage of inhibitors were analysed. The initial results for finite element method show how much percentage of the inhibitors in the nanocontainers are necessary to protect the metal surface which is treated with these healing agents. We also fit with a simplex optimization method diffusion coefficient and diameter of nanocontainers with experimental measurements of the corrosion.

1. Introduction

Corrosion degradation of materials and structures is one of important issues that lead to depreciation of investment goods. There are active and passive approaches for corrosion protection. The passive corrosion protection is achieved by deposition of a barrier layer preventing contact of the material with the corrosive environment. The active corrosion protection decreases the corrosion rate when the main barrier is damaged [1].

Small size defects can appear on a material surface. Such defects have a substantial effect on the mechanical properties of material. To protect this material failure the coating systems are employed on a wide range of engineering structures, from cars to aircrafts, from chemical factories to household equipment. The “self-healing” or “inhibition” are a relatively new terms in material science which means a self-recovery of initial properties of the material after destructive actions of external environment. It is an urgent demand for

industrial applications to initiate development of an active healing mechanism for polymer coatings and adhesives [2].

One of the first examples of self-healing materials was microcapsule [3]. Some authors recently investigated self-healing system with computer simulation [4]. Verberg et al [5] used hybrid approach with coupled lattice Boltzman model (LBM) and the lattice spring model (LSM) to simulate the motion of microcapsules driven by an imposed flow to move on a substrate with an adhesive coating. The microcapsules consist of an elastic shell and enclose a solution of nanoparticles which can diffuse from the interior of the capsule into the host fluid.

In this study we presented FEM for self-healing materials. We begin by describing the details of the nanocontainers healing concept and FEM methodology. We then discuss about fitting of the parameters for varying the nanocontainers fillings, diffusivity parameter. These findings provide guidelines for formulating nanocomposite coatings that effectively heal the surfaces through the self-assembly of the particles into the defects.

2. Methods

The initial process of nanocontainer breaking starts at a random position where a crack occurred. The nanocontainer membrane is approximated by one layer of particles and particles inside the nanocontainers represent healing agents – inhibitors. We consider that nanocontainers are fixed in the coating layer (pretreatment or primer layer) as can be seen in Fig. 1.

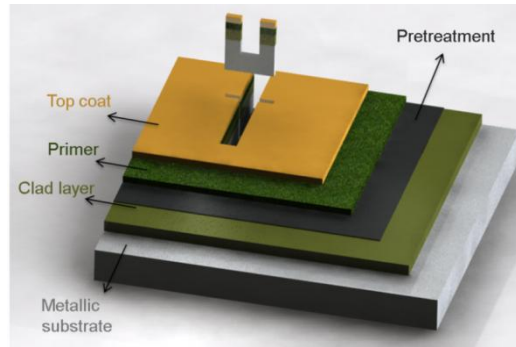


Figure 1. Model with nanocontainers in primer layer.

Nanocontainers release the “self – healing” agent particles which are filling the space inside a crack in order to bond it and to protect crack from further propagation. The continuum model used the process of convective-diffusion for inhibitors binding to the substrate surface.

The mass transport process for inhibition system of coating is governed by convection-diffusion equation,

$$\frac{\partial c}{\partial t} + v_x \frac{\partial c}{\partial x} + v_y \frac{\partial c}{\partial y} + v_z \frac{\partial c}{\partial z} = D \left(\frac{\partial^2 c}{\partial x^2} + \frac{\partial^2 c}{\partial y^2} + \frac{\partial^2 c}{\partial z^2} \right) + q^{wall} \quad (1)$$

where c denotes the concentration of inhibitors; v_x , v_y and v_z are the velocity components in the coordinate system x,y,z ; and D is the diffusion coefficient, assumed to be constant, of

the transported material; and q^{wall} is flux of the binding process for inhibitors which adhere on the substrate surface. Similar concept is using for calculation of the volume of inhibitors which are possible to diffuse on the scratch surface. Diffusivity coefficient and wall binding flux are the fitting parameters in FEM model. The drawback of continuum approach is that particle-particle interaction cannot be modeled but benefit is that a large substrate area is possible to be modeled.

3. Results

The continuum model consists of mesh size of $30 \times 30,000 = 900,000$ 3D finite elements where inhibitors are randomly prescribed as the influx boundary conditions. The scratch dimension is 0.1×100 mm, the primer layer is 4000 nm, nanocontainer diameter is 400 nm. The percentage of inhibitor inside nanocontainers is 20% and the percentage of nanocontainers in the primer or pre-treatment layers is 10%. The convection velocity is assumed to be zero due to dominant diffusion process. The binding flux was prescribed to be unit which depends on mechanical property of scratch, with no water inclusion on the surface. Distribution of inhibitors on the scratch surface for time = 6h is presented in Fig. 2. The inhibitors fluxes are randomly distributed along the plate, which cause higher coverage near these plate sides.

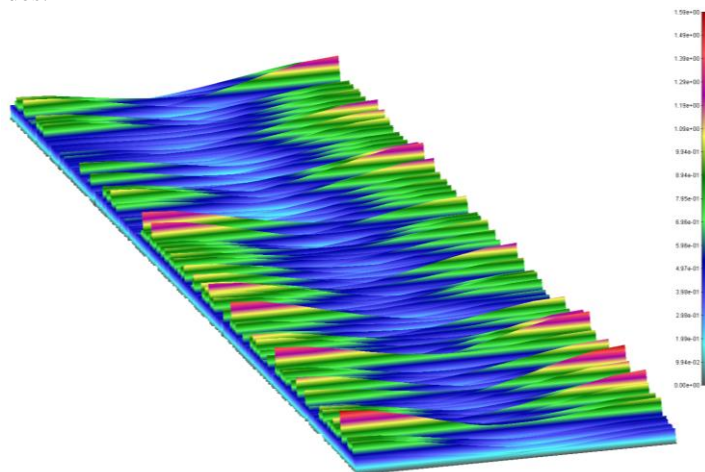


Figure 2. Distribution of inhibitors on the scratch surface for $t=6h$. The width of the scratch is 0.1mm and the length is 100mm.

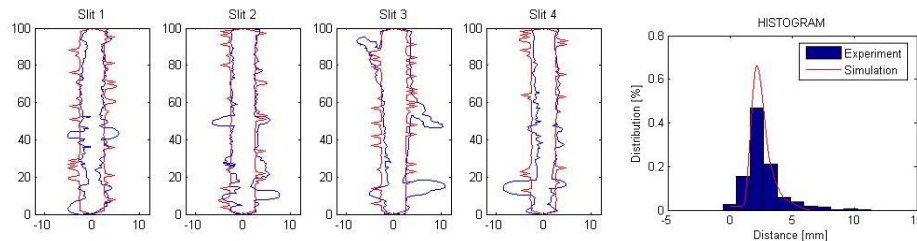


Figure 3. Comparison of experimental and computer simulation results.

The goal is to determine diffusion coefficient and diameter of nanocontainers so that computer simulations match experiments. We used a simplex optimization method developed by Nelder and Mead [7] to reach the best fit. This is nonlinear procedure which involves only function evaluations (no derivatives). The best fit minimizes the sum of squared residuals, a residual being the difference between an experimental value of the creepage distance and the creepage distance provided by a simulation. We have four different experimental creepages defined with 1200 points all together, thus we have 1200 residuals. The sum of squared residuals is calculated as:

(2)

where s_i is the creepage distance for i -th point calculated by simulation and t_i is target (experimental) creepage distance for i -th point. We achieved minimum error (SE=3082) with diffusion coefficient value $0.32 \text{ [m}^2/\text{s]}$ and diameter of nanocontainers 0.092 [nm] .

From the Fig. 3 we see that experimental results (blue color) and results obtained by simulations (red color) are very similar. The reason why error looks high is because high error occurs at points where experiment gave very large creepage distance (for example, third experiment at height around 15mm creepage distance is around 10mm), but from the histogram we can see that most of the point for both, computer simulation and experiment, have creepage distance around 2 mm.

4. Conclusions

In this study FE modeling methods is used in order to simulate self-healing systems with nanocontainers and inhibitors. It has been shown that it was sufficient to have 20% inhibitors in the primer layer with 10% of nanocontainers to completely protect the damaged material. Time for the scratch surface coverage is model parameter which can be fitted by employing real experimental data. The fitting of the diffusion coefficient and diameter of nanocontainers with a simplex optimization method and comparison with experimental measurements of the corrosion was implemented.

Progress in this field can greatly facilitate fabrication of the next generation of adaptive materials which can self-heal themselves before any catastrophic failure can occur.

Acknowledgement. This research was supported by Ministry of Science in Serbia, ON174028, III41007 and FP7 MUST project NMP3-LA-2008-214261.

References

- [1] Zheludkevich, M. L., Shchukin D. G., Yasakau K. A., Mohwald K., and Ferreira M. G. S. (2007) *Chem. Mater.* **19**, pp. 402-411.
- [2] Tyagi S., Lee J. Y., Buxton G. A., Balazs A. C. (2004), *Macromolecules* **37**, pp. 9160-9168.
- [3] White S. R., Sottos N. R., Geubelle P. H., Moore J. S., Kessler M. R., Sriram S. R., Brown E. N., and Viswanathan S. (2001), *Letters to Nature* **409**, pp. 794-797.
- [4] Balazs A. C. (2007), *Materials Today* **19**, 9, pp.18-23.
- [5] Verberg R, Dale A. T., Kumar P., Alexeev A., Balazs A. C. (2007), *J R Soc Interface* **4**, 13, pp.349-357.
- [6] Jovanovic A, and N. Filipovic, J. *Theoretical and Applied Mechanics* **44**, 637-648, 2006.
- [7] Nelder J. and Mead R, (1965), A simplex method for function minimization, *Computer Journal* **7** (4), pp.308-313.

IMAGE-BASED MPM SIMULATION OF THE HUMAN HIP STRUCTURAL FAILURE UNDER IMPACT

Yong Gan¹, Zhen Chen^{2,3}, Yonggang Shen⁴, Andrew Horner³, Ye Duan⁵, Carol Ward⁶ and Jerry Parker⁷

¹ Soft Matter Research Center, Zhejiang University, Hangzhou 310027, China
e-mail: ganyong@zju.edu.cn

² Department of Engineering Mechanics Dalian University of Technology, Dalian 116024, China

³ Department of Civil & Environmental Engineering, University of Missouri, Columbia, MO 65211, USA

e-mail: chenzh@missouri.edu

⁴ College of Civil Engineering and Architecture, Zhejiang University, Hangzhou 310027, China

⁵ Department of Computer Science, University of Missouri, Columbia, MO 65211, USA

⁶ Department of Pathology and Anatomical Sciences, University of Missouri, Columbia, MO 65212, USA

⁷ Office of Dean, School of Medicine, University of Missouri, Columbia, MO 65212, USA

Abstract. The hip damage resulting from a fall or trauma is one of the most common broken-bone injuries for elderly people. The main challenge in promoting the use of a hip protector is the designing and fabrication of the cost-effective, comfortable and personalized hip protector, for which the model-based simulation of the hip structural response to impact loading with a hip protector is necessary. In this interdisciplinary team project, a computational model for the human hip structure, which consists of both bones and soft tissues, is being developed to predict and simulate the damage evolution within the framework of the Material Point Method, based on the CT scan images. The impact-induced damage evolution in the hip will then be investigated by considering different boundary conditions and loading scenarios. As a result, various kinds of hip protectors could be considered to evaluate their effectiveness in reducing the impact damage to hip bones.

1. Introduction

Falls are common in older people and can result in serious injuries, even premature death. It is estimated that one of every three adults age 65 and older falls each year [1,2]. In 2009, over 2 millions of fall injuries among older adults were treated in the US [3].

Hip fracture is one of serious fall-related injuries in older people. It is reported that complications following a hip fracture are a major factor for fall deaths and the death rate for hip fracture patients within a year of the injury is 20% [4,5]. Hip fracture takes a large amount of medicare service, e.g., surgery, hospitalization, nursing and rehabilitation, and has become a public health problem. As the world population is aging, the number of hip fracture might continuously increase.

More than 90% of hip fractures result from falls [6]. However, there are many factors for falls, for example, vision defects, heart problems, poor environments, etc. Due to these multifactorial causes, wearing a hip protector appears to be an effective choice for hip fracture prevention. Currently, existing hip protectors are unpopular with older people for the uncomfortable wearing experience. As a result, there exists an urgent demand for designing personalized hip protectors made of soft materials, for which the impact response of human hip structure must be understood.

In this work, a computational model for the human hip structure consisting of both bones and soft tissues has been established within the framework of the Material Point Method (MPM), based on the CT scan images. The impact-induced structural responses of the hip with and without hip protector are simulated by considering different boundary conditions and protector materials, to examine protector's effectiveness in reducing the impact damage to hip bones.

2. Hip model and simulation procedure

The MPM is an extension to solid mechanics problems of a hydrodynamics code called FLIP [7]. In the MPM, the material is discretized by a set of material points, each of which carries the material properties and is tracked throughout the deformation history. One Eulerian background mesh is constructed to solve the equations of motion, and the internal state variables carried by material points are updated by the interpolation of the solutions at the mesh nodes. With the deformation history recorded at material points for the given history-dependent constitutive equations, the MPM is able to handle engineering problems with discontinuity, large deformation and multiple materials, such as impact/contact, penetration and perforation, and fluid-structure interactions [8].

The MPM model for human hip could be established by converting the pixel points in the CT scan images into the MPM points. The bone pixels are identified in the following method: (1) pixels with a gray value (range of 0-255) of less than 200 are cropped, and (2) extraneous pixels in each image are manually removed. The soft flesh pixels are generated in the same way, except for the gray value range of 25-185. Finally, a program is made to convert the pixel data to material point data with the specified space resolution. It should be noted that the bone structure is assumed homogeneous without further identifying cortical bone, cancellous bone and marrow and such structural refinement will be conducted in the future work. Figure 1 shows the MPM model of human hip structure employed in the following simulations, which is generated based on the CT scan images of a middle-age male. In the model, there are 352,796 material points in total, with 135,053 bone points and 217,743 soft tissue points.

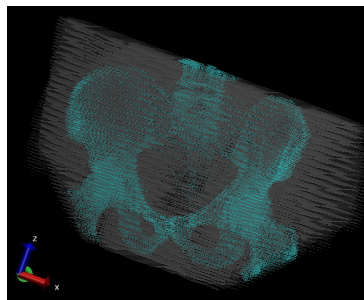


Figure 1. MPM model for human hip structure (bone and tissue points marked by cyan and white, respectively).

3. Results

Figure 2(a) presents the schematic diagram of a sideways fall of human hip against a rigid wall. To study the effect of the hip protector on the hip response, a 2-cm thick soft pad placed between the hip and the wall is also considered in the simulations, as illustrated in Fig. 2(b). Throughout all simulations, the soft tissue and the protector pad are linear elastic,

while the associated von-Mises elasto-plastic model with strain hardening and softening (see Figure 3) is assumed for the hip bone [9]. The Young's modulus for soft tissue is 85.5 kPa, and Poisson's ratios for soft tissue and pad are 0.495 and 0.38, respectively [10]. The velocity of the hip, v , is set as 2 m/s and the rate effect on the material response is neglected. The MPM grid is constructed of cubic elements with the side length being 0.02 m, and a time step of 1×10^{-6} s is employed.

Figure 4(a) shows the snapshot of damaged bone points (plasticity points in red color) at 50 ms without soft pad. The damage at the femur can be clearly seen in the figure, in addition to the pelvis damage. Figures 4(b)-4(c) give the hip damage snapshots at 50 ms with including pads of $E=85.5$ kPa, 855 kPa and 8 GPa, respectively. It is evident that the use of soft pad could substantially reduce the hip bone damage by comparing Figs. 4(a)-4(d). Moreover, less damage in pelvis and femur is generated as the pad becomes softer. Meanwhile, it is also found from Figs. 4(b)-4(d) that the femur is least damaged for the pad of $E=855$ kPa. These simulation results indicate that soft material is able to cushion the impact loading and the femur damage reduction is not monotonically increasing with decreasing pad stiffness.

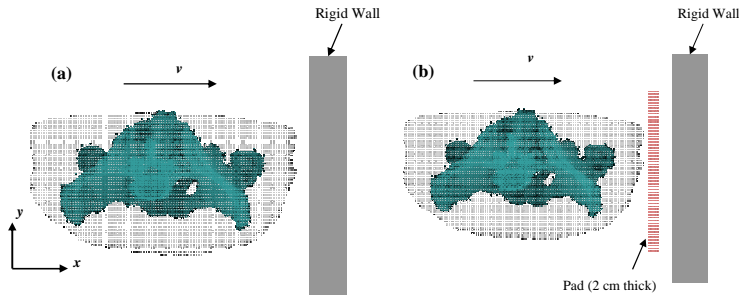


Figure 2. Schematic diagrams of a sideways fall of human hip against a rigid wall

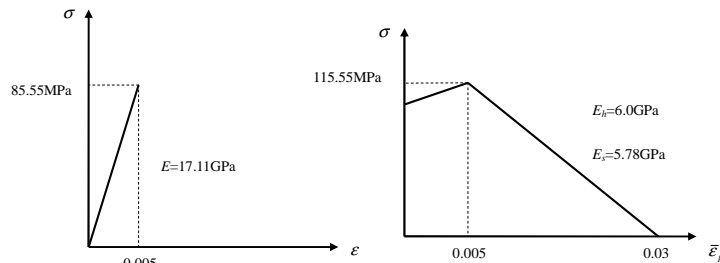


Figure 3. Elasto-plastic model for bone points

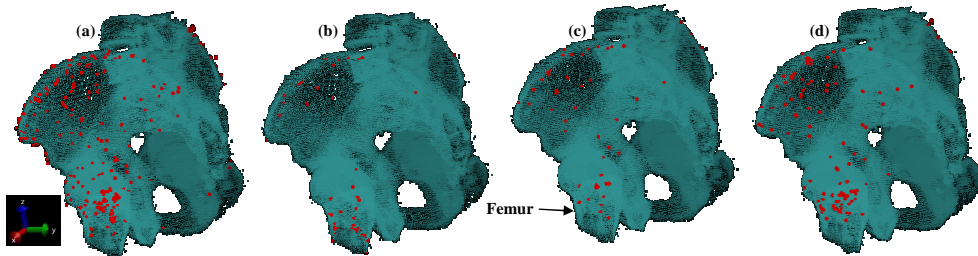


Figure 4. Snapshots for hip bone damage at 50 ms: (a) no soft pad, and soft pads of $E=$ (b) 85.5 kPa, (c) 855 kPa and (d) 8 GPa (damaged bone points marked by red).

4. Conclusions

An MPM model of human hip with soft tissue and bone has been built based on the CT scan images. The model-based simulations of the hip structural response in a sideways fall have been conducted. It is shown that a soft hip protector could reduce the impact-induced hip bone damage, and that the softer the pad, the less the bone damage could occur. However, the least femur damage is found for the pad of $E=855$ kPa, instead of the softest pad. It suggests that there exists an optimal stiffness of soft pad for hip fracture minimization. The present MPM-based modeling provides some preliminary results of the human hip structural damage due to impact loading. In the future, a refined MPM model will be developed based on CT and MRI images, and improved constitutive models for both bone and tissue will be employed in the simulations. It is also proposed that the effect of different hip protector scenarios on hip damage reduction be investigated, in combination with experiments.

Acknowledgement. The work is supported by the Soft Matter Research Center at Zhejiang University, and by the 111 Project (No.B08014), the Program for Changjiang Scholars and Innovative Research Team in University (PCSIRT) and the National Key Basic Research Special Foundation of China (2010CB832704) at Dalian University of Technology.

References

- [1] Hausdorff J. M., Rios D. A. , and Edelber H.K. (2001), Gait variability and fall risk in community-living older adults: a 1-year prospective study, *Archives of Physical Medicine and Rehabilitation*, **82**, pp. 1050–1056.
- [2] Hombrook M. C., Stevens V. J., Wingfield D. J., Hollis J. F., Greenlick M. R., and Ory M. G. (1994) Preventing falls among community-dwelling older persons: results from a randomized trial, *The Gerontologist*, **34**, pp. 16–23.
- [3] Centers for Disease Control and Prevention, National Center for Injury Prevention and Control. Web-based Injury Statistics Query and Reporting System (WISQARS) (<http://www.cdc.gov/injury/wisqars/>). Accessed November 30, 2010.
- [4] Deprey S.M. (2009) Descriptive analysis of fatal falls of older adults in a Midwestern counting in the year 2005, *Journal of Geriatric Physical Therapy*, **32**, pp. 23–28.
- [5] Leibson C. L., Totoson A. N. A., Gabriel S. E., Ransom J. E., and Melton J. L. III (2002) Mortality, disability, and nursing home use for persons with and without hip fracture: a population-based study, *Journal of the American Geriatrics Society*, **50**, pp. 1644–1650.
- [6] Hayes W. C., Myers E. R., Morris J. N., Gerhart T. N., Yett H. S., and Lipsitz L. A. (1993) Impact near the hip dominates fracture risk in elderly nursing home residents who fall, *Calcified Tissue International*, **52**, pp. 192-198.
- [7] Sulsky, D., Chen, Z., and Schreyer, H. L. (1994) A particle method for history-dependent materials, *Computer Methods in Applied Mechanics and Engineering*, **118**, pp. 179-196.
- [8] Sulsky, D., Zhou, S. J., and Schreyer, H. L. (1995) Application of a particle-in-cell method to solid mechanics, *Computer Physics Communications*, **87**, pp. 236-252.
- [9] Song E., Fontaine L., Trosseille X., and Guillemot H. (2005), Pelvis bone fracture modeling in lateral impact, *19th International Technical Conference on the Enhanced Safety of Vehicles*, Paper Number 05-0247.
- [10] Majumdera S., Roychowdhury A., and Pal S. (2007), Simulation of hip fracture in sideways fall using a 3D finite element model of pelvis-femur-soft tissue complex with simplified representation of whole body, *Medical Engineering & Physics*, **29**, pp. 1167–1178.

MATERIAL DAMAGE STUDIED BY THE STRAIN ENERGY DENSITY THEORY

E.E. Gdoutos

School of Engineering
Democritus University of Thrace, GR-671 00 Xanthi, Greece
e-mail: egdoutos@civil.duth.gr

Abstract. In this work the strain energy density theory is used to study the problem of slow stable growth of an inclined crack in a plate subjected to uniaxial tension. The stable crack growth process is simulated by predicting a series of crack growth steps corresponding to a piecewise load increase when the material elements in the direction of crack extension absorb a critical amount of elastic strain energy density. Crack instability takes place when the last increment of crack growth takes a critical value which is a material constant.

1. Introduction

The strain energy density theory has been used to address the problem of rapid unstable crack growth under mixed-mode conditions in a host of engineering problems [1, 2]. The theory was further extended to study the problem of stable crack propagation leading to crack arrest or instability [3, 4]. The conditions of crack initiation and growth have been studied for a variety of crack problems [1]. In such cases, failure always initiates from the crack tips due to the high stress concentration at these points. The directions of crack propagation and maximum yielding are automatically determined by the stationary values of dW/dV along a circumference of a circle centered at the crack tip. Failure by crack growth or yielding takes place when the minimum or maximum values of dW/dV become equal to their respective critical values which are material constants.

2. Strain energy density theory

The strain energy density theory focuses attention in a continuum element in the vicinity of the point of failure initiation. For the case of bodies with cracks the point of failure initiation is the crack tip. The theory is based on the strain energy density function, dW/dV , which can be determined from the stress and strain fields as follows:

$$\frac{dW}{dV} = \int_0^{\varepsilon_{ij}} \sigma_{ij} d\varepsilon_{ij}. \quad (1)$$

where σ_{ij} and ε_{ij} are the stress and strain components.

A material element fails by yielding or fracture when it absorbs a critical amount of strain energy density. This amount for the case of yielding is equal to the area of the true stress – true strain diagram of the material up to the point of yielding, $[(dW/dV)_{max}]_c$, while for the case of fracture it is equal to the area of this diagram up to the point of fracture, $[(dW/dV)_{min}]_c$. For materials with a relatively brittle behavior $[(dW/dV)_{min}]_c$ and $[(dW/dV)_{max}]_c$ are approximately the same, i.e., the onset of yielding and fracture are close to one another. Materials with more ductile behavior, however, are different in that $[(dW/dV)_{min}]_c$ is always greater than $[(dW/dV)_{max}]_c$ due to the manifestation that yielding always precedes fracture.

It is common experience that excessive change in shape can be associated with yielding, while excessive change in volume can be associated with fracture. In a non-uniform strain energy density field the former corresponds to the site of dW/dV maximum or, $(dW/dV)_{max}$, and the latter to dW/dV minimum or, $(dW/dV)_{min}$. Based on these physical arguments, the hypotheses of the strain energy density theory may be stated as follows [1-3]:

- (a) Yielding and fracture are assumed to initiate at locations of maximum and minimum of the strain energy density function $[(dW/dV)_{max}]_l$ and $[(dW/dV)_{min}]_l$, respectively, along the circumference of a circle centered at the point of failure initiation.
- (b) Yielding and fracture are assumed to occur when $[(dW/dV)_{max}]_l$ and $[(dW/dV)_{min}]_l$ reach their respective critical values.

The above conditions apply to the initiation of yielding and fracture of a material element located at a distance r_0 from the site of possible failure. The value r_0 of the radius of a circle called the core region reflects a basic material property in the microstructural level and is considered to be a material constant.

Since material damage once initiated is a rate process, additional assumptions are required to describe the conditions that govern this damage process by yielding and fracture. Without loss in generality, the relation

$$\left(\frac{dW}{dV}\right)_c = \frac{S_1}{r_1} = \frac{S_2}{r_2} = \dots = \frac{S_j}{r_j} = \dots = \frac{S_c}{r_c} \quad (2)$$

can be written in general with S being the strain energy density factor and r a linear distance. Depending on the loading condition, material damage can increase, decrease, or a combination of the two. The following conditions may thus be stated:

- (a) The amount of incremental growth $r_1, r_2, \dots, r_j, \dots, r_c$ by yielding or fracture is assumed to increase or decrease monotonically, i.e.

$$r_1 < r_2 \dots < r_j < \dots < r_c \quad (3)$$

or

$$r_1 > r_2 \dots > r_j > \dots > r_c \quad (4)$$

in accordance with

$$(dW/dV)_{max}^c \text{ or } (dW/dV)_{min}^c = S_1/r_1 = S_2/r_2 = \dots = S_j/r_j = S_c/r_c \text{ or } S_0/r_0 \quad (5)$$

whereby $r = r_c$ corresponds to the onset of unstable damage and $r = r_0$ to damage arrest.

(b) Incremental damage of material may follow relation (3) for part of the loading and relation (4) for another or some combination before reaching S_c/r_c or S_0/r_0

3. Stable growth of a central crack

The problem of slow stable growth of an inclined crack in a plate subjected to a uniaxial tension is studied (Fig. 1). The crack growth process is simulated by predicting a series of crack growth steps corresponding to a piecewise loading increase when material elements along the direction of crack extension absorb a critical amount of strain energy density. Crack instability takes place when the last ligament of crack extension takes a critical value which is a material constant.

Crack initiation starts when $(dW/dV)_{min}$ takes its critical value $(dW/dV)_c$. By expressing dW/dV in terms of the applied load, the critical load for crack initiation is determined.

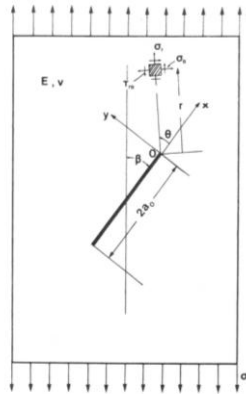


Fig. 1 An inclined crack in a plate subjected to uniaxial tension

In order to obtain numerical results consider a crack of length $2a_0 = 2 \text{ cm}$ in an infinite plate subjected to a remote uniaxial stress σ subtending an angle β to the crack axis. The material of the plate is a steel with the following properties: $E = 207 \text{ GPa}$, $\nu = 0.3$, $(dW/dV)_c = 184 \text{ MJ/m}^3$, $S_c = 13.5 \text{ kN/m}$. The value of r_c is calculated as $r_c = S_c/(dW/dV)_c = 7.33 \times 10^{-3} \text{ cm}$, while $r_0 = 3.05 \times 10^{-3} \text{ cm}$ is used in the subsequent numerical work.

Numerical results were obtained for various values of the crack angle β . Crack initiation takes place when the minimum value of strain energy density along a circle of radius r_0 centered at the crack tip becomes equal to the critical strain energy density, $(dW/dV)_c$. Fig. 2(a) presents the variation of the critical stress σ_i for crack initiation for various values of

the crack angle β . Note that σ_i decreases with β and takes its minimum value when the crack is perpendicular to the applied stress.

Crack initiation is followed by stable crack growth until global instability is reached. In order to study the process of stable crack growth the applied stress is increased by constant increments $\Delta\sigma$ and the corresponding crack increments are obtained. This process is continued until the last crack increment r becomes equal to the critical size r_c which corresponds to global instability. Thus the critical stress at instability, σ_c , is obtained.

Fig. 2(b) presents the variation of the stress σ_c versus the initial crack angle β for $\Delta\sigma$ equal to 3.447 and 13.790 MPa. Higher stress increments correspond to higher loading rates. It is observed that σ_c decreases as the stress increment increases. This trend agrees with experimental observation for specimens with cracks perpendicular to the applied stress ($\beta = 90^\circ$).

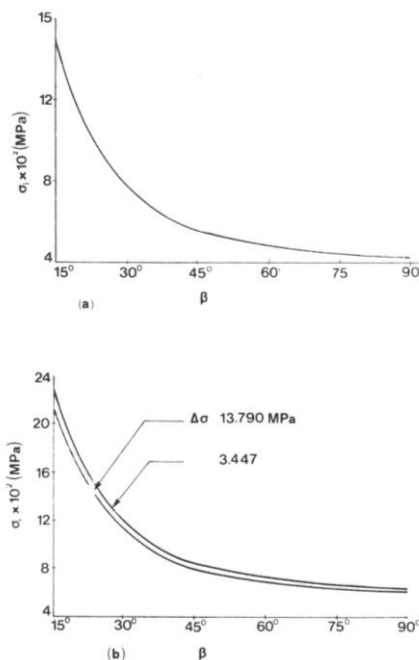


Fig. 2 Critical stress at crack initiation, σ_i , (a) and global instability, σ_c , (b) for two different loading step increments

References

- [1] Sih, G.S., (1974) Strain energy Density Factor Applied to Mixed Mode Crack Problems. *International Journal of Fracture*, **5**, pp. 365-377
- [2] Gdoutos, E.E., (1984) *Problems of Mixed-Mode Crack Propagation*. Martinus Nijhoff, The Hague.
- [3] Gdoutos, E.E., (2005), *Fracture Mechanics – An introduction*, Sec Ed, Springer, Dordrecht, The Netherlands
- [4] Gdoutos, E.E., *Crack Growth Instability Studied by the Strain Energy Density Theory*, *Archive of Applied Mechanics*, to appear

EVALUATION OF CUMULATIVE DAMAGE OF RC STRUCTURES UNDER MULTIPLE EARTHQUAKES

G. Hatzigeorgiou¹, A. Liolios²

¹Department of Environmental Engineering,
Democritus University of Thrace, 67100 Xanthi, Greece
e-mail: gchatzig@env.duth.gr

²Department of Civil Engineering,
Democritus University of Thrace, 67100 Xanthi, Greece
e-mail: liolios@civil.duth.gr

Abstract. This paper develops a new method to evaluate the cumulative damage of reinforced concrete (RC) framed structures under seismic sequences. Two families of regular and vertically irregular frames are examined. The first family has been designed for seismic and vertical loads according to European codes while the second one for vertical loads only, to study structures which have been constructed before the introduction of adequate seismic design code provisions. The whole gamut of frames is subjected to five real and forty artificial seismic sequences. Comprehensive analysis of the created response databank is employed in order to derive significant conclusions. It is found that the cumulative damage due to multiplicity of earthquakes is important and can be accurately estimated using appropriate combinations of the corresponding damage due to single ground motions.

1. Introduction

Modern seismic codes adopt exclusively the isolated and rare 'design earthquake' while the influence of repeated earthquake phenomena is ignored. Recently, Hatzigeorgiou and Beskos [1] and Hatzigeorgiou [2-3] examined the influence of multiple earthquakes in numerous SDOF systems and found that seismic sequences lead to cumulative structural damage. However, these works are concerned with SDOF systems.

This paper presents an extensive parametric study on the inelastic response of eight reinforced concrete planar frames under five real seismic sequences which are recorded by the same station, in the same direction and in a short period of time, up to three days. In such cases, there is a significant damage accumulation as a result of multiplicity of earthquakes, and due to lack of time, any rehabilitation action is impractical. Furthermore, these RC frames are also subjected to forty artificial seismic sequences. More specifically, two families of regular and vertically irregular (with setbacks) frames are examined. The first family of frames has been designed for seismic and vertical loads according to European codes while the second one for vertical loads only, to study structures which have been constructed before the introduction of adequate seismic design code provisions. The time-history responses of these concrete frames are evaluated by means of the structural analysis software Ruaumoko. Comprehensive analysis of the created response databank is employed in order to derive significant conclusions.

2. Description of structures

Four structures (Family A) are considered to represent low-rise (three-storey) and medium-rise (eight-storey) RC buildings for study. They consist of four typical beam–column RC frame buildings without shear walls, located in a high-seismicity region of Europe considering both gravity and seismic loads where a design / peak ground acceleration (*PGA*) of $0.2g$ and soil class B according to EC8 are assumed. Most of the existing reinforced concrete buildings were designed according to early seismic provisions or, sometimes, without applying any seismic provision. In order to examine such buildings designed for gravity only, another family of structures (Family B) is also considered. Families A and B have the same geometry and loads but they have different reinforcement. The dead loads (excluding self-weight) and live loads are equal to 20 kN/m and 10 kN/m , respectively, and they are directly applied on the beams. All floors are assumed to be rigid in plan to account for the diaphragm action of concrete slabs. Material properties are assumed to be 20 MPa for the concrete compressive strength and 500 MPa for the yield strength of both longitudinal and transverse reinforcements. Both the examined 3- and 8-storey buildings have 3 equal bays with total length equal to 15 m . Typical floor-to-floor height is equal to 3.0 m , while for the first floor of the 8-storey buildings the height is equal to 4.0 m . The characteristic interior frames of Family-A structures are shown in Fig. 1.

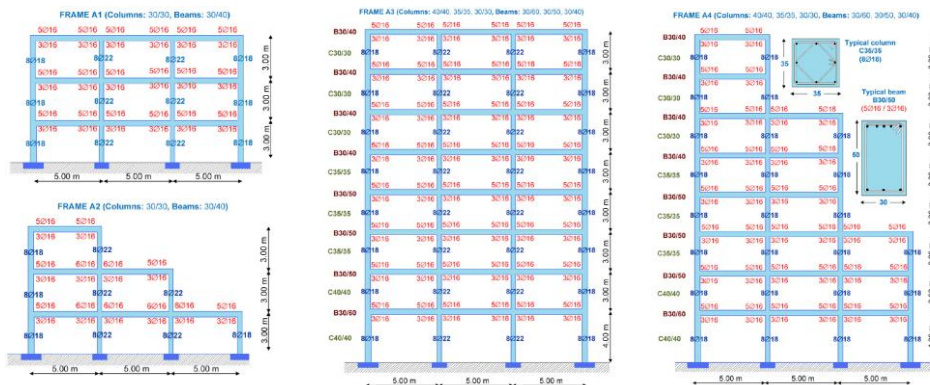


Figure 1. Concrete damage model.

3. Seismic input

3.1 Real seismic sequences

The first strong ground motion database that has been used here consists of five real seismic sequences, which have been recorded during a short period of time (up to three days), by the same station, in the same direction, and almost at the same fault distance. These seismic sequences are namely: Mammoth Lakes (May 1980), Chalfant Valley (July 1986), Coalinga (July 1983), Imperial Valley (October 1979) and Whittier Narrows (October 1987) earthquakes. The complete list of these earthquakes has been downloaded from the strong motion database of the Pacific Earthquake Engineering Research (PEER) Center. These records are compatible with the soil class B, and therefore compatible with the design process as mentioned in the previous section. Between two consecutive seismic events, a time gap equal to 100 sec cease the moving of any structure due to damping.

3.2 Artificial seismic sequences

The second strong ground motion database that has been used here consists of forty artificial seismic sequences. More specifically, 10 artificial accelerograms are considered to generate 20 synthetic sequences of two events and 20 synthetic sequences of three events.

4. Results

The inelastic behaviour of the examined RC framed structures, which are subjected to the aforesaid five real and forty artificial seismic sequences, is investigated in this section. The Park-Ang model [4] is the best known and most widely used damage index (DI), which is defined as a combination of maximum deformation and hysteretic energy:

$$DI = \frac{\delta_m}{\delta_u} + \frac{\beta}{\delta_u P_y} \int dE_h \quad (1)$$

where δ_m is the maximum deformation of the element, δ_u is the ultimate deformation, β is a model constant parameter (usually, $\beta=0.05\sim0.20$) to control strength deterioration, $\int dE_h$ is the hysteretic energy absorbed by the element during the earthquake, and P_y is the yield strength of the element. This damage model can also be extended to the storey and overall scales (global damage index), by summation of damage indices using appropriate multiplication weights. Figure 2a depicts the local DI for the base joint of the left base column of Frame A2, for the Mammoth Lakes seismic sequence. Furthermore, Fig. 2b shows the global DI , for the whole Frame B2, under the Whittier Narrows earthquakes. It is evident that seismic sequences lead to increased damage, both in local and global level. However, the majority of the existing investigations examine these parameters only for the 'idealized' case of isolated earthquakes.

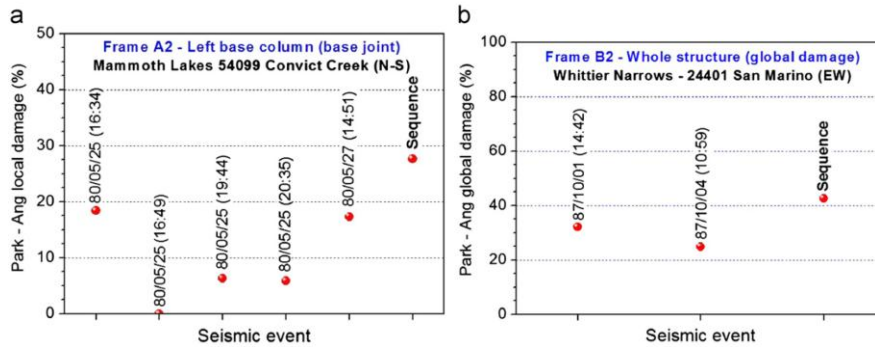


Figure 2. a) Local and b) global cumulative damage due to seismic sequences.

The global damage can be related to global displacement ductility factor, μ , which can be defined in terms of the maximum displacement u_{max} at the top floor and the corresponding yield displacement u_y , as

$$\mu = \frac{u_{max}}{u_y} \quad (2)$$

In order to estimate the cumulative ductility for a sequence of strong ground motions, this work proposes the following simple and rational relation

$$\mu_{seq} = 1 + \left[\sum_{i=1}^n \langle \mu_i - 1 \rangle^{1.3} \right]^{1/1.3} \quad (3)$$

where the cumulative ductility, μ_{seq} , for a sequence of strong ground motions consists of n -seismic events, results from the corresponding ductility demands, μ_i , for each one of them. Furthermore, $\langle \rangle$ symbolizes the Macauley brackets used here in order to eliminate the influence of weak ground motions, i.e., those for $\mu_i < 1$. Figure 3 illustrates the relation between the “exact” cumulative ductility demands and those of the model of Eq.(3). It is clear that the proposed combination of ductility demands of single events is in good agreement with the results obtained from the dynamic inelastic analyses considering directly the sequential ground motions.

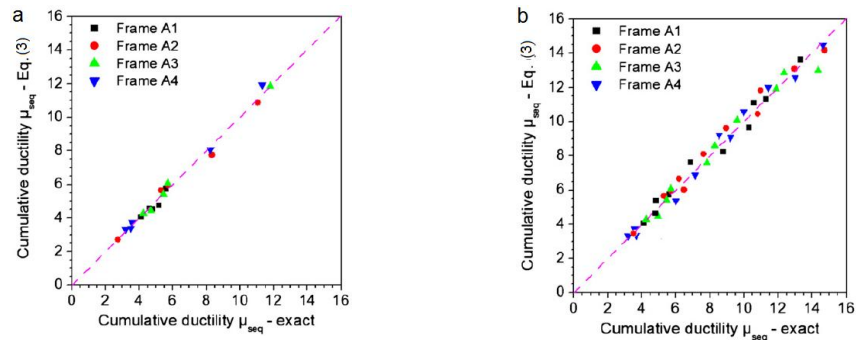


Figure 3. Estimation of cumulative ductility for a) real and b) artificial seismic sequences.

5. Conclusions

This paper examines the inelastic behaviour of planar RC frames under sequential strong ground motions. It is found that the seismic damage for multiple earthquakes is higher than that for single ground motions. Furthermore, a simple and effective empirical expression, which combines the ductility demands of single ground motions, can be used to estimate cumulative ductility demands due to sequential ground motions.

References

- [1] Hatzigeorgiou, G.D. and Beskos, D.E. (2009), Inelastic Displacement Ratios for SDOF Structures Subjected to Repeated Earthquakes, *Engineering Structures*, **31**, pp. 2744-2755.
- [2] Hatzigeorgiou, G.D. (2010), Ductility demand spectra for multiple near- and far-fault earthquakes. *Soil Dynamics and Earthquake Engineering*, **30**, pp. 170-183.
- [3] Hatzigeorgiou, G.D. (2010), Behaviour factors for nonlinear structures subjected to multiple near-fault earthquakes, *Computers and Structures*, **88**, pp. 309-321.
- [4] Park, Y.J. and Ang A.H.S. (1985), Mechanistic seismic damage model for reinforced concrete. *Journal of Structural Division ASCE*, **111**, pp.722-739.

FE-ANALYSIS OF DAMAGE IN STEEL STRUCTURES UNDER DYNAMIC LOADING

Sven Heinrich¹, Ursula Kowalsky¹, Jana Meyer¹, and Dieter Dinkler¹

Abstract. High dynamic excitation of steel structures leads to inelastic material behavior responsible for the dissipation of energy. In addition, the steel suffers from material damage caused by inelastic deformations and cyclic loading. This softening of the material is referred to as ultra low cycle fatigue and influences the stiffness of a structure and its response to dynamic excitation. The proposed material model describes the evolution and distribution of inelastic strains and isotropic ductile damage for mild construction steel by means of a set of internal variables. Viscoplasticity as well as isotropic and kinematic hardening are taken into account. Under tension isotropic ductile damage develops for significant inelastic strains. A nonlocal extension in the form of an implicit gradient formulation is applied to overcome the phenomenon of strain localization. The presented model is used to analyse 3D structures subjected to seismic excitation.

¹Institute for Structural Analysis, Technische Universität Braunschweig, Beethovenstr. 51, 38106 Braunschweig, Germany
e-mail: s.heinrich@tu-bs.de

1. Introduction

Constructions in earthquake regions have to be designed according to the Eurocode 8 that provides a practical approach in order to validate the safety of a structure using a linear response spectrum. As the code also allows nonlinear time-history computations the material model has to be precise as simplified approaches may not be conservative for dynamic loading.

As the material strength influences the stiffness of the structure the presented material model includes hardening effects as well as softening caused by material deterioration. This damage evolves from voids in the microstructure and can finally lead to macrocracks and failure. The softening of the material is accompanied by a mesh-dependent strain localization. An implicit gradient enhanced formulation for a non-local damage variable is introduced to overcome this shortcoming.

Applying the proposed model to a FE analysis of a structure provides the distribution of damage and the identification of damaged zones. To evaluate the overall structural safety a scalar global damage index is formulated.

2. Material Model

The mathematical description of the material behaviour is achieved by a set of internal variables and evolution equations in the form of differential equations of first order. Assuming

small strains, an additive decomposition of elastic and inelastic strain rate is admissible. Based on the principle of energy equivalence, stresses and strains used to compute the internal variables are effective quantities (Eq. 1). The crack closure parameter h takes into account that some but not every microcrack closes under compression ($h < 1.0$) while for tension ($h = 1.0$) all voids reduce the net area [1]. The evolution of elastic strains is given by Hooke's law and contains an isotropic degradation of the modulus of elasticity by the nonlocal damage variable \bar{D} (Eq. 2). The viscoplastic deformation (Eq. 3) follows the approach by CABOCHE & ROUSSELIER [2] with the effective over-stress $\tilde{\sigma}_{ex}$ (Eq. 4) that determines the onset of inelastic material behavior. It corresponds to the yield function and results from a modified criterion based on Gurson [3] and Tvergaard and Needleman [4] with the first and the second invariant of the effective active stress tensor $\tilde{\boldsymbol{\sigma}} - \mathbf{X}$ and the effective active stress deviator $(\tilde{\boldsymbol{\sigma}} - \mathbf{X})^d$, respectively. The yield function considers isotropic hardening k and kinematic hardening \mathbf{X} (Eq. 5) as well as material deterioration. In case of undamaged material, the yield surface corresponds to the v. Mises criterion. Increasing damage leads to a contraction of the yield surface combined with the formation of caps which then initiates inelastic strains also for high hydrostatic stress states.

The onset of damage is determined by a damage threshold surface as experiments have shown that nucleation of cavities does not occur for cyclic loading with small amplitudes. In the model presented here damage evolution is prohibited if the equivalent plastic strain (Eq. 6) is smaller than a parameter ε_D^m (Eq. 7). Furthermore it is assumed that damage does not grow for compression states. The two terms of the damage evolution equation (Eq. 8) consider transient and saturation behavior in damage evolution as well as damage due to volumetric yielding and depend on the damage parameters $c_1 - c_5$.

As experiments reveal the evolution of isotropic hardening depends on the strain loading history. The saturation value Q is therefore coupled with the evolution of a strain memory surface M and its two variables $\boldsymbol{\beta}$ and q . $\boldsymbol{\beta}$ describes the displacement of the surface and q specifies its amplitude. Within this work, a maximum strain amplitude memory [5] is defined in the three-dimensional strain space (Eq. 9-11) where \mathbf{n}_F is the normal to the yield surface, and \mathbf{n}_M is the normal to the strain memory surface. A viscoplastic strain state outside the current strain memory surface leads to the growth and adjustment of the variables q and $\boldsymbol{\beta}$, resulting in a higher saturation value for isotropic hardening. Here, the evolution rule of the saturation value of isotropic hardening Q is assumed to be linear (Eq. 12).

The thermodynamical consistency of the constitutive equations can be shown [6].

$$\tilde{\boldsymbol{\sigma}} = \frac{1}{1 - h \cdot \bar{D}} \cdot \boldsymbol{\sigma} \quad \tilde{\boldsymbol{\varepsilon}} = (1 - h \cdot \bar{D}) \cdot \boldsymbol{\varepsilon} \quad (1)$$

$$\dot{\boldsymbol{\varepsilon}}^{el} = \frac{d}{dt} (\tilde{\mathbf{E}}^{-1} : \boldsymbol{\sigma}) \quad \tilde{\mathbf{E}} = (1 - h \cdot \bar{D}) \mathbf{E} (1 - h \cdot \bar{D}) \quad (2)$$

$$\dot{\boldsymbol{\varepsilon}}^{in} = \frac{\partial \tilde{\sigma}_{ex}}{\partial \tilde{\boldsymbol{\sigma}}} \dot{p} \quad \dot{p} = \dot{\varepsilon}_0 \left\langle \frac{\tilde{\sigma}_{ex}}{\tilde{\sigma}_p} \right\rangle^n \quad (3)$$

$$\tilde{\sigma}_{ex} = \tilde{\sigma}_{eq} - \sigma_Y - k = \sqrt{3J_2(\tilde{\boldsymbol{\sigma}} - \mathbf{X})^d + \bar{D}J_1((\tilde{\boldsymbol{\sigma}} - \mathbf{X}))^2} - \sigma_Y - k \quad (4)$$

$$\dot{k} = b(Q - k)\dot{p} \quad \dot{\mathbf{X}} = b_X \left(\frac{2}{3} Q_X \frac{\partial \tilde{\sigma}_{eq}}{\partial \tilde{\boldsymbol{\sigma}}} - \mathbf{X} \right) \dot{p} \quad (5)$$

$$\varepsilon_{eq}^{in,+} = \sqrt{\frac{2}{3} \left(\langle \varepsilon_{ij}^{in} \varepsilon_{ij}^{in} \rangle \right)} \quad (6)$$

$$\begin{aligned} \boldsymbol{\varepsilon}_{eq}^{in} - \boldsymbol{\varepsilon}_D^{in} \leq 0 &\longrightarrow \dot{D} = 0 \\ &> 0 \longrightarrow \dot{D} > 0 \end{aligned} \quad (7)$$

$$\dot{D} = (c_1 + c_2 e^{-c_3 \frac{1}{(1-\bar{D})} p^+}) \frac{1}{(1-\bar{D})} \dot{p}^+ + c_5 (c_4 - \bar{D}) \left\langle \text{tr} \left(\frac{\partial \tilde{\boldsymbol{\sigma}}_{ex}}{\partial \tilde{\boldsymbol{\sigma}}} \dot{p}^+ \right) \right\rangle \quad (8)$$

$$M = \frac{2}{3} (\boldsymbol{\varepsilon}^{in} - \boldsymbol{\beta}) (\boldsymbol{\varepsilon}^{in} - \boldsymbol{\beta}) - q^2 = 0 \quad (9)$$

$$\dot{q} = H(M) \cdot c \cdot \mathbf{n}_M \cdot \mathbf{n}_F^T \cdot \dot{p} \quad (10)$$

$$\dot{\boldsymbol{\beta}} = H(M) \cdot (1 - c) \cdot \dot{\boldsymbol{\varepsilon}}^{in} \quad (11)$$

$$\dot{Q} = \dot{q} \cdot Q_k \quad (12)$$

2.1. Non-local extension

The dissipation of energy concentrates in small areas of the structure called process zones. For local damage models the solution depends on the fineness of discretization which leads to physically incorrect results for an evanescent volume.

To regularize the solution, the models need to be extended by a material-dependent internal length scale. The proposed approach takes into account a non-local implicit gradient model in 3D-FE structural analysis. Following the derivation of Engelen [7] and using gradients of the damage variables, the non-local damage variable \bar{D} can be determined by the gradient equation with the local damage variable D

$$\bar{D} - l_c^2 \nabla^2 \bar{D} = D. \quad (13)$$

3. Structural Analysis

The structural response to dynamic excitation is described by the equation of motion. The current stiffness of the structure depends on the development of hardening and damage. Stress-deformation analysis of structures implies the solution of the underlying initial boundary value problem. With the principle of virtual work the weak form of the equation of motion can be obtained.

$$\begin{aligned} \int_{\Omega} \delta \mathbf{u} \cdot \rho \ddot{\mathbf{u}} d\Omega + \int_{\Omega} \delta \mathbf{u} \cdot \mathbf{f} d\Omega + \int_{\Omega} \delta \boldsymbol{\varepsilon} : \boldsymbol{\sigma} d\Omega = \\ \int_{\Omega} \delta \mathbf{u} \cdot \mathbf{p} d\Omega + \int_{\partial\Omega} \delta \mathbf{u} \cdot \bar{\mathbf{t}} d\partial\Omega + \int_{\Omega} \delta \mathbf{u} \cdot \rho \ddot{\mathbf{u}}_g d\Omega \end{aligned} \quad (14)$$

The equation is discretized in space with the finite-element method, while the Newmark method with a constant mean acceleration is used for the discretization in time.

Eq. (13) can be assumed to be time-independent. The weak form of the equation for the non-local damage field \bar{D} results from weighted residua

$$\int_{\Omega} (\delta \bar{Y} (\bar{D} - D) - \nabla \delta \bar{Y} \cdot l_c^2 \nabla \bar{D}) d\Omega - l_c^2 \int_{\partial\Omega} \delta \bar{Y} \bar{\mathbf{t}}_{\bar{D}} d\partial\Omega = 0 \quad (15)$$

with the virtual nonlocal energy release rate $\delta \bar{Y}$ and Neumann boundary condition $\bar{\mathbf{t}}_{\bar{D}} - \mathbf{n} \nabla \bar{D} = 0$, which prohibits a damage flux through the boundary of the domain. The gradient equation is discretized in space by the finite-element method.

The material equations are solved using the implicit Euler approach.

3.1. Global damage index

Applying the proposed model provides the distribution of damage for dynamic loading. Therefore, highly stressed regions can be identified, but it is not possible to evaluate the damage state of the structure in general. A scalar global damage index GDI is proposed which bases on the eigenvalue decomposition

$$GDI = (1 - \lambda_r) \frac{\|\mathbf{M}\mathbf{v}_r\|}{\|\mathbf{M}\mathbf{v}_{ref}\|} \quad [\mathbf{K}_t - \lambda_{r,i}^2 \mathbf{K}_0] \mathbf{v}_{r,i} = \mathbf{0} \quad (16)$$

where $\lambda_{r,i}$ are the eigenvalues, $\mathbf{v}_{r,i}$ are the eigenvectors, \mathbf{K}_0 is the initial and \mathbf{K}_t the current stiffness matrix due to hardening and damage. $\|\mathbf{M}\mathbf{v}_{ref}\|$ is the amount of displaced mass for the eigenform \mathbf{v}_{ref} of the first eigenvalue.

3.2. Dynamic excitation of cantilever

To demonstrate the ability of the model a cantilever of 5 m height and an additional top mass is subjected to the north-south component of the Kobe earthquake. The maximum displacement during the vibration is 44 cm. Because of inelastic strains material damage evolves at the base of the cantilever which is shown in Fig. 1(a). It can be seen that damage occurs in the flanges which are subjected to high alternating tension and compression. Evidently the shear bands accumulate damage and weaken the structure. To evaluate the damage state of the cantilever the global damage index is computed for every timestep, see Figure 1(b).

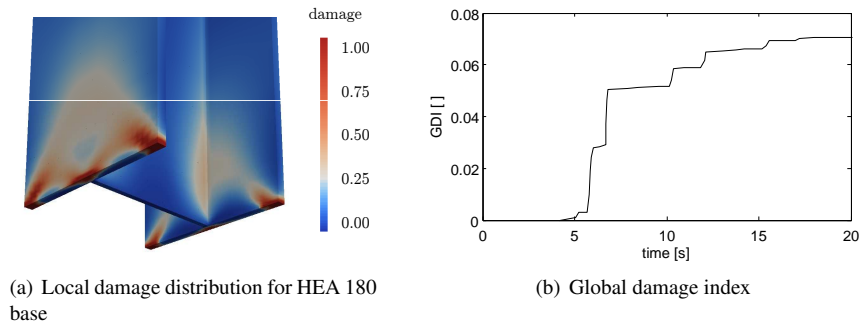


Figure 1. Damage evolution of the cantilever

References

- [1] J. Lemaitre, *A Course on Damage Mechanics*, Springer, 1992.
- [2] J. Chaboche, G. Rousselier, *On the Plastic and Viscoplastic Constitutive Equations - Part I + II: Rules Developed with Internal Variable Concept*, Journal of Pressure Vessel Technology 105 (1983) 153–164.
- [3] A. Gurson, *Continuum Theory of Ductile Rupture by Void Nucleation and Growth: Part I - Yield Criteria and Flow Rules for Porous Media*, Journal of Engineering Materials and Technology 99 (1977) 2–15.
- [4] V. Tvergaard, A. Needleman, *Analysis of the cup-cone fracture in a round tensile bar*, Archives of Mechanics 32 (1984) 157–169.
- [5] J.L. Chaboche, K. Dang Van, G. Cordier, *Modelization of the strain memory effect on the cyclic hardening of 316 stainless steel*, Transaction of the 5th International Conference on Structural Mechanics in Reactor Technology, Paper No. L11/3, Berlin, Germany, 1979.
- [6] J. Velde, U. Kowalsky, T. Zümendorf, D. Dinkler, *3D-FE-Analysis of CT-specimens including viscoplastic material behavior and nonlocal damage*, Computational Material Science 46 (2009) 352–357.
- [7] R. Engelen, M. Geers, F. Baaijens, *Nonlocal implicit gradient-enhanced elasto-plasticity for the modelling of softening behavior*, International Journal of Plasticity 19 (2003) 403–433.

MODELS OF DYNAMICAL DYSLOCATION IN CONTINUUM

Katica R. (Stevanović) Hedrih

¹Department of Mechanics at Mathematical Institute SANU, Belgrade
and Faculty of Mechanical Engineering University of Niš, Serbia, Priv. address: 18000-
Niš, Serbian ul. Vojvode Tankosića 3/22, e-mail: khedrih@eunet.rs

Abstract. A possible model of dynamical dislocation is presented. Basic suppositions are: a core of dislocation is initially chapped by a part of the continuum with mass density higher than mass density of other material and that is located between fictive surfaces with different displacements in same directions. Also, it is proposed that continuum between fictive parallel surfaces can be modeled as a layer with granular structure and with visco-elastic properties including properties of inertia of translation, and inertia of rolling. Taking into account previous listed properties, and that initiation of the dislocation is caused by displacements in same direction of these fictive surfaces. Model of rolling dislocation poses that core of dislocation can be used in the form of disk or cylinder with shot length or in the form of sphere which rolls around two surfaces without slipping. Expressions of kinetic and potential energy as well as function of energy dissipation of the proposed model of dynamical dislocation are composed on the basis of the analogy with standard visco-elastic rolling element with corresponding force-extension constitutive relation. Corresponding constitutive relation of dynamical dislocation model is given by relation between forces and element extension (or compression) is determined. Distribution of the force of interaction between layer with dislocation and fictive surface are expressed by displacements of these surfaces. Also, a model of oscillatory dynamical dislocation with layer of dislocation between two concentric cylindrical surfaces is presented. Characteristic equation of oscillatory waves on a thin plate with a layer containing distributed oscillatory dynamic dislocation is presented.

Key words: dynamical model, oscillatory dislocation, core of dislocation, layer of dislocation, rolling, kinetic energy, potential energy, function of dissipation, constitutive relation of dislocation, characteristic equation.

1. Introduction

When I accepted the invitation for participation in the conference and after submission of an Abstract of my contribution, three reviewer's reports appeared in my e-mail. After my consideration of these reports, numerous dilemmas appeared, and main is: What is dislocation? Are there different definitions of this word dislocation?

One of the reviewers used the following comment: "There is neither rolling nor viscoelasticity in dislocation behavior. Instead, edge and screw dislocations are translational defects in a crystalline structure. Disclinations (appearing in liquid crystals) have rotational imperfection structure but any type of rolling never happens". Same reviewer added: "A spherical inclusion mentioned in the proposed abstract without slip is not a dislocation. Maybe the author thinks on Eshelbian inclusion causing eigenstresses. Modeling like the one proposed in the abstract could be presumably applied to some other physical processes but not to dislocation behavior".

By the same reviewer we learn: "The references (containing only authors papers) listed in the proposed abstract do not have any connection with dislocation physics"

Another reviewer includes in a part of sentence the following:” Author should stress problem of inclusion in the sense of Eshelbian inclusion”.

After consideration of the listed previous reviewers sentences, I conclude that different definitions of the notation “dislocation” are reason for different opinions and understanding or misunderstanding of my ideas presented in the abstract of this contributed lecture. My conclusion is that, by abstract of my contributed lecture only one of three reviewers fully understood my ideas and accepted my definition of dynamic dislocation in continuum on macro and micro-level of the continuum media.

After, my consideration in general notion of the dislocation I am in situation to express the complexity of the notion “dislocation” and in fully keep my ideas in my submitted abstract and that my definition of the dynamic dislocation is real and new in scientific literature and different then those known in literature of dislocation.

Among researchers in the area of technology, dislocation is accepted on the level of the crystals and motion between crystals as crystals dislocation is largely used.

After analysis of the word web literature we can point out the following sentences: “For the syntactic operation, see Dislocation (syntax). For the medical term, see Joint dislocation.” In syntax, dislocation is a sentence structure in which a constituent which could otherwise be either an argument or an adjunct of the clause occurs outside the clause boundaries either to its left or to its right as in English: They went to the store, Mary and Peter. The dislocated element is often separated by a pause (comma in writing) from the rest of the sentence. There are two types of dislocation: right dislocation, in which the constituent is postponed (as in the above example), or a left dislocation, in which it is advanced.

2. New model of dynamical dislocation in continuum

In this paper, a new model of dynamical dislocation in continuum is proposed. We start with the following definition: *Physical dislocation, in general, is any transportation of the part of material in continuum as that his mass is rigid and bounded by fictive boundary surfaces, which separate this bounded material in transportation in relation to other material in continuum.*

Each dynamical dislocation, in sense of previous definition, has kinetic and geometrical parameters. Dislocation has boundary surfaces, inside of boundary surface is core in different forms, surface and point contacts with around material of continuum a known or no known two displacements by which is defined dynamics and kinetic parameters of dynamical dislocation. In continuum is possible to appear one or more dislocations.

Presented, in Figure 1, model of the dynamical dislocation does not cause increase in numbers of degrees of freedom. Presented model of dislocation in the continuum be accepted, not as a model of dynamical dislocation but also as a dynamical actuator of continuum excitation or as a dynamical sensor for of displacement in continuum. Also, appearance of dynamical dislocation model in continuum is element for obtaining a stress concentration in material around dynamical dislocation.

3. Oscillations in plate with layer containing distributed dynamical dislocations

Let us consider an element of the thin plate with continuum layer containing, in parallel positions, continually distributed discrete dislocation elements in the continuum material as it is presented in Figure 1. a*, b* and c*. Material plate is visco-elastic and homogeneous. Denotation of the displacement $w(x, y, t)$ is visible in Figure 1.c*. We propose that oscillatory waves in the plate and in the layer containing dislocations are in plate surface and that other dislocations are not present. By using denotation presented in Figure 1.a*, b* and c* we can derive the partial differential equations with corresponding

initial, boundary and conditions of the continuity and generalized forces of interactions between dynamical dislocations distributed in layer [4,5,6].

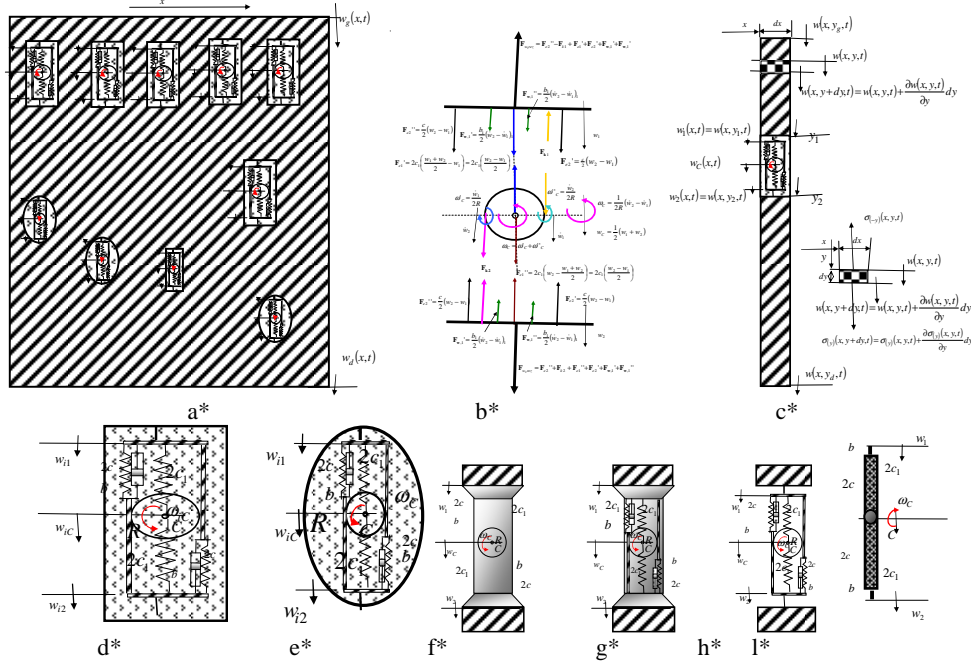


Figure 1. **a*** Model of dynamic dislocations in continuum (plate). **d*** and **e*** two models of elementary dynamic dislocations. **b*** Decomposition of the standard visco-elastic rolling element with properties of inertia translation and inertia rotation: Forces of dynamical interaction between decomposed parts. **f***, **g*** and **h*** experimental pivots of material with dynamic dislocation with visco-elastic and translator and rotator inertia properties and **i*** a standard visco-elastic element with translator and rotator inertia properties. **c*** an elementary part of plate with layer consisting by distributed dynamical dislocation in the form **d*** and decomposition **b***.

Constitutive stress strain relation between normal stress $\sigma_{(y)}(x, y, t)$ and strain ε_y in y direction for ideally visco-elastic plate material is: $\sigma_y = E\varepsilon_y + \mu\dot{\varepsilon}_y$. Partial differential equation of waves in y direction is [1,2,6,7]:

$$\frac{\partial^2 w(x, y, t)}{\partial t^2} = c_0^2 \frac{\partial^2 w(x, y, t)}{\partial y^2} + \frac{\mu}{\rho} \frac{\partial^3 w(x, y, t)}{\partial y^2 \partial t} \quad \text{for } y_g \leq y \leq y_1 \quad \text{and for } y_2 \leq y \leq y_d, \quad (1)$$

where $c_0^2 = \frac{E}{\rho}$. Conditions of the compatibility and continuity between plate continuum and dynamical dislocations in the layer are [6,7,4]: $w_1(x, t) = w(x, y_1, t)$, $w_2(x, t) = w(x, y_2, t)$

$$\left\langle \frac{\partial w(x, y, t)}{\partial y} + \frac{\mu}{E} \frac{\partial^2 w(x, y, t)}{\partial y \partial t} \right\rangle_{y=y_i} = \pm \frac{1}{Ea\delta} \left\{ - \left\langle \frac{d}{dt} \frac{\partial \mathbf{E}_{x, dist}}{\partial w_i(x, t)} - \frac{\partial \mathbf{E}_{x, dist}}{\partial w_i(x, t)} \right\rangle - \frac{\partial \mathbf{E}_{p, dist}}{\partial w_i(x, t)} - \frac{\partial \Phi_{dist}}{\partial w_i(x, t)} \right\}, i=1,2 \quad (2)$$

Boundary conditions of the plate can be different, but in this example, we take into account that ends of the plate are free of the forces, and we can write:

$$F_{1g,d}(x, y_{g,d}, t) = \sigma_{(-y)}(x, y_{g,d}, t) \delta x = \mp \left\langle E \frac{\partial w(x, y, t)}{\partial y} + \mu \frac{\partial^2 w(x, y, t)}{\partial y \partial t} \right\rangle_{y=y_{g,d}} \delta x = 0 \quad (3)$$

Initial conditions of the plate we take as a kinetic state at initial moment starting mathematical description of the waves in plate by initial displacements and velocities.

Characteristic equation of the oscillatory dynamics in plate with layer containing distributed parallel dynamical dislocations is in the form [6,7]:

$$\Delta(\lambda) = \begin{vmatrix} 0 & -\lambda \sin \lambda + \lambda \cos \lambda & \lambda \cos \lambda \\ \left\langle \lambda \sin \kappa_1 \lambda + \left(\lambda^2 E^2 \kappa_m \left(1 - \frac{i_c^2}{R^2} \right) - \frac{c E y_d}{a \delta} \right) \cos \kappa_1 \lambda \right\rangle & \left\langle \lambda^2 E^2 \kappa_m \left(1 + \frac{i_c^2}{R^2} \right) + \frac{c E y_d}{a \delta} \right\rangle \cos \kappa_2 \lambda & \left\langle \lambda^2 E^2 \kappa_m \left(1 + \frac{i_c^2}{R^2} \right) + \frac{c E y_d}{a \delta} \right\rangle \sin \kappa_2 \lambda \\ \left\langle \lambda \sin \kappa_1 \lambda + \left(\lambda^2 E^2 \kappa_m \left(1 + \frac{i_c^2}{R^2} \right) - \frac{c E}{a \delta} \right) \cos \kappa_1 \lambda \right\rangle & \left\langle \lambda^2 E^2 \kappa_m \left(1 - \frac{i_c^2}{R^2} \right) + \frac{c E}{a \delta} \right\rangle \cos \kappa_2 \lambda & \left\langle \lambda^2 E^2 \kappa_m \left(1 - \frac{i_c^2}{R^2} \right) + \frac{c E}{a \delta} \right\rangle \sin \kappa_2 \lambda \end{vmatrix} = 0 \quad (4)$$

By introducing roots of the previous characteristic equation, we obtain infinite set of the characteristic numbers and corresponding eigen amplitude functions and time functions, and oscillatory displacement of the plate parts we obtain in the forms [7.7]:

$$w(x, y, t) = \sum_{s=1}^{\infty} e^{-\delta_s t} C_{1s}(x) \langle A \cos p_{0s} t + B \sin p_{0s} t \rangle \cos k_s y \quad \text{for } y_g \leq y \leq y_1 \quad (11)$$

$$w(x, y, t) = \sum_{s=1}^{\infty} e^{-\delta_s t} \langle A \cos p_{0s} t + B \sin p_{0s} t \rangle [C_{3s}(x) \cos k_s y + C_{4s}(x) \sin k_s y], \quad \text{for } y_2 \leq y \leq y_d, \quad (12)$$

where $\omega_{0s}^2 = k_s^2 c_0^2$, $k_s^2 \frac{\mu}{\rho} = 2\delta_s$, $p_{0s} = \sqrt{\omega_{0s}^2 - \delta_s^2}$.

4. Concluding remarks

Condition for existing visco-elastic plane oscillatory process in plate with layer containing distributed dynamical dislocations with constant characteristic numbers are compatibility between visco-elastic properties of plate and model of dislocations: $\frac{\mu}{E} = \frac{b}{c}$.

Acknowledgement. Parts of this research were supported by the Ministry of Sciences of Republic Serbia through Mathematical Institute SANU Belgrade Grants OI 174001 "Dynamics of hybrid systems with complex structures. Mechanics of materials", and Faculty of Mechanical Engineering University of Niš.

5. References

- [1] Goroško O. A. i Hedrih (Stevanović) K., *Analitička dinamika (mehanika) diskretnih naslednih sistema*, (Analytical Dynamics (Mechanics) of Discrete Hereditary Systems), University of Niš, 2001, Monograph, p. 426, YU ISBN 86-7181-054-2.
- [2] Hedrih (Stevanović) K., The Dissipation Function of a Nonconservative System of Mass Particles, Tensor, N.S., Vol.63, No.2(2002), pp.176-186. Tensor Society, Japan.
- [3] Hedrih (Stevanović) K., (2008), Energy interaction between linear and nonlinear oscillators (Energy transient through the subsystems in the hybrid system), ISSN 1027-3190. Ukr. mat. Ţurn., 2008, t. 60, # 6, pp. 796-814.
- [4] Hedrih (Stevanović) K., (2008), Dynamics of coupled systems, Nonlinear Analysis: Hybrid Systems, Volume 2, Issue 2, June 2008, Pages 310-334.
- [5] Hedrih (Stevanović) K., (2004), *Discrete Continuum Method*, COMPUTATIONAL MECHANICS, WCCM VI in conjunction with APCOM'04, Sept. 5-10, 2004, Beijing, China, © 2004 Tsinghua University Press & Springer-Verlag, pp. 1-11, CD. IACAM Int. Association for Computational Mechanics – www.iacm.info
- [6] Katica (Stevanović) Hedrih, (2006), The frequency equation theorems of small oscillations of a hybrid system containing coupled discrete and continuous subsystems, Facta Universitatis, Series Mechanics, Automatic Control and Robotics, Vol.5, No 1, 2006 pp. 25 - 41 <http://facta.junis.ni.ac.rs/facta/> ISSN 0354 – 2009
- [7] Hedrih (Stevanović) K., (2003), Frequency equations of small oscillations mixed systems of the coupled discrete and continuous subsystems, Mehanika tverdogo tela (Rigid Body Mechanics, Donetsk, UDC 531.1:534.012:534.013; ISSN 0321-1975, vip. 33, pp. 174-189.

AVALANCHES IN THE FRACTURE PROCESS ZONE

P.C. Houlis, A.V. Dyskin

Deep Exploration Technologies Cooperative Research Centre, School of Civil and Resource Engineering, M051, University of Western Australia, 35 Stirling Hwy, Crawley, WA, 6009, Australia
e-mail: pantazis.houlis@uwa.edu.au

Abstract. We investigate damage accumulation in the fracture process zone using the fibre bundle model. The fibres are modelled as springs with a constant stiffness and randomly and independently assigned strengths. The simulations were conducted for uniformly distributed strengths for 300 and 1000 fibres. We found that the value of the normalised deformation modulus with respect to the normalised fibre stiffness controls the process of fibre breakage. The high values of the modulus (equal load sharing) lead to distributed accumulation of broken fibres and relatively low loads of full failure. Low values of the modulus (near neighbour load sharing) lead to clustering of broken fibres, generation of large avalanches and the increase in the ultimate failure load.

1. Introduction

Fracture propagation in brittle heterogeneous materials involves the development of a fracture process zone where the material undergoes transition from the intact to fully damaged states [1]. Amongst possible models of damage accumulation in heterogeneous materials, attractive are the fibre bundle models, which represent the accumulation of local damage in a heterogeneous material prior the ultimate failure as successive breakage of some fibres. The fibres simulate the spatial variability of local strength of the heterogeneous material. Each fibre, in the simplest case, is considered as an elastic spring stretched under the applied force. After loading to a certain limiting force (strength), the fibre breaks and does not offer any resistance to the force. The material heterogeneity is modelled by introducing random distributions of fibre strengths. Usually the uniform or Weibull distributions are used to characterise the strength variability and the fibre strengths are assigned independently.

Here we use a 2D version of the fibre bundle model to simulate the damage accumulation in the fracture process zone. While the fibre strengths are independent, the forces they are acted upon depend upon the numbers and positions of broken fibres. This was investigated previously by modelling the crack as an infinite fibre bundle layer between two elastic beams [2] or semi-planes [3]. In modelling the fracture process zone there is another important factor – the positions of broken fibres with respect to the tip of the fracture process zone. This factor is investigated in the present paper.

2. Fibre bundle model of the process zone

Consider a semi-infinite crack in an isotropic plane with a process zone of length L consisting of a bunch of elastic fibres, Fig. 1. Fibres are considered to be located at equal step r . Uniform tractions p are applied to the crack faces over the process zone length.

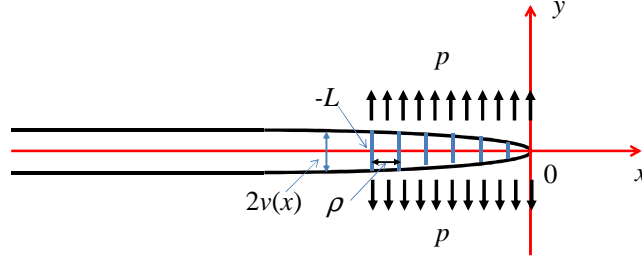


Figure 1. Fibre bundle model of a fracture process zone.

A fibre situated at a point t of the x -axis applies a pair of forces to the opposite faces of the crack. If the magnitude of this force is P , its contribution to the crack opening is [4]:

$$2v_f(x,t) = \frac{1}{E'} G^*(x,t) P, G^*(x,t) = \frac{8}{\pi} \begin{cases} \tanh^{-1} \sqrt{|x|/t} & -t < x \leq 0 \\ \coth^{-1} \sqrt{|x|/t} & x < -t \end{cases} \quad (1)$$

Here for the plane-strain approximation, $E' = E/(1-\nu^2)$, E , ν are the Young's modulus and Poisson's ratio of the material.

We now compute the displacement of the fibre located at point x_m by summing the opening displacement created at a point x_m by all fibres located at points x_n and the opening displacement $2v_0(x_m)$ created by tractions p [4]

$$2v_0(x) = \frac{1}{E'} Q(x,L) p, Q(x,L) = \frac{8L}{\pi} \left[\sqrt{\frac{|x|}{L}} + \left(1 + \frac{x}{L}\right) \begin{cases} \tanh^{-1} \sqrt{|x|/L} & -L < x \leq 0 \\ \coth^{-1} \sqrt{|x|/L} & x < -L \end{cases} \right] \quad (2)$$

Thus for the equilibrium of the upper face at point x_n we have

$$P(x_n) = -k v_n f_n, f_n = \Theta(s_n - 2v_n k) \quad (3)$$

Here k is the fibre stiffness, s_1, \dots, s_N are the (randomly assigned) fibre strengths and $\Theta(s)$ is the Heaviside function. Factor $f_n = 1$ if n^{th} fibre is intact, otherwise it is zero.

The stretch of the fibre located at point x_m consists of the displacement $2v_0(x_m)$ and the total displacement produced by all other fibres leading to the following linear system:

$$v_m + A \sum_{\substack{n=1 \\ n \neq m}}^N f_n v_n G^*(x_m, x_n) = Q(x_m, L) p, \quad A = k/E', \quad m = 1, \dots, N \quad (4)$$

3. Computer simulations

The computer simulations consist of steady increase in load p stepwise. At each step the broken fibres are identified and removed from the computations. The simulations are carried out until all the fibres are broken. In order to avoid the step dependence, we use variable steps; the step value is the minimal one that ensures that a new fibre is broken. The fibre is then removed and (4) is solved. The new distribution of displacements can cause

new fibres to break; these are removed as well. The process is repeated until all fibres that can be broken under the current load p are broken (avalanches can be generated in the process). Then a new load step and new value of p are calculated.

We use uniform strength distribution in interval $(0, 1)$. Thus all force variables are normalised by the maximum fibre strength. We also choose $L=1$ such that all length variables are normalised by the process zone length. We use the dimensionless stiffness (stiffness normalised by the maximum fibre strength and the process zone length) $k=0.1$ and the dimensionless values of the modulus $E \in 10, 100, 10^3, 10^8$.

Since the opening displacement at the crack tip is zero, the displacement in the fibre closest to the tip depends upon the distance to it and hence upon the number of fibres. In order to avoid this dependence we characterise the process zone failure as the load p_{\max} required to break 90% of all fibres. Figure 2 shows the dependence of p_{\max} on the deformation modulus E for the numbers of fibres $N=300$ and $N=1000$. It is seen that p_{\max} is independent of the number of fibres. It is also seen that increase in the modulus leads to increase in the failure load. This can be interpreted in the following way. Let us split the length of the process zone into short intervals such that the load on the fibres within each interval can approximately be considered as uniform. (This can always be done for the intervals not very close to the crack tip.) Then the high modulus means that the broken fibres redistribute the load almost equally to the other fibres within that interval. Thus the high modulus corresponds to the equal load sharing model [5] applied independently to each interval. Decreasing the modulus leads to the increased influence of the elastic redistribution of the load after a fibre is broken. In particular, higher load is applied to the neighbouring fibres (near neighbour load sharing). This leads to clustering of the broken fibres and hence to the decrease in the full breakage load.

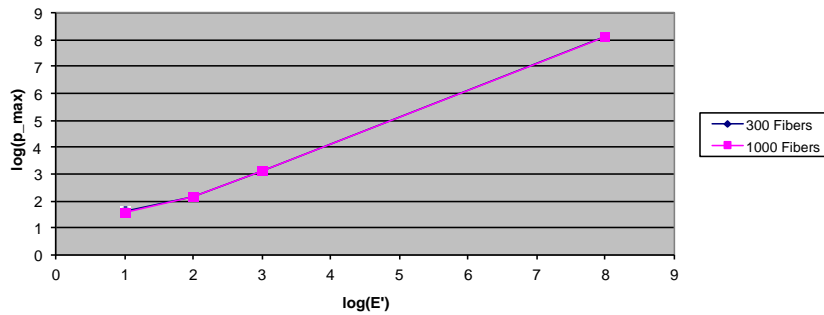


Figure 2. The load of breakage of 90% of fibres vs. the deformation modulus for different numbers of fibres.

We now investigate the values of applied load needed to break a certain fraction of fibres. The fractions of fibres broken in the simulations are split into intervals $(0-0.1)$, $(0.1-0.2)$, ..., $(0.8-0.9)$. Within each interval we compute the mean value of the loads p that produced the fractions of broken fibres within each interval. These values normalised by the maximum loads, p_{\max} , are shown in Figure 3. The picture gives further distinctions between the equal load sharing and the near neighbour load sharing (elastic interaction) cases. Firstly, low values of the modulus (near neighbour load sharing) produce large avalanches (indicated by ovals), which are the rapid increase in the fractions of broken fibres without

any appreciable increase in the load. Also, in the equal load sharing the main fibre failures occur in the beginning of the loading process, while in the near neighbour load sharing.

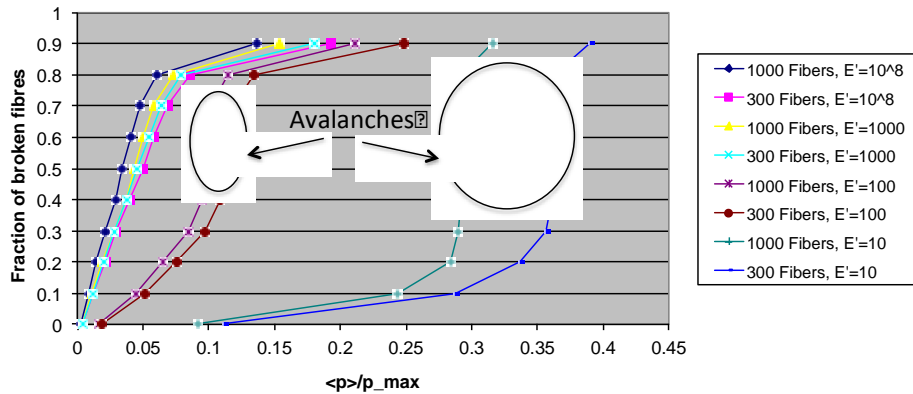


Figure 3. Average values of load p needed to break certain fractions of fibres.

4. Conclusions

The fibre bundle model of the fracture process zone shows that the values of the deformation modulus of the material as compared to the normalised fibre stiffness considerably influence the process of damage accumulation. When the material is stiff, the load supported by the broken fibres gets redistributed equally between all fibres. This produces relatively dispersed damage (broken fibre) accumulation without clustering and avalanches until the load is close to the total failure. Opposite to this, low stiffness of the material leads to increasing effect of elastic stress redistribution with the emphasis on the overloading the fibres near to the broken one. This leads to the reduction in the total failure load and the development of large avalanches.

Acknowledgement. The work has been supported by the Deep Exploration Technologies Cooperative Research Centre whose activities are funded by the Australian Government's Cooperative Research Centre Programme. This is DET CRC Document 2012/001. We also acknowledge the support from ExxonMobil.

References

- [1] Hillerborg, A. 1983. Analysis of one single crack. In: *Fracture Mechanics of Concrete*, F.H. Wittmann (ed.), Elsevier, Amsterdam, pp. 223-249.
- [2] Delaplace, A., S. Roux and G. Pijaudier-Cabot, 2001. Avalanche statistics of interface crack propagation in fiber bundle model - Characterization of Cohesive Crack. *Journal of Engineering Mechanics*, 127, pp. 646-652.
- [3] Delaplace, A., S. Roux and G. Pijaudier-Cabot, 2003. Study of avalanches during the fracture of discrete models. *Engineering Fracture Mechanics* 70, pp. 943-955.
- [4] Tada, H., P. Paris and G. Irwin, 1985, *The Stress Analysis of Cracks Handbook*, Paris Productions.
- [5] Sornette, D. 2000, *Critical Phenomena in Natural Sciences: chaos, fractals, self-organization, and disorder: concepts and tools*, Springer-Verlag Berlin Heidelberg, New York.

EMI SHIELDING SIMULATION OF CNT-EPOXY FILM COATED MORTAR PANELS

Y.Y. Hwang¹, B.J. Yang¹, H.K. Lee^{1*}

¹Department of Civil and Environmental Engineering,
Korea Advanced Institute of Science and Technology, Guseong-dong,
Yuseong-gu, Daejeon 305-701,
South Korea
e-mail: hyn1014@kaist.ac.kr, bumjoo@kaist.ac.kr, leeh@kaist.ac.kr*

Abstract. The CNT-epoxy coat was applied on mortar panels to shield electromagnetic waves originated from the outside in our previous study [1]. Electromagnetic interference (EMI) shielding effectiveness (SE) of CNT-epoxy coated mortar panels is numerically investigated in the present study. The commercial program HFSS (High Frequency Structure Simulator) [2] is used to simulate the EMI shielding performance of the mortar panels. The numerically obtained S-parameters of each specimen are compared with experimental data reported by [1] to assess the potential of proposed framework. Furthermore, the effect of detachment between mortar and CNT-epoxy film on the EMI shielding effectiveness of the panel specimen is addressed.

1. Introduction

During the past few years, the growth in the use of electronic devices has resulted in a high volume of electromagnetic waves in residential and work area [3]. The unintended electromagnetic emissions have caused significant electromagnetic interference problems [4], thus electromagnetic interference (EMI) shielding performance of construction materials has been brought attention especially at the medical and military fields which require high degree of accuracy for using precise electronic devices [1]. Due to the impetus for the development of electromagnetic shield techniques, various kinds of construction materials have been investigated to satisfy both site application and EMI shielding performance [1,5]. In addition, numerical or analytical formulations to predict the EMI shielding effectiveness (SE) of construction materials have been studied.

This study focuses on the simulation of EMI shielding performance of carbon nanotube (CNT)-epoxy film coated mortar panels. The simulation is based on a finite element (FE) program, which has been proven to be an effective and promising method for frequency-domain analysis of volumetric structures [6]. The commercial FE program HFSS (High Frequency Structure Simulator) [2] used for electromagnetic field simulation is used here to analyze EMI shielding performance of CNT-epoxy film coated mortar panels. Appropriate properties of the CNT-epoxy film are determined in accordance with experimental data of [1]. With the determined properties, predictions of the EMI shielding performance on the panels considering various film thicknesses are conducted. In addition, the effect of detachment between the CNT-epoxy film and mortar on the EMI shielding performance is investigated.

2. Theoretical backgrounds

2.1. Electromagnetic wave shielding mechanism

When electromagnetic waves pass through a material, absorption, reflection and transmission of wave occurs coincidentally. Among those phenomena, EMI shielding performance of a material is based on the absorption and reflection ability. During the absorption, electromagnetic waves lose their energy while passing through the shielding material and the lost energy usually transformed to heat energy [7]. The reflection can be divided into external and internal reflections according to the reflecting side of a shielding material. The discontinuity of the impedance at the boundary of shielding material and air causes the reflection of electromagnetic waves [7].

2.2. S-parameter

S-parameter (scattering parameter) is an indicator for the EMI shielding ability of a shielding material [3]. S-parameter is the ratio between output and input voltage in complex number and generally expressed in dB scale. When the wave port j radiates electromagnetic waves, the port i receives the waves. The S-parameter of this system can be written as [3]

$$S_{ij} = \alpha + \beta j \quad (1)$$

or

$$S_{ij}(dB) = 20 \times \log \left(\frac{V_i}{V_j} \right) = 20 \times \log(\sqrt{\alpha^2 + \beta^2}) \quad (2)$$

In Eqs. (1) and (2), α and β are real and imaginary parts of the S-parameter, respectively, and V_i is the voltage receiving at the port i and V_j is the voltage of an incident wave at the radiating port j .

3. Numerical analysis

The commercial program HFSS (High Frequency Structure Simulator, 2008) [2] is used as a simulation tool to predict EMI SE of CNT-epoxy film coated mortar panels. The material properties of CNT-epoxy film coated mortar panels are determined according to Nam et al. (2011) [1]. Two different types of specimen groups (Group A and Group B) are considered. Group A consists of specimens having thicknesses 0.1, 0.2, 0.3, 0.4 and 0.5 mm, while Group B consists of specimens having thicknesses 0.5, 1.0, 1.5, 2.0 and 2.5 mm, as shown in Figs. 1 and 2.

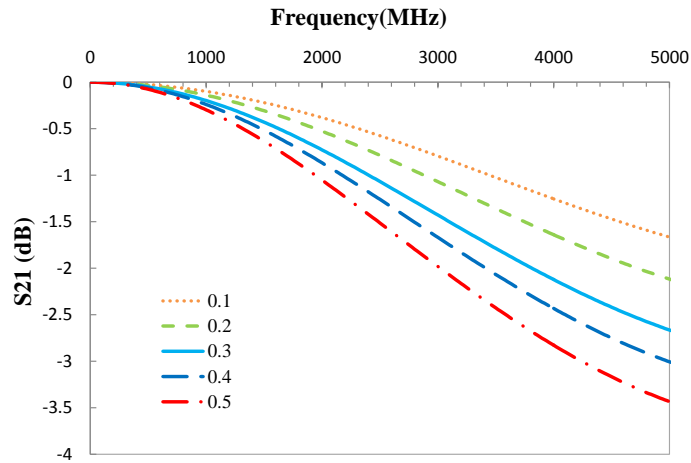


Figure 1. S-parameters for Group A

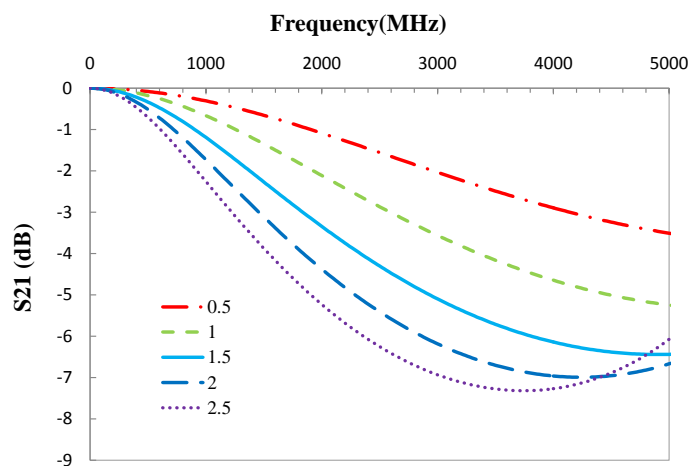


Figure 2. S-parameters for Group B

The detachment between the mortar panel and the CNT-epoxy film is also modeled to examine the influence of the detachment on CNT-epoxy film coated mortar panels. As shown in Fig. 3, three detachment cases (0.04, 0.08 and 0.12mm) are considered and simulated. Details of the EMI shielding simulation of CNT-epoxy film coated mortar panels and influences of the detachment on the EMI shielding performance can be found in [8].

The effect of cracks in CNT-epoxy film on the EMI shielding effectiveness of the panel specimens will be investigated in the future.

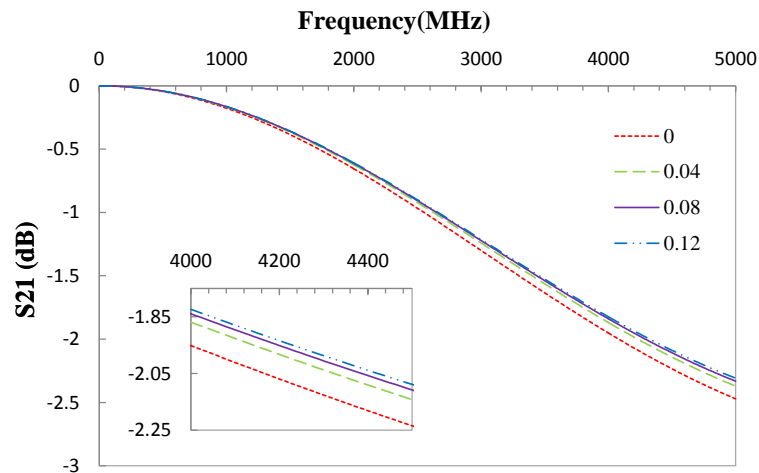


Figure 3. S-parameters for detachment case

Acknowledgement. This research was supported by grants from the Construction Technology Innovation Program (11CCTI-B050520-04-000000) and the U-City Master and Doctor Course Grant Program (07High Tech A01) funded by the Ministry of Land, Transportation and Maritime Affairs of the Korean government.

References

- [1] Nam, I.W., Lee, H.K., and Jang, J.H. (2011). "Electromagnetic interference shielding/absorbing characteristics of CNT-embedded epoxy composites," *Composites Part A: Applied Science & Manufacturing*, Vol. 42, Issue 9, pp. 1110-1118.
- [2] HFSS. (2008): High Frequency Structure Simulation, Ansoft Inc.
- [3] Kwon, S.H. and Lee, H.K. (2009), "A computational approach to investigate electromagnetic shielding effectiveness of steel fiber-reinforced mortar," *CMC: Computers, Materials, & Continua*, **12**, 197-222
- [4] Kwon, S.H., Kim, B.R. and Lee, H.K. (2011), "Electromagnetic shielding effectiveness of grid-mesh films made of polyaniline: a numerical approach," *CMC: Computers, Materials, & Continua*, **21**, 65-86
- [5] Karim, N., Mao, J. and Fan, J. (2010), "Improving electromagnetic compatibility performance of packages and SiP modules using a conformal shielding solution," *2010 Asia-Pacific International Symposium on Electromagnetic Compatibility*, Beijing, China
- [6] Wang, R., Gao, Y., Shi, D. and Shen, Y. (2009), "Application of the transmission line method to the shielding effectiveness with incident wave of arbitrary polarization," *5th Asia-Pacific Conference on Environmental Electromagnetics*, Beijing, China
- [7] Hemming LH. Architectural electromagnetic shielding handbook: a design and specification guide. New York: Institute of Electrical and Electronics Engineers; 1992.
- [8] Hwang, Y.Y., Yang, B.J., and Lee, H.K. (2012), "Predictions for the investigation of the EMI shielding effectiveness of CNT embedded epoxy films", in preparation.

ON ANISOTROPIC ELASTICITY DAMAGE MECHANICS

J. Jarić¹, D. Kuzmanović², D. Šumarac³

Abstract. The anisotropic elasticity damage mechanics is presented within the framework of the classical theory of elasticity. Starting from the principle of strain equivalence, damage tensor components are derived in terms of elastic parameters of undamaged (virgin) material in closed form solution. The procedure was applied for several symmetries that are important for applications.

¹ University of Belgrade, Faculty of mathematics, e-mail: jovojaric@yahoo.com

² Faculty of Transport and Traffic Engineering, e-mail: d.kuzmanovic@sf.bg.ac.rs

³ Faculty of Civil Engineering, e-mail: sumi@eunet.rs

1. Introduction

In most of the existing damage theories, the damaged elastic strain-stress (or stress-strain) response is formulated by using the notion of effective stress (strain) and the hypothesis of strain (stress) equivalence or stress-energy (strain-energy) equivalence (Lemaitre and Chaboche, 1985 [1], Voyiadjis and Kattan, 2006 [2]).

The damage variable (or tensor), based on the effective stress concept, represents average material degradation which reflects the various types of damage at the micro-scale level like nucleation and growth of voids, cracks, cavities, micro-cracks, and other microscopic defects.

The effective stress $\tilde{\sigma}$ is the stress tensor to be applied to a virgin representative volume element in order to obtain the same elastic strain tensor, ϵ^e , produced by applying the actual stress tensor σ , to the damage volume element. Because the same elastic strain is considered in both damaged and undamaged materials, that strain is considered to be the equivalent strain.

By this definition often called the principle of strain equivalence, the actual stress and effective stress satisfy the equations:

$$\sigma_{ij} = C_{ijkl} \epsilon_{kl}^e, \quad \tilde{\sigma}_{ij} = C_{ijkl} \epsilon_{kl}^e. \quad (1)$$

In the virgin state, even in the most general case of anisotropy, there are only 21 independent elements of the fourth-order elastic modulus tensor \mathbf{C} as a result of general symmetry requirements

$$C_{ijkl} = C_{jikl} = C_{ijlk} = C_{klij}, \quad (2)$$

where the first three results from the symmetry of the stress and strain tensors and the last from the existence of a strain energy function. The symmetry of \mathbf{C} in (2) applied to \mathbb{C} as well and dictates a maximum of 21 independent elements.

Following Caivin and Testa (1999) [3], it can be shown that

$$\sigma_{ij} = \mathbb{R}_{ijkl} \tilde{\sigma}_{kl}, \quad (3)$$

where the fourth-order tensor \mathbb{R} possess symmetry in successive pairs of indices.

It can be shown that \mathbb{R} can be written in the form

$$\mathbb{R} = \mathbb{I} - \mathbb{D}, \quad (4)$$

where \mathbb{I} is the unit tensor for the set of tensors with the symmetry of \mathbb{R} is given by

$$\mathbb{I}_{ijkl} = \frac{1}{2} (\delta_{ik} \delta_{jl} + \delta_{il} \delta_{jk}). \quad (5)$$

The fourth-order tensor \mathbb{D} is known as damage tensor.

Caivin and Testa (1999) [3], have been shown that the actual number of independent damage parameters in such a tensor is related to the material and damage symmetry.

2. General consideration

From (1)-(4) one can obtain

$$\mathbb{C} = \mathbf{C} - \mathbb{D}\mathbf{C} \quad \text{or} \quad \mathbb{C}_{ijkl} = \mathbf{C}_{ijkl} - \mathbb{D}_{ijpq} \mathbf{C}_{pqkl}. \quad (6)$$

We note that

$$\mathbb{D}_{ijkl} = \mathbb{D}_{jikl} = \mathbb{D}_{ijlk} \quad (7)$$

and, in general, $\mathbb{D}_{ijkl} \neq \mathbb{D}_{klij}$. Hence, the fourth-order tensor \mathbb{D} does not possess the full symmetry of the elastic modulus tensors \mathbf{C} and \mathbb{C} , and has at most 36 independent components.

Obviously, the number of independent elements of tensor \mathbb{D} and their values are determined by the value of tensors \mathbf{C} and \mathbb{C} . We investigate that assuming that \mathbf{C} is always given, and considering (6) as a linear equation with respect to \mathbb{C} and \mathbb{D} .

First. Assume that we want to find \mathbb{C} for given \mathbb{D} . Then \mathbb{D} cannot be given arbitrary in order to find \mathbb{C} since we assume that \mathbb{C} posses major symmetry. In that case \mathbb{D} must satisfies the condition

$$\mathbb{D}\mathbf{C} = \mathbf{C}\mathbb{D}^T \quad \text{or in indices notation} \quad \mathbb{D}_{ijpq} \mathbf{C}_{pqkl} - \mathbb{D}_{klpq} \mathbf{C}_{pqij} = 0. \quad (8)$$

The symmetries in the elements of \mathbb{C} and \mathbf{C} impose, generally, 15 constraints on the elements of \mathbb{D} . Therefore, tensor \mathbb{D} can not possess more than 21 independent components.

Second. We consider that \mathbf{C} , \mathbb{C} are given and we want to find tensor \mathbb{D} . Since \mathbf{C} is positive definite there is always \mathbf{C}^{-1} such that $\mathbf{C}\mathbf{C}^{-1} = \mathbb{I}$. Thus

$$\mathbb{D} = \mathbb{I} - \mathbf{C}\mathbf{C}^{-1}. \quad (9)$$

Proposition 1 *Damage tensor \mathbb{D} , given by (9), always satisfies the constrain (8).*

Proposition 2 *The corresponding isotropy groups of tensors \mathbb{C} and \mathbb{D} are the same.*

3. Damage tensor for anisotropic body

We proceed further by applying (9) for several crystal classes under the assumption that \mathbf{C} is isotropic elasticity tensor, i.e.

$$\mathbf{C} = \lambda I \otimes I + 2\mu \mathbb{I}. \quad (10)$$

Then, Jarić et al., (2008) [4],

$$\mathbf{C}^{-1} = -\frac{\lambda}{2\mu(3\lambda + 2\mu)} I \otimes I + \frac{1}{2\mu} \mathbb{I}. \quad (11)$$

From this and (9) we obtain

$$\mathbb{D} = \mathbb{I} + \frac{\lambda}{2\mu(3\lambda + 2\mu)} \mathbf{C} I \otimes I - \frac{1}{2\mu} \mathbf{C}, \quad (12)$$

or, in componental form

$$\mathbb{D}_{ijkl} = \mathbb{I}_{ijkl} - \frac{1}{2\mu} \mathbf{C}_{ijkl} + \frac{\lambda}{2\mu(3\lambda + 2\mu)} \mathbf{C}_{ijpp} \delta_{kl}. \quad (13)$$

The term

$$\mathbb{A}_{ijkl} = \frac{\lambda}{2\mu(3\lambda + 2\mu)} \mathbf{C}_{ijpp} \delta_{kl} \quad (14)$$

does not possess major symmetry, i.e.

$$\mathbb{A}_{ijkl} \neq \mathbb{A}_{klij}, \quad (15)$$

and because of them \mathbb{D}_{ijkl} also does not possess major symmetry.

Now we are ready to apply (13) for following crystal classes defined by corresponding elasticity tensor \mathbf{C} (Srinivasan and Nigam (1969), [5]).

Orthotropic damage

$$\begin{aligned} \mathbf{C}_{ijkl} &= \lambda_1 \delta_{ij} \delta_{kl} + 2\lambda_2 \mathbb{I}_{ijkl} + \lambda_3 \alpha_i \alpha_j \alpha_k \alpha_l + \lambda_4 \beta_i \beta_j \beta_k \beta_l + \\ &+ \lambda_5 (\alpha_k \alpha_l \delta_{ij} + \alpha_i \alpha_j \delta_{kl}) + \lambda_6 (\beta_k \beta_l \delta_{ij} + \beta_i \beta_j \delta_{kl}) + \\ &+ \lambda_7 (\alpha_i \alpha_j \beta_k \beta_l + \alpha_k \alpha_l \beta_i \beta_j) + \lambda_8 (\alpha_i \alpha_k \delta_{jl} + \alpha_i \alpha_l \delta_{jk} + \alpha_j \alpha_k \delta_{il} + \alpha_j \alpha_l \delta_{ik}) + \\ &+ \lambda_9 (\beta_i \beta_k \delta_{jl} + \beta_i \beta_l \delta_{jk} + \beta_j \beta_k \delta_{il} + \beta_j \beta_l \delta_{ik}) \\ 2\mu \mathbb{D}_{ijkl} &= 2(\mu - \lambda_2) \mathbb{I}_{ijkl} + \\ &+ \left[\frac{\lambda}{3\lambda + 2\mu} (3\lambda_1 + 2\lambda_2 + \lambda_5 + \lambda_6) - \lambda_1 \right] \delta_{ij} \delta_{kl} - \lambda_3 \alpha_i \alpha_j \alpha_k \alpha_l - \lambda_4 \beta_i \beta_j \beta_k \beta_l - \\ &- \lambda_5 (\alpha_k \alpha_l \delta_{ij} + \alpha_i \alpha_j \delta_{kl}) - \lambda_6 (\beta_k \beta_l \delta_{ij} + \beta_i \beta_j \delta_{kl}) - \lambda_7 (\alpha_i \alpha_j \beta_k \beta_l + \alpha_k \alpha_l \beta_i \beta_j) - \\ &- \lambda_8 (\alpha_i \alpha_k \delta_{jl} + \alpha_i \alpha_l \delta_{jk} + \alpha_j \alpha_k \delta_{il} + \alpha_j \alpha_l \delta_{ik}) - \\ &- \lambda_9 (\beta_i \beta_k \delta_{jl} + \beta_i \beta_l \delta_{jk} + \beta_j \beta_k \delta_{il} + \beta_j \beta_l \delta_{ik}) + \\ &+ \boxed{\frac{\lambda(\lambda_3 + 3\lambda_5 + \lambda_7 + 4\lambda_8)}{3\lambda + 2\mu} \alpha_i \alpha_j \delta_{kl} + \frac{\lambda(\lambda_4 + 3\lambda_6 + \lambda_7 + 4\lambda_9)}{3\lambda + 2\mu} \beta_i \beta_j \delta_{kl}} \end{aligned}$$

Hexagonal damage

$$\begin{aligned}\mathbb{C}_{ijkl} = & \lambda_1 \delta_{ij} \delta_{kl} + 2\lambda_2 \mathbb{I}_{ijkl} + \lambda_3 n_{3i} n_{3j} n_{3k} n_{3l} + \\ & + \lambda_4 (n_{3i} n_{3j} \delta_{kl} + n_{3k} n_{3l} \delta_{ij}) + \\ & + \lambda_5 (n_{3i} n_{3k} \delta_{jl} + n_{3j} n_{3l} \delta_{jk} + n_{3i} n_{3l} \delta_{jk} + n_{3j} n_{3k} \delta_{il}).\end{aligned}$$

$$\begin{aligned}2\mu \mathbb{D}_{ijkl} = & \left[\frac{(3\lambda_1 + 2\lambda_2 + \lambda_4)}{(3\lambda + 2\mu)} - \lambda_1 \right] \delta_{ij} \delta_{kl} + 2(\mu - \lambda_2) \mathbb{I}_{ijkl} - \\ & - \lambda_4 (n_{3i} n_{3j} \delta_{kl} + n_{3k} n_{3l} \delta_{ij}) - \\ & - \lambda_5 (n_{3i} n_{3k} \delta_{jl} + n_{3j} n_{3l} \delta_{ik} + n_{3i} n_{3l} \delta_{jk} + n_{3j} n_{3k} \delta_{il}) - \\ & + \boxed{\frac{\lambda (\lambda_3 + 3\lambda_4 + 4\lambda_5)}{3\lambda + 2\mu} n_{3i} n_{3j} \delta_{kl}}.\end{aligned}$$

Notice that terms in boxes do not possess major symmetry, and so do corresponding damage tensors. **Cubic crystals**

$$\begin{aligned}\mathbb{C}_{ijkl} & = \lambda_1 \delta_{ij} \delta_{kl} + 2\lambda_2 \mathbb{I}_{ijkl} + \lambda_3 n_{\alpha i} n_{\alpha j} n_{\alpha k} n_{\alpha l}, \\ 2\mu \mathbb{D}_{ijkl} & = \frac{1}{3\lambda + 2\mu} [(2\lambda_2 + \lambda_3) - 2\mu \lambda_1] \delta_{ij} \delta_{kl} + \\ & + 2(\mu - \lambda_2) \mathbb{I}_{ijkl} - \lambda_3 n_{\alpha i} n_{\alpha j} n_{\alpha k} n_{\alpha l}.\end{aligned}$$

In this case damage tensor \mathbb{D}_{ijkl} possesses the same symmetry as tensor \mathbb{C}_{ijkl} .

Isotropic damage

$$\mathbb{C}_{ijkl} = \lambda_1 \delta_{ij} \delta_{kl} + 2\mu_1 \mathbb{I}_{ijkl}, \quad \mu \mathbb{D}_{ijkl} = \frac{\lambda \mu_1 - \lambda_1 \mu}{3\lambda + 2\mu} \delta_{ij} \delta_{kl} + (\mu - \mu_1) \mathbb{I}_{ijkl}.$$

Obviously, damage tensor \mathbb{D}_{ijkl} possesses the same symmetry as tensor \mathbb{C}_{ijkl} .

4. Conclusion

In the present paper, starting from the principle of strain equivalence, the closed forms of damaged tensors are derived for orthotropic, hexagonal, cubic and isotropic damage.

References

- [1] Lemaitre J., Chaboche, J.-L., "Mechanics of Solid Materials", Cambridge University Press, (1990).
- [2] G.Z. Voyiadjis and P.I. Kattan, "Damage Mechanics with Fabric Tensors", *Mechanics of Advanced Materials and Structures*, 13, 285-301, 2006.
- [3] Cauvin, A., and Testa, R., (1999) Damage mechanics: Basic variables in continuum theories, *International Journal of Solids and Structures*, 36, pp. 747-761.
- [4] Jarić, J., Kuzmanović, D., and Golubović, Z., "On Tensors of Elasticity", *Theoret. Appl. Mech.* Vol. 35, No. 1-3, pp. 119-136, 2008.
- [5] Srinivasan, T.P., & Nigam, S.D., *Invariant Elastic Constants for Crystals*, *J. Math. Mech.*, Vol. 19., No. 5, (1969).

PREDICTING THE LIFETIME OF FILLED ELASTOMERS UNDER INHOMOGENEOUS LOADING CONDITIONS

D. Juhre, T. Alshuth

¹Department of Simulation and Continuum Mechanics
German Institute of Rubber Technology, Eupener Str. 33, D-30519 Hannover, Germany
e-mail: daniel.juhre@dikautschuk.de

Abstract. In this work, we present some important remarks on the lifetime of complex rubber parts under multiaxial loading conditions like simple shear with rotating axis. The results from the experiment are accompanied by FE simulations, which show the lack of hyperelastic models, used for estimating the inhomogeneous stress distribution in cyclic loaded rubber parts.

1. Introduction

To predict the service life of rubber parts by means of finite element simulations it is necessary to find a unique relationship between the varying operational loads and the corresponding material behavior. In general this relationship is experimentally investigated via cyclic uniaxial tension tests with varying load amplitudes and frequencies. The results are then used for lifetime simulations of complex rubber parts. The very fact of assuming a correlation between the uniaxial material response and the multiaxial stress state in a real rubber part is daring, since experimental tests like the simple shear test with rotating axes show that the service life strongly depends on the applied load type. A further drawback comes along with the wrong choice of material models for the elastomer. In the most components highly filled elastomers are used which show a strong inelastic behavior due to material softening, hysteresis and residual strains. These effects influence the structural behavior as well as the service life of rubber parts most notably in inhomogeneous and cyclic loading conditions. Pure elastic material models (e.g. [1] and [2]) are not able to describe these effects. A material model, which is able to describe the three mentioned phenomena in filled elastomers, is the so-called MORPH (Model Of Rubber PHenomenology) model [3,4]. In this work, we want to utilize this model to compare it with hyperelastic material models (e.g. Yeoh model) to highlight the drawbacks, if we choose pure elastic models in predicting the lifetime of rubber materials.

2. Constitutive model

The MORPH model has been originally proposed by Ihlemann and Besdo [3,4] and it is based on an additional split of the Cauchy stress $\boldsymbol{\sigma}$ into three parts:

$$\boldsymbol{\sigma} = \frac{2\alpha}{J} \mathbf{b}'_{iso} + \boldsymbol{\sigma}'_Z - q(J)\mathbf{1} \quad (1)$$

wherein q is a pressure function depending on the Jacobian J , \mathbf{b}'_{iso} the deviatoric part of the isochoric left Cauchy-Green tensor, $\alpha = \hat{\alpha}(p_1, p_2, p_3, b_s)$ a function depending as well on material parameters p_1, p_2 and p_3 as on the history function b_s , which depends itself on the maximum value of the isochoric part of the equivalent left Cauchy-Green strain b_{iso}^{eq} at each material point during all loading cycles:

$$b_s(t) := \max [b_{iso}^{eq}(\tau), 0 \leq \tau \leq t] \quad (2)$$

The auxiliary stress σ_Z is computed through its time derivative:

$$\dot{\sigma} = \beta \dot{b}_{iso}^{eq} (\sigma_H - \sigma_Z) - \frac{5}{3} (\mathbf{d} : \mathbf{1}) \sigma_Z + \mathbf{d} \sigma'_Z - \sigma'_Z \mathbf{d} \quad (3)$$

wherein \mathbf{d} is the symmetric part of the rate of the deformation gradient, $\beta = \hat{\beta}(p_3, p_4, b_s)$ a function depending on the material parameters p_3 and p_4 and the history function b_s and σ_H the cladding stress defined by:

$$\sigma_H = \frac{\gamma}{J} \exp \left(p_7 \frac{b_{iso}^{eq} \dot{\mathbf{b}}_{iso}}{b_s \dot{b}_{iso}^{eq}} \right) + \frac{p_8}{J} \frac{\dot{\mathbf{b}}_{iso}}{\dot{b}_{iso}^{eq}} \quad (4)$$

with $\gamma = \hat{\gamma}(p_5, p_6, b_s)$. Hence, the MORPH model depends on 8 material parameters (p_1, \dots, p_8) . A detailed derivation of the model can be found in [4].

To compare the model with a standard hyperelastic material model, we choose the Yeoh model defined by the following strain energy function:

$$W = p_1 (I_1 - 3) + p_2 (I_1 - 3)^2 + p_3 (I_1 - 3)^3 + q(J) \mathbf{1} \quad (5)$$

Both models are fitted to a uniaxial tension test for a filled natural rubber (see Fig. 2). The resulting material parameters are summarized in Tab. 1.

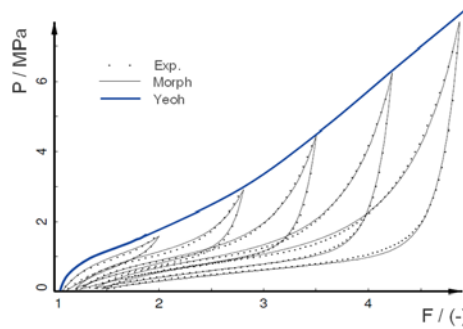


Figure 2: Fitting of Yeoh and MORPH model to experimental data

Material model	Material parameters							
	p1	p2	p3	p4	p5	p6	p7	p8
Yeoh	0.739	-0.019	0.136					
MORPH	0.062	0.364	0.219	3.09	0.00846	5.92	5.70	0.201

Table 1: Material parameters for Yeoh and MORPH model

3. Simple shear with rotating axes

A conclusive evidence for the inappropriate choice of a hyperelastic material model for predicting the lifetime of rubber material is shown by investigating a new experimental approach considering simple shear with rotating axes. The test rig for realizing the exceptional load type is drafted in Fig. 3. It consists of three parts, whereby, during a measurement, the outer parts are fixed in their position. The middle part has a degree of freedom in radial direction. For an experiment, two rotationally symmetric rubber samples are clamped into the rig in a double-sandwich-arrangement, each between one outer and the middle part. The experiment is initiated by the radial displacement of the middle part. Thus, a simple shear deformation is initiated in the samples leading to a radial force F_R . The geometry of the samples is optimized in such a way, that simple shear is the predominating deformation throughout the whole volume. At the same time, the maximum load is located within the sample, far away from surfaces and contact areas, so that a failure is most probable in the interior. After initiating the simple shear deformation, one of the shafts of the outer parts is rotated to start a simple shear deformation with rotating axes. For inelastic materials, the middle part would move sideways due to energy-dissipation, as shown in the third image of Fig. 3. If it is restricted (fourth image in Fig. 3), a resulting circumferential force F_U can be measured instead.

Fig. 4a shows the results of a long time fatigue experiment with the experimental rig, whereby the radial force F_R and the circumferential force F_U during the experiment are plot against the revolutions with a frequency of 1.5 Hz. The experiment has been carried out till failure of one of the samples in the double-sandwich-arrangement. During the first 10000 cycles, stress softening effects can be observed in the curve progression of the two measured forces. The material becomes weaker and both forces decrease in the course of the experiment. Due to the work done by the circumferential force F_U , the samples have a finite lifetime accompanied by an abrupt decrease of the resulting forces.

For simulating this loading type we apply at first a shear load on the sample and afterwards we let rotate the lower and upper surface within one revolution. The resulting forces are plotted in Fig. 4b. By using the MORPH model (solid lines) we get the characteristic progress of the resulting forces F_R and F_U . The magnitude of the values as well as the decreasing of the forces during the first revolution reflect very well the real material behavior as shown in Fig. 4. Since the test rig is fixed in longitudinal direction, the specimen cannot compensate the large shearing deformation thus, an additional positive force F_A in the axial direction is induced. This force cannot be measured with the test rig in

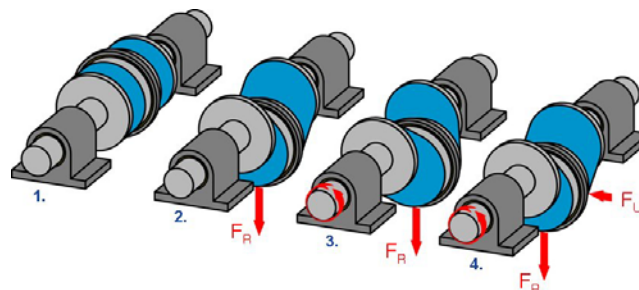


Figure 3: Sketch of the test rig.

its current state, but a modification of the machine concerning this point is in progress. By using the above fitted material models, the magnitude of the axial force is a fifth of the radial force. The ratio generally depends on the type of material. By using a hyperelastic material model like the Yeoh model the resulting forces are captured only partially. The radial force F_R and the axial force F_A can be modeled unless the decrease of both forces during the revolution is not reproduced. Obviously, this is an inelastic effect coming from material softening (Mullins effect). Even worse is the fact that the circumferential force F_U cannot be displayed at all, since it is a force generated by inelastic phenomena, too. If we now want to predict the lifetime of the specimen utilizing a hyperelastic material model, the missing circumferential force in the system leads to a misleading prediction. In the worst case, it results in an infinite lifetime prediction, which is definitely unphysical.

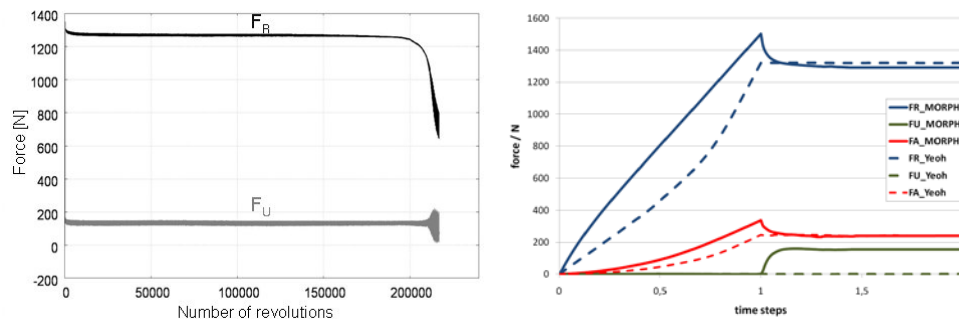


Figure 4: a) Lifetime test with the new test rig: measurement of reaction forces F_R and F_U until material failure. b) Reaction forces F_R , F_U and F_A from FE simulations using MORPH and Yeoh model.

5. Conclusion

In this work, we have presented a new test rig for applying simple shear with rotating axes. Due to these loading conditions, a finite lifetime of filled elastomers can be achieved. However, by simulating this experiment using a hyperelastic material model for the elastomer, no feasible measure can be evaluated, which correlates to the finite lifetime. In case of using the MORPH model, it is possible to analyze the occurring circumferential force and correlate it to the finite lifetime of the elastomer.

References

- [1] Ogden, R. W. (1972). Large Deformation Isotropic Elasticity - On the Correlation of Theory and Experiment for Incompressible Rubberlike Solids, Proc. of the Royal Society of London. Series A, Mathematical and Physical Sciences 326, pp. 565-584.
- [2] Yeoh, O. H. (1993). Some forms of the strain energy function for rubber, Rubber Chemistry and Technology, 66, pp. 754-771.
- [3] Besdo, D. and Ihlemann, J. (2003). A phenomenological constitutive model for rubberlike materials and its numerical applications, International Journal of Plasticity 19, pp. 1019-1036
- [4] Ihlemann, J. (2003). Kontinuumsmechanische Nachbildung hochbelasteter technischer Gummiwerkstoffe. Duesseldorf: VDI.

A FINITE ELEMENT CALCULATION OF STRESS INTENSITY FACTORS IN STRUCTURES WITH MULTI-SITE DAMAGE (MSD)

G. Kastratović¹, A. Grbović², N. Vidanović³, B. Rašuo⁴

¹Faculty of Transport and Traffic Engineering,
The University of Belgrade, ul. Vojvode Stepe 305 11000 Belgrade, Serbia
e-mail: g.kastratovic@sf.bg.ac.rs

²Faculty of Mechanical Engineering,
The University of Belgrade, Kraljice Marije 16, 11120 Belgrade 35, Serbia
e-mail: agrbovic@mas.bg.ac.rs

³Faculty of Transport and Traffic Engineering,
The University of Belgrade, ul. Vojvode Stepe 305 11000 Belgrade, Serbia
e-mail: n.vidanovic@sf.bg.ac.rs

⁴Faculty of Mechanical Engineering,
The University of Belgrade, Kraljice Marije 16, 11120 Belgrade 35, Serbia
e-mail: brasuo@mas.bg.ac.rs

Abstract. The prediction of crack-growth rate, residual strength and fatigue life in the presence of multiple site damage (MSD), requires accurate calculation of the Stress Intensity Factors (SIFs) at each crack tip. The problem becomes more difficult when crack propagation has to be treated and therefore successive calculations are required. This paper describes the estimation of SIFs for typical aero structural configuration by easy-to-use approximate procedure, which is based on the principle of superposition [1]. The results obtained by proposed procedure were compared against values obtained by software for finite element analysis (FEA). Relationship between crack length and SIFs during crack growth was calculated in FRANC2D software, which is well known for its high accuracy. The comparison of the results has shown that solutions obtained by proposed method can be used for the SIFs predictions with acceptable accuracy.

1. Introduction

Multiple site damage (MSD) represents the simultaneous development of fatigue cracks at multiple sites in the same structural element. It became crucial investigation issue since the Aloha accident in 1988 [2, 3]. Many studies and analyses of this phenomenon have been carried out in recent decades. Overviews on analytical methods for MSD are provided in many scientific papers, such as [4]. But, the prediction of crack growth rate and residual strength of cracked structure demands accurate calculation of stress intensity factors. There are some available solutions, but only for simple geometry configurations [5]. However, there are no available analytical methods for SIFs calculations at the crack tips in case of complex structures with MSD.

The solutions for these configurations require usage of finite element method (FEM), which can be very complicated and requires substantial computer resources. In [6] authors proposed an algorithm which can speed up the simulation of crack growth in MSD. Still,

the mutual influence of the adjacent cracks additionally increases the complexity of stress intensity factors determination. This is the main reason for introducing approximation methods and procedures that enable faster and simpler determination of SIFs in supporting aircraft structures with multiple cracks.

So, finite element analysis, along with approximate methods, must be employed in order to provide fairly accurate solutions for SIFs, thus eliminating the need for expensive tests (this is why the experimental results reported in the literature are very limited). The aim of this paper is to show how SIFs calculations for structures with multiple cracks can be performed with the use of FEM based computer program and approximate numerical method based on the principle of superposition.

2. Approximate method for SIFs calculation in a case of MSD

The approximate procedure, for calculating stress intensity factors, was developed in [1]. This procedure is based on principle of superposition.

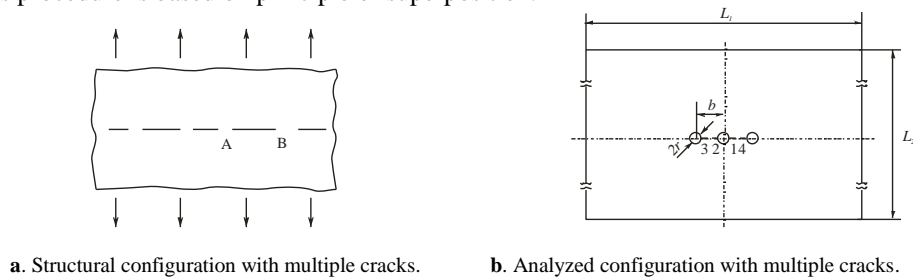


Figure 1. Configuration with multiple cracks.

According to this procedure, the SIF for opening mode of analyzed crack in any given configuration with n cracks (Fig. 1.a.) can be estimated with the use of:

$$K_{IjA,B} = c_{1b,d} \cdot K_{I1} + \dots + c_{jb,d} \cdot K_{Ij} + \dots + c_{nb,d} \cdot K_{In} = \sum_{i=1}^n c_{ib,d} \cdot K_{Ii} \quad (1)$$

where:

$K_{IjA,B}$ - represents stress intensity factor for tip A, or B of analyzed crack in presence of all other cracks in configuration;

K_{Ii} - individual stress intensity factor of all cracks in configuration, i.e., stress intensity factors of auxiliary configurations;

$c_{ib,d}$ - the coefficient that takes into consideration influence of i -th crack on stress intensity factor of analyzed crack, (the influential coefficient of the analyzed crack on itself is $c_{jb,d} = 1$).

In this manner the analyzed complex configuration can be represented as a combination of several simpler (auxiliary) configurations. The number of those configurations is equal to the number of cracks, such that every auxiliary configuration contains only one crack. Hence, the determination of SIF at analyzed crack tip is reduced to determination of influence that every crack in the initial configuration has on the analyzed one. This influence is represented by corresponding coefficients. The influential coefficients were

estimated by the application of presented method on configuration with two unequal cracks in an infinite plate subjected to remote uniform stress, as shown in [7].

2.1. Numerical example

In this paper, the SIFs were determined for a typical aero structural configuration. It is a thin plate with three circular holes subjected to uniform uniaxial tensile stress. Material of the plate is aluminium alloy Al-2024 T3 [8]. Middle hole has two radial cracks and other two holes have one radial crack. This configuration is shown in Fig 1.b.

It should be noticed that for this type of aircraft structural element, the dominant fraction of loading originates from fuselage pressurisation, and thus, tension in the direction perpendicular to the middle line of the plate prevails. Hence, the determination of opening mode SIFs is sufficient enough.

3. Finite element calculations of stress intensity factors

The SIFs for analyzed configuration were also calculated in FRANC2D/L software, which is well known for its accuracy. FRANC2D/L is a highly interactive program for the simulation of crack growth in layered structures.

The results obtained by described approximate procedure and by the use of FRANC2D/L, were compared against results obtained with open source finite element software CAELinux 2010.

The SIFs are calculated for different models with different crack sizes for all the cracks in the configuration, but with same crack increment for all the cracks, because the service data shows that in MSD all cracks are roughly the same length [9] (“catch-up” phenomenon).

The results are presented through normalized stress intensity factors (geometry factors β) for all cracks in analyzed configuration denoted as in Fig.1.b. The length of the cracks 1 and 2 is marked as a_1 , and the length of the cracks 3 and 4 is marked as a_2 (the model is symmetrical). The results are shown on Fig. 2 and Fig. 3.

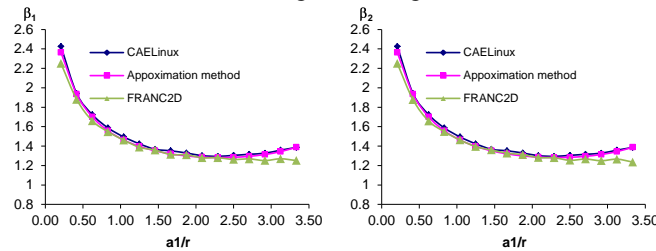


Figure 2. Normalized stress intensity factors for crack tips 1 and 2

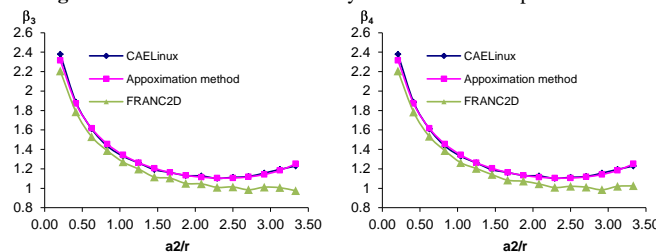


Figure 3. Normalized stress intensity factors for crack tips 3 and 4

As it can be seen from the graphs, there are excellent agreements between results obtained by finite element based computer program, approximate procedure which uses influential coefficients, and FRANC2D/L, especially for cracks 1 and 2. All differences are less than 5%, except in two cases where difference was about 10%. Those cases are the ones where adjacent cracks were large, with plastic zones that suggest link up occurrence.

For cracks 3 and 4, the agreements between results obtained by FEM based software and approximate procedure is excellent, but the solution obtained in FRANC2D/L differs more from these results, as the cracks grow. This can be explained by the fact that the interaction between the cracks was not quite adequate in case of FRANC2D/L model. This could be improved by better meshing of the region between the cracks and even crack numeration.

Nevertheless, the obtained solutions for SIFs are absolutely acceptable from an engineering point of view.

4. Conclusion

Using commercial FEM software, which is currently widely available, the calculations of stress intensity factors for typical aero structural configuration with MSD were conducted. Those factors were also obtained by approximate procedure. The analysis of all results has shown that the obtained solutions can be used for the prediction of SIFs in analyzed configuration with acceptable accuracy, from the engineering point of view. The comparison between results also showed, the significance of accurate calculation of SIFs, in order to provide a better prediction of MSD phenomenon.

References

- [1] Kastratović G. (2006), Određivanje faktora inteziteta napona nosećih vazduhoplovnih struktura sa višestrukim prskotinama, *Doctoral Thesis*, Belgrade
- [2] Schijve J (1995), Multiple-site damage in aircraft fuselage structures, *Fatigue Fracture Eng Mater Struct*, **18**, pp. 329–344.
- [3] Rasuo, B. (2004), *Aeronautical Safeguarding*, Military Academy, Belgrade, (in Serbian).
- [4] Zerbst U, Heinemann M, Donne CD, Steglich D (2009), Fracture and damage mechanics modeling of the walled structures-an overview, *Eng Fract Mech* **76**, pp. 5–43.
- [5] Rooke, D. P., and Cartwright, D. J. (1976), *Compendium of Stress Intensity Factors*, HMSO, London.
- [6] Wang, X., Modarres, M. and Hoffman, P. (2009), Analysis of crack interactions at adjacent holes and onset of multi-site fatigue damage in aging airframes, *Int J Fract*, **156**, pp. 155–163.
- [7] Kastratović, G. (2007), The Effect of Crack Tips Interaction on Stress Intensity Factor, *Proceedings of the 1st International Congress of Serbian Society of Mechanics*, D Šumarac and D Kuzmanović (Eds.), pp. 1059–1064.
- [8] Rasuo, B. (1995), *Aircraft Production Technology*, Faculty of Mechanical Engineering, University of Belgrade, Belgrade, (in Serbian).
- [9] Beuth, J. L. and Hutchinson, J. W. (1994), Fracture analysis of multi-site cracking in fuselage lap joints, *Computational Mechanics*, **13**, pp. 315–331.

DEBONDING IN BEAM-REINFORCED PLATES

J.T. Katsikadelis¹, N.G. Babouskos²

Institute of Structural Analysis and Aseismic Research
National Technical University, Zografou Campus, GR-15773, Athens, Greece

¹e-mail: jkats@central.ntua.gr

²e-mail: babouskosn@yahoo.gr

Abstract. A method is presented to establish accurately the interface forces (shear and tensile) between plate and beams in rib-reinforced plates and, thus, to control debonding. Contrary to other investigations, where the problem is highly simplified by assuming parallel beams, herein the beams may have an arbitrary relative orientation and inclined principal axes with respect to the plate plane. Numerical results are presented, from which useful conclusions are drawn for the response of the plate-beam system.

1. Introduction

A thin plate reinforced with beams is a type of composite structure, used in almost all modern engineering applications such as aircrafts, ship, building, bridges and machines. They offer an economical and functionally way of construction by increasing the strength and minimizing the weight. Ribs also increase considerably the buckling load, which is crucial in light structures. Plates and beams may be connected uniformly or at separate points, especially when they are made of different materials. Therefore, it is important to evaluate accurately the interface shear and tensile forces in order to control debonding and ensure the integrity of the composite structure. The debonding has been examined experimentally [1] and theoretically using semi-analytical [2] and numerical methods, such [3,4]. In all previous investigations the solution was highly simplified by assuming parallel beams with symmetrical principal axes. Herein, the plate-beam system is studied by extending the plate-beam model introduced by Sapountzakis and Katsikadelis [5] to enable analysis of plates stiffened by arbitrary oriented beams with principal axes inclined with respect to the plate plane. First the plate-beam model is presented and the differential equations for the plate and the beams are derived by minimizing the total potential. The AEM (Analog Equation Method) is employed to solve the resulting coupled differential equations and establish the interface forces. Numerical results are presented and useful conclusions are drawn for the response of the plate-beam system. The accurate computation of interface forces enables the control of the debonding between plate and beams.

2. The plate-beam model and the governing differential equations

We consider a thin elastic plate of uniform thickness h stiffened by L beams of length l_i ($i = 0, 1, 2, \dots, L$) having arbitrary orientation under the transverse load $g(x, y)$ and the

inplane boundary forces N_n^*, N_t^* . The plate occupies the two-dimensional multiply connected domain Ω with boundary $\Gamma \cup_{i=0}^K \Gamma_i$ (Fig. 1). The beams have a uniform cross section with principal axes inclined with respect to the plate plane. The plate is supported along the boundary, whereas the beams may have point supports.

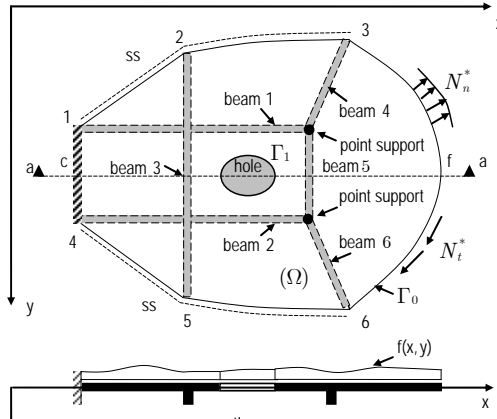


Figure 1: Plate stiffened with beams (f=free, ss=simply supported, c=clamped).

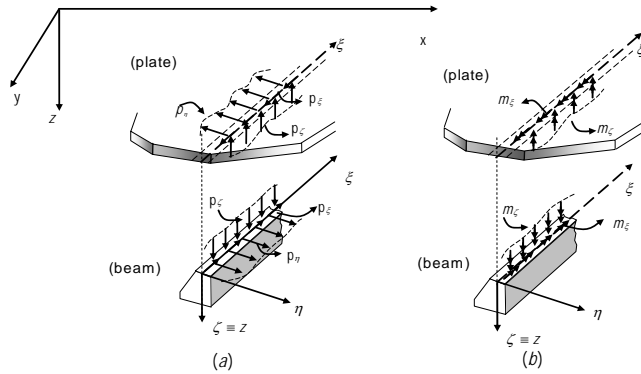


Figure 2: Interface (a) forces (b) moments along the trace of the beam

The model of analysis of the plate-beam system is shown in Fig. 2. The beams are separated from the plate by a section at the lower surface of the plate. Subsequently, the deformation of the plate and the beams under external loading and the unknown interface tractions is considered. The continuity conditions at the interfaces yield the necessary equations for the evaluation of the unknown interface forces. As the variations of the interface tractions t_ξ, t_η and t_ζ along the width t of the contact area are unknown, we work with their resultants. Hence, we define the interface quantities.

$$p_\xi = \int_{-t/2}^{+t/2} t_\xi d\eta, \quad p_\eta = \int_{-t/2}^{+t/2} t_\eta d\eta, \quad p_\zeta = \int_{-t/2}^{+t/2} t_\zeta d\eta \quad (1a,b,c)$$

$$m_\xi = \int_{-t/2}^{+t/2} \eta t_\xi d\eta, \quad m_\zeta = - \int_{-t/2}^{+t/2} \eta t_\zeta d\eta \quad (1d,e)$$

On the basis of the above consideration, we come across the following two problems. The overbar denotes quantities referred to the plate axes or beam principal axes.

2.1. For the plate

The plate undergoes bending combined with inplane deformation.

(i) Transverse deflection

$$D\nabla^4 w - (N_x w_{,xx} + 2N_{xy} w_{,xy} + N_y w_{,yy}) + \sum_j (\bar{p}_\xi w_{,\xi} + \bar{p}_\eta w_{,\eta}) \delta(\eta) = g$$

$$+ \sum_j [\bar{p}_\zeta \delta(\eta) - \bar{m}_\xi \frac{\partial \delta(\eta)}{\partial \eta} + \frac{\partial \bar{m}_\eta}{\partial \xi} \delta(\eta)] \quad \text{in } \Omega \quad (3)$$

$$Vw + N_n^* w_{,n} + N_t^* w_{,t} + k_T w + \varepsilon(s) \bar{m}_t / |n_\xi| = V_n^* \quad \text{or } w = w^* \quad \text{on } \Gamma \quad (4a,b)$$

$$Mw - k_R w_{,n} = M_n^* \quad \text{or } w_{,n} = w_{,n}^*$$

(ii) Inplane deformation

$$\nabla^2 u + \frac{1+\nu}{1-\nu} (u_x + v_y)_{,x} + \frac{1}{hG} \sum_j \left[b_x \delta(\eta) + \bar{m}_z \frac{\partial \delta(\eta)}{\partial \eta} \cos \phi \right] = 0$$

$$\quad \text{in } \Omega \quad (5a,b)$$

$$\nabla^2 v + \frac{1+\nu}{1-\nu} (u_x + v_y)_{,y} + \frac{1}{hG} \sum_j \left[b_y \delta(\eta) + \bar{m}_z \frac{\partial \delta(\eta)}{\partial \eta} \sin \phi \right] = 0$$

$$N_n + \varepsilon(s) n_\eta n_\xi \bar{m}_z / |n_\xi| = N_n^* \quad \text{or } u_n = u_n^* \quad (6a,b)$$

$$N_t - \varepsilon(s) n_\eta^2 \bar{m}_z / |n_\xi| = N_t^* \quad \text{or } u_t = u_t^*$$

2.2. For the beam

The beam undergoes biaxial bending and nonuniform torsion combined with axial deformation.

(i) Axial deformation

$$EA \bar{u}'' = -\bar{p}_\xi \quad 0 < \xi < l \quad (7)$$

$$N_\xi = P_\xi^* \quad \text{or } \bar{u} = \bar{u}^* \quad \text{at } \xi = 0, l, \quad N_\xi = EA \bar{u}' \quad (8)$$

(ii) Bending about the $\bar{\eta}$ axis

$$EI_{\bar{\eta}} (\bar{w}^{IV} + \bar{\eta}_s \theta^{IV}) - N_\xi \bar{w}'' + \bar{p}_\xi \bar{w}' = \bar{p}_\zeta + \bar{m}'_{\bar{\eta}} \quad 0 < \xi < l \quad (9)$$

$$Q_\zeta - N_\xi w' = P_\zeta^* - \bar{m}_{\bar{\eta}} \quad \text{or } \bar{w} = \bar{w}^* \quad \text{at } \xi = 0, l \quad (10a)$$

$$M_{\bar{\eta}} = M_{\bar{\eta}}^* \quad \text{or } \bar{w}' = \bar{w}'^* \quad \text{at } \xi = 0, l \quad (10b)$$

(iii) Bending about the in $\bar{\zeta}$ axis

$$EI_{\bar{\zeta}} (\bar{v}^{IV} - \bar{\zeta}_s \theta^{IV}) - N_\xi \bar{v}'' + \bar{p}_\xi \bar{v}' = \bar{p}_\eta - \bar{m}'_{\bar{\zeta}} \quad 0 < \xi < l \quad (11)$$

$$Q_\eta + N_\xi v' = P_\eta^* + \bar{m}_{\bar{\zeta}} \quad \text{or } \bar{v} = \bar{v}^* \quad \text{and } M_{\bar{\zeta}} = M_{\bar{\zeta}}^* \quad \text{or } v' = v'^* \quad \text{at } \xi = 0, l \quad (12a,b)$$

(iv) Torsion about the ξ axis

$$EI_\omega \theta^{IV} - GI_t \theta'' + \bar{\eta}_s EI_{\bar{\eta}} \bar{w}^{IV} - \bar{\zeta}_s EI_{\bar{\zeta}} \bar{v}^{IV} - \frac{I_C}{A} N_\xi \theta'' + \frac{I_C}{A} p_\xi \theta' = \bar{m}_\xi - \bar{p}'_\xi \phi + \bar{m}'_{\bar{\zeta}} \phi_{,\bar{\eta}} \quad (13)$$

$$M_t + \frac{I_C}{A} N_\xi \theta' = M_\xi^* + \bar{p}_\xi \phi - \bar{m}_{\bar{\zeta}} \phi_{,\bar{\eta}} \quad \text{or } \theta = \theta^* \quad \text{at } \xi = 0, l \quad (14a)$$

$$M_w = -P_\xi^* \phi + M_\xi^* \phi_{,\bar{\eta}} \quad \text{or } \theta' = \theta'^* \quad \text{at } \xi = 0, l \quad (14b)$$

3. Numerical example

The nonlinearly coupled equations combined with the continuity conditions are solved using the AEM [6] and the interface forces are computed. Several problems have been studied. In Fig. 3 results are shown for the rectangular plate of thickness $h = 0.05$ m reinforced with two beams of rectangular cross section (0.40×0.10). The elastic constants of plate and beams are $E = 210$ MPa, $\nu = 0.3$. The results are compared with a FEM solution obtained from a three dimensional analysis (Fig. 3d).

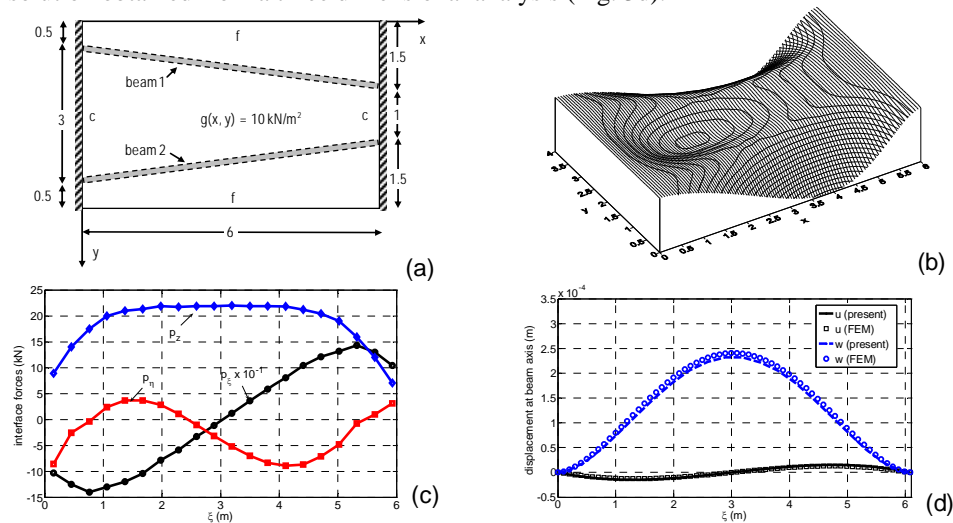


Figure 3: (a) geometry of rib-reinforced plate, (b) transverse deflection surface of the plate, (c) interface forces (beam 1) and (d) displacements at beam 1 axis.

4. Conclusions

In this paper a method is presented for the analysis of plates stiffened with arbitrary orientated beams. The method enables the accurate evaluation of the interface, which may cause debonding, ensuring thus the integrity of the plate-beam system.

5. References

- [1] Bertolini J.B., Castanie B., Barrau J.-J., Navarro J.-P., Petiot C. (2009), Multi-level Experimental and Numerical Analysis of Composite Stiffener Debonding. Part 1: Non-specific Specimen Level, *Composite Structures*, 90, pp. 392-403.
- [2] Pan Y. and Louca L.A. (1999), "Experimental and numerical studies on the response of stiffened plates subjected to gas explosions," *Journal of Constructional Steel Research*, 52, pp. 171-193.
- [3] Sadek E.A. and Tawfik S.A. (2000), "A finite element model for the analysis of stiffened laminated plates," *Computers & Structures*, 75(4), pp. 369-383.
- [4] Sapountzakis E.J. and Katsikadelis J.T. (2007), "Interface forces in composite steel-concrete structure," *International Journal of Solids and Structures*, 37, pp. 4455-4472.
- [5] Sapountzakis E.J. and Katsikadelis J.T., (2000), "Analysis of plates reinforced with beams," *Computational Mechanics*, 26, pp. 66-74.
- [6] Katsikadelis J.T. (1994), "The analog equation method. - A powerful BEM-based solution technique for solving linear and nonlinear engineering problems", in: Brebbia C.A. (ed.), *Boundary Element Method XVI*: 167-182, Computational Mechanics Publications, Southampton.

APPLICATION OF CONSERVATION LAWS TO DEFECT AND DAMAGE MECHANICS

R. Kienzler

Bremen Institute for Mechanical Engineering
University of Bremen, Am Biologischen Garten 2, D-28359 Bremen, Germany
e-mail: rkienzler@uni-bremen.de

Abstract. Material conservation laws and associated path-independent integrals play a prominent role in the assessment of defects in structures. Especially Rice's J Integral is widely used in fracture mechanics. For systems governed by a Lagrangian, the usual tool for the derivation of material conservation laws is the application of Noether's first theorem in combination with Bessel-Hagen's extension. The so-called Neutral-Action (NA) method is a different approach. Its advantage in comparison with the classical Noether's approach lies in the fact that it is applicable to field equations that are not necessarily the Euler-Lagrange equations of a variational principle, i.e., for systems not governed by a Lagrangian. After a short review of the NA method a complete set of characteristics and the associated conserved currents are derived and interpreted in physical terms.

1. Introduction

Noether's first theorem [1] and the Neutral-Action (NA) method [2] are competitive methods to derive conservation laws in field theories governed by a Lagrangian. If a Lagrangian is not available, only the NA method is applicable. Within this paper, we are concerned with the linear theory of elasticity. For a three-dimensional body made of homogeneous isotropic material (Lamé's constants λ and μ) we adopt the Navier-Lamé equations (cf., e.g., [3]), which read in the absence of body forces as

$$\Delta_i = \mu u_{i,jj} + (\lambda + \mu) u_{j,ji} = 0 \quad (1)$$

(displacements u_i , an index following a comma denotes partial differentiation with respect to the indicated independent variable, summation is implied over repeated indices).

The so-called characteristic functions f_i leading to conservation laws are determined via the NA method by

$$E_k(f_i \Delta_i) = 0 \Leftrightarrow f_i \Delta_i = P_{i,i}. \quad (2)$$

$E_k(\cdot)$ are the Euler-Lagrange equations and P_i are the conserved currents. With (2b), a conservation law is obtained, since integration over the volume V of a Body B and application of the divergence theorem (surface A unit outward normal vector n_i) leads to

$$\int_B P_{i,i} dV = \int_{\partial B} P_i n_i dA = 0, \quad (3)$$

giving rise to path-independent integrals. If we restrict the characteristic functions f_i to depend on the independent variables x_j , the dependent variables, i.e., the displacements $u_k(x_j)$ and the displacement gradients $u_{\ell,m}$

$$f_i = f_i(x_j, u_k, u_{\ell,m}), \quad (4)$$

a complete set of conservation laws can be derived [4], [5].

2. Conservation laws

We will concentrate on two different groups of conservation laws. The first group follows from the characteristic

$$f_i = b_k(x_\ell) u_{i,k} + f_{ij}^b u_j. \quad (5)$$

with

$$\begin{aligned} b_k &= \beta_k^{(0)} + \varepsilon_{nmk} x_m \beta_n^{(1)} + x_k \beta + (2x_k x_m - \delta_{km} x_n x_n) \beta_m^{(2)} \\ f_{ij}^b &= \varepsilon_{ijk} \beta_k^{(1)} + \frac{n-2}{2} \delta_{ij} \beta + (n-2) \delta_{ij} x_m \beta_m^{(2)} \end{aligned} \quad (6)$$

and describes material transformations (δ_{ij} and ε_{ijk} are the Kronecker and the permutation symbol, respectively). The value of n is equal to 3 for three-dimensional problems, equal to 2 for two-dimensional problems (plane strain) and equal to 1 for one-dimensional problems (tension and compression of bars).

The four transformations $\beta_j^{(0)}$, $\beta_n^{(1)}$, β and $\beta_m^{(2)}$ lead to the four conservation and balance laws [4], respectively

$$\text{Translation} \quad \beta_j^{(0)} \neq 0: \quad b_{ij,i} = [W \delta_{ij} - \sigma_{ik} u_{k,j}]_{,i} = 0,$$

$$\text{Rotation} \quad \beta_n^{(1)} \neq 0: \quad \varepsilon_{nkj} [x_k b_{ij} + u_k \sigma_{ij}]_{,i} = 0,$$

$$\begin{aligned}
\text{Scaling} \quad & \beta \neq 0 \quad \left[x_j b_{ij} + \frac{2-n}{2} u_j \sigma_{ij} \right]_{,i} = 0, \\
\text{Inversion} \quad & \beta_m^{(2)} \neq 0 \quad \left[(2x_m x_k - x_\ell x_\ell \delta_{mk}) b_{ik} + \right. \\
& \quad \left. + (2x_k u_m + (2-n)x_m u_k - 2x_\ell u_\ell \delta_{mk}) \sigma_{ik} \right. \\
& \quad \left. + n\mu \left(u_m u_i + \frac{1}{2} u_\ell u_\ell \delta_{mi} \right) \right]_{,i} = (n\lambda + (4+n)\mu) u_{\ell,\ell} u_m.
\end{aligned} \tag{7}$$

The term b_{ij} is the by-know well-known Eshelby Tensor involving the strain-energy density W and Cauchy's stress tensor σ_{ik} . On integration over the volume V of a body B and application of the divergence theorem, equation (7a) gives rise to Rice's J integral [6], which describes the energy-release rate due to the translation of a material inhomogeneity within the body. In a similar way, (7b) and (7c) resemble the L and M integrals introduced in [7], but discussed much earlier in [8]. The integrals L and M indicate the energy-release rates due to a rotation and a self-similar expansion of the inhomogeneity.

Inversion does not give rise to a conservation law but rather a (more or less) trivial balance law. The right-hand side of (7d) vanishes either under the unphysical condition $(n=3): 3\lambda + 7\mu = 0$, i.e., Poisson's ratio $\nu = 7/8$ or for the special case of an isochoric deformation, i.e., $u_{k,k} = 0$.

The second class of characteristics are scaled with the parameters of the material under consideration and are given by

$$f_i = c_m(x_\ell) \left[(\lambda + 2\mu) \delta_{jk} \delta_{im} + \mu \delta_{ik} \delta_{jm} \right] u_{j,k} + f_{im}^c(x_\ell) u_m$$

with a similar appearance for $c_m(x_\ell)$ and f_{im}^c as $b_k(x_\ell)$ and f_{ij}^b in (6), respectively. The conservation laws follow to be

$$\begin{aligned}
\text{Translation} \quad & \gamma_i^{(0)} \neq 0: \quad c_{ji,j} = 0, \\
\text{Rotation} \quad & \gamma_i^{(1)} \neq 0: \quad \varepsilon_{ik\ell} \left[(\lambda + \mu) x_k c_{j\ell} + \mu(\lambda + 3\mu) u_k \sigma_{j\ell} \right. \\
& \quad \left. + 2\mu^3 u_k (u_{m,m} \delta_{j\ell} - u_{m,\ell} \delta_{jm}) \right]_{,j} = 0, \\
\text{Scaling} \quad & \gamma \neq 0: \quad \left[x_i c_{ji} + \mu u_i (\sigma_{ji} + \mu u_{k,k} \delta_{ji} - u_{j,i}) \right. \\
& \quad \left. + \mu^2 (u_j u_{i,i} - u_i u_{j,i}) \right]_{,j} = \frac{1}{2} (3\lambda + 7\mu) u_{i,i} u_{j,j},
\end{aligned} \tag{8}$$

$$\begin{aligned}
\text{Inversion} \quad \gamma_i^{(2)} \neq 0: & \left[\left(x_i x_k - \frac{1}{2} x_\ell x_\ell \delta_{ik} \right) c_{jk} + x_k (\sigma_{j\ell} u_m, \right. \\
& \left. u_{j,\ell} u_m, \lambda, \mu) + (u_{j,\ell} u_m, \lambda, \mu) \right]_{,j} \\
& = \frac{1}{2} (3\lambda + 7\mu) (x_i, u_{j,k} u_{m,n}, \lambda, \mu).
\end{aligned}$$

The tensor c_{ij} is given in displacement gradients as

$$\begin{aligned}
c_{ij} = & \frac{1}{2} (\lambda + 2\mu) (\lambda + \mu) u_{k,k} u_{\ell,\ell} \delta_{ij} + \mu^2 u_{j,k} (u_{k,i} - u_{i,k}) \\
& + \mu (\lambda + 2\mu) u_{k,k} u_{i,j}
\end{aligned} \tag{9}$$

and coincides with Q_{ji} in Olver's paper [9]. Rotation leads again to a conservation law (8b), whilst scaling (8c) and inversion (8d) yield rather balance laws, the right-hand side being proportional to the same factor $3\lambda + 7\mu$ as discussed above. The term in round brackets of (8d) are not given explicitly. They involve complicated combinations of the terms indicated within the brackets and do not disclose any physical interpretation.

3. Applications

On evaluating the proposed path-independent integrals around a crack tip, they prove to be favourable tools to calculate stress-intensity factors separately with advantages in the numerical implementation and in the accuracy obtained. In addition, defect interaction problems are investigated in terms of material reciprocity. Further, the potential and possibilities to apply conservation laws and reciprocity theorems in continuum damage mechanics are discussed.

References

- [1] Noether, E. (1918), Invariante Variationsprobleme. *Nachr. Ges. Wiss. Göttingen, Math. Phys. Kl.* **2**, pp. 235-257.
- [2] Honein, T., Chien, N. and Herrmann, G. (1991), On conservation laws for dissipative systems. *Phys. Lett. A* **155**, pp. 223-224.
- [3] Timoshenko, S. P. and Goodier, J. N. (1970), *Theory of Elasticity*, 3rd ed. McGraw-Hill, New York.
- [4] Kienzler, R., Rohde, L. and Schröder, R. (2010), On path-independent integrals within the linear theory of elasticity. *Int. J. Fract.*, **166**, pp. 53-60.
- [5] Kienzler, R., Rohde, L., Schröder, R. and Kutz, K. (2010), Treating mixed-mode problems with path-independent integrals. *Engng. Fract. Mech.* **77**, pp. 3604-3610.
- [6] Rice, J. R. (1968), A path independent integral and the approximate analysis of strain concentrations by notches and cracks. *J. Appl. Mech.* **35**, pp.379-386.
- [7] Budiansky, B. and Rice, J. R. (1973), Conservation laws and energy-release rates. *J. Appl. Mech.* **40**, pp. 201-203.
- [8] Günther, W. (1962), Über einige Randintegrale der Elastomechanik. *Abh. Braunsch. Wiss. Ges.* **14**, pp. 53-72.
- [9] Olver, P. J. (1984), Conservation laws in elasticity, II. Linear homogeneous isotropic elastostatics. *Arch. Rat. Mech. Anal.* **85**, pp.111-129.

HIGH-TEMPERATURE MATERIAL CHARACTERISTICS ANALYSIS OF OFFSHORE STRUCTURAL STEELS CONSIDERING DAMAGE MECHANICS

S. J. KIM¹, Y. H. Choi², M. H. KIM³, J. M. LEE⁴

¹Naval Architecture and Ocean Engineering
Pusan National University, Jangjeon-dong, Geumjeong-gu, Busan 609-735, Republic of Korea

e-mail: sneek@pusan.ac.kr

²Naval Architecture and Ocean Engineering
Pusan National University, Jangjeon-dong, Geumjeong-gu, Busan 609-735, Republic of Korea

e-mail: damien@pusan.ac.kr

³Naval Architecture and Ocean Engineering
Pusan National University, Jangjeon-dong, Geumjeong-gu, Busan 609-735, Republic of Korea

e-mail: kimm@pusan.ac.kr

⁴Naval Architecture and Ocean Engineering
Pusan National University, Jangjeon-dong, Geumjeong-gu, Busan 609-735, Republic of Korea

e-mail: jaemlee@pusan.ac.kr (Corresponding Author)

Abstract. The subsea pipeline fabricated using HSLA-65 steel is used in high-pressure/high-temperature environments. Because of the operation environments, the HSLA-65 steel has a temperature gradient in the thickness direction. Further, pipeline failure occurs frequently in these environments. High temperature and corrosion are known to be two of the major reasons causing pipeline failure. To prevent pipeline failure, an increased number of researchers are conducting extensive research on the structural integrity of these pipelines. In the present study, numerical studies for evaluating and predicting the nonlinear material behaviors as well as the failure characteristics of the HSLA-65 steel are carried out. First, temperature- and rate-dependent constitutive-damage models are introduced for describing the material nonlinearity and damage growth. The introduced constitutive-damage models are implemented using ABAQUS as a user-defined material (UMAT) subroutine. Moreover, a structural analysis using the developed UMAT is carried out.

1. Introduction

Since the 1950s, many pipelines have been laid out for transporting oil and gas across the world. However, the number of accidents related to these pipelines has also increased considerably with the increasing number of operating pipelines [1-2]. Most of the pipelines are exposed to high-pressure/high-temperature (HP/HT) conditions during operation. The HT results in a temperature gradient in the thickness direction of these pipelines. Hence, in the present study, numerical studies for the evaluation and prediction of the nonlinear material behaviors as well as the failure characteristics of the high-strength low-alloy (HSLA)-65 steel are conducted. First, the temperature- and rate-dependent constitutive-damage models are introduced for describing the material nonlinearity and damage growth [3]. The introduced constitutive-damage models are implemented using the ABAQUS as a user-defined material (UMAT) subroutine [4]. The numerical simulations are compared to the uniaxial tensile test results of the HSLA-65 steel to validate the proposed numerical

models and computational methods. Moreover, the developed UMAT is used for carrying out a structural analysis.

2. Material Properties

Table 1 shows the chemical composition of the HSLA-65 steel. The relatively high strength of HSLA steels is attributed to a combination of ferrite grain refinement and precipitation strengthening [5]. HSLA steel has good ductility and plasticity even at low temperatures and high strain rates [6]. Because of these advantages, this metal has been widely used in heavy industries. In particular, it is suitable for use in naval surface vessels, automobiles, and pipelines. Fig. 1 shows the tensile test result of the HSLA-65 steel.

Table 1 Chemical composition of HSLA-65 (wt.%)

C	Mn	Cu	Si	Cr	Mo	V	Ti	Al	Nb	Ni	P	S	Balance
0.08	1.40	<0.01	0.24	0.01	0.02	0.07	0.01	0.03	0.04	<0.01	0.005	0.005	Fe

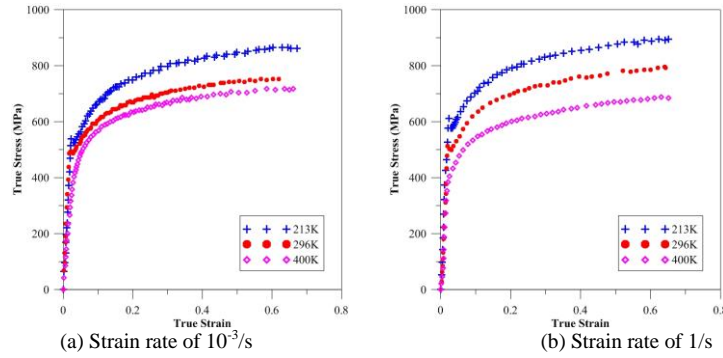


Figure 1 Representative tensile test of HSLA-65 steel [8]

3. Isotropic Viscoplastic-Damage Model for HSLA-65 and Its Application to ABAQUS UMAT

Bodner and Partom proposed a unified viscoplastic constitutive model (BP model) to represent inelastic creep behavior [7]. The BP model is applicable to a wide range of time-dependent problems. In the present study, a viscoplastic constitutive model is developed based on the BP model.

$$\dot{\epsilon}_{ij}^p = D_0 \exp \left\{ -\frac{1}{2} \left(\frac{Z}{\sigma_{eff}} \right)^{2n} \right\} \frac{\sqrt{3} S_{ij}}{\sigma_{eff}} \quad (1)$$

The variable D_0 denotes the assumed maximum plastic strain rate, which is generally in the order of 10^4 [7]. The parameter n has a temperature-dependent value. The loading history-dependent hardening parameter Z is a total hardening variable, which is referred to as an isotropic hardening variable in this study, and indicates the overall resistance level of materials to a plastic flow [7].

A damage evolution model is also taken into account in the constitutive relation to reflect the material damage based on the concept of effective stress [7]. The evolution of the material damage variable is expressed as

$$\dot{\omega} = \frac{b}{H} \left[\ln \left(\frac{1}{\omega} \right) \right]^{(b+1)/b} \omega \dot{Q} \quad (2)$$

$$\dot{Q} = \left[\alpha \sigma_{\max}^+ + \beta \sigma_{\text{eff}} + \gamma I_1^+ \right]^z \quad (3)$$

where b and h in Eq. (2) are the material constants [7] and \dot{Q} is the assumed multi-axial stress function developed by Hayhurst and Leckie [9]. σ_{\max}^+ is the maximum tensile principal stress, I_1^+ is the first stress invariant, r is the material constant, and α , β , and γ are the stress function control parameters satisfying $\alpha + \beta + \gamma = 1$.

The aforementioned isotropic viscoplastic-damage model has been implicitly formulated and implemented using the ABAQUS user subroutine UMAT. In the present study, a constitutive equation is implemented as an implicit formulation using the definition of the algorithmic tangential stiffness (ATS) tensor [10].

4. Comparison of Simulation and Experimental Results

Fig. 3 shows a comparison of the stress–strain relation between the experimental and simulation results. The simulation results, which are obtained using the proposed isotropic viscoplastic-damage model for the RPUF, agree well with the experimental results.

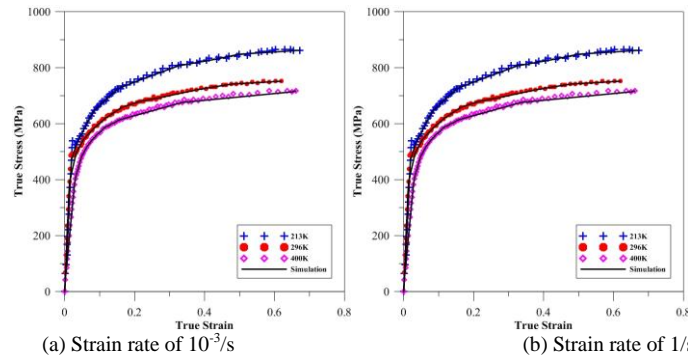


Figure 2 Comparison of stress–strain relation between experimental and simulation results

5. Numerical Simulation applied to Pipeline under Internal Pressure

In this section, we discuss the developed ABAQUS UMAT of the HSLA-65 steel used for making a pipeline under internal pressure. In this study, we use a quarter of the full model under symmetrical conditions. The outer diameter and wall thickness of the considered pipeline are 762 mm and 17.5 mm, respectively. A monotonically hydrostatic pressure is applied to the inner surface of the model. The FEA model considers the temperature

gradient along the thickness direction on the basis of a thermal transfer analysis of the pipeline. Fig. 3 shows the representative results of the pipeline FEA.

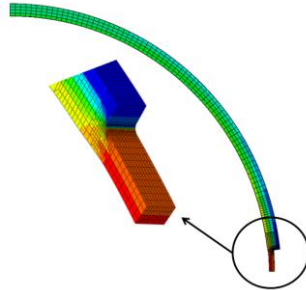


Figure 3 Representative results of pipeline FEA

6. Concluding Remarks

In this study, numerical studies for evaluating and predicting the nonlinear material behaviors as well as the failure characteristics of HSLA-65 steel were carried out. The temperature- and rate-dependent constitutive-damage models were introduced for describing the material nonlinearity and damage growth. Further, the introduced constitutive-damage models were implemented using ABAQUS as a user-defined material (UMAT) subroutine. The simulation results were found to agree well with the uniaxial tensile test results of the HSLA-65 steel. Moreover, we could predict the failure of the pipelines on the basis of the simulated corrosion defects under an internal pressure condition using the developed ABAQUS UMAT.

Acknowledgement. This research was supported by Basic Science Research Program through the National Research Foundation of Korea (NRF) funded by the Ministry of Education, Science and Technology (2011-0004786). This work was also supported by the National Research Foundation of Korea (NRF) grant funded by the Korea government (MEST) through GCRC-SOP (Grant No. 2011-0030667).

References

- [1] P. Hopkins, (1995), Transmission pipelines: how to improve the integrity and prevent failures, *Proceedings of the Second International Pipeline Conference*, Belgium, 1: 683-706
- [2] Office of pipeline safety, US Department of Transportation, pipeline Statistics, 2001. <http://ops.dot.gov/stats.htm>
- [3] S. R. Bodner, K.S. Chan. (1986), Modeling of continuum damage for application in elastic-viscoplastic constitutive equations, *Engineering Fracture Mechanics*, 25: 705-712.
- [4] C. L. Chow, J. Wang, (1988), A finite element analysis of continuum damage mechanics for ductile fracture, *Int. J. Fracture*, 38: 83-102.
- [5] M. Militzer, E.B. Hawbolt, T.R. Meadowcroft. (2000), Micro-structural model for hot strip rolling of high-strength low-alloy steels, *Metall Trans, A* 31A, 1247-1259.
- [6] N.N. Sia, W.G. Guo. (2005), Thermomechanical response of HSLA-65 steel plates: experiments and modeling, *Mechanics of Materials*, 37: 379-405.
- [7] S. R. Bodner, Unified plasticity for engineering applications, first ed., *Kluwer Academic Plenum Publishers*, New York, 2002
- [8] V. Moreno, E. H. Jordan, (1986), Prediction of material thermomechanical response with a unified viscoplastic constitutive model, *International journal of plasticity*, 2: 223-245
- [9] D. R. Hayhurst, (1972), Creep rupture under multi-axial state of stress, *J. Mech. Phys. Solids.*, 20: 1059-1070
- [10] H. Andersson, (2002), An implicit formulation of the Bodner-Partom Constitutive Equations, *Computers & Structures*, 81: 1405-1414

SIMULATION OF ANISOTROPIC DAMAGE IN QUASIFRAGILE MATERIALS USING THE TRUSS-LIKE 3D DISCRETE ELEMENT METHOD

L. Kostascki ¹, I. Iturrioz ², J. D. Riera ³

^{1,2} Post-Graduate Program in Mechanical Engineering (PROMEC), Federal University of Rio Grande do Sul (UFRGS). Rua Sarmiento Leite, 425. CEP: 90050-170 - Porto Alegre, RS, Brazil. Phone: (+55-51) 3308-3182 luiskostascki@hotmail.com, ignacio@mecanica.ufrgs.br

³Civil Engineering Department (DECIV), PPGEC, Universidade Federal do Rio Grande do Sul (UFRGS), Porto Alegre, RS, Brazil: jorge.riera@ufrgs.br

Abstract: Efforts to improve models able to simulate damage distribution and its posterior localization in quasi-fragile materials as concrete and rocks are reported in this paper. The authors use a lattice model, increasingly employed in computational mechanics. The basic tool in the present study is a version of the so-called truss-like Discrete Element Method (DEM), which has been used with success in applications in solid mechanics problems where the simulation of fracture and fragmentation is relevant. It is shown that it constitutes a simple and versatile numerical tool to simulate anisotropic damage and its localization in quasi-fragile materials. Comparisons between several uni-axial constitutive laws are presented. The performance of the models examined in tensile tests allows the derivation of preliminary criteria concerning the influence of the constitutive law on the global results.

Keywords: Fracture mechanics, crack growth, dynamic fracture, truss like discrete element method

1. Introduction

During the 1960s an alternative set of computational methods, which do not use a set of differential or integral equations to describe the problem in its spatial dominium was introduced. Depending on the type of individual elements adopted, such as particles or bars, different methods were developed. In the process, an alternative approach has emerged, called by Munjiza [1] *computational mechanics of discontinua*, which is now an integral part of cutting edge research in different fields of solid mechanics.

The lattice model used in the present paper adopted results from Nayfeh and Hefzy [2] to determine the properties of an equivalent orthotropic elastic continuum to model aircraft panels made of large numbers of small interconnected bars. This allowed the representation of an orthotropic elastic continuum using a regular truss lattice, to develop the DEM for solid mechanical problems, approach proposed by Riera[3] to determine the dynamic response of plates and shells under impact loading when failure occurs primarily by tension, which is generally the case in concrete structures. Numerous applications of DEM to model shells subjected to impulsive loading (Riera and Iturrioz, [4] and [5]); fracture of elastic foundations on soft sand beds (Schnaid et al.[6]); dynamic fracture (Miguel et al. [7]); simulation of earthquake motions (Dalguer et al.[8]); scale effect in concrete (Rios and Riera[9]) and in rock dowels (Miguel et al.[10] and Iturrioz et al.[11]) and crack propagation (Kostascki et al.[11]) were published subsequently. This version of the DEM constitutes a simple and versatile numerical tool to simulate anisotropic damage and its

localization in quasi-fragile materials. In this paper we examine the influence of the shape of the constitutive element law on the global response of the structure and we propose global parameters to evaluate the evolution of damage and quantify the level of localization.

2. Truss-like discrete element method (DEM)

The Discrete Element Method employed in this paper is based on the representation of a solid by means of a regular 3D arrangement of elements able to carry only axial loads shown in Fig 1.a and b. The discrete elements representation of the orthotropic continuum was adopted to solve structural dynamics problems by means of explicit direct numerical integration of the equations of motion, assuming the mass lumped at the nodes. Each node has three degrees of freedom, corresponding to the nodal displacements in the three orthogonal coordinate directions. For an isotropic medium, the equations that relate the properties of the elements with the elastic constants are:

$$\delta = \frac{9\nu}{4-8\nu}, \quad EA_n = EL^2 \frac{(9+8\delta)}{2(9+12\delta)}, \quad EA_d = \frac{2\sqrt{3}}{3} A_n. \quad (1)$$

in which E and ν denote Young's modulus and Poisson's ratio, respectively, while A_n and A_d represent the areas of normal and diagonal elements.

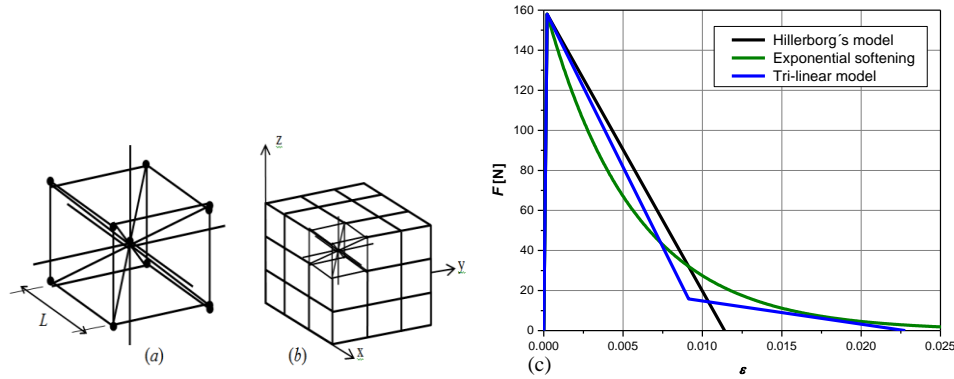


Figure 1. DEM discretization strategy: (a) basic cubic module, (b) generation of prismatic body. (c) comparison between the different ECRs of the uni-axial DEM elements considered in the paper.

The resulting equations of motion may be written in the well-known form:

$$\mathbf{M}\ddot{\vec{x}} + \mathbf{C}\dot{\vec{x}} + \vec{F}_r(t) - \vec{P}(t) = 0. \quad (2)$$

in which \vec{x} represents the vector of generalized nodal displacements, \mathbf{M} the diagonal mass matrix, \mathbf{C} the damping matrix, also assumed diagonal, $\vec{F}_r(t)$ the vector of internal forces acting on the nodal masses and $\vec{P}(t)$ the vector of external forces. Obviously, if \mathbf{M} and \mathbf{C} are diagonal, Equations (2) are uncoupled and may be integrated in the time domain using

the explicit central finite differences scheme. Since the nodal coordinates are updated at every time step, large displacements can be accounted for in a natural and efficient manner.

Riera [3] and Riera and Rocha [13] adopted the softening law for quasi-fragile materials proposed by Hilleborg [14], extending the Discrete Element Model to handle fragile fracture. The first constitutive law was the bilinear shown in Fig 1c, which was extensively used to simulate the behavior of quasi fragile materials. But in the present work alternative Element Constitutive Relationships (ECRs) were studied, namely the tri-linear model and the exponential softening model also shown in Fig 1c. Riera and Rocha [13] defined the toughness G_f as a random variable with a Weibull probability distribution with two parameters.

3. Damage assessment

In the ensuing comparison of the performance of the different laws, damage in an element is quantified by a dimensionless number between 0 and 1. This *damage index* is defined as the relation between the energy dissipated by damage and the energy necessary to fracture the area of influence of the element. This index, denoted as I_D , aims at quantifying the *scalar damage*, by averaging the damage index of all 26 elements in a given cubic modulus. The directional index I_{Dj} , $j=x,y,z$ quantifies damage in the coordinate directions x,y and z. The proposed damage indexes were computed in simulated square plates, fixed at their lower face and subjected to monotonically increasing displacements at nodes on their upper face, which induce a nominally uniform strain rate in the specimens. The plates were analyzed up to complete failure. In all cases, nodal displacements in the normal direction to the plate middle surface were restrained, in order to simulate Plane Strain conditions. It is important to notice that the specific fracture energy G_f is modeled as a random field.

The plate final configurations, obtained with the three ECR examined herein were similar, for which reason only one DEM rupture configuration is shown in Fig 2a. The global response in terms of stress and strain for the models using the three ECR is presented in Fig 2c. Also in this case the global responses are similar up to the maximum stress. After this point, the differences among the responses increase.

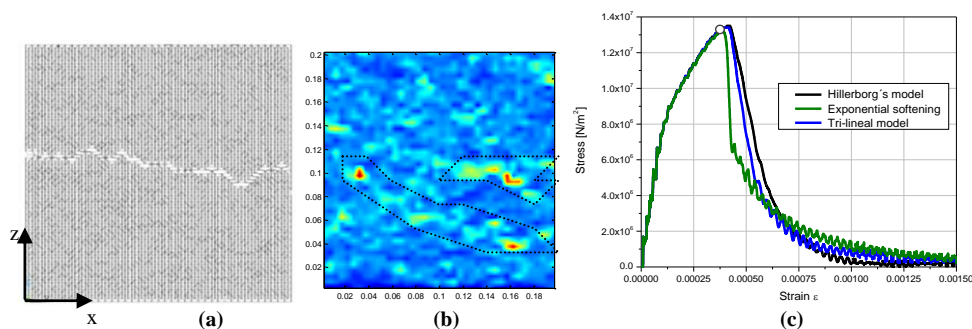


Figure 2. (a) A typical DEM rupture configuration. (b) Damaged map in the white point indicated in Fig (c). (c) Global Stress Strain curves for the ECR proposed.

In Fig 2.b the scalar damage index I_D at the point indicated in Fig 2c is shown for the three laws examined herein. In this case the three models presented similar patterns. Note also that an incipient coalescence of damage clusters, shown within dotted contours in Fig.2.b, may be perceived.

4- Conclusions

The theoretical basis of the truss like Discrete Element Method (DEM) is summarily presented. Three Element Constitutive Relations (ECR) are described: Hilleborg's Model, the tri-linear and the exponential softening models. A preliminary evaluation of these three models in a tensile test simulation is herein presented for only one set of parameters, that is, the same G_f and the same ε_p . It is initially concluded that:

- No perceptible difference was found between the three models up to the peak load. The influence of the softening shape on global results was marginal, possibly due to the filtering effect of the randomness introduced in the models.
- The proposed damage index captures incipient localization at the point indicated in Fig 2b, (see the dotted contours).
- Finally we suggest that the method proposed could be a useful tool to evaluate the transition between damage and fracture in solid mechanics problems.

Acknowledgement. The authors acknowledge the sponsorship of CNPq and CAPES, Brazil.

5. References

- [1]Munjiza, A (2009) Special issue on the discrete element method: aspects of recent developments in computational mechanics of discontinua, Engineering Computations, Vol. 26 Iss: 6, pp.
- [2] Nayfeh A.H., Hefzy M. S.: "Continuum modeling of three-dimensional truss-like space structures". AIAA Journal, 1978; 8:779-787.
- [3] Riera J. D.: "Local effects in impact problems on concrete structures". Proceedings, Conference on Structural Analysis and Design of Nuclear Power Plants, Porto Alegre, RS, Brasil, 1984; Vol. 3,CDU 264.04:621.311.2:621.039.
- [4] Riera J.D., Iturrioz I.: Discrete element dynamic response of elastoplastic shells subjected to impulsive loading. Communications in Num. Meth. in Eng.1995; 11: 417-426
- [5] Riera J.D., Iturrioz I.: "Discrete element model for evaluating impact and impulsive response of reinforced concrete plates and shells subjected to impulsive loading". Nuclear Engineering and Design, 1998; 179: 135-144.
- [6] Schnaid F., Spinelli L., Iturrioz I., Rocha M. : "Fracture mechanics in ground improvement design", Ground Improvement, 2004; 8:7-15.
- [7] Miguel, L.F.F., Iturrioz I., Riera J.D., 2010. Size effects and mesh independence in dynamic fracture analysis of brittle materials. CMES, vol.56, no.1, pp.1-16.
- [8] Dalguer L. A., Irikura K., Riera J. D., Chiu H. C.: "The importance of the dynamic source effects on strong ground motion during the 1999 Chi-Chi, Taiwan, earthquake: Brief interpretation of the damage distribution on buildings". Bull. Seismol. Soc. Am. 2001; 91:1112-1127.
- [9] Rios R.D, Riera J.D.: "Size effects in the analysis of reinforced concrete structures". Engineering Structures 2004; 26:1115-1125.
- [10] Miguel, L. F. F., Riera, J. D., and Iturrioz, I.: "Influence of size on the constitutive equations of concrete or rock dowels". International Journal for Numerical and Analytical Methods in Geomechanics 2008; 32: 1857-188.
- [11] Iturrioz I., Miguel L. F. F., Riera J. D.: "Dynamic fracture analysis of concrete or rock plates by means of the Discrete Element Method". Latin American Journal of Solids and Structures 2009; 6: 229-245.
- [12] Kosteski L, Iturrioz I, Batista RG, Cisilino AP (2011) The truss-like discrete element method in fracture and damage mechanics. Engineering Computations, 28:6, 765-787.
- [13] Riera, J. D., Rocha M. M.: "A note on the velocity of crack propagation in tensile fracture", Revista Brasileira de Ciencias Mecanicas,1991; 3: 217-240.
- [14] Hillerborg A.: "A model for fracture analysis", Cod. LUTVDG/TVBM 1971; 300: 51-81.

ANALYSIS OF CRACK DISPLACEMENTS ON RESIDENTIAL STRUCTURE INDUCED BY BLASTING AND EARTHQUAKE VIBRATIONS AND DAILY CHANGES OF TEMPERATURE AND RELATIVE HUMIDITY

L. Kričak¹, M. Negovanović², I. Janković³, D. Zeković⁴, S. Mitrović⁵

^{1,2,3,4} Blasting Center, Faculty of Mining and Geology
The University of Belgrade, Djusina 7, 11000 Belgrade, Serbia
e-mail: kricak@rgf.bg.ac.rs, milanka@rgf.bg.ac.rs, ivanj@rgf.bg.ac.rs, dario@rgf.bg.ac.rs
⁵ Copper Mining and Smelting Complex Bor, Djordja Vajferta 29, 19210 Bor, Serbia
e-mail: stojanmitrovic@gmail.com

Abstract. The paper presents an analysis of the results of continuous remote monitoring of crack displacements induced by vibrations from blasting and earthquake as well as daily changes of temperature and relative humidity on the house located at 950 m from the final contour of the open pit copper mine Veliki Krivelj Bor, Serbia. Cracks were observed in the period from early August to early November 2010. Along with crack monitoring, vibration monitoring instruments were also placed in the house for continuous measurement of blast-induced vibrations. During continuous remote monitoring, the earthquake occurred on November 3rd 2010 with the epicenter located ten kilometers north of Kraljevo, Serbia. Vibration instruments recorded successfully the vibrations induced by earthquake.

The measurement results showed surprisingly large crack response to daily variations of temperature and relative humidity. Crack displacements were several tens of times larger than the displacements due to vibrations from blasting while the maximum crack response from the earthquake was six times greater than that from blasting.

1. Introduction

Blasting is still the most effective and inexpensive method for primary fragmentation of hard rocks in mines. Some blasting effects are desirable while others are not useful and might be even dangerous for the environment [1]. The owners of residential structures located around the mine sites the appearance of new cracks on structures usually associate with blast-induced vibrations. Damage in buildings can be classified into two types: 1) cosmetic and 2) structural [2]. The formation of minor hairline cracks on drywall surfaces is referred to cosmetic damage while structural damage involves more major cracking. Basically, cracks are found to be caused by the following: differential thermal expansion, structural overloading, chemical changes in mortar, bricks, plaster, and stucco, shrinkage and swelling of wood, fatigue and aging of wall coverings, differential foundation settlement [3]. Crack response is measured in terms of crack displacement, i.e., change in crack width, rather than total crack width [4]. Therefore crack response may be positive or negative since it is a measure of change rather than absolute width.

2. Remote continuous monitoring of crack displacement

Crack displacements were being monitored continuously within the period from early August to early November 2010. Along with crack monitoring outside/inside temperature

and relative humidity were also measured. Sampling intervals were 1 and 2 min. During some blasting operations, crack displacements were measured directly with a sampling interval of 1 s. Also, high-speed crack monitoring was activated so the system recorded crack displacement 100 times per second. Along with the crack displacement measurement, blast vibrations were also measured with two four-channel vibration monitoring instruments [5]. Distances from the instruments to blasting sites were determined by the GPS system. During continuous remote monitoring, the earthquake occurred on November 3rd 2010. The epicenter of the earthquake was located ten kilometers north of Kraljevo. The earthquake had magnitude of 5.3 (Richter magnitude scale) and took place at 01:56 local time. Vibration instruments recorded successfully vibrations from earthquake.

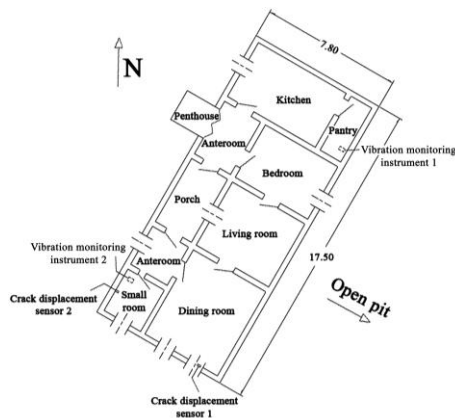
2.1. The system for continuous remote crack displacement monitoring



Figure 1. System for continuous remote crack monitoring

Continuous remote crack displacement monitoring was carrying out using the system [6] shown in Figure 1. The system consists of two data loggers, a device for data transmission and alarming, pc software and crack displacement, air temperature and humidity sensors.

Air temperature and humidity sensors are in data loggers. Measuring and storing rhythm of data loggers are adjusted via pc software. There is an option to activate high-speed crack monitoring with up to 100 Hz. Device for transmission and alarming is fully automated for data transmission via e-mail and for alarming via SMS or e-mail. Start time and data transmission frequency are configurable via pc software.



3. The location of the house and monitoring instruments

The house is located 950 m from the final contour of the open pit copper mine Veliki Krivelj, Bor, Serbia. Positions of the crack displacement sensors and vibration monitoring instruments are shown in Figure 2. Crack displacement sensors were mounted on the wall perpendicularly to the long direction of the crack in the plane of the wall.

Figure 2. Plan view of the house showing the locations of the crack displacement sensors and vibration monitoring instruments, [7]

4. Analysis of results of the crack displacement measurements

Figure 3a. shows blast vibration waveform recorded by vibration monitoring instrument 2 during the blast carried out on August 7th 2010 at 13:05 h. The maximum peak was vertical peak particle velocity 0.66 mm/s with a dominant frequency of 12.5 Hz. Maximum charge weight per delay in this blast was 330 kg and the distance between the house and the

blasting field was 1425 m. Maximum displacements of both cracks induced by this blasting were 3 μm , (Figure 3b).

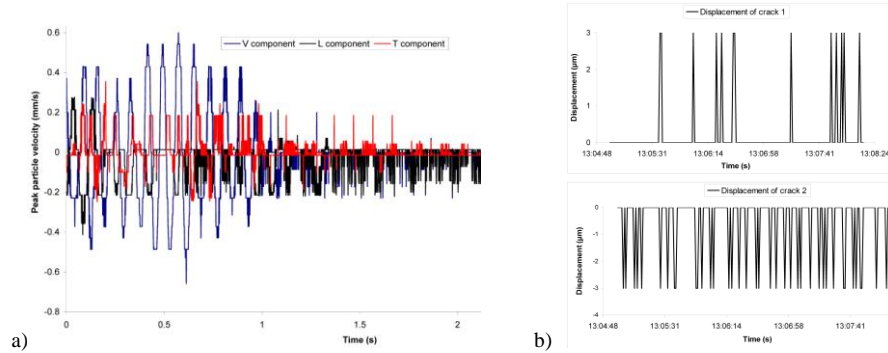
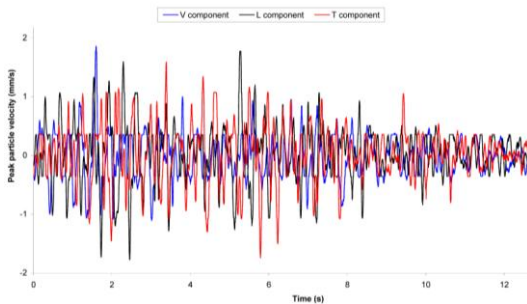


Figure 3. a) Blast vibration waveform and b) maximum displacements of crack 1 and 2 due to the blast performed on August 7th 2010 at 13:05 h

Within the whole observation period, the values of recorded peak particle velocities were far less than 5 mm/s. According to the German standard DIN 4150-3:1999 [8] no cosmetic damage of residential structure is expected when peak value of any of three components of particle velocity is in the range of 5-15 mm/s at frequencies from 10 to 50 Hz. Sometimes the measured vibration velocities were under 0.5 mm/s (trigger level of the instruments). The values of crack displacement induced by blasting were in the range of 3 to 5 μm .

Figure 4. shows measured peak particle velocity due to earthquake occurred on November 3rd 2010 at 01:56 h. The values of peak particle velocities recorded by the same instrument

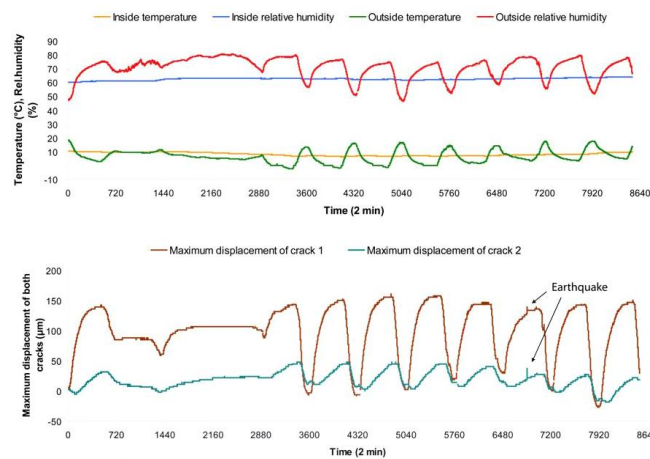


were: vertical peak 1.86 mm/s (freq. 3.54Hz, dominant freq. 3.0Hz), longitudinal peak 1.77 mm/s (freq. 3.64Hz, dominant freq. 2.4Hz) and transversal peak 1.75 mm/s (freq. 5.04Hz, dominant freq. 2.1Hz). Maximum displacement of crack 1 due to the earthquake was 11 μm while the displacement of crack 2 was 18 μm , Figure 5.

Figure 4. Measured peak particle velocities due to earthquake occurred on November 3rd 2010 at 01:56 h

During the whole observation period the weather conditions varied, with outside temperature and relative humidity ranging between -2.5 °C and 35.7° C and 31.9 to 88.3 % respectively [7]. Within this period, the interior of the house was not heated. Figure 5. shows the measured maximum displacements of both cracks due to daily changes in temperature and relative humidity from October 24th 2010 at 14:52 h to November 5th 2010 at 10:58 h. Measuring intervals of temperature, relative humidity and crack displacement were 2 min. Positive values in the graphic show shrinkage of crack while the negative ones show crack expansion. Time axis is divided into 720 (x 2min) or 24 h. Maximum shrinkage of crack 1 of 174 μm (peak to peak) was recorded from November 4th 2010 at 14:42 h to November 5th 2010 at 4:52 h and maximum expansion of 164 μm was recorded from November 4th 2010 at 8:12 h to November 4th 2010 at 14:22 h, [7,9]. These values of shrinkage and the expansion of crack 1 were also the highest values during the whole three

month observation period. Within the whole monitoring period, maximum shrinkage of



crack 2 of 64 μm was recorded from August 23rd 2010 at 20:13h to August 24th 2010 at 8:10 h while maximum expansion was from August 27th 2010 at 10:39 h to August 27th 2010 at 17:14 h of 77 μm [7,9].

Figure 5. Measured maximum displacements of both cracks due to daily changes in temperature and relative humidity from October 24th 2010 at 14:52 h to November 5th 2010 at 10:58 h with the displacements of both cracks induced by earthquake

5. Conclusion

Continuous remote monitoring of crack displacements on residential structure has shown that the effect of weather is not so negligible. Crack displacements caused by daily changes in temperature and relative humidity were several tens of times larger than the displacements due to vibrations from blasting. Some researchers [10] reported that the measured crack displacements induced by blasting when the peak particle velocity was even 10 mm/s were still only 1/6 those induced by daily temperature changes. It should be noted that when the blast operations are control and the levels of blast-induced vibrations are within the prescribed limits [8], there is no risk of damage to residential structures. Measured crack displacements induced by the vibrations from earthquake were six times greater than the displacements induced by blasting vibrations.

References

- [1] Kričak, L.(2006), *Blasting seismic*, Blasting Center, Faculty of Mining and Geology, Belgrade, Serbia, pp.51.
- [2] Gad, E. F., Wilson, J. L., Moore, A. J., Richards, A. B. (2005), Effects of Mine Blasting on Residential Structures, *Journal of Performance of Constructed Facilities*, Vol. 19, No. 3, Baltimore, MD, United States, pp. 222-228.
- [3] Dowding, C.H. (1996), *Construction Vibrations*, Prentice Hall, Englewood Cliffs, NJ, USA, pp.182.
- [4] Kosnik, D.E. (2009), *Autonomous Crack Displacement Monitoring of a Residence Near a Quarry*. pdf, Autonomous Crack Displacement Publications, Northwestern University, Evanston, IL, USA, pp.5.
- [5] ABEM Vibraloc, Sweeden. <http://www.abem.se>
- [6] <http://www.scantronik.de>
- [7] Negovanović, M., Kričak, L., Janković, I., Zeković, D., Ignjatović, S. (2012), Measurement of crack displacement on residential structure due to blast-induced vibrations and daily changes of temperature and relative humidity. Accepted paper, *Journal Technics Technologies Education Management*, Vol. 7. No.1 u II/III.
- [8] German Standards, DIN4150 Part 3 (1999), *Structural vibrations in building, effects on structures*, Berlin, Germany.
- [9] Kričak, L., Negovanović, M., Janković, I., Zeković, D., (2011), Continuous monitoring of crack displacement on residential structure in order to compare the effects of blasting and weather, *Proceedings of the 7th Scientific and Professional Conference "Rating condition, maintenance and repair of buildings and settlements"*, Zlatibor, Serbia, pp.391- 400.
- [10] AMA, (2005), *Structure Response Study*, Report prepared for the City of Henderson, NV by Aimone-Martin Associates.

ON THE CREEP-FATIGUE LIFETIME OF TURBINE HOUSINGS AFFECTED BY APPLICATION-SPECIFIC LOAD CONDITIONS

F. Laengler¹, T. Mao² and A. Scholz²

¹BorgWarner Turbo Systems Engineering GmbH,
Mannheimer Strasse 85/87, 67292 Kirchheimbolanden, Germany
e-mail: flaengler@borgwarner.com

²Institut fuer Werkstoffkunde,
Technische Universitaet Darmstadt, Grafenstrasse 2, 64283 Darmstadt, Germany
e-mail: mao@mpa-ifw.tu-darmstadt.de, scholz@mpa-ifw.tu-darmstadt.de

Abstract. The turbine housing of an exhaust turbocharger is exposed to extensive cyclic thermo-mechanical loading. Consequently, the design of the turbine housing becomes a major challenge in ensuring the guaranteed lifetime in relation to the high-temperature behavior of the materials. In a first step a phenomenological lifetime estimation approach together with a constitutive material model of Chaboche-type was developed and validated. The present study deals with the more detailed analysis of application-specific phenomena. The influence of strain rate and mean strain has been investigated on the austenitic casting material Ni-resist D5S within the framework of turbine housing design adaption.

1. Introduction

The most cost-intensive key component of a turbocharger is the turbine housing (T/H) that provides the kinetic energy required for charging. Numerous test stand runs are generally inevitable in order to find the appropriate combination of the complex design and the material. Hence, there is a demand for reliable calculation methods allowing lifetime assessment with respect to thermo-mechanical fatigue (TMF) early in the design process. Improvements in this respect could be showed in terms of coupling the numerical component structural analysis with a validated phenomenological lifetime estimation approach based on creep-fatigue interaction [1]. Both thermal shock tests on turbine housings and TMF tests on specimens subject to characteristic load conditions have been conducted for identification and verification purposes to adapt the lifetime approach for T/H design [2]. To improve the adaption process, the influence of strain rate and mean strain has been investigated as application-specific phenomena which could occur due to the arbitrary operation conditions.

2. Lifetime assessment

The constitutive material model of Chaboche-type [3], [4] applied in the preceding Finite-Element analysis (FEA) is limited to rate-independent plasticity due to the balance between effort and quality. Time-dependent phenomena such as creep and stress relaxation, which are essential to calculate creep damage, are subsequently recalculated within the lifetime approach.

The lifetime assessment is based on a phenomenological approach, see e.g. [5], to estimate

the number of cycles until crack initiation N_f . By applying the life fraction rule [6] for creep and Miner's rule [7] for fatigue, failure is determined from the cycle at mid-life by the summation of fatigue damage L_A and creep damage L_t , wherein both failure fractions are approximately independent of each other. The damage evaluation follows Equation (1) resulting in the material-specific creep-fatigue damage sum L .

$$L_t + L_A = N_f \left(\sum_j \frac{\Delta t_j(\sigma_j^*)}{t_u(\sigma_j^*)} + \frac{1}{N_{fo}} \right) = L \quad (1)$$

Creep damage is calculated with respect to variation of stress during a cycle. When fulfilling the creep condition at an individual increment j within a cycle, the quotient of the corresponding incremental time interval length Δt_j and the rupture time t_u of the effective stress σ_j^* during the increment is calculated. To obtain the effective acting stress σ_j^* , the stress relaxation of FEA resultant stress σ_j is recalculated by the use of both, the Norton-Bailey power law [8] to describe secondary creep and the time hardening rule. The stress relaxation term in Equation (2) is calculated with backstress X_j correction and by the subtraction of the continuous accumulated creep strain $\varepsilon_{c,j}$ multiplied by the Young's modulus E_j at increment j .

$$\sigma_j^* = \sigma_j - X_j - E_j \varepsilon_{c,j}, \quad \varepsilon_{c,j} = \varepsilon_{c,j-1} + \Delta \varepsilon_{c,j} \quad (2)$$

In the case of fatigue damage, it is proposed that the LCF life curves (see e.g. Figure 1) at maximum cycle temperature T_{\max} and minimum cycle temperature T_{\min} together with the maximum strain width range $\Delta \varepsilon_{\max}$ be considered. In order to calculate a geometric temperature-dependent mean value of fatigue life N_{fo} at mid-life, the relationship in Equation (3) was introduced.

$$\frac{1}{N_{fo}} = \frac{1}{2} \left[\frac{1}{N_f \Delta \varepsilon_{\max}, T_{\max}} + \frac{1}{N_f \Delta \varepsilon_{\max}, T_{\min}} \right] \quad (3)$$

3. Application-specific phenomena

In general, isothermal strain controlled LCF tests are conducted by applying symmetric triangular shaped cycles fully reversed (strain ratio $R_\varepsilon = -1$) without dwell period at a constant strain rate $d\varepsilon = 10^{-3} \text{ s}^{-1}$. The strain load is driven by the constrained thermal expansion of the T/H, so that several strain rates of lower magnitude as well as mean strains ($R_\varepsilon \neq -1$) appear as a function of different T/H positions and time. Therefore, the influences of the application-specific phenomena *strain rate* $d\varepsilon$ and *mean strain* ε_m on the LCF life curves and the deformation behavior at mid-life have been studied for Ni-resist D5S. The deformation behavior affects the calibration of the material model applied in the FEA, and the LCF damage behavior is important for the fatigue damage calculation.

In Figure 1, the effect of the strain rate $d\varepsilon = 10^{-3} \text{ s}^{-1}$ compared to a power of ten lower strain rate of 10^{-4} s^{-1} is shown. At moderate temperature around 200°C up to 500°C the LCF life curves in Figure 1 (a) illustrate two effects. At higher strain width range, the cycle number N_f decreases together with a lower strain rate. Due to the higher strain load and the lower strain rate, the superimposed creep damage should be the main damage mechanism. In

contrast to lower strain width ranges, the cycle number remains in the same range. It seems that in the latter case, the ductility of the material dominates the failure mechanism and creep, especially at lower loads, may become subordinate relevance. By increasing the temperature to 700°C the effect described at higher strains seems to be inverted, the life curves do nearly coincide. The ductility remains as the driving force for the cracking behavior.

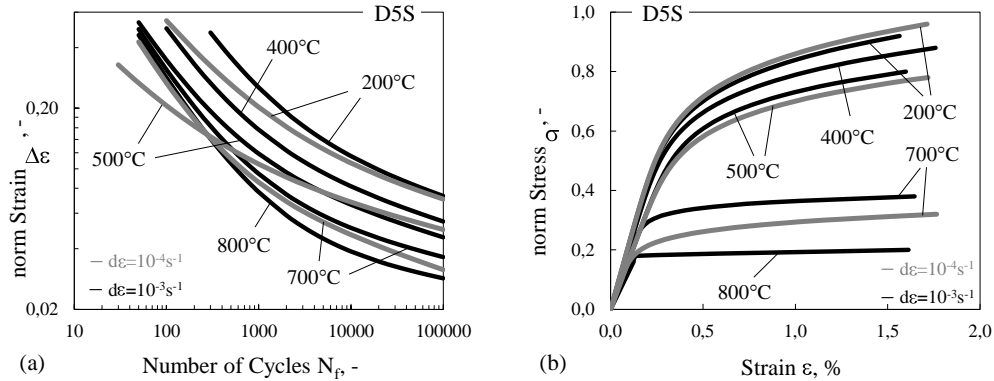


Figure 1. (a) LCF life curves and (b) Cyclic stabilized stress strain curves of D5S at strain rate of $10^{-3}s^{-1}$ (black shaded line) and $10^{-4}s^{-1}$ (gray shaded line), respectively.

In terms of the stress strain behavior Figure 1 (b) demonstrates a significant drop in strength at 700°C caused by lower strain rate. The variation in strain ratio, Figure 2 (a), indicates a loss of cycle numbers together with higher mean strains at 200°C. This trend could also be observed at 500°C, but solely for higher strains. At 700°C together with the higher ductility the difference between these two strain ratios is negligible. Apart from scattering, an effect of mean strain on the cyclic stress strain behavior at mid-life could not be observed, see Figure 2 (b). The curves are nearly identically over the whole temperature range. By reaching the stabilized material condition the stress response is already relaxed.

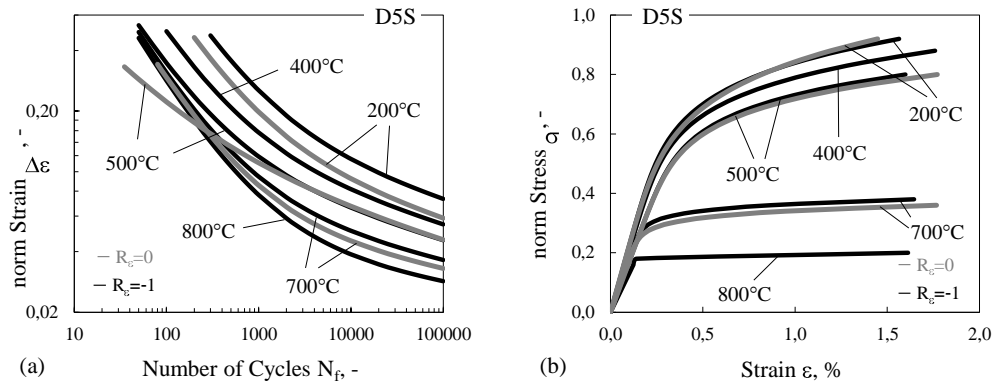


Figure 2. (a) LCF life curves and (b) Cyclic stabilized stress strain curves of D5S at $R_c=-1$ (black shaded line) and $R_c=0$ (gray shaded line), respectively.

4. TMF lifetime validation

In terms of damage evaluation and validation of the lifetime approach, a test series of in-phase TMF tests under characteristic load conditions was performed on smooth specimens [1]. Considering the testing results carried out in the previous chapter, creep damage fraction L_t and fatigue damage fraction L_A until crack initiation have been determined pursuant to Equation (1) by use of a representative cycle at mid-life; the results are shown in Figure 3 (a). By applying the evaluated mean creep-fatigue damage sum, the recalculation of the cycle numbers until crack initiation N_f^c provides the TMF lifetime estimations shown in Figure 3 (b). The results are compared to measured values N_f .

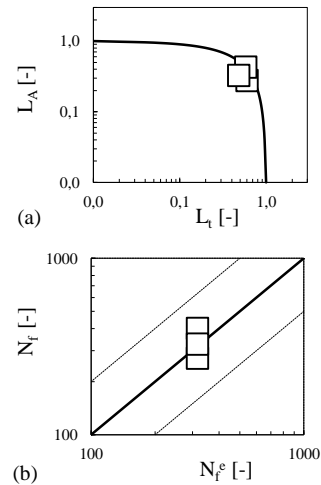


Figure 3. (a) Fatigue (L_A) and creep (L_t) damage fractions, (b) recalculated number of cycles until crack initiation N_f^c of TMF tested specimens compared to experimental results N_f .

5. Conclusion

The lifetime estimation approach demonstrates a satisfactory estimated number of cycles until crack initiation on specimens, while the adaption for T/H design is still ongoing. Alternative fatigue damage methods, e.g. based on micro crack growth, are also focused. It is assumed that tensile and compressive stress has equal effect on creep, and no distinction is made when calculating the creep damage. But there is a demand for a refinement to describe creep characteristics.

References

- [1] Laengler F. et al.(2010), Validation of a phenomenological lifetime estimation approach for application on turbine housings of turbochargers. *9th Int Conference on Turbochargers and Turbocharging*, May 19-20, London, pp. 193-205.
- [2] Laengler F., Mao T. and Scholz A. (2010), Phenomenological lifetime assessment for turbine housings of turbochargers. *9th Int Conference on multiaxial fatigue & fracture*, June 7-9, Parma.
- [3] Chaboche J.L.(1986), Time-independent constitutive theories for cyclic plasticity. *Int J Plast* 2, pp. 149-188.
- [4] Chaboche J.L.(1989), Constitutive equations for cyclic plasticity and cyclic viscoplasticity. *Int J Plast* 5, pp. 247-302.
- [5] Scholz A. and Berger C. (2005), Deformation and life assessment of high temperature materials under creep fatigue loading. *Materialwissenschaft und Werkstofftechnik* 36, pp. 722-730.
- [6] Taira S. (1962), Lifetime of structures subjected to varying load and temperature. *Creep in Structures*, N.J. Hoff (Ed.), Academic Press, New York, pp. 96-119.
- [7] Miner M.A. (1945), Cumulative Damage in Fatigue. *J Appl Mech* 12, A1S9.
- [8] Norton F.H. (1929), *The creep of steel at high temperature*. McGraw Hill, New York.

EFFECT OF ANISOTROPIC CHARACTERISTICS ON FAILURE OF REINFORCED POLYURETHANE FOAM

C.S. Lee¹, C.H. Lee², J.M. Lee³

Department of Naval Architecture and Ocean Engineering
Pusan National Univ., Jangjeon-dong Geumjeong-gu, 609-735 Busan, Republic of Korea
e-mail: ¹rich@pusan.ac.kr, ²changhunlee@pusan.ac.kr, ³jaemlee@pusan.ac.kr (Corresponding Author)

Abstract. This investigation included experimental and numerical studies for the evaluation and prediction of nonlinear material behaviours, as well as the failure characteristics of reinforced polyurethane foam (RPUF). First, the failure phenomenon and stress-strain relations of RPUF are precisely investigated using systematic experiments. Next, in order to predict the directional material nonlinear behaviours, an anisotropic viscoplastic-damage model is developed. The proposed model is coded using the ABAQUS user subroutine UMAT. Finally, the numerical simulations are compared to the uniaxial tensile and compressive test results of RPUF to validate the proposed numerical models and computational methods.

1. Introduction

Reinforced polyurethane foam (RPUF) is commonly adopted in industrial fields owing to its advantages such as excellent thermal barrier performance, impact absorption, and light weight [1]. In order to design and fabricate a robust RPUF-based structure, it is essential to evaluate the static/dynamic material behaviour of RPUF. However, there is scant literature regarding experimental research on RPUF. The existing research focuses on the elastic-dominant material properties, molecular structures, etc.

Hence, the present study examines the experimental basis and numerical studies for evaluation of the material nonlinear behaviours as well as failure characteristics of RPUF. First, the failure phenomenon and stress-strain relations of RPUF were precisely investigated using systematic experiments. Next, in order to predict the directional material nonlinear behaviours, an anisotropic viscoplastic-damage model was developed. The proposed model was coded using the ABAQUS user subroutine UMAT. Finally, the numerical simulations were compared to the uniaxial tensile and compressive test results for RPUF to validate the proposed numerical models and computational methods.

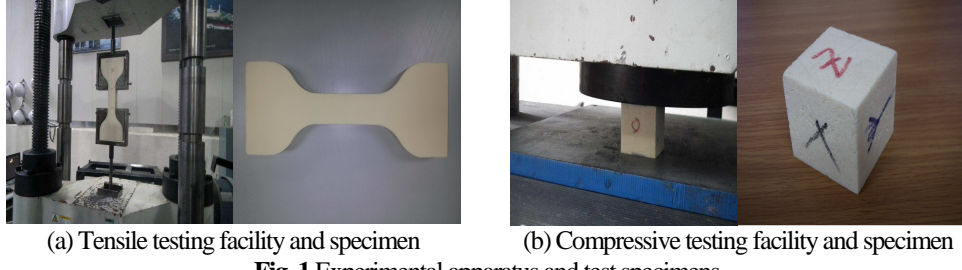
2. Experimental Investigation of Anisotropic Material Behaviours of RPUF

In order to investigate the material characteristics of RPUF, uniaxial tensile and compressive tests were carried out. Fig. 1 shows the experimental setup for each test and specimen. Each test specimen was fabricated regarding to x-, y- and z-axis direction in order to investigate the anisotropic material characteristics.

Fig. 2 shows the tensile and compressive test results. The elastic modulus and yield/fracture stress values for the x- and y-axis are nearly the same. However, results for the z-axis are entirely different owing to its different material properties.

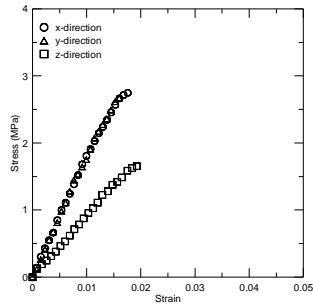
3. Anisotropic Viscoplastic-Damage Model for RPUF and Its Application to ABAQUS UMAT

In this study, a new anisotropic viscoplastic-damage model is proposed. There are lots of anisotropic viscoplastic(-damage) model for metal and nonmetal materials. However, the yield surface and loading dependence were not identified in their studies owing to the difficulty of defining these variables.

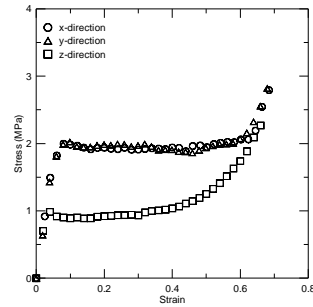


(a) Tensile testing facility and specimen

(b) Compressive testing facility and specimen

Fig. 1 Experimental apparatus and test specimens

(a) Tensile test



(b) Compressive test

Fig. 2 Representative tensile and compressive test results

The current study developed an anisotropic viscoplastic-damage model that is characterized by the explicit yield criterion and loading-unloading conditions. The model was developed based on the Bodner-Partom isotropic viscoplastic model. Moreover, the different material behaviours under tensile and compressive loadings were considered to describe the brittle and ductile material characteristics with regard to the loading directions.

The inelastic strain rate and the plastic multiplier for the anisotropic case can be modified as follows:

$$D_{\alpha} = \sum_{\beta=1}^6 \Lambda_{\alpha\beta} T_{\beta} \quad (1)$$

$$\Lambda_{\alpha\beta} = \frac{D_0}{\sqrt{J_2}} \left(\frac{3J_2}{Z_{\alpha\beta}^2} \right)^n \quad (2)$$

where D_{α} and T_{α} are the six-dimensional strain rate and the deviatoric stress, respectively; $\Lambda_{\alpha\beta}$ is the anisotropic plastic multiplier; $Z_{\alpha\beta}$ is the anisotropic total hardening; D_0 is the limiting shear strain rate; n is the strain rate sensitivity parameter; and J_2 is the second deviatoric invariant. Using the mapping algorithm, the anisotropic variables can be written as

$$\left. \begin{aligned} D_1 &= \dot{\epsilon}_{11}^p, D_2 = \dot{\epsilon}_{22}^p, D_3 = \dot{\epsilon}_{33}^p, D_4 = \sqrt{2}\dot{\epsilon}_{12}^p, D_5 = \sqrt{2}\dot{\epsilon}_{23}^p, D_6 = \sqrt{2}\dot{\epsilon}_{31}^p \\ T_1 &= S_{11}, T_2 = S_{22}, T_3 = S_{33}, T_4 = \sqrt{2}S_{12}, T_5 = \sqrt{2}S_{23}, T_6 = \sqrt{2}S_{31} \end{aligned} \right\} \quad (3)$$

The diagonal anisotropic total hardening rate for $\dot{Z}_{\alpha\alpha}^{\pm}$ can be written as

$$\dot{Z}_{\alpha\alpha}^{\pm} = \begin{cases} \dot{Z}_{\alpha\alpha}^{+} = q\dot{Z}^{+}\hat{e}_{\alpha} + (1-q)\dot{Z}^{+}u_{\alpha}\hat{e}_{\alpha} & \text{if } D_{\alpha} > 0 \\ \dot{Z}_{\alpha\alpha}^{-} = q\dot{Z}^{-}\hat{e}_{\alpha} - (1-q)\dot{Z}^{-}u_{\alpha}\hat{e}_{\alpha} & \text{if } D_{\alpha} < 0 \end{cases} \quad (4)$$

$$u_{\alpha} = \frac{S_{\alpha}}{\sqrt{3}J_2} \quad (5)$$

where $Z_{\alpha\alpha}^{+}$ and $Z_{\alpha\alpha}^{-}$ are the hardness variables for the positive and negative plastic strain rate, respectively; q is the part of the total hardening rate that is isotropic; and S_{α} is related to the direct stress by $S_1 = \sigma_{11}$, $S_2 = \sigma_{22}$, $S_3 = \sigma_{33}$, $S_4 = \sqrt{2}\sigma_{12}$, $S_5 = \sqrt{2}\sigma_{23}$, $S_6 = \sqrt{2}\sigma_{31}$. The anisotropic total hardening rate can be broken down into a hardening part and a softening part, and each component can be defined as follows:

$$\dot{Z}^{\pm} = \dot{Z}_1^{\pm} + \dot{Z}_2^{\pm} \quad (6)$$

$$\dot{Z}_1^{+} = \dot{Z}_2^{+} = 0 \quad (7)$$

$$\dot{Z}_1^{-} = \Lambda_{\alpha\alpha} m \left[\frac{Z_1^{-} - (1-\alpha)Z_{10}}{Z_{10}} \right] T_{\alpha} T_{\alpha} \quad (8)$$

$$\dot{Z}_2^{-} = \Lambda_{\alpha\alpha} h \left(1 - \frac{Z_2^{-}}{Z_{2s}} \right) T_{\alpha} T_{\alpha} \quad (9)$$

where Z_1^{-} is the pressure-free flow resistance, Z_{10} is the initial value of Z_1^{-} , m is the rate of hardening, α is the hardening parameter controlling the resumption of the strain hardening, Z_2^{-} is the asymptotic value of the end of the softening, Z_{2s} is the saturation value of Z_2^{-} , and h is the rate of softening.

In order to evaluate the damage evolution of RPUF, the Gurson-Tvergaard model was adopted. Based on this model, the void nucleation and growth of RPUF can be quantitatively described as follows:

The void volume fraction rate \dot{f} can be broken down into the void growth part \dot{f}_{grow} and the void nucleation part \dot{f}_{nuc} as follows:

$$\dot{f} = \dot{f}_{grow} + \dot{f}_{nuc} \quad (10)$$

The void growth rate is given by the mass conservation principle as follows:

$$\dot{f}_{grow} = 3(1-f)^2 q_1 q_2 f \left(\Sigma_{ij} : \frac{\partial \Phi}{\partial \Sigma_{ij}} \right)^{-1} \sinh \left(\frac{3}{2} q_2 \frac{\Sigma_h}{\sigma_e} \right) \dot{p} \quad (11)$$

where Σ_h is the macroscopic hydrostatic stress, and q_1 and q_2 are material parameters.

To capture the accelerated damage due to the cavitation of voids, according to the phenomenological hydrostatic stress-controlled nucleation law, the cavitation part can be expressed as follows:

$$\dot{f}_{nuc} = \frac{f_N}{sZ_{10}\sqrt{2\pi}} \exp \left[-\frac{1}{2} \left(\frac{\sigma_h - \sigma_N}{sZ_{10}} \right)^2 \right] \dot{\sigma}_h \quad (12)$$

where s is the standard deviation, σ_N is the mean value of the hydrostatic stress, and f_N is the volume fraction of the RPUF particles.

The aforementioned anisotropic viscoplastic-damage model has been implicitly formulated and implemented into the ABAQUS user subroutine UMAT. In the present study, the stress update algorithm is formulated on the basis of algorithmic moduli [2]. The optimal size of the time increment Δt and the corresponding strain increment are determined using the material Jacobian matrix.

4. Comparison with Experimental Results

Fig. 3 shows the comparison of the stress-strain relations between the experimental and simulation results. The simulation result, which was calculated based on the proposed anisotropic viscoplastic-damage model for RPUF, coincided well with the experimental results.

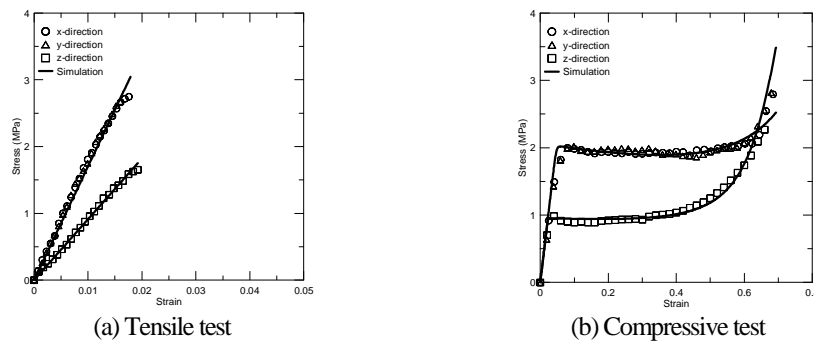


Fig. 3 Comparison of stress-strain relation between experimental and simulation results

5. Concluding Remarks

This study proposed an anisotropic viscoplastic-damage model (with no yield surface and loading independence) for RPUF to predict the tensile and compressive stress-strain relation for this material. The model also considered the effects of the tensile/compressive loading directions and hardening/softening material behaviours. In addition, the proposed model was implicitly formulated and implemented into the ABAQUS user subroutine UMAT. The simulations were compared to the uniaxial tensile and compressive test results of RPUF to validate the proposed models and computational methods; it was confirmed that the simulation result coincided well with the experimental results.

Acknowledgment. This research was supported by the Basic Science Research Program through the National Research Foundation of Korea (NRF), funded by the Ministry of Education, Science and Technology (2011-0004786). This work was also supported by the National Research Foundation of Korea (NRF) grant funded by the Korean government (MEST) through GCRC-SOP (Grant No. 2011-0030667).

References

- [1] Chun, M.S., Kim, M.H., Kim, W.S., Kim, S.H. and Lee, J.M. (2009), Experimental investigation on the impact behavior of membrane-type LNG carrier insulation system, *Journal of Loss Prevention in the Process Industries*, **22**, pp. 901-907.
- [2] Lee, C.S., Chun, M.S., Kim, M.H. and Lee, J.M. (2011), Numerical evaluation for debonding failure phenomenon of adhesively bonded joints at cryogenic temperatures, *Composites Science and Technology*, **71**, pp. 1921-1929.

STOCHASTIC DAMAGE MECHANICS OF CONCRETE: A REVIEW OF RECENT PROGRESSES

J. Li¹, X.D. Ren²

¹Distinguished Professor,
School of Civil Engineering, Tongji University, Shanghai 200092, China
e-mail: lijie@tongji.edu.cn

²Faculty of Structural Engineering,
School of Civil Engineering, Tongji University, Shanghai 200092, China
e-mail: rxdjt@tongji.edu.cn

Abstract. The nonlinear behaviors of concrete are governed by the constitutive model of concrete in the structural analysis. By appropriately considering the randomness and the nonlinearity, the stochastic damage mechanics of concrete has been systematically investigated by the author and collaborators. The achievements and recent developments are briefly reviewed in the present paper. It is found that the behaviors of concrete show strong dependent to the coupling of randomness and nonlinearity. And the random fluctuation of should be carefully considered to handle the failure of concrete structures.

1. Introduction

As is well known, concrete plays an essential role for the construction of infrastructures. On the other hand, some fundamental problems still remain controversial even in nowadays, especially for the constitutive modeling of concrete and nonlinear analysis for concrete structures. Actually, in the past 50 years, the developments of solid mechanics, including the nonlinear elastic theory, the plastic theory, and the fracture mechanics, have been introduced to simulate the mechanical performances of concrete. However, no widely accepted model has been established due to the extraordinary complexity of concrete materials. How to represent the performance of concrete still remains very challenging for the researchers and engineers. Since 1980s, the establishment of damage mechanics [1] has led to a series of substantial changes for the constitutive modeling of concrete. By taking this advantage, especially considering the observed nonlinearities and randomness of concrete, a complete framework of stochastic damage mechanics has been well developed. The present paper intends to present a summary of these works.

2. Stochastic damage model of concrete

We firstly propose a new bi-scalar elasto-plastic damage model [2] as the framework to describe the multi-axial behavior of concrete. Consider the strain split as follows

$$\boldsymbol{\varepsilon} = \boldsymbol{\varepsilon}^e + \boldsymbol{\varepsilon}^p . \quad (1)$$

Define the effective stress as the stress applying on the undamaged material, we have

$$\bar{\boldsymbol{\sigma}} = \mathbf{C}_0 : \boldsymbol{\varepsilon}^e. \quad (2)$$

where the forth order tensor \mathbf{C}_0 denotes the elastic stiffness tensor of the undamaged materials. To consider the tensile and the compressive loading conditions, define the decomposition of effective stress as follows

$$\bar{\boldsymbol{\sigma}} = \bar{\boldsymbol{\sigma}}^+ + \bar{\boldsymbol{\sigma}}^-. \quad (3)$$

Then by introducing the Helmholtz free energy and using the law of thermo-dynamics, we obtain the damage model in multi-dimension. The stress-strain relation is

$$\boldsymbol{\sigma} = (\mathbf{I} - \mathbf{D}) : \mathbf{C}_0 : (\boldsymbol{\varepsilon} - \boldsymbol{\varepsilon}^p). \quad (4)$$

The evolution of plastic strain $\boldsymbol{\varepsilon}^p$ could be defined by the effective space plasticity as follows

$$\begin{aligned} \dot{\boldsymbol{\varepsilon}}^p &= \dot{\lambda}^p \partial_{\bar{\boldsymbol{\sigma}}} F^p(\bar{\boldsymbol{\sigma}}, \boldsymbol{\kappa}), \quad \dot{\boldsymbol{\kappa}} = \dot{\lambda}^p \mathbf{H}(\bar{\boldsymbol{\sigma}}, \boldsymbol{\kappa}) \\ F(\bar{\boldsymbol{\sigma}}, \boldsymbol{\kappa}) &\leq 0, \quad \dot{\lambda}^p \geq 0, \quad \dot{\lambda}^p F(\bar{\boldsymbol{\sigma}}, \boldsymbol{\kappa}) \leq 0 \end{aligned} \quad (5)$$

The forth order damage tensor is

$$\mathbf{D} = d^+ \mathbf{P}^+ + d^- \mathbf{P}^-. \quad (6)$$

where \mathbf{P}^+ and \mathbf{P}^- are projection tensors; d^+ and d^- are tensile and compressive damage variables. The evolution of damage variables could be defined by the energy equivalent strain [3] as follows

$$d^+ = F^+(\boldsymbol{\varepsilon}_{eq}^+), \quad d^- = F^-(\boldsymbol{\varepsilon}_{eq}^-). \quad (7)$$

where $\boldsymbol{\varepsilon}_{eq}^+$ and $\boldsymbol{\varepsilon}_{eq}^-$ double be calculated by

$$\boldsymbol{\varepsilon}_{eq}^+ = \sqrt{\frac{2Y^+}{E_0}}, \quad \boldsymbol{\varepsilon}_{eq}^- = \frac{1}{(\alpha-1)} \sqrt{\frac{Y^-}{b_0}}. \quad (8)$$

As is known, the damage evolution functions, e.g. $F^+(\square)$ and $F^-(\square)$, cannot be solved within the framework of continuum damage mechanics and thermodynamics. Thus we consider the mesoscopic stochastic damage model to develop the random evolutions of damage variables.

On our investigations, noticing the development of the modern damage mechanics, we believe that the damage evolution process could be reflected by two basic damage mechanisms in micro-level: tensional damage and shear damage. Every kind of micro-damage possess random fracture strain belong to specified probability distribution. Meanwhile, the plastic deformation should be considered in these micro models. On this

basic idea, two kinds of micro stochastic rupture-sliding models were suggested based on the classic parallel bundle model [4] (Fig. 1). Here the tensile element represents the tensile damage by the direct tensile rupture of a micro element, while the shear element experiences shear fracture of a micro element under compressive loading [5][6] (Fig. 2). The sliding part is introduced for both of the elements to describe the remnant deformation of concrete induced by the plastic deformation of cement matrix.

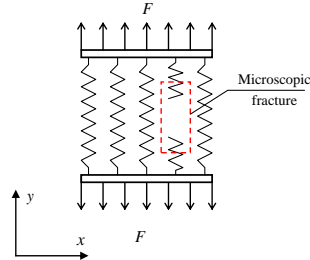


Figure 1. Parallel bundle model

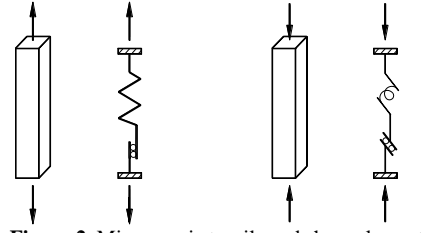


Figure 2. Microscopic tensile and shear elements

The derived stochastic damage evolution function is expressed as

$$D(\varepsilon) = \int_0^1 H[\varepsilon - \Delta(x)] dx . \quad (9)$$

$\Delta(x)$ is a 1-D randomness field defined on coordinate x . The knowledge of probability theory further gives the evolutions of mean value and standard deviation of damage as follows

$$\begin{cases} \mu_D(\varepsilon) = F(\varepsilon) \\ V_D^2(\varepsilon) = 2 \int_0^1 (1-\gamma) F(\varepsilon, \varepsilon; \gamma) d\gamma - F^2(\varepsilon) \end{cases} . \quad (10)$$

By using the stochastic damage evolution (9) to substitute the damage evolutions in Eq. (7), the multi-dimensional stochastic damage model could be established.

3. Stochastic nonlinear simulation of concrete structures

Based on the proposed stochastic damage model, the stochastic nonlinear analysis of RC structures could be implemented. To investigate the stochastic nonlinear behaviors of RC structure and verify the above theory, we designed a series of experiments upon the RC short limb shear wall structures [7]. Four pins of shear wall structure were tested with the same experimental set-up (Fig. 3) and loading procedure, so that the variation of experimental results were totally induced by the randomness of materials. According to the material tests, the compressive strength and Young's modulus of concrete are the primary random variables, with the mean values $f_c = 40\text{MPa}$, $E_c = 40\text{GPa}$ and coefficient of variation 10%.



Figure 3. Experimental set-up

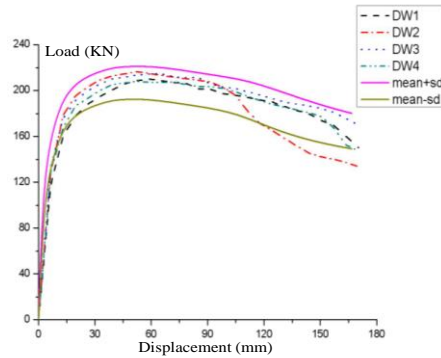


Figure 4. Load-displacement curve

The load-displacement curves are shown in Fig. 4. It is observed that all the tested curves are located within the domain defined by the mean value plus/minus standard deviation. The agreement between the experimentation and the second order results verifies the proposed stochastic damage model.

4. Concluding remarks

Obviously, even though the existing works have established a well-defined framework of the stochastic damage model for concrete, upon which a serious works still need to be done. Which may include: to consider the heterogeneous structure of concrete material in a proficient way; to describe the transfer and fluctuation of randomness among different scales; to design and control a structure based on the stochastic nonlinear analysis, etc.

Acknowledgement. Financial supports from the National Science Foundation of China for key Project (Grant No. 90715033) are gratefully appreciated.

References

- [1] Ju, J.W. (1989), On energy-based coupled elastoplastic damage theories: constitutive modeling and computational aspects, *International Journal of Solids Structures*, **7**, pp. 803-833.
- [2] Wu, J.Y., Li, J. and Faria, R. (2006), An energy release rate-based plastic-damage model for concrete, *International Journal of Solids and Structures*, **3-4**, pp. 583-612.
- [3] Li, J. and Ren, X.D. (2009), Stochastic damage model of concrete based on energy equivalent strain. *International Journal of Solids and Structures*, **11-12**, pp. 2407-2419.
- [4] Kandarpa, S., Kirkner, D.J. and Spencer, B.F. (1996), Stochastic damage model for brittle material subjected to monotonic loading. *Journal of Engineering Mechanics, ASCE*, **8**, pp. 788-795.
- [5] Li J., Zhang Q.Y. (2001), Stochastic damage constitutive law for concrete. *Journal of Tongji University: Natural Science*, **10**, pp. 1135-1141. (in Chinese)
- [6] Li, J., Yang, W.Z. (2009), Elastoplastic stochastic damage constitutive law for concrete. *China Civil Engineering Journal*, **2**, pp. 31-38. (in Chinese)
- [7] Li, K.M., Li, J. (2009), Non-linear stochastic evolution analysis of shortleg shear walls with dual binding beams. *Journal of Tongji University (Natural Science)*, **4**, pp. 432-439. (in Chinese)

MICROMECHANICALLY INFORMED MACRO-DAMAGE CHARACTERIZATION OF GRANULAR MATERIALS

Xikui Li, Youyao Du

The State key Laboratory for Structural Analysis of Industrial Equipment,
Dalian University of Technology, Dalian 116024, P.R.China
e-mail: xikuili@dlut.edu.cn

Abstract. A Voronoi cell model including not only the reference particle laid inside the Voronoi cell but also its intermediate neighboring particles is presented. Based on kinematical and kinetic analysis of a reference Voronoi cell and the homogenization procedure, the micromechanically informed constitutive relation of effective anisotropic Cosserat continuum element for granular materials is formulated. The material damage of effective anisotropic Cosserat continuum is defined as a reduction in the meso-mechanically based macroscopic elastic modular tensor. The anisotropic damage factor tensor and related damage effect tensor for Cosserat continuum are formulated in terms of the micro-structural parameters and their evolutions in the scale of the Voronoi cell. The numerical results demonstrate the applicability and performance of the derived micromechanically informed anisotropic damage factor tensor and its principal directions and values.

1. Introduction

As a micromechanically informed macroscopic constitutive model for granular materials is concerned, one has to perceive its local character due to the heterogeneity and anisotropy of microstructures of granular materials. The homogenization procedure to determine the constitutive model and failure behaviors of macroscopic effective continuum should be performed in the meso-scale, in which one focuses on the mechanical behavior of a typical small group of particles consisting of a reference particle and its surrounding intermediate neighboring particles. To describe mesoscale mechanical behavior of the small group of particles, in which voids and discontinuities exist, a Voronoi cell model including not only the reference particle laid inside the Voronoi cell but also its intermediate neighboring particles is presented. The Voronoi cell model can be used to describe local microstructures including local void ratio around a particle and to characterize contact topology of the particle with its intermediate neighboring particles and its evolution.

2. Constitutive relations and modular tensors for Voronoi cell of Cosserat continuum

To study the mechanical behaviors of the Voronoi cell as an individual Cosserat continuum element it is desired to not involve explicitly the translational and rotational displacements of the intermediate neighboring particles. To achieve this objective the translational displacements of the intermediate neighboring particles should be expressed in terms of the

displacements of the spatial contacting points of the reference particle, which are located on the boundaries of the Voronoi cell and where the neighboring particles contact with the reference particle; meanwhile, the rotational displacements of the intermediate neighboring particles will be approximately expressed in terms of the curvatures defined as the gradients of the micro-rotation for the Voronoi cell and the orientations of the lines linking the reference particle with its intermediate neighboring particles.

With kinematical and static analysis of moving pair of grains in contact and the homogenization procedure, micromechanically informed non-linear constitutive relations for the average Cauchy stresses $\bar{\sigma}_{ji}^A$ and couple stresses $\bar{\mu}_{ji}^A$ exerted on the Voronoi cell A in the two dimensional case can be expressed in the forms

$$\bar{\sigma}_{ji}^A = \bar{\sigma}_{ji}^{Ae} - \bar{\sigma}_{ji}^{Ap}, \quad \bar{\mu}_{j3}^A = \bar{\mu}_{j3}^{Ae} - \bar{\mu}_{j3}^{Ap} \quad (i, j = 1 \sim 2) \quad (1)$$

where $\bar{\sigma}_{ji}^{Ap}$ and $\bar{\mu}_{j3}^{Ap}$ stand for reductions of average Cauchy stresses and couple stresses due to relative plastic displacements of the neighboring particles in contact with the reference particle A, and are determined by means of Coulomb law of friction. The elastic parts of $\bar{\sigma}_{ji}^A$ and $\bar{\mu}_{j3}^A$ are given in terms of the average strains and curvatures $\bar{\varepsilon}_{lk}^A, \bar{\kappa}_l^A$ ($l, k = 1 \sim 2$) of the Voronoi cell A of anisotropic Cosserat continuum

$$\bar{\sigma}_{ji}^{Ae} = D_{jilk}^{e\sigma\varepsilon} \bar{\varepsilon}_{lk}^A + D_{jil}^{e\sigma\kappa} \bar{\kappa}_l^A, \quad \bar{\mu}_{j3}^{Ae} = D_{j3lk}^{e\mu\varepsilon} \bar{\varepsilon}_{lk}^A + D_{j3l}^{e\mu\kappa} \bar{\kappa}_l^A \quad (2)$$

with the micromechanically informed elastic modular tensors given by

$$D_{jilk}^{e\sigma\varepsilon} = \frac{r_A}{V_A} \sum_{c=1}^m h(u_n^{OA_t}) (k_0^c t_i^c n_j^c t_k^c n_l^c + k_n^c (r_A + r_B) n_i^c n_j^c n_k^c n_l^c) \quad (3)$$

$$D_{jil}^{e\sigma\kappa} = \frac{r_A}{V_A} \sum_{c=1}^m h(u_n^{OA_t}) k_B^c (r_A + r_B) t_i^c n_j^c n_l^c, \quad D_{j3lk}^{e\mu\varepsilon} = \frac{r_A^2}{V_A} \sum_{c=1}^m h(u_n^{OA_t}) k_0^c t_k^c n_j^c n_l^c \quad (4)$$

$$D_{j3l}^{e\mu\kappa} = \frac{r_A}{V_A} \sum_{c=1}^m h(u_n^{OA_t}) (r_A + r_B) [r_A r_B (k_s^c - k_r^c) + k_\theta^c] n_j^c n_l^c \quad (5)$$

where m is the number of intermediate neighboring particles of the reference particle A, V_A denotes the volume of the Voronoi cell A associated with particle A. $h(u_n^{OA_t})$ is the Heaviside unit function, depending on the value of $u_n^{OA_t}$ evaluated by relative translational displacements at time t of the center of particle A and the contacting point O of the particle A with one of its neighboring points, and embodies loss and generation of contact for a reference particle with one of its surrounding intermediate neighboring particles. r_A, r_B are radii of the particle A and one of its intermediate neighboring particles. t_i, n_j ($i, j = 1 \sim 2$) are components of the local Cartesian coordinate axes \mathbf{t} and \mathbf{n} assigned to the particle A with the coordinate origin set at the contacting point O . $k_n^c, k_s^c, k_r^c, k_\theta^c$ are stiffness coefficients for normal compression, sliding and rolling frictions, rolling friction moment between two particles in contact, and

$$k_B^c = (k_s^c - k_r^c) r_B, \quad k_0^c = k_s^c (r_A + r_B) + k_r^c (r_A - r_B) \quad (6)$$

It is noted that the m neighboring points are generally distributed in an anisotropic manner around the particle A in both geometrical and material senses. As a consequence, in contrast with the classical isotropic Cosserat continuum, coupled elastic modular tensors

$D_{jil}^{e\sigma\kappa}$ and $D_{j3li}^{e\mu\varepsilon}$ are no longer equal to null.

3. Micromechanically informed macro-damage characterization of anisotropic Cosserat continuum

Eq.(2) can be expressed into a matrix-vector form given by

$$\Sigma' = \mathbf{D}_e \mathbf{E}' \quad (7)$$

where and hereafter for clarity in expression of equations, superscripts or subscripts A, e and the overbars to express the average values of stresses and strains are omitted, i.e.

$$\Sigma' = \left[\{\sigma'\}^T \quad \mu'^T \right]^T, \quad \mathbf{E}' = \left[\{\varepsilon'\}^T \quad \kappa'^T \right]^T \quad (8)$$

$$\{\sigma'\} = \left[\sigma_{xx} \quad \sigma_{yy} \quad \sigma_{xy} \quad \sigma_{yx} \right]^T, \quad \mu' = \left[\mu_{2x} \quad \mu_{2y} \right]^T, \quad \kappa' = \left[\kappa_{2x} \quad \kappa_{2y} \right]^T = \left[\omega_{,x} \quad \omega_{,y} \right]^T \quad (9)$$

$$\{\varepsilon'\} = \left[\varepsilon'_{xx} \quad \varepsilon'_{yy} \quad \varepsilon'_{xy} \quad \varepsilon'_{yx} \right]^T = \left[u_{,xx} \quad u_{,yy} \quad u_{,yx} - \omega \quad u_{,xy} + \omega \right]^T \quad (10)$$

$$\mathbf{D} = \begin{bmatrix} \mathbf{D}^{\sigma\sigma} & \mathbf{D}^{\sigma\kappa} \\ \mathbf{D}^{\mu\sigma} & \mathbf{D}^{\mu\kappa} \end{bmatrix}, \quad \mathbf{D}^{\sigma\sigma} = [D_{(ji)(lk)}^{\sigma\sigma}], \quad \mathbf{D}^{\sigma\kappa} = [D_{(ji)(l)}^{\sigma\kappa}], \quad \mathbf{D}^{\mu\sigma} = [D_{(j3)(lk)}^{\mu\sigma}], \quad \mathbf{D}^{\mu\kappa} = [D_{(j3)(l)}^{\mu\kappa}] \quad (11)$$

Denoting two principal damage axes “1” and “2” with their orientations identified in terms of the inclined angles α, β to the x axis in the x-y orthogonal coordinate system, the stress vectors $\{\sigma\}, \mu$ referred to the two principal coordinates are written in the forms

$$\Sigma = \left[\{\sigma\}^T \quad \mu^T \right]^T, \quad \sigma = \left[\sigma_{11} \quad \sigma_{22} \quad \sigma_{12} \quad \sigma_{21} \right]^T, \quad \mu = \left[\mu_{31} \quad \mu_{32} \right]^T \quad (12)$$

They are related to the stress vectors $\{\sigma'\}, \mu'$ referred to the x-y coordinates as

$$\{\sigma\} = \tilde{\mathbf{T}}(\alpha, \beta) \{\sigma'\}, \quad \mu = \mathbf{T}(\alpha, \beta) \mu' \quad (13)$$

The effective Cauchy stress $\{\tilde{\sigma}\}$ and effective couple stress $\tilde{\mu}$ referred to the principal damage axes may be expressed as

$$\{\tilde{\sigma}\} = \mathbf{M}_\sigma \{\sigma\}, \quad \tilde{\mu} = \mathbf{M}_\mu \mu \quad (14)$$

where the material damage effect matrices $\mathbf{M}_\sigma, \mathbf{M}_\mu$ referred to the principal damage axes are assumed to take the forms as follows

$$\mathbf{M}_\sigma = \text{Diag}(M_\sigma^i) \quad \text{with} \quad M_\sigma^i = \frac{1}{1-d_{11}}, \frac{1}{1-d_{11}}, \frac{1}{1-d_{12}}, \frac{1}{1-d_{21}} \quad (i=1 \sim 4) \quad (15)$$

$$\mathbf{M}_\mu = \text{Diag}(M_\mu^i) \quad \text{with} \quad M_\mu^i = \frac{1}{1-d_{31}}, \frac{1}{1-d_{32}} \quad (i=1 \sim 2) \quad (16)$$

The relations between the effective stress measurements $\{\tilde{\sigma}'\}, \tilde{\mu}'$ and $\{\sigma'\}, \mu'$ referred to the x-y coordinates become

$$\{\tilde{\sigma}'\} = \mathbf{M}'_\sigma \{\sigma'\} \quad \text{with} \quad \mathbf{M}'_\sigma = \tilde{\mathbf{T}}^{-1} \mathbf{M}_\sigma \tilde{\mathbf{T}}, \quad \tilde{\mu}' = \mathbf{M}'_\mu \mu' \quad \text{with} \quad \mathbf{M}'_\mu = \mathbf{T}^{-1} \mathbf{M}_\mu \mathbf{T} \quad (17)$$

In view of the anisotropy in both material modular matrices given by Eq.(10) and material damage effects and the effect of rigid body rotation from the initial (undamaged) to current (damaged) configurations of the Voronoi cell, the damage effect matrices $\mathbf{M}'_\sigma, \mathbf{M}'_\mu$ can be expressed in terms of the degradation in the elastic modular tensors given by

$$\mathbf{M}'_\sigma = \bar{\mathbf{D}}_0^{\sigma\sigma} \cdot (\mathbf{D}_t^{\sigma\sigma})^{-1}, \quad \mathbf{M}'_\mu = \bar{\mathbf{D}}_0^{\mu\kappa} \cdot (\mathbf{D}_t^{\mu\kappa})^{-1} \quad (18)$$

$$\text{where} \quad \bar{\mathbf{D}}_0^{\sigma\sigma} = \hat{\mathbf{R}} \cdot \mathbf{D}_0^{\sigma\sigma} \cdot \hat{\mathbf{R}}^T, \quad \bar{\mathbf{D}}_0^{\mu\kappa} = \tilde{\mathbf{R}} \cdot \mathbf{D}_0^{\mu\kappa} \cdot \tilde{\mathbf{R}}^T \quad (19)$$

The subscripts “0” and “t” stand for the elastic modular matrices at initial and current configurations respectively. $\hat{\mathbf{R}}$ and $\tilde{\mathbf{R}}$ are the 4×4 and 2×2 matrices of rigid body rotation

of of the Voronoi cell for the 4×1 stress vector and 2×1 coupled stress vector respectively. It is assumed that damage effects due to the degradation in the coupled elastic modular tensors $\mathbf{D}^{\sigma\sigma}$, $\mathbf{D}^{\mu\sigma}$ are omitted. With the micromechanically informed \mathbf{M}'_{σ} , \mathbf{M}'_{μ} given by Eq.(18) and Eq.(17), the directions of the principal damage axes α , β and the principal damage values shown in Eqs.(15)-(16) can be determined.

4. Numerical examples

An anisotropic Voronoi cell representing a reference particle with its intermediate neighboring particles at its undamaged configuration is shown by Fig.1(a). It is assumed the small group of particles represented by the Voronoi cell experiences a rigid body rotation of $\theta = 60^\circ$ and a deformation resulting in material damage characterized by loss of contacts of the reference particle with one or two of its intermediate neighboring particles with grey color shown by Fig.1(b) and (c) respectively. It is observed that the principal damage directions and principal damage values to characterize the macroscopic material damage for the Voronoi cell of effective Cosserat continuum are well identified in terms of derived micromechanically informed formulations. In addition, the micro-mechanical mechanisms resulting in macroscopic material damage, i.e. loss of contacts of the reference particle with its intermediate neighboring particles and volumetric dilatation, are revealed.

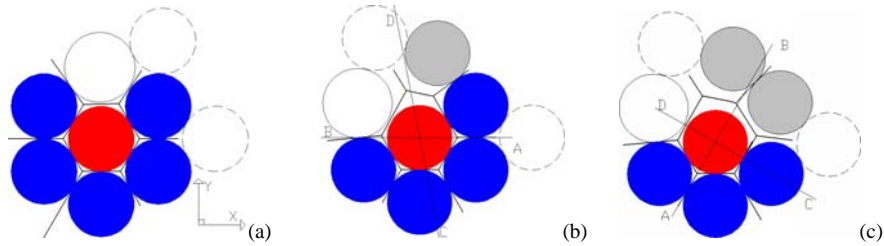


Figure 1. Micromechanically informed macroscopic principal damage directions and values. (a) undamaged cell with void ratio $e = 0.1254$; (b) damaged cell: $\alpha = 0^\circ$, $\beta = 101^\circ$, $d_{31} = 0.0972$, $d_{32} = 0.4357$, $d_{11} = 0.0972$, $d_{22} = 0.4567$, $d_{12} = 0.0972$, $d_{21} = 0.4131$, $e = 0.2466$. (c) damaged cell: $\alpha = 60^\circ$, $\beta = 150^\circ$, $d_{31} = 0.5746$, $d_{32} = 0.3618$, $d_{11} = 0.5746$, $d_{22} = 0.3283$, $d_{12} = 0.5746$, $d_{21} = 0.3922$, $e = 0.3226$.

Acknowledgement. The authors would like to acknowledge the support of this work by the National Natural Science Foundation of China through Grant No. 11072046 and the National Key Basic Research and Development Program (Contract No. 2010CB731502).

References

- [1] Chang C.S. and Kuhn M.R.(2005), On virtual work and stress in granular media, *Int. J. Solids Struct.*, **42**, pp. 3773–3793.
- [2] Walsh, S.D.C., Tordesillas, A. and Peters J.F.(2007). Development of micromechanical models for granular media. The projection problem. *Granular Matter*, **9**, pp.337-352.
- [3] Chow C.L. and Wang J(1987). An anisotropic theory of elasticity for continuum damage mechanics, *International Journal of Fracture*, **33**, pp. 3-16.
- [4] Li X.K., Chu X.H. and Feng Y.T.(2005), A discrete particle model and numerical modeling of the failure modes of granular materials, *Eng. Comput.* **22**, pp. 894–920.
- [5] Li X.K. and Tang H.X.(2005), A consistent return mapping algorithm for pressure-dependent elastoplastic Cosserat continua and modelling of strain localisation. *Comput Struct* **83**, pp.1-10.

FIBER BEAM-COLUMN ELEMENT FOR THE SEISMIC DAMAGE ANALYSIS OF RC FRAMES

Z. Li¹, G. Hatzigeorgiou²

¹China Architecture Design & Research Group,
Beijing 100044, China
e-mail: zhenglitju@163.com

²Department of Environmental Engineering,
Democritus University of Thrace, 67100 Xanthi, Greece
e-mail: gchatzig@env.duth.gr

Abstract. The development of a simple and effective concrete damage model for earthquake engineering applications is examined in this paper. This constitutive model consists of a modified uniaxial version of the Faria– Oliver model and takes into account most of the basic traits of concrete under monotonic static and dynamic loading, like the different response under compression and tension, the stiffness reduction with the increase of external loading and the appearance of softening behavior. A fiber beam-column element is investigated, which adopts the proposed concrete damage model and the Menegotto–Pinto approach for steel rebars. Then, these constitutive models are implemented into the ABAQUS general purpose finite element program to provide simple and effective computational tools for the seismic inelastic analysis of general 3-D reinforced concrete (RC) framed structures. The proposed method is demonstrated and verified by characteristic numerical examples where it is shown that the proposed damage model can describe successfully the complicated behavior of reinforced concrete under extreme seismic loads.

1. Introduction

The seismic inelastic analysis of RC structures is examined in this study based on the principles of damage mechanics. The fiber model involves the subdivision of any shape of concrete and steel rebars' composite section into small elements which are assumed to be in a state of uniaxial stress. The coupled effect between axial force and bi-axial bending moments can be straightforwardly taken into account. Effects such as concrete confinement and steel rebars buckling can be simulated through indirect consideration, through the stress–strain relations. One of the most crucial effects for the concrete behaviour has to do with the cracking process. This phenomenon can also be simulated using smeared crack approaches, e.g. using continuum damage mechanics constitutive models. Among others, one can mention here the concrete damage models of Mazars [1], Faria-Oliver [2], Hatzigeorgiou et al. [3], which have been proposed for the concrete modelling under multiaxial stress or strain state. This work proposes a modification of the uniaxial version of the Faria-Oliver damage model [2].

The paper is organized as follows. In the first part, the formulation of the uniaxial damage model of concrete is presented. Then, the Menegotto-Pinto model [4] for steel rebars is briefly described. These models are efficient for members under axial force with biaxial

bending moment and are implemented into the general purpose finite element program ABAQUS [5]. The paper concludes with critical comments related to the accuracy and applicability of the proposed method examining characteristic numerical examples.

2. Constitutive modeling

In the context of damage mechanics, uniaxial effective tensile and compressive stresses can be expressed as

$$\bar{\sigma}^+ = E_0 \varepsilon \quad \bar{\sigma}^- = E_0 (\varepsilon - \varepsilon^p) \quad (1)$$

where E_0 is Young's modulus of concrete, ε the uniaxial strain, ε^p the plastic strain. The tensile and compressive equivalent effective stress can be defined as

$$\bar{\tau}^+ = \sqrt{E_0^{-1} \bar{\sigma}^+} \quad \bar{\tau}^- = \sqrt{\frac{\sqrt{3}}{3} (K - \sqrt{2}) \bar{\sigma}^-} \quad (2)$$

where $\bar{\sigma}^+$ and $\bar{\sigma}^-$ are uniaxial effective tensile and compressive stress and K is a material constant. The damage criteria will be introduced as

$$\bar{\tau}^+ - r^+ \leq 0 \quad \bar{\tau}^- - r^- \leq 0 \quad (3)$$

where r^+ and r^- are the current damage thresholds, which control the level of the increasing damage state. One can also define the tensile, d^+ , and compressive, d^- , damage indices which describe the tensile and compressive damage effects

$$d^+ = 1 - \frac{r_0^+}{\bar{\tau}^+} e^{A^+ \left(1 - \frac{\bar{\tau}^+}{r_0^+}\right)} \quad d^- = 1 - \frac{r_0^-}{\bar{\tau}^-} (1 - A^-) - A^- e^{B^- \left(1 - \frac{\bar{\tau}^-}{r_0^-}\right)} \quad (4)$$

where A^+ , A^- and B^- are model parameters. The cyclic stress-strain curves of the modified model as well as the original model are shown in Fig.1.

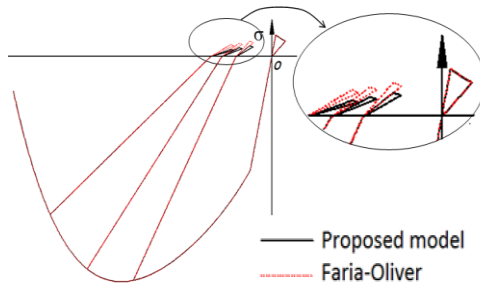


Figure 1. Concrete damage model

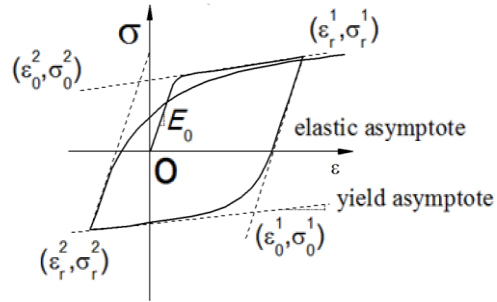


Figure 2. The MP model for steel rebars

The Menegotto-Pinto (MP) model [4] has been extensively applied for the simulation of steel rebars under cyclic loading. The MP model has been adopted by many researchers examining RC structures under seismic loads [1], due to its advantages, e.g., it satisfies with enough accuracy the experimental tests, takes into account the Bauschinger effect, etc. This model appears in Fig. 2.

3. Numerical applications

3.1. Damage analysis of a 3-D frame subjected to earthquake

This section examines the seismic damage analysis of a three-dimensional five-storey RC frame (C30, S335). The ground-plan layout of the frame is shown in Fig.3. The height of the first floor is 4.0 m while the other floors have height equal to 3.3m. The columns section dimensions are 500mm×500mm and for the beams are 300mm×600mm. The thickness of the floor slab is equal to 100mm. The finite element model of the frame is also shown in Fig.3 using sufficient number of fibers in the cross section and number of elements along the members. The bi-directional horizontal components of Imperial Valley earthquake (El-Centro 1940) are examined which excite the base of the structure.

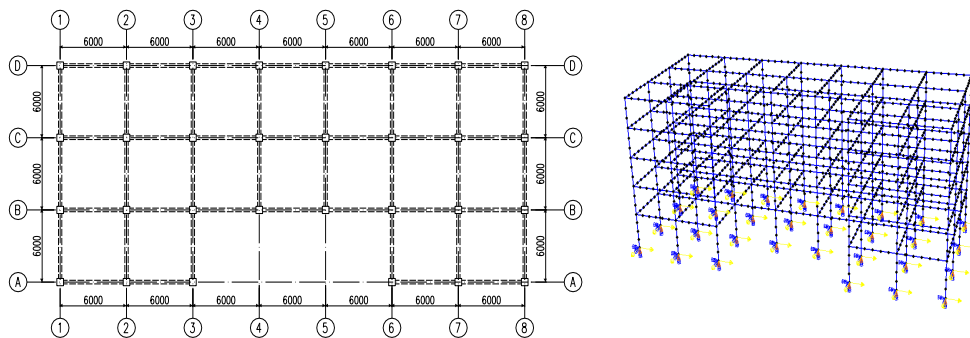


Figure 3. 3-D RC frame under consideration

Figure 4 depicts the damage at various stages where the damage evolution appears to be gentle. Although the frame was damaged severely, local or global collapse does not occur.

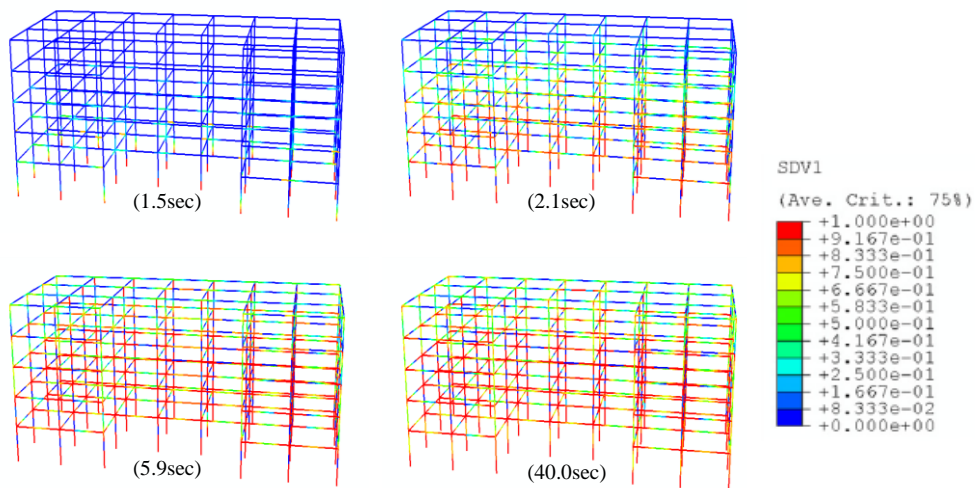


Figure 4. Tensile damage evolution process

3.2. Shaking table test of a RC bridge pier

The simulation of a shaking table experimental test of a RC bridge pier [6] is examined in the following. The geometry of the examined specimen is shown in Fig.5. The top horizontal displacement time history of the examined bridge pier under Kobe earthquake is shown in Fig.6a, where results between the experimental test and the proposed method are in good agreement. Figure 6b depicts the tensile damage evolution process of the external (more distant) concrete fiber.

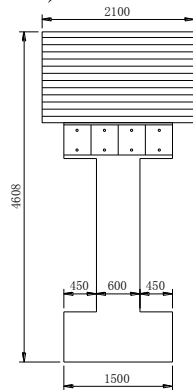


Figure 5. Geometry of bridge pier

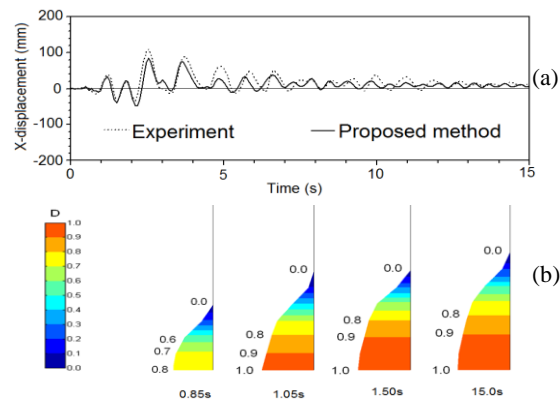


Figure 6. Selected analysis results

4. Conclusions

A new uniaxial damage model of concrete has been proposed and applied to the static and seismic analysis of various reinforced concrete members and structures. The model leads to a unified treatment of monotonic or cyclic, static or dynamic problems. The model simulates the seismic behaviour of reinforced concrete structures in an accurate and efficient way using the fiber model. The proposed constitutive relations have been implemented in the general finite element program ABAQUS. Various numerical examples have demonstrated the accuracy, efficiency and applicability of the proposed method.

References

- [1] Mazars, J. (1986), A Description of Micro- and Macroscale Damage on Concrete Structures, *Engineering Fracture Mechanics*, **25**, pp. 729-737.
- [2] Faria, R. and Oliver, X. (1993), *A Rate Dependent Plastic-Damage Constitutive Model for Large-Scale Computations in Concrete Structures*, Monografia No. 17, CIMNE, Spain.
- [3] Hatzigeorgiou, G.D., Beskos, D.E., Theodorakopoulos, D.D. and Sfakianakis M. (2001), A Simple Concrete Damage Model for Dynamic FEM Applications, *International Journal of Computational Engineering Science*, **2**, pp. 267-286.
- [4] Menegotto, M. and Pinto, P.E. (1973), Method of Analysis for Cyclically Loaded Reinforced Concrete Plane Frames Including Changes in Geometry and Non-Elastic Behaviour of Elements Under Combined Normal Force and Bending, *Proceedings of IABSE Symposium on Resistance and Ultimate Deformability of Structures Acted on by Well Defined Repeated Loads*. Lisbon, pp. 15-22.
- [5] ABAQUS (2007), Theory Manual, Version 6.7 Hibbit, Karlsson and Sorensen Inc., Pawtucket (RI).
- [6] Nishida, H. and Unjoh, S. (2004), Dynamic Response Characteristic of Reinforced Concrete Column Subjected to Bilateral Earthquake Ground Motions, *Proceedings of the 13th World Conference on Earthquake Engineering*. Vancouver BC, Canada, Paper No.576.

DYNAMIC SOIL - PIPELINE INTERACTION UNDER ENVIRONMENTAL DAMAGE EFFECTS: A LINEAR COMPLEMENTARITY NUMERICAL APPROACH

A. Liolios¹, G. Hatzigeorgiou², K. Liolios²

¹Department of Civil Engineering,
Democritus University of Thrace, 67100 Xanthi, Greece
e-mail: aliolios@civil.duth.gr

²Department of Environmental Engineering,
Democritus University of Thrace, 67100 Xanthi, Greece
e-mail: gchatzig@env.duth.gr, kliolios@env.duth.gr

Abstract. A Linear Complementarity numerical approach is presented for the unilateral contact problem of the seismic soil-pipeline interaction under degrading environmental effects. The nonconvex unilateral contact conditions due to tensionless and elastoplastic softening-fracturing behaviour of the soil as well as due to gapping are taken into account. The numerical approach is based on the one hand on a double discretization, in space by FEM and /or BEM and in time, and on the other hand on mathematical programming. The number of the problem unknowns is significantly reduced to the unilateral ones concerning the damage behaviour and a nonconvex linear complementarity problem is solved in each time-step.

1. Introduction

Damage Mechanics problems can be treated numerically as Inequality Problems of Engineering. The governing conditions of latter problems are equalities as well as inequalities. Mathematical Programming methods and optimization procedures have been used successfully for such inequality problems in Contact Mechanics and Elastoplasticity, since long time, see e.g. [1,2,8]. Recently, the Linear Complementarity approach has been also applied for Damage Mechanics problems [3-4].

In this paper, dynamic soil-pipeline interaction under environmental damage effects is considered as a Damage Mechanics problem and treated numerically as an Inequality Problem. The relevant inequalities are first due to interaction stresses on the transmitting interface between the structure and the soil, which are of compressive type only. Further, due to in general nonlinear, elastoplastic, tensionless, fracturing etc. soil behaviour under degrading environmental effects [5-7], gaps can be created between the soil and the structure. Thus, during strong earthquakes or due to high-speed trains, separation and uplift phenomena are often appeared, as the praxis has shown [6,7]. The proposed numerical method is based on a double discretization (in space and time) and methods of nonlinear programming. Thus, in each time-step a non-convex linear complementarity problem involving a reduced number of the problem unknowns is solved.

2. Method of analysis.

First, a discretization in space, by combining the finite element method (FEM) with the boundary element one (BEM), is used for the soil-pipeline system. The horizontal pipeline is discretized into beam finite elements. Each pipeline node is considered as connected to the associate soil nodes on both sides through two unilateral (interface) elements, see e.g. Fig. 1(a). Every such *u*-element consists of an elastoplastic softening spring and a dashpot, connected in parallel, and appears a compressive force $p(t,y)$ only at the time-moments t when the pipeline node comes in contact with the soil node. The relevant constitutive diagramme for the spring non-convex compressive force $p(y)$ is shown in Fig. 1(b).

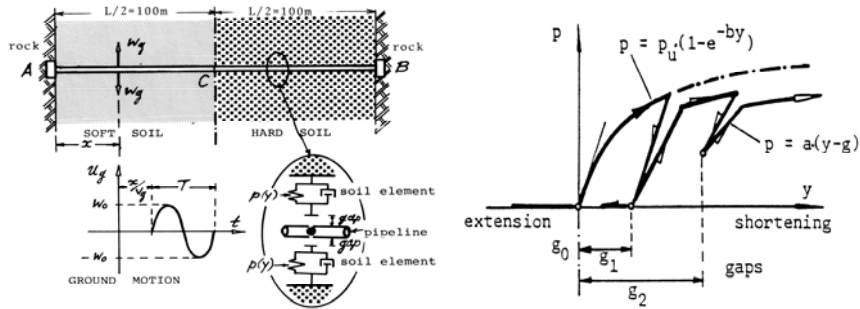


Figure 1: (a) Soil-pipeline system and (b) unilateral, degradation soil behaviour in loading-unloading with remaining gaps under environmental effects.

Function $p(y)$ is mathematically described by the following, in general nonconvex and nonmonotone constitutive relation:

$$p(y) \in C_g P_g(y), \quad (1)$$

where C_g is Clarke's generalized gradient and $P_g(\cdot)$ the symbol of superpotential nonconvex functions [8]. So, rel. (1) expresses in general the elastoplastic-softening soil behaviour, where unloading-reloading, gapping, degradating, fracturing etc. effects are included.

For the herein numerical treatment, $p(y)$ is piece-wise linearized, as in plasticity [1-4], in terms of non-negative multipliers $z(t)$ and interaction forces $r(t)$. So the conditions for the assembled soil-pipeline system are written in matrix form (underlined symbols) as follows:

$$\underline{M} \underline{\ddot{u}}(t) + \underline{C} \underline{\dot{u}}(t) + \underline{K} \underline{u}(t) = \underline{f}(t) + \underline{A} \underline{z}(t), \quad (2)$$

$$\underline{H}(t) = \underline{B} \underline{r}(t) - \underline{H} \underline{z}(t) - \underline{k}, \quad \underline{h}(t) \leq \underline{0}, \quad \underline{z}(t) \geq \underline{0}, \quad \underline{z}^T \underline{h} = 0. \quad (3)$$

Here, eq. (2) is the dynamic equilibrium condition, and relations (3) constitute a Linear Complementarity set, which concerns the unilateral, piece-wise linearized constitutive relations for the damage-interface. Dots over symbols denote, as usually, derivatives with respect to time t . \underline{M} , \underline{C} and \underline{K} are the mass, damping and stiffness matrix, respectively; $\underline{u}(t)$, $\underline{f}(t)$ are the displacement and the force vectors, respectively; \underline{A} , \underline{B} are kinematic transformation matrices; \underline{h} and \underline{k} are the yield potential vector and the unilateral capacity vector, respectively; and \underline{H} is the unilateral interaction square matrix, symmetric and positive semidefinite for hardening elastoplastic soil case. But in the case of soil softening-damage, diagonal entries of \underline{H} are nonpositive [2-4]. The mathematical treatment of the so-formulated inequality problem of rels. (1)-(3) can be realized by the variational and/or hemivariational inequality approach [8].

Further, the procedure described in [9] is followed. So, applying a time discretization and eliminating some problem unknowns, we arrive eventually at relations of the form:

$$\underline{h}_n = \underline{D}_n \underline{z}_n + \underline{d}_n, \quad \underline{z}_n \geq \underline{0}, \quad \underline{h}_n \leq \underline{0}, \quad \underline{z}_n^T \cdot \underline{h}_n = 0. \quad (4)$$

Here $\underline{D}_n, \underline{d}_n$ are known quantities from previous time-steps and the unknowns \underline{z}_n concern unilateral damage-contact quantities of the interface only. Thus, at every time-moment $t_n = n \cdot \Delta t$, where Δt is the time step, the problem of rels.(4) has to be solved. This problem is a *Non-Convex Linear Complementarity Problem (NC-LCP)*, and is solved by available methods and computer codes of nonconvex optimization [8-10].

3. Numerical example

An empty horizontal steel cylindrical pipeline of length $L = 200$ m, outside diameter 1 m, thickness 1.5 cm, elastic modulus $21 \cdot 10^7$ KN/m² and yield stress 50 KN/cm² is considered. As depicted in Fig. 1(a), the pipeline is clamped by the two anchor blocks A and B imbedded into a rock soil. The soil, into which the horizontal pipeline is buried, has an elastoplastic behaviour as in Fig. 1(a) and consists of two regions: the first (I) is soft soil, degraded due to environmental actions [5-7] with a shear modulus $G_i = 5000$ KN/m², the second (II) is hard (non-degraded) soil with a shear modulus $G_{ii} = 100000$ KN/m². The parameters for the soil elastoplastic behaviour in Fig.1(b) are taken to be [6] $a = p_u \cdot b$, $b = 100$ m⁻¹, where it is $p_u = 100$ KN/m² for the soft region (I) and $p_u = 2000$ KN/m² for the hard region (II).

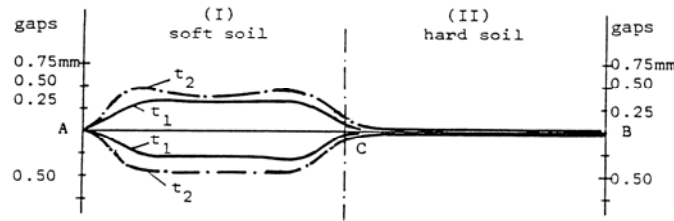


Figure 2: Gaps along the pipeline at times $t_1 = 0.6$ sec and $t_2 = 2.1$ sec.

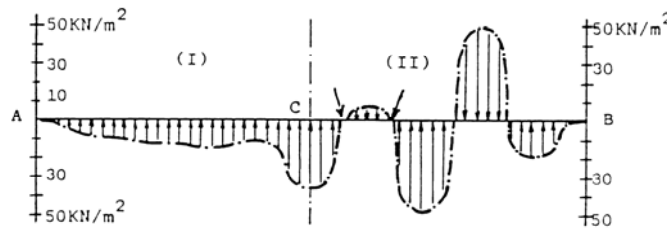


Figure 3: Soil-pressure distribution at the time $t_1 = 0.6$ sec

Further, the seismic ground excitation is assumed to be a sinusoidal horizontal wave propagation parallel to the pipeline axis (Fig. 1), with mean speed $v_g = 0.4$ km/sec in the soft region (I) and $v_g = 0.8$ km/sec in the hard one (II), frequency $f_g = 10$ rad/sec, duration $T = 2 \pi / f_g$ and maximum ground displacement $w_0 = 5$ cm. Thus the horizontal ground motion, perpendicular to the pipeline axis x , is expressed mathematically by the following relation, where $H(t)$ is the Heaviside function:

$$u_g(x,t) = w_0 \sin(t-x/v_g) \cdot \{H(t-x/v_g) - H(t-x/v_g - T)\}. \quad (5)$$

Some representative results from the numerical ones, obtained by applying the presented procedure, are here reported. So in Fig. 2 the gaps along the pipeline due to permanent soil deformations are shown for the time moments $t_1 = 0.6$ sec and $t_2 = 2.1$ sec. The difference of the gap widths in the soft and in the hard soil region is remarkable. On the other hand, in Fig. 3 it is shown the distribution of the soil-pressures at the time $t_1 = 0.60$ sec. The stresses in the soft region are smaller than in the hard one. Furthermore, a concentration of stresses is observed around the pipeline middle C, where the soil quality changes.

4 Concluding remarks

Linear Complementarity approaches can be efficiently applied in Damage Mechanics for simulating and numerically solving praxis problems. As the above indicative results of the numerical example show, unilateral contact effects due to tensionless soil capacity, degraded by environmental effects, and to gapping may be significant and have to be taken into account for the resistant construction, design and control of buried pipelines against earthquakes. These effects can be numerically estimated by the herein presented procedure, which is realizable on computers by using existent codes of the finite element method (FEM), the boundary element method (BEM) and optimization algorithms.

Acknowledgement. The third co-author (K.L.) acknowledges the support by the Project “Herakleitos II, DUTH, NSRF 2007-2013”, Greek Ministry of Education, co-financed by Greece and European Union.

References

- [1] Maier, G., Munro, J. (1982), Mathematical programming applications to engineering plastic analysis, *Applied Mechanics Reviews*, **35**, pp. 1631-1643.
- [2] G. Maier, G. Bolzon, F. Tin-Loi. (2001). *Mathematical programming in engineering mechanics: some current problems*. In: M.C. Ferris, O.L. Mangasarian, J.-S. Pang (eds), *Complementarity: Applications, Algorithms and Extensions*. Applied Optimization, Vol. 50, Kluwer Academic Publisher, Chapter 10, pp. 201-232, 2001
- [3] Bolzon, G.; Maier, G.; Novati, G. (1994): *Some aspects of quasibrittle fracture analysis as a linear complementarity problem*. In: Bittnar, Z.; Jirasek, M.; Mazars, J. (eds.), *Fracture and Damage in Quasi-brittle Structures*, E&FN Spon, London.
- [4] Bolzon, G.; Maier, G.; Tin-Loi, F. (1996): *On holonomic structural analysis as a complementarity problem*. In: Choi, C. K., Yun, C. B., Lee, D. G. (eds.), Proc. Third Asian-Pacific Conference on Computational Mechanics (APCOM '96), Seoul, Korea, Techno Press,
- [5] Wolf, J.P. (1988), *Soil-Structure-Interaction Analysis in Time Domain*. Englewood Cliffs, N.J.: Prentice-Hall.
- [6] Scott, R. (1981), *Foundation Analysis*. London: Prentice-Hall.
- [7] Tchobanoglous, G., Peavy, H. & Rowe, D. (1985), *Environmental Engineering*, MacGraw-Hill, New York.
- [8] Panagiotopoulos, P.D. , (1993), *Hemivariational Inequalities. Applications in Mechanics and Engineering*. Berlin, Springer.
- [9] Liolios, A., Radev, S., Liolios K. and Angelov, T., (2004), A nonconvex numerical approach to the seismic soil-pipeline interaction under instabilizing environmental effects, *Journal Theor. Appl. Mechanics*, vol. 34, no. 3, pp. 21-28.
- [10] Mistakidis, E.S. & Stavroulakis, G.E., (1998), *Nonconvex optimization in mechanics. Smooth and nonsmooth algorithms, heuristic and engineering applications*. Kluwer, London.

NUMERICAL AND EXPERIMENTAL MODELLING CORTICAL BONE TISSUE DEFORMATION PROCESSES

M. Lovrenić-Jugović, Z. Tonković, A. Bakić, D. Pustaić

Faculty of Mechanical Engineering and Naval Architecture,
University of Zagreb, Ivana Lučića 5, 10000 Zagreb, Croatia
e-mail: martina.lovrenic@fsb.hr

Abstract. A new one-dimensional constitutive model for the bovine cortical bone tissue is proposed to predict the experimental viscoelastic-viscoplastic-damage behaviour in creep-recovery tests. The material parameters are determined by fitting experimental results. The derived algorithm for the integration of the proposed constitutive model is implemented in the finite element formulation. The computational algorithm shows an excellent capability to describe the tensile behaviour of bovine cortical bone for the specific mechanical condition analyzed.

1. Introduction

Numerous investigations have been carried out during the past decades to evaluate nonlinear time-dependent response of bone tissue [1]. It has been found that cortical bone behaviour under tensile creep loading is characterized by three crucial regimes. The first regime is linear viscoelasticity for stress levels below some threshold value of stress. Beyond this value, the second and/or third regimes, which correspond to the damage and viscoplasticity modes, start. The second damage mode represents the generation and opening of microcracks leading to a stiffness (modulus) reduction and permanent strains. The third viscoplastic mode is due to friction of the closing (or sliding) of microcracks leading to permanent strains but no extension of damage [2].

In recent years, the ideas and approaches developed for engineering materials are used for the modelling of bone behaviour [3-5]. Numerous attempts have been made to simulate and predict the viscous damage behaviour of bone in a computer model, combining the continuum mechanics theories with the finite element (FE) analysis, but the obtained solutions still have some shortcomings ([2-5]). Constitutive models, which have to represent the bone behaviour realistically, form the core of a finite element formulation.

An algorithm which enables numerical modelling of viscoelastic-damage behaviour of cortical bone is proposed in [6]. The present paper is a continuation of that work where the viscoplastic deformation associated with creep and creep-damage is detailed analyzed for more accurate predictions. The paper is concerned with the experimental and finite element modelling of the viscoelastic-viscoplastic-damaging behaviour of bovine cortical bone. The bone behaviour is modelled by using the theory of viscoelasticity, viscoplasticity and continuum damage mechanics based on the thermodynamics of irreversible process [3]. Based on the experimental results constitutive model is developed and implemented into the finite element code ABAQUS/Standard. The accuracy of the computational procedure is tested by comparing the computed results with the own experimental data.

2. Constitutive model

A schematic representation of the stress history and strain response of cortical bone during the creep and recovery period is presented in Fig. 1.

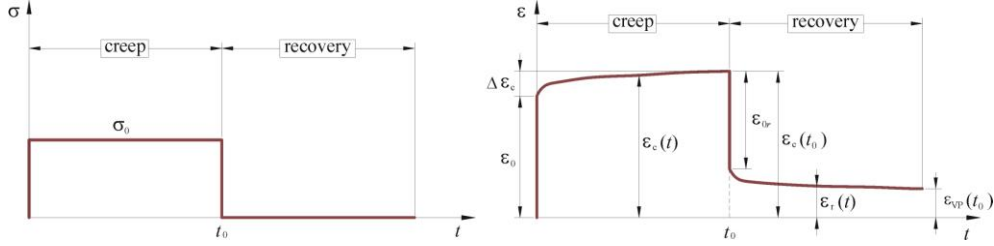


Figure 1. Schematic representation of the stress history and strain response during the creep-recovery period.

Constitutive equations, originally developed by Abdel-Tawab, Weitsman and Dasappa et al. [3, 4] for engineering materials, are employed here to model the viscoelastic–damage–viscoplastic cortical bone response. Assuming small strains, the total creep strain $\varepsilon(t)$ is additively decomposed into the viscoelastic part coupled with damage ε_{VE}^D , and the viscoplastic part $\varepsilon_{VP}(t)$, as follows

$$\varepsilon(t) = \varepsilon_{VE}^D(t) + \varepsilon_{VP}(t). \quad (1)$$

As shown in authors' previous paper [6], the viscoelastic strain coupled with damage may be expressed in the following form

$$\varepsilon_{VE}^D = \begin{cases} K_T \left[J_0 \sigma \left(1 - \frac{t}{t_c} \right)^{\frac{1}{1+r}} + J_1 \sigma t^\gamma \left(1 + \frac{1}{1+r} \cdot \frac{1}{1+\gamma} \cdot \frac{t}{t_c} \right) \right], & \text{for creep } (0 < t < t_0), \\ K_T \left[J_1 \sigma \left(t^\gamma - (t-t_0)^\gamma \right) \left(1 + \frac{1}{1+r} \cdot \frac{1}{1+\gamma} \cdot \frac{t}{t_c} \right) \right], & \text{for recovery } (t > t_0), \end{cases} \quad (2)$$

where J_0 , J_1 and γ are the viscoelastic material parameters. In Eq. (2) K_T is the ratio of “damaged” and initial compliance and t_c is the normalizing constant defined as

$$K_T = \begin{cases} 1 & \text{for } \sigma < \sigma_{th}^D, \\ 1 + a\sigma^b & \text{for } \sigma > \sigma_{th}^D, \end{cases} \quad \text{and} \quad t_c = \frac{(1-w_0)^{1+r}}{1+r} \left[\frac{C}{\langle \sigma - \sigma_{th}^D \rangle} \right]^r, \quad (3)$$

where a , b , C , r and w_0 are the damage parameters. According to Dasappa et al. [4], the following viscoplastic model, initially proposed by Zapas and Chrissman, is adopted

$$\varepsilon_{VP} = \begin{cases} A \cdot \langle \sigma - \sigma_{th}^{VP} \rangle^{m-n} \cdot t^n & \text{for } 0 < t < t_0, \\ A \cdot \langle \sigma - \sigma_{th}^{VP} \rangle^{m-n} \cdot t_0^n & \text{for } t > t_0, \end{cases} \quad (4)$$

where A , m and n denote the viscoplastic material parameters, while σ_{th}^D and σ_{th}^{VP} are the threshold values of damage accumulation and viscoplastic accumulation, respectively. Thus, viscoplastic model considers the viscoplastic strain as a nonlinear function of stress and time.

3. Experiments

The experimental samples for the study were taken from the middle portion of the tibial diaphysis of a 7.5-year-old bovine. The shape and dimensions of the specimens are shown in Fig. 2. By using an industrial water jet cutting device, the samples were cut in the form of plates with a rectangular cross section (thickness $\delta = 3$ mm) along the longitudinal axis of the bone. Thereafter, tensile cyclic creep and recovery tests are carried out at room temperature on a Messphysik Beta 50-5 testing machine at eleven different stress levels between 20 and 120 MPa. Each test consisted of 60 s of tensile creep at constant stress level, followed by 300 s of recovery per cycle. The results presented in Fig. 3 are average values from six tests at each applied stress level. From obtained experimental results, material parameters for the proposed constitutive model are determined, and are listed in Table 1. The value of damage parameter w corresponding to the failure of the material is denoted by w_F in Table 1. The procedure proposed by Dasappa et al. [4] for the determination of material parameters is used in this study.

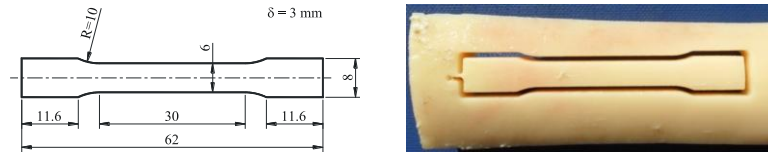


Figure 2. Specimens shape and dimensions.

Table 1. The material parameters determined by fitting experimental results of creep-recovery tests.

Parameters		Values	Parameters		Values
viscoelasticity	J_0 (MPa ⁻¹)	$4.4749 \cdot 10^{-5}$	damage	σ_{th}^D (MPa)	91.4
	J_1 (MPa ⁻¹ s ^{-γ})	$7.7233 \cdot 10^{-7}$		C (MPa s ^{γ})	826.905
	γ	0.2335		r	2.2265
viscoplasticity	σ_{th}^{VP} (MPa)	28.61		w_F	0.9912
	A (MPa ^{-m} s ^{-n})	$1.2913 \cdot 10^{-7}$		w_0	0.0488
	m	2.1711		a	$2.222 \cdot 10^{-19}$
	n	0.6582	b	8.9044	

4. Numerical formulation and results

Within the framework of numerical investigations a computational algorithm for the integration of the proposed constitutive model is derived. The derived integration algorithm and the corresponding tangent stiffness are implemented at the material point level of the one dimensional finite elements in the software ABAQUS/Standard by using the user-defined material subroutine UMAT. In order to validate the numerical algorithm, the creep and recovery simulation results are compared with the experimental data. Fig. 4 shows a comparison between the experimental data and the model predictions for creep strain over one load cycle at stress level of 110 MPa.

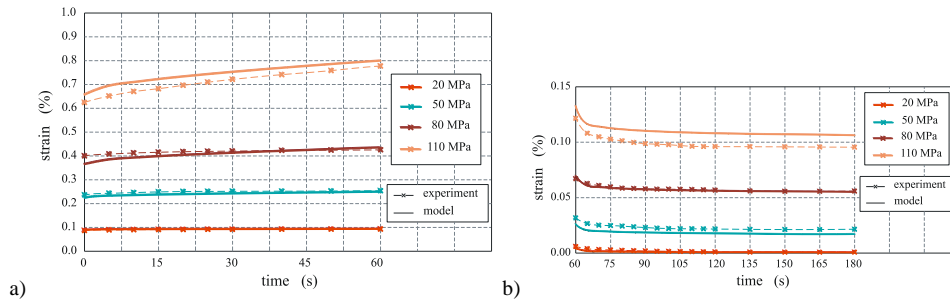


Figure 3. a) Creep and b) recovery deformations as a function of time for stress levels between 20 and 120 MPa

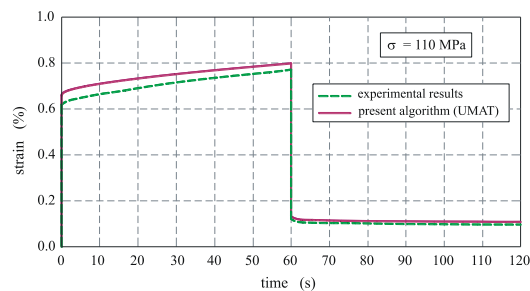


Figure 4. A comparison between the experimental data and the predictions for creep strain ($\sigma=110$ MPa).

5. Concluding remarks

A one-dimensional constitutive model and a computational algorithm for bovine cortical bone are developed to simulate the viscoelastic–viscoplastic–damage behaviour occurring during creep–recovery tests. The accuracy of the computational procedure is verified by comparing the model predictions with the experimental data. Thereby, the creep and creep–recovery deformation processes in cortical bone at different loading levels are considered. The model predictions are found to be in good agreement with the real experimental data.

References

- [1] Fondrk, M., Bahniuk, E., Davy, D.T. and Michaels, C. (1988), Some viscoplastic characteristics of bovine and human cortical bone, *Composites Part B: Engineering*, **41**(1), pp. 48-57.
- [2] Garcia, D., Zysset, P. K., Charlebois, M. and Curnier, A. (2010), A 1-D elastic plastic damage constitutive law for bone tissue, *Archive of Applied Mechanics*, **80**, pp. 543-555.
- [3] Abdel-Tawab, K. and Weitsman, Y.J. (2001), A strain-based formulation for the coupled viscoelastic/damage behavior, *Journal of Applied Mechanics, Transaction ASME*, **68**(2), pp. 304-311.
- [4] Dasappa, P., Lee-Sullivan, P. and Xiao, X. (2010), Development of viscoplastic strains during creep in continuous fibre GMT composites, *Composites Part B: Engineering*, **41**(1), pp. 48-57.
- [5] Marklund, E., Varna, J. and Wallstram, L. (2006), Nonlinear viscoelasticity and viscoplasticity of flax/polypropylene composites, *Journal of Engineering Materials and Technology*, **128**(4), pp. 527-536.
- [6] Lovrenić-Jugović, M., Tonković, Z. and Skozrit, I. (2012), Numerical modeling of damage accumulation in cortical bone tissue, *Technical Gazette*, accepted for publication.
- [7] Lovrenić-Jugović, M., Tonković, Z. and Skozrit, I. (2012), Modelling of Nonlinear Creep and Recovery Behaviour of Cortical Bone, *Key Engineering Materials*, **488-489**, pp. 186-189.

COMPUTATION METHODS AND SOFTWARE IN FATIGUE LIFE ESTIMATIONS OF STRUCTURAL COMPONENTS UNDER GENERAL LOAD SPECTRUM

S. Maksimović¹, I. Vasović², M. Maksimović³, M. Djurić¹

¹Military Technical Institute, Ratka Resanovica 1, Belgrade, Serbia
e-mail: s.maksimovic@open.telekom.rs

²Institute Goša, Milana Rakica 35, Belgrade, Serbia
e-mail: ivanavvasovic@gmail.com

³Water Supply, Belgrade, Serbia
e-mail: maksimovic.mirko@gmail.com

Abstract. Attention in this work is focused on developing computation procedures and software of aircraft structural components with respect fatigue and fracture mechanics. Computation method is based on combining singular finite elements to determine stress intensity factors for cracked structural components with corresponding crack growth laws that include effect of load spectra on number of cycles or blocks up to failure. Procedure is applied to aircraft structural components. In this investigation Strain Energy Density (SED) method is used in domain total fatigue life of structural components under general load spectrum up to crack initiation and crack growth. The SED method is based on using low cycle fatigue (LCF) properties for crack initiation and crack growth analyses [1,2]. To determine analytic expressions for stress intensity factors (SIF), that are necessary in crack growth analysis for residual life estimation, singular finite elements are used. Crack growth analysis of cracked structural elements is based on conventional Forman's low and Strain Energy Density (SED) concepts. To demonstrate efficient computation procedure in fatigue life estimation here numerical examples are included. Computation results are compared with correspond experiments. Good agreement between computation and experimental results is obtained.

1. Introduction

Many failures of structural components occur due to cracks initiating from the local stress concentrations. Attachment lugs are commonly used for aircraft structural applications as a connection between components of the structure. In a lug-type joint the lug is connected to a fork by a single bolt or pin. Generally the structures which have the difficulty in applying the fail-safe design need the damage tolerance design. Methods for design against fatigue failure are under constant improvement. In order to optimize constructions the designer is often forced to use the properties of the materials as efficiently as possible. One way to improve the fatigue life predictions may be to use relations between crack growth rate and the stress intensity factor range. To determine residual life of damaged structural components here are used two crack growth methods: (1) conventional Forman's crack growth method and (2) crack growth model based on the strain energy density method. The last method uses the low cycle fatigue properties in the crack growth model^{1,2}.

2. Determination of Fracture Mechanics Parameters of Lug Structural Components

Here are considered cracked aircraft attachment lugs, Fig 2.1. Once a finite element solution has been obtained, Fig. 2.2, the values of the stress intensity factor can be extracted from it. To determine Stress Intensity Factors of cracked aircraft attachment lugs here two approaches are used: (1) Method based on J-integral approach and (2) Method based on extrapolation of displacements around tip of crack.

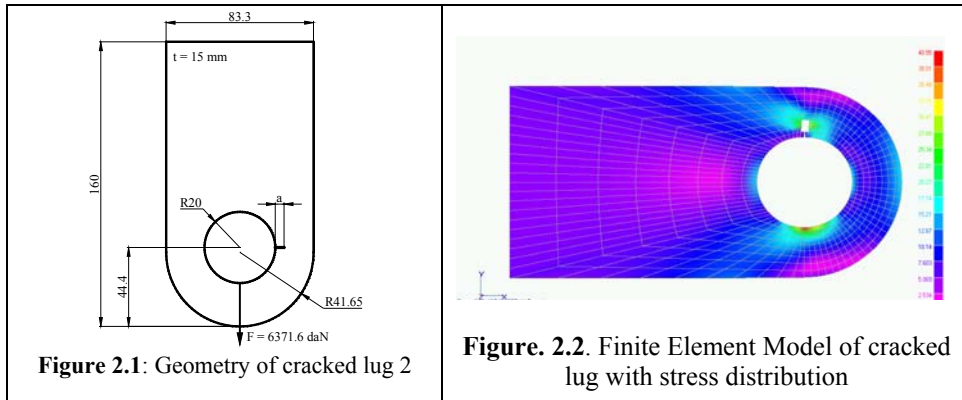


Figure 2.1: Geometry of cracked lug 2

Figure 2.2. Finite Element Model of cracked lug with stress distribution

The path-independent J-line integral which was proposed by Rice is defined as

$$J = \int_{\Gamma} \left(W dx_2 - T_i \frac{\partial u_i}{\partial x_1} ds \right) \quad (2.1)$$

where W is the elastic strain energy density, Γ is any contour about the crack tip, T_i and u_i are the traction and displacement components along the contour and s is arch-length along the contour, x_1 and x_2 are the local coordinates such that x_1 is along the crack.

3. Crack growth models

Conventional Forman's crack growth model is defined in the form³

$$\frac{da}{dN} = \frac{C(\Delta K)^n}{(1-R)K_C - \Delta K} \quad (3.1)$$

where K_C is the fracture toughness C , n – are experimentally derived material parameters. The strain energy density method can be written as^{1,2}

$$\frac{da}{dN} = \frac{(1-n')\psi}{4E I_{n'} \sigma_f' \varepsilon_f'} (\Delta K_I - \Delta K_{th})^2, \quad (3.2)$$

where: σ_f' is cyclic yield strength and ε_f' - fatigue ductility coefficient, ΔK_I is the range of stress intensity factor, ψ - constant depending on the strain hardening exponent n' , $I_{n'}$ - the non-dimensional parameter depending on n' . ΔK_{th} is the range of threshold stress intensity factor and is function of stress ratio i.e.

$$\Delta K_{th} = \Delta K_{th0}(1-R)^\gamma, \quad (3.3)$$

ΔK_{th0} is the range of threshold stress intensity factor for the stress ratio $R = 0$ and γ is coefficient (usually, $\gamma = 0.71$).

4. Numerical validation

Subject of this analyses are cracked aircraft lugs under cyclic load of constant amplitude and spectra. For that purpose conventional Forman crack growth model and crack growth model based on strain energy density method are used. Material of lugs is Aluminum alloy 7075 T7351 with the next material properties: $\sigma_m=432$ N/mm² \Leftrightarrow Tensile strength of material, $\sigma_{02}=334$ N/mm², $K_{IC}=2225$ [N/mm^{3/2}], Dynamic material properties (Forman's constants): $C=3 \cdot 10^{-7}$, $n=2.39$; Low cycle fatigue material properties of material are: $\sigma_f=613$ MPa, $\epsilon_f=0.35$, $n'=0.121$.

4.1. Determination of stress intensity factors

Here are determined stress intensity factors of cracked lug, defined in Figures 2.1 and 2.2 using different computation methods. The stress intensity factors (SIF's) of cracked lugs are determined for nominal stress levels: $\sigma_g = \sigma_{max}=98.1$ N/mm² and $\sigma_{min}=9.81$ N/mm². The corresponding forces of lugs are defined as, $F_{max} = \sigma_g (w-2R) t = 63716$ N and $F_{min}=6371.6$ N, that are loaded of lugs. For stress analyses contact pin/lug finite element model is used. Results of SIF's are given in Table 4.1. Good agreement between FE and analytic results is evident.

Table 4.1. SIFs of cracked lugs using J-integral approach and Displacement Extrapolations

Path of J-integral on locations „w“	Crack Length	J-integral approach		Method of Displacements Extrapolation		
		J-integral	K_I	K_I	K_{II}	K_{III}
	a = 5mm					
	2D	0.581	65.582	69.592	5.7803	0.000
Path 1 w=0.0 mm	3D	0.609	67.136	60.439	10.003	5.967
Path 2 w=4.75 mm	3D	0.637	68.669	66.090	8.221	2.099
Path 3 w=7.50 mm	3D	0.640	68.809	66.180	8.234	0.000

Analytic solution⁴ : $K_I=65.621$
 Results of FEM⁴ : $K_I=68.784$

4.2. Comparisons SED and conventional approach for cracked lug under load spectrum

For cracked lug No.2, Figure 2.1, with crack through the thickness the crack growth behavior under load spectra is considered. Detail experimental investigations of cracked lugs are given in reference [4]. In Figure 4.1 are shown results of crack growth results for cracked lug using two methods: (1) conventional Forman's method³ and (2) strain energy density method⁴ (GED).

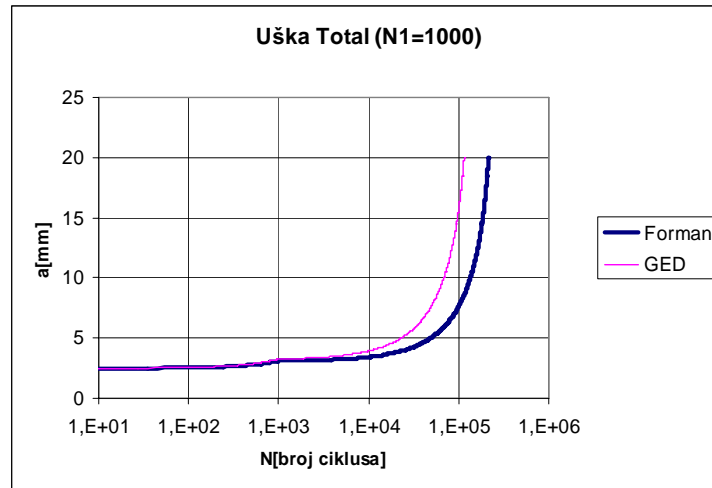


Figure. 4.1 Comparisons crack growth behavior using GED and Forman's methods

5. Conclusions

This investigation is focused on developing efficient and reliable computation methods for residual fatigue life estimation of damaged structural components. A special attention has been focused on determination of fracture mechanics parameters of structural components such as stress intensity factors of aircraft cracked lugs. Computation prediction investigations for fatigue life estimation of an attachment lug under load spectrum were performed. From this investigation followings are concluded: A model for the fatigue crack growth is included which incorporates the low cycle fatigue properties of the material. Comparisons of the predicted crack growth rate using strain energy density method with conventional Forman's model points out the fact that this model could be effectively used for residual life estimations.

Acknowledgments: This work was financially supported by the Ministry of Science and Technological Developments of Serbia under Projects OI174001 and TR-34028.

References

- [1] Sehitoglu, H., Gall, K., Garcia, A.M. (1996), Recent Advances in Fatigue Crack Growth Modelling, *Int. J. Fract.*, **80**, pp. 165-192.
- [2] Maksimovic S., Posavljak S., Maksimovic K., Nikolic-Stanojevic V. and Djurkovic V., Total Fatigue Life Estimation of Notched Structural Components Using Low-Cycle Fatigue Properties, *J. Strain* (2011), **47** (suppl.2), pp 341-349, DOI: 10.1111/j.1475-1305.2010.00775.x
- [3] Forman, R.G., V.E. Kearney and R. M. Engle, Numerical analysis of crack propagation in cyclic loaded structures, *J. Bas. Engng. Trans. ASME* 89, 459, 1967.
- [4] Maksimovic K., Strength and Residual Life Estimation of Structural Components Under General Load Spectrum, Doctoral Thesis, Faculty of Mechanical Engineering, 2009 (in Serbian).
- [5] Maksimović S., Vasović I., Maksimović M., Đurić M., RESIDUAL LIFE ESTIMATION OF DAMAGED STRUCTURAL COMPONENTS USING LOW-CYCLE FATIGUE PROPERTIES, Third Serbian Congress Theoretical and Applied Mechanics, Vlasina Lake, 5-8 July 2011, pp. 605-617, Organized: Serbian Society of Mechanics, ISBN 978-86-909973-3-6, COBISS:SR-ID 187662860, 531/534(082).

DAMAGE AND RECOVERY OF ARS 1400 CONVEYER'S LOWER CONSTRUCTION SUPPORT IN A SURFACE MINE

T. Maneski¹, N. Trišović¹ D. Ignjatović²

¹ University of Belgrade, Faculty of Mechanical Engineering, Kraljice Marije 16, 11120 Belgrade 35, Serbia

e-mail: ntrisovic@mas.bg.ac.rs

² University of Belgrade, Faculty of Mining and Geology, Đušina 7, 11120 Belgrade 35, Serbia

Abstract: Surface mining sites suffer from frequent damages of mining machinery and transporting system components. These damages are the consequences of inadequate design solutions or poor choice of materials used in construction building. This paper explains loading analysis of conveyers, establishment of the root causes of most frequent damage incidents and locations of the critical spots within a construction for different types of loads. In the loading analysis section finite elements method [2] was employed, while the detection of critical points was performed using the stress distribution and deformation energy analysis for a construction [1]. In this paper we propose the procedure for removal of most frequent causes of support damages in surface mines.

1. Introduction

Conveyer ARS 1400 which operates on tailing system within surface mine „Tamnava East field“ has suffered from a damaging incident. The conveyer box support for left transporting caterpillar's semi-axis was damaged. The load analysis has shown that the cause of damage was the inadequate design solution. This paper studies the interaction between the state of vital elements of construction and localization of the critical spots. Insights into distribution of loads, membrane and bending stresses and deformation energy enable highly efficient analysis of state and diagnostics of existing constructions. Many studies that deal with this type of problems have already been published [6, 7, 8, 9, 10].

Analysis and diagnostics of construction behaviour of conveyers was conducted using finite elements method based, computer system for modelling and calculating the construction named KOMIPS, which was developed at Faculty of Mechanical Engineering in Belgrade. The finite elements used in structure modelling are line and surface elements.

2. Damage incident

In the course of the operation, an abrupt stopping of conveyer's transporting tapes occurred. Afterwards, a cracking sound was audible as well as sound of destruction of steel material. All this happened while tape was under 45° inclination. During this event, the box support for the left transporting caterpillar semi-axis occurred, thus causing the upper construction to exert pressure upon the caterpillar's tape. Photos 1-4 in Figure 1 show the position of loader during damage incident, parts of the construction as well as the damaged spot itself.



Figure 1. Position of conveyer and the outlook of the damaged spot

From these photos it can be seen that the path was very good, flat and without longitudinal and transversal inclination, that the loading capacity of the soil foundation was satisfactory. By analysing the machine's position during the damage incident, the dirt found on the conveyer, and the operation technology prior to damage of the support element, it was concluded that no direct evidence exists for improper handling of the machine, and that the cause of the damage incident is a possibility that during machine desing proces, some inadequacies have been included.

3. Diagnostics

3.1. Introduction

The basis for diagnostics as well as recovery of the loading construction is its computer modelling and the appropriate calculation using numerical methods, FEM [2].

Software package KOMIPS which was developed at Faculty of Mechanical Engineering in Belgrade [1] enables us to model and calculate complex constructions and problems.

The analysis of distribution of membrane and bending stresses, as well as normal and tangential stresses facilitates the localization of week points (dominating presence of bending and/or tangential stresses) and strong points (presence of only membrane and/or only normal stresses) [3, 4, 5]. It also points to types of modifications needed for minimizing the negative influence of bending and improve load distribution. Analysis of deformation energy distribution within a construction yields very efficient indicators of load flow and aids in defining the sensitivity to possible modifications.

3.2 Model

The carrying construction of lower support of conveyer is a spatial plate construction which is strengthened by placement of beams in the appropriate spots. Substructures of lower support are: box «damaged» support, upper horizontal plate, middle horizontal plate, lower horizontal plate, plates in between middle and lower plates, upper part of the cylinder, lower part of the cylinder, strengthened supports, connecting elements (shafts) for support and side supports. Figure 2 shows the calculation model.

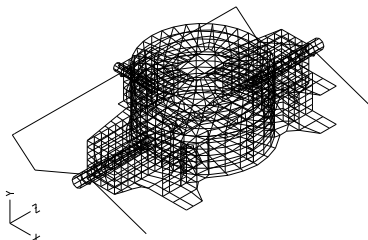


Figure 2. Computational model of conveyer

The numerical analysis is required for lower support but also for the construction of caterpillar's guidance mechanism which is modeled by beams as finite elements.

3.3. Loads

During conveyor's operation, different types of loads occur: main load (the combination of loads that are expected to appear during operation), additional loads, special loads, and limiting loads. The aforementioned loads are combined. This means that we need to analyse the least favourable loads and least favourable positions of separate parts of the construction. In the case of damaging incidents it is necessary to analyse the following loads: permanent loads, loads caused by the transported material, loads caused by the material that sticks onto construction, loads caused by untypical transported material, and loads caused by bunker blockage.

3.4. Calculation

Calculation was conducted for the case of least favourable load (Figure 3). This is an unsymmetrical load with the intensity of 4560 kN centered in the point of radii of 100 cm away from radial-axial bearing and under the angle of 60° in relation of longitudinal X axis which is parallel to caterpillars and pointed towards columns. Figures 3 and 4 show the fields of deformations and equivalent stresses for the model and for the chosen type of load.

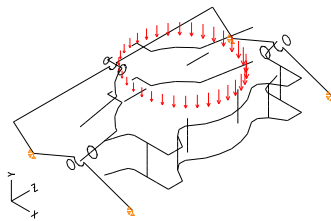


Figure 3. Model contour, load and conveyers lower support.

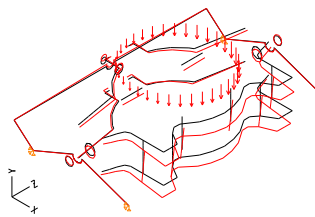


Figure 4. Model's deformation field. Maximum deformation is 3.28 cm.

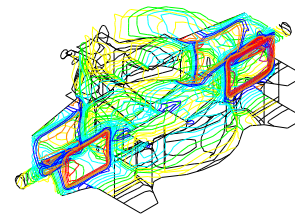


Figure 5. Field of model's equivalent stresses $\sigma_e = 0-18,6 \text{ kN/cm}^2$

3.5 Analysis

Figure 5 shows the high intensity of stresses within vertical critical plate and, very clearly, the concentration of stresses. A high quality construction behaviour diagnostics demands the calculation of percentage distributions for membrane and bending loads situated on each element, the normal and bending loads and deformation energy of construction, as well as distribution of total and specific deformation energy for substructures belonging to conveyor's lower support, under the given loading. This data is displayed in table 2, for box critical supports. The values of other stresses are not given in the table. Box critical support is the most heavily loaded element, with respect to membrane and normal loading, and with respect to energy that outer forces have invested into its deformation (deformation energy). Critical bending and shearing stresses and Oyler's critical stress are described by:

$$\sigma_{kr} = k_\sigma \sigma_E, \tau_{kr} = k_\tau \sigma_E, \sigma_E = \frac{\pi^2 E}{12(1-\nu^2)} \left(\frac{t}{b}\right)^2, k_\sigma = 23.9, k_\tau = 7.2$$

where k_σ, k_τ are the buckling coefficients which are determined by the standards.

Coefficient k_σ has, in this case, large value which points to conclusion that buckling caused by bending cannot be the object of this analysis. In this conditions $\tau_{kr} = 7,2 \cdot 1,81 = 13 \text{ kN/cm}^2$. The intensity of the shear stress obtained by FEM is very close to critical shear

stress. In the critical zone, aside from presence of shear stresses a significant presence of deformation energy exists. It can be concluded that the cause of damaging incident was the inadequate stiffness of the vertical plate within the critical zone.

4. Recovery

From the table 1 it can be seen that the vertical plate 1 is the cause of the damage incident, due to very low value of critical stress which is too close to operation stress value. This plate has a great presence of stresses and deformation energy. Decrease of operation stress is accomplished by increase in the thickness of the vertical plate. Often, in the course of exploitation, it is impossible to alter the thickness of the entire plate, therefore its stiffness is increased by adding new elements on precisely determined locations. In this case the construction stiffness is increased by adding vertical beams after which the operation stresses was decreased to one-half of its previous value, while the concentration of stresses in the vertical critical plates has disappeared. In the table 1, the percentage of participation of all the basic values after the recovery is given. Comparative display of behaviour is given in the table 1, showing how much has the added solution improved the local behaviour of the support, while not disturbing global behaviour of the conveyer's support, at the same time.

Table 1 – Analysis of critical zone before and after recovery

	Mem/bending stresses for each element [%]		Normal/shear stresses [%]		Total/specific deformation energy [%]	
	before	after	before	after	before	after
1-160	14.8 /1.0	13.6/1.5	7.6/8.2	8.7/6.5	16.6/27.8	11.3/16.3
803-962	13.2 /0.9	12.0/1.3	6.7/7.3	7.6/5.7	13.3/22.2	8.9/12.8

5. Conclusion

The damage in the construction of the conveyer is most often caused by the poor design solution of the conveyer's lower box support. During its maximum intensity, the exploitation stresses in that part of the construction can overcome the limiting allowed stresses. This primarily relates to shear stresses which can cause buckling and subsequently even destruction of vertical plates. The recovery of the construction demands a decrease in the value of shear stress by introducing of new elements (stiffening beams) in precisely determined locations. Thus obtained solution does not disturb the global state of stresses within the construction.

Acknowledgments

This work has been performed within the projects TR35040, TR35011 and ON74001 which are supported by the Ministry of Education and Science of the Republic of Serbia, whose financial help is gratefully acknowledged.

References

1. Maneski, T., Contribution to Development of Design via Computational Modeling of Supporting Structure of Machine Tools, Faculty of Mechanical Engineering, Belgrade, PhD, Thesis, 1992.
2. T. Maneski, Computer Modeling and Calculation of Structures, Faculty of Mechanical Engineering, Belgrade, 1998. (in Serbian)
3. T. Maneski, V. Milošević-Mitić, D. Ostrić, The Basis of the Strength of Constructions, Faculty of Mechanical Engineering, Belgrade, 2002. (in Serbian)
4. N. Trišović, T. Maneski, D. Kozak, *Strojstvo - Journal for Theory and Application in Mechanical Engineering*, 52 (2) (2010) 147.
5. N. Trišović, Modifikacija dinamičkih karakteristika u strukturalnoj reanalizi mehaničkih sistema, Ph.d Thesis, Belgrade, 2007.
6. D. Ignjatović, T. Maneski, P. Jovančić, Proc. 26th Danubia-Adria Symposium on Advances in Experimental Mechanics, September 23 – 26, Leoben, Austria, 2009, p.87.

DAMAGE PHENOMENOLOGY IN DYNAMICALLY LOADED BRITTLE LATTICES

S. Mastilovic

Union Nikola Tesla University
Cara Dusana 62-64, 11000 Belgrade, Serbia
e-mail: smastilovic@fgm.edu.rs

Abstract. This study summarizes some general damage and failure features of the brittle systems observed by using dynamic 2D lattice simulations. The expression proposed previously to model the mean tensile strength dependence on the strain rate is developed further to capture the sample size dependence. The continuous evolution of the representative sample size between two asymptotes corresponding to the limiting loading rates is discussed. The 2D simulation results also indicate that the number of broken links corresponding to the stress peak is described by a continuous spectrum of scaling exponents varying between 1 and 2 reflecting predominant damage distribution pattern.

1. Introduction

Ceramic materials are increasingly used for design of structures exposed to extreme dynamic loads, which requires in-depth knowledge of the physics of high rate deformation [2]. This complexity is further enhanced by a well-known sensitivity of the aforementioned materials to a size effect, defined as a change of material properties due to the change in “either the dimensions of an internal feature or structure or in the overall physical dimensions of a sample” [11]. The size effect is also related to the concept of a representative volume element (RVE) whose definition is “perhaps one of the most vital decisions that the analyst makes” [9]. It represents a volume of heterogeneous material statistically representative of the certain local continuum property at the corresponding material point (e.g., [6], [9]). For the purpose of the present investigation, the size of RVE with respect to the dynamic tensile strength is identified with the sample size corresponding to the rate-insensitive tensile strength for the given level of microstructural disorder.

The rapid growth of computer capabilities and advance of the massively parallel molecular dynamics techniques are perpetually probing spatial and time scales accessible by atomistic simulations. At the same time, recent advances in experimental techniques offer opportunity to create and study states of matter under extreme loading conditions and increase the spatial and temporal resolution of shock-loaded experiments allowing analyses on subnanosecond scales (e.g., [2], [4], [11]). Thus, simulations and experiments are slowly converging in the attempt to probe the longer time scales with ever-larger systems. This development calls attention to the question of the RVE size of the material exposed to the extreme conditions and the sample dimensions influence on deformation mechanisms and strength.

2. Computational model

Polycrystalline ceramics are brittle multiphase materials containing hard crystals bonded with an inferior-stiffness matrix. In the present computational model, the mesoscale sample of aforementioned material is approximated by an idealized 2D structure: a Delaunay simplicial graph dual to an Voronoi froth representing grains. It is assumed that the investigation objectives are met by the following model features:

- i. the average grain facet size defines the model resolution length, l_c ;
- ii. the glassy grain boundaries provide the direct, first-order effects on the overall dynamic response; and
- iii. other heterogeneities and defects, such as pores or poorly bound interfaces between hard crystals, are accounted for by stiffness and strength distributions [6].

Consequently, the dominant damage mechanism is intergranular cracking governed by the local fluctuations of stress and energy quenched barriers.

The continuum particles located in lattice nodes interact with their nearest neighbors through the nonlinear central-force links. The randomness of the lattice morphology is defined by the coordination number z and link length λ . The lattice is geometrically and structurally disordered [7]. The rupture criterion of the link between bulk particles i and j is in the present simulation set defined in terms of the critical elongation $\varepsilon_{ij} = \varepsilon_{cr} = \text{const}$.

The unnotched tensile sample is a square of size L . The details of the loading procedure and corresponding effects of the model response are described by Mastilovic et al. [7].

In the present simulation set, the tensile test simulations are limited to 6 different strain rates (100 s^{-1} , $1 \times 10^3 \text{ s}^{-1}$, $1 \times 10^4 \text{ s}^{-1}$, $1 \times 10^5 \text{ s}^{-1}$, $1 \times 10^6 \text{ s}^{-1}$, $1 \times 10^7 \text{ s}^{-1}$) and 8 lattice sizes (specified in Fig. 1) distributed over the wide range from $L/l_c = 9$ to $L/l_c = 765$.

The reduced-units geometric and structural lattice parameters are available in [7] or [8].

3. Discussion of results

An expression is proposed in [8] to model the mean tensile strength dependence on the strain rate. It is also well known that the tensile strength is, as a rule, strongly dependent on the sample size. The commonly observed trend is that with the sample size increase, the stress peak decreases and gradually approaches the asymptotic value corresponding to the size-independent strength (e.g., [1], [3]). Fig. 1 illustrates that the observed stress peak size dependence, is qualitatively similar for all strain rates. These simulation results suggest the following size dependence of the mean tensile strength:

$$\sigma_m(L) = \sigma_m(L \rightarrow \infty) \cdot \left[1 + G \exp(-H \Lambda^2) \right] \quad (1)$$

where the asymptote $\sigma_m(L \rightarrow \infty)$ is the quasi-static strength of unbounded brittle medium, $\Lambda = \log L$, and G and H fitting parameters (Fig. 1).

If the representative sample size corresponding to quasi-static loading is designated as L_r^0 , its rate-driven evolution could be depicted by

$$L_r = L_r^\infty + (L_r^0 - L_r^\infty) \exp \left[- \left(\frac{\log \dot{\varepsilon} + A}{B} \right)^C \right] \quad (2)$$

where fitting parameters define the threshold (A , B) and gradient (C) of the representative sample size decline. The lower asymptote ($L_r^\infty \ll L_r^0$), corresponding to the ordered

homogeneous mesoscale damage patterns [7], depends on the resolution length of the model (i.e., it is individual for each microstructure depending on a dominant internal feature or structure; “underlying essential microconstituents” [6]). The typical damage patterns (e.g., [7], [8])—unambiguous signatures of various loading rates—provide a graphical interpretation of the representative sample size rate-conditioned change described by Eq. (2).

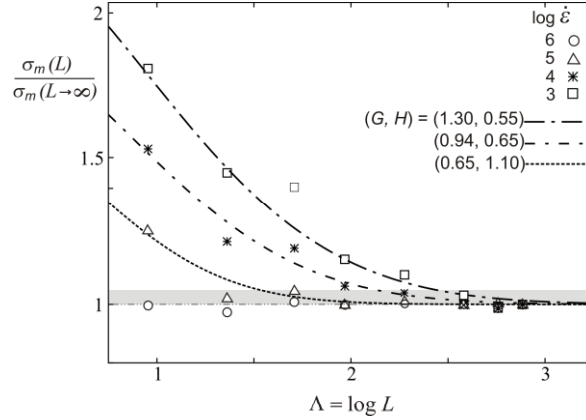


Figure 1. Examples of the rate dependence of strength size effect. (The curves represent the least-square simulation data fit. The sample size L is normalized by resolution length. The shaded area corresponds to 5% deviation from the asymptote. Parameters G and H refer to Eq. (1))

Finally, the attention is also focused on the number of broken lattice links corresponding to the apex of the stress-strain curve. The present dynamic lattice simulations indicate that

$$n_m \propto L^D \quad (3)$$

applies for the entire rate range but it appears, according to the simulation results presented in Table 1 (see also [5], [8]), that the continuous spectrum of rate-dependent scaling exponents is necessary for the complete description of the dynamically loaded disordered brittle 2D system. This “dimensionality” of the continuous spectrum of scaling exponents appears to reflect its predominant damage distribution pattern as illustrated in [7] and [8].

Table 1. Change of scaling exponent with the strain rate

$\log(\dot{\epsilon}) [s^{-1}]$	2	3	4	5	6	7
D	1.14	1.22	1.56	1.95	1.98	1.96

It is tempting to assume that the crossover

$$D = 2 - \exp \left[- \left(\frac{\log(\dot{\epsilon}) + E}{2 \log(\dot{\epsilon}_x)} \right)^F \right] \quad (4)$$

between the two asymptotes corresponds to the rate-driven mean tensile strength evolution; the fitting parameters $(E, F, \dot{\epsilon}_x)$ are described in [8].

4. Summary

The present simulation set emphasizes the link between damage phenomenology and the rate-driven size evolution of the representative sample identified tentatively with the RVE with respect to the tensile strength of the polycrystalline ceramics. From the standpoint of the weakest link theory, existence of the representative sample (characterized by the size-insensitive strength), for the given microstructural statistics, implies negligible probability of finding the dominant crack nucleus with further increase of the sample size. An expression is proposed to model the sample size dependence upon the loading rate. The results of the 2D lattice simulations also indicate that the number of broken links corresponding to stress peak is described by a continuous spectrum of scaling exponents varying between 1 and 2 reflecting predominant damage distribution pattern.

Acknowledgement. This research was sponsored by Ministry of Education and Science of the Republic of Serbia through research project IO 174010.

References

- [1] Bažant Z.P., Planas J. (1998), *Fracture and Size Effect in Concrete and Other Quasibrittle Materials*, CRC Press, Boca Raton.
- [2] Bourne N.K. (2011), Materials' Physics in Extremes: Akrology, *Metallurgical and Materials Transactions A*, 42A, pp. 2975-2984.
- [3] Carpinteri A., Chiaia B., Ferro G. (1995), Multifractal nature of material microstructure and size effects on nominal tensile strength, *Fracture of Brittle Disordered Materials – Concrete, Rock and Ceramics*, A. Baker, B.L. Karihaloo (Eds.), pp. 21-34.
- [4] Field J.E., Walley S.M., Proud W.G., Goldrein H.T., Siviour C.R. (2000), Review of experimental techniques for high rate deformation and shock Studies, *Int. J. Impact Eng.*, 30, pp. 725-775.
- [5] Hansen A., Roux S., Herrmann H.J. (1989), Rupture of central-force lattices, *J. Phys. France*, 50, pp. 733-744.
- [6] Krajcinovic D. (1996), *Damage Mechanics*, North-Holland, Amsterdam.
- [7] Mastilovic S., Rinaldi A., Krajcinovic D. (2008), Ordering effect of kinetic energy on dynamic deformation of brittle solids, *Mech. Mater.*, 40, pp. 407-417.
- [8] Mastilovic S. (2011), Further Remarks on Stochastic Damage Evolution of Brittle Solids Under Dynamic Tensile Loading, *Int. J Damage Mech.*, 20, pp. 900-921.
- [9] Nemat-Nasser S., Hori M. (1999), *Micromechanics: Overall Properties of Heterogeneous Materials*, North-Holland, Amsterdam.
- [10] Ravelo R., Holian B.L., Germann T.C., and Lomdahl P.S. (2004), Constant-stress Hugoniot method for following the dynamical evolution of shocked matter, *Phys. Rev. B*, 70, pp. 014103.
- [11] Uchic M.D., Dimiduk D.M., Florando J.N., Nix W.D. (2004), Sample Dimensions Influence Strength and Crystal Plasticity, *Science*, 305, pp. 986-989.

PLASTICITY OF CRYSTALS AND INTERFACES: FROM DISLOCATION MECHANICS TO SIZE-DEPENDENT CONTINUUM

Sinisa Dj. Mesarovic¹ and Raghuraman Baskaran

School of Mechanical and Materials Engineering
Washington State University, PO Box 642920, Pullman, WA, 99164-2920, USA.

¹Email: mesarovic@mme.wsu.edu

Abstract. Plasticity in heterogeneous materials with small domains is governed by the interactions and reactions of dislocations and interfaces. The rationale for interface dominated plasticity is simple: dislocations glide through the single crystal domain with relative ease, but pile-up at interfaces, so that interface reactions become a critical step in continuing plastic deformation. While the details of dislocation reactions at interfaces take place at the atomic scale, a continuum framework is best suited for large domains. Recently developed size-dependent crystal plasticity theory is capable of representing dislocation pile-ups and their relaxation at interfaces. Using this theory, we obtain solutions to simple problems of single-slip and double-slip shear of sandwiched thin film. Then, we compare the results with available discrete dislocation simulations.

1. Introduction

Below recovery/annealing temperatures, plastic deformation in crystalline materials is mostly the result of dislocation glide. When met with an obstacle such as grain/phase boundaries, dislocations pile-up, resulting in back-stress which impedes further dislocation motion resulting in size effects [1-3]. The pile-ups are high energy configurations and the mobility at interfaces is much higher than in the bulk, so that dislocations react - amongst themselves and with interface structure, to lower the energy (and the back-stress). As a result, plasticity of polycrystals is governed by the reactions of dislocations at/with interfaces [4]. While some experimental observations are available [6, 7], the question of which reaction occurs under given conditions is still open. Indeed, such question can only be answered by atomic level simulations. The complexity of dislocation-boundary relaxation is illustrated in Figure 1.

The general continuum framework capable of accommodating dislocation-interface reactions has been developed [7, 4], based on the earlier analyses [8, 9]. This size-dependent crystal plasticity theory employs the representation of the singular part of dislocation pile-up as jumps in slip at the boundary, representing effectively boundary superdislocation walls. Back-stress relaxation occurs by reaction of these boundary superdislocations to lower the total energy. The relaxation of slip at the boundary is necessarily accompanied by dissipation. Based on the thermodynamic framework developed in [7], dissipation can be computed using the difference between peak energy configurations and final relaxed state.

Motivated by frequent observation of size effects and Ashby's analysis [3] of geometrically necessary dislocations (GND's), a number of gradient theories have been proposed in the past

two decades [10]. While dislocation dynamics simulations [11] confirm that the size-effects are the result of constraint-enforced, high energy pile-ups, they also attest to the failure of phenomenological theories to describe relevant physical processes and emphasize the need for micromechanics-based continuum theory.

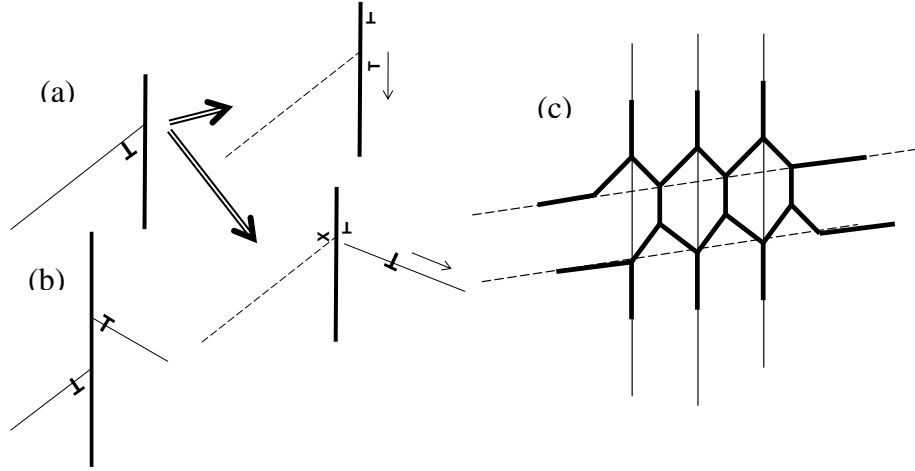


Figure 1. Sketches of dislocation-interface reactions of increasing complexity. (a) Single dislocation impinging on a tilt boundary could dissociate into sessile and mobile components (up), or, it can transmit (down), leaving an interface dislocation and disconnection (X). (b) Two dislocations impinging on a tilt boundary from different sides. (c) Two sets of dislocations impinging from different sides (thin solid and dashed lines). The reaction product is shown as network of thick lines. Ni $\Sigma 11\{311\}$ boundary [5, 6].

2. Problem formulation & the continuum theory

For the system where dislocation reactions at the interface are not allowed, the principle of virtual work for the volume V , bounded by surface S , can be written [7]:

$$\int_S \mathbf{t} \cdot \delta \mathbf{u} dS = \int_V \left[\boldsymbol{\sigma} : \delta \mathbf{e} + \sum_{\alpha} \tau^{\alpha} |\delta \gamma^{\alpha}| + \sum_{\alpha} \mathbf{p}^{\alpha} \cdot \delta \mathbf{g}^{\alpha} \right] dV + \int_S \sum_{\alpha} \mathbf{q}^{\alpha} \cdot \delta \boldsymbol{\Gamma}^{\alpha} dS. \quad (1)$$

The vectors \mathbf{g}^{α} are the in-plane slip gradients, and $\boldsymbol{\Gamma}^{\alpha}$ are the slip jump values at the boundary, effectively representing superdislocation walls. The constitutive relations between work conjugates are based on elasticity solutions [9]. The Peierls stress τ^{α} is considered a material property. The standard procedure of variational calculus then yields a set of governing differential equations and boundary conditions. The equation of classical continuum theory remains unchanged, but an additional differential equations and boundary conditions are given for each slip system. Denote the resolved shear stress as τ_R^{α} , the in-plane gradient operator $\overset{\alpha}{\nabla}$, and the outer normal to the slip plane trace on the boundary \mathbf{N}^{α} . For each slip system, there is an additional differential equation and a boundary condition:

$$\overset{\alpha}{\nabla} \cdot \mathbf{p}^{\alpha} = \tau^{\alpha} - \tau_R^{\alpha} \text{ in } V, \quad \mathbf{N}^{\alpha} \cdot (\mathbf{p}^{\alpha} + \mathbf{q}^{\alpha}) = 0 \text{ on } S. \quad (2)$$

The theory which allows boundary relaxation is given in [7] and [4]. Here we consider a simplified version in which boundary relaxation is accomplished without threshold and thus has no dissipation associated with it. The dislocations on two slip systems react along the boundary to form the resulting dislocation, whose Burgers vector is the sum of the original two, but which has lower energy. In this case, the slip jumps Γ^α in (1) are replaced by the relaxed values, and the sum includes the reaction product dislocations.

3. Results

The stress-strain plots are obtained for the average shear stress τ_{ave} and the total shear strain Γ . We consider two cases of shear in a thin film: single slip, and symmetric double slip. The predictions of the continuum theory are compared to discrete dislocation (DD) simulations in [11].

First, we consider a simple case of constrained shear with only one slip system activated. The overall stress-strain response, as predicted by the current theory, is compared to the results of DD simulations [11] in Figure 2. While the results are in good agreement, note that the single slip case is not realistic; the elastic-plastic stiffness is only little lower than the elastic stiffness. The resulting high stresses are bound to cause activation of other slip systems.

Then, we consider symmetric double slip with identical slips on both slip systems. Stress-strain curves based on DD [11] and the current solutions, for symmetric double slip, are shown in Figure 3.

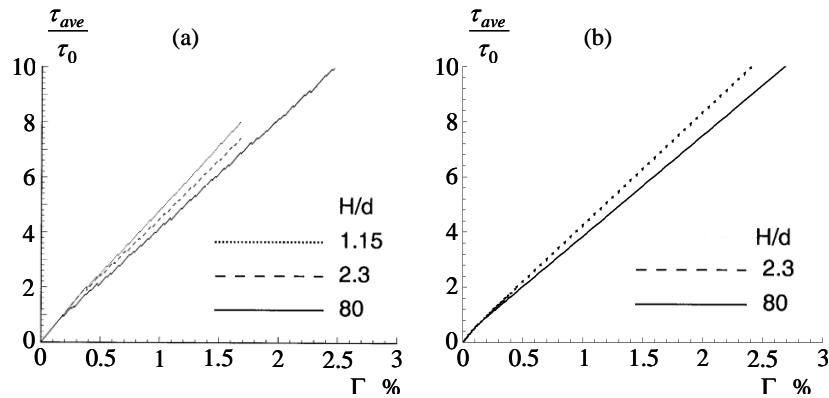


Figure 2. Single slip: (a) DD [11], (b) present continuum theory.

Solutions to the continuum problem match the results of dislocation dynamics simulations. In case of double slip, the elastic-plastic stiffness is much lower than in the single slip case. The small discrepancy between two models - the higher stiffness in Figure 3(a) results from: (i) Neglect of statistical hardening in continuum model. In discrete simulations, random interactions of dislocations in the bulk contribute to the effective yield stress. (ii) Neglect of boundary dissipation. The current simplified version of the continuum theory does not have a “boundary yield condition”, i.e., dislocations in boundary layers react to lower the energy without having to pass an energy barrier.

4. Summary

The size-dependent continuum crystal plasticity [7, 4] is capable of representing dislocation-interface relaxation and matches the results of discrete dislocation simulations. In the absence of dislocation reactions/relaxation, the elastic-plastic thin film is unrealistically stiff. The presence of the second slip system allows for relaxation at the boundary and produces more realistic results. Barring statistical bulk hardening effects and boundary dissipation, the results of continuum theory and discrete dislocation simulations are in agreement. While the details of dislocation-boundary and dislocation-dislocation (at the boundary) relaxation are still an open problem, the continuum theory used here clearly represent a framework in which such processes can be represented.

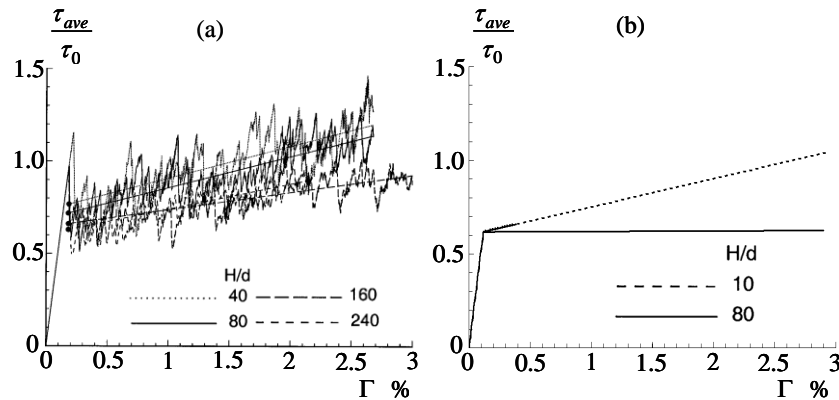


Figure 3. Symmetric double slip: (a) DD [11], (b) current solutions.

References

1. Hall, E.O. 1951 The deformation and aging of mild steel. *Proc. Phys. Soc. B* 64, 747-753.
2. Fleck, N.A., Muller, G.M., Ashby, M.F. & Hutchinson, J.W. 1994 Strain gradient plasticity: Theory and experiment. *Acta metall.* 42(2), 475-487.
3. Ashby, M.F. 1970 The deformation of plastically non-homogeneous materials. *Phil. Mag.* 21, 399-424.
4. Mesarovic, S.Dj. 2011 Plasticity of crystals and interfaces: From discrete dislocations to size-dependent continuum theory. *Theor. Appl. Mech.* 37(4), 289-332.
5. Priester, L. 2001 Dislocation-interface, interaction-stress accommodation processes at interfaces. *Mater. Sci. Eng. A* 309-310, 430-439.
6. Poulat, S., Decamps, B., Priester, L. & Thibault, J. 2001 Incorporation processes of extrinsic dislocations in singular, vicinal and general grain boundaries in nickel. *Mater. Sci. Eng. A* 309-301, 483-485.
7. Mesarovic, S.Dj., Baskaran, R., & Panchenko, A. 2010 Thermodynamic coarsening of dislocation mechanics and the size-dependent continuum crystal plasticity. *J. Mech. Phys. Solids* 58, 311-329.
8. Baskaran, R., Akarapu, S., Mesarovic, S.Dj. & Zbib, H.M. 2010 Energies and distributions of sacked pile-ups. *Int. J. Solids Structures* 47, 1144-1153.
9. Mesarovic, S.Dj. 2005 Energy, configurational forces and characteristic lengths associated with the continuum description of geometrically necessary dislocations. *Int. J. Plasticity* 21, 1855-1889.
10. Tvergaard, V., editor 2007 Special issue. *Mod. Simul. Mater. Sci. Eng.* 15.
11. Shu, J.Y., Fleck, N.A., Van der Giessen, E. & Needleman, A. 2001 Boundary layers in constrained plastic flow: comparison of non-local and discrete dislocation plasticity. *J. Mech. Phys. Solids* 49, 1361-1395.

THERMAL RATCHETTINNG: TENSOR REPRESENTATION VS CLASSICAL APPROACH

M. Mićunović¹, L. Kudrjavceva², A. Sedmak³

¹ Faculty of Engineering Sciences The University of Kragujevac, Sestre Janjića 6a, 34000 Kragujevac, Serbia, e-mail: mmicun@kg.ac.rs

² The State University of Novi Pazar, ul. Vuka Karadžića bb., 36000 Novi Pazar, Serbia, e-mail: ljuta1@gmail.com

³ Faculty of Mechanical Engineering, The University of Belgrade, Kraljice Marije 16, 11120 Belgrade 35, e-mail: asedmak@mas.bg.ac.rs

Abstract. Nonproportional 3D thermoplastic ratchetting of a block made of AISI 316H is considered. Perzyna-Chaboche and MAM models are compared with experimental data.

1. Introduction

Steel mantel of nuclear reactors composed of austenitic stainless steels, such as AISI 316H, is exposed during its exploitation to diverse time-dependent stress-strain histories. The case of plastic saturation when stress frequency in “universal” flow curve diagram (i.e., equivalent Mises stress versus accumulated plastic strain) increases is of special interest. Such behaviour is called *ratchetting*. It has been shown to be the case at multiaxial stress-strain histories especially at nuclear reactors where such histories usually appear.

The paper deals with 3D thermo-viscoplastic strain of a rectangular block made of AISI 316H steel. One of its sides is loaded by constant normal stress σ whereas two lateral side surfaces are acted upon by harmonically variable shear stress τ . Such a history induces progressive but saturated increase of axial strain in the direction of tension stress components. The problem is treated by two constitutive models: (a) Perzyna-Chaboche’s model with incorporated evolution equations for back stress and equivalent flow stress (calibrated by Eleiche in [1]), and (b) the quasi rate independent MAM model. The MAM model, based on tensor representations, was calibrated in [2]. Here a comparison of these two models with experiments reported in [4] has been done.

For finite elastoplastic strains it is commonly accepted that Kröner’s decomposition rule holds in the following form: $\mathbf{F}_P := \mathbf{F}_E^{-1} \mathbf{F}$, where \mathbf{F} is the deformation gradient tensor, \mathbf{F}_E the thermoelastic distortion tensor and \mathbf{F}_P the plastic distortion tensor,

Then as an invariant measure of plastic strain the Hill’s logarithmic tensor $\boldsymbol{\epsilon}_P = 0.5 \ln(\mathbf{F}_P \mathbf{F}_P^T)$ is chosen. Its principal advantage lies in the fact that it is a deviatoric tensor. In other words, its three principal invariants read $\pi_1 = \text{tr} \boldsymbol{\epsilon}_P = 0$, $\pi_2 = \text{tr} \boldsymbol{\epsilon}_P^2 \neq 0$, $\pi_3 = \text{tr} \boldsymbol{\epsilon}_P^3 \neq 0$, if plastic volume change is neglected. Then the symmetric part of plastic “velocity gradient” tensor i.e. plastic stretching tensor equals has nonzero components: $D_{P11} = \dot{e}_P / (1 + e_P)$ and $D_{P22} = D_{P33} = -D_{P11} / 2$. Here the superimposed dot stands for material time derivative.

For the problem stated in the introduction non-zero components of Cauchy stress tensor read: $T_{11} = \sigma, T_{23} = T_{32} = \tau$, with $\sigma = \text{const}$, $\tau = \tau_0 \sin(\omega t)$. In this paper we consider small thermoelastic-plastic strains. Then Cauchy stress differs negligibly from the second Piola-Kirchhoff stress. For small thermoelastic strains we may simplify logarithmic strain tensor and obtain its non-zero components as follows: $\epsilon_{P11} = \epsilon_P$ and $\epsilon_{P22} = \epsilon_{P33} = -\epsilon_{P11}/2$ as well as $\epsilon_{P23} = \epsilon_{P32} = \gamma_P/2$.

A stress controlled test with normal stress $\sigma = 245 \text{ MPa}$, shear stress amplitude $\tau_0 = 75 \text{ MPa}$ and shear stress frequency $\omega = 0.5 \text{ rad/s}$ for ten stress cycles is simulated. Such special choice of history parameters is made in order to acquire results comparable with experimental data reported in [4]. These experiments have been made with AISI 316H at a constant tension of 250 MPa , maximal shear strain of 2.6% and amplitude of shear strain equal to 0.17% . We apply the condition on stress history $\|\dot{\mathbf{T}}(t)\| \leq 16 \text{ MPa/s}$ in order to keep strain rates in the low range of the order of magnitude $\|\mathbf{D}_P\| \leq 10^{-3} \text{ s}^{-1}$. For a given stress history $\mathbf{T}(t)$ a response of the material body determined by plastic strain history is looked for.

2. Constitutive models

Model of Perzyna-Chaboche. For a description of a viscoplastic body Chaboche has extended Perzyna's model to account for an evolution of the residual stress. His evolution equations (for small strains) might be written as follows:

$$\begin{aligned} \dot{\boldsymbol{\epsilon}}_P &= \langle (\mathcal{F} - D)/k \rangle^n (\mathbf{T}_d - \mathbf{B}_d) / \mathcal{F}, & \dot{p} &= \sqrt{2/3} \|\mathbf{D}_P\|, \\ \dot{\mathbf{B}}_d &= c(\mathbf{A}\mathbf{D}_P - \mathbf{B}_d\dot{p}) - \Gamma \|\mathbf{B}_d\|^{m-1} \mathbf{B}_d, & \dot{D} &= b(Q - D)\dot{p}, \end{aligned} \quad (1)$$

where $\mathcal{F} = \|\mathbf{T}_d - \mathbf{B}_d\|$, as well as $\dot{\boldsymbol{\epsilon}}_P \approx \mathbf{D}_P$ - the plastic strain rate (approximately equal to plastic stretching for small strains range), \mathbf{B} - the residual stress (back stress tensor), D - a static equivalent flow stress, p - the accumulated plastic strain scalar and $\mathcal{A}_c = \{k, n, c, A, \Gamma, m, b, Q\}$ - a set of material constants to be determined from experiments.

Here the traditional notations for a second tensor intensity as well as its deviatoric part are employed: $\|\mathbf{A}\| = (\mathbf{A} : \mathbf{A})^{1/2}$, $\mathbf{A}_d = \mathbf{A} - \text{tr}\mathbf{A}/3$, while plastic loading indicator function is determined by means of $2\langle x \rangle = x + |x|$.

An identification of material constants has been made in [1] on the basis of experiments for standard cyclic tension-compression test as well as cyclic torsion test. Their values for AISI 316H as reported in [1] read $\mathcal{A}_c = \{68.38, 5.8, 65, 113.33, 8.7 \cdot 10^{-10}, 1.3, 8.8, 220.45\}$.

For the problem presented in previous section, deviatoric residual stress (cf. also [1]) has the following non-zero components: $B_{d11} = 2B_L/3$ and $B_{d22} = B_{d33} = -B_L/3$. and $B_{d23} = B_{d32} = B_T$ such that $(3/2)\mathcal{F}^2 = (\sigma - B_L)^2 + 3(\tau - B_T)^2$. We are going to consider a relatively small cycle number. This makes it possible to neglect the material constant Γ . Such an assumption simplifies the set (1).

MAM model with loading function based normality. Let us take the tensor representation approach with loading function based normality. Rice's model by itself is based on normality of plastic strain rate tensor on a loading function Ω taking account of microstructural rearrangements during plastic straining. Translated to finite strains and with Ziegler's modification derived from the notion of least irreversible force, the evolution equation reads: $\mathbf{D}_P = \Lambda \partial_{\mathcal{S}} \Omega$, where the microstructural rearrangements are supposed to be completely determined solely by the plastic strain tensor.

An essential generalization of Rice's model was given in [2] where the loading function $\Omega = \Omega(\gamma)$ was assumed to depend on the set $\gamma \equiv (S_2, S_3, \mu_1, \mu_3)$ of proper and mixed invariants of stress and plastic strain tensors $S_2 = \text{tr}\mathbf{S}_d^2$, $S_3 = \text{tr}\mathbf{S}_d^3$, $\mu_1 = \text{tr}\{\mathbf{S}_d \boldsymbol{\epsilon}_P\}$, $\mu_3 = \text{tr}\{\mathbf{S}_d^2 \boldsymbol{\epsilon}_P\}$. If we take for plastic stretching a second-order approximation in stress and linear approximation in plastic strain, we arrive at formula

$$\Lambda^{-1} \mathbf{D}_P = (A_1 + A_3 \mu_1) \mathbf{S}_d + A_2 (\mathbf{S}_d^2)_d + \frac{1}{2} A_3 S_2 \boldsymbol{\epsilon}_P + A_4 (\mathbf{S}_d \boldsymbol{\epsilon}_P + \boldsymbol{\epsilon}_P \mathbf{S}_d)_d, \quad (2)$$

where again subscript d denotes the deviatoric part of a second-rank tensor. The scalar coefficient Λ is obtained from the condition that plastic stretching vanishes when overstress equals zero. Then evolution equation takes its final form:

On the basis of experimental data for tension and shear of AISI 316H ([2]) material constants of this model are here found to be $\mathcal{A}_c = \{A_1, A_2, A_3, A_4, \lambda_1, \lambda_2\} = \{0.01181, 0.01033, -0.008012, -0.01978, 20, 0.2\}$. The two new constants λ_1 and λ_2 appearing in Λ (cf. [2]) arrive from the usual approximation of static equivalent flow stress: $\sigma_{eq,st} = (1 + \lambda_1 p)^{\lambda_2}$ where p is the accumulated plastic strain. The governing set of differential equations is obtained from (2) by substituting constants into it.

3. Comparisons and concluding remarks

If thermoplasticity is treated, then for each constitutive model the first law of thermodynamics is indispensable. If temperature distribution is close to be homogeneous, then it may have the form (cf. [5]):

$$\rho C_\epsilon \dot{\theta} + \alpha(T_0 + \theta) \text{tr} \mathbf{T} = \Pi \mathbf{T} : \mathbf{D}_P. \quad (3)$$

Here ρ is density of matter, C_ϵ - specific heat, α - the coefficient of thermal expansion, $T = T_0 + \theta$ - the absolute temperature and Π is the dissipation coefficient found in [3] to have the form: $\Pi = A \dot{p}^{-\lambda}$ with values $A = 0.7057$, $\lambda = 0.0244$. Also, the reference [6] for AISI 316H gives temperature dependence $\rho = 8084 - 0.4209(T_0 + \theta) - 0.3894(T_0 + \theta)^2$ as well as $C_\epsilon = 462 \cdot 10^{-6} + 136 \cdot 10^{-6}(T_0 + \theta)$. Results of integration of equations (1,3) with $\Gamma = 0$ are

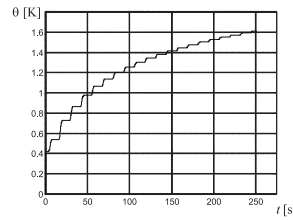


Figure 1. Temperature history at Perzyna-Chaboche model

presented in Fig. 1 and Fig. 2(a). Aside from time-plastic strain component plots the so-called universal flow curve (i.e., equivalent stress versus accumulated plastic strain) as well as phase portrait of plastic strain components are given. The densification feature characteristic for ratchetting has been observed in the "universal" flow curve.

Similarly, integration of equations (2,3) for the given stress history produced the results shown on Fig. 2(b). In the paper [4] the authors have investigated ratchetting behaviour in combined tension-torsion tests. For comparison purposes the paper [4] is especially convenient

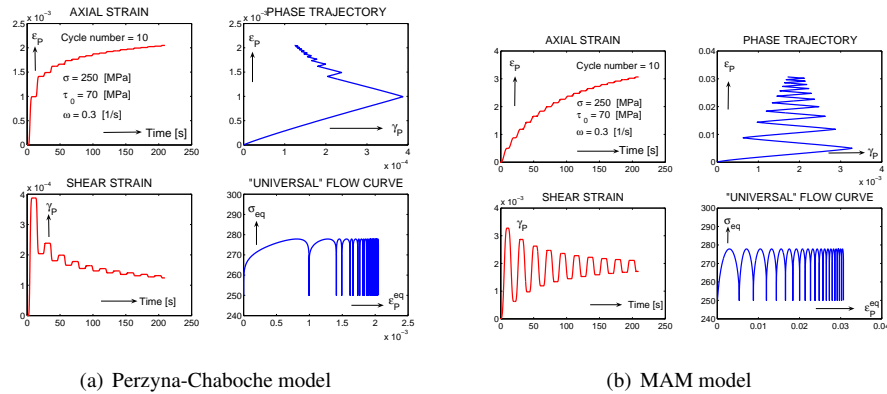


Figure 2. Multiaxial ratchetting with stress control.

since its loading programme was such that after 10 cycles the maximal normal strain was 2.6% at the corresponding tension stress of 250MPa and a prescribed harmonically changed shear strain whose amplitude was 0.17%. Of course, the specimens tested were made of the stainless steel AISI 316H.

Examining the situation of the end point of the phase trajectory calculated by the Perzyna–Chaboche model (Fig. 2(a.)) we see that at these conditions the maximal normal strain has the value of 0.18% which means that the predicted strain is approximately 15 times smaller than the corresponding experimentally acquired strain.

On the other hand, the phase trajectory depicted in Fig. 2(b) gives the maximal tension strain equal to 2.4%. Therefore the relative error amounts to 8%.

A short conclusion could be formulated as follows:

(a) Although handicapped by the absence of compression data which are essential for a good cyclic behaviour prediction, the MAM model [2] has been shown to cover multiaxial variable stress–strain histories in a surprisingly good way. Its extension to include the residual stress tensor into (2) is straightforward but requires new tension–compression tests.

(b) Both models for the given number of stress cycles do not forecast a commencement of elastic strain vibrations, i.e., the shakedown behaviour. However the model of Perzyna–Chaboche aside of poor predictions gives the results very near to these vibrations.

References

- [1] Eleiche A M (1991), Inelastic shear deformation of stainless steels under quasi-static and impact sequential reverse torsion - final report, *Contract No. 2892-55-12 ED ISP ET, JRC CEC Ispra - Cairo University*.
- [2] Mićunović M. (2009), *Thermomechanics of Viscoplasticity - Fundamentals and Applications*, Advances in Mechanics and Mathematics AMMA, Vol. 20, eds. R. W. Ogden and D. Gao, Springer, New York.
- [3] Veljkovic D. (1997), *MSc thesis*, Kragujevac University.
- [4] Lebey J., Roche R. L. and Cousserau P. (1979), Experimental Tests on Ratchet of Tubular Specimens (Torsion and Tension) - Use for Material Characterization, *SMIRT-5, L5/3*.
- [5] Mićunović M. (1992), On the Thermal Elastoplastic Transition in Viscoplasticity of Metals, *Facta Universitatis*, vol. 1, No 2, pp. 155-168.
- [6] Shen W. Q. and Jones N. (1991), Constitutive Equations for Strain Rate History Insensitive, Strain Rate Sensitive Plastic Material, *The University of Liverpool - Impact Research Centre Publication*.

DYNAMIC FAILURE OF INELASTIC RODS

Dragan D. Milašinović

Faculty of Civil Engineering Subotica,
University of Novi Sad, Serbia
e-mail: ddmil@gf.uns.ac.rs

Abstract. This approach uses the rheological-dynamical analogy (RDA) to model the dynamic failure of ductile inelastic rods. The analogy has been developed on the basis of the mathematical-physical analogy between the visco-elasto-plastic rheological model and the dynamical model with viscous damping. Based on the analogy, one very complicated nonlinear problem may be solved as a simpler linear dynamical one. Accordingly, the RDA enables the engineer concerned with materials to utilize simple models, expressible in a mathematically closed form, to predict new notch stress intensities of inelastic rods to examine the fatigue crack growth and failure. Based on this theory, notch-induced fatigue crack growth and failure of rods are quantified by some characterizing parameters namely, fatigue failure frequency, crack depth, fatigue strength, cyclic toughness, crack width, crack opening displacement and cyclic stress intensity factor range. A number of experimental results reported in the literature are used to support the present analysis.

1. Introduction

In the 1960s, linear elastic fracture mechanics (LEFM) was used for the first time for the description of long crack kinetics [1]. According to the original analysis of Paris and his co-workers, the crack growth increment per cycle in fatigue, da/dN , can be described in terms of a power law function of the range of K_I , given by $\Delta K_I = K_{max} - K_{min}$. The LEFM description became generally accepted for both propagation rate of the long cracks and their thresholds in the 1970s.

To quantify the effects of crack closure, Elber [2] attempted to describe, with the aid of a physical model, the connection between load sequence, plastic deformation (by way of crack closure), and crack growth rate. He assumed that crack extension could not take place under cyclic loads until it was fully opened, because only when $P_{op} > 0$ would the crack tip be stressed. Therefore, the bigger P_{op} and the corresponding K_{op} , the less would the effective stress intensity factor (SIF) range $\Delta K_{eff} = K_{max} - K_{op}$ be, and ΔK_{eff} would be the fatigue crack propagation controlling parameter instead of ΔK_I .

2. Rheological-dynamical fatigue crack growth rate and failure of inelastic rods

The RDA model, shown in Fig. 1, of the material behavior of axially cyclically loaded rods has previously been explained by Milašinović [3] and used to predict the fatigue strength. The study [4] presented the physical mechanism and experimental proofs of RDA predictions regarding the fatigue crack growth rate and failure of rods made of ductile

materials. Subsequently, closed-form analytical solutions for the rate of release of inelastic energy $W_d(R)$ as well as characterizing fatigue failure parameters were derived.

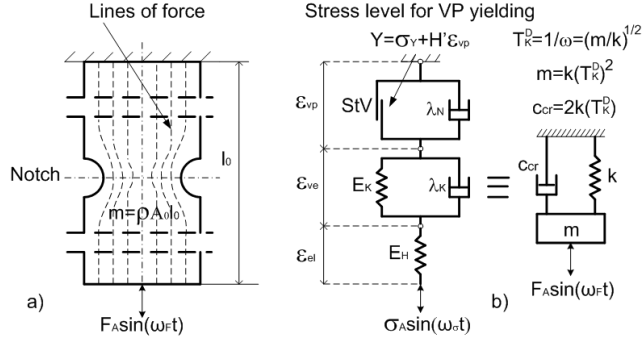


Figure 1. Lowcycle fatigue of a long ductile inelastic rod: a) Cross-section of a circumferentially notched cylindrical rod where fracture finally occurs; b) Model of the rheological body and the discrete dynamical model.

The upper value of the true fracture energy G_c of a circumferentially notched cylindrical rod should be decreased, as shown in Fig. 2, in order to account for the cyclic inelastic energy dissipation within the rod. Consequently, the cyclic SIF range $\Delta K_{Ie}(R)$ would be

$$\Delta K_{Ie} R = \sqrt{G_e R E_H (1 - \nu^2)} = \sqrt{\frac{\sigma_e R - \sigma_f R}{\sigma_k R - \sigma_f R} G_c E_H (1 - \nu^2)} \quad (1)$$

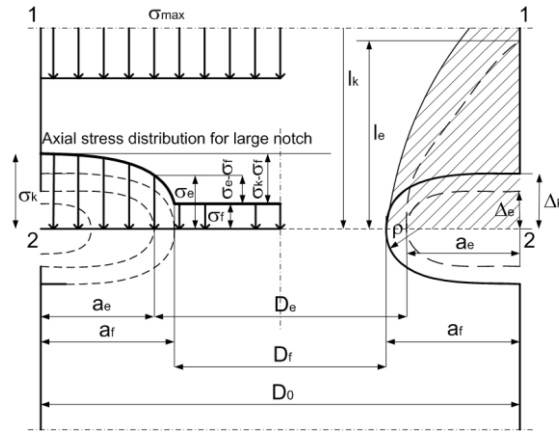


Figure 2. Cross-section of a circumferentially notched cylindrical rod.

From the RDA study [4], the fatigue strength of an inelastic rod can be written as

$$\sigma_e R = \frac{1}{2} \sigma_{max} \left[1 + R + 1 - R \sqrt{\frac{1 + \varphi_{vp}^2 + \delta_e^2}{1 + \delta_e^2}} \frac{1 + \frac{E_H}{H'} \frac{\sigma_Y}{\sigma_{max}}}{1 + \varphi_{vp}} \right] \quad (2)$$

The cyclic inelastic energy dissipation at the crack tip with a relative frequency δ_e which tends to zero will cause the stress concentration

$$\sigma_k R = \lim_{\delta_e \rightarrow 0} \sigma_e R = \frac{1}{2} \sigma_{max} \left[1 + R + 1 - R \left(1 + \frac{E_H}{H'} \frac{\sigma_Y}{\sigma_{max}} \right) \right]. \quad (3)$$

The fatigue failure strength $\sigma_f(R)$ is given by Eq. (2) where $\delta_f(R) = \delta_e$ is the fatigue failure frequency defined by the energy criteria $W_d(R)/W=1$ (W is the elastic potential energy).

$$\delta_f R = \frac{1}{6} \left[2K - \frac{a}{b+c} + 2^{2/3} (b+c)^{1/3} \right]. \quad (4)$$

where

$$a = 2 \cdot 2^{1/3} \left[3(1 + \varphi_{vp}^2 - K^2) \right], \quad b = 18K - 18\varphi_{vp}K - 9\varphi_{vp}^2K + 2K^3, \\ c = \sqrt{4 \left[3(1 + \varphi_{vp}^2 - K^2) \right]^3 + K^2 \left[18\varphi_{vp} + 9\varphi_{vp}^2 - 2(9 + K^2) \right]^2}. \quad (5)$$

The main parameter, which depends on the rod geometry and stress ratio R , is given by

$$K R = 4 \left(\frac{l_0}{\pi D_0} \right)^2 \frac{1}{1-R^2}. \quad (6)$$

The fatigue crack depth of a cylindrical rod is obtained in Ref. [4] as follows

$$a_e R = \frac{1}{2} \left(1 - \frac{D_e R}{D_0} \right) D_0. \quad (7)$$

The localized reduction of the cross-section rod area $A_e(R)$ was derived in Ref. [3] using the equation of continuity and Bernoulli's energy theorem:

$$\frac{A_0}{A_e R} = \sqrt{\frac{\sigma_{max} - \sigma_e R}{\frac{1}{2} \rho \dot{\epsilon}_1^2} + 1}, \quad \frac{D_0}{D_e R} = \sqrt{\frac{A_0}{A_e R}}. \quad (8)$$

The strain rate of a visco-elasto-plastic rod using the RDA is given by

$$\dot{\epsilon}_1 R = \frac{\sigma_0}{\lambda_K} + \frac{\sigma_A}{\lambda_R} = \frac{\sigma_{max}}{2E_H} \left[1 + R \frac{\varphi^*}{T_K^D} + 1 - R \frac{1 + \varphi_{vp}^2}{T_K^D \varphi_{vp}} \right]. \quad (9)$$

The resulting change in the crack depth $a_e(R)$ may be presented in a typical plot where the crack depth increases with the increasing number of loading cycles

$$N_e = \frac{\delta_e}{\delta} = \frac{\delta_e}{2\pi f_\sigma T_K^D}, \quad 0 \leq \delta_e \leq \delta_f R. \quad (10)$$

3. Verification of results

The fatigue crack growth (FCG) rate is determined for the steel rod ($E_H=210$ GPa, $\nu=0.3$): $l_0=50$ cm, $D_0=1.9$ cm, $m=1.114$ kg, $k=119.08 \times 10^6$ N/m, $T_K^D=0.0000967$ s, $K(-1)=70.16702$, $\delta(-1)=70.05285$, $f\sigma=1$ Hz, $N_f(-1)=70.05285/(2\pi \times 1 \times 0.0000967)=0.115 \times 10^6$ cycles. ($\sigma_{max}=142$ MPa, $\varphi^*=2$); ($\sigma_{max}=\sigma_Y=258$ MPa, $\varphi_{vp}=4$, $H'=E_H/2$); ($\sigma_{max}=288$ MPa, $\varphi_{vp}=6$, $H'=E_H/4$). The fracture toughness of the material measured was: $G_c=107$ KJm⁻².

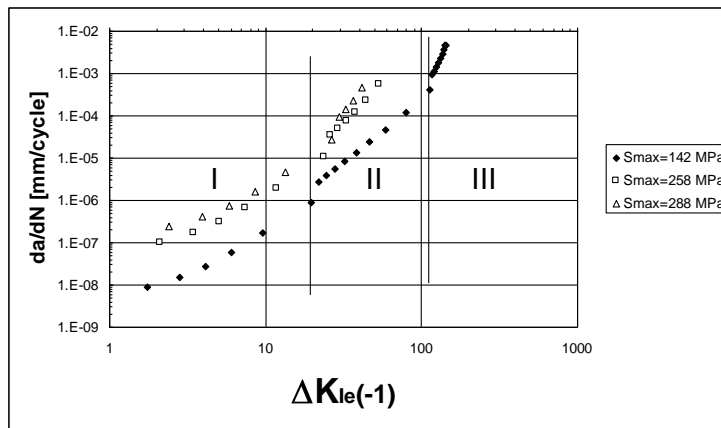


Figure 3. Comparison of the FCG rate curves.

Fig. 3 shows the comparison of the FCG rate curves. The diagrams show three regimes of the FCG response. In Region I, the FCG rate decreases rapidly with the decreasing ΔK_{Ic} ; In Region II, the FCG rate is in the mid-range, with the Paris law prevailing; In Region III, the FCG accelerates, and resulting from a local fracture due to K_{max} equals the fracture toughness K_{Ic} . The K_{Ic} factor gives the overall intensity of the stress distribution. Here, $K_{Ic}=\sqrt{0.107 \cdot 210000 \cdot (1-0.3)^2}=143$ MPa m^{1/2}.

Acknowledgement. The work reported in this paper is a part of the investigation within the research projects: ON 174027 "Computational Mechanics in Structural Engineering" and TR 36017 "Utilization of by-products and recycled waste materials in concrete composites in the scope of sustainable construction development in Serbia: investigation and environmental assessment of possible applications", supported by the Ministry for Science and Technology, Republic of Serbia. This support is gratefully acknowledged.

References

- [1] Paris, P. C., Gomez, M. and Anderson, W. E. (1961), A rational analytic theory of fatigue. *Trends in Engineering* **13**, pp. 9-14.
- [2] Elber, W. (1971), The significance of fatigue crack closure. In: *Damage tolerance in aircraft structures. ASTM STP 486*, pp. 230-42.
- [3] Milašinović, D. D. (2003), Rheological-dynamical analogy: modeling of fatigue behavior. *International Journal of Solids and Structures* **40**, pp. 181-217.
- [4] Milašinović, D. D. (2011), Fatigue crack growth and failure of inelastic rods based on rheological-dynamical analogy. *International Journal of Fatigue* **33**, pp. 372-381.

MICROSTRUCTURAL EFFECTS ON FATIGUE CRACK BEHAVIOR OF A PRESSURE VESSEL WELDED JOINT MADE OF HSLA STEEL

Lj. Milović¹, M. Manjgo², I. Blačić³, T. Vuherer⁴, K. Maksimović⁵, M. Burzić⁶

¹ Faculty of Technology and Metallurgy,
University of Belgrade, Karnegijeva 4, 11120 Belgrade, Serbia
e-mail: acibulj@tmf.bg.ac.rs, misa@tmf.bg.ac.rs

² Faculty of Mechanical Engineering,
University Džemal Bijedić, Univerzitetski kampus, 88104 Mostar, BiH
e-mail: mersida.manjgo@unmo.ba

³ Military Technical Institute,
Ratka Resanovića 1, 11030 Belgrade, Serbia
e-mail: ivo.blacic@gmail.com

⁴ Faculty of Mechanical Engineering,
University of Maribor, Smetanova 17, 2000 Maribor, Slovenia
e-mail: tomaz.vuherer@uni-mb.si

⁵ Republic Serbia, City Administration of City of Belgrade,
Secretariat for Utilities and Housing Services Water Management, Kraljice Marije 1, 11000 Belgrade, Serbia
e-mail: katarina.maksimovic@beograd.gov.rs

⁶ Innovation Center, Faculty of Mechanical Engineering,
University of Belgrade, Kraljice Marije 16, 11120 Belgrade, Serbia
e-mail: mburzic@mas.bg.ac.rs, zradakovic@mas.bg.ac.rs

Abstract: The results of a welding thermal process of low alloyed steels are multiphase microstructures with different amounts of ferrite, martensite, bainite and retained austenite. Different phases in different welded joint regions (weld metal-WM, heat-affected-zone-HAZ and parent metal-PM) along with their different morphologies determine the material mechanical behavior and can affect on propagation rate of the fatigue crack under cycling loading. The aim of the present work is to evaluate the effects of microstructure on fatigue crack growth (FCG) of high strength micro alloyed (HSLA) steel-NIONIKRAL 70.

1. Introduction

Welded structures are widely used in various structures including pressure vessel. The structural integrity and operational safety of welded pressure vessels primarily depends on weldments behaviour.

Determination of parameters of the fatigue crack for characteristic zones of welded joints of HSLA steel type Nionikral-70 (yield strength 700 MPa) is presented in this paper. The results have shown that the position of notch and the initiation of a crack affect the values of stress intensity range of fatigue threshold ΔK_{th} and parameters in equation of Paris.

2. Computations and Experimental Fatigue Crack Growth Behavior

In this section (FCG) predictions of single edge cracked bending (SEN(B)) specimen (L=100 mm, W=16 mm, B=12 mm, $a_0=3.029$ mm) made of NIONIKRAL 70 are considered. In computation fatigue crack growth analysis conventional Paris law [2] is used:

$$da/dN = C (\Delta K_I)^m \quad (1)$$

where: C , m – the material constants, ΔK_I is the stress intensity factor (SIF) range of specimen. The SIF of cracked specimen is defined in the next form [3]:

$$K_I = Y \frac{6M \sqrt{\pi a}}{W^2 B} \quad (2)$$

in which M denotes bending moment and Y the corrective function. Material constants C , m are determined experimentally for three welded joint regions PM, WM and HAZ, Table 1.

Table 1: The material constants of Nionikral 70 in three welded regions

Crack in	C	m	ΔK_{th} [MPam ^{0.5}]	K_{Ic} [MPam ^{0.5}]
PM	$9,05 \times 10^{-14}$	4,76	5,85	158
WM	$6,07 \times 10^{-12}$	2,393	5,82	120
HAZ	$8,06 \times 10^{-12}$	3,054	4,3	147

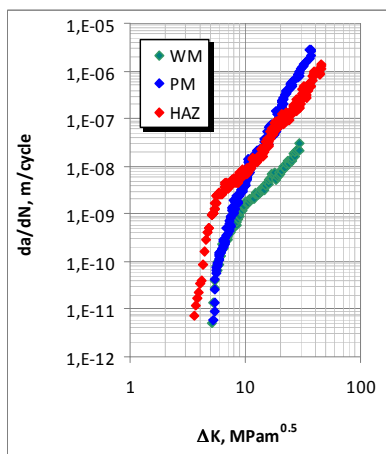


Fig. 1. Comparison of crack growth rate da/dN vs. stress intensity factor range ΔK for welded joint constituents, [1].

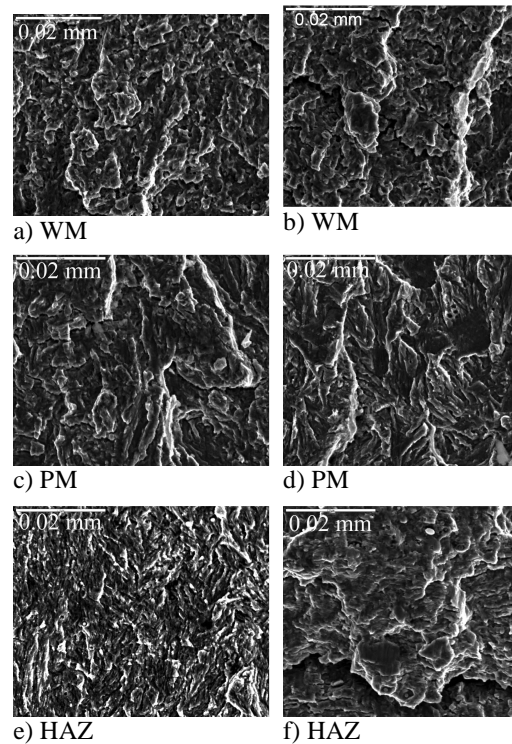


Fig. 2. Fatigue fracture surfaces under: $\Delta K \sim 10 \text{ MPam}^{0.5}$ a,c,e and under $\Delta K \sim 30 \text{ MPam}^{0.5}$ b,d,f.

2.1. Fatigue Crack Growth behavior of PM

Cracked specimen was tested under variable bending moment during crack growth, Fig. 4. Relation (1) can be solved only if bending moment is defined in analytic form, [4]. This moment is approximated in polynomial form as defined in Figure 3.

2.2. Fatigue Crack Growth Behavior of HAZ

Computation crack growth behavior, using eqs (1) and (2), is obtained for constant average bending moment of 28 Nm during crack growth behavior, Fig.5.

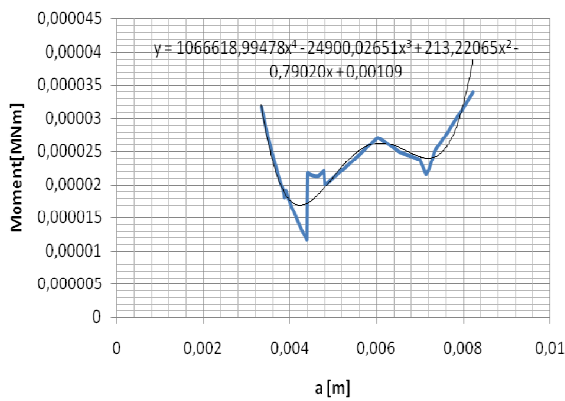


Figure 3 Variable specimen bending moment during crack growth

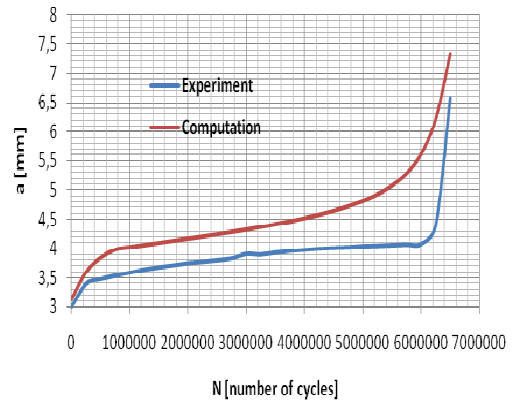


Figure 4 Fatigue crack growth of specimen made from parent metal (steel Nionikral 70)

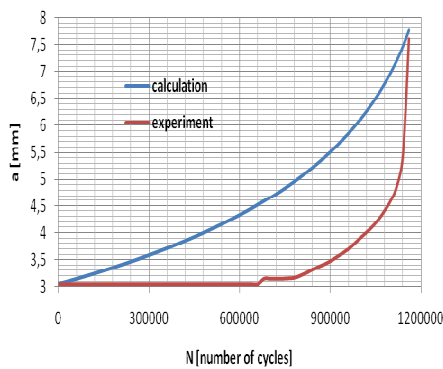


Figure 5 Comparisons Computation with Experimental Crack Growth Behavior of HAZ Structure

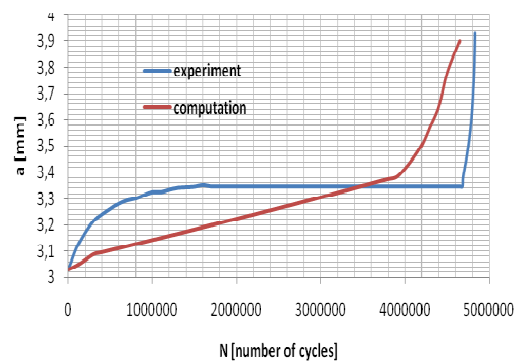


Figure 6 Comparisons Computation with Experimental Crack Growth Behavior of WM Structure

2.3. Fatigue Crack Growth Behavior of WM

Computation crack growth behavior, using eqs (1) and (2), is obtained for constant bending moment of 19.51 Nm during crack growth behavior, Fig. 6

3. Discussions

The most expressively presence of striation is found at HAZ fatigue fracture surface under $\Delta K \sim 30 \text{ MPam}^{0.5}$, Fig.2.f. The presences of secondary cracks among striations indicate their brittle character. Poorly striation was found at HAZ fatigue fracture surface under the value of $\Delta K \sim 10 \text{ MPam}^{0.5}$ Fig. 2.e, and at WM under $\Delta K \sim 10 \text{ MPam}^{0.5}$ and $\Delta K \sim 30 \text{ MPam}^{0.5}$ Fig. 2. a,b. Representative for PM under $\Delta K \sim 30 \text{ MPam}^{0.5}$ is the presence of brittle intercrystalline fracture which is one of static fracture modes. The presence of dimple fracture (which is also one of static fracture modes) at WM fracture surface was also found under $\Delta K \sim 10 \text{ MPam}^{0.5}$ and $\Delta K \sim 30 \text{ MPam}^{0.5}$. Relief at WM, PM and HAZ is more apparent under $\Delta K \sim 30 \text{ MPam}^{0.5}$ Fig. 2. b,d,f, than under $\Delta K \sim 10 \text{ MPam}^{0.5}$ because of the larger plastic zone.

Comparison of computation and experimental fatigue crack growth behavior of different welded joint regions of NIONIKRAL 70 shows good agreement between computation predictions and experimental results in fatigue crack growth behavior in all welded joint regions.

Acknowledgements. The authors acknowledge financial support from the Ministry of Education and Science of the Republic of Serbia under Project TR35011.

References

- [1] Milović, Lj., Vuherer, T., Radaković, Z., Janković., Zrilić, M. and Daničić, D. (2011), Determination of Fatigue Crack Growth Parameters in Welded Joint of HSLA Steel, *Structural Integrity and Life*, **11**(3), pp. 183-187.
- [2] Paris, P.C. and Erdogan, F. (1963), A Critical Analysis of Crack Propagation Laws, *J Basic Engn.*, **85**, pp. 528-538.
- [3] Wiltshire, B. and Knott, J.F. (1980), The Toughness of High Strength Maraging Steels Containing Short Cracks, *Int. J. Fracture*, **16**(1), pp. 19-26.
- [4] Maksimović, K., Đurić, M. and Janković M. (2011), Fatigue Life Estimation of Damaged Structural Components under Load Spectrum, *Scientific Technical Review*, **61**(2), pp. 16-23.

APPLICATION OF THE THEORY OF CRITICAL DISTANCES ON FAILURE ANALYSIS - A CASE STUDY

D. Momčilović¹, R. Mitrović², I. Atanasovska³

¹ Institute for testing of materials IMS
Bulevar vojvode Misića 43, 11000 Belgrade, Serbia
e-mail: dejanmomcilovic@yahoo.com

² Faculty of Mechanical Engineering, The University of Belgrade,
Kraljice Marije 16, 11120 Belgrade 35
e-mail: rmitrovic@mas.bg.ac.rs

³ Institute Kirilo Savić
Bulevar vojvode Stepe 51, 11000 Belgrade Serbia
e-mail: iviatanasov@yahoo.com

Abstract. This paper describes the application of the theory of critical distances (TCD) in the prediction of high-cycle fatigue behaviour in engineering components. The TCD represents a major extension of linear elastic fracture mechanics (LEFM), allowing it to be used for short cracks as well as for stress concentrations of arbitrary geometry, using the results of finite element analysis (FEA) or other computer-based methods.

The classical analytical calculation of shafts has used the Peterson's elastic stress concentration factor charts obtained for conventional values of fillet shaft's transition radius. Finite element method has been used for the simulation of shaft stress state under real load conditions.

This paper illustrates the application of the TCD to a case study on the failure analysis of a turbine shaft from a hydro power plant. The key conclusion of this research is ability of TCD to fully explain cause of failure through accurate crack initiation prediction [1].

Key words: theory of critical distances, high-cycle fatigue, shaft, FEA

1. Introduction

The most frequent causes of failure are defects such as pores or cracks introduced during manufacturing. Also, an inadequate design features, such as sharp corners and other notch like type of stress raisers, cause excessive stress concentration and significantly contribute to failures. In all such cases the common factor which cause failure, is high local stresses. One of the key points in failure analysis is the ability to make accurate predictions of the strength and fracture of materials in complex load-bearing structures. The strength calculation of failed part is also linked with the review of original designer approach in order to check a hidden design error. The majority of failures could be addressed to high-cycle fatigue and prediction of the effect of stress concentrations on fatigue life and fatigue strength is of great importance [2].

Despite this, there is no commonly accepted set of standard methods for predicting the effect of notches, holes, joints, defects and other stress-raisers. This is not due to a shortage of theories and methodologies – there are, in fact, a multiplicity of methods to be found in the literature for the prediction of notch fatigue behaviour. It is rather that the scientific

community has not been able to decide which method, or methods, are most suitable, and under which circumstances [1, 3, 4].

The Theory of Critical Distances (TCD) is a method for the prediction of failure on engineering components and structures with various types of stress raisers. Failure commonly occurs due to the initiation and growth of a crack, through mechanisms such as brittle fracture, fatigue and stress corrosion cracking. In these cases it is well known that both the maximum stress and the stress gradient are important in determining whether failure will occur. It is also well known that materials possess inherent length scales which are related (in complex ways) to their microstructure and modes of deformation and damage. The interaction between the length scale and the stress gradient determines whether failure will occur from a given feature. The major assumption is that cracks, notches and other stress concentration features could be considered in the same way, in particular that cracks are not a special case. This assumption is rather questionable, since it is known that different results can be obtained from, for example, a specimen containing a pre-crack induced by fatigue, and an otherwise identical specimen containing a sharp, machined notch.

The local stress field around a notch, or any other stress concentration, can be represented in a simple form by a plot of the stress as a function of distance along a line beginning at the notch root, Fig. 1. We will assume that the stress analysis is an elastic one, and that it is the maximum principal stress which is being plotted. It is well known that poor accuracy can be expected if one attempts to predict fatigue life based on the range of stress at the notch root (i.e., at a distance of zero in Fig. 1). The use of plastic strain range instead of stress range, has the disadvantage that an elastic–plastic analysis must be performed (or approximated) and in any case it is still quite inaccurate for the prediction of high-cycle fatigue in features with high K_t - stress concentration factor factors (e.g., sharp notches, pits) [3, 5].

This means that the first step in the application of critical distance methods is to use them explicitly, generating stress–distance curves such as Fig. 1 from FEA and calculating the necessary stress values directly.

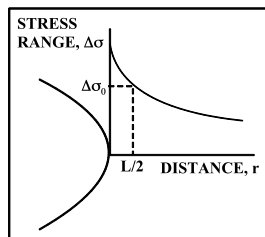


Figure 1. Schematic plot of the stress as a function of distance from the root of a notch or other stress concentration feature. The point method uses the stress at a distance $L/2$ from the notch.

The second step in the updating of these approaches has been the development of a method to calculate the value of the critical distance from first principles. The underlying theory was suggested by Tanaka [3] and by Taylor [4] and validated against experimental data by Taylor [4] and by Taylor and Wang [5]; it is essentially a combination of notch fatigue and linear elastic fracture mechanics concepts. If one assumes that the point method and line method are valid for all types of notches, including sharp cracks, then one can use fracture mechanics to define the stress–distance curve at the fatigue limit for a cracked body (for which the stress intensity range is equal to the threshold value for the material: $\Delta K = \Delta K_{th}$) and thus obtain the critical distances for the two methods. The result [3,4] is that the critical distance for the point method is $L/2$, where:

$$L = \frac{1}{\pi} \left(\frac{\Delta K_{th}}{\Delta \sigma_0} \right)^2$$

In this equation $\Delta \sigma_0$ is the fatigue limit of standard, unnotched specimens of the material, and ΔK_{th} is threshold stress intensity. The fact is that it is often difficult to define an accurate fatigue limit, the stress range corresponding to a given number of cycles, usually in the range 1–10 million, is generally used instead. It has been demonstrated by comparison with experimental data [6] that the use of this value of $\Delta \sigma_0$ for L gives good predictions, not only for notches but also for short cracks, in many different materials.

2. Case study: Failure analysis of hydraulic turbine shaft

The conclusion of shaft failure analysis, Fig 2, was that the combination of several factors leads to failure:

- Inappropriate corrosion protection in the zone of critical radius and lack of procedures of renewing corrosion protection of turbine shaft.
- Corrosion, i.e. corrosion fatigue due to leakage of river water through the sealing box.
- High stresses during start/stop cycles and during regular operating regime in the zone of transition radius for “wet” environment - constant leakage of river water [7].



Figure 2. a) turbine shaft with runner during assembling in the bulb, b) fractured surface

As an integral part of failure analysis, the finite element analysis of turbine shaft was performed under various conditions [8, 9]. The major conclusion was that stress gradient during start up and regular regime had no influence on crack initiation, Fig. 3a) and b). But the simulation of corrosion pits with diameter of $600 \mu m$, Fig. 3c) during start up regime revealed that the stresses under corrosion pit at distance $L/2$ was above the values of fatigue strength of unnotched specimens tested in water. The values of K_t (stress concentration factor) obtained by FEM analysis was, for the case of LC1 (regime during starting) the 3,97 and for case LC2 (regular operation regime) 2,057. The value of K_t on corrosion pit on radius, Fig 3c) was 5,97.

3. Discussion and conclusions

Presented case study is another confirmation, the applicability range of TCD as a method that combines properties of material and geometrical features of engineering component is

very wide. Compared with standard damage mechanics models, which are not generally used to predict cracking processes because they are not well adapted to deal with stress singularities, the TCD can be used as a complementary methodology to modern damage mechanics. On Fig. 3b) the comparative stress gradients from tension as result of axial hydraulic force during starting regime ($F_a=5542.65 \cdot 10^3$ N) without corrosion pit and with corrosion pit are presented.

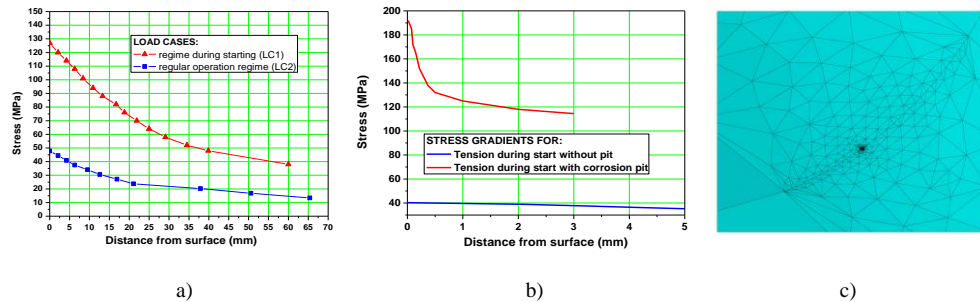


Figure 3. a) Stress gradients on $r=80$ mm radius over two regimes b) Stress gradients over two regimes, c) Simulated corrosion pit with $600\mu\text{m}$ diameter on transition radius

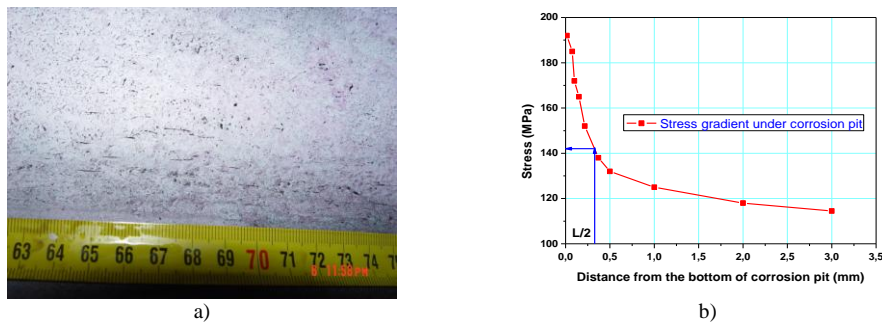


Figure 4. a) Corrosion pits on transition radius b) Stress gradient under the corrosion pit

Acknowledgments. The work has been funded by the Ministry of Education and Science of Republic of Serbia, Grant TR 35029: Development of the methodology for working capacity, reliability and energy efficiency improvement of energetic mechanical systems.

4. References

- [1] Taylor, D (2005), Analysis of fatigue failures in components using the theory of critical distances, *Engineering Failure Analysis* 12, 906–914
- [2] Brooks, R.C. (1993), *Metallurgical failure analysis*. New York: McGraw-Hill; pp 6-11
- [3] Taylor, D (2011), Applications of the theory of critical distances in failure analysis, *Engineering Failure Analysis* 18, 543–549
- [4] D.Taylor et al., (2011), Forni di Sopra (UD), Italy, March 7-9, 2011; ISBN 978-88-95940-35-9, pp 129-135
- [5] Taylor, D., et al. (2000), Prediction of fatigue failure location on a component using a critical distance method, *International Journal of Fatigue* 22 (2000) 735–742
- [6] Taylor D. (1999), Geometrical effects in fatigue: a unifying theoretical model. *Int J Fatigue* 1999;21:413–20
- [7] Momčilović, D. et al. (2012). Failure analysis of hydraulic turbine shaft. *Engineering Failure Analysis*, Elsevier, Volume 20, March 2012, pp. 54-66.
- [8] Atanasovska, I., et al. (2010). FEM model for calculation of Hydro turbine shaft. *Proceedings of the Sixth International Symposium KOD 2010, Palić, Serbia*, pp. 183-188.
- [9] Atanasovska, I., et al. (2011). Influence of transition section of shaft with flange on stress concentration factor. *The 7th International scientific conference Research and development of mechanical elements and systems*, April 2011., Zlatibor, Serbia, pp. 213-218.

EXPERIMENTAL ASSESSMENT OF DAMAGE MECHANISMS IN BOTH ONE-PIECE AND WELDED ALUMINUM FOAM SANDWICH BEAMS

M. Moncada, F. Cognini, U. De Angelis, D. Ferrara, G. De Santis, L. Pilloni, G. Barbieri*, A. Rinaldi*

ENEA, C.R. Casaccia, Via Anguillarese 301, Santa Maria di Galeria, 00123, Rome, Italy
*E-mail: giuseppe.barbieri@enea.it, antonio.rinaldi@enea.it

Abstract. Aluminum foam structures (AFS) have been actively researched over the past decade as a means to develop lighter, more efficient materials for transportation to address sustainability issues. Composite sandwich beams based on a foam core between two flat enclosures are interesting systems for practical purposes due to their mechanical properties optimized for high shock absorption and bending strength. These materials have a ductile microstructure and can hardly be modeled as homogenous effective continua outside the linear elastic regime. The comparison of uniform compression tests vs. 4-points bending tests on one-piece beams, 400mm x 40mm x 30mm (length, width, thickness) in size, demonstrate that the Al foam is damage tolerant only under compression, whereas it undergoes sudden failure in presence of shear due to limited shear strength of the microstructure. Capturing the onset of localization is easy in the first (ductile) case and challenging in the second (brittle) one. Presence of weld joints can alter substantially the intrinsic properties of the native composite panel, introducing weaker spots that cause shift in failure mode. Electron beam welding offered optimal performance in our screening tests, preserving the response of the native one-piece beam in the bending test.

1. Introduction

Metal foams make a class of modern materials with great industrial potential for the development of innovative structural components optimised for several functions, e.g. energy absorption, acoustic isolation, EM shielding, vibration damping, etc. While there exist methods for manufacturing foams for most metals, aluminium foam structures (AFS) are particularly appealing by a sustainable engineering perspective [1]. Figure 1 displays the section of a commercial AFS-based composite beam (AFSC hereafter) for light weight transportation, where the foam core is sandwiched between two skins of bulk Al to deliver optimized mechanical properties (POHLTEC METALFOAM, ECKA Granules, Italy) [2-3]. Amongst the many technological challenges, this paper highlights two important aspects for failure prediction and mechanical design. First, tests on one-piece AFSC beam are analyzed to demonstrate the different damage tolerant behavior under compression and shear (which arises during bending actions). Next, the attention shifts onto two-parts AFSC beams welded by different techniques, a particularly critical aspect for the structural integrity of large span components that are necessarily built from multi-parts joining. The importance of the experimental characterization on modeling is emphasized throughout.

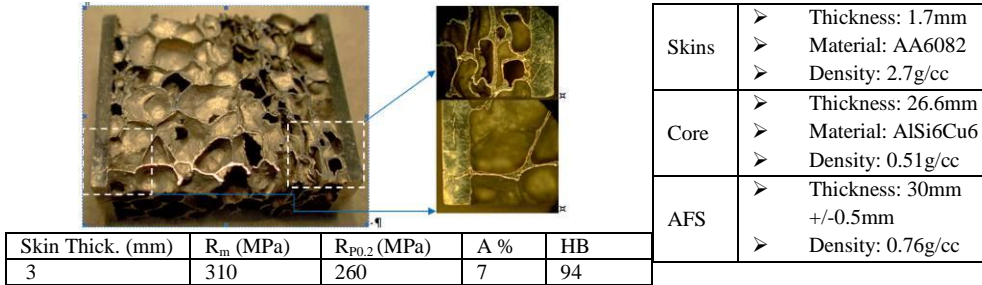


Figure1. Main geometric features of AFSC panels, including mechanical properties of the Al skins

2. One-piece AFS composite beams

For the sake of assessing the different behavior (i.e. strength and failure mode) under compression and shear, the mechanical characterization of AFS panels is performed with uniform compression tests and 4 point bending tests.

2.1. Uniform compression

Uniform compression tests with periodic unloading revealed three stages of deformation. After the elastic regime ($\epsilon < \epsilon_0$, with $E \sim 770$ MPa and compression yield strength $\sigma_0 \sim 4-5$ MPa), the microstructure undergoes two-stages transformation consisting of buckling and collapse of foam pores (stage 2, $\epsilon_0 < \epsilon < \epsilon_1$) followed by compaction and densification ($\epsilon > \epsilon_1$). The extended range of plastic deformation in stage 2 ($\epsilon_1 \sim 0.5$) and stage 3 (test stopped at $\epsilon_{MAX} \sim 70-80\%$), with unchanged unloading slope, indicates the ductile nature of the microstructural response to compression and the lack of cracking.

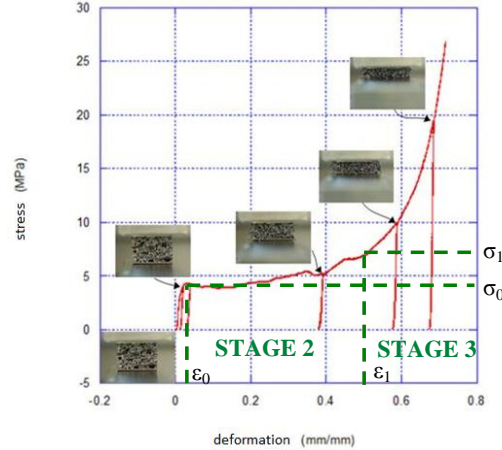


Figure2. Compression test of one piece AFSC sample at strain rates $\sim 0.4 \cdot 10^{-3}$ (1/s). Three stages are observed.

Damage parameter. The plastic deformation ϵ_p does not relate to a bulk process but describes at the macroscopic level the ongoing ductile damage in the microstructure. By a technological standpoint, the stage 2 deformation is the most relevant, as it is directly related to the pores distribution and can be controlled (in terms of ϵ_0 and ϵ_1) by tuning the AFS microstructure and thickness. The damage consists of sequential plastic collapse of individual thin-walled cells (starting from the larger ones) and can be expressed in terms of

a damage parameter (an order parameter D_p ranging from 0 at yielding to 1 at ϵ_1) defined simply as

$$D_p(@ \sigma = 0) = \frac{t - t_0}{t_1 - t_0} = \frac{t_0}{t_1 - t_0} \epsilon_p \tag{1}$$

which is evaluated at rest in terms of ϵ_p and thicknesses both at yielding and at ϵ_1 . Work is being carried out to relate D_p with the tangent stiffness $E_T = \partial\sigma/\partial\epsilon$ and to correlate the latter to the pore distribution via extreme value theory of statistics. The resulting constitutive model throughout the uniform compression test is expressed by the usual relationship for ductile systems $\sigma = E(\epsilon - \epsilon_p)$ specialized for AFSC as

$$\sigma(\epsilon; D_p) = E\left(\epsilon - \frac{t_1 - t_0}{t_0} D_p\right) \tag{2}$$

2.2. Four points Bending

The damage tolerant behavior in compression is not paralleled by an equal damage tolerance to shear. In accordance with ASTM C393 and (input & output) data in Table 1, the information deduced from the bending test in Figure 3 indicates that the onset of failure (point 2 in the stress plot) is due to the “sudden” formation of a localized shear fault in the non-zero shear zone (between the lower support and the nearest upper support) as soon as the AFS core is subject to apparent shear stresses of less than 2 MPa. This corresponds to a brittle, damage intolerant behavior of the AFS and hinders safe application of this type of AFSC in presence of shears. (Accordingly no damage parameter is introduced).

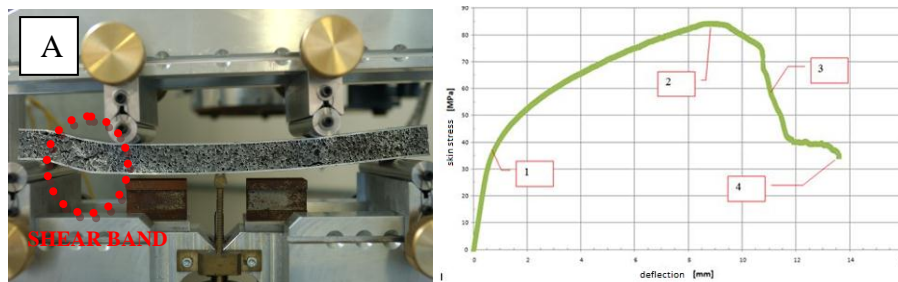


Figure 3. 4/pts bending of one-piece AFSC beam and plot of stresses in the skins as a function of the deflection .

4PBT – OUTPUT PARAMETERS	LIST OF PARAMETERS DEFINITION	
	TEST PARAMETERS	MECHANICAL OUTPUT
$\tau = \frac{P}{(d + c)b}$ $\sigma = \frac{PL}{4t(d + c)b}$ $D = \frac{E(d^3 - c^3)b}{12}$ $U = \frac{G(d + c)^2b}{4c}$ $\Delta = \frac{11 PL^3}{768 D} + \frac{PL}{8 U}$	P = shear load [N] d = sandwich thickness[mm] c = core thickness [mm] b = specimen width [mm] L = distance between the supports [mm]	τ = shear stress in the core [MPa]; σ = bending stress in the skins [MPa]; D = panel bending stiffness [N/mm ²] U = panel shear stiffness [N] Δ = central deflection

Table 1. Summary table for stress determination in bending tests

3. Two-pieces welded AFS composite beams

The “intrinsic” deformation and failure properties of the AFSC described in the previous section may drastically change in presence of welding joint. Our screening tests of the welds in Figure 4, indicates that electron beam welding (although costly) offers best

performance. A representative comparison in Fig.4 between the failure mode of this technique (B) vs. a laser-TIG (C) reveal that the joint section becomes a weaker causing a shift in failure mode from a shear dominated rupture in the AFS to a bending driven one. However, the optimization of the laser-TIG is continuing because it is more convenient for al practical purposes. In particular, preliminary observations indicate a marked improvement by adjusting operational parameters such as the amount of feed material. This first experimental campaign precedes a systematic study of residual stresses from welding and from foaming process itself, which is an important piece of information to obtain reliable materials simulations and understand the underlying mechanisms of the different mechanical failure modes. Preliminary characterization tests of the microstresses have began by means of the technique [4].

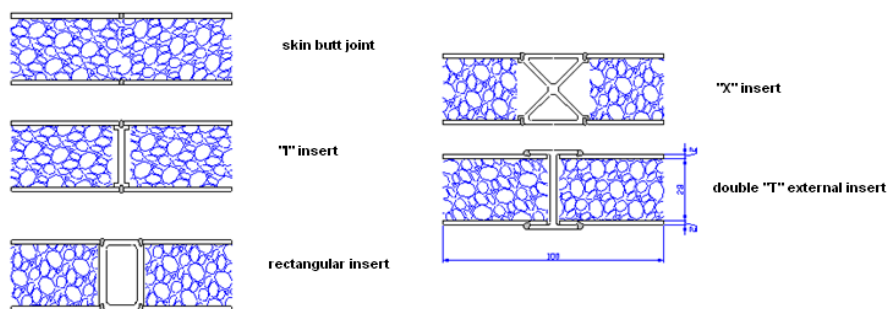


Figure 4. Comparison between different failure modes in a 4-points bending test of two-pieces welded AFSC: (B) shear fault formation in the foam in an electron beam welded AFSC (with insert) (like Fig.3); (C) brittle fracture at the joint location of a laser-TIG beam welding in the middle (without insert).

Acknowledgement. The present work has been performed within the research activities of the “Accordo di Programma MSE-ENEA sulla Ricerca di Sistema Elettrico” (Project 3.5 “Electrical energy saving in transportation: new materials and innovative components for transportation”).

References

- [1] Banhart J. and Seeliger H.-W. (2008), Aluminium Foam Sandwich Panel: Manufacture, Metallurgy and Applications, *Adv. Eng. Mat.*, 10 (9), 793-802.
- [2] Gibson L. J. (2000), Mechanical behavior of metallic foam, *Annu. Rev. Mater. Sci.*, 30, 191.
- [3] Vogel J. et al., (2011), Characterisation of strength behaviour of aluminium foam sandwiches under static load, *Strain*, 47, 234-242.
- [4] Sebastiani, M., Eberl, C., Bemporad, E., and Pharr, G. M. (2011), Depth-resolved residual stress analysis of thin coatings by a new FIB-DIC method, *Mater. Sci. Eng. A*, 528, 27, 7901-7908.

Effect of Micro-alloying on Microstructure and Cyclic Mechanical Durability Response of Sn1.0Ag0.5Cu Joint-scale Solder Specimens

S. Mukherjee¹, A. Dasgupta²

¹Graduate Research Assistant, Department of Mechanical Engineering
University of Maryland, College Park, College Park, USA

E-mail: smukher1@umd.edu

² Professor, Department of Mechanical Engineering,
University of Maryland, College Park, College Park, USA

E-mail: dasgupta@umd.edu

Abstract

The amount of silver in SnAgCu (SAC) alloys has undergone progressive reduction due to cost, concerns related to mechanical properties and toxicity of Ag. Micro-alloying via addition of various amounts of minor/micro dopants, such as manganese (Mn) or antimony (Sb), or rare earth elements, such as lanthanum (La) or cerium (Ce), is currently being explored in these low silver content solders as a means for producing fine-grained, stable microstructures, to improve their reliability under different types of loading conditions. These solders are often termed SAC-X solders, X being the micro-alloying element(s). The current study investigates isothermal cyclic durability of two relatively new SAC105-X solders – Sn1.0Ag0.5Cu (SAC105) doped with 0.05 wt-percent Mn (termed SAC105Mn in this paper) and with 0.55 wt-percent Sb (termed SAC105Sb in this paper). Grain size of these micron-scale specimens is investigated using cross-polarized microscope. Presence of any new phase and due to addition of micro elements is currently under investigation using synchrotron diffraction analysis. Morphology and distribution of intermetallic compounds in as-solidified microstructures have been reported in this study. Cyclic isothermal mechanical durability tests have been conducted at room temperature at a constant strain rate of approx 5.5E-2/s to identify the effect of addition of the trace elements on durability of SAC105 solder. Post failure investigation of these mechanically cycled specimens is conducted to identify the failure mechanisms and modes in these new alloys.

1. Introduction

Research focus on development of new materials for electronic interconnects has recently shifted from the processing issues to tailoring their microstructures and mechanical properties for specific use conditions, by adding minor alloying elements. In the past, silver content in lead free alloys has been kept high (~3 wt-%) to get adequate thermo-mechanical strength but recent investigations have pointed out that low silver content (~1 wt-%) solders perform better under mechanical shock and drop loading conditions due to their lower hardening and low ductility [1-3]. Addition of micro-alloying elements can have a wide range of effects on various physical properties of solders, primarily on (a) bulk microstructure e.g. morphology and/or mechanical properties of the intermetallic compound (IMCs) of solder interconnections and/or, (b) the solidification rate and/or, (c) mechanical properties of the bulk solder. The primary reason for adding Sb in SAC solders is its effect on the strength of the alloy: the ultimate tensile strength (UTS) of the Sn3.5Ag0.7Cu solder alloy increased by about 15 % (strain rate of 1E-4) as the Sb content increased to the range of (1 – 2) wt-percent [4]. Sb dissolves in the Sn-rich phase solid solution as well as Cu₆Sn₅ and Ag₃Sn phases by substituting Sn in the Sn sub lattice as Cu₆(Sn, Sb)₅ and Ag₃(Sn, Sb) [5-7]. Thus, Sb affects mechanical properties of the solder primarily through solid solution strengthening of the Sn matrix. Reports on improved drop reliability with the introduction of trace amount of Mn have made it another interesting new minor alloying element for SAC solders. Liu et al. [8-9] have made an extensive reliability evaluation with BGA component boards assembled with different solder alloys, including the SAC105Mn. Their studies show that, as compared to the SAC105, the drop reliability is improved by about (10 – 50) % depending on the pre-test treatment used in the study and thermal cycling reliability by about (10 – 40) %. Due to the fact that Sb & Mn containing solders are still very little used in the industry, many of the mechanical properties, such as creep and cyclic fatigue in particular, of the Mn & Sb containing SAC solders need to be investigated. A brief summary of the multi-scale microstructure and isothermal cyclic durability response of these two new alloys have been reported in this paper. However, creep constitutive response of the above materials will be reported in details in future publication.

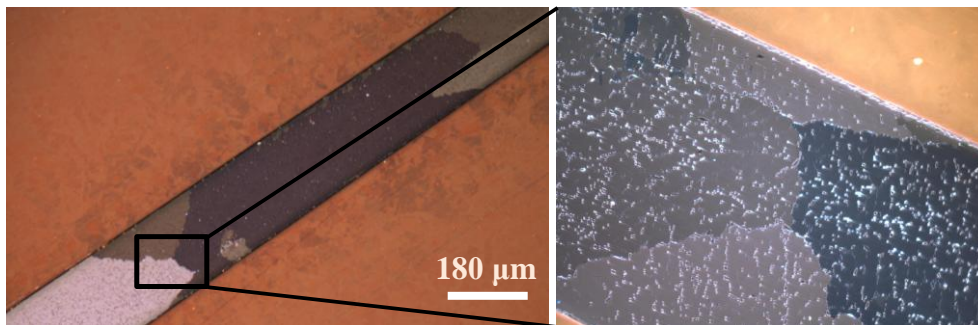
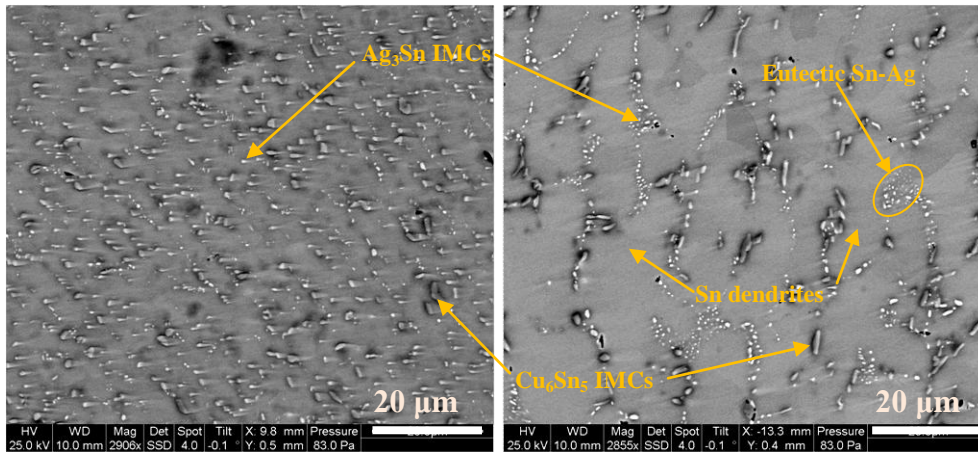
2. Experimental setup & Approach

The constitutive response and cyclic fatigue durability of SAC alloys have been measured using a custom built thermo-mechanical micro-scale (TMM) test system developed at the University of Maryland. The test setup used in this work has been described in more detail elsewhere [10]. The specimen configuration used in the current work is a modified version of the notched shear specimen developed by Iosipescu [11]. The advantage of this specimen configuration is that the stress distribution in the joint volume is quite uniform because of the notches. The specimen width is only about 180 microns; representative of the size of the functional solder interconnects. Complete details of the fabrication procedure are presented elsewhere [11]. In the current work, cyclic tests have been conducted at room temperature and a deformation rate of $10\mu\text{m/s}$. This displacement rate corresponds to a strain rate of approximately $5\text{E-}2\text{ s}^{-1}$. Under these conditions the deformation is believed to be plasticity dominated rather than creep for the solders under study. The displacement controlled loading profile is triangular and all the results presented here are based on a failure criterion of 50% load drop in the specimen, commonly used criterion for isothermal mechanical cycling tests.

3. Results and Discussions

As cast solidified microstructure of the SAC105Mn and SAC105Sb solders and grain morphology are presented in section 3.1. In section 3.2, cyclic mechanical durability behavior of the above two materials has been compared with that of SAC105 at room temperature. Section 3.3 gives a brief summary on failure failure modes and mechanisms of cycled specimens.

3.1 Pre-test microstructure



Several length scales exist in microscale SAC solder joints. SAC105X solder joints are predominantly found to be coarse grained in nature as evident from cross-polarized image of SAC105Mn solder joint (Fig. 3). The next lower length scale (within a single grain) is the micrometer Sn dendrites embedded in the Sn-Ag eutectic region. Load sharing between Sn dendritic phase, eutectic Sn-Ag phase and microscale Cu_6Sn_5 IMCs contribute to reinforcement strengthening of Sn matrix (Fig. 1 & Fig. 2). Next lower length scale is nanoscale Ag_3Sn IMCs dispersed in eutectic Sn-Ag region, which contribute to dispersion strengthening of Sn matrix (circled region in Fig. 2). The above dispersion and reinforcement strengthening mechanisms are being influenced by the microstructural features such as size (length and radius) of IMCs, volume fraction of IMCs; interparticle spacing etc. Micro alloying influences the above microstructural features, which in turn affects the dispersion and reinforcement strengthening mechanisms resulting in change in constitutive and durability properties of solder material. Initial investigations points towards evenly spaced smaller size Ag_3Sn and Cu_6Sn_5 IMCs with reduced interparticle spacing in SAC105Mn solder compared to SAC105 leading to more uniform stabilized microstructure. This is due to addition of trace amount of Mn which reduces the amount of undercooling in SAC solder significantly by about (20-25°C) [8-9]. In case of SAC105Sb, solid solution strengthening of Sn matrix by Sb dissolving in the Sn-rich phase solid solution as well as Cu_6Sn_5 and Ag_3Sn phases is currently under investigation There is no new phase formed across the volume of the SAC105X solder specimens confirmed using synchrotron radiation analysis, which will be discussed in details in future publication.

3.2 Cyclic mechanical durability test results

Cyclic mechanical durability of SAC105Mn and SAC105Sb is compared to that of SAC105 under room temperature isothermal conditions to identify the effect of micro alloys on durability of SAC105 solder. The test is performed under inelastic strain range control. A triangular wave form of with a strain rate of approximately 5E-2/sec is used for this study. A power law relationship is used to fit the various damage metrics (D) and the cycles to failure (N_f) and is given by:

$$D = C \cdot N_f^n, \tag{1}$$

Where, C and n are material constants. Multiple tests have been conducted at varying displacement amplitudes of 6, 8, 10 and 15 μm which corresponds to strain ranges of ± 3 , ± 4 , ± 5 and $\pm 8\%$ at room temperature for above three solders. The damage criteria (D) used in this study is cyclic hysteresis or inelastic work density (W , mJ/mm^3). Number of cycles to failure is defined as the test cycle at which load induced in the specimen reaches 50 percent of its total load bearing capacity. Cyclic softening is evident from the hysteresis loops at different load drops for one such cyclic durability test (Fig 4) for a SAC105Sb specimen. Number of cycles is recorded for 50% load drop criterion and is plotted against the energy density obtained from the area under the hysteresis loop in Fig 5. Addition of trace amounts of Mn and Sb do not improve the cyclic mechanical durability of the above solders compared to SAC105 significantly under tested strain rate (5E-2/sec) at room temperature. Additional tests are currently being conducted at both lower (5E-1/sec) and higher (5E-4/sec) strain rates to identify the dependence of cyclic fatigue durability on strain rate due to addition of these trace elements. Power law material constants for the above three materials under the tested conditions will be detailed in future publication.

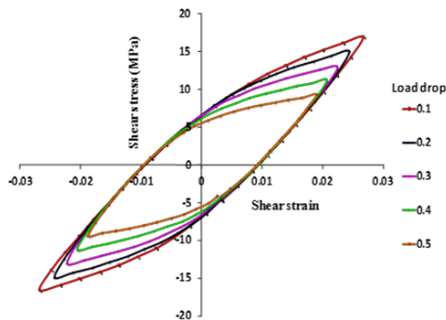


Figure 4. Hysteresis loops for SAC105Sb solder

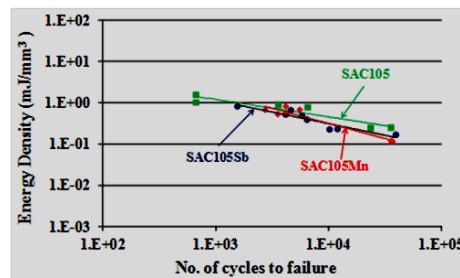


Figure 5. Creep minimized-cyclic fatigue test results

3.3 Post Failure Investigation

The initiation of fatigue cracks in Sn-rich alloys bears a close relationship with the alloy microstructure. In dendritic microstructure, macro cracks are found propagating dominantly through the bulk of the solder taking the path that shows least deformation resistance. Cyclic deformation tends to concentrate in the dendritic phase as

shown by numerous slip bands (Fig. 6). The as solidified dendritic microstructure evolves into a more equiaxed microstructure near the macro crack due to localized recrystallization (Fig. 7). Slip bands (Fig. 6) found in the bulk of the solder is impeded either by possible Sn grain boundaries or dendrite boundaries (shown with arrows), thus causing interfacial discontinuities where a change in orientation of the shear bands is visible across the boundary. Macro cracks are found to subsequently nucleate and propagate along these interfaces.

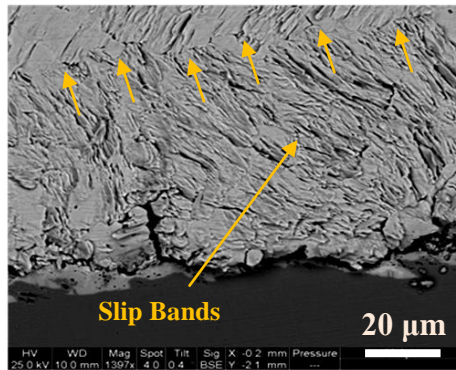


Figure 6. Slip bands in β -Sn dendrite

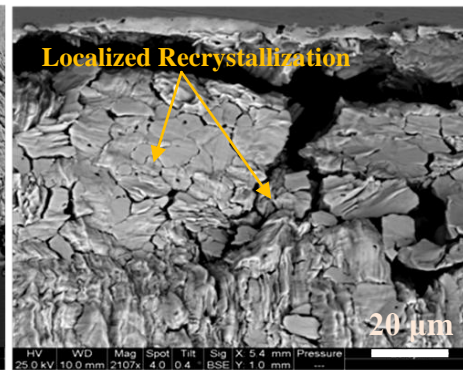


Figure 7. Grain boundary cracking in Sn dendrite

4. Conclusions

As cast solidified microstructure of two SAC105X solders are investigated to identify the microstructural differences due to addition of dopant elements (Mn and Sb) and their effect on cyclic fatigue durability of SAC105 is quantified. SAC105X solder joints are found to be moderately textured coarse grained in nature similar to that of previously found coarse grained SAC105 solder. It is noted that cyclic mechanical durability of SAC105 at room temperature under tested strain rate neither vastly improve nor degrades due to addition of above dopant elements. Effect of strain rate on the durability of the above alloys due to addition of trace element is currently under investigation. However, creep resistance of these two new solders at room temperature is found to be higher than that of SAC105 which is not reported in this paper due to space constraints. Post failure analysis of cycled specimens show shear bands on both sides of grain boundaries and macro-crack propagating dominantly through the bulk of the solder with distributed micro-damage surrounding it.

5. Acknowledgments

This work is sponsored by the members of the CALCE Electronic Products and Systems Consortium at the University of Maryland, College Park.

6. References

- [1] Mattila T. T., Kaloinen E., Syed A., and Kivilahti J. K. (2007), "Reliability of SnAgCu Interconnections with Minor Additions of Ni or Bi under Mechanical Shock Loading at Elevated Temperatures", *The Proceedings of the 57th Electronic Component and Technology Conference*, Reno, NV, IEEE/EIA CPMT, pp. 381-390.
- [2] Kim H., Zhang M., Kumar C. M., Suh D., Liu P., Kim D., Xie M., and Wang Z. (2007), "Improved drop reliability performance with lead free solders of low Ag content and their failure modes," *The Proceedings of the 57th Electronic Component and Technology Conference*, Reno, NV, IEEE/EIA CPMT, pp. 962-967.
- [3] Zhu W.H., Xu L., Pang J. H. L., Zhang X. R., Poh E., Sun Y. F., Sun A. Y. S., Wang C. K., and Tan H. B., (2008), "Drop reliability study of PBGA assemblies with SAC305, SAC105 and SAC105-Ni solder ball on Cu-OSP and ENIG surface finish," *The Proceedings of the 58th Electronic Component and Technology Conference*, Orlando, IEEE/EIA CPMT, pp. 1667-1672.
- [4] Li G. Y., Chen B. L., Shi X. Q., Wong S. C. K., and Wang Z. F. (2006), "Effects of Sb addition on tensile strength of Sn-3.5Ag-0.7Cu solder alloy and joint," *Thin Solid Films*, 504, pp. 421-425.
- [5] Chen B. L. and Li G. Y. (2004), "Influence of Sb on IMC growth in Sn-Ag-Cu-Sb Pb-free solder joints in reflow process," *Thin Solid Films*, 462-463, pp. 395-401.
- [6] Chen B. L. and Li G. Y. (2005), "An investigation of effects of Sb in intermetallic formation in Sn-3.5Ag0.7Cu solder joints," *IEEE Transactions on Components and Packaging Technologies*, 28, 3, pp. 534-541.
- [7] Lee C., Lin C.Y., and Yen Y.W. (2007), "The 260 °C phase equilibrium of the Sn-Sb-Cu ternary system and interfacial reactions at the Sn-Sb/Cu joints," 15, 8, pp. 1027-1037.
- [8] Liu W., Lee N.C., Porras A., Ding M., Gallagher A., Huang A., Chen S., and Lee J. C. (2009), "Shock resistant and thermally reliable low Ag SAC solders doped with Mn or Ce," *The proceedings of the 11th Electronics Packaging Technology Conference*, Singapore, IEEE/CPMT, pp. 49-63.
- [9] Liu W., Lee N.C., Porras A., Ding M., Gallagher A., Huang A., Chen S., and Lee J. C. (2009), "Achieving high reliability low cost lead-free SAC solder joints via Mn or Ce doping," *The proceedings of the 59th Electronics Component and Technology Conference*, San Diego, IEEE/CPMT, pp. 994-1007.
- [10] Haswell P., Dasgupta A. (1999), *Proc. Int. Mech. Congr. Expo.* New York: ASME.
- [11] Iosipescu N. (1967), "New Accurate Procedure for Single Shear Testing of Metals," *J. Materials*, Vol. 2, No. 3, pp. 537-566.

DEVELOPMENT OF HYBRID LAYERED STRUCTURES CONSISTING OF SILICONE AND METAL AND THEIR STATIC TENSILE BEHAVIOR

N. Nestic¹, R. Uhlig², U. Risto², L. Zentner²

¹Faculty of Mechanical Engineering,
The University of Nis, Aleksandra Medvedeva 14, 18000 Niš
e-mail: nnesic@gmail.com

²Faculty of Mechanical Engineering,
Technical University Ilmenau, Max-Planck-Ring 12 (Haus F), Postfach 100 565
D-98684 Ilmenau, Germany
e-mail: lena.zentner@tu-ilmenau.de

Abstract. Silicone is a material which has today many practical applications. Usage of silicone is constantly increasing, especially in medicine (surgical implants, sensors). For development of new medical devices and implants it is important to find more suitable ways to connect different materials that are widely used separately. The aim is to combine the positive characteristics and to create a new material behavior. Therefore, the objective of this investigation is the development of new manufacturing concepts for creating hybrid shouldered test bars and to perform tensile tests on them. The test bars are made of silicone with inserted flat metal springs. Altogether 4 different shapes of springs are considered. For manufacturing of the hybrid shouldered test bars the methods of casting and heat pressing are used. The test bars created by casting have smaller deformation of the leaf spring than the ones produced by heat pressing. During tensile tests most of the bars show damage at strains between 11% and 25% of their lengths depending on the shape of the inserted metal spring. The analysis of the test results shows a high degree of relative movements between the different used materials [1].

Key words: Casting, heat pressing, leaf spring, shouldered test bar, tensile test

1. Introduction

Silicone is a material which has today many practical applications. Usage of silicone is constantly increasing, especially in medicine (surgical implants, sensors) and food industry (packages). It is used because of its properties: human body can be in contact with it for a long time, without consequences; it can be easily shaped; it has great elastic properties. But in some applications, that so big elasticity can be disadvantage. So, if greater toughness is needed, and chemical structure of silicone can not be changed, some other material must be inserted into it. That material is in our case metal.

In the field of technology that concentrates on the combination of different materials, a lot of research has been done. As an example, a cochlear-implant can be mentioned. All of the nowadays applied implants, which are implanted in the cochlea, consist of an electrode array, a receiver and a stimulator unit for signal, an electrical transmission and a receiving antenna. In Fig. 1 is a representation of an implant from MED-EL (MED-EL, Innsbruck, Austria). 12 or more platinum electrode pairs are embedded in one soft silicone-carrier. The electrodes are made with wave-shaped wires for maximum softness and flexibility.

Production procedures are chosen according to recommendations in data sheets of products of Wacker Silicones Company [2, 3]. Two manufacturing concepts are selected and used for production of hybrid test bars. They are casting with liquid silicone and heat pressing with solid silicone.

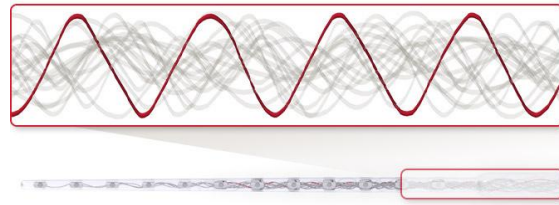


Figure 1: a silicon implant from MED-EL, Innsbruck, Austria (<http://www.medel.com>)

2. Manufacturing concepts

2.1. Test bar

The *complete form closure* was chosen as a connection type between silicone and metal for this research, which means that metal structure is put inside silicone (in the middle of it). Four different shapes of the leaf spring (whole metal part is constructed of a sheet metal) were manufactured (fig. 2). As a material for metal parts of shouldered test bars is used spring steel 1.4310.

Since these test bars were to be stretched in the machine and characteristics (stress and strain) measured, they are made with shoulders. That means that the ends are wider (which means greater contact surface with machine catching part) and middle part narrow (in order to have smaller resistance). Part in the middle of test bar is only important for the results of the stretching tests. Shoulders of the test bars have an insignificantly small influence on accuracy of results.



Figure 2: Example of final produced hybrid test bars with heat pressing

2.2. Heat pressing

Produced model of the heat pressing tool is displayed at the figures 3 and 4. The test bar must be made in a few steps. Firstly, one half of the silicone body is made with first configuration (fig.3 left), and then the second half on the same way. They can be made with cold press (on the room temperature) or with a hot press (for a very short time). Then is the metal part inserted between them, and they are vulcanized with heating press (fig.3 right).

On the next picture (Figure 4) all parts of our press tool can be seen. Purpose of the small screws is to close the small holes on the “red” covers in the process of production of silicone halves. That is done because through high speed of exiting silicone some holes in the silicone half around the exiting holes of the tool can be made. In the process of final pressing and vulcanization these screws are not used.

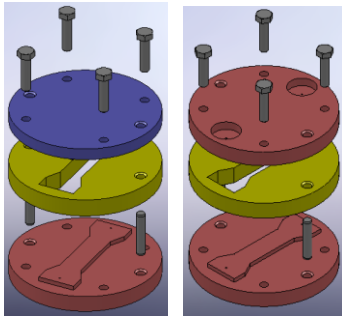


Figure 3: Press tool in 2 configurations



Figure 4: Parts of the produced press tool



Figure 5: Parts of the produced casting tool

2.3. Casting

For the process of casting it is important that tool have two holes, one for injection of the silicone, and another for exiting air. To prevent that silicone flows out of the tool, these two holes must be on the top of the tool. It is also better if the pocket is filled from bottom to top, because in that way is less possible that bubbles of air could be captivated by silicone in the pocket and silicone would press residual air out, through output hole. To solve these problems, pocket is built with an angle (in our case it is 45°), input and output holes are on the top of the tool, and with tunnels is input hole connected with the bottom of the pocket. The output hole is positioned on the top edge of the pocket so the silicone can leave the pocket through it, only if the pocket is completely full with silicone. Build model can be seen on the figures 5 and 6.

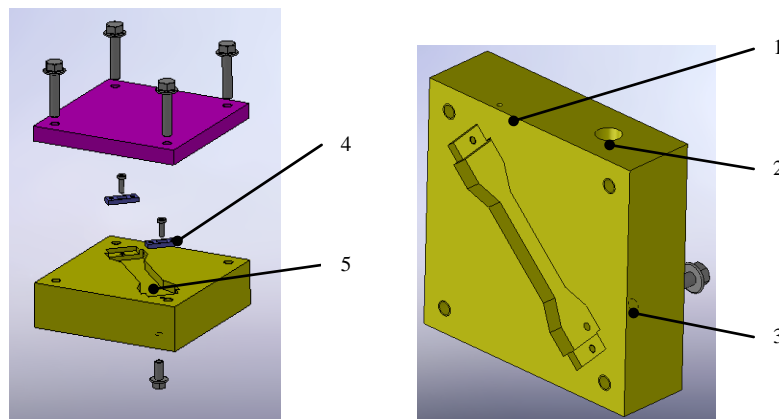


Figure 6: Casting tool: 1 – output hole, 2 – input hole, 3 – cleanout hole (during casting closed with screw), 4 - fixer for metal spring, 5 – pocket.

3. Tensile tests

Tensile tests are performed on the machine shown on the Figure 7. Hybrid test bars are stretched for 12.5% and 25% of their length. Stretching machine is connected to the computer which in appropriate software sketch stress-strain diagram. Diagrams clearly display moment of crack. One of them is displayed on the Figure 8.



Figure 7: Test bar in the stretching machine during uniaxial tensile tests

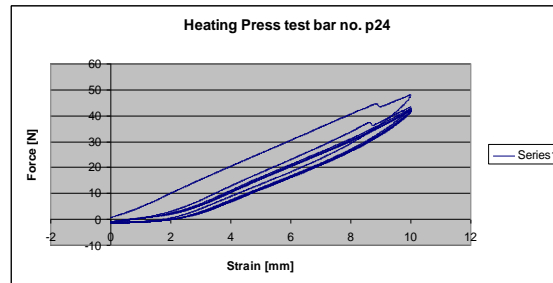


Figure 8: Example of test results

4. Results

There were 4 different types of springs. 8 (2 x 4) test bars are produced by pressing and 4 by casting. 4 of the first ones and 4 of the second ones are 25% stretched (10mm), and in 100% of cases, spring was broken. 4 test bars produced by pressing are stretched up to 12.5% (5mm) and in the 25% of cases spring was broken. During tensile tests most of the bars show damage at strains between 11% and 25% of their lengths depending on the shape of the inserted metal spring. The analysis of the test results shows a high degree of relative movements between the different used materials

5. Discussion

Hybrid test bars produced by casting are giving better results, then ones produced by pressing.

Acknowledgement. This research is realized thanks to cooperation of Technical University Ilmenau in Germany and Faculty of Mechanical Engineering, University of Nis in Serbia. Submitting of this paper is supported by the Ministry of Sciences and Technology of Republic of Serbia through Mathematical Institute SANU Belgrade Grant OI174001 “Dynamics of hybrid systems with complex structures. Mechanics of materials”.

References

- [1] Nesic, N (2010), Development and production of hybrid test bar and investigation of silicone-metal connection for application in surgical implants, *Graduation thesis*, The Faculty of Mechanical Engineering, University of Nis
- [2] Instruction manual, Wacker Silicones, Die Verarbeitung von Elastosil[®] r Festsiliconkautschuk
- [3] Instruction manual, Wacker Silicones, Die Verarbeitung von Elastosil[®] r Flüssigsiliconkautschuk
- [4] Grambow, A. (2002). Bestimmung der Materialparameter gefüllter Elastomere in Abhängigkeit von Zeit, Temperatur und Beanspruchungszustand. *PhD thesis*, RWTH Aachen, Institut für Kunststoffverarbeitung
- [5] Hegemann, B. (2004). Deformationsverhalten von Kunststoffen beim Thermoformen experimentelle und virtuelle Bestimmung, *PhD thesis*, Universität Stuttgart, Institut für Kunststoffkunde und Kunststoffprüfung
- [6] Detrois, C. (2001). Untersuchungen zur Dehnrheologie und Verarbeitbarkeit von Halbzeugen beim Thermoformen sowie Simulation und Optimierung der Umformphase, *PhD thesis*, RWTH Aachen, Fakultät für Maschinenwesen

FRACTURE PHENOMENA – COMBINED DM & FM APPROACH – A TRIBUTE TO PROFESSORS J. JANSON AND J. HULT

M. Pavisic,

¹Independent Consultant, "Bridge Consult"
11070 Belgrade, Bulevar Zorana Djindjica 215, Serbia
E-mail: m.pavisic@gmail.com

Abstract. Two theories – Damage Mechanics and Fracture Mechanics (DM&FM) exist today in parallel both trying to describe the fracture phenomena of many different materials. However, both theories are founded on their own basic assumptions which are highly idealistic considering the real fractographic nature of any fracture of materials. FM assumes and considers a single crack surrounded with medium which is assumed as mechanically intact. On the other side, DM assumes a continuous damage field within the zone of loaded material. The highly idealized base ground of both theories makes them unable to encompass and solve the problem of fracture of any material in general. Much more realistic solution may be obtained by combining these two approaches as it was proposed earlier (1977) by Professors J. Janson and J. Hult from Gethenburg's University [1]. The new assumption implies a single macro crack embedded in the material with continuous damage field. The assumption is derived and based on many NDT investigations of the fracture initiation and propagation of various materials. Actually, it appears that the fracture process within loaded material proceeds continuously and gradually through the several phases following subsequently each other from (a) mechanically intact material to (b) continuous damage field and finally to (c) sharp single crack initiated within damage field [2]. Analyzing Dugdale crack model, plastic flow and damage creation are assumed to occur within the narrow region at the crack tip. The approach has not gained significant attention of researchers so far mainly because of their firm devotion to the one of the mentioned theories. The main objective of this paper is to remind once again all those interested in fracture material phenomena on the great idea of professors Janson & Hult and to point out the way where further research must be directed on the field of fracture material analysis.

1. Introduction

A fracture process initiation and propagation differs for different materials. The nature of this process is different even for the same material depending of environmental conditions – temperature, pressure etc. To describe and to define this process in general for any kind of materials is an extremely complex assignment. Therefore, several theories and sub-theories have been founded so far with the purpose to cover fracture analysis of certain, particular materials. All of them are limited by their basic assumptions and not able to give a general solution which could be applied to any materials. FM assumes and considers a single crack surrounded with medium which is assumed as mechanically intact. On the other side, DM assumes a continuous damage field within the zone of loaded material. However, experience in fracture process analysis of various materials shows the clear evidence that the fracture process, more or less takes place gradually following increased or repeated loads passing

through the different states of material degradation. This material degradation process can be roughly determined with three sequential states: (a) non-damaged, virgin material state (b) material with continuously distributed micro damaged field and (c) material with the macro crack created within the field of continuous damage field. Therefore, professors Janson and Hult (Authors) came to a challenging conclusion that the third state is actually that which should be analysed and considered as a crucial for solving the problem of fracture.

2. Dugdale crack with damage

Already well known Dugdale's model of crack in a thin sheet of elastic ideally plastic material loaded in mode I is assumed but now imbedded in damage field existing in front of the crack tip (Figure 1.)

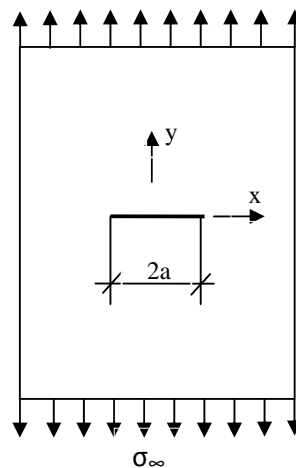


Fig. 1. Sheet with crack loaded in mode I

Since an interaction between the macro crack and micro damage is unavoidable, Authors [1] and further J. Janson [2] by himself introduced the following constitutive relations:

$$\begin{aligned} \varepsilon &= s/E && \text{for } s < s_y \\ \varepsilon &= \text{indefinite} && \text{for } s = s_y \end{aligned} \quad (1)$$

Here s is the net stress with the following relation between stress, net-stress and damage as it was originally introduced by Kachanov and Rabotnov (1958) (1969):

$$\sigma = s(1 - \omega) \quad (2)$$

The mentioned interaction is the main and essential contribution of the new proposed approach. Accordingly, net-stress within the plastic zone at the crack tip is assumed as net

yield stress s_y . Outside of this zone damage field prevails related to the net stress with a power relation (Broberg, 1975):

$$\omega = C_0 s^{\nu_0} \quad (3)$$

At the zone boundary s is s_y and damage is treated as material parameter: $\omega = \omega_0$. Following original Dugdale's work, inside the zone, damage is assumed to depend linearly on the crack opening (Fig. 2.):

$$\omega(x) = \omega_0 + k\eta(x) \quad (4)$$

where k is material parameter.

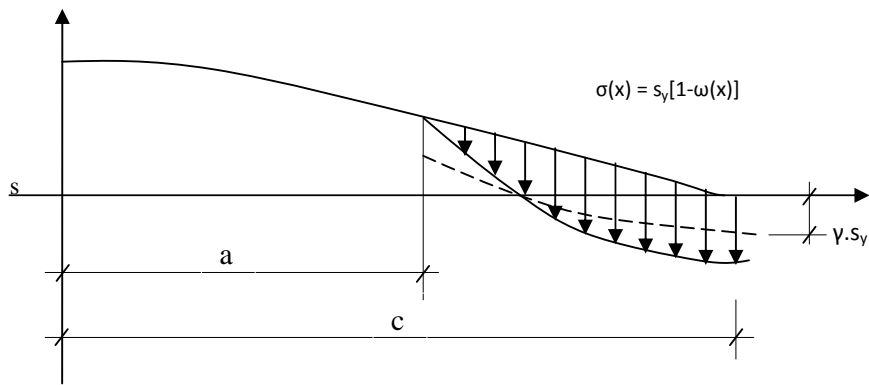


Figure 2. Plastic zone with damage

However, taking now damage in consideration according to the equation (2) the stress σ within the zone is:

$$\sigma(x) = s_y (1 - \omega(x)) \quad (5)$$

or, according to equation (4):

$$\sigma(x) = s_y(1 - \omega_y - k\eta(x)) \quad (6)$$

Using well known Westergard's stress function, J. Janson [2] further made an attempt to define half-opening $\eta(x)$. The procedure based on the initial approximation:

$$1 - \omega_y - k\eta(x) = \gamma = const. \quad (7)$$

may be further followed in [2] as an iterative process to the final outcome – the critical external stress needed to create a damage $\omega(a)=1$ (criterion for crack growth).

3. Conclusions

Two theories (FM & CDM) are dominant today in fracture phenomena analysis and problem solving. However, both are founded on highly idealized assumptions. The proposed combined approach gives more realistic solution. The main point is damage presence within the zone of crack tip and its interaction with the process of plasticization. As a result the critical external stress σ_{∞} as a function of crack length is obtained. When the critical state is reached, the crack will start to grow unstably. For sufficiently small cracks the stress is approximately s_y what is actually Dugdale's result.

References

- [1] Janson, J., Hult, J. (1977), Fracture mechanics and damage mechanics a combined approach, *Journal de Mécanique appliquée*, Vol.1, N°1, pp. 69-84.
- [2] Janson, J. (1978), Damage model of crack growth and instability, *Engineering Fracture Mechanics*, Vol.10, pp. 795-806.

EXPERIMENTAL ANALYSIS OF LOW CYCLE FATIGUE OF DC 90 DAMPERS

Z. Petrašković¹, D. Šumarac²

¹ Research-productive Centre System DC 90, 11000 Belgrade, Serbia,
e-mail: dc90@eunet.rs,

² Faculty of Civil Engineering, Kralja Aleksandra 73, 11000 Belgrade, Serbia, e-mail: sumi@eunet.rs

Abstract: In the present paper experimental analysis of DC 90 dampers is presented. The structure of DC 90 dampers as a patent is thoroughly explained. The advantage of those dampers is that they are without oil, very easy to be applied and almost without any maintenance. They are already very successfully implemented for retrofitting structures on four continents, America, Africa, Asia and Europe. Three types of experiments connecting with DC 90 System are performed. First type is testing of dampers on alternate cyclic loading. Second and third experiments are testing of dampers in applications. Quasy static testing on walls clearly shows how dampers contribute to strengthening of structures. Finally in situ testing on structures shows advantage of those dampers.

Keywords: Dampers, cyclic plasticity, very low cycle fatigue

1. Introduction

Earthquakes are very dangerous impacts on civil engineering structures. Specially this is the case of masonry structures. It is well known that those structures have large mass, and consequently, because of bad cohesion between bricks (stones) and mortar they crack and suffer damage when exposed to earthquakes. In Fig. 1. typical masonry structure in the western part of Serbia, after Kolubara earthquake, 5.3 Richter scale, is shown. The cracks and damage, due to alternating loading are along diagonals. Strong need and desire to find a new effective object protection from seismic loads and realization of the tougher masonry and even concrete structures resulted a new, DC 90 Construction System and associate devices, presented in this article.



Figure 1. Damage of two store building from Kolubara region, Serbia

2. Development of the DC 90 construction system with applications

System DC 90 comprises a number of structural elements which strengthen brittle walls and make them ductile and tough. The application assumes that floor slabs are stiff and

capable to transmit the load in their own plane, and connect them by foundation collars. These elements make structure stronger to accept the horizontal loads. This invention is based on the construction system with damper- absorber which makes the building structures more resistant and lets them withstand the highest values of earth tremors through elastic plastic work and plastic deformation (flow) control.

The construction of the damper of the type "Mionica" is given in Fig. 2. with associated cyclic loop characteristic of this damper. There are more than 15 type of dampers developed so far for different structures to be retrofitted. System DC90 is protected by patents in USA and Australia [1-2]. In this paper the focus will be on damper "Mionica". The damper itself (Fig.2) is cylindrical structure, made from the steel tube (pos 1 $\text{Ø}48.3 \times 3$) and four rings (pos 2 $\text{Ø}54.3 \times 3 \dots 10$). Three of them are fixed and one is free to move. To protect buckling main tube is stiffened by another tube from outside and aluminum tube and micro reinforced concrete from inside. To avoid friction the tubes are lubricated by special graphite lubricant. There is third tube (pos 3 $\text{Ø}60.3 \times 3 \dots 92$) to connect fixed and movable rings in order to control the limit of elongations.

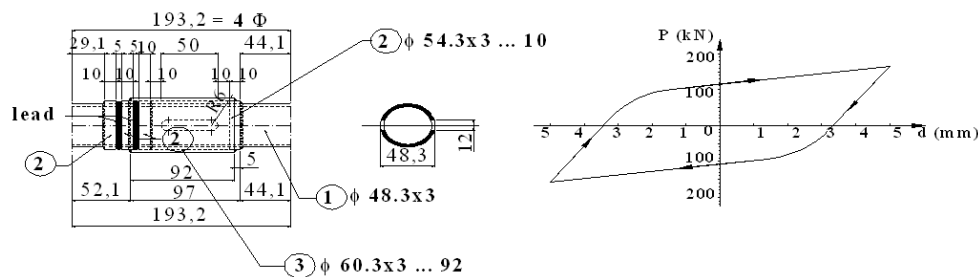


Figure 2. Construction of Damper "Mionica"

The principle of operation of the metal hysteresis damper is based on post elastic (plastic) zone and deformation control by force of four rings, one of them is free to move. Its movement is defined and limited by fixed side rings. To prevent the local buckling there are two systems (inside and outside). The inside surface of the damper is filled with micro reinforced concrete reached by super plastificator and other additives used in construction chemistry for construction members of relatively small cross-sections. The concrete centre and damper body are adjoined by aluminum tube. The outside surface of the aluminum tube is lubricated by special permanent graphite lubricant. The metal tube finished in a special way prevents the outside local buckling. The above mentioned quality level eliminates the possibility of crack initialization on the damper body.

3. Testing of dampers

Dampers for DC 90 system (Fig. 3) were tested by variable loading on MTS servo-hydraulic closed-loop machine (Fig. 4). The test was performed on 18 specimens and obtained hysteresis loop diagram is given in Fig. 5 for 1mm displacement, in Fig.6 for displacement of 2mm and in Fig.7 for displacement of 4mm. Associated Force-number of cycles to rupture diagrams are presented to on the same Figures.



Figure 3. Typical dampers of DC 90 system



Figure 4. Damper testing on MTS machine

On the same Figures, diagram energy-number of cycles is presented to.

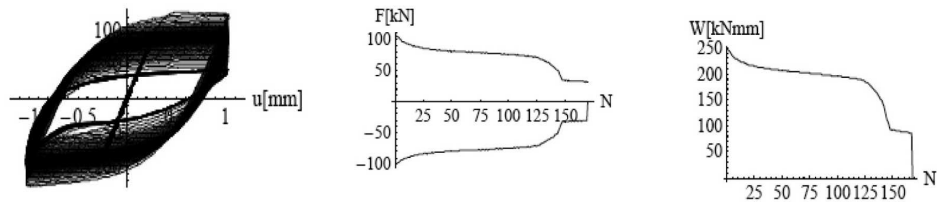


Figure 5. Hysteresis loop diagram, Force - Number of cycles diagram, Energy - Number of cycles diagram for cycle loading at constant displacement range ± 1 mm.

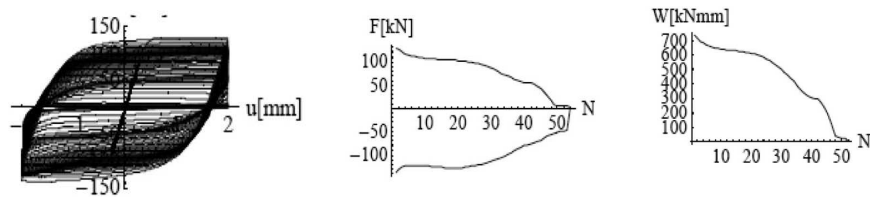


Figure 6. Hysteresis loop diagram, Force - Number of cycles diagram, Energy - Number of cycles diagram for cycle loading at constant displacement range ± 2 mm.

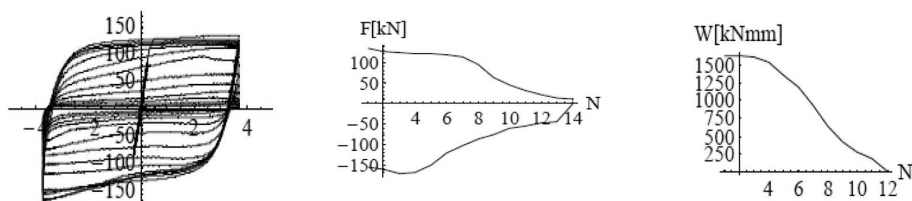


Figure 7. Hysteresis loop diagram, Force - Number of cycles diagram, Energy - Number of cycles diagram for cycle loading at constant displacement range ± 4 mm.

From the diagrams force-displacement, Fig.5, 6 and 7, one can conclude that classic low cycle fatigue is in question [6]. During operation, in displacement control, permanent plastic deformations appear, or in another words, with increasing number of cycles material weakens and maximum force reduces: when force decreases for the same deflection, material is weaker. It can be seen that with increasing of plastic deformation during a single cycle (larger amplitude of loading, for instance 4mm) number of cycles to failures is

decreasing from 150 in case of amplitude of 1mm to 14 in the case of 4mm amplitude. For smaller amplitude displacement, number of cycles needed for failure is greater. From Dufailly and Lemaitre paper [6] it is clear that behavior of dampers shown in Fig.5, 6 and 7 belongs to very low cycle fatigue.

4. Testing by quasidynamic loading of hollow blocks wall

Figure 8 presents testing by quasidynamic loading of experimental two store wall, made of hollow blocks 19x19x25, framed by girders, as classical solution, (left), as strengthened according to DC 90 system (middle) and during testing after few cycles (right): for displacement 10 mm of console top point, extended flaws of 8-10 mm appeared in the first area from the point of force application. In the area to the wall constraint, cracks typical for dominant bending stresses appeared. Wall behaves much tougher at cyclic loading. For loading of 60 kN, for top displacement of 25 mm far less cracks occurred, with openings 2 to 3 mm.



Figure 8. Two-store wall model, before retrofit, after retrofit and during testing

5. Conclusion

The numerous testing of the construction DC90 system and DC90 Damper as well as numerous analyses define the sphere and the possibility of implementation of our technology. The Canada HQL Type Damper can be used in case of low range plastic displacements (from tenth of millimeters to several millimeters), for example, displacement range from 4 to 5 mm. In case of the constructions that demand plastic displacements over 100mm we recommend the using of "Bridge" Type Damper with maximum displacement range of 120 mm. Besides, the accumulated strain capacity in low cycle area is double in comparison with standard construction member's capacity. The damper ability to define the limits of plastic displacements and to prevent the construction from failure is of significant importance. The construction mechanism provides the stability of its members even at higher values of strain in low cycle area as it is cited in patents.

References

- [1] Petraszkovic, Z. (2006), System of Seismic Strengthening of Structure, United States Patent and Trademark Office, Pub. No US 2006/0207196 A1, Serial No. 10/555,131.
- [2] Petraszkovic, Z. (2004), System of Seismic Strengthening of Structure, Australian Patent Office, Application No. 2003254327, WIPO No. WO04/097146, 11.23.
- [3] Popov, E.P. (1984), Bond and Anchorage of Reinforcing Bars under Cyclic Loading, *ACI Structural Journal*, July-August 1984., pp 340-349.
- [4] Šumarac, D., Krajinović D. (1990), Elements of Fracture Mechanics, Scientific book, Belgrade, (in Serbian).
- [5] Šumarac, D., Petrašković, Z., Miladinović, S., Trajković, M., Andjelković, M., Trisović, N. (2006), Absorbers of Seismic Energy for Damaged Masonry Structures, Fracture of Nano and Engineering Materials and Structures, Proceedings (CD) of the 16th ECF, Greece, Ed. E.E. Gdoutos, pp. 1041-1042, Springer.
- [6] Dufailly, J. and Lemaitre, J. (1995), Modeling Very Low Cycle Fatigue, *Int. J. Damage Mechanics*, 4, pp. 153-170.

A TWO-DIMENSIONAL SHELL ELEMENT FOR COUPLED VISCO-HYPERELASTIC AND DAMAGE BEHAVIOR OF POLYMERIC FABRICS

G.P. Potirniche¹, D. Stillman², T.-L. Lin²

¹ Department of Mechanical Engineering,
University of Idaho, Moscow, ID 83843, USA
e-mail: gabrielp@uidaho.edu

² CAE Solutions Corporation,
40935 Camero Place, Fremont, CA 94539-3730, USA
e-mail: stillman.douglas@gmail.com

Abstract. Owing to their high strength-to-weight ratio, materials incorporating polymeric fabrics are key structural components in numerous engineering applications. Fabrics are used extensively for protection against various projectiles, thus understanding their ballistic impact properties becomes vital for ensuring adequate protection. In this paper a two-dimensional finite element was developed for modeling the deformation and failure of Nylon 6.6 and Kevlar 29 fabrics upon impact. The interaction between crossover yarns in a fabric material is incorporated into a continuum mechanics formulation for the shell element. The constitutive material modeling is based on a coupled visco-hyperelastic and damage model for one-dimensional rope elements accounting for the damage evolution by individual yarn failure. The model also incorporates the strain rate and temperature effects on the stress-strain behavior of Nylon and Kevlar fibers. The shell element is considered as a unit cell with the yarn interaction and deformation behavior resulting from the yarn crossover. The advantage of this modeling approach is that, while incorporating the details of yarn interaction, it does not explicitly model the geometrical details of the yarns, but including these details into a continuum element, and consequently reducing the computational time.

1. Introduction

Fabrics are used extensively in applications that involve protection against various projectiles, thus understanding their impact properties becomes vital for ensuring adequate protection for personnel and equipment. Several continuum models for ballistic properties of fabrics have been developed over the years [1,2]. These models capture the geometry of the three-dimensional interaction between yarns into a continuum description of the fabric behavior. In this paper a model for fabric behavior is presented, whereas the interaction between the crossover yarns is incorporated into a continuum description of a two-dimensional membrane element. The advantage of this approach is that while incorporating the details of yarn interaction, it does not explicitly model the geometrical details of the yarns, but including these details into a continuum element, thus reducing the computational time. The proposed approach has been used before in [3-5]. The main

improvement of the present study compared with the previous research efforts is a more accurate description of the rate dependent behavior of the individual yarns and also a more accurate description of the damage evolution in yarns, thus improving the failure predictions for the membrane elements representing the fabric to be analyzed.

2. Constitutive equations for two-dimensional polymeric shell elements

The numerical implementation assumes a known visco-hyperelastic behavior for the yarns, and captures their interaction into a representative membrane element as a continuum representation of this interaction. The model is applied to Nylon and Kevlar fabrics. Figure 1 indicates the position and the contact forces between two crossover yarns, as part of a larger fabric. The force in the fill yarn is denoted F_f while the force in the weft yarn is F_w . The spans are denoted s_f and s_w , while h_f and h_w represent the heights of the two yarns. Given these dimensions, the orientation angle α_f and α_w of the two fibers can be calculated, and the two fiber forces F_f and F_w resolved into their corresponding components T_f and N_f , and respectively T_w and N_w . The equilibrium between the two yarns is achieved when

$$N_f = N_w \quad (1)$$

where

$$N_f = F_f \sin \alpha_f, \quad N_w = F_w \sin \alpha_w \quad (2)$$

The forces in the fill and warp are computed from the stresses developed in each of these yarns

$$F_f = \sigma_f A, \quad F_w = \sigma_w A \quad (3)$$

where A is the cross-sectional area of each yarn. The stress is given by the amount of stretch experienced by each yarn, following the model developed for one-dimensional rope elements by Potirniche et al. in [6]. According to this model, the stress developed as a result of the deformation process quantified by the total stretch is given by the sum of the hyperelastic, damage and visco-elastic stress components. Thus, one can write

$$\sigma_f = \sigma_f^{eh} + \sigma_f^{ed} + \sigma_f^v \quad \text{and} \quad \sigma_w = \sigma_w^{eh} + \sigma_w^{ed} + \sigma_w^v \quad (4)$$

Each of the stress components from the previous equations is calculated using the following equations [6]

$$\sigma^{eh} = \sum_{m=1}^3 \mu_m \left(\lambda^{\alpha_m} - 2\lambda^{-\alpha_m/2} \right) \quad (5)$$

$$\sigma^{ed} = -A_1 \left(\lambda - \lambda^{-1/2} \right) - \lambda A_2 \exp \left[A_2 (\lambda - 1) \right] + \lambda^{-1/2} A_2 \exp \left[A_2 \left(\lambda^{-1/2} - 1 \right) \right] \quad (6)$$

$$\sigma^v = \left(\lambda^3 + \frac{1}{2} \lambda^{-3} \right) \dot{\lambda} A_3 \exp \left(A_4 \sqrt{\frac{I_2}{3}} \right) A_5 \left[1 - \exp \left(-\frac{t}{A_4} \right) \right] \quad (7)$$

where λ is the stretch, μ_m , α_m ($m=1,2$ and 3), A_1 , A_2 , A_3 , A_4 , and A_5 are material constants defined for Kevlar 29 and Nylon 6.6, and t is the total time elapsed during deformation. I_2 represents the stretch invariant defined as $I_2 = \lambda^{-2} + 2\lambda$. The material constants for Kevlar and Nylon have been presented in [6]. Writing Eqs. (5)-(7) for both fill and weft yarns, and substituting Eqs. (2)-(7) into Eq. (1), a non-linear equation will result from which the fiber deformation can be found using a Newton-Raphson algorithm.

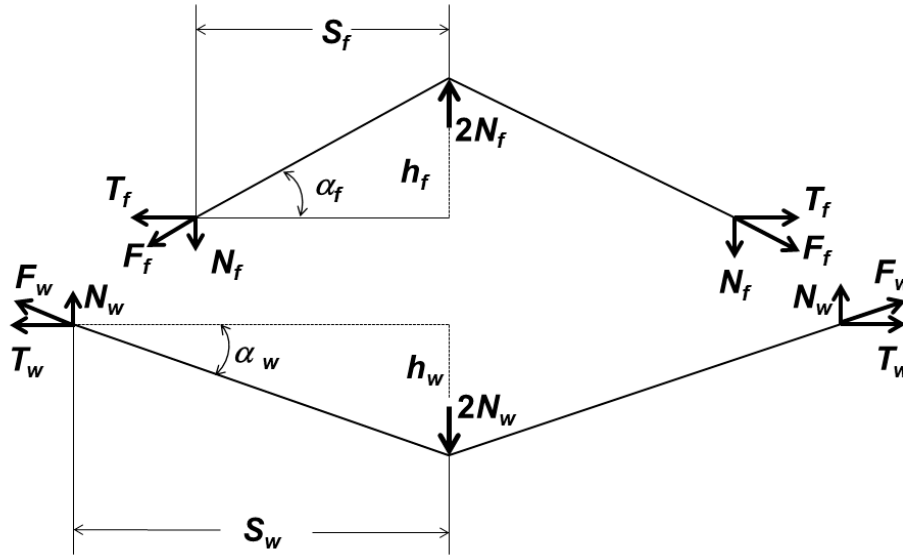


Figure 1. Relative position of the fill and warp yarns with dimensions and applied forces.

The stresses computed with equations (5)-(7) for the fill and warp yarns are used to compute the stresses in the membrane element.

$$\bar{\sigma} = T_f^T \sigma_f T_f, \quad \bar{\sigma} = T_w^T \sigma_w T_w \quad (8)$$

where the transformation matrix T from the local system of fiber coordinates to the global system of coordinates of the membrane element as explained in [5]. Finally, the stresses in the membrane element are defined as

$$\sigma_x = \frac{\bar{\sigma}_{fx} + \bar{\sigma}_{wx}}{2}, \quad \sigma_y = \frac{\bar{\sigma}_{fy} + \bar{\sigma}_{wy}}{2}, \quad \tau_{xy} = \frac{\bar{\tau}_{fxy} + \bar{\tau}_{wxy}}{2} \quad (9)$$

3. Application

The membrane element has been implemented in the finite element code Javelin [7] as a user element. The implementation has been tested by simulating the behavior of a unit cell of the Kevlar 29 membrane element loaded under a simple tension test, as illustrated in Fig. 2. The element is fixed in the warp direction and stretched in the fill direction. Fig. 2 indicates that the strength of the element is much higher in the fill direction compared with the weft direction.

Fig. 3 shows a computer simulation for a ballistic impact scenario in which a patch of fabric is firmly clamped and impacted by a bullet at given velocity. Velocities tested included 26 m/s, 37 m/s, 46 m/s and 59 m/s. The velocities of 26 and 37 m/s resulted in the bullet rebound, while the 46 and 59 m/s velocities resulted in the fabric being penetrated and significant fabric damage. Fig. 3 shows an example of the Kevlar 29 fabric impacted by a bullet at 46 m/s. Tests and numerical simulations were performed to characterize the ballistic resistance and fracture properties of single layer fabrics at four impacting velocities. Bullet velocities after impact were computed from the finite element simulations,

and it was observed that the Kevlar fabric undergoes a larger amount of damage compared with the Nylon fabric. The ballistic resistance of fabrics is the result of both the fiber strength and fiber density in the fabric.

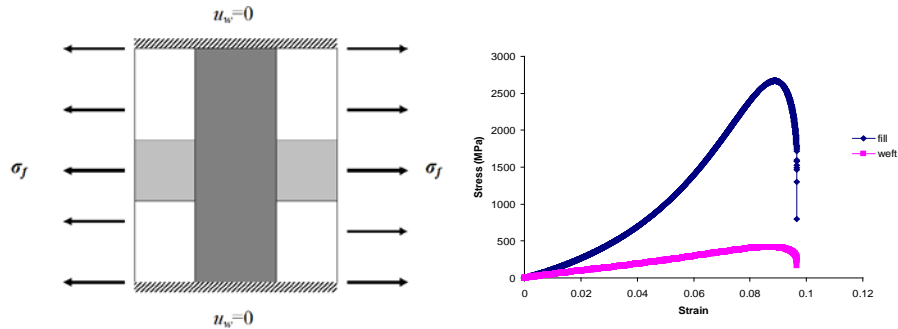


Figure 2. Typical tension test of a membrane element stretched in the fill direction and fixed in the warp direction.

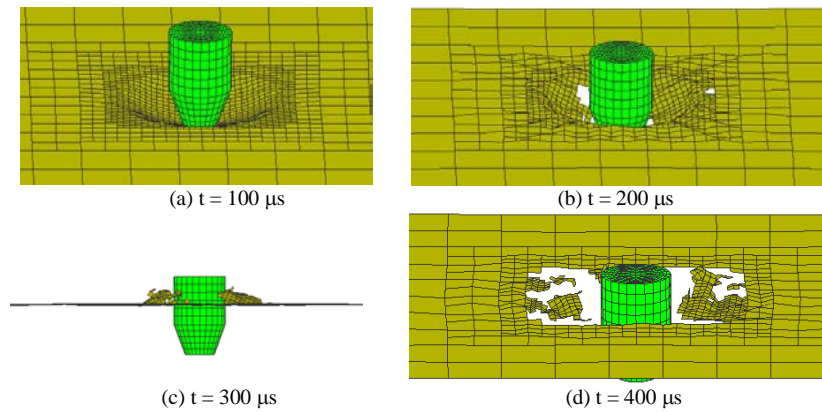


Figure 3. Kevlar fabric impacted at 46 m/s.

Acknowledgement. The support of this work by DoD-SBIR under grant W15QKN-06-C-0184 is gratefully

References

- [1] Shockey, D.A., Erlich, D.C., and Simons, J.W. (2000), Improved barriers to turbine engine fragments, *SRI International*, Menlo Park, California
- [2] Duan, Y., Keefe, M. Bogetti, T.A. and Cheeseman, B.A. (2005), Modeling friction effects on the ballistic impact behavior of a single-ply high strength fabric, *International Journal of Impact Engineering*, **31**, pp. 996-1012.
- [3] Kawabata, S., Niwa, M., and Kawai, H. (1973), The finite-deformation theory of plain-weave fabrics. Part I: The biaxial-deformation theory, *Journal of the textile Institute*, **64**, pp. 21-46
- [4] Shahkarami, A, and Vaziri, R.(2006), An efficient shell element based approach to modeling the impact response of fabrics, *9th International LS-DYNA Users Conference*, pp. 4-1 - 4-11
- [5] Ivanov, I. and Tabiei, A. (2004), Loosely woven fabric model with viscoelastic crimped fibers for ballistic impact simulations, *International Journal for Numerical Methods in Engineering*, **62**, pp.1565-1583
- [6] Potirniche, G.P., Pascu, A., Stillman, D., Lin, T.-L., Wang, P.T. and Horstemeyer, M.F. (2011), A visco-hyperelastic model for the thermo-mechanical behavior of polymer fibers, *International Journal of Damage Mechanics*, **20**, pp. 1002-1020
- [7] Javelin (2008), CAE Corporation.

MODELS & ROBUST ALGORITHMS IN CRASH SIMULATIONS

R. Prohl¹, A. Grillo², G. Wittum³

¹ Steinbeis Center “Simulation in Technology”
Schillerstraße 21, D-75248 Ölbronn, Germany
e-mail: raphael@techsim.org

² DISMA (Dept. of Mathematical Sciences),
Polytechnic of Turin, C.so Duca degli Abruzzi 24, I-10129 Turin, Italy
e-mail: alfio.grillo@polito.it

³ G-CSC,
University of Frankfurt, Kettenhofweg 139, D-60325 Frankfurt, Germany
e-mail: Wittum@gcsc.uni-frankfurt.de

Abstract. We examined the stability of some algorithms taken from the industrial crash simulations, where full-vehicle-models are normally used. We reduced these models in order to investigate their main features and developed a new plasticity algorithm with better mathematical properties. We studied the functionality of the well-established return-mapping-algorithm by performing some numerical tests in our simulation framework UG. In our mathematical models, we considered large elastic and plastic strains as well as both geometric and kinematic nonlinearities.

1. Introduction

The simulations of crash tests are very sensitive numerical procedures, which require very accurate and robust algorithms in order to handle numerical instabilities. In addition to these, also physical instabilities, which may be due, for example, to the bifurcation behavior of the material under asymmetric loading, have to be detected and correctly treated by the numerical procedures in order to obtain reliable results. In this context, our task is to identify and eliminate numerical instabilities and improve the mathematical analysis of the physical ones.

For our purposes, we firstly formulated simplified versions of some full-vehicle-models used by automotive industries. By “simplified versions” we mean that our models are purely mechanical, take into account only a selected number of physical effects and are implemented for relatively simple (unrealistic) geometries. These preliminary steps are necessary for providing computationally cheap benchmark problems to be used for testing numerical codes and improving their functionalities, when needed. With this attitude, we focused on the stability of some algorithms used in crash test simulations. In particular, we closely investigated the return-mapping-algorithm [6]. By reviewing this computational procedure in the context of nonlinear programming (cf. [9]), we developed a new class of solution methods with better mathematical properties.

Our next step is to adopt the methods exposed in [3] in order to include large-deformation contact in our problem. After the stability of our numerical algorithms has been proven, the

goal is to formulate a reliable criterion for identifying physical instabilities within a crash-simulation.

2. Reduced model for finite elasto-plasticity

In our mathematical model of crash tests, we consider large elastic and plastic strains as well as nonlinear material behavior. Initially we concentrate on geometric and kinematic nonlinearities as well as on nonlinear material properties and elasto-plastic material behavior. The theoretical bases of our work were taken from [2][4][6].

2.1. Balance laws

We consider the balance of linear momentum in local, material form:

$$\begin{aligned} -\operatorname{DIV}(FS) &= \rho_0 B & \text{in } \Omega \\ u &= d & \text{on } \Gamma_d \end{aligned} \quad (1)$$

In (1), F denotes the deformation gradient, S is the 2nd Piola-Kirchhoff stress tensor, ρ_0 is the reference density, B is the body force per unit mass, and d represents the prescribed displacement on the Dirichlet boundary of the computational domain. For the first part of our study, inertial terms are not accounted for the force $\rho_0 B$. Apparently, dropping inertial terms in a mathematical model that should be the basis for crash test simulations may sound as a strong contradiction. However, our task here is to analyze and compare algorithms that should be applied in the numerical simulations of crash tests. In this respect, inertial terms are, at this stage, only “temporarily” switched off. This saves computational resources when different algorithms are compared, and allows for focusing on the possible numerical instabilities that, hidden behind a given algorithm, may exist independently on the consideration of inertial terms.

We restrict our investigations to a purely mechanical framework. Consequently, thermal phenomena are excluded from the outset and dissipation is expressed in terms of mechanical quantities only.

2.2. Constitutive equations, associative flow rule and Karush-Kuhn-Tucker conditions

We consider the formulation of the J_2 flow theory at finite strains for hyperelastic-plastic materials [6]. The constitutive equations, the flow rule and the KKT-conditions read:

$$S = 2 \frac{\partial W}{\partial C} \quad (2)$$

$$\frac{\partial \bar{C}_p^{-1}}{\partial t} = -\frac{2}{3} \gamma \operatorname{tr}[b^e] F^{-1} \frac{\operatorname{dev}[\tau]}{\|\operatorname{dev}[\tau]\|} F^{-T} \quad (3)$$

$$\gamma \geq 0, f(\tau) \leq 0, \gamma f(\tau) = 0 \quad (4)$$

In (2)-(4), W is a stored energy-function, C is the Cauchy-Green strain tensor, b^e is the elastic part of the finger tensor, τ is the Kirchhoff stress tensor, f is the von-Mises flow-condition and γ is the (Karush-Kuhn-Tucker) plastic multiplier.

3. Numerical methods

The numerical computations of the quasi-static case are performed by an incremental procedure, which contains a nonlinear sub-problem in every single incremental step.

3.1. Discretization

We obtain the discrete material model by an implicit Euler method in time for the evolution of the internal parameters, e.g. plastic strains or hardening variables. Inserting this update in the constitutive equation (2), we get a nonlinear incremental stress response, which has to satisfy the balance of momentum (1). Thus, we have to solve a nonlinear variational problem for the displacements. In order to discretize our equations in space we use a standard finite-element-method with tri-linear hexahedron elements for the displacements.

3.2. Plasticity algorithm

To start with the treatment of the governing equations of plasticity, we adopt the return-mapping-algorithm (RMA) [6]. As remarked in [9], this well-established procedure, which requires low computational effort, may be turn instable because it computes stresses that do not necessarily satisfy the global equilibrium equations. This drawback can be improved by having recourse to an algorithm based on the linearization of (2)-(4). In [9], it is shown that such a criterion leads to a computational method with higher robustness in the case of small strains. The additional iteration, introduced due to the linearization of (2)-(4), defines an algorithm, which now iterates along stresses satisfying equilibrium, until (2)-(4) are “sufficiently” fulfilled. We extended this method to the case of finite deformations.

3.3. Solution methods

In our code the nonlinear variational problem is solved by a Newton method. The consistent tangent operator [7] provides the basis for the linearization therein. We use a parallel multigrid solver for solving the linear sub-problems featuring in the Newton scheme [10].

4. Numerical tests

The implementation of the RMA in our software framework *UG* (“Unstructured Grids” [1][8]) has been tested by some benchmark problems.

4.1. Benchmark problems

As a reference for our numerical tests, we used a shear/compression-test of the unit-cube with perfect plastic behavior [5]. Additionally, we simulated the well-documented necking of a circular bar as an example for exponential hardening behavior [6].

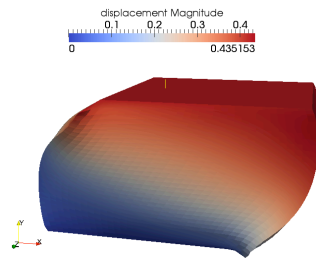


Figure 1. Unit cube in a shear/compression test.

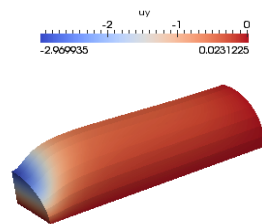


Figure 3. 1/8th of a circular bar in a tensile test

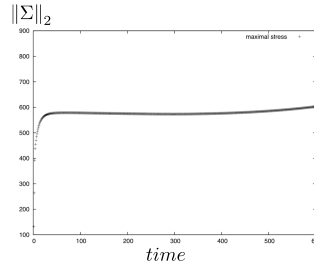


Figure 2. Max. Stress at the midpoint of the cube.

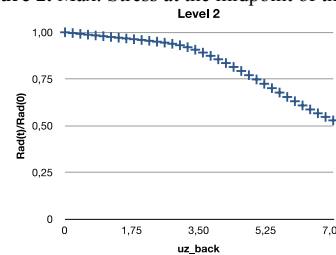


Figure 4. Change of necking area in time

4.2. Software framework UG

UG ([1][8]) is a general-purpose library for the solution of partial differential equations, which supports parallel adaptive multigrid-methods on high-performance computers. A novel implementation ensures the complete independence of grid and algebra. Cache aware storage for algebra structures and a parallel communication layer make UG4 well suited for current and next hardware-architectures.

Acknowledgements. This work is supported by the *Baden-Württemberg Stiftung* in the project “Reduction of Numerical Sensitivities in Crash-Simulations on HPC-Computers”

References

- [1] Bastian, P., Birken, K., Johannsen, K., Lang, S., Neuss, N., Rentz, H. and Wieners, C. (1997), UG – a flexible software toolbox for solving partial differential equations, *Computing and Visualization in Science*, **1**, pp. 27-40.
- [2] Cleja-Tigoiu, S. and Maugin, G.A. (2000), Eshelby’s stress tensors in finite elastoplasticity, *Acta Mechanica*, **139**, pp. 231-249.
- [3] Krause, R. (2009), A Non-Smooth Multiscale Method for Solving Frictional Two-Body Contact Problems in 2D and 3D with Multigrid Efficiency, *SIAM Journal on Scientific Computing*, **31**, no. 2, pp. 1399-1423.
- [4] Micunovic, M.V. (2009), *Thermomechanics of viscoplasticity*, Fundamentals and Applications, Springer.
- [5] Neff, P. and Wieners, C. (2003), Comparison of models for finite plasticity: A numerical study, *Computing and Visualization in Science*, **6**, pp. 23-35.
- [6] Simo, J.C. and Hughes, T.J.R. (1998), *Computational Inelasticity*, Springer.
- [7] Simo, J.C. and Taylor, R.L. (1985), Consistent Tangent Operators for Rate Independent Elasto-Plasticity, *Computer Methods in Applied Mechanics and Engineering*, **48**, pp. 101-118.
- [8] UG: <http://atlas.gesc.uni-frankfurt.de/~ug/>
- [9] Wieners, C. (2007), Nonlinear solution methods for infinitesimal perfect plasticity, *Journal of Applied Mathematics and Mechanics*, **87**, no. 8-9, pp. 643-660.
- [10] Wieners, C., Lang, S. and Wittum, G. (2002), *The application of adaptive parallel multigrid methods to problems in nonlinear solid mechanics*, Adaptive Methods in Solid Mechanics, J. Wiley.

MODELLING OF OVERALL MATERIAL PROPERTIES AND CRACK REINFORCEMENT BY BRIDGING FIBRES IN METAL-CERAMIC COMPOSITES WITH INTERPENETRATING PHASE MICROSTRUCTURE

Z. Poniznik¹, M. Basista²

^{1,2}Institute of Fundamental Technological Research
Polish Academy of Sciences, Pawińskiego 5b, 02-106 Warsaw, Poland

¹e-mail: zponizni@ippt.gov.pl

²e-mail: mbasista@ippt.gov.pl

Abstract. The objective of this paper is the analytical and numerical modelling of the overall elastic properties and the crack bridging toughening mechanism in metal-ceramic composites with interpenetrating phase microstructure (IPC). The specific microstructure of the IPC makes the effective media/field models based on Eshelby's solution inapplicable to the estimation of the effective elastic properties of the IPC. The effective material constants were calculated analytically extending the Tuchinskii-Feng models devised for the IPC microstructure. Numerical FEM models were developed for two types of IPC microstructure: simplified 3-D cross structure and real microstructure obtained with computer micro-tomography scans. The micro-CT scans were transformed into FEM meshes using the Simpleware ScanIP/FE commercial software. The crack bridging mechanism was investigated assuming the metal ligament undergoing large plastic deformations (necking) and delamination from the surrounding elastic material (ceramic matrix). As a first step towards the numerical determination of J integral from the simulation of the CT (compact tension) test, the σ - u relationship in the metal fiber was determined numerically and applied to compute the stress and displacement fields in the CT specimen. The numerical solution agrees well with the analytical one obtained by Mataga et al. [4].

1. Introduction

The metal-ceramic interpenetrating phase composites (IPC) are usually processed by pressure assisted or pressureless infiltration of molten metals into porous ceramic performs. They have characteristic microstructure different from typical MMC's or CMC's with particulate or fiber reinforcement. The main difference is that both metal and ceramic phases are spatially continuous forming complementary 3D skeletons of non-zero stiffness. The uniform microstructure and the enhanced mechanical and thermal properties are the main advantages of IPC. A state-of-the art in fracture and damage modelling of IPC can be found in [1], while models of effective properties of the IPC in [2] and [3]. The objective of this paper is twofold: (i) to model the effective elastic properties of IPC, and (ii) to model the fracture in IPC with the crack bridging being the major toughening mechanism. The developed models are verified on the example of Al_2O_3 -Cu infiltrated composites.

2. Modelling of overall elastic properties

The effective elastic constants of IPC can be determined using a number of different methods. Firstly, simple estimates of Voigt, Reuss and Hashin-Shtrikman were computed. Secondly, analytical models of Tuchinskii and Feng [2] based on the cross unit cell (Fig. 1) were implemented since the models based on the Eshelby solution are inapplicable for IPC. Here the generic Tuchinskii's model was corrected and extended (cf. curves denoted as "extended bounds" and "extended model" in Fig. 3). Thirdly, numerical methods accounting for a real composite microstructure were developed and used for Al_2O_3 -Cu microstructure acquired from the computer micro-tomography (micro-CT) images (Fig. 2a). The following numerical approaches were compared: the 3D cross microstructure model (Fig. 1), and two models based on the real microstructure obtained from the micro-CT scans: a voxel model, and a model with smoothed interfaces obtained with Simpleware ScanIP/FE software. With the +ScanFE software a FEM mesh was created and a smoothing of the material interfaces and optimization of the size of the elements was done (Fig. 2b). Three effective elastic constants were modelled: Young's modulus (Fig. 3), Poisson's ratio and the shear modulus (here only E modulus is shown for brevity).

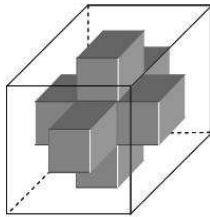


Figure 1. Cross model of interpenetrating microstructure of an IPC.

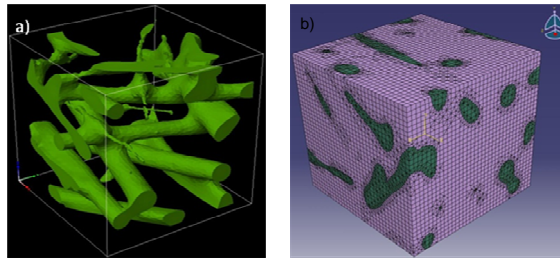


Figure 2. Real microstructure of Al_2O_3 -Cu IPC from micro-CT images (metal phase) (a). FE representation in ABAQUS via Simpleware ScanIP/ScanFE (b).

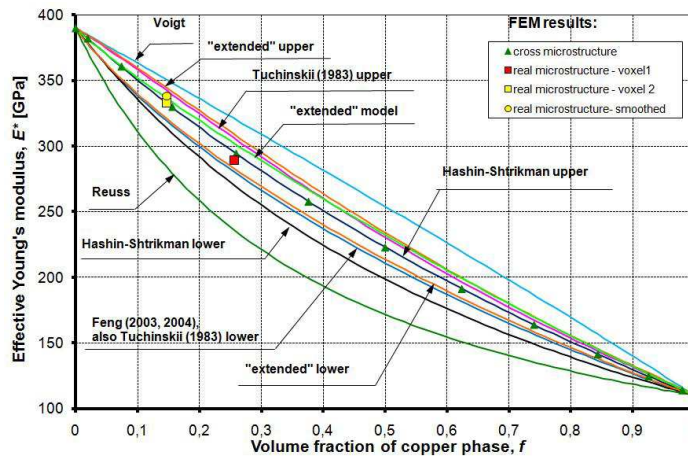


Figure 3. Effective Young's modulus of Al_2O_3 -Cu IPC: analytical and numerical models and micro-CT measurements results.

3. Modelling of crack reinforcement by bridging fibres

One of the main toughening effects occurring in metal-ceramic IPC during fracture is the crack bridging by metal ligaments, [4]. These ligaments deform plastically contributing to the composite's fracture toughness. The J -integral, or energy release rate G in this case, can be expressed as

$$J = G = \int_0^{u^*} \sigma(u) du \quad (1)$$

where σ is the nominal stress in the bridging ligament at stretch u ($\sigma \rightarrow 0$ at $u=u^*$, with u^* being the crack opening displacement COD at rupture). A non-trivial problem is to determine the physical relation $\sigma(u)$. This problem was solved numerically in this paper using the model of an elasto-plastic cylindrical ligament in an elastic matrix undergoing delamination from the surrounding material and large strains due to necking. Fig. 4 shows an exemplary FEM solution of axial stress distribution in the ligament for a chosen value of delamination parameter ψ . The obtained $\sigma(u)$ relationships in function of the delamination parameter ψ are presented in Fig. 5 together with the corresponding analytical solutions of Mataga [4] based on purely geometrical considerations.

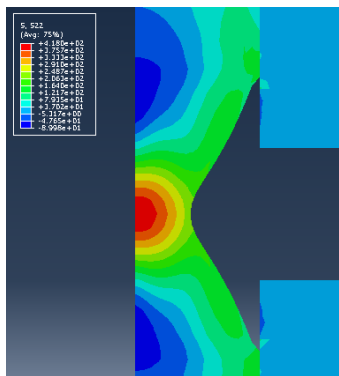


Figure 4. Axial stress distribution in the metal ligament at large plastic deformation and delamination from the matrix; numerical solution by ABAQUS.

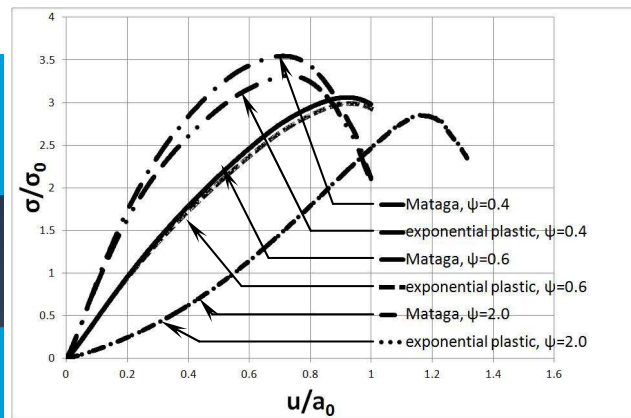


Figure 5. Normalized (σ - u) relationships in metal ligament derived numerically by FEM for three delamination parameters ψ ; σ and σ_0 denote the nominal and the yield stress of the ligament material (Cu); a_0 is the ligament's initial radius. Relevant analytical solutions by Mataga [4] are also shown for comparison.

Having determined the stress-displacement relationship in the bridging fibre, it was possible to apply it as a material model for the fibre in the numerical simulation of the Compact-Tension test. The truss element was introduced similarly as in Emmel [5] to model the bridging of the crack faces. The matrix material of the composite was Al_2O_3 ceramics and the ductile fiber was that of copper. The plastic behaviour of the fibre was modelled using the input data furnished by the constitutive relation $\sigma(u)$ (Fig. 5) which were then used in the UMAT procedure in ABAQUS. The truss element T2D2 was chosen for the fibre. The FEM mesh with boundary conditions and force loading is presented in Fig. 6.

An illustrative example of the computed stress field in the CT specimen with a single metal ligament bridging the crack faces is shown in Fig. 7.

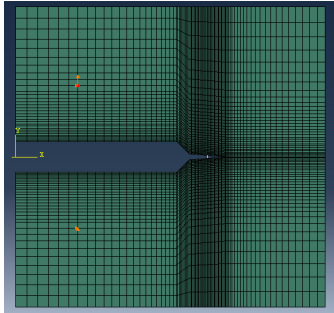


Figure 6. The FEM mesh of a CT specimen with the metal ligament modelled as truss element connecting the crack faces.

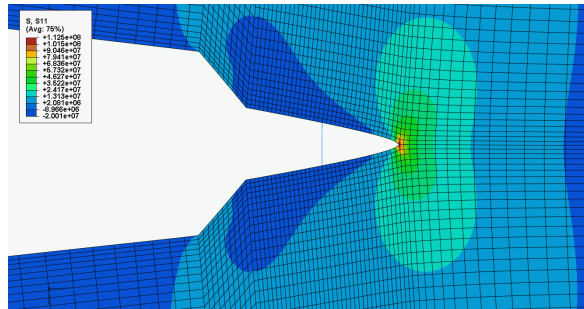


Figure 7. Vertical stress distribution (numerical solution by ABAQUS)

4. Conclusions

A set of analytical estimates and numerical models have been employed to determine the effective elastic constants of the interpenetrating phase composites. The micro-CT images have been incorporated in the developed FEM models leading to the most realistic estimates of elastic constants. A problem of crack bridging with ligament undergoing delamination and necking has been modelled by FEM for an idealized ligament geometry. The resulting σ - u relationship for the crack bridging fibre was used in the FEM model of the Compact-Tension test. The obtained numerical results enable calculation of the J integral which is now in progress.

Acknowledgement. The present research was supported in part by the EU FP7 project “Micro and Nanocrystalline Functionally Graded Materials for Transport Applications” (MATRANS) under Grant Agreement no. 228869 with the European Commission.

5. References

- [1] Basista M. and Węglewski W. (2006), Modelling of damage and fracture in ceramic-matrix composites – an overview, *Journal of Theoretical and Applied Mechanics*, **44**, pp. 455-484.
- [2] Feng X., Tian Z., Liu Y. and Yu S. (2004), Effective elastic and plastic properties of interpenetrating multiphase composites, *Applied Composite Materials*, **11**, pp. 33-55.
- [3] Poniżnik Z., Salit V., Basista M. and Gross D. (2008), Effective elastic properties of interpenetrating phase composites, *Computational Materials Science*, **44**, pp. 813-20.
- [4] Mataga P. A. (1989), Deformation of crack-bridging ductile reinforcements in toughened brittle materials, *Acta Metallica*, **37**, pp. 3349–3359.
- [5] Emmel Th. (1995), *Untersuchung des Bruchverhaltens von Metall – Keramik Verbundwerkstoffen*, Diplomarbeit, Technische Hochschule Darmstadt.

MULTISCALE MODELING OF COLLECTIVE BEHAVIOR OF CARBON NANOTUBES

H. Radhakrishnan, S.Dj. Mesarovic¹, A. Qiu and D.F. Bahr

School of Mechanical and Materials Engineering
Washington State University, PO Box 642920, Pullman, WA, 99164-2920, USA.

¹Email: mesarovic@mme.wsu.edu

Abstract. To analyze the collective behavior of a large number of carbon nanotubes (CNTs) we consider two computational models, covering two different length and time scales. To model a large number of interacting CNTs in a turf, we represent the segments of CNTs forming the turf, as elastica finite elements. During compression, the predominant deformation of CNTs is due to bending and buckling. The van der Waals forces of interaction between adjacent tubes are modeled as distributed loads. An explicit time integration technique is used to integrate the equations of motion. The resulting computational model is robust and is capable of modeling the collective behavior of CNTs. The generation of the computational model of a turf is accomplished by means of the restricted random walk and subsequent relaxation. The continuum model is a nonlinear viscoelastic model. We show that it is capable of representing different experimental conditions.

1. Introduction

The properties of individual carbon nanotubes (CNTs) have been studied extensively, and are now well understood. The collective behavior of CNTs arranged in complex structures, *turfs* (Figure 1) is of interest in practical applications, such as nanoscale sensors and thermal switches. Their microstructure is the result of the growth process from the substrate [1], during which an interplay of elastic bending energy and adhesive energy produces a local energy minimum in the configurational space [2].

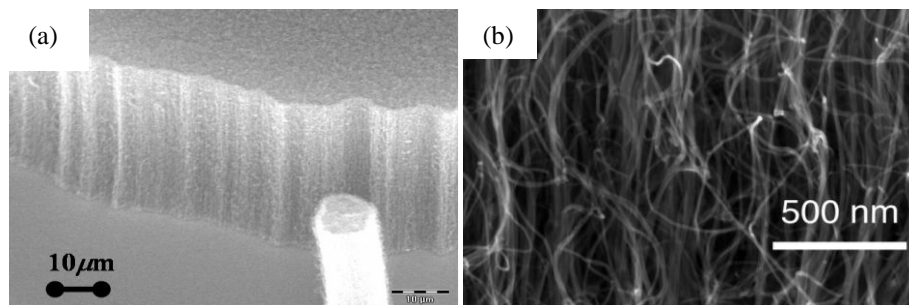


Figure 1. SEM images of the carbon nanotube turf: (a) corner view, (b) detail.

Given the growth method, the following question arises: Is the CNT turf a *material*, describable by a standard mathematical apparatus of continuum mechanics with effective properties, or – is it a *structure*, in which case a continuum model is not relevant?

Moreover, the uniform compression experiments reveal a curious type of nonlocal behavior – collective reorientation and buckling of a layer [3, 4]. The curious aspect of this behavior is that the nonlocality occurs under uniform loading, but not under non-uniform loading such as nanoindentation [1, 5]. We have shown [6] that the turf is indeed a material, with negligible variation in local mechanical properties. Our uniform compression experiments [3] indicate that collective reorientation and buckling of the boundary layer is the result of intrinsic length scale, associated with CNT wavelengths.

In the present communication, we first address the nonlocal reorientation and buckling using the discrete model based on elastica elements, then formulate a local continuum model to simulate the behavior under localized loading.

2. Discrete model

The segments of each CNT are modeled as elastica elements [7]. Their extensional and bending stiffness are calculated from atomistic model. The extensional stiffness is very high compared to the bending stiffness, so inextensional constraint was imposed by means of Lagrange multipliers. The van der Waals interactions between the segments are modeled as distributed forces using the Lennard-Jones potential. The algorithm for interaction detection was developed. The preliminary results are shown in Figure 2.

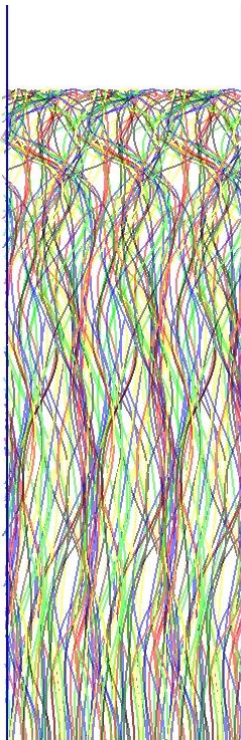


Figure 2. Uniform compression of a turf by 10%. The initial configuration was created by means of a constrained random walk algorithm, and subsequent relaxation, taking into account van der Waals interactions. Such initial configuration is characterized by the average curvature, number of contacts per unit length and density. Periodic boundary conditions are imposed on the sides. The turf is then gradually compressed vertically. Formation of buckled layer on top preceded by collective reorientation of bowed segments is observed. A study of dependence of buckle wavelength on the parameters of initial configuration is underway.

3. Continuum model

The continuum model CNT turfs is the isotropic compressible elastomeric hyperfoam [8] with a Kelvin-Voigt relaxation component. The time dependent relaxation seen in the nanoindentation experiments is due to thermal sliding of contacts between the tubes. To obtain an economical 2D problem, we approximate the Berkovich three-sided pyramid with the equivalent conus. The adhesive contact between the tip and the turf (arising from van der Waals interactions) is modeled with the Lennard-Jones contact law. The details of numerical procedure are given in [9]. We consider two different nanoindentation setups: (a) load-controlled experiment (Hysitron triboscope) with a blunt (spherical), and, (b) depth-controlled experiment (Hysitron triboindenter) with a sharp tip.

The fit between computational and experimental results in Figure 3a is satisfactory. The differences between the experiments and the model can be attributed to the equivalent cone approximation of the Berkovich indenter. The results shown in Figure 4a also indicate a satisfactory fit. A notable exception is the sharp change in the slope during computational unloading (point c^1 in Figure 4a), which is the result of our neglecting the time-dependence of adhesion at the contact between the turf and indenter, resulting in delayed onset of peel-off (Figure 4b).

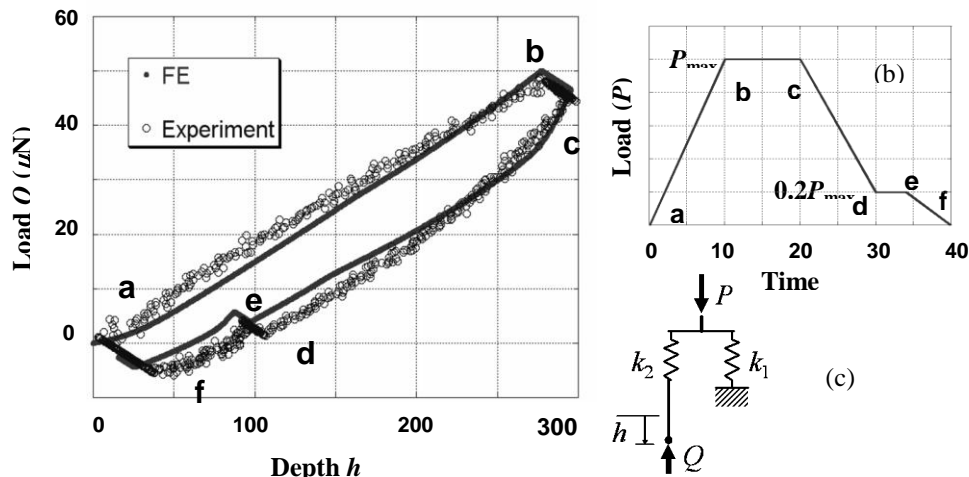


Figure 3. (a) Comparison between FE results and controlled load nanoindentation experiments. (b) Loading history. (c) The loading mechanism of the Hysitron Triboscope. Note that the force P is controlled, not the contact force Q .

3. Discussion

In contrast to nanoindentation results, CNT turfs under uniform loading exhibit irreversible reorientation of CNTs and collective buckling of a layer. The question of why such collective buckling does not occur under localized load can perhaps be answered at this time. Buckling of nanotubes will be irreversible only if it involves collective rearrangements of large number of segments, i.e., large volume. In contrast,

buckling of a single segment with fixed ends (contacts) is expected to be fully reversible. Even if the ends (contacts) slide, they can slide back under reversed loading if the topology of the segments is not changed. Only the changes in topology (connectivity) are expected to yield mechanically irreversible behavior. Under localized loading, the segments in a small affected volume buckle, but the changes in topology are minimal or nonexistent, hence the mechanical reversibility.

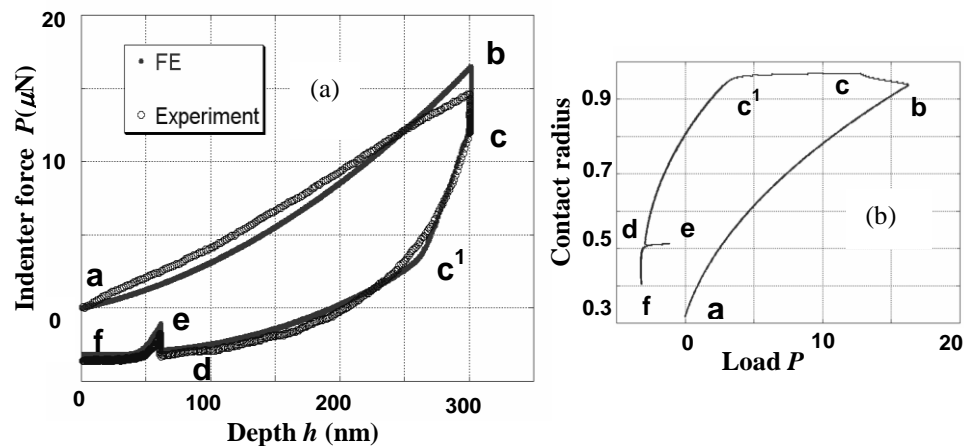


Figure 4. (a) Comparison between FE results and controlled-depth nanoindentation experiments. (b) Contact radius as a function of indentation depth.

Acknowledgements. This work has been supported by the US National Science Foundation, grant # CTS-0856436. The authors are grateful to J. Jiao and D. McClain, Portland State University, for providing the initial turf samples.

References

1. McCarter CM, Richards RF, Mesarovic SDj, Richards CD, Bahr DF., McClain D, Jiao J 2006 Mechanical compliance of photolithographically defined vertically aligned carbon nanotube turf. *J Mater Sci* **41**(23), 7872-7878.
2. Mesarovic SDj, McCarter,CM, Bahr DF, Radhakrishnan H, Richards RF, Richards CD, McClain D, Jiao J 2007 Mechanical behavior of a carbon nanotube turf. *Scripta Mat.* **56**, 157-160.
3. Zbib AA., Mesarovic SDj, Lilleodden E, McClain D, Jiao J, Bahr D 2008 Coordinated buckling of carbon nanotube turf under uniform compression. *Nanotechnology* **19**(17), 1757-1763.
4. Cao, A., Dickrell, P.L., Sawyer, W.G., Gahasemi-Nejhad, M.N. & Ajayan, P.M. 2005 Super-compressible foamlike carbon nanotube films. *Science* **310**(5752), 1307-1310.
5. Qiu A, Bahr DF, Zbib AA.,Bellou A., Mesarovic SDj, McClain D, Hudson W, Jiao J, Kiener D, Cordill MJ 2010 Local and nonlocal behavior of CNT turfs and coordinated buckling of turf layers. *Carbon* **49**(4), 1430-1438.
6. Qiu A, Fowler SP, Jiao J, Kiener D, Bahr DF 2011 Time-dependent contact behavior between diamond and a CNT turf. *Nanotechnology* **22**(29), 2957-2963.
7. Nordgren RP 1974 On Computation of the Motion of Elastic Rods. *J Appl Mechanics*, **41**, 777-780.
8. Storakers B 1986 On material representation and constitutive branching in finite compressible elasticity. *J. Mech. Phys. Solids* **34**(2), 125-145.
9. Radhakrishnan H, Mesarovic SDj 2009 Adhesive contact of elastic spheres revisited: numerical models and scaling. *Proc. R. Soc. Lond A.* **465**, 2231-2249.

DAMAGE AND FAILURE ASSESSMENT OF PIPES WITH LOCAL THIN AREAS

M. Rakin^{1,*}, B. Medjo¹, M. Arsić², Ž. Šarkoćević³, V. Grabulov², A. Sedmak⁴

¹ Faculty of Technology and Metallurgy,
University of Belgrade, Karnegijeva 4, 11120 Belgrade
* e-mail: marko@tmf.bg.ac.rs

² Institute for Testing of Materials (IMS),
Bulevar vojvode Mišića 43, 11000 Belgrade

³ High Technical School of Professional Studies,
Nušićeva 6, 38227 Zvečan

⁴ Faculty of Mechanical Engineering,
University of Belgrade, Kraljice Marije 16, 11120 Belgrade

Abstract. The subject of this study is application of local approach to ductile fracture in order to estimate the integrity of pipes with local thin areas (e.g. corrosion defects). Majority of the procedures for determining the load carrying capacity of such structures are based on limit loads, i.e., plastic collapse criteria. However, they can also fail by ductile fracture mechanism, which is modelled in this work using the complete Gurson model - CGM. This model is applied to predict the damage development in the pipes with simulated corrosion defects (machined notches with different sizes). The failure criterion is considered fulfilled when damage parameter reaches its critical value in the bottom of a notch. Bearing in mind that one of the main problems in application of local approach to fracture is the mesh sensitivity, a study has been conducted to determine the dependence of maximum pressure on the size and formulation of the finite elements in the defect area.

1. Introduction

Many procedures for estimation of remaining strength of the pipes with corroded (local thin) areas have been developed in the last decades, including solutions from ASME B31G code, Det Norske Veritas procedure, SINTAP/FITNET procedure and several groups of authors dealing with this topic [1-7]. In this work, a local criterion for determining the maximum pressure in damaged pipe for drilling rigs is discussed. A capped pipe segment, with corrosion defects simulated by machined notches, was subjected to hydrostatic pressure to determine the spreading of plasticity in damaged areas. Local approach to fracture is applied to assess the failure criterion for the pipe, and results are compared with existing solutions from the literature and a finite element stress-based criterion.

2. Experimental

API J55 steel is used for fabricating the examined seam casing pipe; yield strength 380 MPa, tensile strength 562 Mpa (more data about the material is given in [8]). Having in

mind that damage is modelled in this work using a micromechanical model, quantitative microstructural analysis was performed to obtain the microstructural parameters (Table 1).

Table 1. Microstructural parameters of the examined material.

Material	f [%]	λ [μm]
API J55 steel	2.7648	69.39

Pressure test is conducted on a segment of the pipe capped at both ends, with nominal diameter $\phi 139.7$ mm and wall thickness 6.98 mm. Corrosion defects were simulated by machining circular notches at the outer surface of the pipe. Different levels of material degradation (local thin areas) were represented by varying the notch depth: 75%, 50% and 25%. During the increase of pressure, the strains were measured inside each notch.

3. Numerical analysis

Numerical analysis of the behaviour of the pipe under internal pressure is conducted using the finite element (FE) software package Abaqus [9]. FE meshes consist of 20-node reduced integration elements, Figure 1; defect length is varied in order to check its influence on the load carrying capacity. Due to the symmetry, one quarter of the pipe is modelled, with appropriate symmetry boundary conditions defined at the model boundaries. Loading is defined by prescribing the pressure at the inner surface and axial loading at one side of the FE model for simulating the effect of the dished end.

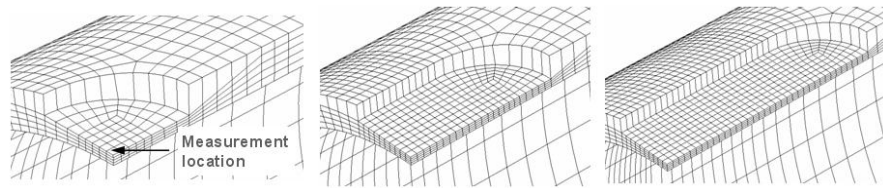


Figure 1. Finite element meshes.

4. Micromechanical modelling

A significant accumulation of stress and plastic strain emerges in the bottom of a defect, which leads to development of ductile damage in this area. The complete Gurson model – CGM [10] (with porosity as damage parameter) is used for damage quantification in this work. In the initial stage of ductile fracture of steel, the voids nucleate mostly around non-metallic inclusions. Hence the initial porosity f_0 is here assumed to be equal to the volume fraction of non-metallic inclusions f_v , Table 1. CGM is applied through Abaqus UMAT subroutine created by Zhang, based on [10]. The value of f is monitored in the element nearest to the middle of the defect. When it reaches the critical value f_c , the pipe failure is predicted and the corresponding maximum pressure is determined.

In the literature [11 - 13], local approach to fracture has been previously used for analysis of load carrying capacity of pipes with crack-like flaws. The present work aims at extending this approach to pipes containing blunt surface defects, like those caused by local corrosion. Local approach to fracture was previously applied for similar purpose in [14],

but the procedure included so-called uncoupled modelling - calculating the damage parameter during post-processing procedure, without its influence on the yield criterion.

5. Failure criteria comparison

In addition to the micromechanical criterion, several solutions from literature are applied in this paper for calculating the maximum pressure of the analysed pipe: ASME B31G code [1], modified ASME B31G [2] and the solution of Choi et al. [5] (in the remainder of the paper - Choi's solution/equation). All the expressions give the limit pressure dependence on defect depth and length, geometry of the pipe and material properties.

The dependence of the maximum pressure in a damaged pipeline on the defect length is shown in Figure 2 for damage levels 75% and 50%; the results were obtained using the three mentioned expressions, the FE stress-based solution and the CGM solution. FE stress-based failure criterion is considered to be fulfilled when the von Mises stress value reaches the reference stress throughout the entire ligament, *i.e.*, it is also a plastic collapse criterion, like the expressions mentioned in the previous paragraph. The reference stress was chosen as 85 % of the ultimate tensile strength, as a moderately conservative solution [15].

Local approach (CGM) can predict the trend of decrease in maximum pressure with increase of defect length and depth. Having in mind that it is strain-based and that it includes damage development in the material, it is physically suitable for the materials often used for pipe manufacturing. Namely, such materials exhibit ductile behaviour in the working conditions (except for those operating at low temperatures) and their failure is usually accompanied with plastic deformations.

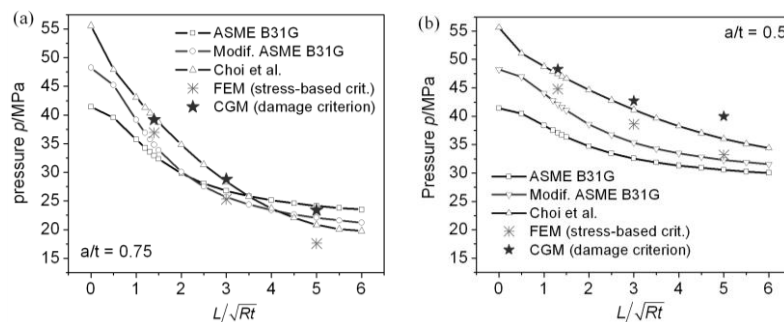


Figure 2. Maximum pressure for defects with depth 75% (a) and 50% (b) of the pipe wall thickness - dependence on defect length.

Bearing in mind that the prediction of the initiation of ductile fracture using the local approach to fracture typically exhibits mesh dependency, the calculations were performed with several mesh refinements. The results did not vary significantly [16], which can be attributed to the fact that crack initiation is assessed in this work as a failure criterion, and the stress concentration on the analysed geometries was not pronounced.

6. Conclusions

Ductile fracture initiation can be used as the failure criterion for examined damaged pipes, especially bearing in mind the exploitation conditions and materials used for their manufacturing. Micromechanical modelling, unlike most solutions for integrity assessment of corroded pipes, includes analysis of damage initiation which must occur before total failure. This approach can be used for determining the fracture initiation moment in structures without a pre-crack, which cannot be achieved by application of fracture mechanics criteria. It is found that influence of the FE mesh on the applied failure criterion is negligible, which can be attributed to a lack of significant stress concentration.

Acknowledgement. The authors acknowledge the support from the Serbian Ministry of Science under the projects ON 174004 and TR 35002. The authors would also like to thank Z.L. Zhang for the CGM user subroutine and I. Cvijović-Alagić for help in microstructural analysis.

References

- [1] American Society of Mechanical Engineers (1991) *ASME B31G: Manual for Determining the Remaining Strength of Corroded Pipelines*, New York.
- [2] Kiefner J, Vieth P (1989) *A modified Criterion for Evaluating the Strength of Corroded Pipe - Final Report on Project PR 3-805 to the Pipeline Supervisory Committee of the American Gas Association*, Ohio: Battelle.
- [3] Det Norske Veritas (2004) *DNV RP-F101: Corroded Pipelines - Recommended Practice*, Hovik.
- [4] FITNET: European Fitness-for-Service Network, <http://www.eurofitnet.org>
- [5] Choi J B, Goo B K, Kim J C, Kim Y J, Kim W S (2003) Development of Limit Load Solutions for Corroded Gas Pipelines, *International Journal of Pressure Vessels and Piping*, **80**, pp. 121-128.
- [6] Adib-Ramezani H, Jeong J, Pluvinage G (2006) Structural Integrity Evaluation of X52 Gas Pipes Subjected to External Corrosion Defects Using the SINTAP Procedure, *International Journal of Pressure Vessels and Piping*, **83**, pp. 420-432.
- [7] Chiodo M, Ruggieri C (2009) Failure Assessments of Corroded Pipelines with Axial Defects Using Stress-Based Criteria: Numerical Studies and Verification Analyses, *International Journal of Pressure Vessels and Piping*, **86**, pp 164-176.
- [8] Šarkočević Ž, Arsić M, Medjo B, Kozak D, Rakin M, Burzić Z, Sedmak A (2009) Damage Level Estimate of API J55 Steel for Welded Seam Casing Pipes, *Strojarstvo: Journal for Theory and Application of Mechanical Engineering*, **51**, pp. 303-311.
- [9] Abaqus FEM software package, www.simulia.com
- [10] Zhang Z L, Thaulow C, Odegard J (2000) A Complete Gurson Model Approach for Ductile Fracture, *Engineering Fracture Mechanics*, **67**, pp. 155-168.
- [11] Bezensek B, Miyazaki K (2009) Alignment Criteria for Through-Wall Flaws in Plates and Pipes, *Proceedings of the 2009 ASME Pressure Vessels and Piping Division Conference*, Prague, published on CD.
- [12] Dotta F, Ruggieri C (2004) Structural Integrity Assessments of High Pressure Pipelines with Axial Flaws Using a Micromechanics Model, *International Journal of Pressure Vessels and Piping*, **81**, pp. 761-770.
- [13] Saxena S, Ramakrishnan N, Chouhan J S (2010) Establishing Methodology to Predict Fracture Behaviour of Piping Components by Numerically Predicting Specimen Fracture Data Using Tensile Specimen Test, *Engineering Fracture Mechanics*, **77**, pp. 1058-1072.
- [14] Oh C K, Kim Y J, Baek J H, Kim Y P, Kim W S (2007) A Phenomenological Model of Ductile Fracture for API X65 Steel, *International Journal of Pressure Vessels and Piping*, **84**, pp. 512-525.
- [15] Arsić M, Rakin M, Šarkočević Ž, Medjo B, Burzić Z, Sedmak A (2011) Remaining Strength of Damaged API J55 Steel Casing Pipes, *submitted to International Journal of Pressure Vessels and Piping*
- [16] Medjo B, Rakin M, Arsić M, Šarkočević Ž, Zrilić M, Putić S (2012) Determination of the Load Carrying Capacity of Damaged Pipes using Local Approach to Fracture, *Materials Transactions*, **53**, pp. 185-190

USE OF GLOBAL MINIMUM OPTIMIZATION IN IDENTIFYING DAMAGE MICROMECHANICAL MODEL PARAMETERS WITH A DAMAGE DEACTIVATION PHENOMENON

D. RAZAFINDRAMARY^{a,b} and A. ABDUL-LATIF^{a,b}

^a Université Paris 8

^b Laboratoire d'Ingénierie des Systèmes Mécaniques et des Matériaux (LISMMA),

Supméca, 3, rue Fernand Hainaut - 93407 St Ouen Cedex – France

e-mail: donneraza@iu2t.univ-paris8.fr

e-mail: aabdul@iu2t.univ-paris8.fr

Abstract. Motivated by a low-cyclic fatigue micromechanical model proposed recently [1], a study is performed emphasizing the concept of damage induced anisotropy. The numerical solution of these nonlinear constitutive relations represents an important topic since it needs relatively important computational time. For such a model coupled with damage having a high nonlinearity, the identification of model parameters represents always an important issue. Therefore, a combination of the genetic algorithm with pattern search is proposed. A comparative study is conducted under complex cyclic loadings showing the ability of such approach in identifying model parameters.

1. Introduction

Despite the existence of increasingly powerful computers, the progress in the constitutive relations development is necessary and can be performed via computational optimization process. Several types of constitutive relations like micromechanical models are formulated for describing several complex physical phenomena. Under cyclic loadings, a strong non-linearity response makes their resolution very expensive in computing times as well as in memory capacity. From the numerical simulation viewpoint, it has been recently reported [2] that the algorithm of Burlisch–Stöer gives the best compromise between the computational time and its precision compared to other very well-known algorithms tested with a micromechanical model [1].

In this work, our focus goes towards the identification of the model parameters particularly these related to damage evolution. The used applications deal with cyclic plasticity behavior with damage induced anisotropy behavior of polycrystals and its related phenomena under complex history of external paths. To conduct the identification process, a combination of genetic algorithm (GA) with pattern search (PS) is developed. The two methods are complementary and have different applications. The GA optimizes globally the model parameters leaving the field open for the local method (here, the pattern search algorithm) to determine the final values of these parameters. Then, in order to evaluate the performances of the proposed method, a comparative study is conducted showing the ability of such approach to identify the model parameters.

2. Employed Micromechanical Model

The used micromechanical model utilizes three operating levels which are: microscale (slip system), mesoscale (granular) and macroscale (overall). The theoretical formulation of the developed model is presented in detail in [1]. However, a short description of the main features of the mesoscale model equations is illustrated in Table 1.

Table 1 macroscopic model equations coupled with damage

At the macroscopic level	
$\underline{\underline{\Sigma}} = \sum_{i=1}^3 \Sigma_i^* p_i \otimes p_i \quad (1)$	$\underline{\underline{Q}} = \sum_{i=1}^3 p_i \otimes p_i \quad (2);$
$\underline{\underline{Q}}^+ = \sum_{i=1}^3 H(\Sigma_i^*) p_i \otimes p_i \quad (3);$	$P_{ijkl}^+ = Q_{ia}^+ Q_{jb}^+ Q_{ka} Q_{lb} \quad (4)$
$\underline{\underline{D}} = D^T \underline{\underline{P}}^+ \quad (5);$	$\underline{\underline{R}}^d = (\underline{\underline{I}} - \underline{\underline{D}}^T) : \underline{\underline{R}}^o \quad (6)$
$\underline{\underline{R}}^d = \left(\dot{D}^T \underline{\underline{P}}^+ + D^T \dot{\underline{\underline{P}}}^+ \right) : \underline{\underline{R}}^o \quad (7);$	$\dot{\underline{\underline{\Sigma}}} = \underline{\underline{R}}^d : \underline{\underline{E}}_e + \underline{\underline{R}}^d : \dot{\underline{\underline{E}}}_e + \dot{\underline{\underline{M}}} \quad (8)$
$\dot{\underline{\underline{M}}} = -\frac{1}{2} \dot{D}^T \frac{\partial \underline{\underline{P}}^+}{\partial \underline{\underline{E}}_e} : \underline{\underline{R}}^o : \underline{\underline{E}}_e : \underline{\underline{E}}_e - \frac{1}{2} D^T \left[\frac{\partial \underline{\underline{P}}^+}{\partial \underline{\underline{E}}_e} \right] : \underline{\underline{R}}^o : \underline{\underline{E}}_e : \underline{\underline{E}}_e - D^T \frac{\partial \underline{\underline{P}}^+}{\partial \underline{\underline{E}}_e} : \underline{\underline{R}}^o : \dot{\underline{\underline{E}}}_e : \underline{\underline{E}}_e \quad (9)$	

To determine the overall damage tensor $\underline{\underline{D}}$ (Eq. 5), the spectral decomposition of stress tensor is deduced (Eqs. 1-4). Σ_i^* is the i th principal strain and p_i the i th corresponding to the unit principal direction of eigenvalue and eigenvector of Σ_i^* , and the symbol \otimes represents the tensor product. The 4th order positive spectral projection tensor $\underline{\underline{P}}^+$ given in (4) is determined by equations (2) and (3). According to (5), the damage is considered to be entirely active when all the eigenvalues are positive in the three principal directions; whereas, it becomes fully passive once the eigenvalues are negative, i.e., depending on the $\underline{\underline{P}}^+$ configuration. Hence, $\underline{\underline{P}}^+$ allows verifying naturally the complexity of the damage activation/deactivation phenomenon whatever the applied loading path. The overall rigidity tensor for a damaged material $\underline{\underline{R}}^d$ and its evolution $\dot{\underline{\underline{R}}^d}$ are defined respectively by equations (6) and (7), where $\underline{\underline{R}}^o$ is the classical 4th order rigidity tensor for an initially isotropic material. As recently proposed [1], the overall stress tensor evolution coupled with damage activation/deactivation phenomenon is mathematically described by equation (8). In (9), the second term in the right-hand side depends explicitly on the eigenvectors variation during cyclic loading. Thus, when the loading is applied according to laboratory reference axes, the principal vectors coincide with the latter. In this case, these vectors are constant, i.e., their characteristics vary neither with respect to time, nor according to the deformation. Hence, the second and third terms in the right-hand side of equation (9) vanishes. As a result, equation (8) has the advantage to successfully treat a great number of loading types especially the multiaxial ones.

3. Numerical approaches

The identification process is to numerically find a set of coefficients, which correlates the best possible predictions and experimental results. It is to minimize the difference between the recorded model response and the given experimental result. Such a difference can never be zero. However, the rule states that when the difference is smaller, the set of coefficients is better. In this work, identification of the model parameters is to find a search space where these values should minimize the gap between experimental results and predictions. Solving this problem is realized by minimizing the following function:

$$F(P) = \sum_{n=1}^N F_n(P) \quad \text{with} \quad F_n(P) = \frac{1}{(t_1 - t_0)} \int_{t_0}^{t_1} (V_{\text{exp}} - V_s)^T \cdot D \cdot (V_{\text{exp}} - V_{\text{sim}}) dt$$

where, P: Model parameters, N: number of tests, [t₀, t₁]: time interval of the test n, V_{exp}-V_{sim}: difference between observed variables and their simulations for the test n, D: weighting matrix of the test n.

The complexities of research space give in general the minimum function using radically different methods of resolutions. As a first approximation, it seems that deterministic method is suitable for search in small state-space; whereas for complex and large search state-space, this requires rather a method of stochastic search (genetic algorithm, pattern search ...).

The difficulties of these problems via conventional optimization methods give rapidly this family of algorithms able to handle large combinatorial problems with mixed variable. It is more interested for solving practical problems by a general classification of optimization problems and solved methods [3,4]. Briefly, genetic algorithms are adaptive heuristic search algorithm based on the evolutionary idea of natural selection and genetic. Moreover, they are a part of evolutionary computing, a rapidly growing area of artificial intelligence.

4. Numerical applications

The performance evaluation of the proposed numerical approach for identification issue is performed describing polycrystals elastic-inelastic cyclic behavior under uniaxial tension-compression (TC), biaxial tension-torsion with 90° out-of-phase angle (TT90). An aggregate of 400 grains is used assuming a single-phase FCC. Initially, a database for both cyclic loading (TC and TT90) is numerically made up to final damaging of the material point (grains aggregate) using these coefficients given in table 1. Such a database is considered as an experimental one. Thereafter, the identification process of model parameters related to the damage is started by setting the parameters of elasticity and plasticity changing all the damage parameters. Therefore, the identification process by the global minimum optimization concept is made through the genetic algorithm. Several iterations are made obtaining several families of model parameters followed by a local identification using the pattern search algorithm. The optimized model parameters are summed up in table 2.

Table 2 Constants of the model

Model parameters	MPa				MPa MPa				MPa		Damage parameters							
	E	v	α	z	K	b	ko	Q	h1=h2=...=h5	h6	C	a	S	so	w	d1	d2	γ0
initial coef	215000	0.32	1	20	50	13	240	256	1	2.4	95100	10	4	0.95	1	1	1.4	7
Optimized coeff.	215000	0.32	1	20	50	13	240	256	1	2.4	95100	10	5.24	4.07	1.38	1	1.82	7

One of the main reasons which promotes this association is that both algorithms are parallelizable as shown in [3,4]. This allows gaining in computation time by exploiting computer multiprocessor. The experimental recorded fatigue lives are 186, and 67 cycles for TC and TT90, respectively. The model predicts these lives faithfully giving therefore 195 and 67 cycles in TC and TT90, respectively.

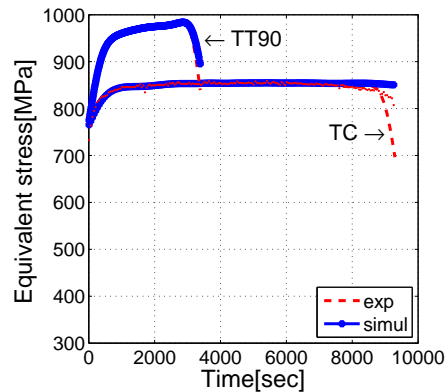


Figure 1. Evolution of the overall stress during TC, TT90 up to the final fracture

Figure 1 represents the typical evolutions of the maximum overall stress (pick stress value for each cycle) versus cyclic time using the same maximum von-Mises equivalent macro-strain for the two cyclic loading paths (TC and TT90). The predicted responses describe properly the experimental results. Note that these predicted results are computed with the optimized model parameters summarized in table 2.

5. Conclusion

The objective of this work is to optimize the identification of the micromechanical model parameters under different cyclic loading complexities. Hence, a combination of genetic algorithm (GA) with pattern search (PS) is developed. The GA optimizes globally the model parameters the PS (considered as a local method) has a role to determine the final values of these parameters. It is recognized that this combination shows its ability to optimize the identification process. Consequently, the predicted responses describe faithfully the experimental results

References

- [1] Abdul-Latif, A., and Mounounga T., B. S., (2009), Damage Deactivation Modeling under Multiaxial Cyclic Loadings for Polycrystals, *International Journal of Damage Mechanics*, **18**, 177-198.
- [2] Razafindramary, D., and Abdul-Latif A., (2011), On the Efficiency of Algorithms for Computing a Micromechanical Constitutive Equations Coupled with Damage, *Computational Materials Science*, **50**, pp. 2001-2008.
- [3] Dréo J., Pétrowski A., Siarry P., and Taillard E. (2003), *Métaheuristiques pour l'Optimisation Difficile*, Eyrolles, ISBN : 2-212-11368-4.
- [4] Smith R.E., Perelson A.S., and Forrest S., (1993), Searching for diverse, cooperative populations with genetic algorithms, *Evolutionary Computation*, 1(2), pp.127-149.

ANISOTROPIC PLASTIC DEFORMATION AND DAMAGE IN COMMERCIAL AL 2198 T8 SHEET METAL

D. Steglich¹, H. Wafai, J. Besson²

¹ Helmholtz-Zentrum Geesthacht Zentrum für Material- und Küstenforschung, Institute of Materials Research, Materials Mechanics, Max-Planck-Str. 1, 21502 Geesthacht, Germany
e-mail: dirk.steglich@hzg.de

² Mines ParisTech, Centre des Matériaux, CNRS UMR 7633, BP87 91003 Evry Cedex, France
e-mail: Jacques.Besson@mat.ensmp.fr

Abstract. Deformation anisotropy of sheet aluminium alloy 2198 (Al-Cu-Li) has been investigated by means of mechanical testing of notched specimens and Kahn-type fracture specimens, loaded in the rolling direction (L) or in the transverse direction (T). Contributions to failure are identified as growth of initial voids accompanied by a significant nucleation of a second population of cavities and transgranular failure. A model based on the Gurson-Tvergaard-Needleman (GTN) approach of porous metal plasticity incorporating isotropic voids, direction-dependent void growth, void nucleation at a second population of inclusions and triaxiality-dependent void coalescence has been used to predict the mechanical response of test samples. The model has been successfully used to describe and predict the direction-dependent deformation behaviour, crack propagation and, in particular, toughness anisotropy.

1. Introduction

Characterisation of alloys with respect to resistance against ductile crack extension has become an essential part of a damage-tolerance concept, which acknowledges the existence of cracks and structural damage. Damage mechanics provides a unified approach of combining constitutive equations for anisotropic deformation with equations describing the degradation of the material, taking full advantage of the potential of the local approach. Ductile damage is usually approached by using isotropic damage models, in which voids are assumed to be spherical while the matrix material is assumed to be isotropic. Assuming plastic isotropy of the matrix only, many authors have investigated the influence of the void geometry on the homogenised response of the material. Apparently, there is a coupling between anisotropy and void growth due to the constraint added in the vicinity of the void. In order to account for this effect in a general way, a homogenisation procedure has to be accomplished, which finally leads to a set of constitutive equations comprising plastic potential, flow rule and an evolution equation for the porosity. For the sake of simplicity, porosity is commonly expressed as a scalar quantity; its evolution is therefore assumed to be isotropic. To the contrary, evolution equations for non-isotropic voids require at least a non-scalar damage measure, e.g. for the modelling of ellipsoidal voids [1-3] or general anisotropic damage [4-6]. For orthotropic material like rolled sheets, various yield criteria are available. Anisotropy is expressed by using a structural tensor, which is based on the axes of orthotropy. In damage models this framework may be used together with the assumption that effects caused by matrix anisotropy and void shape are independent [7]. The material considered in the present study is a new member of the Al-Cu family. These alloys are specifically designed to have good mechanical properties in order to use them for structural components in aircrafts. It has superior yield strength than the well established alloy Al 2024. This template should help the authors of plenary lectures and accepted papers

for the ICDM - International Congress on Damage Mechanics to prepare their papers. The length of full papers should be 4 pages. The authors are kindly asked to follow the instructions about formatting of the document in order to reduce further interventions during the preparation of Proceedings.

2. Constitutive Model

For commercial aluminium alloys, non-quadratic yield criteria are recommended. In a previous investigation [8], it was proven that the Bron model [9] based on an anisotropic yield surface is able to predict the direction-dependent deformation response of different types of flat specimens machined from rolled sheets. This particular constitutive model has been extended in order to incorporate the effect of hydrostatic pressure on the growth of micro-voids. This was done by replacing the (von Mises) equivalent stress usually used in the yield function of a voided aggregate by the respective definition of the anisotropic deformation model, $\bar{\sigma}$:

$$\frac{\bar{\sigma}^2}{R^2(p)} + 2q_1 f^* \cosh\left(q_2 \frac{3\sigma_h}{2R(p)}\right) - 1 - (q_1 f^*)^2 = 0. \quad (1)$$

For the nucleation term different functions have been proposed. Following the popular assumption to link nucleation rate to plastic equivalent strain, a constant nucleation rate starting at a threshold value of the plastic equivalent strain is used in the present contribution,

$$\dot{f}_{nuc} = A H(p - \varepsilon_0), \quad (2)$$

with H being the Heaviside function and A and ε_0 model parameters. This was chosen to support void nucleation at high plastic strains on a phenomenological basis. Hardening and damage evolution are assumed to be isotropic, expressed by the plastic equivalent strain, p, and the void volume fraction, f. The mathematical model has been realised in the object-oriented FE code Zébulon [10]. It has been linked via the material library Z-Mat to the commercial finite element program ABAQUS/Standard, which is used to perform the simulations in the present contribution.

The model parameters have been identified sequentially. The strain hardening function in terms of true stress and true (logarithmic) plastic strain was taken from a tensile test in L-direction up to the load maximum and extrapolated using a power-law function

$$\sigma = 468 \text{ [MPa]} (1 + 40.95 p)^{0.1202} \quad (3)$$

The shape parameters of the yield surface a, b1, b2 and α as well as parameters describing the orthotropy cik were calibrated based on force-elongation and reduction of width signal taken from smooth and notched samples [8]. The model is used in the following to determine parameters associated to damage and to predict the mechanical behaviour of notched tensile specimens and Kahn-specimens. The void volume fraction at the beginning of coalescence has been derived from 3D-unit-cell calculations and found to be dependent on stress triaxiality, T. An exponential decay functions have been used for the respective main loading directions.3. Equations

3. U-notch tensile specimens and Kahn specimens

Two different kinds of notched specimens were used: specimens with notch radius of 1 mm and notch radius of 2 mm. Specimens were machined in three directions with respect to the rolling direction of the sheet:

- along the rolling direction, L “Longitudinal”, three specimens each radius,
- perpendicular to the rolling direction, T “Transversal”, three specimens each radius,
- 45° to the rolling direction, D “Diagonal”, three specimens each radius.

Despite the fact that the specimen thickness is comparably small, 3D discretisation has to be used for the simulations to properly capture the void evolution.

Kahn specimens were machined in two directions with respect to the rolling direction of the sheet:

- along the rolling direction, L “Longitudinal”,
- perpendicular to the rolling direction, T “Transversal”.

For the FE-model of the specimen, one fourth of the specimen is modelled due to the twofold symmetry. The complete specimen was constructed with 3D quadratic solid elements with reduced integration.

Figure 1 displays the experimental results obtained from the notched specimens in the three directions and the corresponding simulation results. The maximum force of the specimen oriented in T-direction is highest for notch radii of 1 mm and 2 mm, while D-orientation shows a significantly lower force level. The elongation at failure observed in the experiments is sorted in increasing order L, T, D for both notch geometries. While L and T-orientation differ only slightly, D shows a significantly higher failure strain. This effect correlates well with the fracture surface appearance, where the amount of dimples is significantly higher on D-oriented specimens compared to L and T orientation revealing an increased ductility.

Figure 2 displays the experimental results of the two representative Kahn-type specimens and the corresponding simulation results. One can see from the simulation results that slight differences in specimen’s “pre-fracture” deformation behaviour between L- and T-orientation exist. The simulations under predict the maximum force, but meet the decreasing part of the load-CMOD curve. This implies that the stable crack extension phase is not exactly met by the simulations, whereas the mixed-mechanism-phase is. This goes back on the calibration of the nucleation function used, eqn. (2), which is based on the sudden load decrease obtained from the notched samples originating from a turn to a slanted failure mode. Consequently, the use of the strong nucleation rate aims rather on an assessment of the slanted failure mode instead of meeting the stable crack extension correctly.

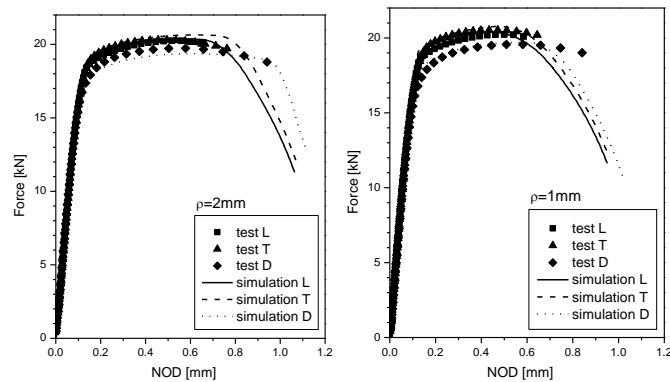


Figure 1. Response of the U-notched samples $\rho=2$ mm (a) and $\rho=1$ mm (b) – experiment and simulation using the damage model

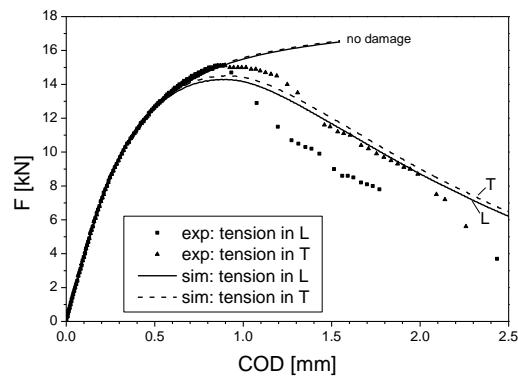


Figure 2. Results of the FE-simulations of the Kahn tear tests in comparison with experimental data

4. References

- [1] M. Gologanu, J.-B. Leblond, and J. Devaux, "Approximate models for ductile metals containing non-spherical voids - case of axisymmetric prolate ellipsoidal cavities," *J. Mech. Phys. Solids*, vol. 41, pp. 1723-1754, 1993 1993.
- [2] T. Pardoen and J. W. Hutchinson, "An extended model for void growth and coalescence," *J. Mech. Phys. Solids*, vol. 48, pp. 2467-2512, 2000 2000.
- [3] D. Steglich, W. Brocks, J. Heerens, and T. Pardoen, "Anisotropic ductile fracture of Al 2024 alloys," *Engineering Fracture Mechanics*, vol. 75, pp. 3692-3706, 2008.
- [4] P. Ladeveze, "Towards a fracture theory," in *Computational Plasticity: Fundamentals and Applications*, Barcelona, 1992, pp. 1369-1400.
- [5] D. Krajcinovic, J. Lemaitre, J. Hult, S. Murakami, D. Sumarac, F. A. Leckie, and J. Najjar, "Continuum Damage Mechanics - Theory and Applications," in *Courses and lectures no. 295*: Springer-Verlag, 1987.
- [6] J. Lemaitre, R. Desmorat, and M. Sauzay, "Anisotropic damage law of evolution," *European Journal of Mechanics a-Solids*, vol. 19, pp. 187-208, Mar-Apr 2000.
- [7] A. A. Benzerga, J. Besson, R. Batisse, and A. Pineau, "Synergistic effects of plastic anisotropy and void coalescence on fracture mode in plane strain," *Modelling Simul. Mater. Sci. Eng.*, vol. 10, pp. 73-102, 2002 2002.
- [8] D. Steglich, H. Wafai, and W. Brocks, "Anisotropic Deformation and Damage in Aluminium 2198 T8 Sheets," *Int. J. Damage Mechanics*, 2009.
- [9] F. Bron and J. Besson, "A yield function for anisotropic materials: Application to aluminium alloys," *Int. J. Plast.*, vol. 20, pp. 937-963, 2004 2004.
- [10] J. Besson and R. Foerch, "Large scale object-oriented finite element code design," *Computer Methods in Applied Mechanics and Engineering*, vol. 142, pp. 165-187, 1997.

DAMAGE PREDICTION OF A GRADED POROUS BIOCOMPOSITE IMPLANT USING THE FINITE ELEMENT METHOD

^{1a}C.P. Tsui, ^{1b}C.Y. Tang, ^{1c}H.Y. Wang, ^{1d}L.C. Chan

¹ Department of Industrial and Systems Engineering, The Hong Kong Polytechnic University, Hung Hom, Hong Kong, P.R. China

^ae-mail: mfgary@inet.polyu.edu.hk, ^be-mail: mfcytang@inet.polyu.edu.hk

^ce-mail: wanghui@inet.polyu.edu.hk, ^de-mail: mflcchan@inet.polyu.edu.hk

Abstract. In this study, the mechanical response and progressive damage behavior of a graded porous implant made of hydroxyapatite reinforced polyetheretherketone (HA/PEEK) biocomposite under tensile and compressive loads have been investigated. In the macro-scale, a finite element (FE) model was constructed with brick elements and beam elements with gradient variation in their cross-section areas for mimicking the entire implant. In a micro-scale, a repeated unit FE cell model developed previously was used to determine the constitutive behavior of the base material, which was subsequently exported to the macro-scale FE model. By incorporating a material failure criterion in the micro-scale FE model, the mechanical response and the damage evolution of the graded porous implant under either tension or compression could be simulated. The advantages and limitations of the graded porous biocomposite implant are also discussed. The results show that the proposed method can provide useful information for the design of graded porous biocomposite implants.

Keywords: Finite element method, Mechanical response, Damage behaviors, Graded porous biocomposite implant

1. Introduction

Porous biocomposite structures have been widely used as biomimetic materials in the medical and pharmaceutical fields for bone replacement and implants, and scaffolds for bone tissue or cell growth [1-2]. The previous studies on porous biocomposite structures focused on the mechanical properties of homogenous uniform cellular solids such as open-cell foams [3] and porous scaffolds [4]. However, study of the elasto-plastic response of graded porous structures for mimicking the bone structure is very limited. The multi-level finite element (FE) method has been used for studying the effects of shapes, sizes and locations of microscopic inclusions on the structural performance of elasto-plastic two-dimensional structures [5]. This method was also used to analyze local cellular deformation in bone tissue for determining the relation between pore pressure and local tissue strain [6]. Pore size and distribution in porous structures are important factors, affecting the effectiveness of bone implants. In clinical engineering applications, too small pore size could prevent cellular penetration, and a too large pore size could hinder the adhesion and proliferation of adjacent cells, highly weakening the structural integrity [7]. In this study, a multi-level FE method is proposed to predict the mechanical response and damage behavior of a graded porous implant made of hydroxyapatite reinforced polyetheretherketone (HA/PEEK) biocomposite under tensile and compressive load. A micro-scale model was firstly developed to determine the mechanical properties and damage behavior of the base material. A macro-scale model was constructed with brick elements and beam elements

with gradient variation in their cross-section areas for mimicking the graded porous structure. By exporting the behavior of the micro-scale model with damage initiation and evolution to the macro-scale model, the damage behavior of the graded porous structure could be simulated. The proposed method can be extended to model the mechanical properties of bone, which possesses a multi-level hierarchical structure.

3. Interface Damage Initiation and Evolution

The damage initiation for the interface layer between HA and PEEK was assumed to occur due to a stress-based damage criterion. A threshold parameter φ , is defined as follows

$$\varphi = \sqrt{\left(\frac{\sigma_n}{\sigma_n^M}\right)^2 + \left(\frac{\tau_s}{\tau_s^M}\right)^2 + \left(\frac{\tau_t}{\tau_t^M}\right)^2} \quad (1)$$

where σ_n , τ_s and τ_t represent the nominal stresses when the deformation is either purely normal to the interface or purely in the first or the second shear direction, respectively. M represents the peak value of each corresponding quantity. When the value of φ , reaches unity, damage is initiated. The damage evolution function for the interface is defined [8].

$$d = \frac{\delta_m^f (\delta_m^{\max} - \delta_m^0)}{\delta_m^{\max} (\delta_m^f - \delta_m^0)}, \quad (0 < d < 1) \quad (2)$$

where δ_m^0 and δ_m^f represent the relative displacements for the damage initiation and total decohesion, respectively. The maximum relative displacement is δ_m^{\max} . The relation between the effective plastic displacement δ_p and effective plastic strain is ε_p given by $\delta_p = L\varepsilon_p$, where L is the characteristic length of the material. This relation can be rewritten as $\dot{\delta}_p = L\dot{\varepsilon}_p$. A linear evolution of the damage variable, d , with $\dot{\varepsilon}_p$ is assumed. Then

$$d = \frac{L\dot{\varepsilon}_p}{\varepsilon_p^{\max}} \quad (3)$$

where ε_p^{\max} is the maximum effective plastic displacement. When the effective plastic displacement δ_p increases to ε_p^{\max} , the value of d reaches unity, meaning that the material stiffness of the interface layer is totally degraded and the HA/PEEK interfacial debonding occurs. During the damage process, the contact stress components are revised as

$$\bar{\sigma}_n = (1-d)\sigma_n, \quad \bar{\tau}_s = (1-d)\tau_s, \quad \bar{\tau}_t = (1-d)\tau_t \quad (4)$$

where $\bar{\sigma}_n$ is the newly obtained normal stress, and similarly for the symbols of $\bar{\tau}_s$ and $\bar{\tau}_t$. From Eq.(4), there is no stress between HA and PEEK at debonding when $d = 1$.

4. Numerical Results and Discussion

4.1. FE results of micro-scale model (base material)

When the micro-scale model was subjected to a tensile normal displacement along the x -axis, the maximum von Mises stress was initiated at the pole of the interface, inducing the initiation of interfacial debonding along the interface beyond the nominal tensile strain of 4% and leading to a significant debonding at a tensile strain of 20%, as shown in Fig.2(a). When a compressive displacement was applied to the cell model, the maximum von Mises stress in the interface changed to its centre portion, leading to the occurrence of debonding in this area at the compressive normal strain of 20%, as shown in Fig.2(b). The normal stress-strain relations of HA/PEEK, the base material predicted from the micro-scale model is shown in Fig.3. For the model subjected to a tension, the normal stress decreases more

significantly for a material with a high particle content (e.g. PVF=40%) beyond the tensile strain of 0.06, because the cross-section occupied by the particles in the material with PVF=40% is higher than that for PVF=10%, hence the load-bearing capacity for the material with high PVF after interfacial debonding drops more sharply. This response is not significant for the model under compression. For example, the material with PVF=30% has a similar stress level as that with PVF=10% at a compressive strain of 0.1, because the debonded particles can still contribute to the load-bearing capacity of the material.

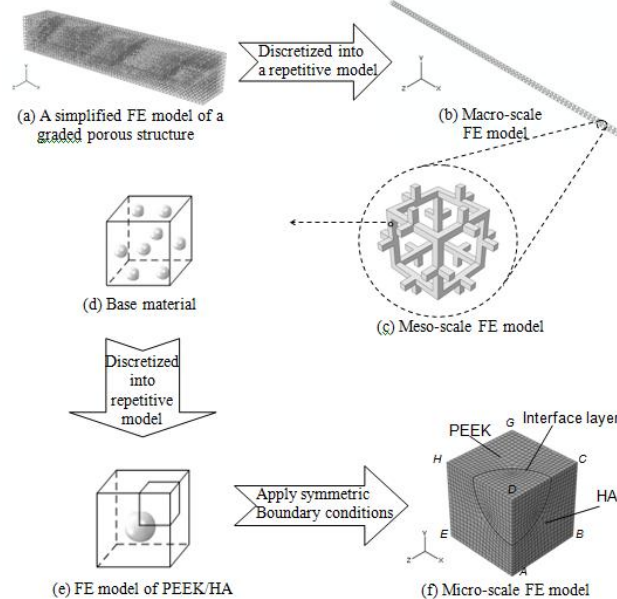


Figure 1. Schematic diagram of the graded porous structure and multi-level FEM models.

4.2. FE results of macro-scale model (graded porous structure)

The normal stress-strain relation of the graded porous structure under tension, as shown in Fig.4, is similar to that of the base material shown in Fig.3. The tensile strength of the structure drops from 12.9MPa to 7.2MPa at a tensile strain of 0.1 when PVF is increased from 10% to 40%. However, for the structure under compression, elastic behavior is dominant. The normal stress on the structure increases linearly to the maximum value, and then the structure crashes before it exhibits a plastic response. The difference between the tensile and compressive response of the structure is attributable to the effect of the debonding damage criteria in the micro-scale model. The proposed method can be applied to structures with more complex variations in porosity levels, because the beam cross-sectional area in the meso-scale FE model serves as the controlling parameter.

5. CONCLUSION

In this paper, the mechanical response and damage evolution of a graded porous structure made of HA/PEEK biocomposite was analyzed by using a multi-level finite element method. By using the micro-cell model incorporating the criteria for the interface damage initiation and evolution, the normal stress-strain relation of HA/PEEK undergoing interfacial debonding could be obtained. The macro-scale model constructed from the beam elements with variable cross-sectional areas was also effective in mimicking the structure

with a gradient change in porosity, and hence could predict the stress-strain response of the structure. The results showed that the proposed method can provide useful information for the design of graded porous biocomposite implants, which can be extended to model multi-level hierarchical bone structures.

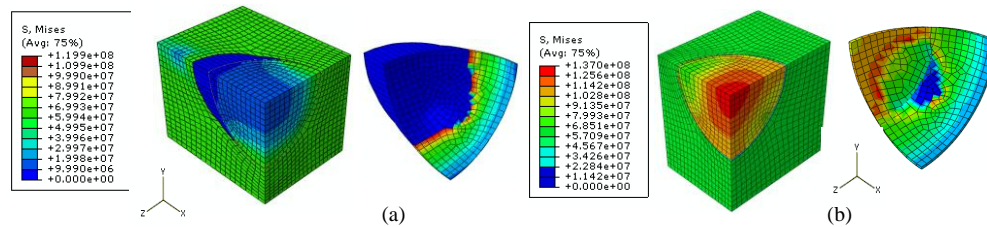


Figure 2. The contour plots of von Mises stress field in the micro-scale model with PVF = 10% under, (a) nominal tensile strain of 20% and (b) nominal compressive strain of 20%

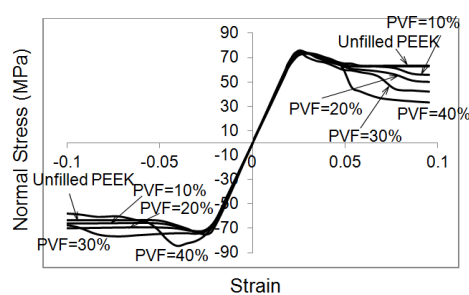


Figure 3. Stress-strain relation of the base material predicted by the micro-scale model

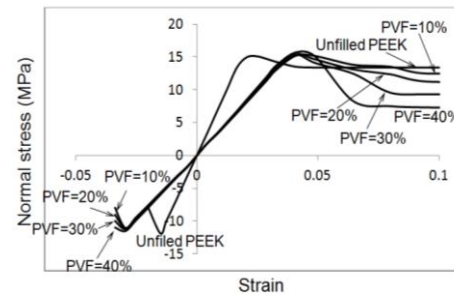


Figure 4. Stress-strain relation of graded porous material predicted by the macro-scale model

Acknowledgements

The authors would like to thank the substantial support from the Research Committee of the Hong Kong Polytechnic University (Project code: G-YG18) and the Research Grants Council of the Hong Kong Special Administrative Region, China (Project no.: PolyU 511511).

References

1. Rezwan K., Chen Q. Z., Blaker J. J., Boccaccini A. R. Biodegradable and bioactive porous polymer/inorganic composite scaffolds for bone tissue engineering, *Biomaterials*, Vol. 27, 2006, pp. 3413-3431.
2. Tampieri A., Celotti G., Sprio S., Delcogliano A., Franzese S. Porosity-graded hydroxyapatite ceramics to replace natural bone, *Biomaterials*, Vol. 22, 2001, pp. 1365-1370.
3. Zhu H. X., Knott J. F., Mills N. J. Analysis of the elastic properties of open-cell foams with tetrakaidecahedral cells, *Journal of the Mechanics and Physics of Solids*, Vol. 45, 1997, pp. 319-325.
4. Fang Z., Starly B., Sun W. Computer-aided characterization for effective mechanical properties of porous tissue scaffolds, *Computer-Aided Design*, Vol. 37, 2005, pp. 65-72.
5. Ghosh S., Lee K., Moorthy S. Two scale analysis of heterogeneous elastic-plastic materials with asymptotic homogenization and Voronoi cell finite element model, *Computer methods in applied mechanics and engineering*, Vol. 132, 1996, pp. 63-116.
6. Deligianni D. D., Apostolopoulos C. A. Multilevel finite element modeling for the prediction of local cellular deformation in bone, *Biomechan model mechanobiol*, vol. 7, 2008, pp. 151-159.
7. Schlenk R. P., Stewart T., Benzel E. C. The biomechanics of iatrogenic spinal destabilization and implant failure, *Neurosurg Focus*, Vol. 15, 2003, pp.1-11.
8. Fan J. P., Tsui C. P., Tang C. Y., Chow C. L. Influence of interphase layer on the overall elasto-plastic behaviors of HA/PEEK biocomposite, *Biomaterial*, Vol. 25, 2004, pp. 5363-5373.

MODELLING DAMAGE AND FAILURE IN HIGH VELOCITY IMPACT ON CFRP

R. Vignjevic¹, N. Djordjevic, J. Campbell

¹ Applied Mechanics and Astronautics department,
Cranfield University-SoE, Cranfield, MK43 0AL, UK
e-mail: v.rade@cranfield.ac.uk

Abstract. The primary objective of this investigation is to develop a thermodynamically consistent constitutive model for carbon fibre reinforced composite (CFRP) materials under high velocity impact loading. The constitutive model is capable of modelling formation and propagation of shock wave in anisotropic material and damage and failure including damage induced by shock wave propagation. The model comprises two parts: equation of state (EOS) which defines the material response to isotropic volumetric deformation and the strength part which defines the material response to pure shear deformation. Solution proposed by Anderson [1] was not capable of predicting material response accurately, thus the alternative decomposition of stress tensor was used [2].

The damage model is based on the assumption that damage within continuum can be represented as a second order tensor, ω_{ij} which is divided into the damage which results in volume change of the damaged (e.g. voids, cavities) material and damage related to shear deformation. Damage evolution based on the concept proposed in [3] is coupled with a thermo elastic model and the shock EOS. The initiation of failure is based on a critical value of a specific dissipation function. The constitutive model was implemented into Lawrence Livermore National Laboratory (LLNL) transient nonlinear finite element code DYNA3D [4]. The performance of the model is illustrated by few numerical examples where experimental data from high velocity impact tests [5] is compared with the numerical results.

1 Introduction

The CFRP composites are often exposed to the impact loading high strain rates in the range from 10^3 s^{-1} to 10^6 s^{-1} (debris, hail stone and ice impact, bird strike, armour penetration). These extreme impact loadings are almost always involve generation and propagation of shock waves within the material. Therefore, the material behaviour under such a complex loading need to be properly understood and accurately predicted, in order to optimise design of a structure and to minimise the risk of its catastrophic failure due to the impact hazards.

The objective of this investigation is to develop a constitutive model capable of predicting dynamic deformation and failure in the woven CFRP composites, which are widely used in aerospace and defence.

A thermoelastic damage model was developed in the framework of irreversible thermodynamics with internal variables. Due to the evident brittle properties of the composites, the elastic strains were assumed to be small and the plastic deformation was neglected (plastic deformation in CFRP considered does not exceed 1%). These assumptions significantly simplify the formulation of the constitutive model in the configurational and thermodynamic frameworks, in a way that it can be derived in the current configuration and the dissipation of energy in the material during deformation process is due to damage only.

2 Thermoelastic damage model

In this material model damage was incorporated through a damage effect tensor operating on the material elastic stiffness tensor [6]-[7]. It is defined using the principle of strain energy equivalence, originally derived by Cordebois and Sidoroff as a generalization of pioneering work of Kachanov. Damage effect tensor defines a relationship between the effective and nominal Cauchy stress tensors:

$$\bar{\boldsymbol{\sigma}} = \mathbb{M}(\boldsymbol{\omega}) : \boldsymbol{\sigma} \quad (1)$$

where $\bar{\boldsymbol{\sigma}}$ denotes effective Cauchy stress applied to the virgin material and $\mathbb{M}(\boldsymbol{\omega})$ is a damage effect tensor, which is a function of a second order damage tensor $\boldsymbol{\omega}$. In order to maintain the symmetry of the effective stress tensor, the damage effect tensor is defined using a product type symmetrisation [6]-[7], in the following form:

$$\mathbb{M}(\boldsymbol{\omega}) = (\mathbf{I} - \boldsymbol{\omega})^{-\frac{1}{2}} (\mathbf{I} - \boldsymbol{\omega})^{-\frac{1}{2}} \quad \mathbb{M}_{ijkl} = (\delta_{ik} - \omega_{ik})^{-\frac{1}{2}} (\delta_{jl} - \omega_{jl})^{-\frac{1}{2}} \quad (2)$$

The damage effect tensor was defined in terms principle damage components (directions) as a fourth order diagonal tensor.

The relationships between the damaged material stiffness (or compliance) tensor \mathbb{C} and the virgin material stiffness tensor $\bar{\mathbb{C}}$ obtained using the energy equivalence principle is:

$$\mathbb{C}(\boldsymbol{\omega}) = \mathbb{M}^{-1}(\boldsymbol{\omega}) : \bar{\mathbb{C}} : \mathbb{M}^{-1}(\boldsymbol{\omega}) \quad \mathbb{C}^{-1}(\boldsymbol{\omega}) = \mathbb{M}(\boldsymbol{\omega}) : \bar{\mathbb{C}}^{-1} : \mathbb{M}(\boldsymbol{\omega}) \quad (3)$$

The dissipation rate in the model is determined by the rate of change of damage tensor and a definition of damage effect tensor (2) as:

$$\Delta = \frac{1}{2} \boldsymbol{\sigma} : \mathbb{M}(\boldsymbol{\omega}) : \bar{\mathbb{D}} : \frac{\partial \mathbb{M}(\boldsymbol{\omega})}{\partial \boldsymbol{\omega}} : \boldsymbol{\sigma} : \dot{\boldsymbol{\omega}} \geq 0 \quad (4)$$

The damage evolution equations were derived by modifying Tuler Bucher criterion [3], in the following form:

$$\dot{\omega} = \dot{\omega}(\omega, \sigma) = \Omega_{\omega} \left(\frac{\sigma}{C_m (1 - \omega)} - \frac{\sigma_{CR}}{C_m} \right) H \left(\frac{\sigma}{C_m (1 - \omega)} - \frac{\sigma_{CR}}{C_m} \right) \quad (5)$$

$$\dot{\omega}_{del} = \dot{\omega}_{del}(\omega, \sigma) = \Omega_{del} \left(\frac{\sigma_{33}}{C_{33} (1 - \omega_3)} - \frac{\sigma_{CRdel}}{C_{33}} \right) H \left(\frac{\sigma_{33}}{C_{33} (1 - \omega_3)} - \frac{\sigma_{CRdel}}{C_{33}} \right) \quad (6)$$

where: Ω_{ω} , Ω_{del} are material parameters determined by time to failure, σ_{CR} and σ_{delCR} are critical effective stress and critical out of plane stress, C_m and C_{33} are maximum in-plane and through thickness stiffness member, respectively; H is Heaviside function.

The proposed damage model was implemented into the LLNL code DYNA3D [4] and coupled with an orthotropic elastic constitutive model and the Mie Gruneisen EOS, as detailed in [2].

3 Numerical results

Thermoelastic damage model for composites was validated through a series of plate impact tests [8] and sphere impact tests; the latter is presented in this section. Mesh density of the models was defined to minimise mesh sensitivity and ensure that all main physical effects are modelled with required fidelity. Material elastic properties and parameters for the

damage model for the CFRP woven composite are given in [2] and [9], respectively. The data for the EOS are obtained in the experiments described in [9].

The normal sphere impact tests were carried out for a range of velocities from 186 m/s (velocity just above the ballistic limit) to 1875 m/s, [5]. In all test cases, a 6mm thick woven CFRP plate, which consisted of 16 plies, was impacted by an annealed stainless steel sphere, which was 12 mm in diameter. A quarter of the FE model of the sphere impact test and an asymmetric layout of the target plate are shown in Figure 1. The plate was modelled as a quasi-orthotropic material, with three hexagonal solid elements per thickness in order to properly capture delamination.

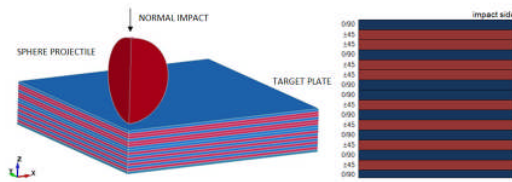


Figure 1. FE model of a quarter of the sphere impact test

The experimental data for the impact velocities 194 m/s and 354 m/s were obtained by using X-ray computed tomography (XCT) [10] and the cross sections of the specimens after the impact with relevant parameters of damage are shown in Figure 2. The size of the damaged area and crater of the holes after a high velocity impact at 1199m/s were obtained from the C scans [5].

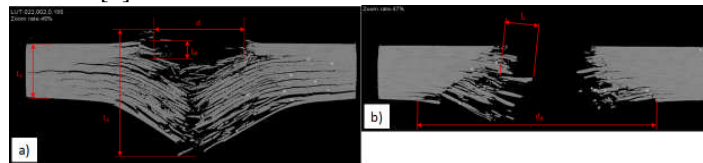


Figure 2 Post impact XCT, cross section of the target plates, impact velocity: a) 194 m/s b) 354m/s

From the XCTs of the impacted test samples for impacts at 194m/s and 354m/s, the elliptical shape of damage in the plane normal to the impact was observed in each ply. The same shape of the damaged area was also obtained by modelling. The comparison of size of the numerically obtained and experimentally observed damaged area for each ply through the thickness for the two impact velocities are illustrated in Figure 3. The simulation results agree well with the experimental observations. For the lower impact velocity, the model underestimated the size of the damaged area at the back of the target plate, which can be attributed to the quasi orthotropic equivalent properties of composite, which in turn made the model stiffer in the fibre direction (tensile fibre failure is dominant failure mechanism).

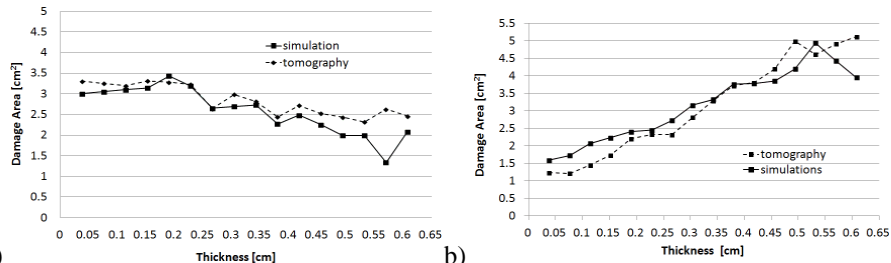


Figure 3. Comparison of the damage area calculated from the simulation results and tomography data: a) normal impact at 194m/s; b) normal impact at 354m/s

The simulation results for 354m/s impact (shear plugging failure mode) shows that damaged area is increasing from the top towards the bottom plies, resulting in a conical profile of the hole and the damaged zone in the target cross section (see Figure 2b). This shape of the crater agrees well with the experimental data, as illustrated in Figure 3b.

The hole and the damaged zone in the specimens impacted at 1199 m/s (high velocity range), had an hourglass profile of in the cross section of the target plate with the wide damage (delamination) zone in the top and bottom plies of a target plate. The validation of the model was based on the measurements of the diameter of the hole, and diameter of the damage zone in the front and rear face (ply) of the target for two perpendicular directions. The comparison of the quantities measured is shown in Table 1. The numerical results compare well with the experiments: 1) simulations captured hourglass shape of delaminated zone; 2) bigger delamination zone at the back of the target plate compared to the front plies; 3) calculated average diameter of the hole differs below 5%; 4) numerically obtained size of delamination zone at the back of the target differed below 8%.

Table 1. Simulation results and C-scan measurements for the diameter of the crater and delamination zone for the impact at 1199 m/s

sample	t [mm]	Nominal Velocity [m/s]	x ₁		x ₂		Impact face		Rear face	
			[mm]	[mm]	[mm]	[mm]	y ₁ [mm]	y ₂ [mm]	y ₁ [mm]	y ₂ [mm]
simulations	6	1199	11.7	12.8	19.8	24.3	36.5	23.3		
C scan C-3	6.1	1199	11.2	12.2	19.02	26.2	36.98	24.5		
Error %	-	-	4.27	4.69	3.94	7.82	1.32	5.15		

4 Summary

This paper describes a part of the validation process of the thermoelastic damage model proposed for the orthotropic materials including woven composites. This includes modelling of three sphere impact tests at 194, 354 and 1199 m/s. The extent of damage in the impacted samples was determined using X ray tomography and compared with the equivalent numerical results. The comparison showed that the model is capable of accurately predicting damage distribution and extent in plane and through thickness, especially for the high velocities, when the shock significantly influenced the material response.

References

- [1] Anderson Jr., C. E., Cox, P. A., Johnson, G. R. and Maudlin, P. J. (1994), "A constitutive formulation for anisotropic materials suitable for wave propagation computer programs-II", *Comp. Mech.*, 15(3), 201-223.
- [2] Vignjevic, R., Campbell, J. C., Bourne, N. K. and Djordjevic, N. (2008), "Modeling shock waves in orthotropic elastic materials", *Jrnl of App Physics*, vol. 104, no. 4.
- [3] Tuler, F. R. and Butcher, B. M. (1968), "A criterion for the time dependence of dynamic fracture", *Int J Fracture Mechanics*, 4 (4), pp. 431-437.
- [4] Liu, J., (2004), *Dyna3D: A Nonlinear, Explicit, Three-Dimensional Finite Element Code for Solid and Structural Mechanics*, University of California, LLNLL, USA.
- [5] Hazell, P. J., Cowie, A., Kister, G., Stennett, C. and Cooper, G. A. (2009), "Penetration of a woven CFRP laminate by a high velocity steel sphere impacting at velocities of up to 1875 m/s", *Int J Imp Eng*, 36 (9)
- [6] Krajcinovic, D. (1996), *Damage mechanics*, Elsevier, Amsterdam ; New York.
- [7] Carol, I., Rizzi, E. and Willam, K. (2001), "On the formulation of anisotropic elastic degradation. I. Theory based on a pseudo-logarithmic damage tensor rate", *Int J of Sol and Struct.*, 38 (4), pp. 491-518.
- [8] Vignjevic, R., Djordjevic, N. and Campbell, J. C. (2009), "High velocity impact on CFRP", ICCM, Edinburgh
- [9] Campbell, K. (2004), *Material characterisation - 5HS/RTM 6*, ELRIPS-WP7b-Bom-TREP-02.
- [10] Penumadu, D. (2010), Woven CFRP Composite Materials Damage From Steel Sphere Impact: Visualization and Analysis Using X-ray Micro CT, X-ray CT Experimental data for the ELRIPS project, Tennessee

STABILITY OF QUASI-STATIC FRACTAL CRACKS AT MESO AND NANO SCALE LEVELS

Michael P. Wnuk¹

¹College of Engineering and Applied Science, University of Wisconsin – Milwaukee, USA, ph. +1-414-962-0687, E-mail: mpw@uwm.edu

Abstract. Problems of damage accumulation and evolution are intrinsically related to the phenomenon of crack propagation in inelastic solids. Attention is focused on mathematical modeling of the stable quasi-static phase of crack propagation that precedes the catastrophic fracture in dissipative materials. All materials exhibit certain degree of irreversible straining and energy dissipation due to either plastic or visco-plastic phenomena associated with the deformation and fracture processes in inelastic solids. Later, Wnuk and Kriz (1985), and also Wnuk and Read (1986) provided some arguments that connected crack growth and damage accumulation. Analysis presented here is founded on the structured cohesive crack model, in which both the crack and the cohesive zone are described by the fractal geometry.

1. Introduction

The phenomenon of slow stable crack extension or subcritical crack growth (SCG) so ubiquitous in ductile and quasi-brittle fracture is not addressed in Griffith's theory of brittle fracture. Ultimately the analysis of this process leads to solutions for advancing crack, which significantly differ from those valid for stationary cracks. Physically this type of continuing crack growth resembles time-dependent or creep fracture observed in polymers. A noteworthy phenomenon in the studies of fractal fracture mechanics is the change of the order of singularity for the near-tip stresses, from $r^{-1/2}$ for the smooth crack to a somewhat weaker singularity, $r^{-\alpha}$ for a rough crack. Therefore, the exponent α can be used as a measure of the degree of roughness as suggested by the "embedded crack model" of Wnuk and Yavari [3], and it is related to the dimension D of the fractal representing the crack, $\alpha = (2-D)/2$, in which $1 < D < 2$. The effect of another important parameter, the material ductility measured by the index ρ , has been investigated in this research. It has been shown that the ductility index can be related to the micro-structural parameters, $\rho = R_{ini}/\Delta$, or to macro material parameters such as the yield strain ε_Y and the plastic component of the strain at fracture ε_{pl}^f , namely $\rho = 1 + \varepsilon_{pl}^f / \varepsilon_Y$. Symbol R_{ini} denotes the length of the cohesive zone at the onset of crack growth, and Δ is the size of the process zone adjacent to the crack front.

2. Mathematical analysis

Let us now review the essential results of these studies. Since the delta-COD criterion of Wnuk [8,9] requires a priori knowledge of the crack opening displacement within the cohesive zone, say $v(x_1, R)$, we shall focus attention on the following results, cf. Wnuk [8,9]

for the smooth crack and Khezzadeh et al. [10] for a rough crack. If x_1 denotes the distance measured outward from the physical crack tip, the opening displacements read

$$v(x_1, R(x_1)) = \frac{4S}{\pi E'} \left[\sqrt{R - x_1} - \frac{x_1}{2} \ln \left(\frac{\sqrt{R} + \sqrt{R - x_1}}{\sqrt{R} - \sqrt{R - x_1}} \right) \right] \quad (1)$$

for the smooth crack, and

$$v(x_1, R(x_1)) = \frac{4S\kappa(\alpha)}{\pi E'} \left[\sqrt{R^f - x_1} - \frac{x_1}{2} \ln \left(\frac{\sqrt{R^f} + \sqrt{R^f - x_1}}{\sqrt{R^f} - \sqrt{R^f - x_1}} \right) \right] \quad (2)$$

for a rough crack. The following notation has been used in equation (2)

$$R^f = N(\alpha, X, Y)R$$

$$N(\alpha, X, Y) = 4\pi^{\frac{1}{2\alpha}} \left[\frac{\alpha\Gamma(\alpha)}{\Gamma\left(\frac{1}{2} + \alpha\right)} \right]^{\mu^2} \left(\frac{2Y(X)}{X} \right)^{\frac{1}{\alpha} - 2} \quad (3)$$

$$X = a / R_{ini}$$

$$Y(X) = R(a) / R_{ini}$$

$$\kappa(\alpha) = \frac{1 + (\alpha - 1)\sin(\pi\alpha)}{2\alpha(1 - \alpha)}$$

It is seen that X denotes the dimensionless crack length and Y is the dimensionless length of the cohesive zone. Symbol κ is used to name the so-called “fractal constraint factor”. The displacements defined by (1) and (2) are then inserted into the Wnuk’s “final stretch” criterion, which governs the subcritical crack growth, namely

$$v(0, R(0)) - v(\Delta, R(\Delta)) = const = \delta / 2 \quad (4)$$

Note that R is viewed as a function of x_1 , while δ is used to denote the “final stretch” equivalent to an increment of the displacement measured at the outer edge of the process zone and considered a material constant, see Fig. 1. Since the variable R depends on the current crack length, it is time dependent (because the crack is extending), and thus we have the following Taylor expansion

$$R(0) = R(\Delta) + \frac{dR}{da} \Delta \quad (5)$$

We chose to use the coordinate $x_1 = x - a$ as a time-like variable, and we have considered two states: STATE ONE, $x_1 = \Delta$, and STATE TWO, $x_1 = 0$, see Fig. 1. Thus the quantity R becomes a function of x_1 , as indicated in (4) and (5). Substitution of (1), (2) and (5) into the criterion for slow crack propagation (4) leads to the following equations that govern motion of the quasi-static crack. For a smooth crack we obtain

$$\frac{dR}{da} = M - \frac{1}{2} - \frac{1}{2} \ln \left(\frac{4R}{\Delta} \right), M = 1.1 \left[\frac{1}{2} + \frac{1}{2} \ln 4\rho \right] \quad (6)$$

compare Wnuk [8]. For a rough crack this equation reads

$$\frac{dR}{da} = \frac{1}{N(\alpha, X, Y)} \left\{ M_{fractal} - \frac{1}{2} - \frac{1}{2} \ln 4\rho N(\alpha, X, Y)R / R_{ini} \right\}, M_{fractal} = M / \kappa(\alpha) \quad (7)$$

Both of these moduli are determined by the group of material constants $\frac{\delta}{2} \frac{\pi E'}{4S\kappa(\alpha)}$ and both

can be related to the experimentally determined Paris modulus, which in turn is related to the initial slope of the R-curve, namely

$$T_j = \frac{E'}{\sigma_y^2} \left(\frac{dJ_R}{da} \right)_{ini} = \frac{\pi}{8} \left(\frac{dR}{da} \right)_{ini} \quad (8)$$

Numerical integration of the governing equations (6) and (7) results in generating the R-curves (R vs. a) as shown in Fig. 2. The R-curves are then used to determine the point at which a quasi-static crack attains the size of the critical (catastrophic) crack. This critical point of fracture transition can be determined from the energy condition involving the total potential energy of the cracked and loaded solid

$$\Pi(\sigma, a) = \frac{1}{2} \int_V \sigma_{ij} \epsilon_{ij} dV - \int_{S_f} T_i u_i dS - SE(a) \tag{10}$$

Here SE(a) designates the surface energy, which for a Griffith crack equals $4\gamma a$, and for the quasi-brittle solids it equals the product of the Irwin's critical driving force G_c and the length (2a). At the onset of fracture the derivative

$$J = - \frac{d\Pi}{d\ell}, \ell = 2a \tag{11}$$

is set equal the doubled specific fracture energy 2γ , or G_c for quasi-brittle materials. In the present study the apparent surface energy is measured by either J_R or directly by the length R, which is contained in the range

$$R_{ini} \leq R \leq R_{unstable} \tag{12}$$

Evaluation of the coordinates of the point of transition to unstable crack propagation ($X_{unstable}$, $Y_{unstable}$) involves solving these simultaneous equations

$$G(\sigma, a) = G_R(a) \tag{13}$$

$$- \frac{\partial^2 \Pi}{\partial a^2} = \left[\frac{\partial G}{\partial a} \right]_X = \frac{dG_R(a)}{da}$$

or

$$J(\sigma, a) = J_R(a) \tag{14}$$

$$- \frac{\partial^2 \Pi}{\partial a^2} = \left[\frac{\partial J}{\partial a} \right]_X = \frac{dJ_R(a)}{da}$$

Equations (13) and (14) result from the energy considerations associated with the material resistance curves, so-called R-curves. The solutions are obtained numerically and they are indicated by the little circles shown in Fig. 2. They correspond to the unstable state. An additional effect, also beneficial, can be expected from the interaction between the growing dominant crack and the field of the micro-damage accumulated within the material in the volume adjacent to the crack front, compare Wnuk and Kriz [11] and Wnuk and Read [12].

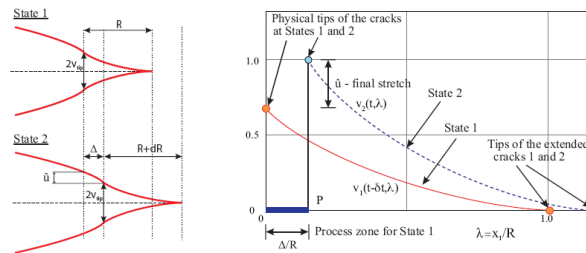


Fig. 1. Distribution of the COD within the cohesive zone corresponding to two subsequent states in the course of quasi-static crack extension (Wnuk's criterion of delta COD).

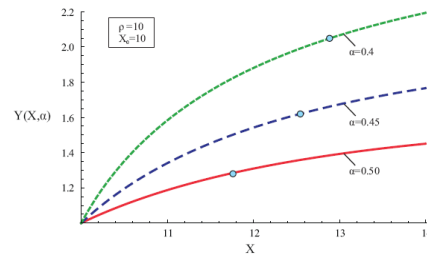


Fig. 2. Material resistance curves obtained for $X_0 = 10$, ductility index $\rho = 10$ and three values of the fractal exponent $\alpha = 0.50, 0.45$ and 0.40 . It is seen that for rough cracks the R-curves are more pronounced.

References

1. J. R. Rice, 1968, "Mathematical Analysis in the Mechanics of Fracture", in Liebowitz, editor, "Fracture", Vol.2, pp. 191 – 311.
2. V. V. Novozhilov, 1969, "On a necessary and sufficient criterion for brittle strength", *J. Appl. Mech – USSR*, Vol. 33, pp. 212 – 222 (in Russian).
3. M. P. Wnuk and A. Yavari, (2003), "On Estimating Stress Intensity Factors and Modulus of Cohesion for Fractal Cracks", *Eng. Fract. Mechanics*, Vol. 70, pp. 1659 – 1674.
4. L. M. Alves, R. V. da Silva, L. A. Lacerda, (2010), "Fractal Model of the J-R curve and the Influence of the Rugged Crack Growth on the Stable Elastic-Plastic Fracture Mechanics", *Engng. Fract. Mech.* 2010, 77, pp. 2451-2466.
5. N. Pugno and R. S. Ruoff, (2004), "Quantized Fracture Mechanics", *Philos. Mag.* 2004, 84(27), 2829–45.
6. D. Taylor, (2008), "The Theory of Critical Distances", *Engng. Fract. Mech.* 2008, 75, 1696–705.
7. M. P. Wnuk and A. Yavari, (2008), "Discrete Fractal Fracture Mechanics", *Engng. Fract. Mech.* 2008, 75(5), pp. 1127 – 1142.
8. M. P. Wnuk, (1974), "Quasi-static Extension of a Tensile Crack Contained in a Viscoelastic-plastic Solid", *J. Appl. Mech.* 1974, Vol. 41, pp. 234–242.
9. M. P. Wnuk, (1980), "A Model for Stable Crack Growth", *Prikladnaya Matematika i Mekhanika (PMM)*, Russian Academy of Sciences, Vol. 1, No. 4, pp. 758 – 764.
10. H. Khezradeh, M. P. Wnuk and A. Yavari, (2011), "Influence of Material Ductility and Crack Surface Roughness on Fracture Instability", *Journal of Physics D*, Vol. 44, (395302) 22 pages.
11. M. P. Wnuk and R. Kriz, (1985), "CDM Model of Damage Accumulation in Laminated Composites", *Int. J. Fracture*, Vol. 28, pp. 121 – 138.
12. M. P. Wnuk and D. Read, (1986), "Essential Work of Fracture (w_e) versus Energy Dissipation Rate (J_c) in Plane Stress Ductile Fracture", *Int. J. Fracture*, Vol. 31, pp. 161 – 171.
13. M. P. Wnuk, Z. Bazant and E. Law, 1984, "Stable Growth of Fracture in Brittle Aggregate Materials", *Int. J. Fracture*, Vol. 2, pp. 259 – 286.

MODELLING OF COMPRESSIVE FAILURE IN Z-PINNED COMPOSITE LAMINATES

Shunli Xie¹, Junqian Zhang^{2,3}

¹ Shanghai Institute of Applied Mathematics and Mechanics, Shanghai University, Shanghai 200072, China, e-mail: applexie007@gmail.com

² Department of Mechanics, Shanghai University, Shanghai 200444, China, e-mail: jqzhang2@shu.edu.cn

³ Shanghai Key Laboratory of Mechanics in Energy Engineering, Shanghai University, Shanghai 200072, China, e-mail: jqzhang2@shu.edu.cn

Abstract. The progressive failure analysis of z-pinned composite laminates under compressive loading has been carried out to identify failure modes. The fiber waviness and the fiber volume content concentration, which are inhomogeneously distributed, as well as the resin-rich pocket, are taken into account. Failure mode pictures and stress-strain curve under compressive load are obtained. The results indicate that kinking/micro-buckling is the main failure mode in z-pinned carbon/epoxy composites under compression. Z-pins reduce the compressive strength of composites. The effects of pin parameters on the compressive strength of z-pinned laminates are discussed in details.

1. Introduction

The relatively poor interlaminar properties of traditional composite laminates can be substantially improved by the introduction of the through-the-thickness pins, called z-pins. The z-pinning, however, causes the distortion of fibers which stimulate buckling or kinking of fibers, and forms a resin-rich zone around pins. These conditions have adverse effects on in-plane properties, especially on compressive strength [1-2]. Therefore, an important scientific and engineering issue is how to appropriately evaluate the loss of compressive strength caused by insertion of z-pins.

The finite element code FLASH developed by Fleck et al has been used to predict the compressive strength of z-pinned unidirectional laminates [3]. The compressive strength of z-pinned woven composites was predicted by the single pin and multiple-pin finite element models with the results indicating that the composite strength decreases with the increasing z-pin density and diameter [4]. The detailed and comprehensive review on z-pinned composite laminates has been made [1].

This work will summarize our recent work on prediction of compressive failure in z-pinned unidirectional composites. First, a progressive failure analysis of z-pinned composite plate under compressive loading will be carried out to identify failure modes. Secondly, the progressive failure analysis will be used to justify our strength model [5], in which fibers and matrix are treated as discrete layers with kinking failure mode.

2. Progressive analysis of compressive failures

We consider the unidirectional composite laminates that are reinforced with z-pins in the square configuration with 0.28mm pin diameter and 1.75mm pin-spacing (2% pin density). The laminate thickness is 1.5 mm. One unit cell with periodic boundary condition can be chosen as the representative volume element (RVE), Fig.1. RVE is subdivided into four regions for characterizing the inhomogeneous properties due to change in local structure around the pin, i.e., (I) the fiber distortion region, (II) the undistorted region, (III) the resin-rich pocket and (IV) pin. The regions and finite element mesh are shown in figure 1. In the fiber distortion region the material properties vary from element to element. We use the formula in [6] to evaluate the material properties at Gauss points in the elements in this region. The other three regions are assumed to be homogeneous. The failure criterion for the matrix in resin-rich pocket is based on Mises yield criterion. Hashin failure criteria [7] are employed for initiation of local failures in composite regions (I and II). The stiffness-discount rules suggested in [8] are used to characterize the residual stiffness of damaged material elements.

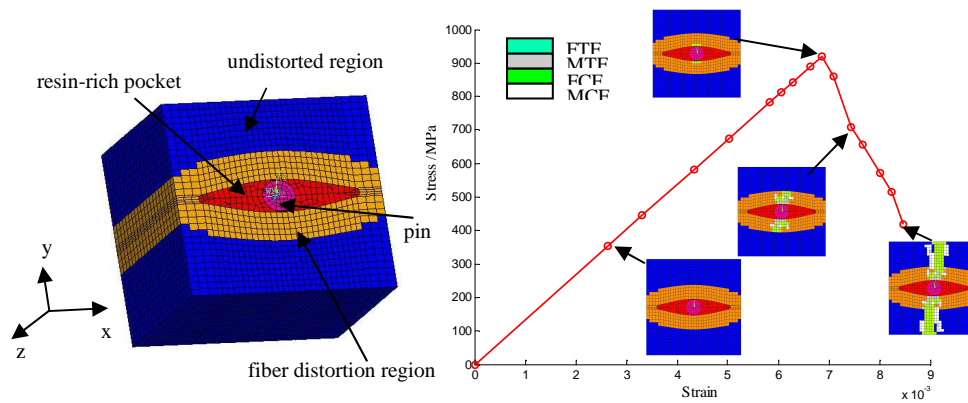


Figure 1. FE mesh of RVE of z-pinned composite **Figure 2.** Compressive stress-strain curve and failure patterns

The overall stress-strain curve and the progressive failure patterns of the z-pinned carbon/epoxy unidirectional laminate under compressive loading is shown in Figure 2. It can be seen that the stress increase with the applied strain in linear manner before the ultimate strength, 920MPa, is reached. As the applied compressive strain increases further the stress decreases rapidly. In the linear stress-strain regime no failure is observed. The observed main failure mode is the fiber compressive failure (FCF), accompanied with the some matrix tensile failure (MTF) and the matrix compressive failure (MCF). At the peak stress the FCF occurs in a few elements in the fiber distortion region near the pin. The FCF extends rapidly from the edge of the fiber distortion region to the edge of the RVE, forming a fiber compressive failure band spanning the width of specimen. This suggests that once the fiber compressive failure (FCF) occurs in the elements in the fiber distortion region near the pin the unstable FCF takes place leading to the catastrophic failure of the z-pinned composite.

3. Compressive strength model

In our recent work [5], the compressive strength model based upon variational principle and fiber kinking failure mode has been developed to predict the compressive strength of z-pinned composites. The fibers and matrix are treated as discrete layers. Failure criterion of composites is established on fiber and matrix scale. When the maximum shear stress at the fiber/matrix interface reaches the shear strength of matrix, the composite failure will occur by fiber kinking, i.e. $\tau_m^{\max} = \tau_Y$. This assumption has been justified by the progressive failure analysis.

Figure 3 shows influence of the pin diameter on the compressive strength of unidirectional laminate with 2% pin volume content. Both the compressive strength model and the progressive failure model agree well. The compressive strength of laminate decreases for the given pin volume content as the pin diameter increases. The fast reduction of compressive strength with pin diameter is observed for pins with small diameter. When the diameter of pin is larger than a certain value, roughly say 0.6mm, further reduction of the compressive strength is relatively slow. The reason is that shear stress in matrix can reduce the compressive strength by promoting micro-buckling and kinking with increasing of amplitude of fiber waviness (in connection with diameter of pin). When diameter of pin is up to critical value, increase of local fiber volume content makes fibers closely spaced, which slack down the effect of shear stress in matrix between fibers.

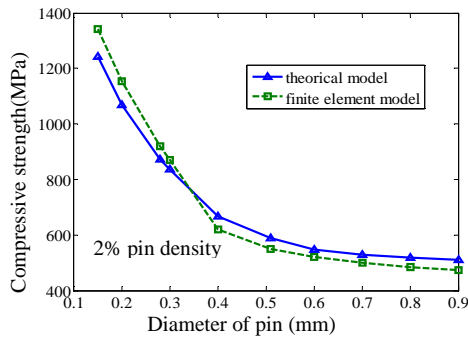


Figure 3. Effect of pin diameter on compressive strength

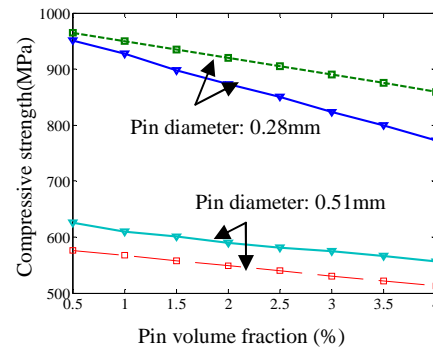


Figure 4. Effect of pin volume fraction on compressive strength

Influence of pin volume fraction on the compressive strength of the unidirectional laminate is shown in figure 4. The plot shows the relationship of pin volume fraction and compressive strength for two kinds of pin diameter, which are used in engineering. It is indicated that the compressive strength of composite reinforced by both thinner pin and bigger pin decreases at a linear rate with increasing of pin volume fraction. It is seen that the rate of reduction of the compressive strength against the pin volume fraction for the bigger diameter of pin is smaller than the rate of reduction for the thinner diameter pin.

That means that the influence of pin volume fraction on compressive strength is more notable for smaller pin.

4. Conclusion

A progressive failure analysis has been used to identify the failure modes in z-pinned carbon/resin composites under compressive loading. Both the progressive failure model and the strength model have been used to predict the in-plane compressive strength of z-pinned unidirectional composites, which take into account the influence of micro-structural changes caused by z-pinning. The results have shown that the kinking or micro-buckling is the main failure mode for z-pinned carbon/resin composites bearing compressive load. The compressive strength decreases gradually with increasing volume content and diameter of z-pins. Under the same pin volume content the smaller pin has a lesser loss on the compressive strength than the bigger pin.

Acknowledgement. The authors gratefully acknowledge the financial support of the National Science Foundation of China under grant numbers 10772105 and 11172159, and of Shanghai Leading Academic Discipline Project under number S30106.

References

- [1] Mouritz, A.P. (2007), Review of z-pinned composite laminates, *Composites Part A- Applied Science and Manufacturing*, **38**, pp. 2383-2397.
- [2] Mouritz, A.P. (2007), Compression properties of z-pinned composite laminates, *Composites Science and Technology*, **67**, pp. 3110-3120.
- [3] Steeves, C.A. and Fleck, N. A. (2006), In-plane properties of composite laminates with through-thickness pin reinforcement, *International Journal of Solids and Structures*, **43**, pp. 3197-3212.
- [4] Huang, H. and Waas, A. M. (2009), Compressive response of z-pinned woven glass fiber textile composite laminates: Modeling and computations, *Composites Science and Technology*, **69**, pp. 2338-2344.
- [5] Xie, S. L., Zhang, J. Q., Guo, Z. S. and Hu, H. J. (2012), Prediction of compressive strength of z-pinned unidirectional composite laminates, *Journal of Composite Materials*, DOI: 10.1177/0021998311419875.
- [6] Wei, Y. Q. and Zhang, J. Q. (2008), Characterization of microstructure in stitched unidirectional composite laminates, *Composites Part A: Applied Science and Manufacturing*, **39**, pp. 815-824.
- [7] Hashin, Z. (1980), Failure criteria for unidirectional fiber composites, *Journal of applied mechanics*, **47**, pp. 329.
- [8] McCarthy, C., M. and Lawlor, V. (2005), Progressive damage analysis of multi-bolt composite joints with variable bolt-hole clearances, *Composites Part B: Engineering*, **36**, pp. 290-305.

QUASI-STATIC TEST TILL FAILURE OF THE CONNECTION OF REINFORCED PAN SLAB WITH FLOOR SUPPORT JOISTS

S. Zdravković¹, T. Igić², D. Zlatkov³, D. Turnić⁴

¹ Ph D, full professor, Expert of the Federal Ministry of Science, technology and development, The Faculty of Civil Engineering and Architecture of Niš, Aleksandra Medvedeva 14. 18000 Niš

e-mail: slavko.zdravkovic@gaf.ni.ac

² Ph D, full professor, The Faculty of Civil Engineering and Architecture of Niš, Aleksandra Medvedeva 14. 18000 Niš

e-mail: tigić@gaf.ni.ac

³MA Teaching Assistant, The Faculty of Civil Engineering and Architecture of Niš, Aleksandra Medvedeva 14. 18000 Niš

e-mail: dragan.zlatkov@gmail.com

⁴ Grad. Civ. Eng. Assistant, The Faculty of Civil Engineering and Architecture of Niš.

e-mail: dragana.turnić@gaf.ni.ac

Abstract. In order to determine the data about bearing capacity and deformability of the connections of reinforced pan slabs K-45 at the support point above the T-70 ceiling joists, two almost identical test models EM-1 and EM-2 were constructed in full scale. The bearing capacity and deformability of the joist connections with the reinforced concrete layer providing their continuity were tested in the conditions when the cyclical forces were applied, and in this way the cyclic negative moments with increasing intensity until connection failure were simulated. The difference of the models is reflected in the number of prefabricated reinforcement Q 131, one in the model EM-1 and two in the model EM-2. Both models show the same trend of relationship behavior that are mutually confirmed and can be successfully used. Nonlinear analytical model was formed which realistically simulate the degree of fixation of reinforced pans tested only to negative moments. However, during earthquakes there may occur the positive moments too, but then it is necessary to perform significant structural modifications. A detailed procedure for performing tests with all the diagrams and relevant photographs has been provided showing the flow from the formation of the first cracks to the model failure.

1. Introduction

In order to determine the data about bearing capacity and deformability of the connections of reinforced pan slabs K-45 at the support point above the T-70 ceiling joists, two almost identical test models EM-1 and EM-2 were constructed in full scale. The bearing capacity and deformability of these joists with the reinforced concrete layer providing continuity was tested by applying the cyclical force, and in this way cyclical negative moments with the increasing intensity until connection failure were simulated. In this way was determined the degree of fixation of floor pan slabs during their final construction. The difference of these models reflects in the quantity of prefabricated reinforcement placed in the continuity

layer. In the EM-1 model, only one mesh Q-131 was installed, and in EM-2 model, two such meshes were installed. Also, in the EM-2 model, additional pouring of concrete on the lateral contact of the flange of the main girder T-70 with the webs of pan slabs K-45 was done. Calculation M_{1max} and w_{1max} for EM-1.

$$M_{1max} = \frac{Pl}{4} = \frac{120 \times 2,7}{4} = 81,0kNm, \quad \text{and it was measured } M_{1max} \approx 81kNm$$

$$w_{1max} = \frac{Pl^3}{48EI} = \frac{117 \times 10^2 \times 270^3}{48 \times 2858 \times 2,1 \times 10^5} = 8,0cm, \quad \text{and it was measured } w_{1max} \approx 8cm.$$

Calculation and the measured values coincide, as it was expected.

2. Experiment procedure and testing results

The sketch design of both models is provided in figure 1, and designations of all the components (elements) are included, as follows:

Testing of EM-1 and EM-2 models were performed on the basis of the previously prepared loading program. This program defined the way and sequence of application of transverse cyclic movements. A large servo-actuator started the application of monotonous conditional application of cyclic movements. This actuator successively monotonously increased the amplitude of displacement of web of T-70 beam, until the behavior of the connection of inter-floor pan slabs became nonlinear. The displacement was being applied in the middle of two shortened cycles with the same maximum amplitude, whereby the maximum amplitude in each series was higher than that of the previous series.

2.1 Results of EM-2 model quasi-static testing

A large servo-actuator successively and monotonously increased the amplitude of T-70 beam web until the behavior of the connection of inter-floor pan slabs became nonlinear and they failed (as in the EM-1 case). The history of application of cyclic displacements of the T-70 beam web (i.e. movement of servo-actuator piston) and the force realized in the servo-actuator required for the displacement can be seen in figures 2 and 3. The displacement was applied in cycles whereby the maximum amplitude at each level of cycle is higher than that in the previous cycle [2]. The value of maximum amplitudes in realized cycles during experiments range from 1mm, 2mm, 3mm, 4mm, 6mm, 8mm, 12mm, 15mm, 17mm, 18mm, 25mm, 30mm, 50mm, up to 90mm which is the amplitude at the end of the experiment.

Diagram of the cyclic force P – displacement of T-70 beam web is presented in figure 4. In the next figure 5 were given the diagrams moment-curve of the K-45 structure at the location of supporting on the T-70 beam. In figure 6 are given the measured displacement diagrams. The measured strains in the reinforcement were presented in figure 7. In the photos 8, 9 and 10, behavior of the model in testing, propagation of the cracks along with the increase of the load, as well as the failure of the connection of inter-floor reinforced pans with two spans at the location of their support on the T-70 beam, are given.

3. Result analysis and conclusion

The experimental data very successfully demonstrate the non-linear characteristics of transmission of negative moments to the phase of large strain and failure.

3.1 Guidelines of potential structural improvement.

The describe experimental results show hysteretic semi-cycles, that is, nonlinear characteristics of transmission of negative moments. The capacity of the cross-sections for transmission of positive moments was not explored as it is evidently very small. The mentioned positive moments may occur due to earthquake two-sign forces [1]. For this reason, it is very important, in analytical considerations to take into account the actual characteristics of this connection [3] to the action of two-sign moment, that is the conditions of dynamic response of the system [4].

If in the future one may wish to increase the bearing capacity of connections to positive moments, it is necessary to perform significant structural modifications. This requirement could be topical in the zones of high seismicity, after the thorough examination of economic justification for its practical application [5].

This research was conducted in the framework of the Republic research of technological development in the period 2011-2014, (project no. 36016), entitled Experimental and theoretical research of linear and planar systems with semi-rigid joints from the aspect of second order theory and stability”, University of Niš.

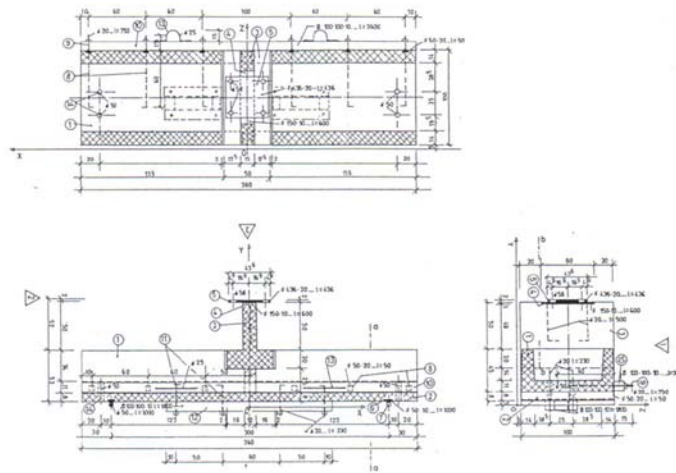


Figure 1 Experimental models EM-1 and EM-2, connections of inter-floor reinforced pans with the beam

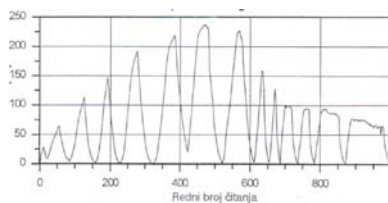


Figure 2 History of cyclic force in the web of the beam

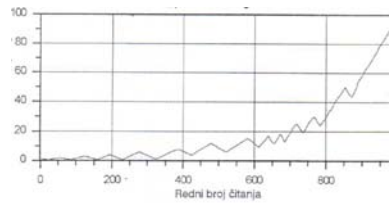


Figure 3 History of the beam web displacement

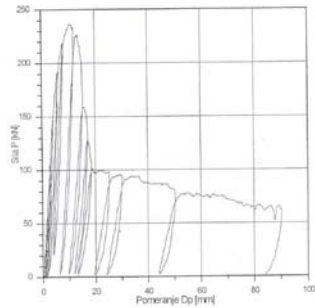


Figure 4 Diagram of the cyclic force P – displacement

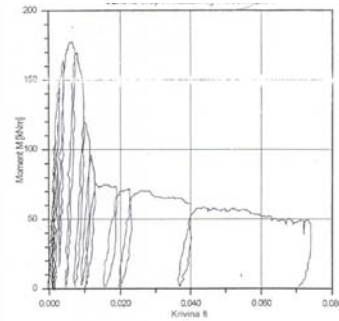


Figure 5 Relation moment – curve

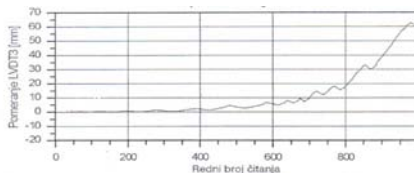


Figure 6 Diagram of displacements measured by the instrument LVDT-3

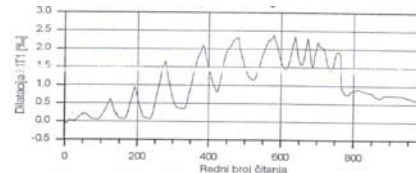
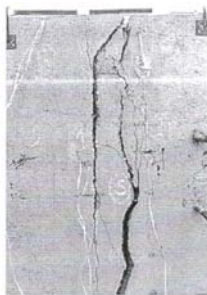
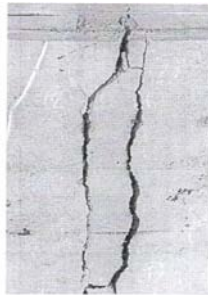


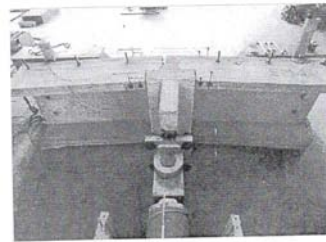
Figure 7 Diagram of displacements measured by the MT-1 measuring tape



Ph. 8 Presentation of the propagation of cracks in the model



Ph. 9 EM-3: Failure of the model



Ph. 10 Model failure

Acknowledgement. We would like to thank Prof. Dr Danilo Ristić, UN expert, Skopje.

5. References

- [1] S. Zdravković, T. Igić, D. Turnić (2011), Kraljevo Earthquake and the Necessary measures to be taken in the Affected Area, *6th International Conference on Risk and Safety Engineering*, Kopaonik, pp. 139-145.
- [2] Kvazi-statičko ispitivanje karakteristika nosivosti i deformabilnosti do stadijuma loma karakterističnih modela veza sistema „AMONT“ u realnoj razmeri, nosilac projekta sa Građevinskog fakulteta, Prof. Dr. Slavko Zdravković, Građevinski fakultet Niš, učesnici: D. Ristić, M. Zisi, V. Mícov, T. Dimitrovski; IZIIS-Skoplje, 1998., knjiga II.
- [3] T. Igić, S. Zdravković, B. Mladenović (2011), Safety and Stability of Structures With Semi-Rigid Connections of Members in Joint, *International BCCCE*, Epoka University, Tirana, pp. 1-8, 19.
- [4] D. Ristić, N. Šešov, M. Zisi, V. Mícov, S. Zdravković: knjiga IV; Atestna analiza nelinearnog dinamičkog ponašanja dvospratne hale „AMONT“ na dejstvo realnih zemljotresa primenom verifikovanog toaldno-nelinearnog matematičkog modela, IZIIS 98-39, Skoplje, 1998.
- [5] D. Ristić, S. Zdravković; Atestni dokument, Modul 1, Dvospratna tipska hala sistema „AMONT“, IZIIS 98-40, Skoplje, 1998.

Index of Contributors

- Abdul-Latif A., 285
Achouri M., 45
Alshuth T., 157
Altenbach H., 49
Andrade F. X. C., 53
Andrade Pires F. M., 53
Arsić M., 57, 281
Atanasovska I., 241
- Babouskos N. G., 165
Baczmanski A., 33
Badreddine H., 37
Bahr D. F., 277
Bakić A., 209
Balos D., 121
Barbieri G., 245
Basista M., 273
Baskaran R., 225
Besson J., 117, 289
Bhat S., 61
Blačić I., 237
Bobyř M., 65
Bošnjak S., 57
Breslavsky D., 69
Bruhns O. T., 73
Brünig M., 77
Bundara B., 89
Burzić M., 237
- Campbell J., 297
Cesar de Sa J. M. A., 53
Challamel N., 81
Chan L. C., 293
Chen Z., 85, 125
Chiaruttini V., 117
Choi Y. H., 173
Chow C. L., 1
Cid Alfaro M. V., 49
Cognini F., 245
Cuvilliez S., 97
Cvelbar R., 89
Cvijović Z., 93
Cvijović-Alagić I., 93
- Dal Santo P., 45
Dartois S., 113
Dasgupta A., 101, 249
De Angelis U., 245
De Santis G., 245
Dinkler D., 137
Djoković J. M., 105
Djordjevic N., 297
Djuric M., 213
Dolicinan C., 109
Dragon A., 113
Du Y., 197
Duan Y., 125
Dyskin A. V., 145
- Faghihi D., 7
Feld-Payet S., 117
Ferrara D., 245
Feyel F., 97, 117
Filipovic N., 121
François M., 33
- Gan Y., 125
Gdoutos E. E., 129
Gerić K., 93
Gerke S., 77
Germain G., 45
Ghozzi Y., 25
Grabulov V., 57, 281
Grbović A., 161
Grillo A., 269
Gubeljak N., 93
- Hagenbrock V., 77
Halm D., 113
Hamed M., 29
Hatzigeorgiou G., 133, 201, 205
Hedrih Stevanović K. R., 141
Heinrich S., 137
Hellesland J., 81
Horner A., 125
Houlis P. C., 145
Hwang Y. Y., 149

- Ignjatović D., 217
Iturrioz I., 177
- Janković I., 181
Jarić J., 153
Jovanovic A., 121
Jovanovic S., 121
Ju J. W., 13
Juhre D., 157
- Kastratović G., 161
Katsikadelis J. T., 165
Khalimon O., 65
Khanna S. K., 85
Kienzler R., 169
Kim M. H., 173
Kim S. J., 173
Kojic M., 121
Kosteski L., 177
Koval V., 65
Kowalsky U., 137
Kozhar S., 49
Kričak L., 181
Kudrjavceva L., 229
Kuzmanović D., 153
- Labergere C., 25
Laengler F., 185
Lazarević M. P., 89
Le Joncour L., 33
Lee C. H., 189
Lee C. S., 189
Lee H. K., 149
Lee J. M., 173, 189
Li J., 193
Li X., 197
Li Z., 201
Lin T. L., 265
Liolios A., 133, 205
Liolios K., 205
Lorentz E., 97
Lovrenić-Jugović M., 209
- Maksimovic K., 109
Maksimovic M., 109, 213
- Maksimović K., 237
Maksimović S., 213
Maneski T., 217
Manjgo M., 237
Mao T., 185
Mastilovic S., 221
Medjo B., 281
Mesarovic S. Dj., 225, 277
Meyer J., 137
Michel-Ponnelle S., 97
Mićunović M., 229
Milašinović D. D., 233
Milović Lj., 237
Mitrović R., 241
Mitrović S., 181
Momčilović D., 241
Moncada M., 245
Morachkovsky O., 69
Mosler J., 73
Mukherjee S., 249
- Nadot-Martin C., 113
Naumenko K., 49
Negovanović M., 181
Nesic N., 253
Nguyen T. D., 37
Nikolic-Stanojevic V., 109
Nikolić R. R., 105
- Obradovic M., 121
Odanović Z., 57
- Panicaud B., 33
Parker J., 125
Patibandla R., 61
Pavisc M., 257
Petrašković Z., 261
Petrovic D., 121
Pilloni L., 245
Ponižnik Z., 273
Potirniche G. P., 265
Prohl R., 269
Pustaić D., 209
- Qiu A., 277

- Radhakrishnan H., 277
Radovic M., 121
Radulovic R., 73
Rajhi W., 41
Rakin M., 93, 281
Razafindramary D., 285
Ren X. D., 193
Riera J. D., 177
Rinaldi A., 245
Risto U., 253
- Saanouni K., 19, 25, 29, 37, 41
Saidane D., 45
Scholz A., 185
Sedmak A., 229, 281
Shen J., 1
Shen L., 85
Shen Y., 125
Sidhom H., 41
Steglich D., 289
Stillman D., 265
Suban M., 89
- Šarkočević Ž., 281
Šumarac D., 153, 261
- Tang C. Y., 293
ten Horn C. H. L.j., 49
Tonković Z., 209
Trišović N., 217
Trombini M., 113
Tsui C. P., 293
- Uhlig R., 253
- Vasić V., 89
Vasovic I., 213
Vidanović N., 161
Vignjevic R., 297
Vistać B., 57
Voyiadjis G. Z., 7
Vuherer T., 237
- Wafai H., 289
Wang H. Y., 293
Ward C., 125
- Wittum G., 269
Wnuk M. P., 301
- Xie S., 305
- Yanase K., 13
Yang B. J., 149
- Zeković D., 181
Zentner L., 253
Zhang J., 305
Zhu H., 85